Nano-Optics for Enhancing Light-Matter Interactions on a Molecular Scale

Plasmonics, Photonic Materials and Sub-Wavelength Resolution

Edited by
Baldassare Di Bartolo
John Collins

Assistant Editor
Luciano Silvestri

Springer

Nano-Optics for Enhancing Light-Matter
Interactions on a Molecular Scale

NATO Science for Peace and Security Series

This Series presents the results of scientific meetings supported under the NATO Programme: Science for Peace and Security (SPS).

The NATO SPS Programme supports meetings in the following Key Priority areas: (1) Defence Against Terrorism; (2) Countering other Threats to Security and (3) NATO, Partner and Mediterranean Dialogue Country Priorities. The types of meeting supported are generally "Advanced Study Institutes" and "Advanced Research Workshops". The NATO SPS Series collects together the results of these meetings. The meetings are coorganized by scientists from NATO countries and scientists from NATO's "Partner" or "Mediterranean Dialogue" countries. The observations and recommendations made at the meetings, as well as the contents of the volumes in the Series, reflect those of participants and contributors only; they should not necessarily be regarded as reflecting NATO views or policy.

Advanced Study Institutes (ASI) are high-level tutorial courses intended to convey the latest developments in a subject to an advanced-level audience

Advanced Research Workshops (ARW) are expert meetings where an intense but informal exchange of views at the frontiers of a subject aims at identifying directions for future action

Following a transformation of the programme in 2006 the Series has been re-named and re-organised. Recent volumes on topics not related to security, which result from meetings supported under the programme earlier, may be found in the NATO Science Series.

The Series is published by IOS Press, Amsterdam, and Springer, Dordrecht, in conjunction with the NATO Emerging Security Challenges Division.

Sub-Series

A.	Chemistry and Biology	Springer
B.	Physics and Biophysics	Springer
C.	Environmental Security	Springer
D.	Information and Communication Security	IOS Press
E.	Human and Societal Dynamics	IOS Press

http://www.nato.int/science
http://www.springer.com
http://www.iospress.nl

Series B: Physics and Biophysics

Nano-Optics for Enhancing Light-Matter Interactions on a Molecular Scale

Plasmonics, Photonic Materials and Sub-Wavelength Resolution

edited by

Baldassare Di Bartolo

Boston College, Chestnut Hill, MA, USA

John Collins

Wheaton College, Norton, MA, USA

and

Luciano Silvestri

Assistant Editor
Boston College, Chestnut Hill, MA, USA

⌂ Springer

If a man will begin with certainties, he will end in doubts;
but if he will be content to begin with doubts, he shall end in certainties.

Francis Bacon

Preface

This book presents an account of the NATO Advanced Study Institute on "Nano-Optics for Enhancing Light-Matter Interactions on a Molecular Scale: Plasmonics, Photonic Crystals, Metamaterials and Sub-Wavelength Resolution," held in Erice, Sicily, Italy, from 3 to 18 July 2011. This meeting was organized by the International School of Atomic and Molecular Spectroscopy of the "Ettore Majorana" Center for Scientific Culture.

Quoting one of our lecturers (L. Novotny): "Nano-optics is the study of optical phenomena and techniques on the nanometer scale, that is, near or beyond the diffraction limit of light. It is an emerging field of study, motivated by the rapid advance of nanoscience and nanotechnology which require adequate tools and strategies for fabrication, manipulation and characterization at this scale."

The Institute provided a comprehensive overview of the rapidly expanding field of nano-optics, and outlined the current state of the art both in terms of the theory and applications to various technologies. The topics presented covered a broad range of subjects within the field of nano-optics, and included both the fundamental and advanced treatments of the following topics: plasmonics, photonic crystals, metamaterials, imaging with sub-wavelength resolution, ultrafast spectroscopy for coherent control of biomolecules, fluorescence resonant energy transfer, photovoltaics, photonic structures for information delivery and processing, non-linear phenomena, luminescence of nanostructures, waveguide arrays of nanostructrures, and terahertz spectroscopy for imaging at the nanoscale. The applications of nano-optics presented included: bio-imaging with subwavelength resolution, plasmonics for cell manipulation and materials processing at the nanoscale, transfection and nano-surgical techniques using ultrafast lasers, the enhancement of fluorescence for bioimaging, sensors based on plasmonics and various nano-structured materials, photovoltaics using nano-materials, photonic crystals for fiber communication, and ultrasensitive techniques (optical microcavities and waveguide arrays) for detection of chemical and biological molecules and explosives in the field.

Each lecturer started at a fundamental level, ultimately reaching the frontier of knowledge in a systematic and didactic fashion. The participants were encouraged to ask questions both during and after the lectures, which often led to lively

interactions. The formal lectures were complemented by additional seminars and discussions. The Institute gave the participants an opportunity to present their research work in the form of short seminars or poster presentations. In all, 10 short seminars and 42 posters were presented.

The participants came from 21 different countries: United States, England, Germany, Italy, Canada, France, Spain, The Netherlands, Finland, Denmark, Norway, Poland, Switzerland, Russia, Ukraine, Czech Republic, Uzbekistan, Belarus, Estonia, Croatia, and Egypt. Over the 2 weeks of the course, participants were given numerous opportunities to interact with one another, at both formal (poster sessions, seminars) and informal (e.g. dinners, excursions) events. The goal was to allow the participants to learn from one another about their scientific work and to expose them to others researchers from various cultures.

Two roundtable discussions were conducted during the course. The first discussion, conducted early in the course, allowed for the organizers and lectures to get immediate feedback from the participants regarding the organizational aspects of the course. The second roundtable meeting, held on the last day of the course, assessed the overall effectiveness of the course from the view of the participants. All participants filled out an evaluation form for the course and were given the opportunity to express their views at the meeting. The discussion and the evaluation forms indicated that the participants overwhelmingly felt that the course was a success. They appreciated the didactic nature of the course and found some of the lecturers very inspiring. They felt that the scientific level of the course was very high, and that both the breadth and balance of the subjects covered were appropriate. They believed the atmosphere of the course helped to promote interaction between all participants, especially between students and lecturers, and that these interactions often led to creative discussions. They also appreciated that the lectures were made available to all the participants online.

The evaluations provided many helpful suggestions that we will implement in the next course. Several participants suggested that additional information be made available online regarding some practical aspects of coming to Erice (accommodations, food, climate, etc.). They indicated a desire to have an online form on the web site to submit abstracts for posters and short seminars. Generally, they believed that a greater online presence would help in disseminating information about the course. Many participants also expressed a desire for additional events with a non-scientific focus, such as the special session given by one lecturer on his recent climb of Mt. Kilimanjaro.

Overall, it seemed that all the students enjoyed meeting and discussing their work not only with the lecturers, but also with one another. They appreciated the opportunity to meet with fellow graduate students and post-doctoral researchers from other countries who are working in the same field, or in related fields that could enhance their own work. They generated friendships and contacts that will very likely lead to new collaborations and opportunities for the enhancement of their research work.

The evaluations allowed us to gather new ideas on how to further improve the course, and revealed a consensus that the course will benefit their research work.

The following quotes from the evaluation forms give insights into how the students viewed their experience at the Institute.

"Very useful and interesting. The atmosphere is very special and very creative. The lineup of the speakers is fantastic . . . . A great service to the community."

"The most valuable thing I got out of the conference was meeting the other people who are involved in my field . . . . This was especially true for those of us from a small group, who maybe don't have as many people to bounce ideas off of."

"Very nice atmosphere among participants. Professors available for questions and willing to answer was highly important."

Summaries of the lectures, seminars, and posters are presented in this report.

I wish to acknowledge the sponsorship of the meeting by the NATO Organization, the Karlsruhe School of Optics, Boston College, the Italian Ministry of Scientific Research and Technology, and the Sicilian Regional Government.

I am looking forward to our activities at the Ettore Majorana Center in years to come, including the next 2013 meeting of the International School of Atomic and Molecular Spectroscopy.
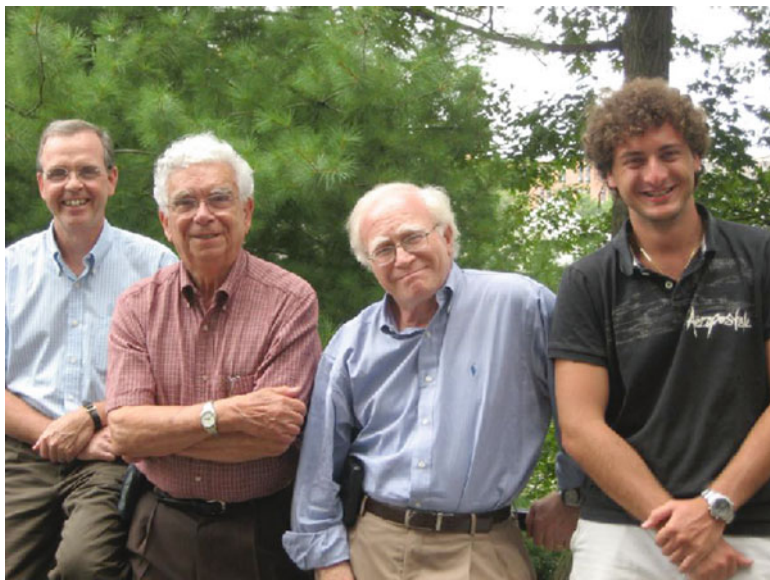
Baldassare (Rino) Di Bartolo
Director of the International School
Of Atomic and Molecular Spectroscopy
Of the "Ettore Majorana Center"

Nano-Optics Summer School
Erice, July 3–18, 2011

The Co-Directors

The Team

Contents

INTERNATIONAL SCHOOL
OF ATOMIC AND MOLECULAR SPECTROSCOPY

B. Di Bartolo, Director

Advanced Study Institutes Held at the
"Ettore Majorana" Center in Erice, Sicily, Italy

1974 – Optical Properties of Ions in Solids
1975 – The Spectroscopy of the Excited State
1977 – Luminescence of Inorganic Solids
1979 – Radiationless Processes
1981 – Collective Excitations in Solids
1983 – Energy Transfer Processes in Condensed Matter
1985 – Spectroscopy of Solid-State Laser-Type Materials
1987 – Disordered Solids: Structures and Processes
1989 – Advances in Nonradiative Processes
1991 – Optical Properties of Excited States in Solids
1993 – Nonlinear Spectroscopy of Solids: Advances and Applications
1995 – Spectroscopy and Dynamics of Collective Excitations in Solids
1996 – Workshop on Luminescence Spectroscopy
1997 – Ultra-fast Dynamics of Quantum Systems: Physical Processes
    and Spectroscopic Techniques
1998 – Workshop on Advances in Solid State Luminescence Spectroscopy
1999 – Advances in Energy Transfer Processes
2000 – Workshop on Advanced Topics in Luminescence Spectroscopy
2001 – Spectroscopy of Systems with Spatially Confined Structures
2002 – Workshop on the Status and Prospects of Luminescence Research
2003 – Frontiers of Optical Spectroscopy
2004 – Workshop on Advances in Luminescence Research
2005 – New Developments in Optics and Related Fields: Modern
    Techniques, Materials and Applications
2006 – Workshop on Advances in the Study of Luminescent Materials
2007 – Frontier Developments in Optics and Spectroscopy
2008 – Workshop on Advances in Luminescence Spectroscopy
2009 – Bio-Photonics: Spectroscopy, Imaging, Sensing, and Manipulation
2010 – Luminescence of Inorganic Materials and Bioimaging

Part I
Lectures

1
Real-Time Optical Detection of Single Nanoparticles and Viruses Using Heterodyne Interferometry

Anirban Mitra and Lukas Novotny

1.1 Introduction

Nanoparticles play a significant role in various fields such as biomedical imaging and diagnostics [1–4], process control in semiconductor manufacturing [5], explosives [6], environmental monitoring and climate change [7, 8], and various other fields. Inhalation of ultrafine particulates in air has been shown to have adverse effects, such as inflammation of lungs or pulmonary and cardiovascular diseases [9, 10]. Nano-sized biological agents and pathogens such as viruses are known to be responsible for a wide variety of human diseases such as flu, AIDS and herpes, and have been used as biowarfare agents [11, 12].

Rapid and accurate detection and characterization of viruses has become increasingly important over the years. Accurate quantification of the presence of human viruses such as HIV, herpes or influenza in blood samples is essential for clinical diagnosis and also for vaccine development. The ability to distinguish between different kinds of viruses present in a sample is also highly desirable. For example, a single patient may be coinfected with multiple viral pathogens such as HIV and HCV, and being able to identify and quantify both viruses is crucial for the patient to be treated appropriately.

Most of the existing virus particle quantification techniques either suffer from significant technical glitches or are extremely time and cost consuming. Techniques such as quantitative-PCR [13] only indirectly determine the number of viral particles in a sample, while the plaque titer method [14] quantifies only those which

A. Mitra • L. Novotny (✉)
Department of Physics and Astronomy, University of Rochester, Rochester, NY 14627, USA

L. Novotny
Institute of Optics, University of Rochester, Wilmot Annex 101, 275 Hutchison Avenue, Rochester, NY 14627-4936, USA
e-mail: lnovotny@ethz.ch

cause visible cell-damage. Quantitative Electron Microscopy (QEM) [15] is limited by its low resolution for small particles such as viruses, whereas quantification by Image Enhanced Microscopy (IEM) [16] is unreliable due to experimentally unconfirmed efficiency of labeling with fluorescent dyes. At present there does not exist any virus quantification method available to biologists which can quickly and reliably detect, quantify and characterize virus particles with single particle sensitivity.

In recent years several studies have focused on developing new and improved optical techniques for nanoparticle detection [17–23]. Optical methods have proved particularly attractive because of their noninvasive nature and high sensitivity [24]. A lot of these methods have specifically concentrated on label-free viral biosensing. Optical techniques based on sensing discrete resonance shifts in whispering gallery mode (WGM) microcavities due to binding of single virus particles have proved really promising [25–29], but they cannot be used to distinguish between viruses of different sizes present in a heterogeneous mixture. Other optical sensing platforms such as those based on nanoplasmonics [30] or interferometry [31, 32] have proved to be sensitive to single viruses; but while some of them need to be run for a long time and hence are unsuitable for real-time sample characterization, others rely on extensive surface preparation steps or availability of specific antibodies for the target viruses in a sample. Electrical sensors have been demonstrated to be able to detect single viruses in solution [33, 34], but they suffer from the drawback that they are extremely sensitive to changes in ionic strengths of the media [35]. A single label-free method which can quickly and accurately quantify levels of different viruses present in clinically relevant samples without additional sample preparation steps, has remained elusive for practical implementation.

Several optical methods for detection and characterization of nanoparticles that have been developed in the past have relied on light scattering [36], since light scattering measurements are usually highly sensitive to small variations in particle sizes or optical properties. Various optical particle counters (OPCs) have been developed, some of which such as the Flow Cytometer [37] are capable of detection single nanoparticles, while some others such as those based on Dynamic Light Scattering (DLS) [38] detect ensembles of particles. However, the methods capable of single particle detection are usually sensitive only for particles down to $\sim$200 nm in diameter. Methods such as DLS can be used to detect very small particles down to less than $\sim$10 nm diameter, but they cannot attain single particle sensitivity.

Optical detection of nanoscale biological agents (such as viruses) using light scattering is difficult due to their low scattering cross-section and low index contrast to the surrounding medium. Light scattering from a homogeneous sphere has a rigorous solution, as derived by Mie [39]. In the limiting case, particles much smaller than the wavelength of the excitation light can be described by a dipolar polarizability α given by Bohren and Huffmann [36]

$$\alpha = 4\pi\varepsilon_o R^3 \frac{\varepsilon_p - \varepsilon_m}{\varepsilon_p + 2\varepsilon_m}, \qquad (1.1)$$

where R is the particle radius, and ε_p and ε_m are the dielectric permittivities of the particle and the surrounding medium, respectively. An incident oscillating electric

field $\mathbf{E}_{exc}$ induces a dipole $\mathbf{p}$ in the particle parallel to the incident field, given by $\mathbf{p} = \alpha \mathbf{E}_{exc}$. The induced dipole radiates (i.e. scatters) a secondary electric field $\mathbf{E}_s \propto \alpha \mathbf{E}_{exc}$. Evidently, α defines the scattering and absorption efficiencies and bears information on both particle size (R) and composition (ε_p), and hence is highly significant in nanoparticle characterization. Nanoparticle detection techniques such as DLS probe the intensity of the scattered light $I \propto |\mathbf{E}_s|^2$, and hence the detector signal scales with $|\alpha|^2 \propto R^6$. The strong size dependence makes it extremely difficult to detect small particles based on standard light scattering.

It would therefore be expected that a detection principle that hinges on an optical interaction mechanism that has a weaker size dependence than standard light scattering-based techniques would provide a better Signal to Noise Ratio (SNR) and hence would be sensitive to single particles of smaller sizes. This is where interferometric detection [40–42] comes in. Unlike other light-scattering based detection techniques, interferometric detection exhibits a weaker size dependence and therefore provides significantly better signal-to-noise for small particles. For interferometric detection, the detector signal is proportional to the amplitude of the scattered light $|\mathbf{E}_s|$, and hence scales with $\alpha \propto R^3$. Interferometric detection can provide *single* particle sensitivity and has the potential for real-time detection [43–46].

In real-time interferometric nanoparticle monitoring, particles typically are made to traverse a stationary laser focus, and the scattered field from a single particle is combined with a reference field and recorded interferometrically with a photodetector. Using this standard (also called homodyne) scheme for interferometric detection, it has been shown that nanoparticles can be detected in real-time with high sensitivity [43,47]. However, the phase sensitivity of homodyne interferometric measurements makes it difficult to accurately assess α of a target particle traversing a stationary laser focus. Slight variations in the particle's position have a significant influence on the phase of the scattered field, thereby affecting the detector signal and hence the resolution of the measurement. This in turn makes it difficult to clearly distinguish between particles of slightly different sizes present in a heterogeneous mixture. In the following sections, we present a nanoparticle detection scheme based on heterodyne interferometry, using which amplitude and phase of the interferometric signal from a nanoparticle can be effectively decoupled, hence improving the size resolution of particle characterization. Furthermore, combining heterodyning with differential detection greatly reduces background and laser power noise, and helps achieve high detection sensitivity.

1.2 Differential Optical Heterodyne Detection

Let us consider a detection scheme as illustrated in Fig. 1.1. A collimated excitation laser beam $\mathbf{E}_{exc}$ with frequency ω is incident on a high-NA inverted microscope objective, and is brought to a diffraction-limited tightly focused spot at the interface of a nanofluidic channel [48] through which a nanoparticle solution is made to flow. Let the particle be located at $\mathbf{r} = (x, y, z)$, and the flow direction be in the
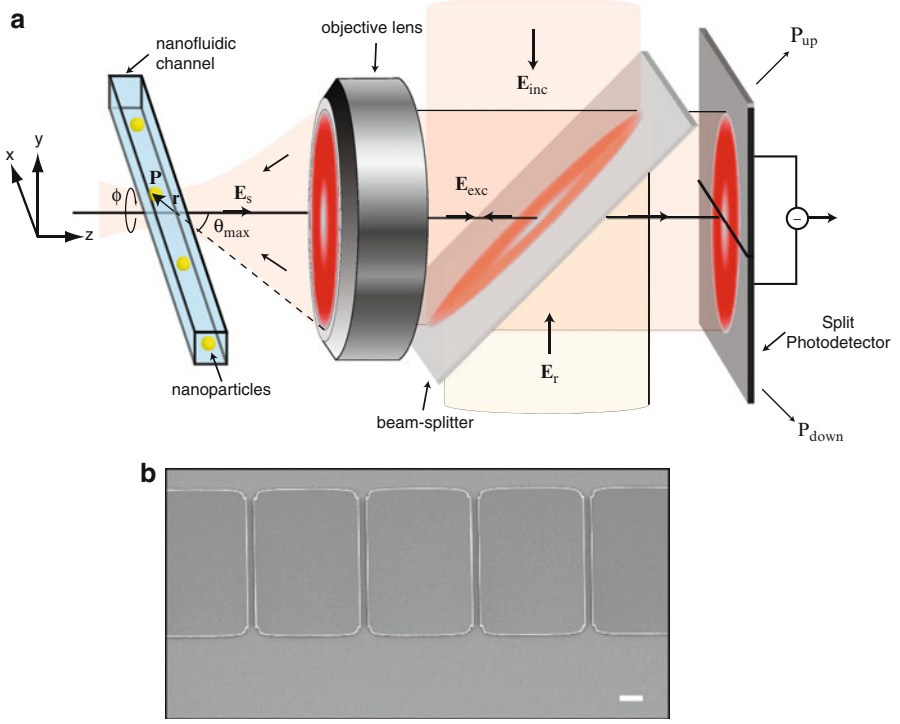
Fig. 1.1 (**a**) Heterodyne interferometric detection of the light scattered by a nanoparticle or a virus (*yellow*) as it traverses a laser focus. The scheme employs an excitation laser ($\mathbf{E}_{exc}$) with frequency ω that is reflected off a beamsplitter and focused via an objective into a nanofluidic channel. The scattered light ($\mathbf{E}_s$) is superimposed to a reference beam ($\mathbf{E}_r$) with frequency $\omega + \Delta\omega$ and directed onto a split photodetector. (**b**) SEM micrograph of a series of nanofluidic channels in the flow-cells used in the experiments. Scale Bar = 2 μm (Color figure online)

x-direction, transverse to the optical axis z. The focused electric field induces a dipole moment $\mathbf{p}$ in the particle, given by

$$\mathbf{p}(\mathbf{r}) = \alpha\,\mathbf{E}_{exc}(\mathbf{r}), \tag{1.2}$$

with α being the polarizability of the particle. The particle (the oscillating dipole) scatters a field $\mathbf{E}_s$, which is given by

$$\mathbf{E}_s(\mathbf{r}) = \omega^2\,\mu\,\mu_0\,\overleftrightarrow{G}(\mathbf{r})\,\mathbf{p}(\mathbf{r}) \tag{1.3}$$

where ω is the frequency of the incident field, μ and μ_0 are the relative permittivity of the medium surrounding the particle and the permittivity of free space respectively. $\overleftrightarrow{G}$ is the far-field dyadic Green's function [49],

$$\overleftrightarrow{G}(\mathbf{r}) = \frac{\exp(ikR - i\omega t)}{4\pi R}\left[\mathbf{I} - \mathbf{RR}/R^2\right] \tag{1.4}$$

where $k = n\omega/c$ with n being the index of refraction, and $\mathbf{R} = \mathbf{r}_\infty - \mathbf{r}$ is the vector from dipole to the field point $\mathbf{r}_\infty$. The field radiated by the dipole is collected by the same objective lens characterized by a focal length f and numerical aperture $NA = n \sin\theta_{max}$, with θ_{max} being the maximum collection angle measured from the optical axis (cf. Fig. 1.1). The dipole's farfield can be written from Eqs. (1.3) and (1.4) as

$$\mathbf{E}_s(\mathbf{r}_\infty) = \frac{k^2}{\varepsilon_o n^2} \frac{\exp(ikR - i\omega t)}{4\pi R} \left[\mathbf{I} - \mathbf{R}\mathbf{R}/R^2\right]\mathbf{p}. \tag{1.5}$$

where we have used the fact that $\mu \approx 1$ for most mediums and that $\mu_0 = \frac{1}{c^2\varepsilon_o}$. For $\mathbf{r}_\infty$ located on the reference sphere of the lens and for small deviations of the dipole from the focus $\mathbf{r} = 0$, R can be expanded as

$$R = f - \frac{1}{f} \left[x x_\infty + y y_\infty + z z_\infty\right] + .. \tag{1.6}$$

Retaining only terms up to first-order in the phase and terms up to zeroth-order in the amplitude yields

$$\mathbf{E}_s(\theta, \phi) = \frac{k^2 \exp(ikf - i\omega t)}{4\pi\varepsilon_o n^2 f} \left[\mathbf{I} - \mathbf{r}_\infty\mathbf{r}_\infty/f^2\right]\mathbf{p}$$
$$\times \exp(-ik[x\sin\theta \sin\phi + y\sin\theta \cos\phi + z\cos\theta]) \tag{1.7}$$

where we expressed $(x_\infty, y_\infty, z_\infty)$ in spherical coordinates (f, θ, ϕ). For our purposes $k|\mathbf{r}| < 1$ and hence we expand the last exponential term to first order, i.e. $\exp(x) \approx 1 + x$. This substitution makes a later integration over θ and ϕ possible. Also, using the paraxial approximation, $\left[\mathbf{I} - \mathbf{r}_\infty\mathbf{r}_\infty/f^2\right] \approx 1$. The lens collimates the field of the dipole and projects it on the plane of the detector. In the detector plane the field can be represented as

$$\mathbf{E}_s(\theta, \phi) = \frac{k^2 \exp(ik[f + \Delta z] - i\omega t)}{4\pi\varepsilon_o n^2 f}\mathbf{p}$$
$$\times (1 - ik[x\sin\theta \sin\phi + y\sin\theta \cos\phi + z\cos\theta]) \tag{1.8}$$

where Δz is the distance from the lens to the detector plane.

Let us now consider the reference field $\mathbf{E}_r$ that is incident on the photodetector, along with $\mathbf{E}_s(\theta, \phi)$. In heterodyne interferometry, a frequency-shift $\Delta\omega$ is introduced into the reference field (with respect to the excitation field), usually with the help of a pair of acousto-optic modulators [44]. The magnitude of $\Delta\omega$ is usually chosen to be relatively high (80 kHz for the experiments described below), so that the signal processing can be done beyond the range till which $1/f$ noise [50] can affect the signal-to-noise (SNR) of the system. The reference field can be written as

$$\mathbf{E}_r = E_r e^{i(k\Delta z - [\omega + \Delta\omega]t - \Delta\phi)} \mathbf{n}_p, \tag{1.9}$$

where $\mathbf{n}_p$ is the unit vector in direction of $\mathbf{p}$, $\Delta\phi$ is a constant phase shift, and $\Delta\omega$ is the frequency shift introduced in the reference field. For nanoparticles or

viruses suspended in an aqueous medium, there is a refractive index difference at the interface between the glass nanofluidic channel and the medium inside. Since the excitation laser beam is tightly focused at this interface (Fig. 1.1), a part of if it is reflected back along the same path as the scattered light and interferes with the reference and the scattered fields. We will call this field as the background field $\mathbf{E}_b$ in the rest of the article.

1.2.1 Differential Detection with a Split Photodetector

We have seen above that even without any particle traversing the laser focus, the fields $\mathbf{E}_r$ and $\mathbf{E}_b$ are incident of the surface of the photodetector, which would inevitably produce a background in the detector, unless the effect of this background is somehow negated. This is usually done by performing differential detection using a split photodetector or a pair of balanced photodiodes. In the experiments we will describe below, a split photodetector is used for differential detection. A particle traversing the laser focus in the x-direction (cf. Fig. 1.1) produces a position-sensitive signal in the y-direction on the detector surface, and two independent power readings P_{up} and P_{down} can be obtained out of the detector. Let us first consider the total intensity I of the light that is incident on the detector

$$I(\theta, \phi) \propto |\mathbf{E}_s + \mathbf{E}_r + \mathbf{E}_b|^2$$
$$\propto |\mathbf{E}_s|^2 + |\mathbf{E}_r|^2 + |\mathbf{E}_b|^2 + 2\,\mathrm{Re}\left\{\mathbf{E}_r^* \cdot \mathbf{E}_s\right\} + 2\,\mathrm{Re}\left\{\mathbf{E}_b^* \cdot \mathbf{E}_s\right\} + 2\,\mathrm{Re}\left\{\mathbf{E}_b^* \cdot \mathbf{E}_r\right\}.$$
$$(1.10)$$

The differential output of the detector is the difference of the intensities integrated over the areas of the two halves of the detector

$$S = [P_{up} - P_{down}]. \tag{1.11}$$

By centering the reference and the background beams on the surface of the detector in the absence of a particle at the laser focus, the contribution of the terms in Eq. (1.10) that do not contain $\mathbf{E}_s$ can be eliminated. This is how a perfectly aligned split detector helps in *background-free* detection. So, the differential signal S from a perfectly centered detector is given by

$$S = |\mathbf{E}_s|^2 + 2\,\mathrm{Re}\left\{\int_{up} \mathbf{E}_r^* \cdot \mathbf{E}_s\, da\right\} + 2\,\mathrm{Re}\left\{\int_{down} \mathbf{E}_b^* \cdot \mathbf{E}_s\, da\right\}$$

$$-2\,\mathrm{Re}\left\{\int_{down} \mathbf{E}_r^* \cdot \mathbf{E}_s\, da\right\} - 2\,\mathrm{Re}\left\{\int_{down} \mathbf{E}_b^* \cdot \mathbf{E}_s\, da\right\} \tag{1.12}$$

where $\int_{up}$ stands for integration over the top half of the detector, and $\int_{down}$ over the bottom half. Now, since $|\mathbf{E}_s|^2$ is much weaker than the rest of the terms in the above
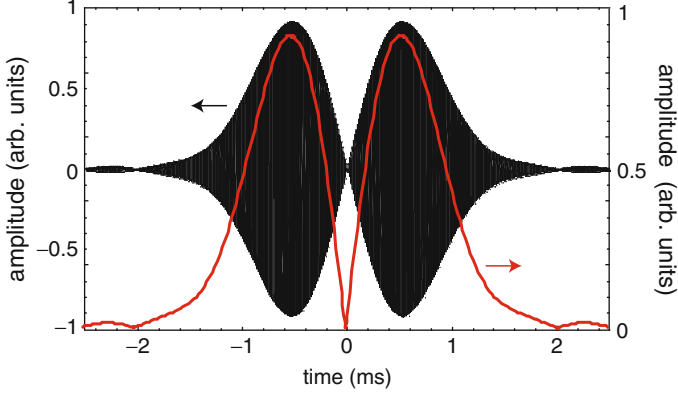
Fig. 1.2 Differential detector signal $S(\mathbf{r})$ for a particle moving along x with speed $v = 1\,\text{mm/s}$ through the focal plane of a laser beam ($\lambda = 532\,\text{nm}$, $w_o = 0.5\,\mu\text{m}$), obtained via numerical calculations. The reference beam is frequency shifted by 80 kHz. The *red curve* is the demodulated amplitude (Color figure online)

equation, we can neglect it. Let us also not consider the terms containing $\mathbf{E}_b$ for now (we will see later that their contribution will be eliminated after processing with a lock-in amplifier). Equation (1.12) reduces to

$$ S = 2\,\text{Re}\left\{ \int_{\text{up}} \mathbf{E}_r^* \cdot \mathbf{E}_s \, da - \int_{\text{down}} \mathbf{E}_r^* \cdot \mathbf{E}_s \, da \right\}. \qquad (1.13) $$

Introducing the expressions for $\mathbf{E}_s$ and $\mathbf{E}_r$ from Eqs. (1.8) and (1.9) and carrying out the integrations in Eq. (1.13) yields

$$ S(\mathbf{r}) = \frac{16\pi^2}{3\varepsilon_o} \frac{NA^3 f}{n^5} \frac{x}{\lambda^3} E_r \,\text{Re}\{\mathbf{n}_{\text{P}}\cdot\mathbf{p} \exp[i\,\Delta\omega t + i\,\Delta\phi]\}, \qquad (1.14) $$

where we made use of the small angle approximation $\sin\theta \approx \theta$. We find that the signal depends linearly on the dipole's deviation in the flow direction (x) measured from the geometric focus $\mathbf{r} = 0$. Note that we consider that the particle moves in the x direction exactly through the center of the focus (hence $y = 0$ and $z = 0$).

For simplicity, we assume that the exciting field $\mathbf{E}_{\text{exc}}$ is a Gaussian beam of the form

$$ \mathbf{E}_{\text{exc}}(x, y, z) = \frac{\mathbf{E}_o\, e^{i k z}}{(1 + 2\,i\,z/kw_o^2)}\, e^{-\frac{(x^2+y^2)}{w_o^2}\frac{1}{(1+2\,i\,z/kw_o^2)}}, \qquad (1.15) $$

where w_o is the beam waist radius. For high NA, Eq. (1.15) is only a rough approximation and more accurate models for the focal fields are necessary [49]. The black curve in Fig. 1.2 shows the calculated signal $S(\mathbf{r})$ for the parameters used in the experimental validation described in the later sections.

If the terms containing $\mathbf{E}_b$ are retained in Eq. (1.13) and the next few steps of the analysis, the split detector signal would be given by

$$S(\mathbf{r}) \; \propto \; E_s E_r \; \cos(\Delta\omega\, t + \Delta\phi) + E_s E_b \; \cos(\Delta\phi_b) \qquad (1.16)$$

which is a simplified form of Eq. (1.14) where E_s is the amplitude of the scattered field; with an additional term for the interference between the scattered and the background fields, where $\Delta\phi_b$ is the phase difference between the two fields. Processing of the split detector signal with a lock-in amplifier gets rid of the second term, as we will see below.

1.2.2 Signal Demodulation

At the output of the split detector, the heterodyne signature of a single nanoparticle rides over carrier frequency $\Delta\omega$, and needs to be demodulated. A lock-in amplifier of suitable operating range and bandwidth is used to demodulate the signal. The lock-in amplifier is given a reference TTL signal which has a frequency equal to $\Delta\omega$, the modulation frequency of the detector output signal. The phase-locked loop (PLL) in the lock-in amplifier locks an internal reference oscillator to this external reference frequency, which results in a reference sinusoidal wave at $\Delta\omega$ and a fixed phase shift of ϕ_{ref}. The lock-in reference can be written as

$$V_{lockin} = V_L \; \cos(\Delta\omega\, t + \Delta\phi_{\mathrm{ref}}). \qquad (1.17)$$

Now the lock-in amplifies the detector output signal and multiplies it by the lock-in reference using a Phase-Sensitive Detector (PSD) whose output is given by

$$S_x \propto \; E_s E_r V_L \; \cos(\Delta\omega\, t + \Delta\phi) \; \cos(\Delta\omega\, t + \Delta\phi_{\mathrm{ref}})$$
$$+ \, E_s E_b V_L \; \cos(\Delta\phi_b) \; \cos(\Delta\omega\, t + \Delta\phi_{\mathrm{ref}}), \qquad (1.18)$$

where we have written the detector signal including the terms containing $\mathbf{E}_b$, as in Eq. (1.16). Equation (1.18) can be simplified to

$$S_x \propto \frac{1}{2} E_s E_r V_L \; [\cos(\Delta\phi - \Delta\phi_{\mathrm{ref}}) + \cos(2\Delta\omega\, t + \Delta\phi + \Delta\phi_{\mathrm{ref}})]$$
$$+ \frac{1}{2} E_s E_b V_L \; [\cos(\Delta\omega\, t + \Delta\phi_{\mathrm{ref}} - \Delta\phi_b) + \cos(\Delta\omega\, t + \Delta\phi_{\mathrm{ref}} + \Delta\phi_b)]. \qquad (1.19)$$

The lock-in passes this output through a narrow-bandwidth low-pass filter, where the AC parts of the output are removed. This reduces Eq. (1.19) to

$$S_x \; \propto \; \frac{1}{2} E_s E_r V_L \; (\cos(\Delta\phi - \Delta\phi_{\mathrm{ref}}). \qquad (1.20)$$

Note that all contribution of the terms containing E_b is removed, justifying the simplification used to obtain Eq. (1.13) in the previous section. The phase dependency in Eq. (1.20) is removed by the lock-in with the help of a second PSD, which essentially shifts the reference oscillator by 90° and then multiplies with the detector signal. The output of this second PSD also passes through a narrow-bandwidth low-pass filter, where the AC parts of the output are removed. Performing similar derivation steps as for S_x we get

$$S_y \; \propto \; \frac{1}{2} E_s E_r V_L \; (\sin(\Delta\phi - \Delta\phi_{\text{ref}}). \qquad (1.21)$$

S_x and S_y are the two output signals from the lock-in amplifier. The phase-sensitivity of these signals can be eliminated by calculating

$$A = [S_x^2 + S_y^2]^{1/2} \propto \; [E_r \, \alpha \, E_{\text{exc}}]^2, \qquad (1.22)$$

where we have used the fact that $E_s \propto \alpha E_{\text{exc}}$, where α is the particle's polarizability and E_{exc} is the excitation electric field. It can be seen that the signal amplitude A reflects α (which gives a measure of the particles's size), and is phase-independent. The red curve in Fig. 1.2 corresponds to this signal amplitude A, which we get after demodulation of the raw detector signal (the black curve) using the lock-in amplifier. Here lies the big advantage of heterodyne interferometry when it comes to particle detection, which is that the phase sensitivity of the detector signal can be eliminated and hence detection accuracy can be improved over standard homodyne detection. In homodyne detection, only one of the phase-sensitive signals (S_x or S_y) would be recorded, and hence particle detection accuracy is affected by phase. The red curve in Fig. 1.3b shows the theoretically expected variation of the homodyne signal (considered to be S_x) for the parameters of the experiments described in the following sections.

1.2.3 Experimental Validation of Predicted Signal

With the theoretical understanding of heterodyne interferometric detection developed in the preceding sections, we will now experimentally validate our predictions using an experimental scheme similar to that illustrated in Fig. 1.1. Instead of particles in solution flowing through nanofluidic channels, we use an immobilized 100 nm polystyrene sphere as a test particle. A drop of water is used to cover the immobilized particle to mimic the surrounding medium for a particle in solution. By means of a piezo scan stage, the particle is first positioned in the focus $\mathbf{r} = (x, y, z) = (0, 0, 0)$ of the stationary excitation beam and then periodically scanned in the transverse x direction. The black curve in Fig. 1.3a shows the raw detector signal according to Eq. (1.16) and the blue curve is the corresponding demodulated signal amplitude A. The inset shows the oscillations at the carrier frequency $\Delta\omega$.
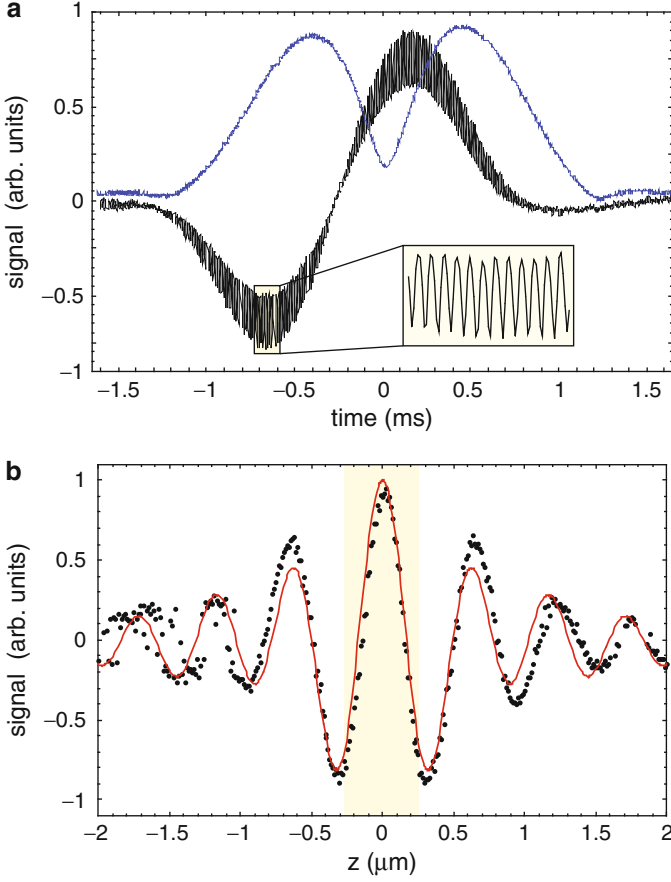
Fig. 1.3 Experimental signals recorded with a test particle scanned through the laser focus. (**a**) The *black curve* shows the raw detector signal according to Eq. (1.16) and the *blue curve* is the demodulated modulus A. The amplitude of A is a measure for the particle polarizability α. Inset shows the oscillations at the carrier frequency $\Delta\omega$. (**b**) Demonstration of the phase sensitivity of homodyne detection. The figure shows the maximum value of S_x recorded by scanning a test particle through the laser focus in different transverse planes $z = const$. The *shaded region* corresponds to the width of the nanofluidic channels used in our experiments with particles in solution. Phase variations across the nanochannel dimensions have a strong influence on the signal strength of S_x (homodyne detection). *Dots*: experimental data; *red curve*: theoretical curve (Color figure online)

Because of the presence of the background field $\mathbf{E}_b$, the raw detector signal exhibits a time-dependent baseline (hence different from the black curve in Fig. 1.2, where we don't consider $\mathbf{E}_b$). The blue curve, however, can be directly compared to that of the theoretically predicted red curve in Fig. 1.2. While the width of the blue curve is associated with the size of the laser focus and the particle velocity, its height reflects the particle polarizability α.

To characterize the influence of the phase on the signal strength for homodyne detection S_x, the experiment is repeated for different offsets ($z =$ const.) along the optical axis, representing the typical range of particle trajectories. For each z position, the maximum value of S_x is evaluated. The result, shown in Fig. 1.3b, represents the signal variations in a standard homodyne detection scheme. Evidently the phase variations cause the signal to vary rapidly with z. Therefore, different particle trajectories affect the homodyne signal strongly, which diminishes the measurement accuracy and makes it difficult to assess the particle size and polarizability. In heterodyne detection, on the other hand, the phase can be eliminated. The resulting signal $A = [S_x^2 + S_y^2]^{1/2}$, which corresponds to the envelope of the oscillating curve shown in Fig. 1.3b, no longer varies across the typical range of particle trajectories (highlighted stripe, which denotes the lateral extent of nanofluidic channels). As will be discussed in the following, the elimination of phase variations leads to improved measurement accuracy.

1.3 Characterization of the Performance of a Heterodyne Detection Scheme

A given set of particle measurements will have a characteristic size distribution, whose width represents the actual particle size distribution as well as the measurement uncertainty. The width can be estimated as the standard deviation

$$\sigma_{\text{total}} = \sqrt{\sigma_{\text{system}}^2 + \sigma_{\text{trajectory}}^2 + \sigma_{\text{size}}^2}, \tag{1.23}$$

which has several contributing terms. Here, σ_{system} is due to the system response, which is the distribution that would be obtained for a single particle crossing the laser focus several times on the same trajectory, and $\sigma_{\text{trajectory}}$ represents the signal variation due to the various trajectories a particle may take. A heterodyne system eliminates the phase dependence of this variation, but the modulus A is also affected to a small degree. Finally, σ_{size} represents the actual distribution of particle sizes, which is the quantity we generally wish to determine.

In the following sections, we present experimental results obtained with the above-introduced heterodyne detection scheme, that characterize the system response, σ_{system}, and the trajectory uncertainty, $\sigma_{\text{trajectory}}$. Once these quantities are known for a given experimental configuration, it is straightforward to isolate the particle size distribution, σ_{size} of a given sample of nanoparticles.

1.3.1 System Response

To investigate the effect of the system's response function in the performance of the detection scheme, we use a single immobilized nanoparticle that is repeatedly
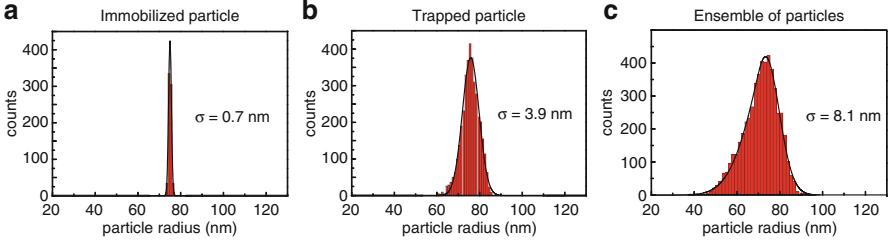
Fig. 1.4 Experimental particle size distributions measured with the heterodyne approach for (**a**) a single immobilized 75 nm polystyrene particle that is repeatedly scanned through the laser focus, (**b**) a single 75 nm polystyrene particle electroosmotically trapped in a nanochannel, and (**c**) an ensemble of 75 nm polystyrene particles freely flowing through a nanochannel. The standard deviations for the respective size measurements (reflecting the size resolutions in the measurements) are indicated by the σ values

scanned through the laser focus. This configuration eliminates the problems associated with particle heterogeneity and different particle trajectories.

Polystyrene spheres 75 nm in radius are immobilized on a microscope cover-slip, covered with a drop of water, and a single particle is scanned several times back-and-forth through the laser focus. Each detection event, corresponding to the particle passing through the laser focus, renders the signals $S_x(t)$ and $S_y(t)$ as described by Eqs. (1.20) and (1.21), from which we calculate the modulus $A(t) = [S_x^2 + S_y^2]^{1/2}$. As seen in Fig. 1.3a (blue curve), the amplitude $A(t)$ of an individual detection event has a characteristic double-peak structure. This information is used to distinguish detection events from system noise. For each detection event we evaluate the maximum peak amplitude of $A(t)$ and use the resulting value as a data point in a histogram. A sufficiently large number of detection events generates a characteristic signal distribution. The signal can be calibrated to the particle's size because the signal magnitude scales linearly with the polarizability α (cf. Eq. 1.1) and hence with the third power of particle size R. Figure 1.4a shows a size histogram obtained for an immobilized 75 nm polystyrene particle. In essence, this size distribution represents the system response function, and the width of the distribution, 0.7 nm, defines the resolving power of the measurement approach.

Homodyne detection yields a size distribution that is significantly wider, which can be demonstrated by plotting a histogram of sizes obtained from the signal $S_x(t)$ [or $S_y(t)$] by itself. This increase in width originates from the fact that the homodyne signal is affected by phase variations due to interferometer instabilities and by small deviations in particle trajectories.

1.3.2 Particle Trajectories

Having quantified the system's response, we next characterize the influence of different particle trajectories and Brownian motion. As shown in Fig. 1.1, we use

a flow-through scheme that employs a nanofluidic channel to direct single nanoparticles through a stationary laser beam. The characterization of particle trajectories requires that the particle size does not vary between measurements. However, commercial nanoparticle solutions come with a finite size distribution. In order to eliminate this ambiguity we implemented an electroosmotic recycling scheme, which allows the interrogation of the *same* single particle over and over again.

The nanofluidic channels used in our experiments are fabricated in fused silica wafers using UV lithography. The nanochannels are $15\,\mu$m long, have a 500×500 nm square cross-section, and are connected to two reservoirs [48]. A single nanochannel is positioned in the laser focus by means of the scan stage. A nanoparticle solution is introduced into one of the reservoirs and a particle flow is established using the electroosmotic effect [47].

To repeatedly interrogate the same nanoparticle, the electroosmotic voltage is controlled by a feedback loop. The signal from a single particle traversing the laser focus is used to flip the electroosmotic voltage immediately after the passage, causing the nanoparticle to reverse its direction of motion and pass through the laser focus again. In order for the trap to be stable, the particle's passage time τ through the laser focus (size $\Delta x \approx 500$ nm) needs to be shorter than the timescale associated with Brownian motion, i.e. $\tau < \Delta x^2/2D$, where D is the diffusion coefficient. In water $D \approx 10^{-11}$ m^2/s and hence $\tau < 8$ ms. In our experiments $\tau \leq 1$ ms, which typically allows us to detect a single nanoparticle more than 10^4 times before it escapes due to Brownian motion.

A characteristic time trace for a single electroosmotically trapped nanoparticle is depicted in Fig. 1.5a. The top curve (red) shows the periodic switching of the electroosmotic potential, the center curve (blue) is the homodyne signal $S_x(t)$, and the bottom curve (black) is the heterodyne signal $A(t)$. As discussed earlier, the phase variations due to different particle trajectories are fully contained in $S_x(t)$ but are eliminated in $A(t)$. Therefore, as shown in Fig. 1.5a, the variations between individual detection events are considerably larger in the homodyne signal than in the heterodyne signal, supporting the hypothesis that the phase should be eliminated for accurate particle characterization.

The maximum value of $A(t)$ for each particle passage is then evaluated and a distribution of the values is established. The resulting histogram is shown in Fig. 1.4b. Since the *same particle* is detected repeatedly, the factors contributing to signal variations are system noise and variations in particle trajectories. The latter gives rise to a broadened size distribution as compared to the immobilized particle case shown in Fig. 1.4a. The width of the distribution is evaluated to be $\sigma = 3.9$ nm. A comparison of the heterodyne distribution with that obtained with homodyne detection (S_x or S_y) is shown in Fig. 1.5b, c. The homodyne distribution in Fig. 1.5c is much wider ($\sigma = 7.9$ nm) than the heterodyne distribution in Fig. 1.5b, because of phase variations due to different particle trajectories. This difference in width clearly illustrates the importance of eliminating the effect of phase variations with heterodyne interferometry, hence improving the accuracy of particle characterization.
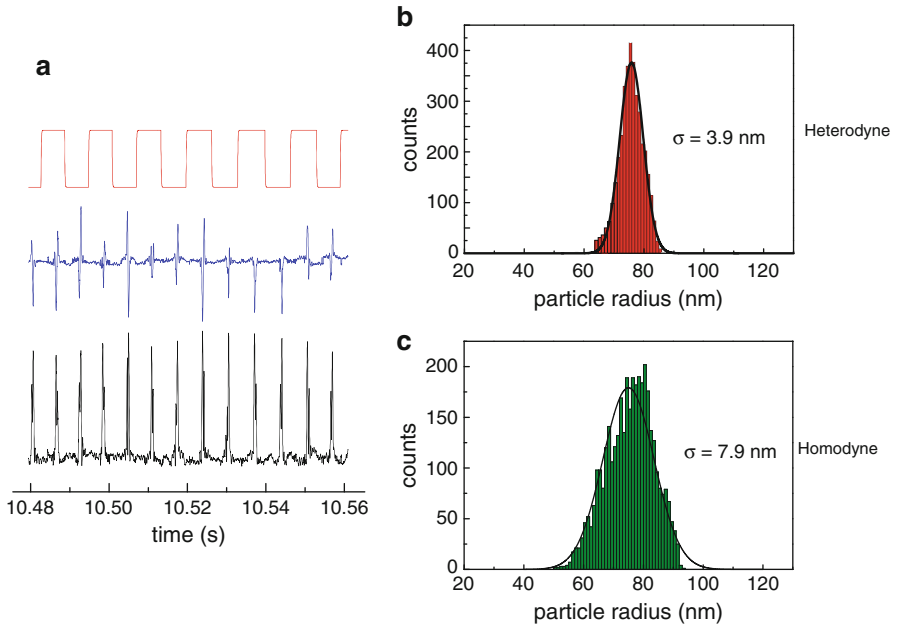
Fig. 1.5 Characterization of the influence of particle trajectories. (**a**) Time trace for a single 75 nm polystyrene particle repeatedly passing through the laser focus. The figure shows the periodic switching of the electroosmotic potential (*top*), the homodyne signal $S_x(t)$ (*center*), and the heterodyne signal $A(t)$ *bottom*. It is evident that the signal variations between detection events are lower for $A(t)$ than for $S_x(t)$, proving that the elimination of phase variations due to different particle trajectories improves the detection accuracy. (**b** and **c**) Comparison of the size distributions obtained using the heterodyne (*red*) and the homodyne (*green*) signals. The effect of phase variations is clearly evident from the significantly greater width of the distribution in the homodyne case (Color figure online)

1.3.3 Ensembles of Single Nanoparticles

The particle distributions further broaden if different nanoparticles from particle solutions are used. Having characterized the detector response and the influence of varying particle trajectories we now concentrate on the size distribution of particles in a solution.

To detect different particles from solutions we open the feedback loop controlling the electroosmotic trapping. Under this condition, a constant electroosmotic potential propels single nanoparticles through the nanochannel. Figure 1.4c shows the recorded size distribution for $\sim$5,000 different 75 nm polystyrene spheres. The distribution is slightly asymmetric with a standard deviation of $\sigma_{\text{total}} = 8.1$ nm, from which we determine the particle size uncertainty σ_{size} according to Eq. (1.23). Now, $\sigma_{\text{system}} = 0.7$ nm is the contribution of the system response to the width (Fig. 1.4a), and $\sigma_{\text{trajectory}} = \sqrt{3.9^2 - 0.7^2}$ nm $= 3.8$ nm is the width associated with

the variations in particle trajectories (Fig. 1.4a, b). The size uncertainty is found to be $\sigma_{\text{size}} = 7.1$ nm.

The optical detection scheme introduced here can be employed for measuring the homogeneity of particle samples and for testing the specifications of commercially available particle solutions. Most particle sizing methods make use of surface immobilization, which is generally less effective for small particles as compared to larger ones. The variation in binding strength affects the measured particle size distributions and hence the specified standard deviations. On the other hand, the present heterodyne detection scheme does not rely on immobilization, which makes the measured distributions more reliable. For example, the asymmetry of the measured distribution in Fig. 1.4c is likely the result of the manufacturer's filtering process, which is effective for the removal of large particles but less effective for the smaller ones.

1.4 Characterization of Nanoparticle Mixtures

Using the above method, it is possible to distinguish between nanoparticles of different sizes or materials in the same solution. In this section we present some results obtained with mixtures of gold and polystyrene particles of different sizes.

Figure 1.6a, b show the particle size distributions recorded for a mixture of polystyrene particles with mean radii of 50 and 75 nm, using the heterodyne (red) and homodyne (green) signals. Using heterodyne detection, one can clearly resolve the two particle sizes, with very little overlap. On the other hand, the individual particle distributions are wider in the homodyne case, and hence the distributions partly overlap. This illustrates the superior size resolution obtainable with heterodyne detection for a heterogeneous mixture of particles.

In order to test the capability of the detection scheme in resolving the distributions of similar particles with slightly different sizes, we used a mixture of gold nanoparticles with mean radii of 30, 40, and 50 nm. The size distributions obtained using the heterodyne (red) and homodyne (green) signals are shown in Fig. 1.6c, d respectively. The heterodyne detection scheme resolves the particles although the individual distributions are largely overlapping, whereas in the homodyne case joint particle distribution is too broad to identify individual particle peaks.

1.5 Detection and Classification of Viruses

We have demonstrated above that heterodyne interferometry can be used very effectively to detect single nanoparticles in solution with high sensitivity and selectivity. Now we explore the possibilities of detecting and distinguishing between viruses in solution using heterodyne interferometry.
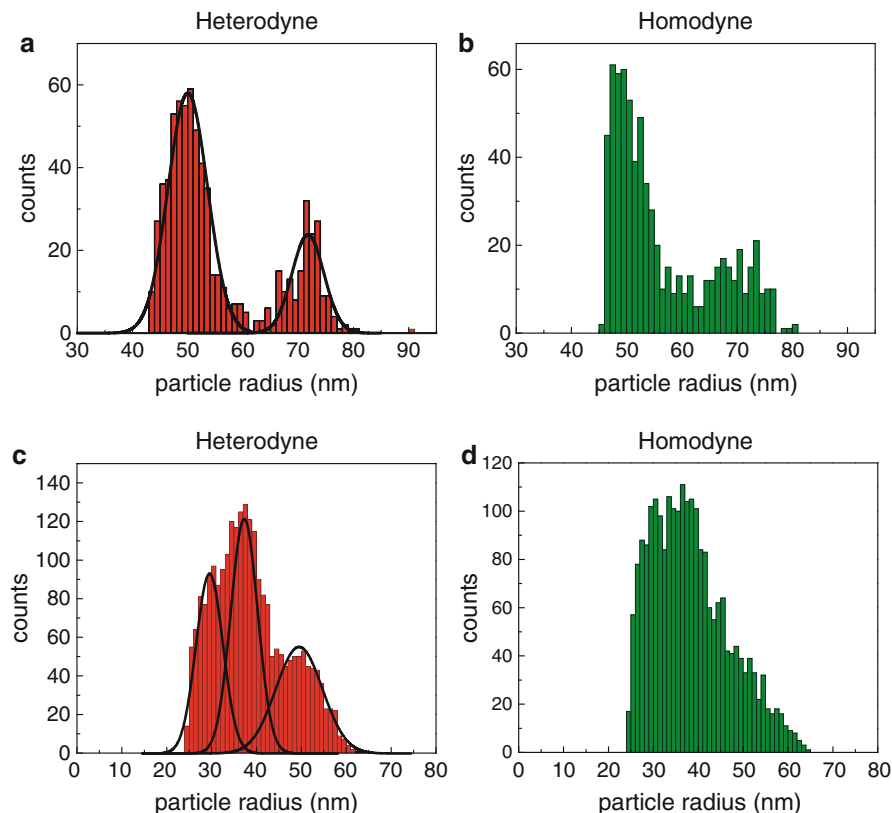
Fig. 1.6 Particle size distributions for mixtures of particles flowing through a nanochannel, obtained using the heterodyne and homodyne detection schemes. (**a** and **b**) Size distributions for a mixture of 50 and 75 nm polystyrene nanoparticles. (**c** and **d**) Size distributions for a mixture of 30, 40, and 50 nm gold nanoparticles. Heterodyne: *red histograms*, and Homodyne: *green histograms* (Color figure online)

The size of most human viruses is in the range of 20–200 nm [51], which is well suited to the capabilities of the heterodyne detection scheme. In general it is difficult to detect nanoscale biological particles such as single viruses in solution using scattering based techniques due to their weak refractive index contrast (refractive index of a virus particle $n \sim 1.5$ [52]) with the suspending medium, which is predominantly water-based ($n = 1.33$ for water). We show below that heterodyne detection helps overcome this difficulty.

Using the heterodyne detection technique, we could successfully detect HIV, Influenza, Sindbis, Vaccinia, Parainfluenza (Sendai), and Baculovirus in separate samples on the single virus level. For virus detection using nanofluidic channels, a pressure-driven flow scheme [44] was used instead of electroosmotic flow. The velocity profile and flow-speed control of the two methods are similar, but electroosmotic flow tends to heat the buffer solution of the viruses [53]. When added

Fig. 1.7 Size distributions for different virus types. (**a**) HIV (ADA strain) and (**b**) Sindbis virus. (**c**) Size distribution for a mixture of HIV and Sindbis viruses
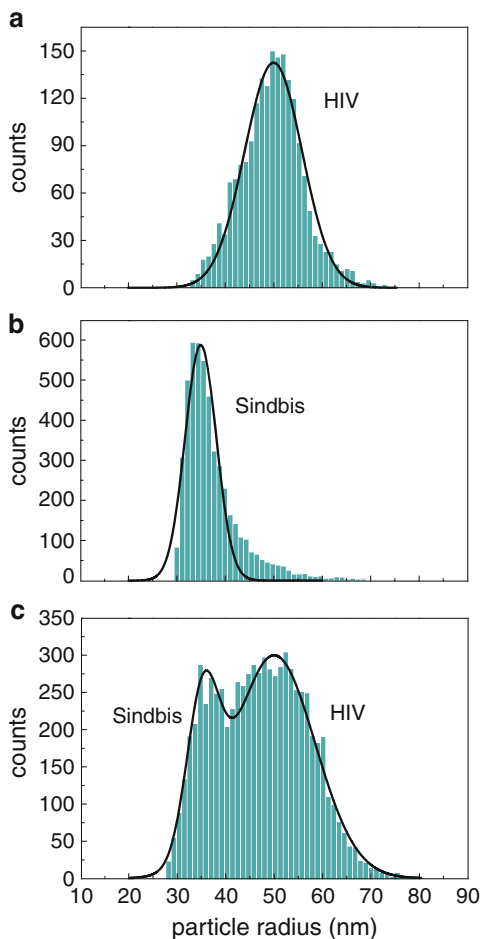
to heating due to the light focus, this can cause the formation of vapor bubbles [54] and decomposition of the sample, which clogs the nanofluidic channels and disrupts the measurement process. Pressure-driven flow does not heat the buffer solution.

In Fig. 1.7 shows some representative results for virus detection using the heterodyne detection scheme. Figure 1.7a shows the size distribution recorded for a sample of HIV virus (ADA strain). To calibrate the HIV size distributions, the mean radius of HIV particles is taken to be 50 nm, as determined from TEM measurements [55]. In Fig. 1.7b we show the size distribution for a sample of Sindbis virus. For calibration purposes, the mean radius of Sindbis virus particles is assumed to be 35 nm according to TEM measurements [56].

To demonstrate the ability to distinguish between HIV and Sindbis viruses in solution, the size distribution for a mixture of the two viruses is recorded. Figure 1.7c shows that the two virus types can be resolved. The size distribution is calibrated with respect to the mean size of a HIV virus particle (50 nm). Note, that according

to this calibration, the mean size of Sindbis viruses turns out to be ~ 35 nm, which is in good agreement with the TEM measurements, and indicates that the optical properties (ε_p) of the two virus types are similar. The results indicate that it is possible to distinguish by size individual viruses in a mixture of different virus types, provided we know, for calibration purposes, the mean size of at least one virus type.

1.6 Conclusions

In this article we have presented heterodyne interferometry as an effective method for accurate characterization of nanoparticles, including those of biological importance such as viruses. It has been established from both theoretical and experimental standpoints that heterodyne interferometric detection is more viable than other presently available label-free techniques, when it comes to accurate real-time characterization of nanoparticles in solution. It has been shown that such a system can detect single viruses in a sample and also distinguish between different kinds of virus types in a heterogeneous mixture. Such a real-time single particle detection scheme can also be used to accurately determine the concentration of nanoparticles present in a sample, which can be of great importance for virological research where the infection levels due to a viral pathogen need to be determined. It can be anticipated that these abilities will find application in label-free biosensing, environmental contamination and quality control, and also for clinical research.

References

1. Yezhelyev M et al (2006) Emerging use of nanoparticles in diagnosis and treatment of breast cancer. Lancet Oncol 7:657–667
2. Loo C et al (2004) Nanoshell-enabled photonics-based imaging and therapy of cancer. Technol Cancer Res Treat 3:33–40
3. Choi M et al (2007) A cellular trojan horse for delivery of therapeutic nanoparticles into tumors. Nano Lett 7:3759–3765
4. Huang X, Jain PK, El-Sayed IH, El-Sayed MA (2007) Nanoparticles for cancer diagnosis and therapeutics. Nanomedicine 2:681–693
5. Wali F, Knotter DM, Mud A, Kuper FG (2009) Impact of particles in ultra pure water on random yield loss in ic production. Microelectron Eng 86:140–144
6. Brousseau L (2008) Enhanced nanocomposite combustion accelerant and methods for making the same. US Patent 7,338,711, 3 Apr 2008
7. Ramanathan V, Carmichael G (2008) Global and regional climate changes due to black carbon. Nat Geosci 1:221–227
8. Morawska L (2010) Airborne engineered nanoparticles: are they a health problem? Air Qual Clim Change 44:18–20
9. Oberdörster G (2000) Pulmonary effects of inhaled ultrafine particles. Int Arch Occup Environ Health 74:1–8
10. Somers CM, McCarry BE, Malek F, Quinn JS (2004) Reduction of particulate air pollution lowers the risk of heritable mutations in mice. Science 304:1008–1010

11. Krug RM (2003) The potential use of influenza virus as an agent for bioterrorism. Antivir Res 57:147–150
12. Anderson B, Friedman H, Bendinelli M (eds) (2006) Microorganisms and bioterrorism, 1st edn. Springer, New York
13. Hockett RD et al (1999) Constant mean viral copy number per infected cell in tissues regardless of high, low, or undetectable plasma hiv rna. J Exp Med 189:1545–1554
14. Dulbecco R, Vogt M (1954) Plaque formation and isolation of pure lines with poliomyelitis viruses. J Exp Med 99:167–182
15. Tsai W, Conley S, Kung H, Garrity R, Nara P (1996) Preliminaryin vitrogrowth cycle and transmission studies of hiv-1 in an autologous primary cell assay of blood-derived macrophages and peripheral blood mononuclear cells. Virology 226:205–216
16. Dimitrov D et al (1993) Quantitation of human immunodeficiency virus type 1 infection kinetics. J Virol 67:2182–2190
17. Clark NA, Lunacek JH, Benedek GB (1970) A study of brownian motion using light scattering. Am J Phys 38:575–585
18. Blom MT, Chmela E, Oosterbroek R, Tijssen R, van den Berg A (2003) On-chip hydrodynamic chromatography separation and detection of nanoparticles and biomolecules. Anal Chem 75:6761
19. Prikulis J et al (2004) Optical spectroscopy of single trapped metal nanoparticles in solution. Nano Lett 4:115–118
20. Bouhelier A, Beversluis MR, Novotny L (2003) Characterization of nanoplasmonic structures by locally excited photoluminescence. Appl Phys Lett 83:5041–5043
21. Yguerabide J, Yguerabide EE (1998) Light-scattering submicroscopic particles as highly fluorescent analogs and their use as tracer labels in clinical and biological applications. Anal Biochem 262:157–176
22. Sönnichsen C, Geier S, Hecker NE, von Plessen G, Feldmann J (2000) Spectroscopy of single metallic nanoparticles using total internal reflection microscopy. Appl Phys Lett 77:2949–2951
23. Schultz S, Smith D, Mock J, Schultz D (2000) Single-target molecule detection with nonbleaching multicolor optical immunolabels. Proc Natl Acad Sci USA 97:996–1001
24. Lindfors K, Kalkbrenner T, Stoller P, Sandoghdar V (2004) Detection and spectroscopy of gold nanoparticles using supercontinum white light confocal microscopy. Phys Rev Lett 93:037401
25. Arnold S, Khoshsima M, Teraoka I (2003) Shift of whispering-gallery modes in microspheres by protein adsorption. Opt Lett 28:272–274
26. Arnold S, Ramjit R, Keng D, Kolchenko V, Teraoka I (2008) Microparticle photophysics illuminates viral bio-sensing. Faraday Discuss 137:65–83
27. Vollmer F, Arnold S (2008) Whispering-gallery-mode biosensing: label-free detection down to single molecules. Nat Methods 5:591–596
28. Vollmer F, Arnold S, Keng D (2008) Single virus detection from the reactive shift of a whispering-gallery mode. Proc Natl Acad Sci USA 105:20701–20704
29. Zhu J et al (2009) On-chip single nanoparticle detection and sizing by mode splitting in an ultrahigh-q microresonator. Nat Photon 4:46–49
30. Yanik AA et al (2010) An optofluidic nanoplasmonic biosensor for direct detection of live viruses from biological media. Nano Lett 10:4962–4969
31. Ymeti A et al (2007) Fast, ultrasensitive virus detection using a young interferometer sensor. Nano Lett 7:394–397
32. Daaboul GG et al (2010) High-throughput detection and sizing of individual low-index nanoparticles and viruses for pathogen identification. Nano Lett 10:4727–4731
33. Patolsky F et al (2004) Electrical detection of single viruses. Proc Natl Acad Sci USA 101:14017–14022
34. Fraikin J-L, Teesalu T, McKenney CM, Ruoslahti E, Cleland AN (2011) A high-throughput label-free nanoparticle analyser. Nat Nanotechnol 6:308–313. doi:10.1038/nnano.2011.24
35. Stern E et al (2007) Importance of the debye screening length on nanowire field effect transistor sensors. Nano Lett 7:3405–3409

36. Bohren CF, Huffmann DR (1983) Absorption and scattering of light by small particles. Wiley, New York
37. Givan AL (2001) Flow cytometry: first principles, 2nd edn. Wiley-Liss, New York
38. Berne BJ, Pecora R (2000) Dynamic light scattering: with applications to chemistry, biology, and physics, 1st edn. Dover Publications, New York
39. Mie G (1908) Beiträge zur optik trüber medien, speziell kolloidaler metallösungen. Ann d Phys 330:376–445
40. Batchelder JS, Taubenblatt MA (1991) Measurement of size and refractive index of particles using the complex forward-scattered electromagnetic field. US Patent 5,037,202
41. Batchelder JS, DeCain DM, Taubenblatt MA, Wickramasinghe HK, Williams CC (1991) Particulate inspection of fluids using interferometric light measurements. US Patent 5,061,070
42. Plakhotnik T, Palm V (2001) Interferometric signatures of single molecules. Phys Rev Lett 87:183602
43. Ignatovich FV, Novotny L (2006) Real-time and background-free detection of nanoscale particles. Phys Rev Lett 96:013901
44. Mitra A, Deutsch B, Ignatovich F, Dykes C, Novotny L (2010) Nano-optofluidic detection of single viruses and nanoparticles. ACS Nano 4:1305–1312
45. Person S, Deutsch B, Mitra A, Novotny L (2011) Material-specific detection and classification of single nanoparticles. Nano Lett 11:257–261
46. Deutsch B, Beams R, Novotny L (2010) Nanoparticle detection using dual-phase interferometry. Appl Opt 49:4921–4925
47. Ignatovich FV, Topham D, Novotny L (2006) Optical detection of single nanoparticles and viruses. IEEE J Sel Top Quantum Electron 12:1292–1300
48. Ignatovich FV, Novotny L (2003) Experimental study of nanoparticle detection by optical gradient forces. Rev Sci Instrum 74:5231–5235
49. Novotny L, Hecht B (2006) Principles of nano-optics. Cambridge University Press, Cambridge
50. Keshner M (1982) 1/f noise. Proc IEEE 70:212–218
51. Strauss EG (2001) Viruses and human disease, 1st edn. Academic, New York
52. Oster G (1950) Two-phase formation in solutions of tobacco mosaic virus and the problem of long-range forces. J Gen Physiol 33:445–473
53. Tang G et al (2006) Assessment of joule heating and its effects on electroosmotic flow and electrophoretic transport of solutes in microfluidic channels. Electrophoresis 27:628–639
54. Knox JH, McCormack KA (1994) Enhanced dielectric contrast in scattering-type scanning near-field optical microscopy. Chromatographia 38:207–214
55. Takasaki T, Kurane I, Aihara H, Ohkawa N, Yamaguchi J (1997) Electron microscopic study of human immunodeficiency virus type 1 (hiv-1) core structure: two rna strands in the core of mature and budding particles. Arch Virol 142:375–382
56. Zhang W et al (2002) Placement of the structural proteins in sindbis virus. J Virol 76:11645–11658

2
Photonic Metamaterials and Transformation Optics: A Very Brief Introduction and Review

Martin Wegener

2.1 Introduction

The major aim of optics & photonics is to obtain complete control on light propagation and light-matter interaction. In this context, materials play a crucial role. In materials, the propagation of light is influenced by the local refractive index n. The refractive index tells us by what factor thfe phase velocity of light inside the material is slower than the vacuum speed of light. Thus, one should actually rather call the refractive index *the slowness factor* of light. Microscopically, in usual materials at optical frequencies, the phase velocity is modified by electric dipoles (formed by the negatively charged electrons and the positive nuclei) that are excited by the electric component of the electromagnetic light wave. These electric dipoles re-radiate waves just like an antenna in radio engineering. The re-emitted wave excites further electric dipoles in the material that again re-radiate, etc. Thus, it is intuitively clear that, inside the material, light will propagate with a velocity different from that in free space. Usually, it is slower than in free space. Equivalently, the refractive index is larger than unity, *i.e.*, $n > 1$. Under these conditions, the refractive index is the square root of the electric permittivity ε. $n > 1$ clearly implies that $n > 0$, which means that the phase-velocity vector and the vector of the electromagnetic energy flow, the Poynting vector, point into the same direction. Waves with this property are called *forward waves*.

At optical frequencies, magnetic dipoles play no role at all. Mathematically, this can be expressed by stating that the magnetic permeability, μ, is equal to one.

M. Wegener (✉)
DFG-Center for Functional Nanostructures (CFN), Institute of Applied Physics (AP), Institute of Nanotechnology (INT), Karlsruhe Institute of Technology (KIT), Wolfgang-Gaede-Straße 1, Karlsruhe, 76131 Germany

Institut für Angewandte Physik, Universität Karlsruhe, D-76128 Karlsruhe, Germany
e-mail: martin.wegener@physik.uni-karlsruhe.de

This obviously limits the opportunities in optics: One can only directly influence the electric component of the electromagnetic light wave but not its magnetic component. In other words, one half of optics has been missing. Just one example is that *backward waves* (equivalent to $n < 0$) were unheard of in optics for many years. Artificial materials called metamaterials have changed that in the last decade (Sect. 2.2).

In more general, one can also consider intentionally spatially inhomogeneous magneto-dielectric metamaterial structures – a generalization of graded-index optics. This field called transformation optics (Sect. 2.3) is strongly inspired by the concepts and the mathematics of Albert Einstein's theory of general relativity.

The present brief paper gives a first flavor for these ideas and is based on the much more thorough and fairly recent reviews [1–4], in which numerous references to the literature have been given (especially see [4] regarding photonic metamaterials).

2.2 Photonic Metamaterials

Effective magnetic properties can be obtained in artificial man-made structures called metamaterials. In these structures, the usual atoms of materials are replaced by sub-wavelength-scale functional building blocks that are sometimes called *meta-atoms*. These meta-atoms can be packed densely into an effective material. In usual materials at optical frequencies, the lattice constant, a, is about thousand times smaller than the wavelength of light λ ($\lambda/a = 1{,}000$). Thus, the light wave effectively averages over the fine lattice periodicity. The same holds true in metamaterials, however, the lattice constant is typically only about ten times smaller than the wavelength of light here ($\lambda/a = 10$). As a result, the averaging is less perfect. It is not possible to unambiguously define a sharp borderline, where a description in terms of effective materials completely breaks down. However, the well-known fundamental Bragg condition corresponds to a wavelength of light that is only twice as large as the lattice constant ($\lambda/a = 2$). Under these conditions, pronounced Bragg reflection/scattering is likely to occur. If the wavelength of light equals the lattice constant itself ($\lambda/a = 1$), an incident plane wave of light generally even leads to diffracted orders emerging from the structure (giving rise to the Wood or Rayleigh anomaly). At this point, one can certainly no longer treat the periodic structure as an effective homogeneous material.

The paradigm building block of metamaterials is the metallic split-ring resonator (SRR), which is depicted in Fig. 2.1. This metallic ring with a slit can be viewed in different ways. First, one can think of it as a rolled-up half-wavelength antenna. In this picture, the SRR eigen-wavelength is given by 2π times the diameter of the ring. If densely packed, the lattice constant is only slightly larger than the ring's diameter and the operation wavelength is more than six times larger than the lattice constant ($\lambda/a = 2\pi$). Secondly, one can think of the SRR as a tiny *LC*-circuit. Here, the ring forms (almost) one winding of an inductor with inductance L. The ends of the wire form the plates of a capacitor with capacitance C. The resulting *LC*
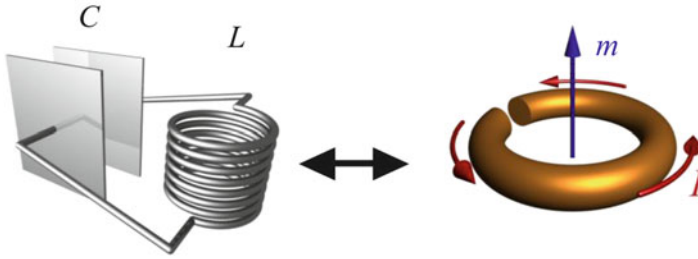
Fig. 2.1 Illustration of the split-ring resonator (*SRR*), a paradigm building block of metamaterials (Figure provided by Stefan Linden)

eigen-wavelength is about ten times larger than the ring's diameter for the structure shown in Fig. 2.1. However, one can influence the eigen-wavelength by the width of the slit. If the slit becomes very narrow, the capacitance eventually goes to infinity, and so does the eigen-wavelength.

The magnetic component of the electromagnetic light wave can induce a circulating and oscillating electric current I in the ring (see Fig. 2.1). This current gives rise to a magnetic-dipole moment, m, which is oriented normal to the plane of the ring. When excited with light at a frequency above the LC eigen-frequency, the current develops a 180-degree phase shift with respect to the excitation – just like any harmonic oscillator. For many densely packed SRR, this means that the local magnetic field can be opposite to the external magnetic field of the incident light wave. Mathematically, the magnetic permeability becomes negative, *i.e.*, $\mu < 0$.

In optics, the LC-circuit has to be so small that its eigen-frequency lies in the optical frequency range. Thus, it is interesting to ask how the eigen-frequency scales with the size of the LC-circuit. In the macroscopic world, both the inductance and the capacitance are simply proportional to SRR size. Thus, the eigen-wavelength is proportional to the SRR size as well. This finding is an immediate consequence of the scalability of the Maxwell equations. However, scalability implies that the constituent material properties (*i.e.*, those of the metal) must not change significantly. In the electric-circuit language, this means that the resistance must be negligible. Interestingly, the resistance of the SRR wire is inversely proportional to the SRR size. This means that the resistive contribution increases upon decreasing the SRR size to approach optical frequencies, whereas L and C decrease. Ohm's law for the resistance $R(\omega) = R + i\omega L_{\text{kin}}$ has two contributions. The first one is the usual resistance R, which is frequency-independent. The second contribution is frequency dependent and stems from the fact that the metal electrons acquire a phase lag for frequencies above the collision frequency. This 90-degrees phase lag is cast into the imaginary unit, i, and means that a usual metal wire also acquires an inductive response – regardless of its shape. The corresponding inductance L_{kin} is connected to the kinetic energy of the electron system and scales inversely with SRR size. Thus, it eventually overwhelms the usual (Faraday) inductance L at small SRR sizes, hence at high operation frequencies. As a result, the LC eigen-frequency saturates

and becomes size independent below a certain SRR size range. For SRRs shaped like the one shown in Fig. 2.1, the saturation occurs at around 1-μm SRR resonance wavelength [1]. For variants of the SRR, *e.g.*, with two slits to reduce capacitance and, hence, increase the eigen-frequency, visible operation frequencies have been achieved [1, 2].

Furthermore, by combining $\mu < 0$ with $\varepsilon < 0$, negative refractive indices (more precisely, backward waves) at visible frequencies have been accomplished [1]. In addition, fabrication advances have meanwhile made truly three-dimensional structures experimental reality as well [2–4]. For example, this allows for realizing compact circular polarizers based on arrays of three-dimensional gold helices exhibiting a bandwidth around one octave – an early real-world application of the far-reaching ideas of photonic metamaterials [2, 5]. Three-dimensional helices can be viewed as a transformed version of planar SRR [2, 5].

Reduction or even complete elimination of the very large photonic metamaterial losses remains to be an important and demanding future challenge [3].

2.3 Transformation Optics

Further interesting opportunities arise for intentionally *inhomogeneous* magneto-dielectric metamaterial structures. Transformation optics is a corresponding design tool: Suppose you take the rubber sheet shown in Fig. 2.2 with a Cartesian grid drawn onto it [2]. An observer looking normal onto the rubber sheet will see an
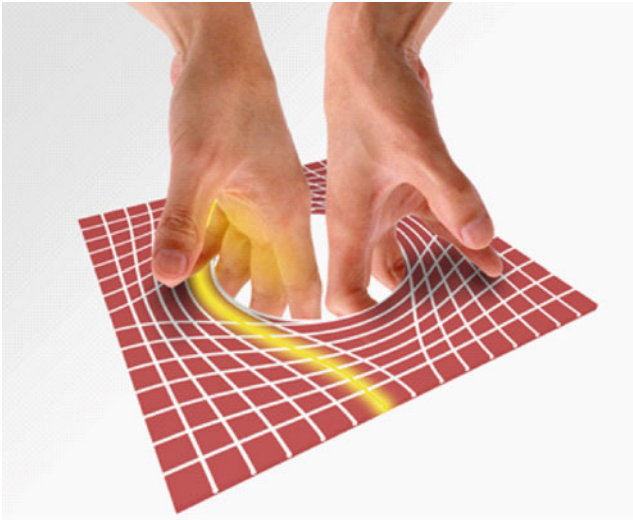
Fig. 2.2 Transformation optics connects the geometry of curved space with propagation of light in inhomogeneous magneto-dielectric materials (Taken from Ref. [3])
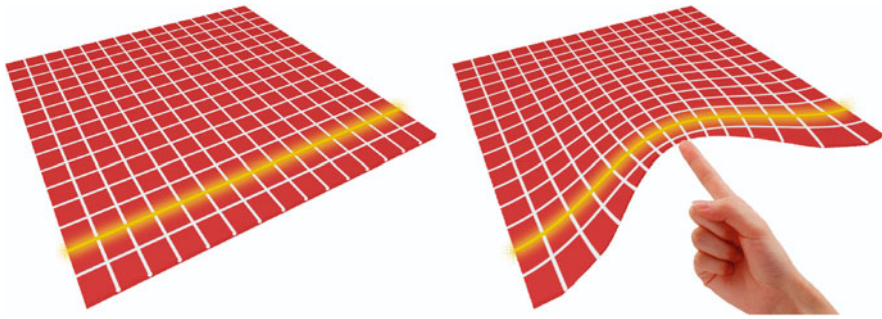
Fig. 2.3 Illustration of the carpet-invisibility-cloak transformation (Figure provided by Michael S. Rill)

undistorted rectangular grid. Upon stretching the rubber sheet within the plane or by even pulling and distorting the rubber sheet in the third dimension (mathematically, by performing a coordinate transformation), the observer will see a distorted set of lines. Any of these lines represents the potential path of a light ray [2]. By appropriate pulling on the rubber sheet, essentially any light path can be tailored. For example, if we take a screw driver and punch a hole into the rubber sheet and then open up this hole to macroscopic size in Fig. 2.2, no grid line will pass this hole. Hence light does not enter the hole, we have created an invisibility cloak [2]. Any person within the hole cannot be seen and cannot look outside his/her hole either. Amazingly, by a purely mathematical manipulation on Maxwell's equations, the effect of any such transformation on electromagnetic light waves can be shown to be exactly the same as in usual Cartesian space with a certain spatial distribution of the (real) tensor quantities $\varepsilon = \mu$. Transformation optics tells us explicitly and constructively how to derive the distribution $\varepsilon = \mu$ from the metric tensor for the complete Maxwell equations [2]. The condition $\varepsilon = \mu$ ensures that the material impedance Z is equal to the vacuum impedance everywhere, avoiding any undesired reflections of light.

Experimental realization of such complex anisotropic three-dimensional low-loss magneto-dielectric structures is presently not quite possibly yet. Often, singularities occur at the edges of the structures. However, the simple and special case of the carpet cloak illustrated in Fig. 2.3 avoids singularities, requires only locally isotropic refractive indices, and approximately gets away without a magnetic response (*i.e.*, $\mu = 1$).

Basically, the carpet cloak in Fig. 2.3 does not start from a single point (compare Fig. 2.2), but rather from the edge of a fictitious two-dimensional space. In practice, the edge corresponds to a mirror. Thus, an object can be hidden underneath a metallic carpet. To make the resulting bump in the carpet disappear (which can be viewed as a particularly demanding example of aberration correction), a graded-index structure needs to be put on top of it. Transformation optics allows for designing this graded-index profile, metamaterials for realizing any refractive index. Corresponding experiments in three-dimensional space have recently been published at telecom [2, 6] and at visible [7] frequencies.

However, invisibility cloaking is just a demanding benchmark example for the strength of the design tool called transformation optics. After all, invisibility cloaking was believed to be impossible by many just a few years ago. Presently, several researchers are searching for real-world applications designed by transformation optics.

References

1. Soukoulis CM, Linden S, Wegener M (2007) Negative refractive index at optical wavelengths. Science 315:47–49
2. Wegener M, Linden S (2010) Shaping optical space with metamaterials. Phys Today 63:32–36
3. Soukoulis CM, Wegener M (2010) Optical metamaterials: more bulky and less lossy. Science 330:1633–1634
4. Soukoulis CM, Wegener M (2011) Past achievements and future challenges in the development of three-dimensional photonic metamaterials. Nat Photon 5:523–530. doi:10.1038/nphoton.2011.154
5. Gansel JK, Thiel M, Rill MS, Decker M, Bade K, Saile V, von Freymann G, Linden S, Wegener M (2009) Gold helix photonic metamaterial as broadband circular polarizer. Science 325:1513–1515
6. Ergin T, Stenger N, Brenner P, Pendry JB, Wegener M (2010) Three-dimensional invisibility cloak at optical wavelengths. Science 328:337–339
7. Fischer J, Ergin T, Wegener M (2011) Three-dimensional polarization-independent visible-frequency carpet invisibility cloak. Opt Lett 36:2059–2061

3
Plasmonic Enhancement of Light Emission and Scattering in Nanostructures

Sergei V. Gaponenko

3.1 Introduction

In this paper, a general consideration of nanoplasmonic enhancement of light–matter interaction is proposed in terms of incident field concentration and photon density of states concentration providing a rationale for huge enhancement factors for Raman scattering and noticeable enhancement factors for luminescence. Experimental performance of enhanced secondary emission for atomic, molecular systems, semiconductor quantum dots and inorganic microcrystals using multilayer and spatially organized metal-dielectric nanostructures is discussed in detail.

Metal-dielectric nanostructures with characteristic surface relief of the order of 10...100 nm are known to modify spatial distribution of incident electromagnetic field. Local field enhancement results in enhanced absorption of photons by atoms, molecules or nanocrystals adsorbed at the surface. The effect is promoted by surface plasmon resonance. A systematic application of the field enhancement in Raman scattering enhancement and in photoluminescence enhancement with respect to molecular probes is followed nowadays by application of the effect with respect to nanocrystals (quantum dots) adsorbed at metal-dielectric nanotextured surfaces. It is the purpose of this paper to outline mechanisms of photoluminescence enhancement and Raman scattering enhancement beyond incident field raise-up and discuss their application in novel luminophores and high sensitive spectral analysis.

Starting from a rather general and straightforward consideration which is valid for resonant (Rayleigh-like) scattering, off-resonant (Raman) scattering and spontaneous emission (luminescence) of incident photons, one readily arrives at the conclusion that not only the local field enhancement in terms of excitation

S.V. Gaponenko (✉)
Stepanov Institute of Physics, National Academy of Sciences of Belarus,
Nezalezhnasti Ave 68, Minsk, 220072 Belarus
e-mail: s.gaponenko@dragon.bas-net.by

process but also photon density of states enhancement effect on photon scattering/emission processes should occur. In this consideration, scattering of light experiences enhancement as spontaneous emission does. Differences in scattering and luminescence enhancement are due to quenching processes which are crucial for luminescence and less pronounced for scattering.

The proposed model sheds light on the so-called "hot spots"' as such places on a nanotextured metal surface or near metal nanobodies where simultaneous spatial redistribution of electromagnetic field occurs both at the frequency of the incident radiation ω and at the frequency of scattered radiation ω'. Recalling the original Purcell's idea [1] on Q-fold enhancement of spontaneous emission rate in a cavity, local density of states enhancement can be treated as high Q-factor development in certain portion of space near a metal nanobody. Therefore, a "hot spot" in surface enhanced Raman scattering can be treated as a place where high Q-factor develops simultaneously at the incident light frequency and emitted light frequency.

We consider ultimate experiments on single molecule detection by means of enhanced Raman scattering and photoluminescence enhancement of atoms, molecules and quantum dots and the approaches to efficient substrates fabrication for the purposes of ultrasensitive spectroscopy. Feasibility of 10- to 10^2-fold enhancement is highlighted for luminescence. Rationale is provided for 10^{14} enhancement factor for Raman scattering which has been claimed for the first time in 1997 based on experimental observations [2, 3] but has never been reported in the theory prior to our works [4].

Experimental performance and relevant techniques are discussed for (i)superior Raman enhancement for molecules; (ii) superior Raman enhancement for inorganic crystals; (iii) luminescence enhancement for rare-earth based luminophors; (iv) luminescence enhancement for molecular fluorophors; (v) luminescence enhancement for semiconductor quantum dots. The basic theory and representative experimental examples can be found, e.g. in the recent book [5].

3.2 Mechanisms for Secondary Emission Enhancement

3.2.1 Basic Principles

For each of the three known types of secondary radiation, namely resonance (Rayleigh) scattering, non-resonant (Raman) scattering, and spontaneous emission, a straightforward single formula can be written as shown in Fig. 3.1.

Such consideration basically dates back to the pioneering paper by Dirac at the very dawn of quantum electrodynamics [6]. The consideration immediately points at the two possible ways of photon scattering and photon spontaneous emission enhancement.
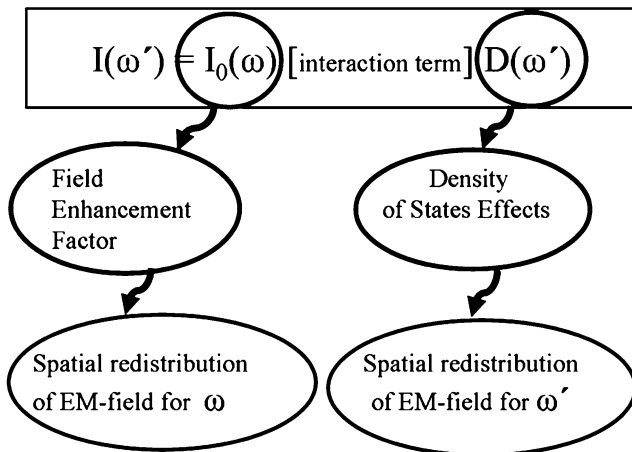
Fig. 3.1 A general formula for all types of secondary radiation

The first way is to enhance the incident photon density at the position of the emitter in question. A straightforward pump-up by means of an incident light source power supply is not meant here. Instead, incident light concentration and accumulation at certain hot points within the metal–dielectric nanostructures, inside a microcavity or within a photonic crystal defect should be exploited purposefully. The proper enhancement factor is referred to as the *local field enhancement factor*. It is this factor which is widely examined, discussed and analyzed with respect to Surface Enhanced Raman Scattering (SERS) since the very first SERS detection [7] to nowadays [8]. The factors up to 10^8–10^{10} orders of intensity enhancement have been demonstrated in model metal–dielectric nanostructures for frequencies near surface plasmon resonance. Though these numbers look quite impressive, these are still well far from the ultimate enhancement of 10^{14} documented in the experimental observations for single molecule Raman scattering [2, 3].

The second way is to make use of the possible density of photon states concentration for the frequency ω'. This can be performed by development of local areas in space with high Q-values for ω' as has been proposed with respect to spontaneous emission by Purcell [1] and has been extended towards spontaneous scattering later on in Ref. [9]. In other words, local density of states for photons should be enhanced. Notably, local density of states (LDOS) can only be redistributed over a frequency range with concentration in certain intervals at the expense of depletion otherwise. This universal sum rule was derived by Barnett and Loudon in 1996 [10]. Huge enhancement of radiative decay rate up to 10^4 has been predicted for plasmonic nanostructures at certain points (areas) in a close vicinity of metal nanobodies indicating of the proper enhancement (concentration) of the local photon density of states [11].

3.2.2 Light Intensity in Plasmonic Structures

Surface plasmon oscillations give rise to local increase in light intensity after some time the light enters the vicinity of a metal nanoparticle. The local areas of high intensity do coexist with other areas where light intensity may even be depleted as compared to a continuous dielectric medium.

Even for a single isolated particle the thorough electrodynamical calculations are very cumbersome. It is the general opinion that the ideal case would be a small particle (preferably a prolate ellipsoid or spheroid as well as cone-like or other sharp tip) or, better, a couple of particles of material with low damping rate and minor interband transitions. Damping rate defines directly the sharpness of resonant response in terms of spectral width of the resulting real part of dielectric function of the metal-dielectric structure under consideration. Interband transitions give rise to finite imaginary contribution to the complex dielectric function and bring dissipative losses.

Because of the complexity of calculations we refer to the books [5, 9, 12–14] where computational techniques are reviewed in detail. In what follows only final numerical results will be discussed.

In the list of metals promising superior local field enhancement, the first place is given to silver, the second to gold and the third to copper in accordance with damping rates and interband transitions that diminish surface plasmon resonances. The crucial parameter is also the crossover point in the dielectric function where it passes through the zero value. For the above metals this point falls in the optical range. Alkali metals even in spite of the minor contribution from interband transitions are not suitable for local light intensity enhancement because their zero-crossover points in dielectric permittivity get deep in the ultraviolet region. Additionally, alkali metals (and most common metals) are actually not suitable for surface enhanced spectroscopy experiments in air because of the rapid oxidation. Because of the above arguments, silver is a typical material for all model calculations.

For a single isolated silver particle local electric field enhancement factors $|\mathbf{E}| / |\mathbf{E_0}|$ of the order of 10 are reported [9] for 30 nm particle which corresponds to the intensity enhancement $I / I_0 \propto |\mathbf{E}|^2/|\mathbf{E_0}|^2 \approx 10^2$. The enhancement dominates in the spectral range of 370–400 nm i.e. close to the extinction peak typically observed for dispersed silver nanoparticles.

The enhancement depends on a particle shape and gets higher for prolate particles. For example, for the bottom plane of a truncated tetrahedron with in plane size $167 \times 167 \times 50$ nm the intensity enhancement about $5\cdot10^4$ was calculated [9]. Unlike smaller particles, in this case enhancement occurs at a wavelength of 646 nm. The red shift comes from the scattering contribution to the extinction. For a prolate silver spheroid (length 120 nm, diameter 30 nm) intensity enhancement about 10^4 was obtained in calculations at a wavelength of 770 nm. Notably the extreme above enhancement numbers are inherent in very restricted space portions, typically measuring 1–5 nm in one dimension.

Coupled particles show higher enhancement in the area between particles, the enhancement factors being strongly dependent on electric field orientation with

respect to a dimer axis. 10^4 intensity enhancement was predicted between two silver spherical particles of 30 nm diameter and 2 nm spacing at wavelength of 520 nm [9].

A transition from a single particle to coupled nanoparticles provides a hint towards engineering of plasmonic nanostructures with superior enhancement of incident electromagnetic field. Further steps can be made based on more complex geometries. Sarychev and Shalaev [15] computed surface field distribution for electromagnetic wave impinging the nanotextured surface formed by irregular particles with dense enough concentration to develop percolation clusters. They found in certain "hot spots" intensity may rise up by more than 10^4 times.

Stockman with co-workers [16] proposed an ingenious self-similar plasmonic "lens". It resembles three aligned nanospheres with scalable size and spacing. The external field with frequency close to the nanosphere surface-plasmon resonance excites the local field around the largest nanosphere enhanced by a factor of approx. 10. This local field is nearly uniform on the scale of the next, smaller nanosphere and plays the role of an external excitation field for it. This in turn creates the local field enhanced by an order of the magnitude. Similarly, the local fields around the smallest nanosphere are enhanced by a factor of 10^3 for the field amplitude. The "hottest" spot in the smallest gap at the surface of the smallest nanosphere was found to exhibit the field enhancement by a factor of $|\mathbf{E}|/|\mathbf{E}_0| \approx 1,200$.

3.2.3 Photon Density of States Enhancement

The local photon density of states modification in plasmonic structures can be traced by means of analysis of radiative decay rate for a probe emitter. An extensive overview of various spatial configurations, sizes and shapes of plasmonic structures can be found in the works by Klimov and Guzatov [11, 14, 17]. For a silver spherical nanoparticle they calculated radiative rate increase by the factor of $100 \ldots 500$ depending on specific configuration. For the position of an emitter between two identical silver spheres the enhancement is about 10^3 times.

Superior increase in radiative decay rate was predicted for an emitter near a prolate silver spheroid. In this case the optimal displacement can result in 10^4-fold enhancement of the radiative decay rate.

One can conclude the photon local density of states (LDOS) in all above structures modifies accordingly since the radiative rate is proportional to LDOS.

3.2.4 Application to Raman Scattering

Combining the incident field enhancement and photon density of states enhancement, the rationale has been proposed for the ultimate enhancement factor in single molecule Raman spectroscopy [4]. As is seen in Fig. 3.2, a metal spheroid
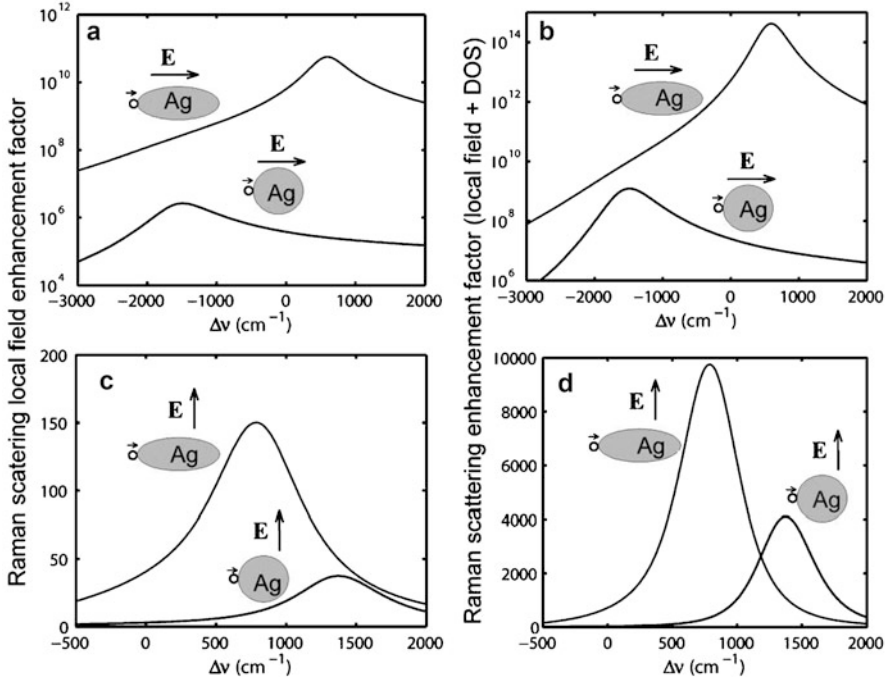
Fig. 3.2 Calculated Raman scattering cross-section enhancement factors for a molecule with polarizability $\alpha = 10^3$ Å attached to a spheroidal and spherical silver nanoparticle as a function of spectral shift $\Delta \nu = (\omega - \omega')/2\pi$ [4]. Molecule position, its dipole moment orientation and incident field orientation are indicated near every curve. Panels (**a**) and (**b**) show enhancement based on incident field enhancement only. Panels (**c**) and (**d**) show enhancement including both incident field and local DOS factors

can offer the desirable enhancement. Though the SERS theory is far of being complete, the consideration based on the two factors looks plausible and should be further extended toward more complex plasmonic structures and more specific experimental configurations (angles, wavelengths, binary and ternary nanoparticle ensembles, sharp tips etc.).

The proposed model sheds light on the so-called 'hot spots' in SERS theory. These appears to be such places in plasmonic structures where simultaneous spatial redistribution of electromagnetic field occurs both at the frequency of the incident radiation ω and at the frequency of scattered radiation ω'. Enhancement of photon LDOS starting from the pioneering paper by Purcell [1] can be interpreted as development of the certain Q-factor in the space region where a probe emitter (atom or other quantum system) is placed. The Q-factor implies a system is capable to accumulate energy. Then the Q value equals the ratio of energy accumulated in the system to the portion of energy the system looses in a single oscillation period. Therefore, one can treat the formation of high LDOS areas as development of multiple microcavities at ω' frequency over a nanotextured metal surface.

From the other side, such microcavities promote electromagnetic wave tunneling including light leakage towards the surface in the scanning near-field optical microscopy (SNOM). Therefore mapping of surface distribution of high LDOS areas can be performed by means of SNOM-ography for SERS-active structures.

Let us discuss in more detail incident field enhancement. Noteworthy, local field enhancement for incident light cannot be interpreted as surface redistribution of incident light, i.e. as a kind of local light 'microfocusing' as anticipated by many authors. Remembering that SERS is considered within the framework of linear light–matter interaction contrary to e.g. surface enhanced second harmonic generation, the totally scattered signal harvested from a portion of surface with large number of molecules will be the same independently of surface redistribution of light intensity because total incident light intensity integrated over a piece of area remains the same. Therefore within the framework of linear light–matter interaction, Raman signal enhancement by means of incident field enhancement can only be understood in terms of high local Q-factors for incident light, i.e. in terms of light accumulation near the surface rather than light redistribution over the surface. To summarize, Q-fold rise up of light intensity occurs near hot spots as it happens in optical microcavities and interferometers.

However, accumulation of light energy needs certain time. Therefore huge Raman signals can develop only with certain delay which is necessary for transient processes to finish. Transient SERS experiments will therefore be important to clarify Q-factor effects in hot spots formation.

3.2.5   Raman Scattering Enhancement Factor

We arrived to a consistent consideration of so-called "hot spots" in surface enhanced spectroscopy and can make the statement that *hot spots are local areas in plasmonic nanostructures where high Q-factors develop both for the incident light frequency and for the emitted (or scattered) light frequency.*

Many authors ignore the role of density of states effect on Raman scattering. Trying to explain huge experimental enhancement exceeding 10^{10} times, enhancements of incident and *emitted* fields are typically discussed to arrive at the hypothetical SERS enhancement factor

$$G = \frac{|\mathbf{E}(\mathbf{r}, \omega)|^2 |\mathbf{E}(\mathbf{r}, \omega')|^2}{|\mathbf{E}_0(\omega)|^2 |\mathbf{E}_0(\omega')|^2} \approx \left| \frac{\mathbf{E}(\mathbf{r}, \omega)}{\mathbf{E}_0(\omega)} \right|^4 \tag{3.1}$$

instead of the correct one

$$G = \frac{|\mathbf{E}(\mathbf{r}, \omega)|^2}{|\mathbf{E}_0(\omega)|^2} \frac{D(\mathbf{r}, \omega')}{D_0(\omega')} \tag{3.2}$$

In these formulas **E** means electric field amplitude and D stands for photon density of states. The subscript "0" means original values for vacuum.

The calculations presented in Fig. 3.2 clearly show that:

(i) LDOS contribution can give up to several orders of the magnitude to the overall SERS enhancement factor;

(ii) Contribution from LDOS is lower than primary contribution from incident field enhancement;

(iii) At the very edge of a metal spheroid the 10^{14} factor becomes affordable as has been searched for since experimental single molecule detection in Raman spectroscopy [2, 3].

Note, the relative contribution from each of the two enhancement factor will definitely depend on the specific excitation and scattered wavelength, configuration of the experimental set-up and the precise position of a molecule in a plasmonic structure. One principal difference between the LDOS factor and the incident field factor is the independence of the former on incident light polarization. One can further suppose that LDOS factor will be independent on incident wavelength but will be strongly dependent on scattered wavelength. These arguments additionally prove that simple $|\mathbf{E}\left(\mathbf{r},\omega\right)|^{4}$factor assumed by Eq. (3.1) and adopted by many authors is by no means justified.

The approach based on LDOS factor involved needs to be extended toward various metal bodies shape/configurations as well as towards various metals, wavelengths etc. The important parameter is local position of an emitter in the problem in question. In Fig. 3.3 an example is given of the distance dependence of total SERS enhancement factor calculated for a silver nanosphere [18].

In the context of the LDOS factor proposed in the SERS theory it is important to discuss possible merging or contradiction of the LDOS factor with respect to the typical consideration expressed by the relation

$$G = \frac{|\mathbf{E}\left(\mathbf{r},\omega\right)|^{2}}{|\mathbf{E}_{0}\left(\omega\right)|^{2}} \frac{|\mathbf{E}\left(\mathbf{r},\omega'\right)|^{2}}{|\mathbf{E}_{0}\left(\omega'\right)|^{2}}. \tag{3.3}$$

The second term accounts for the possible plasmonic enhancement of electric field emitted in the course of the scattering event. Can it be compared/reduced with/to the LDOS contribution? In fact, local DOS enhancement in a sense accounts for concentration of electromagnetic field at ω'. This statement unambiguously implies probe, non-existing field. Nevertheless, concentration of real emitted field by many authors was anticipated to offer the second term in Eq. (3.3). That anticipation is by no means justified if real experimental conditions for SERS observation are accounted for. Notably, enhancement of $|\mathbf{E}\left(\mathbf{r},\omega'\right)|^{2}$occurs only in the close subwavelength-scale vicinity of a nanobody like incident field enhancement does and cannot directly contribute to light harvesting in typical far-field experiments. LDOS enhancement means immeasurable concentration of electromagnetic vacuum field rather than emitted light concentration.

However, LDOS term and $|\mathbf{E}\left(\mathbf{r},\omega'\right)|^{2}$-based approach do merge if the latter is correctly calculated for the specific experimental conditions, i.e. enhancement of

Fig. 3.3 Calculated Raman scattering enhancement factor G versus distance r_{eff} between a point-like probe and the surface of a silver particle with diameter 20 nm for (**a**) normal and (**b**) tangential orientation of the induced dipole moment of a probe. The insets show G (r_{eff}) dependences in the close vicinity of a silver particle
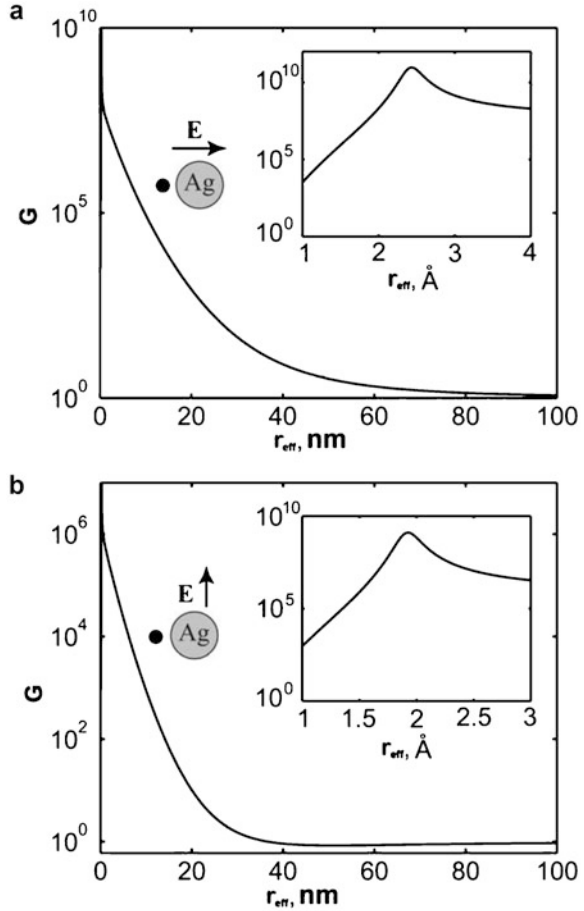
emitted field $|\mathbf{E}(\mathbf{r}_0, \omega')|^2$ reaching a detector (located at $\mathbf{r}_0$) is precisely calculated. Then enhancement of the emitted field can be interpreted in classical notions as *nanoantenna effect* [19]. Such a compromise looks reasonable with one comment. It is entirely calculation-related coincidence since within classical electrodynamice the event of a photon creation with the energy differing from that of an incident photon remains unexplained.

3.2.6 Photoluminescence Enhancement

Plasmonic environment in metal-dielectric nanostructures modifies spontaneous emission, i.e. photoluminescence, as well. However huge enhancement factors predicted by the relation (3.3) should be modified since metal proximity gives rise

to only to incident intensity concentration and radiative decay rate enhancement. Metal proximity promotes efficient non-radiative channel for an excited atom, molecule or nanocrystal (quantum dot). The finite lifetime of every real excited state in a quantum system makes its efficient "by-passing" by a non-radiative channel possible. Nonradiative rate enhancement measures $10^5 \ldots 10^6$ well dominating over radiative rate enhancement at distances less than 5 nm [11, 14, 17]. Therefore the maximal field enhancement factors occurring within a few nanometers from the metal surface cannot entirely contribute to luminescence enhancement.

For the correct calculation of the luminescence enhancement the relation (3.3) should be modified as follows:

$$G = \frac{|\mathbf{E}(\mathbf{r}, \omega)|^2}{|\mathbf{E}_0(\omega)|^2} Q \tag{3.4}$$

where Q is *quantum yield*. The latter in turn can be written as

$$Q = \frac{\gamma_{rad}}{\gamma_{rad} + \gamma_{non}} = \frac{\gamma_{rad}^0 \dfrac{|D(\mathbf{r}, \omega)|^2}{|D_0(\omega)|^2}}{\gamma_{rad}^0 \dfrac{|D(\mathbf{r}, \omega)|^2}{|D_0(\omega)|^2} + F\gamma_{non}^0} = \frac{\dfrac{|D(\mathbf{r}, \omega)|^2}{|D_0(\omega)|^2}}{\dfrac{|D(\mathbf{r}, \omega)|^2}{|D_0(\omega)|^2} + F Q_0} \tag{3.5}$$

with F being the enhancement factor for non-radiative decay rate, and

$$Q_0 = \frac{\gamma_{non}^0}{\gamma_{rad}^0} \tag{3.6}$$

being the original quantum yield. This consideration shows that (i) photoluminescence enhancement and inhibition are equally possible in plasmonic structures and (ii) photoluminescence enhancement can be more likely foreseen for systems with originally low quantum yield. In the latter case the FQ_0 product in Eq. (3.5) becomes less pronounced and high local density of states term can dominate. By and large, the fine balance in the product of manifold filed enhancement and manifold quantum yield decrease is to be attained to give photoluminescence enhancement in the real experiments and devices.

3.2.7 New Tasks for the Theory

A huge incident field may in certain experimental situations result in a *non-linear* response of an atom or a molecule. A few milliwatts per mm^2 in the incident light beam results in many megawatts per cm^2 in a hot point which is enough to observe nonlinearities. Additionally, a huge concentration of emitted field can result in stimulated emission and scattering. Neither stimulated secondary emission nor

nonlinear responsivity of an atom or a molecule in plasmonic nanostructures has been introduced in the theoretical considerations when speaking about luminescence and scattering enhancement in nanoplasmonics.

These issues remain as further factors in the theory and in experimental performance to be perceived for superior optical response of plasmonic structures.

3.3 Experimental Performance

3.3.1 Plasmonic Structures for Surface Enhanced Spectroscopy

The very first nanotextured structures for surface enhanced spectroscopy were made by electrochemical etching of silver, gold or platinum surface in 1970-ies. These pioneering observations were thoroughly reviewed in Ref. [7]. A non-exhaustive list of approaches used in modern experiments includes [5]:

  (i) Single-tip techniques,
 (ii) Electron-beam lithography design of shaped metal islands with desirable arrangement,
(iii) Vacuum deposition of metals with subsequent annealing to give island-like structure,
 (iv) Chemical deposition of metal nanoparticles on dielectric substrates,
  (v) Metal deposition on a template made of colloidal crystal (so called "photonic crystal"),
 (vi) Metal deposition on a template offered by spontaneously grown semiconductor quantum dots on a semiconductor surface [18],
(vii) Implementation of multiple metal-dielectric layers [19] (Fig. 3.4).

3.3.2 Surface Enhanced Raman Scattering for Organic Species

There is extensive list of reports on SERS for various molecular systems with potential applications in biomedical research [8, 20], medical diagnostics [21, 22], in forensic analyses [23] Not only in research but in practical medical diagnostics can SERS be useful. E.g. oral cancer has been found to give rise in three additional lines in patients' saliva Raman spectrum as compared to the reference healthy group [22]. Plasmonic enhancement of Raman signal can be highly enhanced to offer both earlier diagnostics and cheaper cost of analyses because of simpler detecting system. The less explored area of SERS applications includes studies of cultural heritage where identification of components by fine non-destructive analysis is necessary [24–28].
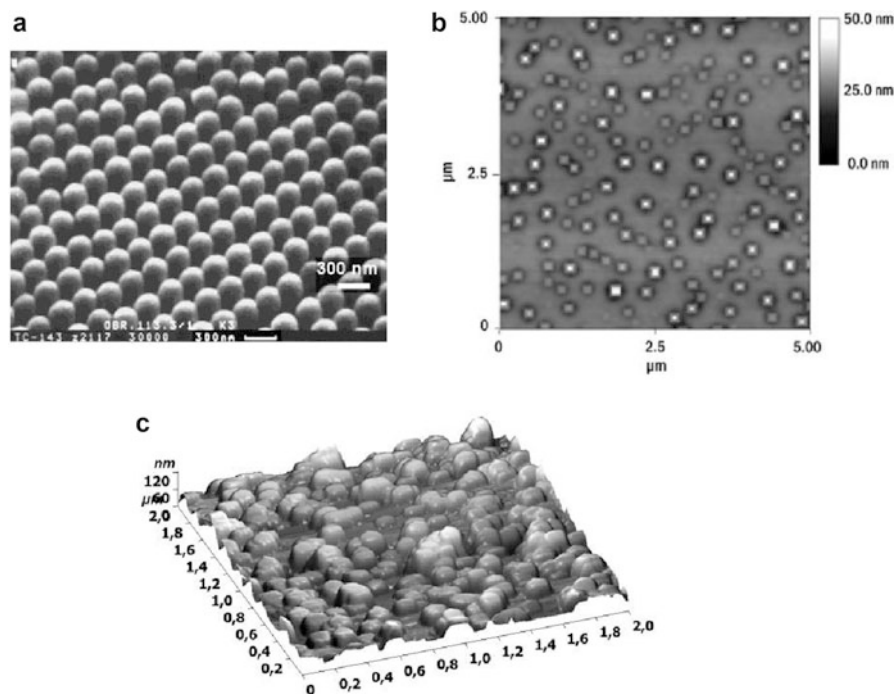
Fig. 3.4 The representative examples of plasmonic nanostructures for surface enhanced spectroscopy: (**a**) regular arrangement of silica nanospheres covered with gold, (**b**) Ge dots on Si substrates covered with gold; (**c**) silver nanoparticles on a glass substrates

3.3.3 Surface Enhanced Raman Scattering for Inorganic Crystallites

The whole wealth of experimental findings for SERS essentially reduces to molecular spectroscopy. Interestingly enough, there just a few publications on SERS application to inorganic crystallites and semiconductor quantum dots.

We found recently that up to 10^9 local SERS enhancement factor is feasible in experiments with micrometer size ultramarine crystallites on top of a mica substrate covered with nanometer sized silver spherical particles [29]. This huge enhancement factor gives overall 10^2–10^3 enhancement in ensemble averaged detection. The data are presented in Fig. 3.5. Note that because of the striking difference in size between metal and ultramarine particles only very small portion of ultramarine actually contributes to the harvested Raman signal. Similar enhancement has also been observed for Au-coated Ge-Si quantum dots on a Si substrate [18]. These results indicate that SERS can be purposefully applied for detection of negligible inorganic analytes, e.g. in forensic or in cultural heritage research.
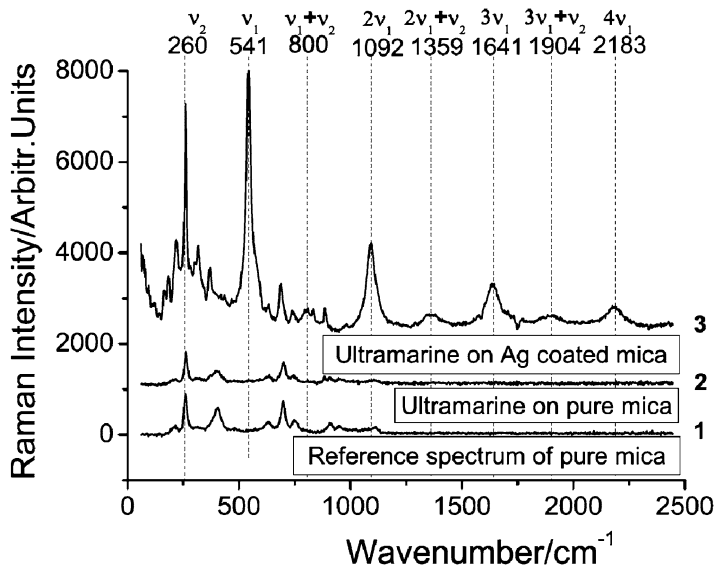
Fig. 3.5 Raman spectra of ultramarine microcrystallites: (*1*) mica reference without ultramarine, (*2*) ultramarine on a mica surface without silver, (*3*) ultramarine on a mica surface with silver nanoparticles. *Vertical lines* indicates the identified ultramarine bands with number measuring the spectral shift in cm^{-1}

3.3.4 Plasmonically Enhanced Luminescence

There are numerous reports on experimental observations of photoluminescence enhancement for various plasmonic nanostructures. The brief list of active experimental groups in the field is presented by Refs. [18, 30–39]. Unlike Raman scattering, luminescence experiences not only promotional effects but also quenching near a metal surface. Therefore keeping the optimal spacing between emitters and metal surface becomes of crucial importance. This is done either by Langmuir–Blodgett films or by fine polyelectrolyte layers. Typical enhancement does not exceed the factor of 10. The bigger values were reported either for specially engineered regular nanostructures with lithographic templating or for originally poor luminophores with low quantum yield.

One may state that, unlike SERS studies, there is the reasonable agreement between experiments and theory with respect to plasmonically enhanced luminescence. In model structures the coincidence between theory and experiments becomes perfect. The good example is tip-enhanced luminescence reported by Novotny with coworkers [37]. With a single gold nanosphere on top of a tip with precise scanning over the surface with organic molecules eight-fold enhancement was observed, the optimal distance being in the range from 5 to 7 nm. Luminescence intensity becomes insensitive to the tip at distance approx. 50 nm.
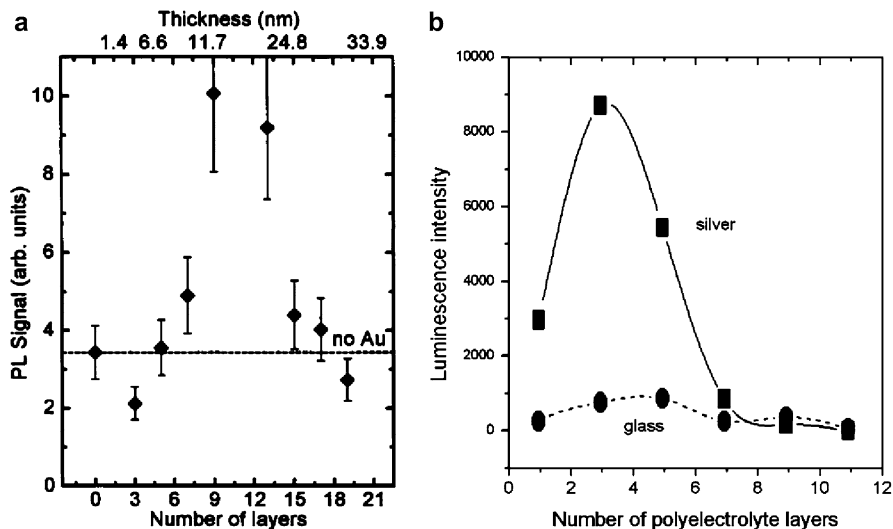
Fig. 3.6 Photoluminescence intensity as a function of the number of polyelectrolyte layers forming a dielectric spacer over a metal surface. (**a**) Core-shell CdSe/ZnS semiconductor nanocrystals with the mean diameter 4 nm on a nanotextured gold surface (Kulakovich et al. [38]); (**b**) Albumin-fluorescein isothiocyanate conjugate of bovine serum on a nanotextured silver surface (Kulakovich et al. [39])

The representative examples are given in Fig. 3.6 of photoluminescence enhancement of semiconductor nanocrystals and organic fluorophores. Semiconductor nanocrystals (so-called quantum dots) are novel luminescent species whose absorption and emission spectra as well as transition probabilities are essentially controlled by quantum confinement of electrons and holes. These factors offer tunability of emission spectra simply by size variation. Simultaneously, superior stability of luminescent properties has been found which is more than 100 times higher than that of traditional organic luminophores like rhodamines or fluorescein. Quantum dots are therefore promising candidates for novel commercial luminophores as well as for novel bioluminescent labels at the single molecule level. Their optical properties in more detail are discussed, e.g. in Ref. [5].

For fluorescein-labeled protein (Fig. 3.6b) approx. ten-fold enhancement has been observed. The odd number of polyelectrolyte layer in every case is predefined by the desire to keep on fluorophore on the same surface every time. It is clearly seen that luminescence intensity is sensitive to the distance between the silver island film and the fluorophore and exhibits a maximum at around three polyelectrolyte layers, which corresponds to a spacer thickness of about 4.2 nm. This value is perfectly agrees with the report on tip-enhanced single molecule spectroscopy using a spherical gold ball [37]. For semiconductor core-shell quantum dots the optimal distance has been found to be about 10 nm for CdSe/ZnS dots adsorbed on a gold colloidal film. This discrepancy could be due to the different metal–fluorophore system, in particular due to a different length scale of surface roughness

and also due to the relatively large size of labeled protein molecules (which are oblate ellipsoids with dimensions of 140×4 nm) in comparison with the 4 nm size of nanocrystals. Progress in synthesis of semiconductor nanoparticles in various ambient environments, understanding of their optical properties combined with an idea of using quantum dots as efficient luminophores in light emitting devices and as fluorescent labels in high sensitive biospectroscopy do stimulate extensive experiments on purposeful application of field enhancement and DOS effects for quantum dot based nanostructures.

3.4 Conclusion and Outlook

Surface enhanced spectroscopy as a field of science has 40 years long history. Surprisingly enough, it has not entered the routine analytical laboratory practice. The poor reproducibility of results and tricky techniques for fabrication of active metal nanostructures seem to be the principal obstacles. Most probably it is the right time to consider extension of the field from research labs to practical analytics and diagnostics.

From one side, cheap techniques are promising of metal nanoparticles deposition on dielectrics in ambient atmosphere which can become a commercial issue in the nearest future or even can be performed *in situ* as a part of routine measurement procedure.

From the other side, using silicon based nanostructures as templates for surface enhanced techniques can offer mass production of substrates by means of microelectronics facilities. Moreover, silicon basis could potentially provide a route towards lab-on-chip solutions since a light source, a light detector, a filter and a plasmonic signal enhancing texture can be all implemented in a single construction measuring size of a few micrometers.

In all potential application of plasmonically enhanced luminescence it is important to keep in mind that emission gets brighter mainly because of heavier excitation of emitters. This necessarily brings the enhancement of the whole variety of photoinduced phenomena and photochemical processes into play. Therefore molecules will be exhausted in shorter time, and the light emitting devices will become less durable

References

1. Purcell EM (1946) Spontaneous emission probabilities at radiofrequencies. Phys Rev 69:681
2. Kneipp K, Wang Y, Kneipp H, Perelman LT, Itzkan I, Dasari RR, Feld MS (1997) Single molecule detection using surface-enhanced raman scattering (SERS). Phys Rev Lett 78: 1667–1670

3. Nie S, Emory SR (1997) Probing single molecules and single nanoparticles by surface enhanced Raman scattering. Science 275:1102–1105

4. Gaponenko SV, Guzatov DV (2009) Possible rationale for ultimate enhancement factors in single molecule Raman spectroscopy. Chem Phys Lett 477:411–414

5. Gaponenko SV (2010) Introduction to nanophotonics. Cambridge University Press, Cambridge

6. Dirac PAM (1927) The quantum theory of the emission and absorption of radiation. Proc R Soc Lond Ser A 114:243–265

7. Chang RK, Furtak TE (eds) (1982) Surface enhanced Raman scattering. Plenum Press, New York

8. Kneipp K, Moskovits M, Kneipp H (eds) (2006) Surface-enhanced Raman scattering. Springer, Berlin

9. Gaponenko SV (2002) Effects of photon density of states on Raman scattering in mesoscopic structures. Phys Rev B 65:140303(R)

10. Barnett SM, Loudon R (1996) Sum rule for modified spontaneous emission rates. Phys Rev Lett 77:2444–2448

11. Guzatov DV, Klimov VV (2005) Radiative decay engineering by triaxial nanoellipsoids. Chem Phys Lett 412:341–346

12. Novotny L, Hecht B (2007) Principles of nano-optics. Cambridge University Press, Cambridge

13. Maier SA (2007) Plasmonics: fundamentals and applications. Springer Verlag, Berlin

14. Klimov VV (2009) Nanoplasmonics. Nauka, Moscow, in Russian

15. Sarychev AK, Shalaev VM (2000) Electromagnetic field fluctuations and optical nonlinearities in metal-dielectric composites. Phys Rep 335:275–371

16. Li K, Stockman MI, Bergman DJ (2003) Self-similar chains of metal nanospheres as an efficient nanolens. Phys Rev Lett 91:227402

17. Klimov VV, Guzatov DV (2007) Optical properties of an atom in the presence of a cluster consisting of two nanospheres (invited paper). Quantum Electron 37:209–231

18. Klyachkovskaya E, Strekal N, Motevich I, Vaschenko S, Harbachova A, Belkov M, Gaponenko S, Dais C, Sigg H, Stoica T, Grützmacher D (2001) Enhanced Raman scattering of ultramarine on Au-coated Ge/Si-nanostructures. Plasmonics 6:413–418

19. Ozel T, Nizamoglu S, Sefunc MA, Samarskaya O, Ozel IO, Mutlugun E, Lesnyak V, Gaponik N, Eychmuller A, Gaponenko SV, Demir HV (2011) Anisotropic emission from multilayered plasmon resonator nanocomposites of isotropic semiconductor quantum dots. ACS Nano 5:1328–1334

20. Kneipp K, Kneipp H, Itzkan I, Dasari RR, Feld MS (1999) Ultrasensitive chemical analysis by Raman spectroscopy. Chem Rev 99:2957–2975

21. Huang X, Jain PK, El-Sayed IH, El-Sayed MA (2007) Gold nanoparticles: interesting optical properties and recent applications in cancer diagnostics and therapy. Nanomedicine 2:681–693

22. Kah JCY, Kho KW, Lee CGL, Sheppard CJR (2007) Early diagnosis of oral cancer based on the surface plasmon resonance of gold nanoparticles. Int J Nanomedicine 2:785–798

23. Ryder AG (2005) Surface enhanced Raman scattering for narcotic detection and applications in chemical biology. Curr Opin Chem Biol 9:489–493

24. Leona M, Lombardi JR (2007) Identification of berberine in ancient and historical textiles by surface-enhanced Raman scattering. J Raman Spectrosc 38:853–858

25. Chen K, Leona M, Vo-Dinh T (2007) Surface-enhanced Raman scattering for identification of organic pigments and dyes in works of art and cultural heritage material. Sens Rev 27:109–120

26. Leona M, Stenger J, Ferloni E (2006) Application of surface enhanced Raman scattering techniques to the ultrasensitive identification of natural dyes in works of art. J Raman Spectrosc 37:981–992

27. Lau D, Livett M, Prawer S (2008) Application of surface enhanced Raman spectroscopy to the analysis of natural resins in artworks. J Raman Spectrosc 39:545–552

28. Whitney AV, Casadio F, Van Duyne RP (2007) Identification and characterization of artists' red dyes and their mixtures by surface-enhanced Raman spectroscopy. Appl Spectrosc 61: 994–1000

29. Klyachkovskaya EV, Guzatov DV, Strekal ND, Vaschenko SV, Harbachova AN, Belkov MV, Gaponenko SV (2011) Enhancement of Raman scattering of light by ultramarine microcrystals in presence of silver nanoparticles. J Raman Spectrosc 43:741–744. doi:10.1002/jrs.3088

30. Strekal N, Maskevich A, Maskevich S, Jardillier J-C, Nabiev I (2000) Selective enhancement of Raman or fluorescence spectra of biomolecules using specially annealed thick gold films. Biopolymers (Biospectroscopy) 57:325–328

31. Ozel T, Soganci IM, Nizamoglu S, Huyal IO, Mutlugun E, Sapra S, Gaponik N, Eychmuller A, Demir HV (2008) Giant enhancement of surface-state emission in white luminophore CdS nanocrystals using localized plasmon coupling. New J Phys 10:083035

32. Aslan K, Malyn SN, Geddes CD (2007) Metal-enhanced fluorescence from gold surfaces: angular dependent emission. J Fluoresc 17:7–13

33. Ray K, Chowdhury MH, Lakowicz JR (2007) Aluminum nanostructured films as substrates for enhanced fluorescence in the ultraviolet-blue spectral region. Anal Chem 79:6480–6487

34. Aslan K, Malyn SN, Geddes CD (2008) Plasmon radiation in SEF as the reason of angular dependence: angular-dependent metal-enhanced fluorescence from silver island films. Chem Phys Lett 453:222–228

35. Kuehn S, Hakanson U, Rogobete L, Sandoghdar V (2006) Enhancement of single molecule fluorescence using a gold nanoparticle as an optical nanoantenna. Phys Rev Lett 97:017402

36. Bek A, Jansen R, Ringler M, Mayilo S, Klar TA, Feldmann J (2008) Fluorescence enhancement in hot spots of AFM-designed gold nanoparticle sandwiches. Nano Lett 8:485–490

37. Anger P, Bharadwaj P, Novotny L (2006) Enhancement and quenching of single molecule fluorescence. Phys Rev Lett 96:113002

38. Kulakovich O, Strekal N, Yaroshevich A, Maskevich S, Gaponenko S, Nabiev I, Woggon U, Artemyev M (2002) Enhanced luminescence of CdSe quantum dots on gold colloids. Nano Lett 2:1449–1452

39. Kulakovich O, Strekal N, Artemyev M, Stupak A, Maskevich S, Gaponenko S (2006) Improved method for fluorophore deposition atop a polyelectrolyte spacer for quantitative study of distance-dependent plasmon-assisted luminescence. Nanotechnology 17:5201–5206

4
Sub-Wavelength Optical Fluorescence Microscopy for Biological Applications

P.N. Hedde and Gerd Ulrich Nienhaus

Abstract Visualization of sub-cellular structures and their temporal evolution contributes substantially to our understanding of biological processes. Far-field optical microscopy is arguably the most powerful imaging technique for cells and tissues because it allows live specimens to be studied over extended periods of time with only minimal perturbation due to the measurement. In fluorescence microscopy, biomolecules or supramolecular structures of interest are specifically labeled by light-emitting moieties and thus can be imaged with excellent contrast. A disadvantage of standard optical microscopy is its moderate spatial resolution, which is restricted to about half the wavelength of visible light ($\sim$200 nm) by fundamental physical laws governing wave optics. Consequently, molecular interactions occurring on spatial scales of 1–100 nm cannot be resolved. However, a variety of super-resolution fluorescence microscopy techniques have recently been developed that overcome the resolution limitation. Here we present a brief overview of these techniques and their application to cellular biophysics.

4.1 Introduction

For more than 400 years, optical microscopy has been utilized to study the microcosm. Hans and Zacharias Janssen in Middelburg in the Netherlands were probably the inventors of the compound microscope in the late sixteenth century. After gradual improvements during the following centuries, the resolution of

P.N. Hedde • G.U. Nienhaus

Institute of Applied Physics and Center for Functional Nanostructures (CFN), Karlsruhe Institute of Technology (KIT), Karlsruhe 76128, Germany

G.U. Nienhaus (✉)

Department of Physics, University of Illinois at Urbana-Champaign, Urbana, IL 61801, USA
e-mail: uli@uiuc.edu

47

conventional light microscopes was pushed to its physical limits in the second half of the nineteenth century, especially due to the work of Ernst Abbe, Otto Schott and Carl Zeiss in Jena, Germany. Abbe, among others, realized that in order to resolve a structure, e.g., a regular grating, at least the first-order diffraction has to be captured by the objective lens, resulting in a fundamental limitation to the resolution, known as the famous Abbe resolution law [1],

$$d = \frac{\lambda}{2n \sin \alpha}. \tag{4.1}$$

Consequently, two objects can only be resolved in an image if their lateral separation is larger than a minimal distance, d, which depends on the wavelength, λ, and the numerical aperture, $n \sin \alpha$, with refractive index, n, of the medium between the object and the objective lens, and half-angle α of the objective lens aperture. For visible light, this popular relation yields a minimal distance of 200 nm. For a long time, it was widely believed that smaller structures cannot be resolved by using far-field optical microscopy with visible light. Various other techniques have been developed to resolve biological structures even down to atomic resolution. Kendrew [2] and Perutz [3] were the first to determine the molecular structures of proteins by x-ray crystallography [4] after solving the phase problem. For high-resolution protein structure determination of two-dimensional protein crystals [5], electron microscopy [6] is an excellent method. More recently, structures of large biomolecular aggregates have been unraveled by electron tomography [7]. Atomic force microscopy [8], although limited to surface measurements, has nevertheless proven useful for structural studies especially of membrane proteins [9]. Nuclear magnetic resonance (NMR) spectroscopy is a spectroscopic method that only indirectly probes spatial scales via their effects on magnetic transitions of nuclear spins, but has become an important tool for protein structure determination [10], providing – in addition to structural data – a wealth of information on the dynamics [11].

However, X-ray diffraction, electron microscopy and NMR all require special sample preparations and are mainly restricted to in-vitro studies. Light microscopy, by contrast, is easy to use, fast and non-invasive, and thus ideally suited for visualization of biological structures and processes inside living organisms. These advantages have already been appreciated in the seventeenth century by famous scientists including Hooke, Malpighi and van Leeuwenhoek. Later, in the nineteenth century, Schleiden, Schwann, Flemming and others laid the foundations of cell biology using optical microscopy.

Optical microscopy with fluorescence detection is particularly powerful for cellular imaging [12]. By specific attachment of fluorophores, structures of interest can selectively be made visible due to their reemission of the absorbed light. Fluorescence light can be well separated from the incident and elastically scattered light since it is delayed in time and red-shifted in wavelength (Stokes's shift), leading to excellent image contrast. Most often, organic dyes and fluorescent proteins are used as fluorescence markers. Organic dyes are molecules of comparatively small (1–2 nm) size that can be attached to cellular structures in various ways, most

commonly by using antibody staining. A great variety of fluorescent dyes with excellent brightness, resistance to photobleaching and widely varying absorption and emission wavelengths have been developed. Fluorescent proteins are a family of small proteins ($\sim$3 nm) that contain a fluorescent chromophore in their interior [13]. These marker proteins can be genetically encoded and, therefore, produced by the cell itself; no further staining steps are necessary prior to the experiment [14]. They can be attached to the protein under study by fusing the DNA encoding the fluorescent protein to the gene of the protein. Consequently, the cell expresses a so-called fusion protein, which has an additional fluorescent protein domain that often does not interfere with the biological function of the original protein. The photophysical and photochemical properties of fluorescent proteins are, however, still inferior to those of the best synthetic dyes.

In recent years, novel fluorescent biomarkers of $\sim$5–10 nm diameter have been introduced that are based on nanocrystals, including metal [15], semiconductor [16] and nanodiamond [17] quantum dots. They show great promise as fluorescent markers due to their excellent brightness and photostability. Yet, their specific attachment to biological structures is more difficult and, therefore, these markers have not yet found as wide-spread application as organic dyes in the life sciences.

Approximately 20 years ago, exciting new developments took off in the field of light microscopy, driven by both progress in fluorescence labeling technology and tremendous advances in key microscope components, e.g. detectors performing close to their physical limits (CCD cameras, avalanche photodiodes), powerful laser light sources (pulsed and cw lasers), optoelectronics and nanomechanical devices for beam steering and sample positioning. Furthermore, the field has also benefited greatly from the availability of affordable, high-performance computers capable of storing vast amounts of data and processing of images in reasonable amounts of time.

Evidently, diffraction is a fundamental physical property of the wave nature of light, and so the resolution of an optical image in a light microscope will always be limited. Nevertheless, in recent years, researchers have been able to find clever strategies that exploit the non-linear response of fluorescent dyes to light irradiation to retrieve spatial information beyond the Abbe barrier. In these ingenious microscope implementations, the image resolution is no longer limited by diffraction. A survey of those methods will be presented in this contribution.

4.2 Microscope Designs, Linear Widefield and Confocal Techniques

There are two basic far-field fluorescence imaging modes, widefield and confocal, which both use a set of lenses, namely the objective lens, to image an object onto a detector. The process of image formation can mathematically be described by two Fourier transforms in succession. The Fourier transform is limited to a range

of spatial frequencies given by a filter function termed the optical transfer function (OTF) because the objective lens cannot capture all the information, as shown by Abbe [1]. By applying the convolution theorem, we find that the image is blurred by the point spread function (PSF),

$$\Phi_I (X, Y) = \Phi_0 (x, y) \otimes PSF (x, y), \qquad (4.2)$$

where Φ_0 describes the object with spatial coordinates x and y, and Φ_I describes the image with spatial coordinates X and Y, respectively. Thus, image formation can be described by repainting the image using a broad brush, with its line width determined by the extension of the PSF.

4.2.1 Widefield Epifluorescence Microscopy

In standard widefield epifluorescence microscopy, the excitation light reaches the sample via the objective lens. All planes along the optical axis are illuminated equally (for optically thin samples) and thus contribute to the fluorescence image. The objective collects the reemitted fluorescence, and the entire field of view is imaged with an area-sensitive detector (frequently a CCD camera). A sharp image is only formed from the signals emanating close to the focal plane. Because there is no rejection of light from planes beneath and above the focal plane, a blurred background is always present that obfuscates the sharply imaged features in the focal plane. To avoid the strong background in widefield microscopy, researchers often resort to very thin sample slices ($z < 2\,\mu$m).

4.2.2 Total Internal Reflection Fluorescence

Alternatively, total internal reflection fluorescence (TIRF) can be used for selective excitation [18]. In this microscopy mode, the excitation light is reflected off the interface between a medium of high refractive index, n, (e.g. glass, $n \sim 1.5$) and a medium of lower n (e.g. water, $n \sim 1.3$), resulting in an evanescent wave in this medium that decays exponentially in axial direction with a decay parameter, z,

$$I(z) = I_0 \cdot e^{-d/z} \qquad (4.3)$$

Here, I_0 and d represent the intensity of the incident light and the penetration depth, respectively. The decay parameter depends on the wavelength of the incident light, the angle of incidence, and the refractive indices of the media forming the interface. Typically, only fluorophores within 100 nm from the surface are efficiently excited. Thus, TIRF microscopy features an excellent axial selectivity but lacks 3D capability.
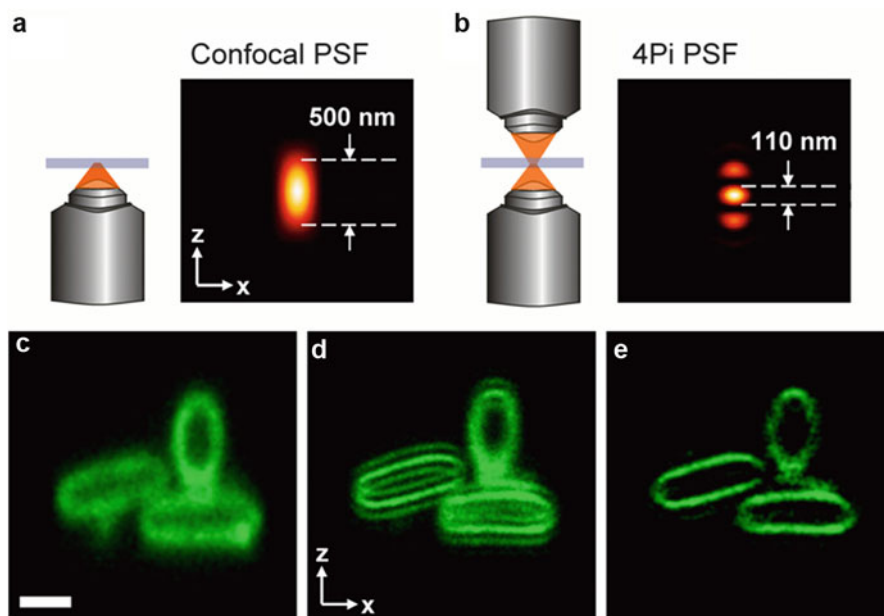
Fig. 4.1 4Pi microscopy. (**a**) By using a single objective lens, only fluorescence photons from less than one half the total solid angle (2π) can be collected. Therefore, the PSF of a standard confocal microscope is elongated in the axial direction. With two objectives in an interferometric arrangement, coverage of the full solid angle (4π) is approximated more closely, leading to an interference pattern with a sharp maximum in the axial direction. (**b**) Side lobes appear due to the limited aperture angles of the objectives but can be removed by mathematical deconvolution. (**c**) Confocal image of membrane-stained (DiI) E. coli bacteria; scale bar, 500 nm. (**d**) Raw 4Pi image of the same specimen; the effects of the side lobes are visible as ghost images. (**e**) 4Pi image after deconvolution

4.2.3 Confocal Microscopy

Confocal microscopy is a raster-scanning technique. A point source is imaged to a point in the focal plane of the sample by means of the microscope objective lens. A pinhole that is geometrically confocal to the point source is used to collect the fluorescence emanating from this point. A dichroic mirror separates excitation and emission light paths. The pinhole blocks light emanating from out-of-focus planes, only light from the focal plane is efficiently transmitted, resulting in an axial resolution of $\sim$500–800 nm with this method. By scanning either the sample or the laser laterally (*x*-, *y*-directions) as well as in the *z*-direction, 3D images can be acquired. The point spread function (PSF, Fig. 4.1a), i.e., the image of a point-like object, is the product of the PSFs for excitation and emission in confocal microscopy,

$$\Phi_I(X, Y) = \Phi_0(x, y) \otimes [PSF_{\text{exc}}(x, y) \times PSF_{\text{det}}(x, y)], \qquad (4.4)$$

so the method features a slightly improved lateral resolution over standard microscopy.

In spinning disk confocal microscopy, an array of pinholes is used for multiplex imaging of ~1,000 confocal spots. Because the transmission of light through the pinhole disk is low, the pinhole disk is rotated in tandem with another disk carrying an identical array of microlenses to enhance the light throughput. The spots are moved by rotation of the disks, and light from all pinholes is collected simultaneously by using a large area detector (CCD camera), resulting in much faster image acquisition than with single-spot confocal scanning.

4.2.4 Two-Photon Excitation

Two-photon excitation is an alternative way to achieve depth discrimination. Instead of exciting fluorescence with a single photon transition, two photons of half the energy, or twice the wavelength, are used in a non-linear process. To achieve a sufficiently high yield, two-photon excitation requires both a high spatial and temporal density of photons. The temporal density can be provided by using powerful pulsed laser sources, often titanium-sapphire (Ti:Sa) lasers with pulse durations in the picosecond region. Even then, the spatial density is only sufficient close to the focus of the high numerical-aperture objective but not in neighboring axial planes due to the quadratic dependence of the fluorescence emission on the excitation intensity. Therefore, out-of-focus excitation is suppressed, leading to optical sectioning in the axial direction [19]. An additional benefit of two-photon excitation is the improved imaging depth in scattering media due to the weaker Rayleigh scattering of the long-wavelength infrared excitation light, allowing for deep tissue imaging [20].

4.2.5 Interferometric Microscopy

An interferometric arrangement of two opposing objectives is implemented in 4Pi confocal microscopy [21]. This design further improves the axial resolution and the collection efficiency of the incoherent photons emanating from the sample in all directions, i.e., into the entire solid angle, 4π. The observation volume is sharpened in the axial direction by a two-source interference pattern caused by two counterpropagating wavefronts that are coherently superimposed at the excitation spot, at the detector, or at both (Fig. 4.1b). The side lobes of the interference pattern lead to ghosting in the 4Pi image but can be suppressed by two-photon excitation and confocal detection. Finally, side lobes are removed by applying a mathematical deconvolution algorithm to the raw data. As an example, confocal, 4Pi raw and 4Pi deconvolved images of *Escherichia coli* bacteria are compared in Fig. 4.1.

An axial resolution of ~100 nm is typically achieved with 4Pi confocal microscopy [22, 23]. Even though the lateral resolution is not affected, structures are imaged more sharply because of the excellent sectioning in axial direction.
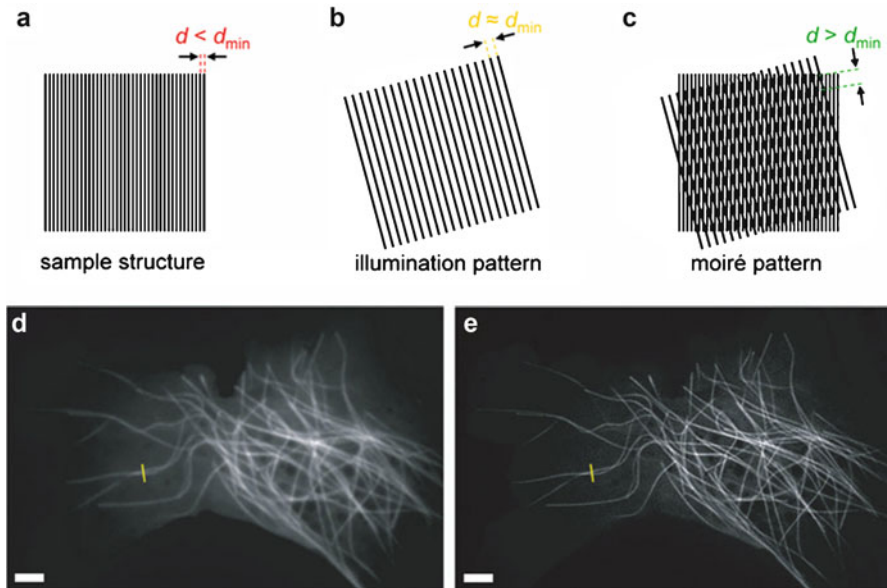
Fig. 4.2 Structured illumination microscopy (SIM). (**a**) Structures of a specimen that are too close to be resolvable by conventional widefield microscopy. (**b**) The sample is illuminated with a periodic pattern having a lattice constant close to the resolution limit. (**c**) In the overlay of the two patterns, the unresolvable sample structures become visible as a Moiré pattern with lower spatial frequency, which can be resolved by the objective lens. (**d**) Conventional TIRF image and (**e**) TIRF-SIM image of the microtubule cytoskeleton in a single S2 cell, scale bars, 2 μm. The intensity profile along the *yellow lines* reveals two microtubules at a distance of 150 nm in the SIM image, whereas this feature cannot be resolved in the conventional image. The images in *panels* **d** and **e** were reprinted from [34] with kind permission

A related interferometric approach has also been implemented in a widefield design called I5M [24]. The 4Pi and I5M techniques have been employed in studies of subcellular organelles in 3D [24–28]. Both concepts are still diffraction-limited, but they have been combined with super-resolution techniques including 4Pi-STED [29] and I5S [30], as will be discussed below.

4.2.6 Structured Illumination Microscopy

Structured-illumination microscopy (SIM) takes advantage of the fact that local information can be transformed into global information by using a Fourier transform [31]. The absence of high spatial frequencies in Fourier space, i.e., the OTF cutoff of the objective lens, results in a lack of detail and, thus, the resolution limitation in real space. By illuminating the sample (Fig. 4.2a) with a regular pattern, e.g., a line grid that still can be optically resolved (Fig. 4.2b), a beat pattern (Moiré fringes) with lower spatial frequency than the original structures emerges in the resulting image

(Fig. 4.2c). The image in Fourier space, $\psi_I(k)$, is given by the Fourier transform of the convolution of the object, $\Phi_0(r)$, with the illumination pattern, $\Phi_{ill}(r)$, finally convolved with the OTF,

$$\Psi_I\left(\vec{k}\right) = FT\left[\Phi_0\left(\vec{r}\right) \times \Phi_{ill}\left(\vec{r}\right)\right] \times OTF\left(\vec{k}\right). \qquad (4.5)$$

The beat pattern contains information about higher spatial frequencies, which can be extracted from the acquired image since the structure of the illumination pattern is known. Patterned illumination is used in combination with widefield or TIRF imaging. To be able to reconstruct a full image, the pattern has to be translated at least three times. Moreover, to enhance the resolution in all lateral directions, the pattern has to be rotated, and images have to be taken in 120° separations. Altogether nine images are, therefore, required using two-beam interference illumination. Because the spatial frequency of the illumination pattern is limited by diffraction, the resolution enhancement of SIM in the linear mode is restricted to a factor of two. Similarly, the resolution can be improved in confocal microscopy, but there, the pinhole size becomes so small in practice that the light throughput is no longer sufficient. SIM also offers axial resolution by using three coherent beams (3D-SIM) [32]. By combining SIM with the interferometric approach I5M, an axial resolution of ∼100 nm has been achieved. This design has been termed I5S [30]. A key advantage of SIM is that the technique works with all types of fluorophores, uses only a single excitation wavelength and can thus easily be extended to multicolor applications [33]. As an example, Fig. 4.2d shows a conventional TIRF image in comparison with a TIRF-SIM image (Fig. 4.2) of the microtubule cytoskeleton of a S2 cell [34]. Another advantage of the SIM principle is its relatively fast image acquisition. A frame rate of up to 11 Hz has been reported [34], making SIM an excellent tool for live cell imaging experiments [35].

4.3 Non-Linear Techniques, Super-Resolution Microscopy

All microscopy techniques discussed in Chap. 2 are – despite their finesse – still diffraction-limited and provide an enhancement in resolution by at most a factor of two over the conventional Abbe limit. True super-resolution techniques have been introduced that provide theoretically unlimited image resolution. The common theme in all these techniques is to utilize the intrinsically non-linear response of the fluorescence markers to light irradiation to circumvent the Abbe barrier.

4.3.1 Photoactivatable Fluorescence Markers

For many fluorescence-based microscopy techniques (except for STED and SSIM, for which regular dyes can be used), photoactivatable fluorophores are key to super-resolution imaging.

4.3.1.1 Photoactivatable Fluorescent Proteins

Fluorescent proteins are ideally suited as markers for optical imaging of living cells and organisms. For super-resolution imaging, photoactivatable fluorescent proteins, which contain a fluorophore with emission properties that can be controlled by light, have become very popular. Two different modes of photoactivation are presently known. Irreversible photoactivation, also known as photoconversion, involves a permanent photochemical modification of the fluorescent protein, whereas reversible photoactivation, also known as photoswitching, involves an isomerization between a bright cis and a dark trans state [36].

The first photoconvertible fluorescent protein, photoactivatable green fluorescent protein (PA-GFP), was generated by mutagenesis of the original GFP [37]. It is initially non-fluorescent but acquires a green fluorescence after intense irradiation with 400-nm light. The diffusion coefficient of hemagglutinin in live fibroblasts was determined using PA-GFP and fluorescence photoactivation localization microscopy (FPALM, see Sect. 4.3.2.2) imaging [38]. Later, a monomeric red fluorescent protein PA-mRFP1-1 has also been introduced [39]. However, both of these photoactivatable proteins are not ideal for super-resolution imaging because of their low contrast ratio between the active and inactive states. Another class of photoconverting fluorescent proteins features a photoactivation mode in which the emission color is irreversibly altered from green to red upon irradiation with 400-nm light, such as in Kaede [40], KikGR [41] and EosFP [42]. Photoconverters feature a high dynamic range and are excellent tools for most localization based super-resolution microscopy approaches.

For reversible saturable optical fluorescence transitions (RESOLFT, see Sect. 4.3.3) imaging, however, reversible photoswitchers are required that can be turned on and off repeatedly [43]. The first application of RESOLFT utilized asFP595 [44] followed by Dronpa [45] and rsEGFP [46]. Dual-color super-resolution imaging was shown with the Dronpa/EosFP and PS-CFP2/EosFP pairs [47], and the first monomeric photoswitchable red fluorescent protein was rsCherry [48]. IrisFP is a fluorescent protein that combines two photoactivation modes [49, 50]. It is reversibly switchable in the green and, after photoconversion with 400 nm light, turns into a reversibly switchable red fluorescent protein. With the combination of two photoactivation modes, entirely new experiments have become available, such as pulse-chase imaging with superresolution.

4.3.1.2 Photoactivation of Organic Dyes

In addition to fluorescent proteins, organic dyes can also be reversibly photo-switched and used for super-resolution imaging, including photochromic rhodamine [51] and cyanine dyes, which were employed in the first stochastic optical reconstruction microscopy (STORM, see Sect. 4.3.2.2) experiment [52]. Photoswitchable dyes are usually a lot brighter than fluorescent proteins. Unfortunately, their application in living cells is compromised by their rather limited ability to permeate

the plasma membrane. Moreover, thiol reagents at millimolar concentrations are typically required in the sample to induce photoswitching, which may not be compatible with the live cell environment. Irreversibly photoactivatable dyes for super-resolution imaging have also become available, e.g. Q-rhodamine [53, 54].

4.3.1.3   Nanocrystalline Quantum Dots

In comparison with synthetic dyes and fluorescent proteins, semiconductor nanocrystalline quantum dots exhibit superior photostability and brightness, and are therefore commonly used in single-molecule imaging including single-particle tracking. Recently, by using direct light driven modulation of Mn-doped ZnSe quantum dot fluorescence, RESOLFT imaging has been reported [55]. Often regarded as a nuisance in single-particle tracking, the intermittency of quantum dots has been taken advantage of in a further super-resolution technique termed super-resolution optical fluctuation imaging, SOFI (see Sect. 4.3.5) [56]. Small noble metal nanoparticles also appear promising as fluorescence labels [57]. Their quantum yields are still comparatively low, but they can be excited at a high rate to emit bright fluorescence.

4.3.2   *Localization-Based Super-Resolution Microscopy*

From single-particle tracking experiments, researchers have long been aware that the position of a single fluorescence emitter can be determined with a precision significantly exceeding the width of the PSF, which governs the resolution in standard imaging. Actually, using single-molecule optical imaging assays, individual steps of motor proteins along filaments were analyzed with an accuracy of 1 nm [58, 59]. Single-molecule, localization-based super-resolution microscopy exploits this fact and uses photoactivatable fluorochromes to disperse spatial information in the time domain.

4.3.2.1   Principle of Localization-Based Super-Resolution Imaging

A high density of fluorescence markers is required to faithfully image fine structures in conventional fluorescence microscopy. Because all fluorophores contribute simultaneously to the image, their PSFs overlap and their positions thus cannot be determined individually. However, using photoactivatable fluorophores as markers, the emission properties can be controlled externally by light, thus allowing localization of individual fluorophores with high precision. At the beginning of localization-based super-resolution image acquisition, all markers are maintained in their inactive (off) state. Subsequently, they are sparsely activated, so only a few appear in each image frame taken with a dwell time of typically 1–100 ms. Since the PSFs do not overlap, each marker can be localized individually. A large
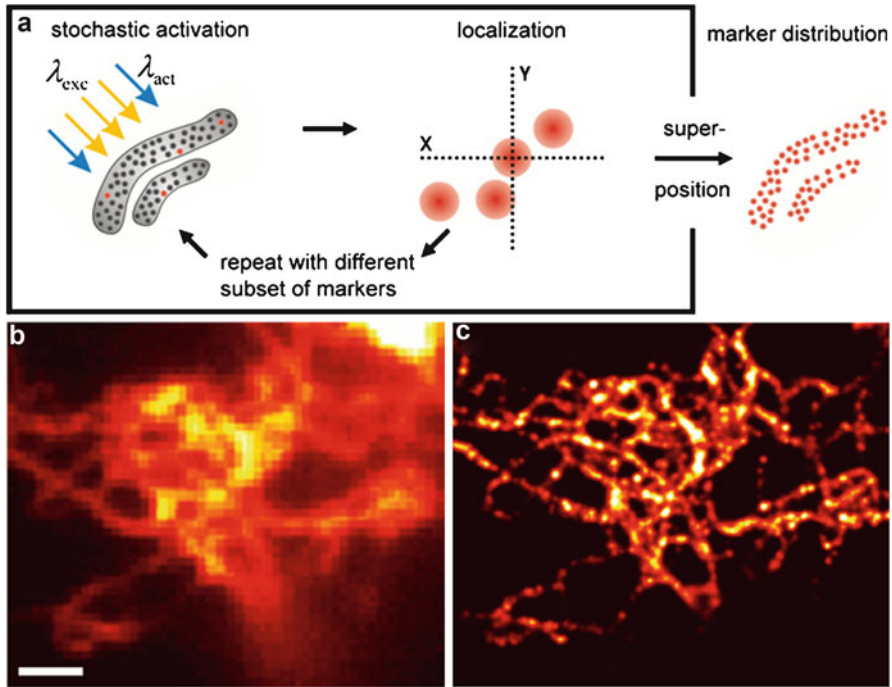
Fig. 4.3 Photoactivation localization microscopy (PALM). (**a**) Schematic depiction of the principle. By weak illumination with light of a specific wavelength, a small subset of spatially well separated fluorophores is photoactivated to a fluorescent state. The activated molecules are imaged by using a laser that excites their fluorescence until photobleaching occurs. Because the individual PSFs do not show significant overlap, each marker can be localized with a precision in the range of a few 10 nm. Typically, up to several thousand image frames are recorded sequentially so that a sufficient number of fluorophores can be localized. The final high resolution image is reconstructed from all fluorophore locations, depicting the density of fluorophores within the specimen. (**b**) Conventional widefield image and (**c**) PALM image of a live SW13 cell expressing a desmin-mEosFPthermo fusion construct, scale bar, 1 μm

number of frames (102–104) are taken by repeated acquisition and are all analyzed individually. Green-to-red photoconvertible fluorescent proteins such as EosFP have been shown to be very useful for localization-based imaging [36, 42, 60]. By an appropriate adjustment of the 400-nm activating laser intensity, only a small number of molecules are converted to red emitters and registered in the red color channel during acquisition of a CCD camera frame of 1–100 ms integration time. Consequently, photoconversion and photobleaching are kept in balance until the supply of fluorescent markers is depleted. Sophisticated software has been developed to determine the positions of the fluorophores in each individual image. Finally, a density map depicting the distribution of emitters is produced with a resolution in the range of a few tens of nanometers. Figure 4.3a illustrates the entire process. The two-dimensional localization precision, i.e., the standard error of the mean,

$$\sigma^2 = \frac{\sigma_{\text{PSF}}^2}{N} + \frac{a^2/12}{N} + \frac{8\pi\sigma_{\text{PSF}}^4 b^2}{a^2 N^2}, \qquad (4.6)$$

is governed by the number of photons, N, detected from each fluorophore; σ_{PSF} is the standard deviation of the PSF, a is the camera pixel size and b the background noise [18]. The localization precision consists of three contributions: the first term represents photon statistics, the second term results from the finite size of the detector pixels, and the last term arises from background noise. As is evident from this equation, the resolution in localization-based super-resolution microscopy is theoretically unlimited because the uncertainty in the determination of the mean of the distribution approaches zero with increasing number of collected photons. The only limitation is the finite size and labeling accuracy, and the number of photons collected from individual fluorescent markers.

4.3.2.2   Concepts of Localization-Based Super-Resolution Imaging

In 2006, three variants of localization-based super-resolution imaging were introduced independently, photoactivated localization microscopy (PALM) [61], FPALM [62] and STORM [52]. In general, synthetic dyes provide a higher localization precision because they are more photostable than fluorescent proteins. As an example, ∼6,000 detected photons were reported per molecule per switching cycle using the photoswitchable fluorophore pair Cy3-Cy5 [63, 64], whereas tdEosFP, arguably the brightest photoactivatable fluorescent protein for PALM imaging [47], emits ∼2,600 photons per molecule. Monomeric FPs often yield only a few hundred photons [50], which, however, still leads to a ten-fold increase in resolution. FPs are expressed by the cell itself and are, therefore, easy to use and ideally suited for in vivo experiments [38, 65]. Synthetic dyes require specific buffer conditions involving high concentrations of reductants for photoswitching and additional labeling procedures, and so they are predominantly used for studies of fixed specimens [63, 66]. Direct STORM (dSTORM) is a simplified version of STORM that works without a second dye molecule for activation [67], and PALM with independently running acquisition (PALMIRA) [68] is a simplified version of PALM that uses only a single laser line for readout as well as photoactivation. In blink microscopy (BM), the off- and on-times of single oxazine dyes are controlled using oxidizing and reducing agents for continuous switching, respectively [69]. The speed of PALM imaging was increased by introducing a simultaneous two-color stroboscopic illumination (S-PALM) for fast switching of variants of the fluorescent protein Dronpa [70]. The triplet state of dye molecules can also be employed as a dark state: In a method called ground state depletion followed by individual molecule return (GSDIM), dye molecules are shelved in the triplet state from which they return spontaneously [71]. In point accumulation for imaging in nanoscale topography (PAINT), fluorescent molecules switch to the on-state only upon binding to the structure to be imaged and are in their non-fluorescent off-state while diffusing freely [72].

Due to the popularity of localization-based super-resolution microscopy, various new developments have emerged in fluorescence marker design, especially in the field of photoactivatable fluorophores. Dual color PALM experiments using different emission spectra were performed [47, 64, 73–76]. Cellular dynamics has been studied on the nanoscale [65]; high resolution pulse-chase experiments have also been implemented [50]. A key advantage of localization-based super-resolution methods is that they do not require any specialized microscopy hardware. Equipped with suitable lasers for excitation and photoactivation of the fluorophores and a fast, sensitive CCD camera, any existing widefield microscope can be used with these techniques. Additionally, special image analysis software is required to localize individual fluorophores and to reconstruct the final, high-resolution images. Frequently, a TIRF microscope is preferred for its improved contrast in comparison to standard widefield microscopy as a result of its axial sectioning capability.

Localization microscopy has also been extended to the third dimension in various ways. In the astigmatism-based method, a cylindrical lens is placed into the detection path to distort the PSF, and the distance to the focal plane can be extracted from the shape of the distorted PSF [77]. Another way is to introduce a spatial light modulator (SLM) in the Fourier plane of the imaging system [78]. The light is modulated such that every object point is convolved with two double-helical lobes, with the angular orientation of the lobes depending on the axial location of the object above or below the focal plane. In biplane PALM (BP-PALM) two image planes of slightly different focus are captured simultaneously, and the z-position of a fluorophore between the two focal planes is computed by fitting a three-dimensional model of the PSF to the two images of the fluorophore [79]. Axial sectioning can also be achieved by using two-photon photoactivation [51] or interferometric designs (iPALM) [80]. In iPALM, as in 4Pi microscopy, two opposing, interferometrically coupled objectives collect photons emitted by the fluorophores. The distance of the emitter from the focal plane can be determined with a very high precision of 10–20 nm, because of photon self-interference for equal path lengths. As an additional benefit, the number of photons collected is twice as large, improving the lateral localization precision as well. The vertical composition of focal adhesions was studied with this technique in great detail [81]. Finally, yet another method involves positioning of a tilted mirror close to the sample, so that a side view is captured in addition to the front view, thereby yielding isotropic 3D resolution termed virtual volume super-resolution microscopy (VVSRM) [82].

Recent years have also witnessed enormous improvements in PALM image analysis. Reconstruction of excellent high resolution images by localization of single molecules requires sophisticated image analysis algorithms. Until very recently, image reconstruction took much longer than data acquisition because image analysis is computationally demanding and, therefore, researchers were only able to assess the quality of their data long after the actual measurement. By using a single step triangulation algorithm instead of an iterative fitting procedure, localization can be performed during data acquisition [83], yielding an instant high-resolution preview and making the data acquisition procedure more intuitive and interactive

[84]. Modern graphics processing units (GPUs) have also been employed instead of conventional central processing units (CPUs) to parallelize single-molecule localization so that image reconstruction can be accelerated by orders of magnitude while maintaining a high localization precision [85, 86]. Further improvements will be necessary to cope with the data flow from faster cameras that will soon become available. Localization software has been made available as an ImageJ plugin for an out-of-the-box application [87], including even a 3D reconstruction algorithm. Beyond increasing camera frame rates [88], faster imaging can also be achieved by analyzing images with a higher density of fluorophores, which reduces the total number of frames necessary to reconstruct an image fulfilling the Nyquist theorem. However, the fraction of overlapping PSFs will be significant, and the analysis software needs to be capable of reliably decomposing these signals [89, 90].

4.3.3 Reversible Saturable Optical Fluorescence Transition-Based Super-Resolution Microscopy

The earliest super-resolution technique, stimulated emission depletion (STED) microscopy [91] or, more generally, RESOLFT microscopy [43, 46, 92] is based on a targeted, point-scanning approach in a raster-scanning confocal microscope. STED microscopy is closely related to saturated structured illumination microscopy (SSIM), in which regular illumination patterns are used instead of point-scanning [93, 94]. All these techniques utilize non-linear responses of the fluorophores to light irradiation, i.e., switching between dark and bright states.

In a STED microscope, stimulated emission is induced with a depletion beam that has an annular shape in the focal plane, with zero intensity in the center. By spatially overlaying the exciting focused spot of a confocal microscope with the depletion beam, fluorophores that do not reside close to the center are efficiently deexcited by stimulated emission of photons in the direction of the depletion beam and thus do not reach the detector. Spontaneous fluorescence photons are only emitted by fluorophores near the center. Consequently, application of the STED beam yields a smaller effective size of the excitation PSF than the usual diffraction-limited PSF (Fig. 4.4a). The higher the intensity of the depletion beam, the more the fluorescence is confined to the central region [95]. The achievable resolution is given by

$$d = \frac{\lambda}{2n \, \sin \alpha \sqrt{1 + I_{\text{STED}}/I_{\text{s}}}}, \tag{4.7}$$

where λ is the wavelength, n the refractive index, α the half-angle under which the fluorescence is collected, and I_{S} and I_{STED} are the characteristic saturation intensity of the fluorophore and the intensity of the STED beam, respectively. No special switching capabilities of the fluorescence markers are needed since STED exploits stimulated emission as a general physical principle of light-matter interaction. However, the fluorophores are required to undergo a large number of
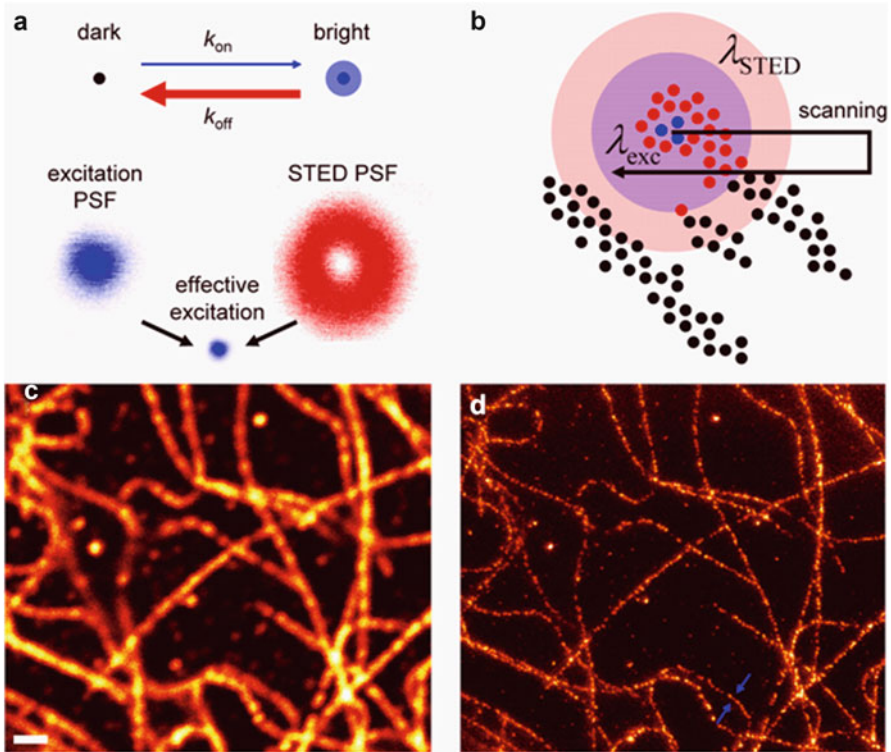
Fig. 4.4 Reversible saturable optical fluorescence transition (RESOLFT) microscopy. (**a**) A fluorophore can be optically switched between a *dark* state and a *bright* state. An illumination pattern featuring at least one intensity-zero can be applied to reduce the effective size of the point spread function (PSF), for example, by stimulated emission depletion (STED). (**b**) Sketch of the scanning procedure. A *donut-shaped* depletion beam with zero intensity in the center is overlayed with the excitation beam. Thus, all markers further away from the center (*red dots*) are efficiently deexcited by stimulated emission before they fluoresce; only markers close to the center emit fluorescence (*blue dots*). (**c**) Confocal image of β-tubulin in fixed HeLa cells labeled with primary and secondary antibodies. (**d**) STED image of the same region. The cross section marked by *blue arrows* features a width of 58 nm, scale bar, 1 μm

excitation-depletion cycles while both excitation and STED beams are scanned across the sample. Thus, excellent photostability of the fluorophores is a prerequisite (Fig. 4.4b). Confocal and STED images of β-tubulin in HeLa cells labeled with primary and secondary antibodies are shown in Fig. 4.4c, d.

The use of continuous-wave lasers for stimulated depletion avoids the need for temporal synchronization of the excitation and the depletion beam that is required with pulsed laser sources [96, 97]. The rather complex design of a STED microscope can be drastically simplified with a combination of wave plates as beam shaping devices [98]. Thus the excitation and depletion beams are intrinsically overlayed and do not require any additional alignment.

To improve the axial as well as the lateral resolution, STED microscopy can be further combined with 4Pi microscopy [29]. Another way to enhance the resolution in axial direction is to shape the pattern imprinted on the wavefront of the depletion beam in a way that depletion also confines the emission along the z-axis, which avoids the considerable complexity introduced by using two objectives [99]. A variety of STED applications to biological specimens have been published. Live cell imaging was shown to be feasible using photostable variants of fluorescent proteins [100, 101]. Fast beam-scanning was applied to study the movement of synaptic vesicles in living neurons at video frame rates [102]. Two-color STED at a resolution down to 30 nm has also been employed to study synaptic proteins in neurons [103] as well as the distribution of proteins in the mitochondrial membrane [104]. Moreover, because STED microscopy is a confocal technique, fluorescence correlation spectroscopy (FCS) can also be performed with a significantly reduced observation volume [105]. STED-FCS was applied in the direct observation of the nanoscale dynamics of membrane lipids in the plasma membrane of a living cell [106]. Fluorescent nitrogen-vacancy centers in diamond were imaged with a resolution of 8 nm using STED microscopy, and these defect centers were even localized with sub-nanometer precision [107]. Yet, effective stimulated depletion requires high laser intensities at the focal spot (MW-GW/cm²) that may damage biological samples. The key problem is the short excited-state lifetime, during which the depletion has to occur. Mechanisms other than stimulated emission can be used to deplete the active state of the fluorescent markers around the center of the excitation beam more efficiently. Those include pumping of a triplet state [108, 109], which permits a reduction of the laser intensity to ∼1 kW/cm² or exploiting a photoswitching mechanism, e.g., cis-trans isomerization of fluorophores between bright and dark states [43, 110, 111], for which ∼1 W/cm² is sufficientf.

4.3.4 *Saturated Structured Illumination Microscopy*

Recently, the SIM method has also been extended to take advantage of a nonlinear fluorophore response to push the image resolution beyond the Abbe limit. Indeed, saturated structured illumination microscopy (SSIM), like STED and localization microscopy, provides theoretically unlimited resolution. A nonlinear response of the fluorescence signal to the excitation intensity is achieved by optically saturating the fluorescence markers in the sample. Consequently, the periodic excitation pattern created in the sample contains higher harmonics of its fundamental frequency, which is key to resolution enhancement beyond the diffraction limit [112]. For SSIM, a lateral resolution of ∼50 nm was demonstrated using fluorescent beads [113]. A problem of SSIM is the fast photobleaching that occurs under saturation conditions. However, similar to RESOLFT, saturation may also be achieved using a photoswitching mechanism, enabling application of this technique to live-cell imaging.

4.3.5 Super-Resolution Optical Fluctuation Imaging

SOFI relies on higher-order statistical analysis of temporal fluctuations, e.g., fluorescence blinking of quantum dots, to obtain subdiffraction optical resolution in all three dimensions [55]. The fluorescence signal of a distribution of markers can be described as

$$F\left(\vec{r}, t\right) = \sum_{k}^{N} U\left(\vec{r} - \vec{r}_k\right) \cdot \varepsilon_k \cdot s_k(t), \tag{4.8}$$

where $U\left(\vec{r} - \vec{r}_k\right)$ is the PSF of marker k, ε_k the molecular brightness and $s_k(t)$ the temporal fluctuation of the marker signal. A second-order autocorrelation can be applied to each pixel of a series of images resulting in

$$G_2\left(\vec{r}, \tau\right) = \sum_{k}^{N} U^2\left(\vec{r} - \vec{r}_k\right) \cdot \varepsilon_k^2 \cdot \langle \delta s_k\left(t + \tau\right) \cdot \delta s_k(t) \rangle \tag{4.9}$$

The intensity value assigned to each pixel of the SOFI image is then given by the integral over the correlation function, yielding a smaller effective PSF. Figure 4.5 shows a conventional widefield image (a,b) of QD625 labeled 3T3 cells versus the second-order SOFI image (panels c, d). Using a camera pixel size well below the diffraction limit, the effective PSF can be further reduced by a factor $\sqrt{n}$ using n-th order cumulants. However, we note that the signal in a SOFI image does not represent the emission intensity but its temporal fluctuations. As an additional benefit, background from non-fluctuating sources such as autofluorescence is efficiently removed.

4.4 Considerations and Limitations

It is evident that the higher the desired image resolution in microscopy the higher the demands on the fluorophores. Linear approaches such as 4Pi, I5M and SIM do not rely on special dye properties and are, therefore, not more demanding on the dyes than conventional fluorescence microscopy techniques. However, it should be evident that, to achieve a higher resolution with concomitantly reduced pixel/voxel size, more photons are required to reach a certain signal-to-noise level for mere statistical reasons.

4.4.1 Limitations of Localization-Based Techniques

For localization-based techniques, the precision of fluorophore localization and, consequently, the achievable resolution, depends on the number of photons emitted
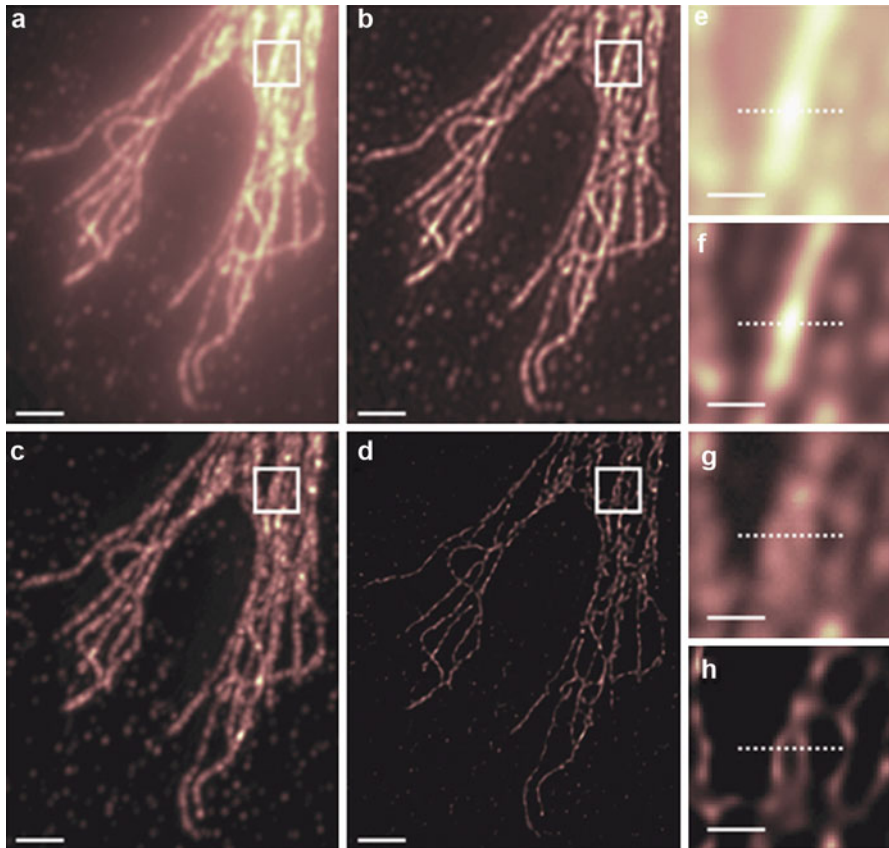
Fig. 4.5 Super-resolution optical fluctuation imaging (SOFI). The intensity value assigned to each pixel of the SOFI image is given by the integral over the autocorrelation function of fluorescence fluctuations from individual emitters. (**a**) Conventional widefield image of QD625 labeled 3 T3 cells generated by time averaging over all frames recorded, scale bar, 2 μm. (**b**) The image in *panel***a** deconvolved. (**c**) Second-order SOFI image. (**d**) The image in *panel***c** deconvolved. (**e–h**) Magnified views of the *boxed* regions, scale bars, 500 nm. The images were reprinted from [56] with kind permission

by the individual emitter [18]. A more subtle issue is the lifetime of the dark and bright states of the fluorescent markers employed. For best possible localization accuracy, the PSFs of the single emitters should not overlap. Therefore, the fluorophores must be kept in their inactive, dark state considerably longer than in their active, bright state [114]. While this condition can easily be satisfied with photoconverting fluorophores, care has to be taken when using photoswitchers. Another important criterion is the dynamic range of the photoactivation mechanism, i.e., the intensity ratio between bright and dark statesf. To achieve a reasonable contrast for single molecule localization, the probability that a fluorophore emits a photon while in its inactive state, which is ideally completely non-fluorescent, must be sufficiently low.

4.4.2   Limitations in Resolft Microscopy

In RESOLFT microscopy, contrary to localization microscopy, the brightness of the individual molecule is less important. In principle, a single detected photon per molecule is enough for image formation as long as the density of emitters is sufficient to produce a strong signal above background. However, for localization-based approaches, only a single switching cycle per molecule is required, whereas in RESOLFT microscopy, the resolution is determined by the number of switching cycles that a molecule can undergo. With decreasing pixel size, the fluorescence markers have to undergo increasingly more transitions between the fluorescent and non-fluorescent states before contributing appreciably to the image. Therefore, they have to be exquisitely resistant to switching fatigue. Additionally, in STED microscopy, the high intensity of the depletion beam (>1 GW/cm²) may cause photodamage to living specimens [115].

4.4.3   General Limitations

A general requirement of all types of fluorescence microscopy, regardless of a particular type, is that the labeling density has to be at least twice as large as the desired resolution [116]. Therefore, the ultimate resolution limitation in super-resolution optical microscopy is posed by the ability to precisely label the structure of interest. Evidently, each fluorescent marker has a certain size and cannot reside where the structure itself is located. Frequently, linkers of considerable lengths connect the fluorophores specifically to a target, which further adds to uncertainties in marking the structure. In live-cell imaging, too dense labeling may interfere with the processes under study. Conditions are even more demanding when imaging dynamic processes. In localization-based techniques, a single high-resolution image is finally reconstructed from a large number of individual frames, each with a dwell time of 1–100 ms using current CCD camera technology. Thus, acquisition of super-resolved images presently takes a few seconds at the very minimum, and processes on the sub-second timescale are too fast to be studied. STED microscopy of live cells at video rate has been demonstrated, yet it is confined to micron-sized regions of interest [102].

4.5   Conclusions

A multitude of super-resolution light microscopy techniques have emerged in recent years that are likely to be extremely helpful for unraveling the molecular details underlying biological processes in cells and tissues. These techniques have been designed to address specific problems in specific ways. For example, they may

provide multi-color, 3D, or video-rate imaging, but not all of these features will be available simultaneously in one and the same microscope. There are strong efforts toward simplified designs that hopefully will allow for a widespread application of these sophisticated techniques even by non-specialists. Apart from stable and easy-to-operate microscope designs, efficient and easy-to-handle labeling systems, featuring brighter, more photostable and smaller fluorescence markers are of crucial importance. The first commercial implementations of STED, SIM and PALM microscopes have become available, and exciting further developments are likely to soon appear on the horizon.

References

1. Abbe E (1873) Beiträge zur Theorie des Mikroskops und der mikroskopischen Wahrnehmung. Arch Mikr Anat 9:413–468
2. Kendrew JC, Dickerson RE, Strandberg BE, Hart RG, Davies DR, Phillips DC, Shore VC (1960) Structure of myoglobin: a three-dimensional Fourier synthesis at 2 A. resolution. Nature 185:422–7
3. Perutz MF, Miurhead H, Cox JM, Goaman LC, Mathews FS, McGandy EL, Webb LE (1968) Three-dimensional Fourier synthesis of horse oxyhaemoglobin at 2.8 A resolution: (1) x-ray analysis. Nature 219:29–32
4. Friedrich W, Knipping P, Laue M (1913) Eine quantitative Prüfung der Theorie für die Interferenzerscheinungen bei Röntgenstrahlen. Ann Phys 41:989–1002
5. Henderson R, Unwin PN (1975) Three-dimensional model of purple membrane obtained by electron microscopy. Nature 257:28–32
6. Knoll M, Ruska E (1932) Das Elektronenmikroskop. Z Physik 78:318–339
7. Lucic V, Forster F, Baumeister W (2005) Structural studies by electron tomography: from cells to molecules. Annu Rev Biochem 74:833–65
8. Binning G, Quate C, Gerber C (1986) Atomic force microscope. Phys Rev Lett 56:930–933
9. Müller DJ, Wu N, Palczewski K (2008) Vertebrate membrane proteins: structure, function, and insights from biophysical approaches. Pharmacol Rev 60:43–78
10. Wüthrich K (1987) Nuclear magnetic resonance–from molecules to man. Q Rev Biophys 19:3–5
11. Lange OF, Lakomek NA, Fares C, Schröder GF, Walter KF, Becker S, Meiler J, Grubmüller H, Griesinger C, de Groot BL (2008) Recognition dynamics up to microseconds revealed from an RDC-derived ubiquitin ensemble in solution. Science 320:1471–5
12. Pawley JB (2006) Handbook of biological confocal microscopy, 3rd edn. Springer
13. Nienhaus GU (2008) The green fluorescent protein: a key tool to study chemical processes in living cells. Angew Chem Int Ed Engl 47:8992–4
14. Shimomura O (2006) Discovery of green fluorescent protein. Methods Biochem Anal 47:1–13
15. Zheng J, Nicovich PR, Dickson RM (2007) Highly fluorescent noble-metal quantum dots. Annu Rev Phys Chem 58:409–31
16. Michalet X, Pinaud FF, Bentolila LA, Tsay JM, Doose S, Li JJ, Sundaresan G, Wu AM, Gambhir SS, Weiss S (2005) Quantum dots for live cells, in vivo imaging, and diagnostics. Science 307:538–44

17. Fu CC, Lee HY, Chen K, Lim TS, Wu HY, Lin PK, Wei PK, Tsao PH, Chang HC, Fann W (2007) Characterization and application of single fluorescent nanodiamonds as cellular biomarkers. Proc Natl Acad Sci U S A 104:727–32
18. Thompson RE, Larson DR, Webb WW (2002) Precise nanometer localization analysis for individual fluorescent probes. Biophys J 82:2775–83
19. Denk W, Strickler JH, Webb WW (1990) Two-photon laser scanning fluorescence microscopy. Science 248:73–6
20. Helmchen F, Denk W (2002) New developments in multiphoton microscopy. Curr Opin Neurobiol 12:593–601
21. Hell SW, Stelzer EHK (1992) Fundamental improvement of resolution with a 4Pi-confocal microscope using two-photon excitation. Opt Commun 93:277–282
22. Gugel H, Bewersdorf J, Jakobs S, Engelhardt J, Storz R, Hell SW (2004) Cooperative 4Pi excitation and detection yields sevenfold sharper optical sections in live-cell microscopy. Biophys J 87:4146–52
23. Glaschick S, Röcker C, Deuschle K, Wiedenmann J, Oswald F, Mailander V, Nienhaus GU (2007) Axial resolution enhancement by 4Pi confocal fluorescence microscopy with two-photon excitation. J Biol Phys 33:433–43
24. Gustafsson MG (1999) Extended resolution fluorescence microscopy. Curr Opin Struct Biol 9:627–34
25. Nagorni M, Hell SW (1998) 4Pi-confocal microscopy provides three-dimensional images of the microtubule network with 100- to 150-nm resolution. J Struct Biol 123:236–47
26. Egner A, Verrier S, Goroshkov A, Soling HD, Hell SW (2004) 4Pi-microscopy of the Golgi apparatus in live mammalian cells. J Struct Biol 147:70–6
27. Medda R, Jakobs S, Hell SW, Bewersdorf J (2006) 4Pi microscopy of quantum dot-labeled cellular structures. J Struct Biol 156:517–23
28. Ivanchenko S, Glaschick S, Röcker C, Oswald F, Wiedenmann J, Nienhaus GU (2007) Two-photon excitation and photoconversion of EosFP in dual-color 4Pi confocal microscopy. Biophys J 92:4451–7
29. Dyba M, Jakobs S, Hell SW (2003) Immunofluorescence stimulated emission depletion microscopy. Nat Biotechnol 21:1303–4
30. Shao L, Isaac B, Uzawa S, Agard DA, Sedat JW, Gustafsson MG (2008) I5S: wide-field light microscopy with 100-nm-scale resolution in three dimensions. Biophys J 94:4971–83
31. Gustafsson MG (2000) Surpassing the lateral resolution limit by a factor of two using structured illumination microscopy. J Microsc 198:82–7
32. Gustafsson MG, Shao L, Carlton PM, Wang CJ, Golubovskaya IN, Cande WZ, Agard DA, Sedat JW (2008) Three-dimensional resolution doubling in wide-field fluorescence microscopy by structured illumination. Biophys J 94:4957–70
33. Schermelleh L, Carlton PM, Haase S, Shao L, Winoto L, Kner P, Burke B, Cardoso MC, Agard DA, Gustafsson MG, Leonhardt H, Sedat JW (2008) Subdiffraction multicolor imaging of the nuclear periphery with 3D structured illumination microscopy. Science 320:1332–6
34. Kner P, Chhun BB, Griffis ER, Winoto L, Gustafsson MG (2009) Super-resolution video microscopy of live cells by structured illumination. Nat Methods 6:339–42
35. Hirvonen LM, Wicker K, Mandula O, Heintzmann R (2009) Structured illumination microscopy of a living cell. Eur Biophys J 38:807–12
36. Wiedenmann J, Nienhaus GU (2006) Live-cell imaging with EosFP and other photoactivatable marker proteins of the GFP family. Expert Rev Proteomics 3:361–74
37. Patterson GH, Lippincott-Schwartz J (2002) A photoactivatable GFP for selective photolabeling of proteins and cells. Science 297:1873–7
38. Hess ST, Gould TJ, Gudheti MV, Maas SA, Mills KD, Zimmerberg J (2007) Dynamic clustered distribution of hemagglutinin resolved at 40 nm in living cell membranes discriminates between raft theories. Proc Natl Acad Sci U S A 104:17370–5
39. Verkhusha VV, Sorkin A (2005) Conversion of the monomeric red fluorescent protein into a photoactivatable probe. Chem Biol 12:279–85

40. Ando R, Hama H, Yamamoto-Hino M, Mizuno H, Miyawaki A (2002) An optical marker based on the UV-induced green-to-red photoconversion of a fluorescent protein. Proc Natl Acad Sci U S A 99:12651–6

41. Tsutsui H, Karasawa S, Shimizu H, Nukina N, Miyawaki A (2005) Semi-rational engineering of a coral fluorescent protein into an efficient highlighter. EMBO Rep 6:233–8

42. Wiedenmann J, Ivanchenko S, Oswald F, Schmitt F, Röcker C, Salih A, Spindler KD, Nienhaus GU (2004) EosFP, a fluorescent marker protein with UV-inducible green-to-red fluorescence conversion. Proc Natl Acad Sci U S A 101:15905–10

43. Hofmann M, Eggeling C, Jakobs S, Hell SW (2005) Breaking the diffraction barrier in fluorescence microscopy at low light intensities by using reversibly photoswitchable proteins. Proc Natl Acad Sci U S A 102:17565–9

44. Lukyanov KA, Fradkov AF, Gurskaya NG, Matz MV, Labas YA, Savitsky AP, Markelov ML, Zaraisky AG, Zhao X, Fang Y, Tan W, Lukyanov SA (2000) Natural animal coloration can Be determined by a nonfluorescent green fluorescent protein homolog. J Biol Chem 275:25879–82

45. Ando R, Mizuno H, Miyawaki A (2004) Regulated fast nucleocytoplasmic shuttling observed by reversible protein highlighting. Science 306:1370–3

46. Grotjohann T, Testa I, Leutenegger M, Bock H, Urban NT, Lavoie-Cardinal F, Willig KI, Eggeling C, Jakobs S, Hell SW (2011) Diffraction-unlimited all-optical imaging and writing with a photochromic GFP. Nature 478:204–208

47. Shroff H, Galbraith CG, Galbraith JA, White H, Gillette J, Olenych S, Davidson MW, Betzig E (2007) Dual-color superresolution imaging of genetically expressed probes within individual adhesion complexes. Proc Natl Acad Sci U S A 104:20308–13

48. Stiel AC, Andresen M, Bock H, Hilbert M, Schilde J, Schönle A, Eggeling C, Egner A, Hell SW, Jakobs S (2008) Generation of monomeric reversibly switchable red fluorescent proteins for far-field fluorescence nanoscopy. Biophys J 95:2989–97

49. Adam V, Lelimousin M, Boehme S, Desfonds G, Nienhaus K, Field MJ, Wiedenmann J, McSweeney S, Nienhaus GU, Bourgeois D (2008) Structural characterization of IrisFP, an optical highlighter undergoing multiple photo-induced transformations. Proc Natl Acad Sci U S A 105:18343–8

50. Fuchs J, Böhme S, Oswald F, Hedde PN, Krause M, Wiedenmann J, Nienhaus GU (2010) Imaging protein movement in live cells with super-resolution using mIrisFP. Nat Methods 7:627–630

51. Fölling J, Belov V, Kunetsky R, Medda R, Schönle A, Egner A, Eggeling C, Bossi M, Hell SW (2007) Photochromic rhodamines provide nanoscopy with optical sectioning. Angew Chem Int Ed Engl 46:6266–70

52. Rust MJ, Bates M, Zhuang X (2006) Sub-diffraction-limit imaging by stochastic optical reconstruction microscopy (STORM). Nat Methods 3:793–5

53. Mitchison TJ, Sawin KE, Theriot JA, Gee K, Mallavarapu A (1998) Caged fluorescent probes. Methods Enzymol 291:63–78

54. Gee KR, Weinberg ES, Kozlowski DJ (2001) Caged Q-rhodamine dextran: a new photoactivated fluorescent tracer. Bioorg Med Chem Lett 11:2181–3

55. Irvine SE, Staudt T, Rittweger E, Engelhardt J, Hell SW (2008) Direct light-driven modulation of luminescence from Mn-doped ZnSe quantum dots. Angew Chem Int Ed Engl 47:2685–8

56. Dertinger T, Colyer R, Iyer G, Weiss S, Enderlein J (2009) Fast, background-free, 3D super-resolution optical fluctuation imaging (SOFI). Proc Natl Acad Sci U S A 106:22287–92

57. Shang L, Dong SJ, Nienhaus GU (2011) Ultra-small fluorescent metal nanoclusters: synthesis and biological applications. Nano Today 6:401–418

58. Yildiz A, Forkey JN, McKinney SA, Ha T, Goldman YE, Selvin PR (2003) Myosin V walks hand-over-hand: single fluorophore imaging with 1.5-nm localization. Science 300:2061–5

59. Yildiz A, Selvin PR (2005) Fluorescence imaging with one nanometer accuracy: application to molecular motors. Acc Chem Res 38:574–82

60. Nienhaus GU, Nienhaus K, Holzle A, Ivanchenko S, Renzi F, Oswald F, Wolff M, Schmitt F, Röcker C, Vallone B, Weidemann W, Heilker R, Nar H, Wiedenmann J (2006) Photoconvertible fluorescent protein EosFP: biophysical properties and cell biology applications. Photochem Photobiol 82:351–8

61. Betzig E, Patterson GH, Sougrat R, Lindwasser OW, Olenych S, Bonifacino JS, Davidson MW, Lippincott-Schwartz J, Hess HF (2006) Imaging intracellular fluorescent proteins at nanometer resolution. Science 313:1642–5

62. Hess ST, Girirajan TP, Mason MD (2006) Ultra-high resolution imaging by fluorescence photoactivation localization microscopy. Biophys J 91:4258–72

63. Bates M, Blosser TR, Zhuang X (2005) Short-range spectroscopic ruler based on a single-molecule optical switch. Phys Rev Lett 94:108101

64. Bates M, Huang B, Dempsey GT, Zhuang X (2007) Multicolor super-resolution imaging with photo-switchable fluorescent probes. Science 317:1749–53

65. Shroff H, Galbraith CG, Galbraith JA, Betzig E (2008) Live-cell photoactivated localization microscopy of nanoscale adhesion dynamics. Nat Methods 5:417–23

66. Heilemann M, Margeat E, Kasper R, Sauer M, Tinnefeld P (2005) Carbocyanine dyes as efficient reversible single-molecule optical switch. J Am Chem Soc 127:3801–6

67. Heilemann M, van de Linde S, Schuttpelz M, Kasper R, Seefeldt B, Mukherjee A, Tinnefeld P, Sauer M (2008) Subdiffraction-resolution fluorescence imaging with conventional fluorescent probes. Angew Chem Int Ed Engl 47:6172–6

68. Egner A, Geisler C, von Middendorff C, Bock H, Wenzel D, Medda R, Andresen M, Stiel AC, Jakobs S, Eggeling C, Schönle A, Hell SW (2007) Fluorescence nanoscopy in whole cells by asynchronous localization of photoswitching emitters. Biophys J 93:3285–90

69. Vogelsang J, Cordes T, Forthmann C, Steinhauer C, Tinnefeld P (2009) Controlling the fluorescence of ordinary oxazine dyes for single-molecule switching and superresolution microscopy. Proc Natl Acad Sci U S A 106:8107–12

70. Flors C, Hotta J, Uji-i H, Dedecker P, Ando R, Mizuno H, Miyawaki A, Hofkens J (2007) A stroboscopic approach for fast photoactivation-localization microscopy with Dronpa mutants. J Am Chem Soc 129:13970–7

71. Fölling J, Bossi M, Bock H, Medda R, Wurm CA, Hein B, Jakobs S, Eggeling C, Hell SW (2008) Fluorescence nanoscopy by ground-state depletion and single-molecule return. Nat Methods 5:943–5

72. Sharonov A, Hochstrasser RM (2006) Wide-field subdiffraction imaging by accumulated binding of diffusing probes. Proc Natl Acad Sci U S A 103:18911–6

73. Bock H, Geisler C, Wurm CA, von Middendorff C, Jakobs S, Schönle A, Egner A, Hell SW, Eggeling C (2007) Two-color far-field fluorescence nanoscopy based on photoswitchable emitters. Appl Phys B 88:161–165

74. Schönle A, Hell SW (2007) Fluorescence nanoscopy goes multicolor. Nat Biotechnol 25:1234–5

75. Andresen M, Stiel AC, Fölling J, Wenzel D, Schönle A, Egner A, Eggeling C, Hell SW, Jakobs S (2008) Photoswitchable fluorescent proteins enable monochromatic multilabel imaging and dual color fluorescence nanoscopy. Nat Biotechnol 26:1035–40

76. van de Linde S, Endesfelder U, Mukherjee A, Schuttpelz M, Wiebusch G, Wolter S, Heilemann M, Sauer M (2009) Multicolor photoswitching microscopy for subdiffraction-resolution fluorescence imaging. Photochem Photobiol Sci 8:465–9

77. Huang B, Wang W, Bates M, Zhuang X (2008) Three-dimensional super-resolution imaging by stochastic optical reconstruction microscopy. Science 319:810–3

78. Pavani SR, Thompson MA, Biteen JS, Lord SJ, Liu N, Twieg RJ, Piestun R, Moerner WE (2009) Three-dimensional, single-molecule fluorescence imaging beyond the diffraction limit by using a double-helix point spread function. Proc Natl Acad Sci U S A 106:2995–9

79. Juette MF, Gould TJ, Lessard MD, Mlodzianoski MJ, Nagpure BS, Bennett BT, Hess ST, Bewersdorf J (2008) Three-dimensional sub-100 nm resolution fluorescence microscopy of thick samples. Nat Methods 5:527–9

80. Shtengel G, Galbraith JA, Galbraith CG, Lippincott-Schwartz J, Gillette JM, Manley S, Sougrat R, Waterman CM, Kanchanawong P, Davidson MW, Fetter RD, Hess HF (2009) Interferometric fluorescent super-resolution microscopy resolves 3D cellular ultrastructure. Proc Natl Acad Sci U S A 106:3125–30

81. Kanchanawong P, Shtengel G, Pasapera AM, Ramko EB, Davidson MW, Hess HF, Waterman CM (2010) Nanoscale architecture of integrin-based cell adhesions. Nature 468:580–4

82. Tang J, Akerboom J, Vaziri A, Looger LL, Shank CV (2010) Near-isotropic 3D optical nanoscopy with photon-limited chromophores. Proc Natl Acad Sci U S A 107:10068–73

83. Andersson SB (2008) Localization of a fluorescent source without numerical fitting. Opt Express 16:18714–24

84. Hedde PN, Fuchs J, Oswald F, Wiedenmann J, Nienhaus GU (2009) Online image analysis software for photoactivation localization microscopy. Nat Methods 6:689–90

85. Smith CS, Joseph N, Rieger B, Lidke KA (2010) Fast, single-molecule localization that achieves theoretically minimum uncertainty. Nat Methods 7:373–5

86. Quan T, Li P, Long F, Zeng S, Luo Q, Hedde PN, Nienhaus GU, Huang Z-L (2010) Ultra-fast, high-precision image analysis for localization-based super resolution microscopy. Opt Express 18:11867–11876

87. Henriques R, Lelek M, Fornasiero EF, Valtorta F, Zimmer C, Mhlanga MM (2010) Quick-PALM: 3D real-time photoactivation nanoscopy image processing in Image. J Nat Methods 7:339–40

88. Zhuang XW, Jones SA, Shim SH, He J (2011) Fast, three-dimensional super-resolution imaging of live cells. Nat Methods 8:499–508

89. Quan TW, Zhu HY, Liu XM, Liu YF, Ding JP, Zeng SQ, Huang ZL (2011) High-density localization of active molecules using Structured Sparse Model and Bayesian Information Criterion. Opt Express 19:16963–16974

90. Holden SJ, Uphoff S, Kapanidis AN (2011) DAOSTORM: an algorithm for high- density super-resolution microscopy. Nat Methods 8:279–80

91. Hell SW, Wichmann J (1994) Breaking the diffraction resolution limit by stimulated emission: stimulated-emission-depletion fluorescence microscopy. Opt Lett 19:780–2

92. Bossi M, Belov V, Polyakova S, Hell SW (2006) Reversible red fluorescent molecular switches. Angew Chem Int Ed Engl 45:7462–5

93. Hell SW (2009) Microscopy and its focal switch. Nat Methods 6:24–32

94. Heintzmann R, Gustafsson MGL (2009) Subdiffraction resolution in continuous samples. Nat Photon 3:362–364

95. Hell SW (2007) Far-field optical nanoscopy. Science 316:1153–8

96. Willig KI, Harke B, Medda R, Hell SW (2007) STED microscopy with continuous wave beams. Nat Methods 4:915–8

97. Moneron G, Medda R, Hein B, Giske A, Westphal V, Hell SW (2010) Fast STED microscopy with continuous wave fiber lasers. Opt Express 18:1302–9

98. Reuss M, Engelhardt J, Hell SW (2010) Birefringent device converts a standard scanning microscope into a STED microscope that also maps molecular orientation. Opt Express 18:1049–58

99. Wildanger D, Medda R, Kastrup L, Hell SW (2009) A compact STED microscope providing 3D nanoscale resolution. J Microsc 236:35–43

100. Hein B, Willig KI, Hell SW (2008) Stimulated emission depletion (STED) nanoscopy of a fluorescent protein-labeled organelle inside a living cell. Proc Natl Acad Sci U S A 105:14271–6

101. Nagerl UV, Willig KI, Hein B, Hell SW, Bonhoeffer T (2008) Live-cell imaging of dendritic spines by STED microscopy. Proc Natl Acad Sci U S A 105:18982–7

102. Westphal V, Rizzoli SO, Lauterbach MA, Kamin D, Jahn R, Hell SW (2008) Video-rate far-field optical nanoscopy dissects synaptic vesicle movement. Science 320:246–9

103. Meyer L, Wildanger D, Medda R, Punge A, Rizzoli SO, Donnert G, Hell SW (2008) Dual-color STED microscopy at 30-nm focal-plane resolution. Small 4:1095–100

104. Donnert G, Keller J, Wurm CA, Rizzoli SO, Westphal V, Schönle A, Jahn R, Jakobs S, Eggeling C, Hell SW (2007) Two-color far-field fluorescence nanoscopy. Biophys J 92:L67–9
105. Kastrup L, Blom H, Eggeling C, Hell SW (2005) Fluorescence fluctuation spectroscopy in subdiffraction focal volumes. Phys Rev Lett 94:178104
106. Eggeling C, Ringemann C, Medda R, Schwarzmann G, Sandhoff K, Polyakova S, Belov VN, Hein B, von Middendorff C, Schönle A, Hell SW (2009) Direct observation of the nanoscale dynamics of membrane lipids in a living cell. Nature 457:1159–62
107. Han KY, Willig KI, Rittweger E, Jelezko F, Eggeling C, Hell SW (2009) Three-dimensional stimulated emission depletion microscopy of nitrogen-vacancy centers in diamond using continuous-wave light. Nano Lett 9:3323–9
108. Hell SW, Kroug M (1995) Ground-state depletion fluorescence microscopy, a concept for breaking the diffraction resolution limit. Appl Phys B 60:495–497
109. Bretschneider S, Eggeling C, Hell SW (2007) Breaking the diffraction barrier in fluorescence microscopy by optical shelving. Phys Rev Lett 98:218103
110. Hell SW (2003) Toward fluorescence nanoscopy. Nat Biotechnol 21:1347–55
111. Dedecker P, Hotta J, Flors C, Sliwa M, Uji-i H, Roeffaers MB, Ando R, Mizuno H, Miyawaki A, Hofkens J (2007) Subdiffraction imaging through the selective donut-mode depletion of thermally stable photoswitchable fluorophores: numerical analysis and application to the fluorescent protein Dronpa. J Am Chem Soc 129:16132–41
112. Heintzmann R, Jovin TM, Cremer C (2002) Saturated patterned excitation microscopy–a concept for optical resolution improvement. J Opt Soc Am A Opt Image Sci Vis 19:1599–609
113. Gustafsson MG (2005) Nonlinear structured-illumination microscopy: wide-field fluorescence imaging with theoretically unlimited resolution. Proc Natl Acad Sci U S A 102:13081–6
114. van de Linde S, Wolter S, Heilemann M, Sauer M (2010) The effect of photoswitching kinetics and labeling densities on super-resolution fluorescence imaging. J Biotechnol 149:260–266
115. Klar TA, Jakobs S, Dyba M, Egner A, Hell SW (2000) Fluorescence microscopy with diffraction resolution barrier broken by stimulated emission. Proc Natl Acad Sci U S A 97:8206–10
116. Shannon CE (1949) Communication in the presence of noise. Proc IRE 37:10–21

5

Raman Spectroscopy and Optical Coherence Tomography on a Micro-Chip: Arrayed-Waveguide-Grating-Based Optical Spectroscopy

Markus Pollnau, N. Ismail, B.I. Akca, K. Wörhoff, and R.M. De Ridder

Abstract We review our recent results on integrating biomedical optical systems onto a silicon chip.

5.1 Introduction

Miniaturization of optical instruments by integration onto an optical micro-chip will lead to smaller size and weight, reduction of optical coupling losses, avoidance of mechanical instabilities and the necessity for alignment, enormous cost reduction, and the potential for mass fabrication. Currently, individual waveguide components can be produced at the micrometer scale, such that total device footprints in the range of a few cm^2 can be obtained, but in the future individual device dimensions will scale down to the nanometer range by exploiting plasmonic waveguides, thereby allowing for complex optical systems to reach dimensions comparable to − and probably integrated with – electronic micro-chips.

In this chapter, we review our recent results on integrating optical systems for biomedical applications onto a silicon chip. Firstly, we investigated light collection from external samples by individual optical waveguides, showing that integrated waveguide probes can be more efficient than fiber probes when investigating thin samples. Then we extended this knowledge to confocal light delivery and collection by use of arrayed-waveguide gratings, thereby improving the light collection efficiency by an order of magnitude. Finally, we employed arrayed-waveguide gratings as integrated spectrometers in Raman spectroscopy and optical coherence tomography and demonstrated performance parameters that are well comparable to

M. Pollnau (✉) • N. Ismail • B.I. Akca • K. Wörhoff • R.M. De Ridder
Integrated Optical MicroSystems Group, MESA+ Institute for Nanotechnology,
University of Twente, P.O. Box 217, Enschede, 7500 AE The Netherlands
e-mail: m.pollnau@ewi.utwente.nl

those of bulky and costly standard equipment. This achievement represents the first important step toward fully integrated biomedical optical instruments.

Our devices are fabricated in silicon oxynitride (SiON) technology. SiON is a promising material for integrated optical applications. Its refractive index can be chosen between the values of silicon dioxide (1.45) and silicon nitride (2.0), thus allowing for a flexible channel waveguide design [1]. A small bending radius of the channel waveguides down to several micrometers can be obtained by employing the highest refractive index contrast with an appropriate waveguide geometry. Furthermore, SiON is transparent in a broad wavelength range from 210 nm to beyond 2,000 nm [2], so that devices can be fabricated for both, the visible and infrared wavelength ranges by use of the same material system.

5.2 Efficiency of Integrated Waveguide Probes for the Detection of Backscattered Light

Numerous medical diagnostic methods are based on optical techniques such as Raman or fluorescence spectroscopy. One of the key challenges for their applicability is the realization of an efficient interface between the sample under investigation and the optical instrument, especially when a compact set-up is envisaged. Fiber-optic probes represent an excellent solution for *in-vivo* and *in-situ* measurements, if small dimensions and high flexibility of the probe are required [3], and fiber probes with different geometries have been extensively studied and characterized.

We explored the use of integrated optical waveguide probes as an alternative to fiber-optic probes. In particular, we compared their collection efficiency with those of large-core multi-mode and small-core single- and multi-mode fiber probes. For this purpose, we developed a semi-analytical model for integrated waveguide probes, under the condition that the sample is a weakly scattering medium [4]. For the case of highly scattering media, we performed Monte-Carlo simulations to understand quantitatively the collection of backscattered light by integrated waveguide probes [5].

We designed and fabricated an integrated waveguide probe having the geometry shown in Fig. 5.1. The probe has one excitation waveguide and eight collector waveguides with a silicon oxynitride (SiON) core and silicon oxide cladding. The propagation losses in SiON waveguides are approximately 0.4 dB/cm for the wavelengths of 532 and 693 nm used in our measurements [6]. The distance d between the waveguides is fixed to 11 μm, and each waveguide cross-section is 5×0.82 μm. The refractive indices of core and cladding at a wavelength of 532 nm have been estimated as 1.5321 (TE polarization) with a birefringence $\Delta n_{TM-TE} = 2.1 \times 10^{-3}$, and 1.4631 (TE polarization) with a birefringence of 1×10^{-3}, respectively. The channels are equally spaced and all the collector waveguides are positioned on the same side with respect to the excitation waveguide. In this way it is possible to measure the backscattered light intensity as a function of lateral distance from the excitation point.

Fig. 5.1 Top view of a multi-waveguide silicon oxynitride (SiON) integrated probe for backscattered light collection. The *inset* shows an expanded view of the probe tip together with the waveguide cross-section, where $w = 5\ \mu m$ and $h = 0.82\ \mu m$. The separation between adjacent waveguides is $d = 11\ \mu m$ (Figure taken from Ismail et al. [5])
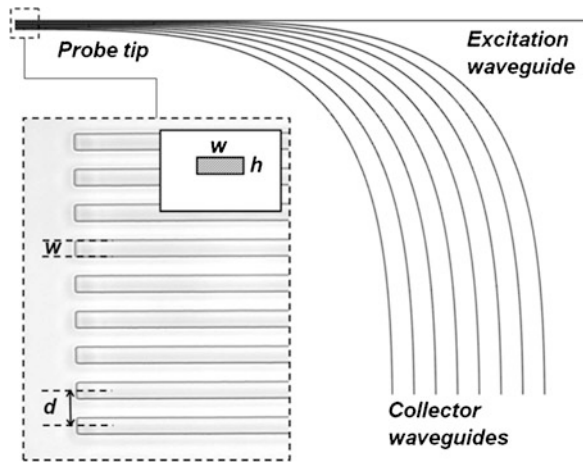
Using the semi-analytical model, we compared our integrated waveguide probe and a similar probe with $d = 6\ \mu m$ with three different fiber probes: a typical Raman large-core multi-mode dual-fiber probe (core diameter of 200 µm) with $d = 210\ \mu m$, a small-core multi-mode dual-fiber probe (core diameter of 5 µm) with $d = 11\ \mu m$, and a small-core single-mode dual-fiber probe (core diameter of 3 µm) with $d = 11\ \mu m$. For all fiber probes a refractive index contrast of 0.01 was assumed and the distance d between the excitation and collection channels was chosen such to prevent coupling of the waveguides through the evanescent tails of their modal fields. In all the simulations the excitation wavelength is 532 nm, while the wavelength of the collected signal is 693 nm.

Within the semi-analytical model we defined a figure of merit S, which is a measure of the collection efficiency of the different probes [4]. The results calculated for the different probes are shown in Fig. 5.2, in which the efficiency of each probe is displayed as a function of sample thickness. It becomes clear that, in case of thin samples (thicknesses t smaller than typically 110–150 µm), integrated waveguide probes provide efficiencies exceeding those of the investigated fiber probes. This result is relevant for various applications, e.g. Raman spectroscopy of the skin for determination of water content in the stratum corneum [7], which requires to detect the signal from regions within 100 µm underneath the sample surface. Furthermore, integrated probes have higher efficiency with respect to the investigated small-core fiber probes regardless of the sample thickness. Although it is not problematic to fabricate micro-fiber arrays with cores of, e.g., 5 µm diameter and similar distance apart from each other providing higher refractive index contrast than that investigated in our simulations, the advantages of integrated probes, such as reproducibility, low cost, and on-chip integration with other components, make them more suitable for applications that require probing of thin samples.

We carried out fluorescence measurements on a ruby rod [4]. The choice for ruby was made because the fluorescent signal in the red spectral region is very
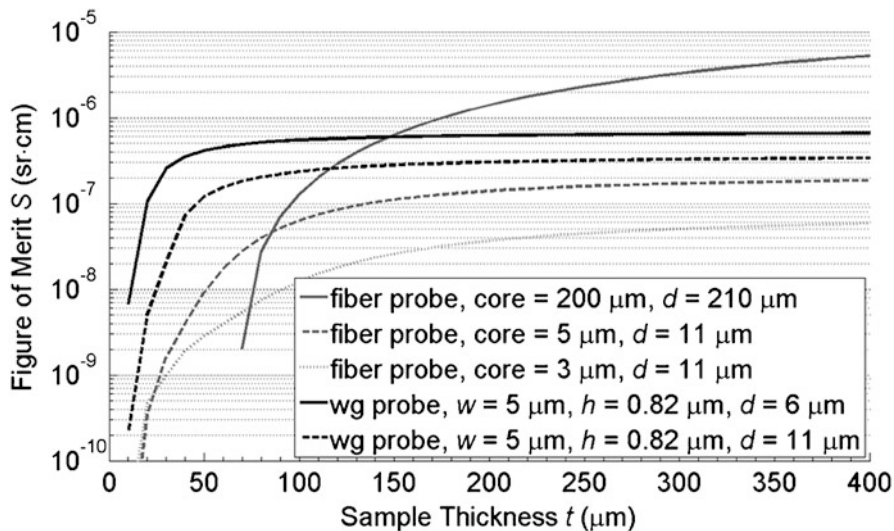
Fig. 5.2 Figure of merit S as a function of sample thickness t for two integrated dual-waveguide probes with cross-sections 5×0.82 µm and distances $d = 11$ µm and $d = 6$ µm (*black lines*), compared to those (*gray lines*) of a large-core dual-fiber probe with core diameter of 100 µm and $d = 210$ µm, and two small-core dual-fiber probes with $d = 11$ µm and core diameters of 5 and 3 µm, respectively (Figure taken from Ismail et al. [4])

strong and can easily be detected and distinguished from possible cross-talk of the excitation light. The measurements were performed using the integrated waveguide probe introduced in Fig. 5.1. Light from a Nd:YAG/SHG laser source at 532 nm was coupled into the excitation waveguide. With the ruby rod positioned in contact with the chip, fluorescence measurements were separately carried out on each of the eight collector waveguides. A small fraction of the fluorescence generated inside the ruby was captured by each of the eight collector waveguides. The comparison between the experimental results and the calculation performed with the semi-analytical model is shown in Fig. 5.3a. A second measurement was carried out by fixing d to 11 µm and measuring the power collected by the first collector waveguide of the probe at different distances of the ruby rod from the probe. The measurements compared to the simulation results are shown in Fig. 5.12b. In both, Fig. 5.12b, the comparison between measurements and simulations is achieved by normalizing each curve to its maximum value. The reasonable agreement between simulation and experiment validates our analytical model of integrated waveguide probes [4].

We also investigated excitation and light collection from a scattering medium by an integrated waveguide probe. Experiments were performed on light collection from a highly scattering water suspension of latex nanospheres. By use of the Monte-Carlo model, the propagation of light through the highly scattering medium was simulated and good agreement with the experimental data was found [5].
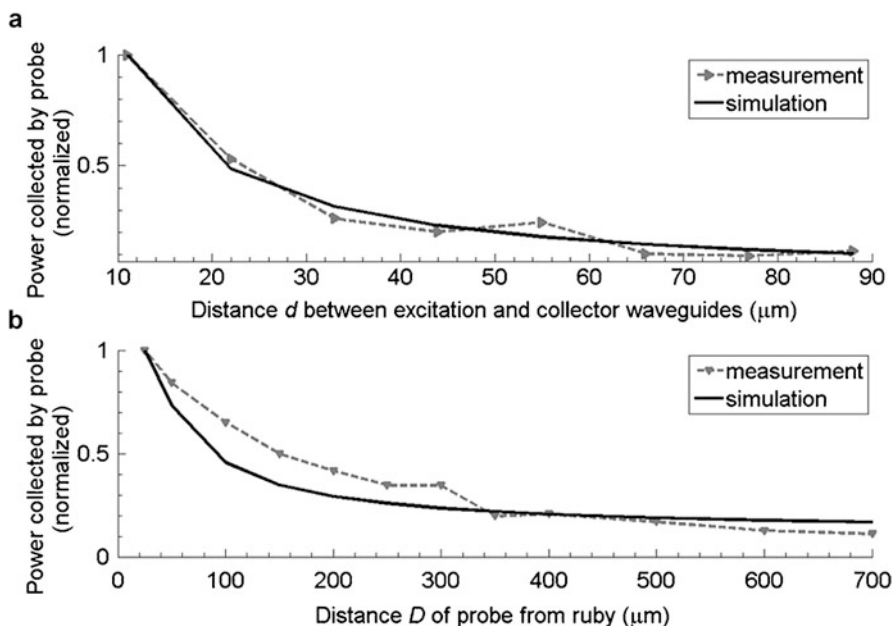
Fig. 5.3 (**a**) Fluorescence measured by a waveguide probe as a function of the distance d between excitation and collector waveguides; (**b**) Fluorescence measured by a dual-waveguide probe with $d = 11$ μm as a function of the distance D between the probe and the ruby (Figure taken from Ismail et al. [4])

5.3 Arrayed-Waveguide Gratings

The most important optical element for performing spectroscopy on a micro-chip is the integrated spectrometer. We have chosen to employ the arrayed-waveguide grating (AWG) [8]. Until now AWGs have been used for wavelength (de)multiplexing in telecommunication, offering high resolution over a small bandwidth [9]. Its working principle is schematically shown in Fig. 5.4a. Light from an input waveguide diverges in a first planar free propagation region (FPR) and illuminates the input facets of an array of channel waveguides. The channel waveguide array has a defined optical-path-length difference between adjacent channels. For a central wavelength λ_c, the phase difference at the output facets of adjacent array waveguides is an integer multiple of 2π. Since these facets are arranged on a circle, a cylindrical wavefront is formed at the beginning of a second FPR, which generates a focal spot at the central output channel. The phase shift caused by the length differences between arrayed waveguides is linearly dependent on wavelength, hence the resulting wavelength-dependent phase gradient implies a tilt of the cylindrical wavefront at the beginning of the second FPR. This causes the focal spot to shift with wavelength, i.e., different wavelengths are diffracted to different locations at the end of the FPR, at which either output channels or the pixels of a detector array can be positioned.
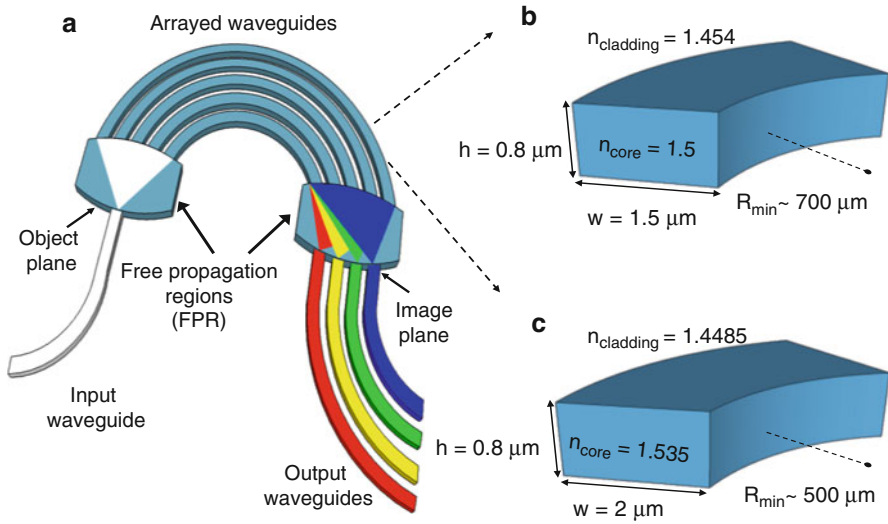
Fig. 5.4 (**a**) Schematic layout of an arrayed waveguide grating (AWG). Channel waveguide geometry for (**b**) an AWG with its central wavelength at 800 nm and (**c**) an AWG with its central wavelength at 1,300 nm (Figure taken from Akca et al. [10])

Compared to conventional spectrometers, the AWG has a small size ($\sim$cm^2) and can be integrated in a handheld device. Typical parameters of the individual waveguides for AWGs fabricated in SiON technology for the spectral ranges of 800 and 1,300 nm are displayed in Fig. 5.4c. A potential disadvantage of an AWG, the limited free spectral range (FSR) achievable for a given device size, can be overcome by a technology platform providing larger refractive index contrast, e.g. silicon photonics, or by accepting spectrally folded, yet non-overlapping peaks, as demonstrated in an example presented later in this chapter.

We described an improved AWG layout which applies identical bends across the entire array. In this way systematic phase errors arising from different bends that are inherent to conventional AWG designs are completely eliminated. In addition, for high-order AWGs our design resulted in more than 50% reduction of the occupied area on the wafer. A low-order device fabricated according to this geometry was experimentally characterized [11].

5.4 Confocal Light Delivery and Collection Using Arrayed-Waveguide Gratings

We invented a compact integrated optical device that combines the functions of light focusing, collection, and wavelength selection [12]. It makes use of two AWGs in a confocal arrangement. In its simplest design, displayed in Fig. 5.5, both AWGs
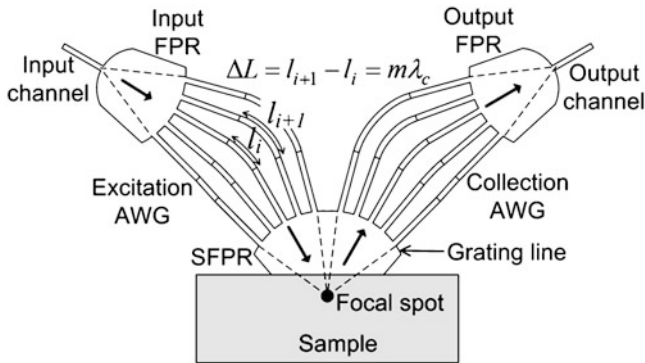
Fig. 5.5 Schematic of the confocal arrangement of two AWGs (with central wavelength λ_c and order m) which allows efficient illumination of, and signal collection from, a small focal volume below the sample surface (Figure taken from Ismail et al. [12])

have order $m = 0$, such that they form two lenses, the first one focusing a single excitation beam into the focal spot at a desired depth inside the sample and the second one collecting the light backscattered from this focal spot into a central output channel. In this arrangement the device behaves like a confocal microscope in one lateral direction. Enhanced functionality can be achieved without increasing device complexity by use of an AWG design exploiting the phase relation between the individual channels, thereby adding wavelength selectivity. As a result, the focusing AWG can have more than one input channel, allowing one to focus several excitation wavelengths into the same focal spot. Likewise, the collecting AWG can resolve different wavelengths emitted from the focal spot, thereby enabling spectral analysis of the backscattered light, if designed with the required wavelength spacing and FSR. In the particular case in which all excitation and signal wavelengths fall into the FSR of a single AWG, the same AWG can be used for both excitation and collection.

The focusing and collecting AWG are arranged in such a way that the output grating line – the interconnection line between the arrayed waveguides and the FPR – of the focusing AWG lies on the same circle and, hence, is concentric with the input grating line of the collecting AWG (Fig. 5.1). In this way the output FPR of the focusing AWG and the input FPR of the collecting AWG merge together, forming a single sample-side FPR. Ideally, its length is chosen such that when in contact with a sample the focal spot is located at the desired depth d below the sample surface (for a given sample refractive index n_S) in order to allow for maximum collection efficiency in the direction perpendicular to the device plane.

In our investigations, we focused on demonstrating that our approach improves the collection efficiency of signal light by more than an order of magnitude compared to standard light collection using a single-mode waveguide. Two similar AWGs were compared. The "reference" AWG is of a conventional design, having a single monomodal input channel for light collection and an AWG for spectral

Fig. 5.6 Input sections of (**a**) a "reference" (standard) AWG and (**b**) a "collector" AWG (the proposed device), both positioned at a distance d from a source S (Figure taken from Ismail et al. [12])
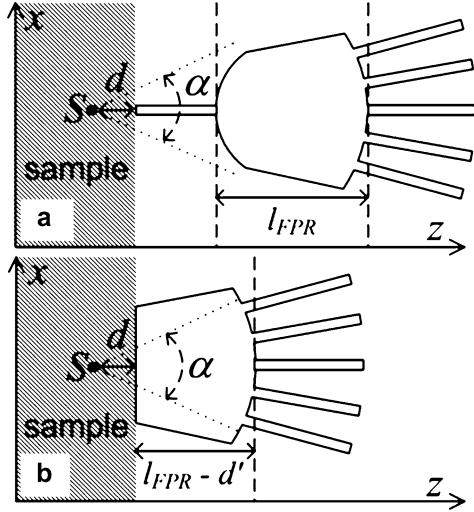
analysis with an input FPR of length l_{FPR}, see Fig. 5.6a. In contrast, the "collector" AWG is of the proposed design; see Fig. 5.6b. Its input FPR is shortened to a length $l_{SFPR} = l_{FPR} - d'$, where d' depends on the distance d of the input facet to the source (if n_S is equal to the effective index of the sample-side FPR, then $d' = d$).

As a source of signal light at point S we used light at a wavelength of 1284.6 nm emitted from either a standard 9-μm fiber with an angular aperture of $\alpha = 9.2°$ or an ultra-high-numerical-aperture fiber with $\alpha = 29°$, with air (refractive index $n_d = 1$) between source and device. Subsequently, index-matching liquid was placed between each fiber and the chip to reduce the angular aperture to $\alpha = 5.7°$ and 19.6°, respectively. The fiber output end was positioned at variable distance d from the chip. Firstly, we performed measurements with the reference AWG for all four α at varying distance d. Secondly, measurements were performed on the repeatedly diced collector AWG at four distances $d = 50, 100, 150,$ and $200\ \mu$m. The collector AWG was measured only with index-matching liquid ($\alpha = 5.7°$ and 19.6°) to average out the roughness of the diced facet. The measured output power of reference and collector AWG is shown in Fig. 5.7b, respectively, as a function of d. Furthermore, the collection efficiency of both devices was calculated as a function of d. Experiments and calculations show that, as d increases, all curves exhibit a monotonous decay which is steeper for the reference compared to the collector AWG, because light collection by the former is limited in both, horizontal and vertical directions by the cross-section of the input channel, while for the latter this limitation occurs only in the vertical direction. This difference results in higher collection efficiency of the collector AWG compared to the reference AWG. Finally, also multi-wavelength imaging was demonstrated utilizing this device [12].
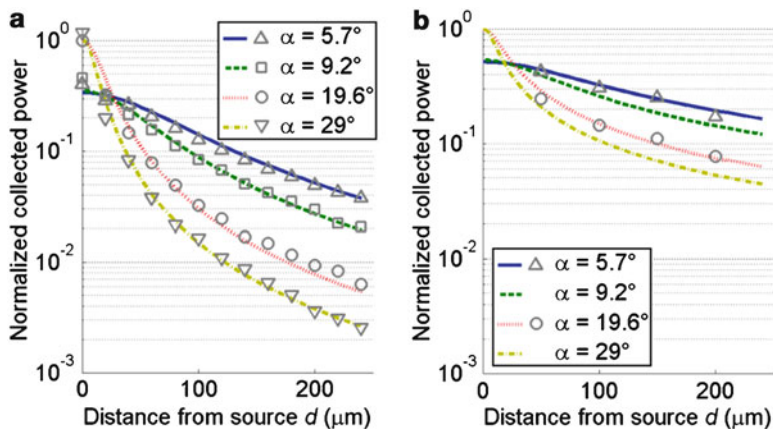
Fig. 5.7 Comparison of measured (*symbols*) and calculated (*lines*) power collected by (**a**) the reference AWG and (**b**) the collector AWG, normalized to the power collected by the reference AWG at $d = 0$ and $\alpha = 19.6°$, versus source-to-input facet distance d for different values of the source angular aperture α (Figure taken from Ismail et al. [12])

5.5 Integrated Raman Spectroscopy with an Arrayed-Waveguide Grating

In numerous applications, Raman spectroscopy is utilized to monitor unique ("fingerprint") Raman scattering in order to identify specific molecules or structures. We aimed at developing a low-cost, compact, hand-held apparatus for polarized Raman spectroscopy, specifically for the detection of dental caries at an early state [13]. A critical function of such a system is spectral separation of the Raman-scattered signals. In our case, the core element of such a device is an AWG.

We chose an excitation wavelength of $\lambda_0 = 830$ nm and designed the wavelength-selective AWG to have a central wavelength of $\lambda_c = 901$ nm and a FSR of ∼22 nm between 890 and 912 nm, with a resolution of 0.2 nm. The center-to-center spacing between the 271 arrayed waveguides at the FPR interface was 6 μm, and so was the spacing between the output channels of the AWG. From these parameters it is possible to calculate the dispersion angle of the AWG from well established equations [9], and determine the length R of the FPR (see inset to Fig. 5.8), which results in approximately 4 mm. The AWG layout was drawn by imposing a minimum bending radius of 1,700 μm to guarantee bending losses below 0.1 dB/cm when taking into account fabrication tolerances.

The setup used in the Raman experiments is shown in Fig. 5.1. Light from a linearly polarized, tunable Ti:Sapphire laser at 830 nm is sent through a polarization beam splitter (PBS) oriented parallel to the laser polarization. A half-wave plate is
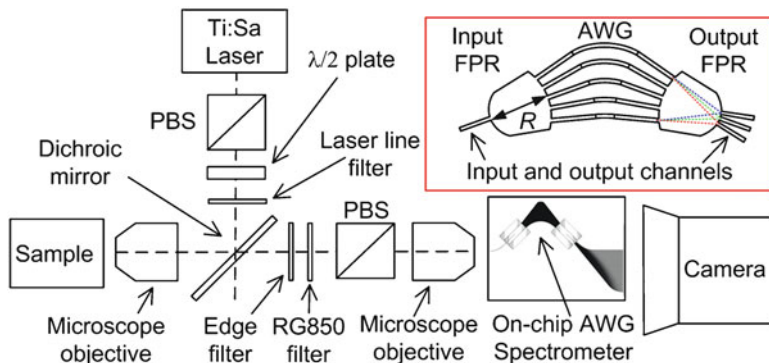
Fig. 5.8 Setup used for the polarized Raman experiments. *Inset*: schematic of arrayed waveguide grating (AWG) (Figure taken from Ismail et al. [14])

positioned after the PBS, initially with one of its optical axes parallel to the laser polarization, so that the polarization is not rotated. The laser light exiting the λ/2 plate, after passing through a laser-line filter, is reflected from a dichroic mirror and focused onto the sample with a microscope objective. The light backscattered from the sample is then collected by the same optics. The Rayleigh-scattered component is again reflected (rejected) by the dichroic mirror, which transmits the Raman-scattered wavelengths. An edge filter and an additional red-glass filter are used to further suppress residual reflected and Rayleigh-scattered light at the laser wavelength, that entering the AWG would be imaged at a higher order on the lateral output channels. At this point the light passes through another PBS with the same orientation as the first PBS, and is focused onto the input channel of the integrated AWG spectrometer by a microscope objective. The output channels of the AWG are imaged onto an electron-multiplying charge-coupled device (EMCCD) through a camera lens. In order to perform the measurements for perpendicular polarization, we rotate the λ/2 plate by ∼45°, so that the polarization of the excitation laser is rotated by 90°. In both, parallel and cross-polarization measurements light entering the AWG is always horizontally polarized (TE polarization with respect to the input waveguide).

We performed Raman measurements on cyclohexane [14]. The inset of Fig. 5.9 displays the unpolarized Raman spectrum of cyclohexane in the fingerprint region (400–1,600 cm^{-1}), as measured using a bulk Raman spectrometer (based on a Model 2,500 High Performance Raman Module, River Diagnostics B.V.). With the excitation wavelength of 830 nm, the Raman signals of cyclohexane occur in the wavelength range between 859 and 957 nm. Since this wavelength range exceeds almost fivefold the FSR of 22 nm (at the central wavelength λ_c) of our AWG, the different parts of the Raman spectrum fall into five different diffraction orders ($m = 39, 40, 41, 42,$ and 43) of the AWG, as indicated in the inset.
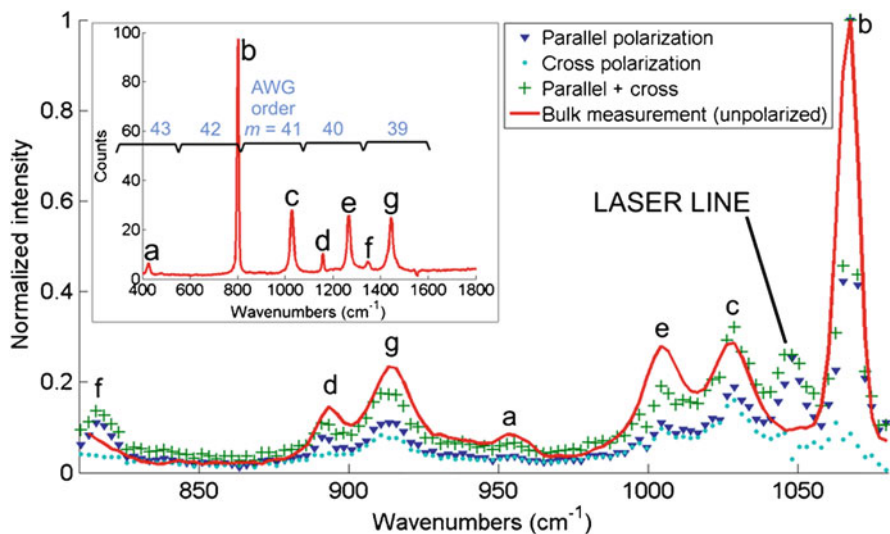
Fig. 5.9 Normalized Raman spectra of cyclohexane for parallel (*triangles*) and cross (*dots*) polarization, measured with the AWG spectrometer; normalized sum of the two spectra (*crosses*). Unpolarized Raman spectrum (*solid line*) measured with a conventional spectrometer, folded into diffraction order $m = 41$ of the AWG. *Inset*: original unfolded spectrum, extending over diffraction orders $m = 39$, 40, 41, 42, and 43 of the AWG. The individual Raman peaks in both, folded and unfolded spectrum, are assigned by letters (*a–g*). An additional peak at 1,050 cm^{-1} is attributed to the laser line imaged at a higher order ($m = 45$) (Figure taken from Ismail et al. [14])

The same Raman spectrum, with the different diffraction orders folded into the diffraction order $m_{AWG} = 41$, for which the AWG was designed, is calculated with the AWG grating equation [15] and shown as a red line in Fig. 5.9. The individual peaks in the original and folded spectrum are assigned by letters (a–g). Using our AWG spectrometer, polarized Raman signals were measured. Figure 5.9 shows the signals measured for parallel (triangles) and cross (dots) polarization, normalized to the intensity of peak b for parallel polarization. Comparison of the normalized sum of these two signals (green crosses) with the unpolarized spectrum (red line) of cyclohexane, as measured using the bulk spectrometer and folded into the diffraction order of the AWG, shows very good qualitative agreement: first of all, we observe the presence of strongly polarized Raman bands at the locations of peaks b and d, in agreement with the results found in the literature [16]. Furthermore, all the peaks of cyclohexane in the fingerprint region can be clearly distinguished. This test result demonstrates that a measurement with an AWG spectrometer can unambiguously identify the Raman fingerprint of a measurand, even if its Raman spectrum exceeds the FSR of the AWG, thus allowing us to design and apply an AWG with high spectral resolution. Furthermore, polarized Raman spectra were measured of extracted human teeth containing localized initial carious lesions [14].

5.6 Integrated Optical Coherence Tomography with an Arrayed-Waveguide Grating

Optical coherence tomography (OCT) [17] is a non-invasive optical technique for high-resolution cross-sectional imaging of biological tissue, with many applications in clinical medicine. The measurement principle of OCT is based on low-coherence interferometry (LCI) in which interference patterns due to the superposition of a multitude of waves with a large spread in wavelengths are studied. These distinctive patterns enable one to determine the location at which light is reflected back and to measure the depth profile of the scattering amplitude. By performing multiple LCI measurements at different lateral coordinates on a sample, a three-dimensional cross-sectional image of the scattering amplitude can be constructed.

Current state-of-the-art OCT systems operate in the Fourier-domain [18], using either a broad-band light source and a spectrometer, known as spectral-domain OCT (SD-OCT), or a rapidly tunable laser, known as swept-source OCT (SS-OCT), because they offer a significant sensitivity advantage over time-domain OCT. SD-OCT systems can utilize simple broadband sources, however they suffer from severe signal roll-off in depth and require complicated detection optics, i.e., linescan cameras and spectrometers. Current commercial SD-OCT systems typically achieve ∼5 µm axial resolution with ∼25–27 kHz axial scan rates over an imaging range of ∼2.0–2.6 mm. OCT systems contain a multitude of fiber and free-space optical components which make these instruments costly and bulky. The size and cost of an OCT system can be decreased significantly by the use of integrated optics. In addition, integrated optics can enhance the performance of OCT by, for example, parallelization [19, 20] of OCT devices on a chip.

A key component of an SD-OCT system is the high-resolution spectrometer. We employ the same type of AWG that we successfully used in Raman spectroscopy (Sect. 5.5). We investigated AWG spectrometers with high resolution and large FSR for the spectral ranges near 800 and 1,300 nm in interferometric depth ranging and OCT imaging, thereby demonstrating the first important step toward miniaturization of an SD-OCT system.

The essential parameters that determine the imaging quality of FD-OCT systems are center wavelength, axial resolution, maximum imaging depth, signal-to-noise ratio (SNR), and sensitivity roll-off in depth. The shorter center wavelength of 800 nm is used for imaging ophthalmic structures to avoid the water absorption losses dominant in this application, whereas for dermal imaging 1,300 nm is used to avoid the dominant scattering losses. The axial resolution of an SD-OCT system is determined by the effective bandwidth of the detected light, which depends on the bandwidth of the light source and the FSR of the spectrometer. Matching the FSR of the AWG with the bandwidth of the light source is the most economical configuration. The maximum imaging depth in SD-OCT is determined by the spectral sampling interval. The imaging range of SD-OCT is limited by the signal roll-off, which is the attenuation of the OCT signal due to washout of the interference fringe visibility with increasing depth. The roll-off in depth of
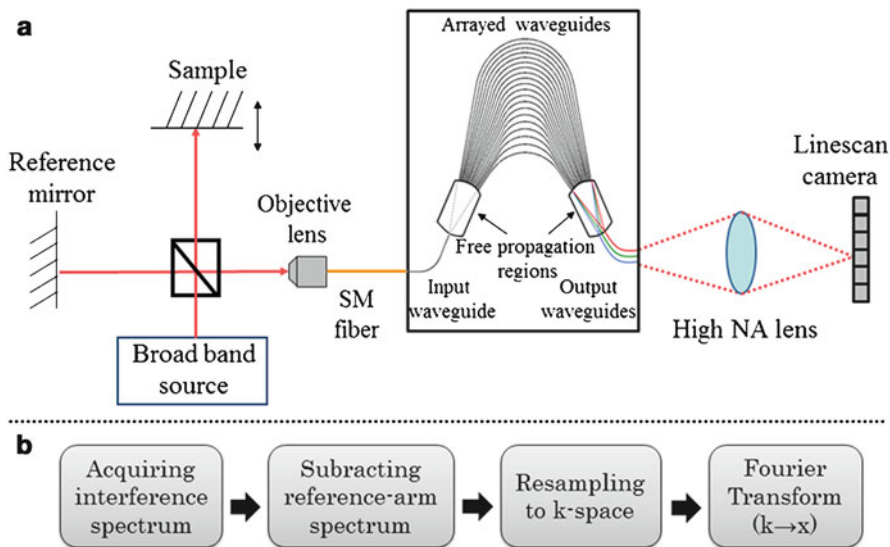
Fig. 5.10 (**a**) Optical measurement set-up of the SD-OCT system with free-space Michelson interferometer and integrated AWG spectrometer; (**b**) signal processing steps for SD-OCT (Figure taken from Akca et al. [10])

the SD-OCT signal is determined by the spectral content of the spectrometer and the camera pixel size. Finally, for maximum SNR, the spectrometer loss should be minimized in the design stage. Typical SNR values for high-quality OCT imaging are on the order of 100 dB. For more details, see [10].

A schematic of the SD-OCT system with integrated AWG spectrometer is shown in Fig. 5.10a. The measurement technique for the 800 and 1,300 nm spectral ranges is similar, except for the different specifications of the light source and the linescan camera. The free-space Michelson interferometer (MI) is illuminated with a superluminescent diode emitting a Gaussian-like spectrum. Light from the source is directed to the reference and sample arms by a 50:50 beam splitter. The reference mirror is kept stationary, while the sample mirror is moved during the experiments. Light returning from the two arms is focused by an objective lens into a single-mode fiber and directed to the AWG spectrometer. The output power of the MI is measured to be 0.1 and 0.9 mW for the 800 and 1,300 nm spectral ranges, respectively. In the AWG spectrometer, the optical spectrum is dispersed by the arrayed waveguides and imaged by a camera lens with high numerical aperture onto the camera. The acquired spectra are processed by subtracting the reference-arm spectrum and resampling to k-space, as indicated in Fig. 5.10b. The reflectivity depth profile is obtained by performing a Fourier transformation of the digitized camera output. The measured spectra have an absolute wavelength scale defined by the center wavelength and FSR value of the AWG.

The spectrum shown in Fig. 5.11a is the spectrum from the reference arm at 1,300 nm. The optical bandwidth of the spectrum is measured as 39 nm.

Fig. 5.11 Measured data for an 1,300-nm AWG: (**a**) Reference spectrum of the AWG spectrometer on the linescan camera. The *inset* shows the interference spectrum measured at 200 µm depth after background subtraction. (**b**) OCT signal as a function of depth for a mirror reflector and fit of the roll-off (*dashed line*). The maximum depth range is 1 mm. (**c**) OCT axial resolution (*solid circles*) in comparison with the theoretical axial resolution (*dashed line*) (Figure taken from Akca et al. [10])
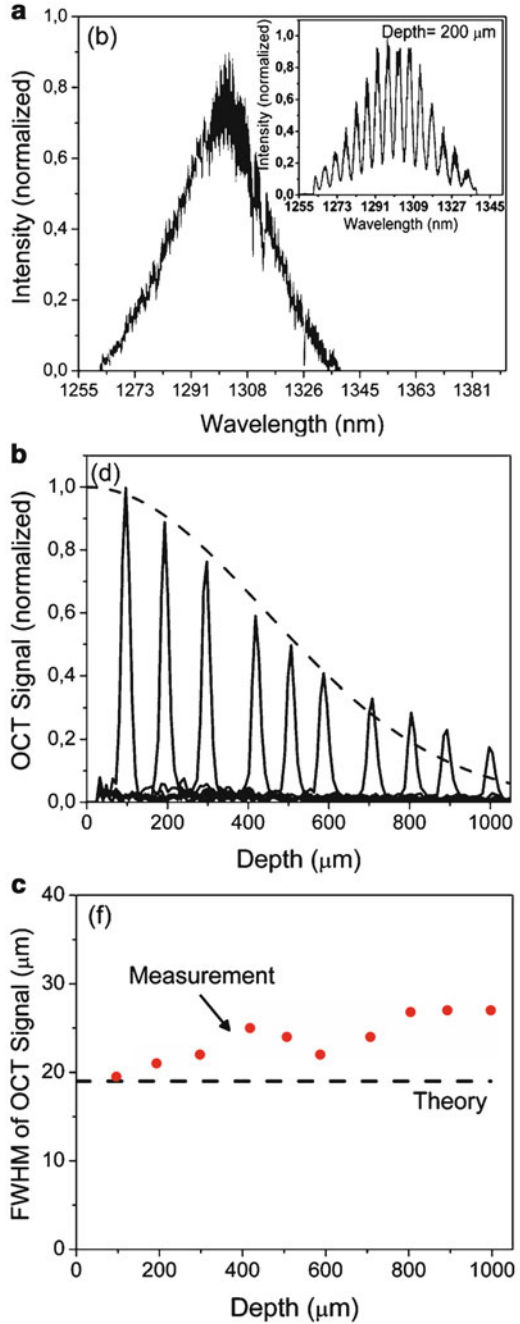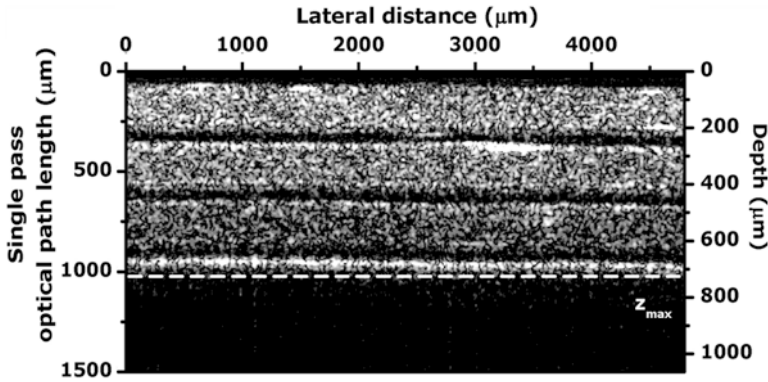
Fig. 5.12 OCT image of a three-layered scattering phantom measured with the AWG as spectrometer in SD-OCT. The *dashed line* indicates the maximum imaging depth (Figure taken from Nguyen et al. [22])

This value corresponds to an axial resolution of 19 μm. The inset shows the measured interference spectrum after background subtraction, measured at a depth of 200 μm. The modulation on the spectrum due to interference can be clearly observed. The OCT signals measured for different depths, i.e. for different path length differences between sample and reference arm of the MI, are shown in Fig. 5.11b. The depth scale corresponded one-to-one with the physical distance of the sample arm position change. We achieved imaging up to the maximum depth range of 1 mm. The measured signal-to-noise ratio (SNR) was 75 dB at 100 μm depth, which includes 10 dB fiber-to-chip coupling loss, 7 dB free-space interferometer loss, and 5 dB chip-to-camera coupling losses. By reducing losses and increasing the output power of the light source, the sensitivity of the SD-OCT system using an AWG spectrometer can be improved to the level of state-of-the-art OCT systems. The FWHM values of the point spread functions at various depths are plotted in Fig. 5.11c. An experimental axial resolution of 20 μm at 100 μm depth was obtained. A decrease in resolution was found at larger depths.

As a demonstration of OCT cross-sectional imaging using the AWG spectrometer, an image of a three-layered scattering phantom was obtained when using part of a fiber-based OCT set-up [21] with the AWG as spectrometer, see Fig. 5.12 [22]. As expected, all three scattering layers are observed up to the maximum single-pass optical path length of 1 mm (725 μm depth for the average refractive index of 1.38 of the phantom). The current imaging resolution and depth are sufficient for biological imaging but can be improved by increasing the FSR and the number of output channels.

Finally, the effect of discrete output channels and polarization dependency of an AWG spectrometer was investigated [23]. By removing the output waveguides of the AWG, the depth range was enhanced from 1 to 3.3 mm. In addition, the effect of polarization dependency of the AWG on sensitivity roll-off was investigated and, for

partial polarization, a beat effect was observed in the depth ranging measurements, which leads to signal fading at specific depths. By controlling the polarization state of the light carefully, the signal fading could be eliminated. A polarization-independent AWG was investigated, which eliminated without the use of extra components for polarization control.

5.7 Conclusions

Exploiting the spectral properties of AWGs, we have demonstrated confocal light delivery and collection as well as Raman spectroscopy and SD-OCT with the spectrometer integrated on a silicon chip. Integration of additional optical components onto the same micro-chip will enable low-cost mass fabrication of integrated optical instruments for various applications. Considerable size reduction of the optical structures, e.g. by exploiting plasmonic structures, could provide sufficient compatibility in lithography and processing for the combination of optical with electronic functions, e.g. signal processing, on the same chip.

References

1. Wörhoff K, Roeloffzen CGH, de Ridder RM, Driessen A, Lambeck PV (2007) Design and application of compact and highly tolerant polarization-independent waveguides. IEEE J Lightwave Technol 25:1276–1282
2. Wörhoff K, Klein EJ, Hussein MG, Driessen A (2008) Silicon oxynitride based photonics. In: Proceedings of the international conference on transparent optical networks, Athens, Greece, pp 266–269
3. Utzinger U, Richards-Kortum RR (2003) Fiber optic probes for biomedical optical spectroscopy. J Biomed Opt 8:121–147
4. Ismail N, Civitci F, Wörhoff K, de Ridder RM, Pollnau M, Driessen A (2011) Efficiency of integrated waveguide probes for the detection of light backscattered from weakly scattering media. Appl Opt 50:935–942
5. Ismail N, Sun F, Wörhoff K, Driessen A, de Ridder RM, Pollnau M (2011) Excitation and light collection from highly scattering media with integrated waveguides. IEEE Photon Technol Lett 23:278–280
6. Wörhoff K, Hilderink LTH, Driessen A, Lambeck PV (2002) Silicon oxynitride: a versatile material for integrated optics applications. J Electrochem Soc 149:85–91

 7. Caspers PJ, Lucassen GW, Carter EA, Bruining HA, Puppels GJ (2001) In vivo confocal Raman microspectroscopy of the skin: noninvasive determination of the molecular concentration profiles. J Invest Dermatol 116:434–442
 8. Smit MK (1988) New focusing and dispersive planar component based on an optical phased array. Electron Lett 24:87–88
 9. Smit MK, van Dam C (1996) PHASAR-based WDM-devices: principles, design and applications. J Sel Top Quantum Electron 2:236–250
10. Akca BI, Nguyen VD, Kalkman J, Ismail N, Sengo G, Sun F, Driessen A, van Leeuwen TG, Pollnau M, Wörhoff K, de Ridder RM (2012) Toward spectral-domain optical coherence tomography on a chip. IEEE J Sel Top Quantum Electron 18:1223–1233
11. Ismail N, Sun F, Sengo G, Wörhoff K, Driessen A, de Ridder RM, Pollnau M (2011) Improved arrayed-waveguide-grating layout avoiding systematic phase errors. Opt Express 19:8781–8794
12. Ismail N, Akca BI, Sun F, Wörhoff K, de Ridder RM, Pollnau M, Driessen A (2010) Integrated approach to laser delivery and confocal signal detection. Opt Lett 35:2741–2743
13. Ko CT, Choo-Smith LP, Hewko M, Sowa MG, Dong CCS, Cleghorn B (2006) Detection of early dental caries using polarized Raman spectroscopy. Opt Express 14:203–215
14. Ismail N, Choo-Smith LP, Wörhoff K, Driessen A, Baclig AC, Caspers PJ, Puppels GJ, de Ridder RM, Pollnau M (2011) Raman spectroscopy with an integrated arrayed-waveguide grating. Opt Lett 36:4629–4631
15. Takahashi H, Oda K, Toba H, Inoue Y (1995) Transmission characteristics of arrayed waveguide N × N wavelength multiplexer. J Lightwave Technol 13:447–455
16. Pelletier MJ (1999) Effects of temperature on cyclohexane Raman bands. Appl Spectrosc 53:1087–1096
17. Huang D, Swanson EA, Lin CP, Schuman JS, Stinson WG, Chang W, Hee MR, Flotte T, Gregory K, Puliafito CA, Fugimioto JG (1991) Optical coherence tomography. Science 254:1178–1881
18. Fercher AF, Hitzenberger CK, Kamp G, Elzaiat SY (1995) Measurement of intraocular distances by backscattering spectral interferometry. Opt Commun 117:3–48
19. Bourquin S, Seitz P, Salathé RP (2001) Optical coherence tomography based on a two-dimensional smart detector array. Opt Lett 26:512–514
20. Bourquin S, Laversenne L, Rivier S, Lasser T, Salathé RP, Pollnau M, Grivas C, Shepherd DP, Eason RW (2005) Parallel broadband fluorescent light source for optical coherence tomography. In: Proceedings of the SPIE, coherence domain optical methods and optical coherence tomography in biomedicine IX, vol 5690. San Jose, CA, USA, pp 209–213
21. Kalkman J, Bykov AV, Faber DJ, van Leeuwen TG (2010) Multiple and dependent scattering effects in Doppler optical coherence tomography. Opt Express 18:3883–3892
22. Nguyen VD, Akca BI, Wörhoff K, de Ridder RM, Pollnau M, van Leeuwen TG, Kalkman J (2011) Spectral domain optical coherence tomography imaging with an integrated optics spectrometer. Opt Lett 36:1293–1295
23. Akca BI, Chang L, Sengo G, Wörhoff K, de Ridder RM, Pollnau M (2011) Performance improvement of spectral-domain optical low-coherence reflectometry using an arrayed-waveguide grating, submitted

6
Introduction to Fluorescence Spectroscopy with Applications to Biological Systems

Baldassare Di Bartolo

Abstract Optical technologies can provide novel opportunities and tools for the life sciences. In turn, biological applications continue to stimulate novel optical technologies. The purpose of this article is to present several applications to biological systems of the techniques of fluorescence spectroscopy. This presentation is divided into seven parts. In the first part we review the fundamental principles of fluorescence spectroscopy, starting with the consideration of fluorophores and of the characteristics of fluorescence spectroscopy. The techniques that produce absorption spectra, excitation spectra, fluorescence under continuous excitation and response to pulsed excitation are also examined. In the second part we present the technique of Fluorescence Anisotropy together with the information it can provide. In the third part we present the technique of Fluorescence Resonance Energy Transfer (FRET) and its applications to distance-distribution analysis in biological systems. In the fourth part we deal with the excitation of fluorescent systems by multiple photons and present its advantage in some instances over the one-photon excitation. In the fifth part we present the technique of fluorescence correlation spectroscopy and we show how it may provide information regarding concentration and diffusion of fluorescent molecules. The sixth part deals with single molecule detection whose application may avoid ensemble averaging. The final part deals with the tools that may increase the quantum efficiency and radiative emission rate by placing emitting fluorophores close to metals. We offer some conclusions at the end.

B. Di Bartolo (✉)
Department of Physics, Boston College, Chestnut Hill, MA 02467, USA
e-mail: dibartob@bc.edu

6.1 Introduction to Fluorescence

6.1.1 Fluorescence and Phosphorescence

Luminescence is the spontaneous emission of light from excited electronic states of physical systems.

The emission is preceded by the process of *excitation*, which may be produced by a variety of agents. If it is achieved by the absorption of light it is called *photoluminescence*, if by the action of an electric field *electroluminescence*, if by a chemical reaction *chemiluminescence*, and so on.

Following the excitation, if the system is left alone, without any additional influence from the exciting agent, it will emit spontaneously.

Even in absolute vacuum an excited atom, devoid of any external influence, will emit a photon and return to its ground state. The spontaneity of the emission presents a conceptual problem. A tenet of physical science, expressed by the so-called *fluctuation-dissipation* theorem sets forth the fact that any dissipation of energy from a system is the effect of its interaction with some external entity that provides the perturbation necessary for the onset of the process. Such an entity seems to be missing in the case of an isolated atom. If we hold a classical view of natural phenomena, we cannot explain the presence of spontaneous emission.

In the quantum world things are very different. The harmonic radiative oscillators that populate the vacuum and that classically hold no energy when in their ground state, have each in this state energy $\frac{1}{2}h\nu$ and may produce a fluctuating electric field at the site of the atom, setting the perturbation necessary for the onset of spontaneous emission.

Luminescence is divided into two categories: *fluorescence* and *phosphorescence*, depending on the nature of the excited state. For most organic molecules in their ground state, the highest occupied molecular orbital is a singlet and is the seat of two electrons. The spins of these electrons are antiparallel resulting in a singlet for the ground state.

The excitation of an electron from the ground state orbital to an upper orbital results in the formation of two states,

– a singlet in which the electron in the excited orbital is paired by opposite sign to the electron in the ground state orbital and
– a triplet, lower in energy than the singlet, in which the electron in the excited orbital and the electron in the ground state orbital have parallel spin.

The decay of an excited state singlet to the ground state singlet is spin allowed and occurs by the rapid emission of a photon. Such an emission is called *fluorescence*; it has typical rates of 10^8 s^{-1}. The average time between excitation and return to the ground state is then 10^{-8} s $= 10$ ns (in 1 ns light travels 30 cm).

The systems that exhibit fluorescence are called *fluorophores* [1]. Several fluorophores have lifetimes shorter than 10 ns.
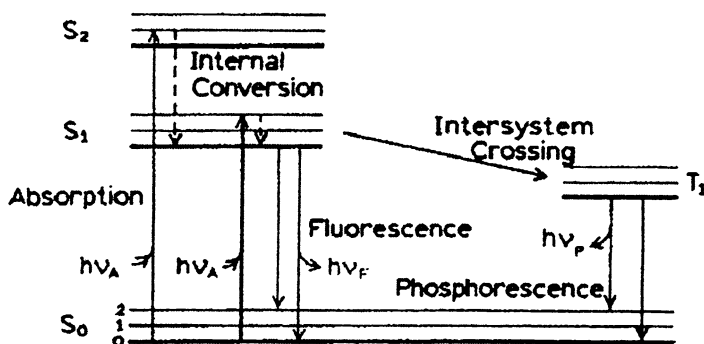
Fig. 6.1 The Jablonski Diagram

Two types of measurements are generally used, the *steady-state fluorescence* and the *time-resolved fluorescence*. Due to the short lifetimes, time-resolved measurements require sophisticated optics and electronics; they provide, however, additional important information.

The emission of light from triplet excited states is called *phosphorescence*. It is related to forbidden transitions, because of the difference in the spins of the electron in the excited orbital and of the electron in the ground state orbital; its rates are typically 10^3–1 s^{-1}, so that phosphorescence lifetimes are typically milliseconds to seconds. On account of this long radiative lifetime phosphorescence is not usually seen in fluid solutions at room temperature: various deactivation processes such as non-radiative decay and quenching processes compete successfully with the radiative decay of the triplet state.

Aromatic molecules, the stable molecules with rings of atoms, are typically fluorophores. Among them quinine, a substance present in quinine water, when exposed to ultraviolet light from the sun, emits light with wavelength close to 450 nm. *John Frederick William Herschel* first reported this process in 1845 in an article titled "on a case of superficial colour presented by a homogeneous liquid internally colourless" [2].

6.1.2 *Timescale of Molecular Processes in Solution*

Once an excited system decides to undergo a transition, the ensuing process is instantaneous. This is the reason why in the *Jablonski diagram* the transitions are indicated as vertical lines [3]. (See Fig. 6.1.)

Transitions actually occur in 10^{-15} s and during this time the nuclei do not undergo significant displacements: this statement expresses the *Franck-Condon Principle*.

The difference between fluorescence and absorption is that the latter is an induced process and the former is a spontaneous process. Even if the actual transition, once started, takes place instantaneously, molecules in an excited state remain in such a state in a time whose average length is the *fluorescence lifetime*.

The lifetime provides an expansion of time and distance that allows the excited molecule to interact with other molecules in solution. For this reason, while the absorption measurements are sensitive only to the immediate and instantaneously averaged environment of the fluorophore, fluorescence measurements may provide information about such dynamical processes as collisional quenching, and vibrational or solution relaxation.

6.1.3 Basic Rules and Measurements of Fluorescence Spectroscopy

It is appropriate at this point to recount the basic rules of fluorescence:

1. The *Franck-Condon Principle*: the nuclei are stationary during the electronic transitions, and, for this reason, excitation occurs to vibrationally excited levels of the excited electronic state.
2. *Kasha's rule*: fluorescence emission occurs generally from the lowest excited singlet state [4].
3. The *Stokes shift*: emission is always of lower energy than absorption due to the nuclear relaxation in the excited state [5].
4. The *mirror image rule*: emission spectra are mirror images of the lowest absorption band.

The basic measurements related to fluorescence are:

1. *Absorption*: these measurements are mainly used to set the energy level scheme.
2. *Steady state fluorescence*: the steady state spectra are used to identify the fluorescent state(s).
3. *Excitation spectra*: these spectra tell us in what spectral region we have to pump the system in order to obtain the emission that is being monitored.
4. *Response to pulsed excitation*: the decay constant τ of an exponentially decaying fluorescence signal is the lifetime of the state from which the transition originates. Deviation of the decay pattern from exponentiality may indicate the presence of other processes such as energy transfer.

In addition to the above, we want to point out some of the relevant information that can be derived from particular techniques.

1. *Emission spectra and Stokes shift*: the shifts between absorption and fluorescence wavelengths are most effective for measuring the interaction of a fluorophore with its immediate surroundings. An important property of many fluorophores is their sensitivity to their immediate environment.

2. *Quenching of fluorescence*: a number of molecular interactions can result in the quenching of fluorescence: excited state reactions, molecular rearrangements, energy transfer, ground state complex formation, and collisional quenching. Fluorescence quenching is studied both as fundamental phenomenon and as a source of information regarding biochemical systems. These biochemical applications are due to the molecular interactions that produce the quenching. Quenching studies can be used to reveal the localization of fluorophores in proteins and membranes, and their permeability to quenchers. Also, the rate of collisional quenching can be used to measure the diffusion coefficient of the quencher.

6.2 Fluorescence Anisotropy

6.2.1 The Process of Fluorescence Anisotropy

Fluorophores absorb light along a particular direction with respect to the molecular axes. The extent to which a fluorophore rotates during its excited state lifetime determines its polarization and anisotropy.

Measurements of anisotropy of light emitted by fluorescent molecules are used in biochemical applications and provide information on the size and shape of proteins or the rigidity of the molecular environment.

The basic idea of fluorescence anisotropy is that a fluorescent molecule excited by polarized light will emit polarized fluorescence. However, if the molecule is moving, it will tend to scramble the polarization of light depending on the rotational diffusion (see Fig. 6.2).

Rotational diffusion is a process by which the overall orientation of molecules is maintained or restored. It represents the counterpart of translational diffusion, which maintains or restores the equilibrium statistical distribution of the particles' position in space.

In the random re-orientation process, because of the equipartition theorem, larger molecules re-orient more slowly than small molecules, and, for this reason, measurements of the re-orientation times can provide information regarding the mass and distribution of mass within a molecular complex.

The scrambling effect is greatest with fluorophores freely tumbling in solution. Protein interactions can be detected when one interacting protein is fused to a fluorophore: upon binding of this protein to another protein, a larger, more stable complex is formed, which will tumble more slowly and will increase the polarization of the emitted light.

The technique of fluorescence anisotropy works best if the fluorophore is fused to a small molecule and binds to a large partner, thus maximizing the difference in polarization between bound and unbound states.
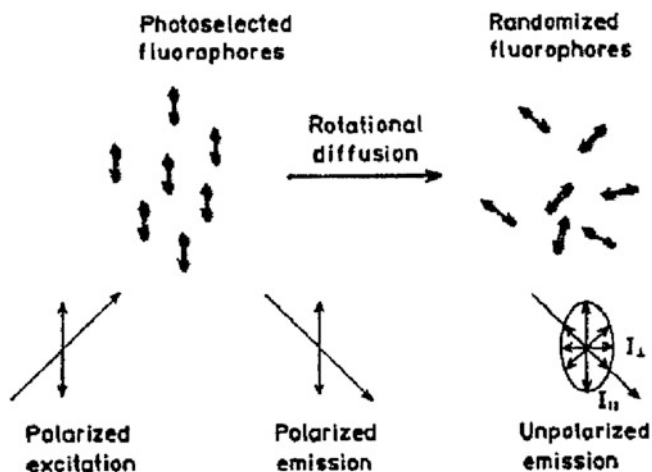
Fig. 6.2 Effects of polarized excitation and rotational diffusion on the polarization or anisotropy of the emission

6.2.2 Fluorescence Under Continuous and Pulsed Excitation

Under continuous excitation a sample is illuminated by a continuous beam of light and the intensity of the emitted light is recorded versus the wavelength. Because of the nanosecond time scale of fluorescence, steady state is reached almost immediately after the sample has been exposed to light.

Under pulsed excitation the sample is exposed to a light pulse whose width is typically shorter than the decay time. The decaying fluorescence intensity is recorded with a high-speed detection system that may measure the intensity or anisotropy on a time scale.

We shall now consider the relation between steady state and time-resolved measurements. The steady-state observation is an average of a time-resolved parameter over the intensity decay of the signal.

The intensity and anisotropy decay are given by the two relations:

$$I(t) = I_0 e^{-t/\tau} \tag{6.1}$$

$$r(t) = r_0 e^{-t/\theta} \tag{6.2}$$

where I_0 and r_0 are the intensity and anisotropy at time $t = 0$, following immediately the exciting pulse, respectively. τ is the lifetime of the fluorescent state and θ is the *rotational correlation time* of the fluorophore, a parameter that describes how fast a molecule tumbles in solution and is given by

$$\theta = \eta V / RT \tag{6.3}$$

where η = viscosity, V = volume of the rotating unit, R = gas constant and T = temperature in K.

The steady state anisotropy is given by the time average of r(t) weighed by I(t):

$$r = \int_0^\infty r(t)I(t)dt \Big/ \int_0^\infty I(t)dt = r_0/(1 + \tau/\theta) \tag{6.4}$$

The above formula is known as *Perrin equation* [6].

If the correlation time is much shorter than the lifetime ($\theta \ll \tau$) the anisotropy is zero and the molecules will randomize in solution during the emission and, as a result, the emitted light of the fluorophore will be depolarized. If the correlation time is much larger than the lifetime ($\theta \gg \tau$), then the measured anisotropy is equal to the fundamental anisotropy r_0 and the excited molecules will stay aligned during the process of emission and, as a result, the emission will be polarized.

We note also the simpler relation of the steady state intensity to the decay time:

$$I_{ss} = \int_0^\infty I_0\ e^{-t/\tau}\ dt = I_0\tau \tag{6.5}$$

I_0 is a parameter that depends on the fluorophore concentration and on a number of instrumental parameters.

It is appropriate to note that, despite the above relations tying the steady state to time-resolved parameters, much of the molecular information available from fluorescence is lost during the time averaging process. For this reason, pulse-excited fluorescence ends up providing additional data.

The precise shape of the anisotropy decay, lost during the averaging process over the decay time, may contain information about the shape of the molecule and its flexibility.

The precise shape of the intensity decay contains also information lost during the averaging process. Macromolecules may exist in more than one conformation and the decay pattern of a probe bound to such a molecule could depend on the conformation. The shape of excited donor decay may provide information regarding the distribution of acceptors around the donor. Time-resolved measurements may also provide information regarding the quenching processes.

6.3 Fluorescence Resonance Energy Transfer (FRET)

6.3.1 Resonance Energy Transfer

The process of resonance energy transfer (RET) takes place in the excited state of a fluorophore. It occurs whenever the emission spectrum of a fluorophore called the *donor* overlaps with the absorption spectrum of another molecule called the *acceptor*.

Energy transfer takes place via dipole-dipole interaction and without the intervention of photons. For this process the expression fluorescence resonance energy transfer (FRET) is also commonly used.

The rate of energy transfer is determined by the distance between donor and acceptor and by the extent of the spectral overlap. This overlap is described in terms of the so-called *Förster distance* (R_0) [7]. The rate of energy transfer is given by

$$w_T(R) = 1/\tau_D \left(R_0{}^6/R^6\right) \tag{6.6}$$

where R = distance between donor (D) and acceptor (A), and τ_D = lifetime of the donor in the absence of the acceptor.

The efficiency of the energy transfer process is given by the fraction of photons absorbed by the donor whose energy is transferred to the acceptor:

$$E = w_T(R) \big/ \left[\tau_D{}^{-1} + w_T(R)\right] \tag{6.7}$$

This expression represents the ratio of the transfer rate to the total decay rate of the donor in the presence of the acceptor. Taking into account the formula for wT(R) the expression for E becomes

$$E = R_0{}^6 \big/ \left[R_0{}^6 + R^6\right] \tag{6.8}$$

The extent of the energy transfer depends on the distance R.

Conveniently the Förster distances are of the same size of biological molecules: 30–60 Å. Therefore in principle energy transfer can be used as a ruler for measurements of distances between sites in proteins.

6.3.2 The Uses of Fret in Biology

The usage of FRET provides a rather unique chance to observe previously inaccessible physical phenomena related to the arrangement and separation of molecules in solution and in solids on a molecular scale [1, 8].

Particularly useful is found the possibility of measuring directly the molecular separation between two molecules Donor (D) and Acceptor (A), counting on the strong dependence of the rate and efficiency of energy transfer on the sixth power of the D-A distance.

The usage of FRET has expanded considerably since the early 1950s, with its applications to such various fields as physics, chemistry, biology and polymer science. However its greatest usage has been with biological macromolecules.

Biological systems are complex molecular entities involving macromolecules (e.g. proteins, nucleic acid, polymers, fatty acids, lipids, and poly-carbohydrates) that associate to form supramolecular structures e.g. multi-protein assemblies, membranes, chromosomes, that, in turn, comprise living cells and their respective parts.

All biological systems in general present intricate and interdependent organization in their various structures. In order to understand and manipulate the functions of biological systems, it is necessary to study the structures of their components and to determine how these components are associated into larger molecular organizations.

FRET is unique in its capacity to supply accurate spatial information about molecular structures at distances ranging from 10 to 100 Å. In many cases geometrical information can also be obtained.

FRET is observed only if D and A are in proximity ($R < 2R_0$). This possibility of detecting and quantifying molecular proximities has led to numerous applications of FRET to biology over the past 30 years and continues to generate much of the present interest in the subject.

6.3.3   A Summary of Fluorescence Resonance Energy Transfer

6.3.3.1   General Characteristics

1. The distance at which FRET is 50% efficient is called the *Förster distance*, and is typically in the range 20–60 Å.
2. The *rate of energy transfer from a D to an A* in the case of dipole-dipole interaction is given by

$$w_{DA}(R) = 1/\tau_D (R_0/R)^6 \tag{6.9}$$

   When $R = R_0$, $w_{DA}(R_0) = 1/\tau_D$.
3. The value of R_0 can be reliably predicted from the knowledge of the spectral properties of donors and acceptors and of the orientation factor.
4. FRET is a through-space interaction that is mostly independent of intervening solvent and/or micromolecules.
5. FRET does not involve emission and re-absorption of photons.
6. FRET contains molecular information that is different from that revealed by solvent relaxation, excited state reactions, fluorescence quenching or fluorescence anisotropy. These fluorescence phenomena depend on interactions of the fluorophore with other molecules in the surrounding solvent shell.

FRET is effective over much longer distances, and the intervening solvent or macromolecule has little effect on the efficiency of the process that depends primarily on R.

6.3.3.2   The Orientation Factor

Biological systems encountered in fluorescence spectroscopy are usually complex objects consisting of supramolecular structures and large organizations of molecular components.
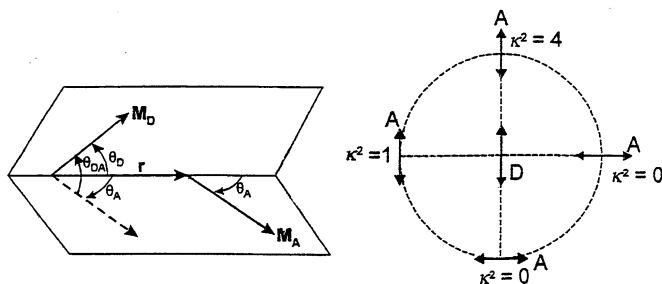
Fig. 6.3 (*Left*) angles that define the orientation factor K^2 and (*right*) examples of various situations and related values of K^2

Spectroscopic probes that interact with biological material are often oriented and undergo less rotational motion than they do in less organized surroundings.

The proximity of immobilized molecular species leads to directional interactions between neighboring molecules, and the mutual orientation of closed spaced D and A molecules affects the effect of FRET through the variations of an *orientation factor*, called K^2.

One must be careful in quantitatively interpreting FRET measurements made on highly structured biological samples. The orientation factor K^2 is often considered the limiting factor for estimating accurate D-A distances from FRET data. K^2 can vary from 0 to 4 although its actual values rarely, if ever, extend over this total range.

In general we do not have sufficient information (often none at all) regarding D-A orientations and approximations must be made. The D and A fluorescence anisotropy values, and consequently the range of K^2 values, depend on the extent to which D and A rotate while D is in its excited state.

6.3.3.3 Calculation of the Orientation Factor

The magnitude of the time-dependent field strength of an oscillating dipole in the near-field zone is identical to that of a static dipole.

The electric interaction between two static electric dipoles is a dot product between the dipole moment of one dipole with the electric field of the other, and K is the factor describing the relative orientation.

No generality is lost by discussing K in terms of classical static dipoles. The rate of energy transfer w_{DA} is proportional to K^2 because w_{DA} is proportional to the square of the interaction energy between D and A.

Considering the angles that define the orientation factor K in Fig. 6.3, K^2 is given by

$$K^2 = (\cos \theta_{DA} - 3 \; \cos \theta_D \cos \theta_A)^2 \tag{6.10}$$

θ_{DA} is the angle between the emission transition dipole of the donor M_D and the absorption transition dipole of the acceptor M_A.

Experimental results show that the value of K^2 affects the rate of energy transfer.

When sufficient orientation information is lacking, the assumption is made that $<K^2> = 2/3$, a value corresponding to an average made when both D and A are randomly oriented.

6.3.4 Energy Transfer in Solution

Energy transfer may take place for donors and acceptors randomly distributed in three-dimensional solutions.

The rate of transfer in the case of dipole-dipole interaction is given by:

$$w_{DA}(R) = 1/\tau_D (R_0/R)^6 \qquad (6.11)$$

R_0 is now related not only to the overlap integral and to the quantum efficiency of the donor, but also to the orientation factor: it is proportional to $(K^2)1/6$.

The response of the donor to pulsed excitation is given by the formula [3–10]

$$\bar{\rho}(t) = \exp\left(-t/\tau_D - c_A/c_0 \sqrt{\pi\, t}/\tau_D\right)^{1/2} \qquad (6.12)$$

where c_A = concentration of acceptors and $c_o^{-1} = 4\pi/3R_0^3$.

6.3.5 Distance Distributions

Up to this point we have considered two situations:

1. The donor and the acceptor are at a fixed distance R.

   In this case the pattern of donor's decay is exponential with a time constant given by

   $$\tau_{DA} = 1/\tau_D + w_{DA}(R) \qquad (6.13)$$

   with $w_{DA}(R) = 1/\tau_D (R_0/R)^6$.

   The assumption of a single D-A distance R allows the calculation of R from the quantum yield of the donor in the presence of the acceptor.

2. The distribution of D-A distances is uniform in a volume V of a solution:

   $$w_{DA}(R) = 1/V \qquad (6.14)$$

We shall now consider the case of flexible D-A pairs, i. e. the case when the range of D-A distances can be expressed by a probability distribution. Some of the D-A pairs are closely spaced and display shorter decay times, and other D-A pairs are further apart and display longer decay times.

The range of distances results in a range of decay times, so that the decay pattern becomes more complex than a single exponential.

The goal of most distance distribution studies is to recover the D-A probability distribution from the non-exponential pattern of the donor. This pattern is the summation of the intensity decays for all accessible distances:

$$I_{DA}(t) = \int_{o}^{\infty} w(R) \exp\left[-t/\tau_D - 1/\tau_D(R_o/R)^6\right] dR \qquad (6.15)$$

The response of the donors to a pulsed excitation is given in the form of an integral that represented the weighted average of the decays for all D-A distances.

The task of the researcher is to try to recover the probability distribution $w(R)$ from the decay pattern of the donor system.

6.3.6   Effect of Diffusion on Linked D-A Pairs

In the preceding sections we have considered donors and acceptors to be static in space and to remain at the same distance during the donor lifetime. However, depending on the donor lifetime and the mutual diffusion coefficient

$$D = D_D + D_A \qquad (6.16)$$

there can be changes in the linked D-A distances during the donor lifetime. It is found that, as diffusion increases, the patterns of donors' decay become more rapid, indicating a more rapid energy transfer.

This seems surprising, since one would think that diffusion is just as likely to move donors and acceptors apart, as it is likely to bring them closely together.

A deeper understanding of diffusion and FRET can be obtained by pondering the following considerations:

1. The distance dependence of $w_{DA}(R)$ causes the more closely spaced D-A pairs to transfer more rapidly.
2. For rapid D-A diffusion the population of D-A at shorter distance is replenished by diffusion and the closely spaced D-A pairs by diffusion result in increased energy transfer with increased rates of diffusion.

6.3.7   Effect of Diffusion on Unlinked D-A Pairs

The theory of energy transfer for unlinked D-A pairs in the presence of diffusion is very complex. No general expression for the decay pattern of the donor system in this situation has been found. However, an expression for this pattern has been obtained by Yokota and Tanimoto [11] for the case, of interest here, of dipole-dipole interaction:

$$\phi(t) = \exp\left\{\left(-t/\tau_D - c_A/c_o\sqrt{\tau}t/\tau_D\right)^{1/2}\left[(1+10.86x+15.5x^2)/(1+8.743x)\right]^{3/4}\right\}$$

(6.17)

For $D = 0$ this formula becomes equivalent to the formula (6.12).

6.4   Multi-photon Excitation

6.4.1   Basic Principles

The usual mode of excitation of a fluorescent system is by a single photon with wavelength within the absorption band of the system. In such a case the intensity of the fluorescence emission is generally proportional to the intensity of the light absorbed.

Multiphoton excitation has become practically possible with the introduction in the laboratory of sharp-pulsed lasers that may concentrate a high intensity of radiation in a few femtoseconds. This high intensity may ensure the simultaneous absorption of two or more long wavelength photons.

The selection rules for two-photon absorption transitions are different than those for one-photon transitions; this difference may provide information regarding the symmetry of the excited states of the system.

6.4.2   Applications of Multi-photon Excitation

The two-photon excited fluorescence is used to produce an imaging technique known as two-photon fluorescence spectroscopy (TP2).

A fluorophore placed at a specific location is excited by two photons with energy $h\nu_1$ and emits a single photon of energy $h\nu_2 > h\nu_1$ which is then detected. The rate of the two-photon absorption is proportional to the square of the exciting radiation intensity [12].

This dependence of the two-photon absorption on intensity represents an advantage of TP2. If a beam is focused the two-photon absorption takes place in the focus region allowing for greater resolution. The emission takes place at a spot within the sample and fluorophores outside the focal volume are not excited, so that the background light or out of focus fluorescence is strongly reduced.

The two-photon absorption process presents an additional advantage when used to investigate biological systems since longer wavelengths can penetrate more deeply in biological tissues. To ensure that the exciting radiation will not damage the tissues, the femtosecond pulses of a mode-locked laser with high pulse intensity but low average energy may be used.

Multi-photon fluorescence spectroscopy (TPk) operates in the same fashion except that in this case the rate of the emitted fluorescence is proportional to the kth power of the intensity.

6.5   Fluorescence Correlation Spectroscopy

6.5.1   Basic Principles

The basic idea of Fluorescence Correlation Spectroscopy (FCS) resides in a measuring system that may excite and detect the fluorescence of molecules in solution in a very small volume, called *volume of detection*.

Molecules will enter and leave this volume randomly and the fluorescence signal, proportional to the number of molecules in the volume, will fluctuate in time.

The theory of FCS is based on the Poisson distribution that governs the number of molecules present at any time in the volume of detection. According to this distribution the following expression

$$p(n, \bar{n}) = \frac{(\bar{n})^n}{n!} e^{-\bar{n}} \tag{6.18}$$

represents the probability that n fluorophores are present in the volume of detection when the average number of molecules in this volume is $\bar{n}$.

The fluctuations observed in the volume are smaller if the average number in the volume is high. This can be seen from the following considerations.

In a Poisson distribution the variance is equal to the average value:

$$\sigma^2 = \bar{n^2} - (\bar{n})^2 = \bar{n} \tag{6.19}$$

The root mean square fluctuation of the particle number is given by

$$\frac{\sqrt{(n - \bar{n})^2}}{\bar{n}} = \frac{\sigma}{\bar{n}} = \frac{1}{\sqrt{\bar{n}}} \tag{6.20}$$

The fluctuations in the occupation number of fluorescent molecules in the volume of detection are reflected in the changes of the fluorescence intensity.

If we assume a constant exciting power, the fluctuations of the fluorescence signal are defined as follows

$$\delta F(t) = \overline{F(t)} - F(t) \tag{6.21}$$

where

$$\overline{F(t)} = \frac{1}{T} \int_0^T F(t)dt \tag{6.22}$$

The time-varying fluorescence signal is correlated with a time-shifted replica of itself whose value depends on the time shift τ. A measure of this correlation is represented by the autocorrelation function

$$R(\tau) = \overline{F(t)F(t+\tau)} = \frac{1}{T} \int_0^T F(t)F(t+\tau) \tag{6.23}$$

where $T = $ time of the accumulation of data.

$R(\tau)$ represents a measure of the probability to detect the present signal taken at time t after a period τ of time.

We note that

$$R(0) = \overline{[F(t)]^2} = \text{second moment} \tag{6.24}$$

$$R(\infty) = \left[\overline{F(t)}\right]^2 \tag{6.25}$$

$$R(0) - R(\infty)\overline{[F(t)]^2} - \left[\overline{F(t)}\right]^2$$
$$= \text{variance of the signal distribution} \tag{6.26}$$

The autocorrelation function can be expressed as follows:

$$R(\tau) = \overline{F(t)F(t+\tau)} = \overline{\left[\overline{F} - \delta(t)\right]\left[\overline{F} - \delta(t+\tau)\right]} =$$
$$= (\overline{F})^2 + \overline{\delta F(t)\delta F(t+\tau)} = (\overline{F})^2 + \overline{\delta F(0)\delta F(\tau)} \tag{6.27}$$

assuming the stationarity of the process. Normalizing this function to the average intensity squared we obtain

$$r(\tau) = \frac{R(\tau)}{(\overline{F})^2} = 1 + \frac{\overline{\delta F(0)\delta F(\tau)}}{(\overline{F})^2} \tag{6.28}$$

Some authors use the following function instead of the expression (6.28)

$$G(\tau) = \frac{\overline{\delta F(0) \delta F(\tau)}}{\left(\bar{F}\right)^2} \qquad (6.29)$$

6.5.2 Correlation Spectroscopy

The autocorrelation function G(τ) of (6.29) is a measure of the relative interdependence of the fluorescence signal at time t and of the signal at time t + τ.

If the fluctuations are slow with respect to τ, and F(t) is larger than $\bar{F}$, then F(t + τ) is likely to be larger than $\bar{F}$ and the autocorrelation will be large.

If the fluctuations are fast relative to τ, then F(t) and F(t + τ) will be independent and the autocorrelation will be zero.

If the average number of molecules in the volume of detection is large (e.g. several hundred) the arrival or departure of an additional fluorescent molecule will cause a small fluctuation in the fluorescence signal.

If, on the other hand, the number of fluorescent molecules in the volume of detection is small (say, one) then the arrival or departure of an additional molecule will cause a large fluctuation in the fluorescent signal.

For these reasons, FCS can provide information about the concentration and diffusion of fluorescent molecules and any process that changes one or both of these parameters can be measured by FCS.

An example of such a process is provided by the binding of two proteins in solution [13]. If the protein of one type is labeled with a fluorescent label, by monitoring the changes in the diffusion coefficient of the labeled molecules upon binding with their partners one can measure directly binding affinities and kinetics.

The applications of FCS include many processes that may produce intensity fluctuations of the fluorescence signal. These include translational diffusion, ligand-macromolecule binding, rotational diffusion, internal macromolecule dynamics, intersystem crossing and excited state reactions [1, 14].

6.5.3 Instrumentation

The standard instrumentation for the performance of FCS is based on a *confocal epifluorescence microscope* [13].

Fluorescence microscopy is different from all other microscopic techniques because the visible light in the microscope eyepieces is not the original light emitted by the light source, but the light emitted by the fluorescing sample.

The excitation is provided by a laser with high beam quality, temporal stability and the detection by a low noise single-photon detector.

The microscope makes use of a dichroic mirror that is reflective at the laser's wavelength and transmissive at the longer wavelength of the fluorescence emission.

It is of importance to make the detection volume as small as possible by the use of the sharpest light focus. The fluorescence light emitted by the sample is transmitted through the dichroic mirror and focused onto a circular confocal aperture, which rejects the fluorescence emission that is out of focus.

The light through the aperture is refocused onto a sensitive light detector, usually a single-photon avalanche diode or a specially configured photomultiplier.

The combined presence of a nearly perfect excitation focus and of a confocal detection optics of the fluorescence may generate an effective detection volume of 0.5 μm in diameter in the focal plane and a few micrometers along the optical axis.

As reported in [13]:

> The exact shape and size of the detection volume determine the shape and temporal decay of the autocorrelation function. For example the smaller the detection volume, the faster molecules will diffuse out of it and the faster is the decay of the autocorrelation function, and vice versa.
>
> Thus the features of the detection volume are weaved into the shape of the autocorrelation function. Knowing the exact shape of the detection volume makes it possible to calculate the shape of the autocorrelation function. The autocorrelation function can then be used to fit experimental data and to obtain the diffusion constants and/or concentration value of the fluorescent molecules.

6.6 Single Molecule Detection

6.6.1 Basic Principles

The ultimate goal of analytical chemistry is achieved in single molecule detection (SMD) for which fluorescence is the choice, since it provides a bright signal against a dark background.

The study of single molecules is possible if the volume of detection is small and the fluorophore is immobilized on a surface; generally fluorophores are chosen for their high quantum yields and stability.

SMD is widely used to detect, analyze and manipulate single molecules in samples with various complexities, from controlled in vitro conditions to the inside of living cells [15].

The most important reason for using SMD is to avoid ensemble averaging.

6.6.2 Instrumentation and Performance

A typical setup for SMD consists of laser excitation through a microscope objective, a scanning stage to move the sample and confocal optics to reject unwanted fluorescence signals [1].

Practically all experimental techniques other than SMD observe a large number of molecules and measure ensemble averages of the properties under study. Only with SMD one can observe a single molecule and study its behavior.

The SMD technique may include the measurement of the lifetime of single molecules while intensity images are collected.

6.7 Radiative Decay Engineering (RDE)

6.7.1 Basic Principles

The radiative lifetime of an excited fluorophore emitting in free space is determined by the interaction of the fluorophore with the photonic modes of free space.

The probability of spontaneous emission in free space is given by [16]:

$$A = \frac{8\pi\nu^2}{c^3} h\nu \frac{8\pi^2\mu^2}{3h^2} s^{-1} \tag{6.30}$$

where $\frac{8\pi\nu^2}{c^3}$ is the number of photonic oscillators per unit volume per unit frequency range, and μ is the matrix element of the transition.

If the medium's index of refraction is n, the expression for A has to be multiplied by n, and small changes in the radiative lifetime may occur. In this situation the changes in the measured lifetime that may occur are mainly due to changes in the non-radiative decay rate.

As emphasized by Purcell [17], the spontaneous emission rate depends on the local photonic mode density. Drastic changes in this rate may be produced if the mode density is modified by changing the boundary conditions on the electromagnetic field in the proximity of the emitting fluorophore [18,19]. The field of *cavity quantum electrodynamics* is based on this concept [20].

In this section we shall be concerned with the effect that the proximity of a metal surface can have on the fluorescence process. A light-emitting molecule can be thought of as an oscillating dipole that can induce oscillations of the electrons in the metal. In turn the field created by these oscillations can interact with the emitting molecule and affect its fluorescent output.

These interactions may produce a number of desired effects such as an increased quantum yield, increase distances for FRET and shorter lifetimes with the possible accompanying increased sensitivity, and decreased interference from background emission [21].

All these effects go under the expression Metal Enhanced Fluorescence (MEF).

Another phenomenon may occur when a fluorophore is close to a metal. If proper conditions are met a fluorophore can interact with a metallic surface and create surface-bound oscillations of electrons called *plasmons*.

If the metal is thin and the substrate material is appropriate the plasmons may radiate energy into the substrate. This phenomenon is called *Surface-Plasmon Coupled Emission* (SPCE).

6.7.2 About Metal-Enhanced Fluorescence (MEF)

Fluorescence experiments are usually performed in solutions that are macroscopic compared with the size of a fluorophore. The main effect of the environment on the emission of the fluorophore is due to the index of refraction of the solvent. The effect of metal surfaces on the fluorescence is negligible due to the small dimension of the fluorophore compared to those of the experimental set-up. The fluorescence represents the far field emission of the fluorophore.

Experimenters know that appropriate reflecting surfaces may be used to gather radiation that would be lost in free space. Reflection takes place after emission and is not to be considered in regard to RDE, since it has no effect on the lifetime of the excited fluorophore.

The effects we are considering are the changes in the rate of emission and spatial distribution of the radiation due to the closeness of a metal surface to the radiating (dipole) emitter.

How many interactions may be present?

1. Interaction of the exciting light with the metal surface,
2. interaction of the fluorophore oscillating dipole with the metal surface, and
3. interaction due to the induced field in the metal.

A Jablonski diagram is presented in Fig. 6.4

Let us now define the following:
Γ = rate of radiative decay
k_{nr} = rate of non-radiative decay

The quantum yield and the lifetime in the absence of any metal are given by

$$Q_0 = \frac{\Gamma}{\Gamma + k_{nr}} \tag{6.31}$$

and

$$\tau_0 = \frac{1}{\Gamma + k_{nr}} \tag{6.32}$$

respectively.

The radiative decay rate Γ is almost constant for any fluorophore; therefore Q_0 can only be increased by decreasing the rate of non-radiative decay k_{nr}.

Fig. 6.4 Jablonski diagram without (*top*) and with (*bottom*) the effects of near metal surfaces. For distances over 50 Å the effect of quenching by the metal (k_m) is expected to be minimal (Reproduced from Lacowicz [1] by permission granted by Springer Science and Business Media)
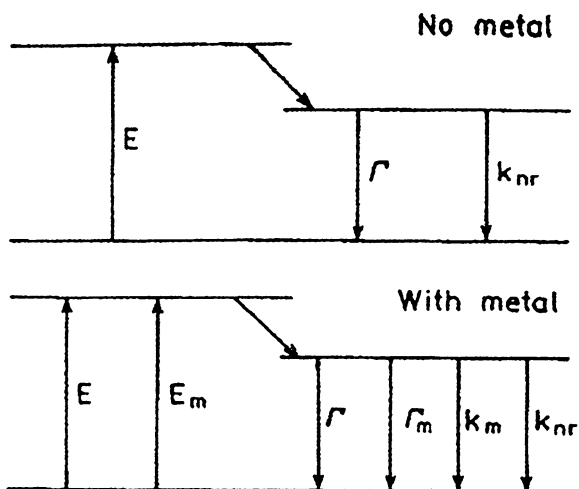
Now, with a look at the Jablonski diagram at the bottom of Fig. 6.4, we can say the following:

1. If the presence of the metal increases the rate of excitation to (E + Em), this will increase the fluorescence output, without any change in the quantum efficiency and in the lifetime. This metal-enhanced excitation may allow smaller incident intensities to obtain the same fluorescence output. In addition it may allow the selective excitation of fluorophores near the metal.

2. The presence of the metal may also increase the radiative decay rate Γ. In this case the quantum yield and the lifetime are given by

$$Q_m = \frac{\Gamma + \Gamma_m}{\Gamma + k_{nr} + \Gamma_m} \tag{6.33}$$

and

$$\tau_m = \frac{1}{\Gamma + k_{nr} + \Gamma_m} \tag{6.34}$$

respectively. We can re-express the above entities in the following ways:

$$Q = \frac{1 + \frac{\Gamma_m}{\Gamma}}{\frac{\Gamma + k_{nr}}{\Gamma} + \frac{\Gamma_m}{\Gamma}} = \frac{Q_0 + Q_o \frac{\Gamma_m}{\Gamma}}{1 + Q_o \frac{\Gamma_m}{\Gamma}} \tag{6.35}$$

$$\tau_m = \frac{1/\Gamma}{\frac{\Gamma + k_{nr}}{\Gamma} + \frac{\Gamma_m}{\Gamma}} = \frac{\tau_0}{1 + Q_0 \frac{\Gamma_m}{\Gamma}} \tag{6.36}$$

The relations (6.35) and (6.36) allow us to set up a diagram for Q_m as a function of Γ_m/Γ for given Q_0 and a diagram for τ_m as a function of Γ_m/Γ with given τ_0 and Q_0.

Fig. 6.5 Effect of an increase in the metal-induced radiative rate on the lifetime and quantum yields of fluorophores. To clarify this figure we note that for $Q = 0.5$, $\Gamma = 5 \times 10^7 \, s^{-1}$ and $k_{nr} = 5 \times 10^7 \, s$. For $Q = 0.1$, $\Gamma = 1 \times 10^7 \, s$ and $k_{nr} = 9 \times 10^7 \, s$ (Reproduced from Birks and Georghiou [22] by permission granted by Springer Science and Business Media)
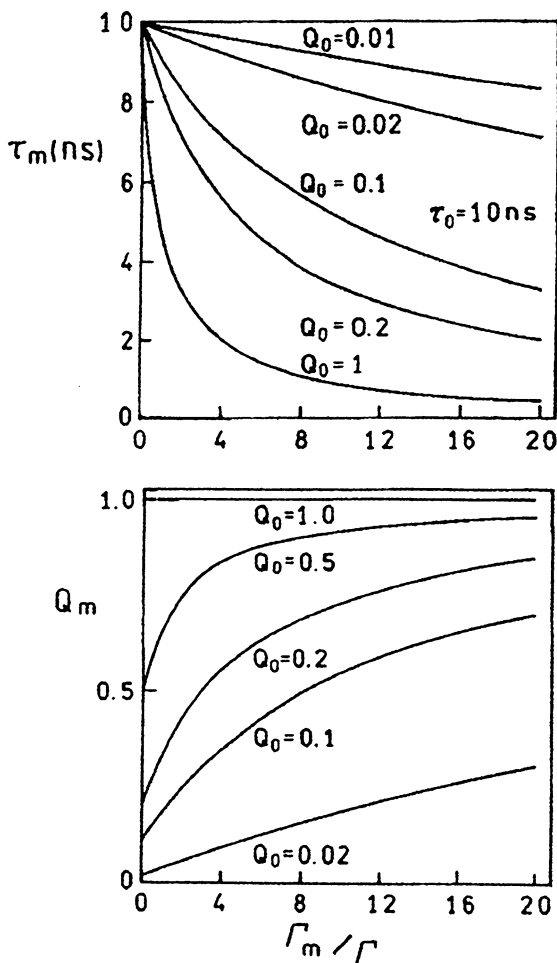
These two diagrams are presented in Fig. 6.5.

We find in Eq. (6.35) that, if Q_0 is equal to 1, Q_m is also equal to 1, i.e. the presence of the metal cannot increase Q_m any further. However, from (6.34) for $Q_0 = 1$ we get

$$\tau_m = \frac{\tau_0}{1 + \frac{\Gamma_m}{\Gamma}} \tag{6.37}$$

This means if $Q_0 = 1$, the presence of Γ_m may increase the probability of spontaneous emission, without changing the quantum yield.

The effect of Γ_m on Q_m is larger for fluorophores with low quantum efficiency Q_0, since Γ_m has no effect when $Q_0 = 1$.
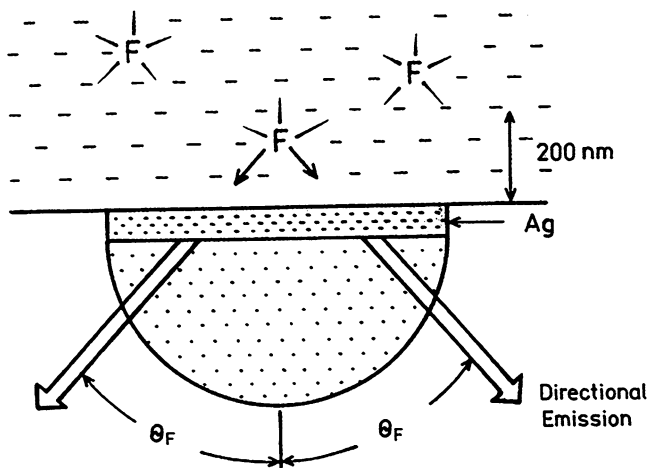
Fig. 6.6 Surface plasmon-coupled emission. F is a fluorophore (Reproduced from Birks and Georghiou [22] by permission granted by Springer Science and Business Media)
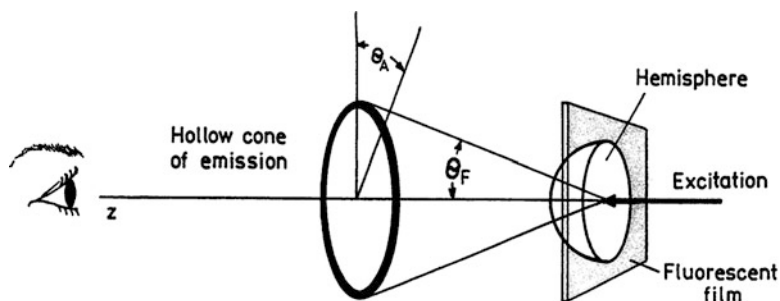
Fig. 6.7 Surface Plasmon-coupled cone of emission for fluorophores near a metallic film (Reproduced from Lacowicz [1] by permission granted by Springer Science and Business Media)

6.7.3 About Surface-Plasmon Coupled Emission (SPCE)

6.7.3.1 General Aspect

The SPCE process is illustrated in Fig. 6.6 [1], in which F represents a fluorophore set above a continuous silver film 50 nm thick.

The fluorescence emission from the fluorophore is not reflected, but passes through the film. The spatial pattern of the fluorophore emission is nearly isotropic, but the emission seen through the film is at an angle θ_F with respect to the normal. The sample being symmetrical about the normal z-axis, the emission through the film occupies a cone around the z-axis (see Fig. 6.7).
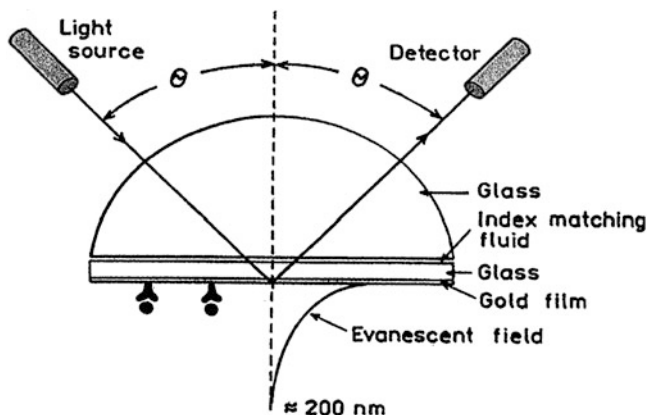
Fig. 6.8 Typical configuration for surface-plasmon resonance analysis. The incident beam is p-polarized (Reproduced from Lacowicz [1] by permission granted by Springer Science and Business Media)

The emission on the cone, about a half of the total emission (the rest being free space emission away from the film) is called *Surface-Plasmon Coupled Emission* (SPCE). This name reflects the fact that the emission in the cone is radiated by the plasmons.

The following can be said:

1. The spectral distribution of the cone emission is the same as that of the fluorophore.
2. The plasmons are not the result of RET because the distance at which SPCE takes place (200–2,000 Å) are too large for RET, for which the Förster distance is 50 Å.
3. The emission is radiated by the plasmons into the substrate at an angle determined by the optical properties of the metal and of the substrate.
4. The emission is 100% p-polarized, even if the fluorophores are randomly oriented and excited by unpolarized light.

The appropriate conditions for the conical plasmon emission reside on the requirement that the incident beam must be matched in both frequency and momentum with that of the surface-plasmon waves.

6.7.3.2 Surface Plasmon Resonance

The phenomenon of *surface-plasmon resonance* (SPR) is closely related to SPCE. Figure 6.8 is illustrative in this regard, for it presents a schema of the measurement of light interaction with a thin metal film (typically made of gold 40–50 nm thick).
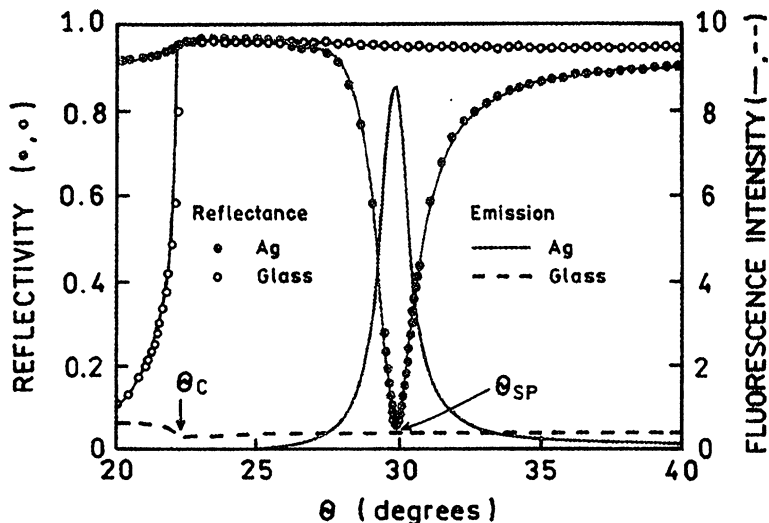
Fig. 6.9 Reflectivity curves for a bare glass and silver-coated glass, both spin coated with a fluorophore in polyvinyl alcohol. The prism is LaSFN9 glass, 633 nm. Also shown is the fluorescence from the labeled PVA film on the glass and silver surfaces [23]

The set up, called *Kretschman configuration*, measures the light reflected from the gold film at various angles of incidence, keeping, of course, the angle of reflection equal to that of incidence.

The reflectivity of the gold film depends on the index of refraction of the solution immediately above the film.

The evanescent field penetrates approximately 200 nm into the solution at the plasmon resonance, and when there is no resonance it vanishes and the reflectivity becomes large.

The presence of an evanescent field brings to mind another case when such a field is present, i.e. the case of *total internal reflection* (TIR) which occurs when the incident light beam angle exceeds a critical value θ_{crit}. TIR occurs in Fig. 6.9 for a bare glass.

The angles θ_{crit} and θ_{spr} are not related, but the origin for both of them resides in the wave vector matching at the interface. The evanescent field due to SPR is much larger than that due to TIR.

Figure 6.9 presents a comparison of the reflectivity curves for a bare glass and for a silver-coated glass. We note the following:

1. The reflectivity of the bare glass is low below the critical angle θ_{crit}, but increases sharply to nearly 100% at θ_{crit} and remains high at larger angles.
2. An evanescent wave exists for bare glass at angles greater than θ_{crit}.
3. No evanescent wave exists for the silver-coated glass at angles that are not close to θ_{spr}. At angles consistently different than θ_{spr} the reflection is high.

4. The strength of the evanescent fields was measured by the fluorescence from the fluorophores near the surface. These fluorophores were concentrated within the polyvinyl alcohol (PVA) that resided in the evanescent field zone.
5. For the glass surface the emission is low for $\theta < \theta_{crit}$, but as the angle exceeds θ_{crit}, it drops about twofold because the incident beam experiences TIR. Above θ_{crit} the intensity that remains is due to the evanescent wave. This result seems to indicate that in the conditions of TIR the incident field is about equal in strength to the evanescent field.
6. Things are different for the silver-coated glass. The emission is close to zero for angles different than θ_{crit} due to the high selectivity of the silver film. The light does not penetrate the sample even if $\theta < \theta_{crit}$, but near the SPR angle there is an increase of the emission intensity by a factor of 15. This increase is due to an increase of the evanescent wave field above the silver 10–40-fold with respect to the intensity above the glass under TIR conditions.
7. This increase is at the basis of the increased sensitivity that can be obtained with plasmon-coupled emission.
8. The SPR angles are strongly dependent on the wavelengths, decreasing as the wavelength decreases. This dependence is responsible for the spectral resolution presented by the SPR emission.

6.7.3.3   Surface-Plasmon Coupled Emission (SPCE)

We can look now at the surface-plasmon coupled emission in Figs. 6.6 and 6.7. An electromagnetic field traveling in the $\vec{r}$ direction can be described by the expression

$$\overrightarrow{E}(\overrightarrow{r}, t) = \overrightarrow{E}_0 \cos(\omega t - \overrightarrow{k} \cdot \overrightarrow{r}) \tag{6.38}$$

where $\vec{k}$ is the *wave vector* whose absolute value, called *propagation constant* is related to the frequency ω and to the wavelength λ as follows:

$$k = 2\pi/\lambda = n\omega/c = nk_0 \tag{6.39}$$

where
n = index of refraction
$\lambda = \lambda_0/n$ with $\lambda_0 =$ wavelength in vacuum
$k_0 =$ propagation constant in vacuum

The component of the vector $\overrightarrow{E}$ in the x-direction, to be considered for the SPR emission is

$$E(x, t) = E_{0x} \cos(\omega t - k_x x) \tag{6.40}$$

In the metal the propagation constant of the electromagnetic wave is given by [1]

$$k_{sp} = k_0[\varepsilon_r\varepsilon_s / (\varepsilon_r + \varepsilon_s)]^{1/2} \tag{6.41}$$

where ε_s = dielectric constant in the region of the evanescent field ε_r = dielectric constant in the metal

In order for the incident light beam to excite surface plasmons, it is necessary for the x-component of its $\vec{k}$ vector to be equal to the propagation constant for the surface plasmons.

The propagation constant for the incident light in the prism is given by

$$k_p = k_0 n_p \tag{6.42}$$

where n_p = index of refraction of the prism.

The component of the wave vector $\vec{k}_p$ along the x-axis is

$$k_{px} = k_0 n_p \sin\theta_p \tag{6.43}$$

where θ_p = angle of incidence in the prism.

The SPR absorption occurs when

$$k_{sp} = k_x = k_0 n_p \sin\theta_{sp} \tag{6.44}$$

when θ_{sp} = angle of incidence in the metal for surface-plasmon resonance to occur.

Simply, SPR takes place when the $\vec{k}$ vector in the prism has an x-component that matches the k constant of the surface plasmons. This proves the fact that θ_{sp} must increase as the frequency of the incident beam increases.

As for the surface-plasmon coupled emission we can say the following [21]:

1. The fluorophores are randomly distributed and the sample can be excited by unpolarized light.
2. Since there is no preferential direction around the z-axis, the SPCE will appear as a cone about the z-axis.
3. The SPR occurs at different angles of incidence. The analogy of SPCE with SPR suggests that SPCE also will occur at different angles, as a circular rainbow.
4. In SPR only p-polarized light is absorbed. Then the SPCE light will also be p-polarized around the z-axis.

6.8   Conclusions

The large number of applications of fluorescence spectroscopy to biological systems points to the great usefulness of such a technique. The range of these applications stimulates the interest of researchers and the desire to expand the limits of fluorescence-based techniques.

Considering the points of encounters between the fluorescence spectroscopy of solids and the fluorescence spectroscopy of biological systems collaboration between researchers in these two fields is desirable and potentially profitable.

References

1. Lacowicz JR (2006) Principles of fluorescence spectroscopy, 3rd edn. Springer
2. Herschel JFW (1845) Philos Trans R Soc Lond 135:143–145
3. Jablonski A (1935) Z Phys 94:38–46
4. Kasha M (1950) Discuss Faraday Soc 9:14–19
5. Stokes GG (1852) Philos Trans R Soc Lond 142:463
6. Jablonski A (1960) Bull Acad Pol Sci A 8:259
7. Förster Th (1949) Z Naturforsch 4a:321
8. Clegg RM (1966) In: Wang XF, Herman B (eds) Fluorescence imaging spectroscopy. Wiley, New York, p 179
9. Bennett RG (1964) J Chem Phys 41:3037–3041
10. Eisenthal KB, Siegel S (1964) J Chem Phys 41:652–655
11. Yokota M, Tanimoto O (1967) J Phys Soc Jpn 22(3):779–784
12. Saleh EA, Teich MC (2007) Fundamentals of photonics, 2nd edn. Wiley Interscience, New York
13. Deringer T, von Hocht I, Loman A, Gregor I, Enderlein J (2009) In: Goldys EM (ed) Fluorescence applications in biotechnology and the life sciences. Wiley-Blackwell, Hoboken
14. Schwille P, Ries T (2011) In: Di Bartolo B, Collins J (eds) Biophotonics: spectroscopy, imaging, sensing and manipulation. Springer, Dordrecht
15. Walter NG (2008) In: Meyers RA (ed) Encyclopedia of analytical chemistry. Wiley, Chichester
16. Fermi E (1932) Rev Mod Phys 4:87
17. Purcell EM (1946) Phys Rev 69:681
18. Amos RM, Barns WL (1997) Phys Rev B 55:7249
19. Goy P, Raimond JM, Gross M, Haroche S (1983) Phys Rev Lett 50:1903
20. Berman PR (ed) (1994) Cavity quantum electrodynamics. Academic, San Diego
21. Lakowicz JR (2001) Anal Biochem 298:1
22. Birks JB, Georghiou S (1968) Proc R Soc (J Phys B) 1:958–965
23. Neumann T, Johanssan ML, Kambhampati D, Knoll W (2002) Adv Funct Mater 12:575

7
Nanophotonics: Linear and Nonlinear Optics at the Nanoscale

Christopher C. Evans and Eric Mazur

7.1   Introduction

Light propagation in sub-wavelength waveguides enables tight confinement over long propagation lengths to enhance nonlinear optical interactions. Not only can sub-wavelength waveguides compress light spatially, they also provide a tunable means to control the spreading of light pulses in time, producing significant effects even for nanojoule pulse energies. By exploring linear and nonlinear light propagation, first for free-space conditions, then for sub-wavelength guided conditions, we demonstrate how sub-wavelength structure can enhance nonlinear optics at the nanoscale. We demonstrate key applications including wavelength generation and all-optical modulation. Lastly, we show how to assemble these devices to form all-optical logic gates.

We begin by developing a fundamental understanding of light propagation in materials that we will build upon as we cover linear and nonlinear light propagation in nano-scale structures. We introduce plane-wave propagation in bulk materials and develop a simple model to explain the frequency dependence of the dielectric function. We observe how this frequency dependence affects optical pulse propagation. With this foundation, we will later explore light-on-light modulation using nonlinear optics.

C.C. Evans (✉)
Department of Physics, Harvard University, 9 Cambridge St. McKay 321, Cambridge, MA 02138, USA

E. Mazur
School of Engineering and Applied Sciences, Harvard University, Pierce Hall 225, Cambridge, MA 02138, USA

C.C. Evans • E. Mazur
School of Engineering and Applied Sciences, Harvard University, 9 Oxford Street, Cambridge, MA 02138, USA
e-mail: evans@fas.harvard.edu

7.1.1 Plane Waves

Throughout this chapter, we will develop and use several different wave equations. Each wave equation makes assumptions to localize energy both in time, using pulses, and in space, using waveguides. The first wave equation assumes *plane waves at a single frequency* (continuous wave). To localize in time, an optical pulse requires the interference of multiple frequencies. Therefore, we model a pulse as a single frequency modulated by an envelope function using the *slowly varying envelope approximation*. We use waveguides to confine light spatially by taking advantage of sustained propagating solutions of Maxwell's equations, known as modes. Light guided within a mode propagates in an analogous way to plane waves using the *guided-wave equation*. Finally, we will augment this equation using the slowly varying envelope approximation to form a fourth wave equation to describe pulses in a waveguides. Strong light-matter interactions create a nonlinear polarization that we must include. We will introduce the physics of nonlinear optics in the simplest way possible, using plane waves. Lastly, we will modify the pulsed waveguide equation to include third-order nonlinear optical effects to form the Nonlinear Schrodinger Equation (NLSE).

7.1.1.1 Wave Equation for Plane Waves

We start with Maxwell's equations in a linear, homogeneous material with no free charges or currents:

$$(i)\ \vec{\nabla} \cdot \vec{E} = 0 \quad (iii)\ \vec{\nabla} \times \vec{E} = -\frac{\partial \vec{B}}{\partial t}$$

$$(ii)\ \vec{\nabla} \cdot \vec{B} = 0 \quad (iv)\ \vec{\nabla} \times \vec{B} = \frac{\mu_r \varepsilon_r}{c^2} \frac{\partial \vec{E}}{\partial t}. \tag{7.1}$$

In this set of coupled differential equations, the vectors $\vec{E}$ and $\vec{B}$ are the electric and magnetic fields, ε_r and μ_r are the relative electric permittivity and the relative magnetic permeability and define we $c \equiv 1/\sqrt{\varepsilon_0 \mu_0}$, which is the speed of light in vacuum. If we take the curl of equation (iii) and substitute equations (i) and (iv), the wave equation is commonly derived as [1]:

$$\nabla^2 \vec{E} - \frac{\mu_r \varepsilon_r}{c^2} \frac{\partial^2 \vec{E}}{\partial t^2} = 0. \tag{7.2}$$

To gain physical insight into this equation, we define $k^2/\omega^2 \equiv \mu_r \varepsilon_r/c^2$ and solve this differential equation in one dimension for $\vec{E}(z, t)$:

$$\vec{E}(z, t) = \frac{1}{2}\left[\vec{E}_0 e^{i(kz-\omega t)} + c.c.\right] = \text{Re}\left[\vec{E}_0 e^{i(kz-\omega t)}\right], \tag{7.3}$$

where $\vec{E}_0$ is the complex electric field vector, z is the position, t is the time and $c.c.$ denotes the complex conjugate of the previous term, insuring the field is a real quantity. The last expression uses phasor notation, which is mathematically more compact. Consequently, we will use phasor notation occasionally and leave it to the reader to take the real part.

7.1.1.2 Velocity of Plane Waves in a Material

The first question one might ask is: what is the speed of this wave? For a fixed location, the time between crests is $T = 2\pi/\omega = 1/f$, where f is the frequency and the quantity $\omega = 2\pi f$ is the angular frequency. In a similar way, the spacing between crests is given by the wavelength in the material, $\lambda_{mat} = 2\pi/k$, and we refer to $k = 2\pi/\lambda_{mat}$ as the wavevector. In three dimensions, k is a vector that points in the direction of the phase velocity; however, we will use it as a scalar for one dimension. This wavelength in the material λ_{mat} should not be confused with the wavelength in vacuum λ_0. For most materials we can approximate $\mu_r \approx 1$ [1]. We also allow the relative permittivity ε_r to be frequency dependent using $\varepsilon_r(\omega)$. We determine the speed of the wave v by observing how long it takes a single crest to propagate one wavelength:

$$v = \frac{\lambda_{mat}}{T} = \lambda_{mat} f = \frac{\omega}{k} = \frac{c}{\sqrt{\varepsilon_r(\omega)}} \equiv \frac{c}{n(\omega)}. \tag{7.4}$$

Here, we define the index of refraction as $n(\omega) \equiv ck(\omega)/\omega$. If ε_r and μ_r are unity (their values in vacuum), the velocity is the speed of light in vacuum c. We refer to the velocity at which the crests and the troughs of the wave propagate as the *phase velocity,* to distinguish it from the pulse or group velocity.

7.1.1.3 Propagation Losses

We have defined the refractive index in terms of the square root of the dielectric function. What happens if the dielectric function is complex? A complex dielectric constant causes k to be complex and we must consider the consequences of a complex index of refraction, $\tilde{n}(\omega)$. Therefore, we must further define the index of refraction as:

$$n(\omega) \equiv \mathrm{Re}\left[\frac{ck(\omega)}{\omega}\right] = \mathrm{Re}\left[\sqrt{\varepsilon_r(\omega)}\right]. \tag{7.5}$$

Considering a complex wavevector for a single frequency given by $\tilde{k} = k' + ik''$, we get immediate physical insight by observing the propagation of a plane wave in a medium with a complex wavevector:

$$\vec{E}(z,t) = \frac{1}{2}\left[\vec{E}_0 e^{i[(k'+ik'')z-\omega t]} + c.c.\right] = \frac{1}{2}\left[\vec{E}_0 e^{-k''z} e^{i(k'z-\omega t)} + c.c.\right] \quad (7.6)$$

We see that k'' exponentially attenuates the wave as it propagates.

We rarely measure the electric field directly and instead measure the time-averaged power. For a plane wave, the time-averaged power per unit area is the intensity or irradiance I defined by

$$I = \frac{c\varepsilon_0 n}{2}\left|\vec{E}(z,t)\right|^2. \tag{7.7}$$

Writing Eq. (7.6) in terms of intensity, the expression becomes

$$I = \frac{1}{2}c\varepsilon_0 n\left|\vec{E}_0\right|^2 e^{-2k''z}, \tag{7.8}$$

and the imaginary part of the wavevector k'' is responsible for intensity attenuation. Attenuation is important because high intensities are critical for efficient nonlinear interactions, thus, attenuation is a limiting factor. We use this expression to define the attenuation coefficient given by $\alpha = 2k''$, having units of inverse length. When the attenuation is due to absorption, we refer to α as the absorption coefficient. In a similar manner, if we allow the index of refraction to become complex, we define $\tilde{n} \equiv n + i\kappa$ and this new term κ is known as the extinction coefficient $\kappa(\omega) \equiv ck''(\omega)/\omega$.

In the optical engineering literature, losses are usually notated in units of decibels per length, and it is convenient to relate this convention to the absorption coefficient. For a distance L, the intensity decreases from I_0 to $I(L)$ and the loss is given by [2]:

$$\text{loss in dB} = -10\log_{10}\left(\frac{I(L)}{I_0}\right) = -10\log_{10}\left(\frac{I_0 e^{-\alpha L}}{I_0}\right) = 10\,(\alpha L)\log_{10}(e) \approx 4.34\alpha L. \tag{7.9}$$

Using this equation and assuming the losses are due to absorption, we can relate all of these quantities:

$$\kappa(\omega)\,[\text{unitless}] = k''(\omega)\,\frac{c}{\omega}\,\left[k''\text{in m}^{-1}\right]$$

$$= \frac{\alpha(\omega)}{2}\frac{c}{\omega}\,\left[\alpha\text{ in m}^{-1}\right] \approx \frac{\text{loss}}{8.68}\frac{c}{\omega}\,\left[\text{loss in dB/m}\right]. \tag{7.10}$$

We have assumed that the loss of light is due to absorption. However, any source of attenuation, such as absorption and scattering from inhomogeneities within the materials, limits nonlinear interactions. Therefore, we should use the inclusive definition of α (the attenuation coefficient) when analyzing nonlinear devices.

7.1.2 Dielectric Function

The frequency-dependent dielectric function produces a frequency-dependent wavevector that is important for pulse propagation. To understand the origins of the frequency dependent dielectric function, we will develop a simple model here.

7.1.2.1 Drude-Lorentz Model

We classically model the interaction between an electromagnetic wave and electrons bound to their respective ion-cores using the Drude-Lorentz model. By modeling the electron-ion interaction as a one-dimensional simple harmonic oscillator, we explore the features of the dielectric function. The binding force between an electron and its ion is given by

$$F_{binding} = -m\omega_0^2 x, \tag{7.11}$$

where m is the mass of the electron, ω_0 is the resonant frequency of the electron-nucleus system, and x is the displacement of the electron. While in motion, the electron is also subject to a damping force with strength proportional to a constant γ, resisting its movement. The damping force is given by

$$F_{damping} = -m\gamma \frac{dx}{dt}. \tag{7.12}$$

Lastly, a steady oscillating electric field, using Eq. (7.3) with $z = 0$, provides the driving force given by:

$$F_{driving} = -eE = -eE_0 e^{-i\omega t}, \tag{7.13}$$

proportional to the charge of the electron e. The equation of motion thus becomes:

$$m \frac{d^2 x}{dt^2} + m\gamma \frac{dx}{dt} + m\omega_0^2 x = -eE_0 e^{-i\omega t}, \tag{7.14}$$

whose solution is:

$$x(t) = x_0 e^{-i\omega t}, \qquad x_0 \equiv -\left(\frac{e}{m}\right) \frac{1}{(\omega_0^2 - \omega^2) - i\gamma\omega} E_0. \tag{7.15}$$

The oscillating electron creates a dipole moment given by

$$p(t) = -ex(t) = \left(\frac{e^2}{m}\right) \frac{1}{(\omega_0^2 - \omega^2) - i\gamma\omega} E_0 e^{-i\omega t}. \tag{7.16}$$

Fig. 7.1 The displacement
amplitude x_0 and phase φ
versus frequency for the
Drude-Lorentz model (*left*).
The complex
frequency-dependent
dielectric function for a single
resonance (*right*)
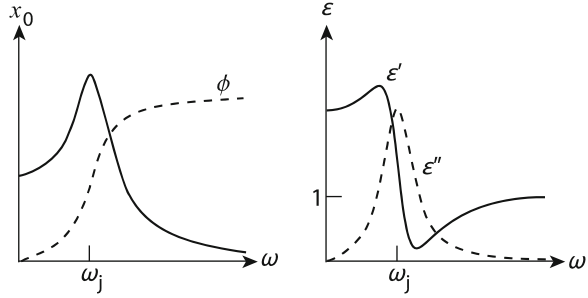
In a bulk material, we have N of these dipoles per unit volume and we must express the dipole moment as a vector:

$$\vec{P}(t) = \frac{Ne^2}{m} \frac{1}{(\omega_0{}^2 - \omega^2) - i\gamma\omega} \vec{E}(t) \equiv \varepsilon_0 \chi_e \vec{E}(t). \qquad (7.17)$$

From the polarization, with the definitions for the susceptibility $\vec{P}(t) \equiv \varepsilon_0 \chi_e \vec{E}(t)$ and the relative dielectric function $\varepsilon_r(\omega) \equiv 1 + \chi_e$, we solve for the relative dielectric function:

$$\varepsilon_r(\omega) = 1 + \frac{Ne^2}{m\varepsilon_0} \frac{1}{(\omega_0{}^2 - \omega^2) - i\gamma\omega}. \qquad (7.18)$$

7.1.2.2 Dielectric Function for a Single Resonance

We realize that the relative dielectric function is a complex quantity $\varepsilon_r(\omega) = \varepsilon_r'(\omega) + i\varepsilon_r''(\omega)$. For a single resonance, we separate Eq. (7.18) into real and imaginary parts:

$$\varepsilon_r'(\omega) + i\varepsilon_r''(\omega) = \left(1 + \frac{Ne^2}{m\varepsilon_0} \frac{(\omega_0{}^2 - \omega^2)}{(\omega_0{}^2 - \omega^2)^2 + \gamma^2\omega^2}\right) + i\left(\frac{Ne^2}{m\varepsilon_0} \frac{\gamma\omega}{(\omega_0{}^2 - \omega^2)^2 + \gamma^2\omega^2}\right). \qquad (7.19)$$

Plotting the displacement of the electron x as a function of frequency ω in Fig. 7.1 (left, solid line), we see that the amplitude on-resonance is largest. The phase shift (dashed line) is initially in-phase for frequencies below resonance and lags behind at higher frequencies. This results in a complex dielectric function which has a strong imaginary component $\varepsilon_r''(\omega)$ on resonance (Fig. 7.1, right, dashed line). Observing the real component $\varepsilon_r'(\omega)$ the bound charges keep up with the driving field and the wave propagates more slowly, corresponding to a higher refractive index. At resonance, energy is transferred to the bound charges and the wave is attenuated. Above the resonance, the bound charges cannot keep up and the dielectric acts like a vacuum.

Fig. 7.2 Schematic
illustration of the various
contributions to the dielectric
constant across the
electromagnetic spectrum
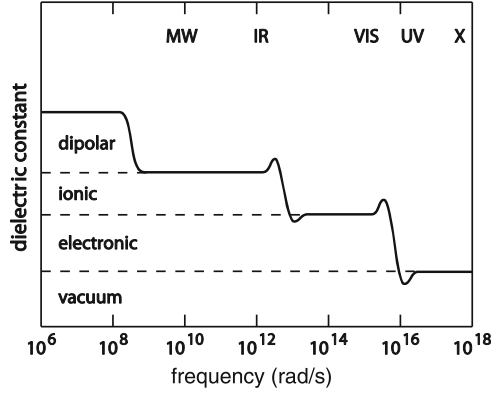
7.1.2.3 Multiple Resonances

In a bulk material, the electric field becomes a vector and we sum over all dipoles,
creating a material polarization given by

$$\vec{P}(t) = \left(\frac{Ne^2}{m}\right) \sum_j \frac{f_j}{(\omega_j{}^2 - \omega^2) - i\gamma_j\omega} \vec{E}_0(t) \equiv \varepsilon_0 \chi_e \vec{E}(t). \qquad (7.20)$$

Here, we sum over the individual electrons for each molecule of the bulk
material. The subscript j corresponds to a single resonant frequency ω_j with a
damping coefficient γ_j, of which there are f_j electrons per molecule and there are
N molecules per unit volume. This model is most quantitatively accurate in the dilute
gas limit [1]; however, it provides a qualitative insight into solid materials. Using
this polarization, the complex relative dielectric function is given by

$$\varepsilon_r(\omega) = 1 + \left(\frac{Ne^2}{\varepsilon_0 m}\right) \sum_j \frac{f_j}{(\omega_j{}^2 - \omega^2) - i\gamma_j\omega}. \qquad (7.21)$$

We can extend the dielectric function to include other resonances, as shown in
Fig. 7.2. At very high frequencies, the dielectric acts like a vacuum. At ultraviolet
and visible frequencies, electronic resonances play a dominant role. Lastly, for low
frequencies, the driving fields are slow enough to access both ionic and dipolar
resonances.

7.1.2.4 Metals

Now, let us consider the case where the binding energy is very weak, as in the case
of a metal. Here, we have $F_{binding} \approx 0$. Then equation of motion reduces to

$$m\frac{d^2x}{dt^2} + m\gamma\frac{dx}{dt} = -eE_0e^{-i\omega t}, \qquad (7.22)$$

which has a solution of

$$x(t) = \left(\frac{e}{m}\right) \frac{1}{\omega^2 + i\gamma\omega} E_0 e^{-i\omega t}. \tag{7.23}$$

Metals are known for their conductivity. In the low frequency limit, where $\omega \ll \gamma$ the generated current J is proportional to the velocity, charge, and number of electrons per unit volume, given by:

$$J = -Ne\frac{dx}{dt} = \frac{Ne^2}{m}\frac{1}{\gamma - i\omega}E(t) \approx \frac{Ne^2}{m\gamma}E(t) \equiv \sigma E(t). \tag{7.24}$$

From this expression, we readily defined the conductivity σ. In the high frequency limit $\omega \gg \gamma$ we find that

$$J = \frac{Ne^2}{m}\frac{1}{\gamma - i\omega}E(t) \approx -i\frac{Ne^2}{m\omega}E(t) \equiv \sigma E(t), \tag{7.25}$$

and that the conductivity σ is complex and that J is out of phase with $E(t)$.

At optical frequencies, if the frequency is large relative to the damping ($\omega \gg \gamma$) we can approximate $\gamma \approx 0$, and we obtain the free electron model:

$$\varepsilon(\omega) = 1 - \frac{Ne^2}{m\varepsilon_0}\frac{1}{\omega^2} \equiv 1 - \frac{\omega_p{}^2}{\omega^2}. \tag{7.26}$$

Here, we define the plasma frequency as $\omega_p \equiv Ne^2/m\varepsilon_0$. For a typical metal, having 10^{22} electrons/cm^3, this density corresponds to a plasma frequency of 6×10^{15} rad/s or a vacuum wavelength of 330 nm. When the frequency of light is above the plasma frequency, $\varepsilon_r{}'' = 0$ and the metal is transparent. At the plasma frequency, the real part of the dielectric function becomes zero. Below the plasma frequency, the dielectric function is completely imaginary; the wave does not propagate and is reflected instead. Therefore, the metal acts as a high-pass filter and can be used as a mirror.

7.1.3   Pulse Propagation

Short optical pulses are a key tool for nonlinear optical research as they can achieve high intensities even with small pulse energies and low average powers. However, pulsed transmission requires multiple frequencies propagating coherently together, as shown in Fig. 7.3 (left). The frequency-dependent phase velocity causes the pulse envelope to propagate at its own velocity and can lead to temporal pulse spreading during propagation show in Fig. 7.3 (right). In this section, we will address these issues and develop the mathematical framework to handle pulses.
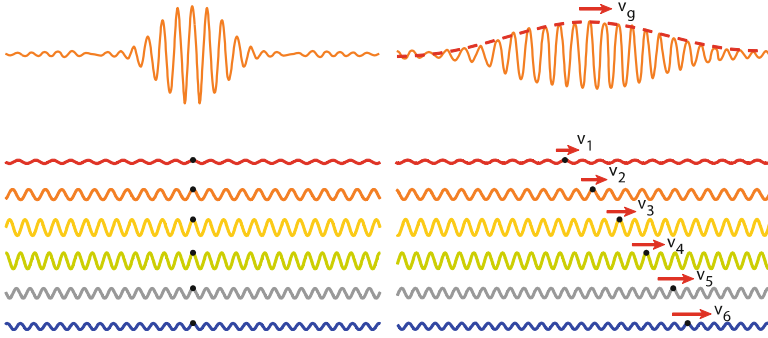
Fig. 7.3 A pulse is made up of many frequencies (*left*) which can propagate with their own phase velocities, leading to temporal pulse spreading (*right*)

7.1.3.1 Phase Versus Group Velocity

To understand how a pulse propagates, let us begin with a simple model (two continuous waves of differing angular frequencies and wavevectors) and explore what happens when they propagate together. The two propagating waves are given by:

$$y_1 = A \sin (k_1 z - \omega_1 t) \ \text{and} \ y_2 = A \sin (k_2 z - \omega_2 t). \tag{7.27}$$

Where A is the amplitude of the waves (identical values here), k_1 and k_2 are the wave vectors, and ω_1 and ω_2 are the frequencies for the first and second waves (respectively). Each wave has a speed, or phase velocity, given by:

$$v_1 = \frac{\omega_1}{k_1} = f_1 \lambda_1 \ \text{and} \ v_2 = \frac{\omega_2}{k_2} = f_2 \lambda_2. \tag{7.28}$$

If we superimpose these waves by adding then, then apply the trigonometric identity,

$$\sin \alpha + \sin \beta = 2 \cos \left(\frac{\alpha - \beta}{2} \right) \sin \left(\frac{\alpha + \beta}{2} \right), \tag{7.29}$$

we arrive at the following result:

$$y \equiv y_1 + y_2 = 2A \cos \left[\frac{1}{2} (z (k_1 - k_2) - t (\omega_1 - \omega_2)) \right] \sin \left[\frac{k_1 + k_2}{2} z - \frac{\omega_1 + \omega_2}{2} t \right]. \tag{7.30}$$

We can simplify this expression using the following definitions:

$$\Delta k \equiv k_1 - k_2 \ \text{and} \ \Delta \omega \equiv \omega_1 - \omega_2$$

$$k \equiv \frac{k_1 + k_2}{2} \ \text{and} \ \omega \equiv \frac{\omega_1 + \omega_2}{2}, \tag{7.31}$$

Fig. 7.4 Two waves
interfere, forming a simple
pulse train whereby a carrier
wave is modulated by a
slowly varying envelope
$\cos(z\Delta k/2)$
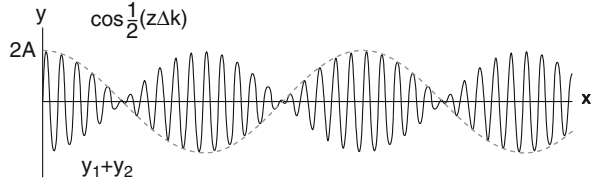
Table 7.1 Types of linear
dispersion

$\dfrac{dn}{d\omega} > 0$	Normal dispersion	$v_g < v_p$
$\dfrac{dn}{d\omega} = 0$	No dispersion	$v_g = v_p$
$\dfrac{dn}{d\omega} < 0$	Anomalous dispersion	$v_g > v_p$

to show

$$y = 2A \cos\left[\frac{1}{2}(z\Delta k - t\Delta\omega)\right]\sin(kz - \omega t). \tag{7.32}$$

This expression takes the form of a fast oscillating term (the sine function) modulated slowly by the cosine function. To visualize this behavior, we set $t = 0$ and plot Eq. (7.32) in Fig. 7.4. We see the beating between these two frequencies forms the basis of a simple pulse or group. We call the cosine function the *envelope*, and the fast oscillatory part the *carrier*.

Observing Eq. (7.32), we see two relevant velocities. The velocity of the carrier wave from the sine term is:

$$v_p = \frac{\omega}{k} = f\lambda. \tag{7.33}$$

We refer to this velocity as the *phase velocity*. Similarly, the envelope has a velocity given by

$$v_g = \frac{\Delta\omega}{\Delta k} \rightarrow \frac{d\omega}{dk}, \tag{7.34}$$

which we refer to as the *group velocity*. If we consider the case of no dispersion, the phase velocities of the two waves are the same $v_p = \frac{\omega_1}{k_1} = \frac{\omega_2}{k_2}$ and we find that:

$$\begin{aligned}
v_g &= \frac{\Delta\omega}{\Delta k} = \frac{\omega_1 - \omega_2}{k_1 - k_2} = \frac{\omega_1/(k_1 k_2) - \omega_2/(k_1 k_2)}{1/k_2 - 1/k_1} \\
&= \frac{v_p/k_2 - v_p/k_1}{1/k_2 - 1/k_1} = v_p \frac{1/k_2 - 1/k_1}{1/k_2 - 1/k_1} = v_p,
\end{aligned} \tag{7.35}$$

and therefore the group velocity and the phase velocity are identical. There are several categories of linear dispersion as shown in Table 7.1.

If we consider a single optical element, such as a mirror, lens, or length of fiber, the group velocity will cause a fixed time-delay for the pulse, known as the *group delay*. The group delay can deviate substantially from the delay caused by the phase velocity (inversely dependent on the index) in a dispersive media. The difference between the phase and group velocity within a single optical element will cause an offset between the absolute phase of the carrier and the envelope of the pulse, known as the *carrier-envelope offset*.

7.1.3.2 Gaussian Pulse

In our simple model, we have only considered two propagating waves. As we add more waves in between these initial waves, the envelope is no longer defined by a simple cosine function and the pulses can separate in time, as shown Fig. 7.3. To describe such a pulse, we use the slowly-varying envelope approximation (in phasor notation):

$$\vec{E}\,(z,t) = A\,(z,t)\,e^{i\,(kz - \omega_0 t)}\hat{x}. \tag{7.36}$$

Here, $A\,(z,t)$ is the envelope function and $\exp\,(i\,(kz - \omega_0 t))$ is the carrier. A Gaussian is a common shape for an ultrashort pulse, given by:

$$
\begin{aligned}
\vec{E}\,(z,t) &= \vec{E}_0 \exp\left(-\frac{1}{2}\left(\frac{t}{\tau}\right)^2\right) e^{i\,(kz - \omega_0 t)} \\
&= \vec{E}_0 \exp\left(-2\ln(2)\left(\frac{t}{\tau_{FWHM}}\right)^2\right) e^{i\,(kz - \omega_0 t)},
\end{aligned}
\tag{7.37}
$$

Here, $\vec{E}_0$ is the amplitude of the electric field, t is time and both τ and τ_{FWHM} reflect the pulse duration. Additionally, ω_0 and k are the angular frequency and wavevector of the carrier wave (respectively).

We can measure the pulse duration in several ways by applying different clipping levels ($1/e, 1/e^2$, full-width at half maximum) and calculating these in terms of either the electric field or the power. Using Eq. (7.37), we define two definitions for the pulse duration with respect to the time-averaged power:

$$P(t) = P_p \exp\left(-(t/\tau)^2\right) = P_p \exp\left(-4\ln(2)(t/\tau_{FWHM})^2\right). \tag{7.38}$$

Here, $P(t)$ is the power as a function of time t, and P_p is the peak power. In the first pulse-duration definition, τ is the duration from the peak to the $1/e$-clipping level and is often used for its mathematical simplicity. Experimentally, we use the full-width at half-maximum duration, related to τ using $\tau_{FWHM} = 2\sqrt{\ln 2}\tau$.

A Gaussian pulse is very convenient because the spectrum also takes the shape of a Gaussian. A pulse is as short as possible if the spectral phase is frequency-independent. We refer to such a pulse as being *transform limited* and we use the time-bandwidth product: $\tau \Delta \nu \approx 0.44$ (for a Gaussian). Alternatively, we can write this expression in terms of wavelength to show: $\tau \approx 0.44 \lambda^2 / (c \Delta \lambda)$. Thus, the transform limited pulse duration is inversely dependent on the spectral width. For example, a transform limited 100-fs pulse has a spectral width of $\Delta \lambda \approx 9.4$ nm at 800 nm and a width of $\Delta \lambda \approx 35.3$ nm at 1,550 nm.

7.1.4 Temporal Pulse Broadening

We observed how a frequency-dependent propagation constant gives rise to phase velocity and group velocity. If we continue to expand the propagation constant in a Taylor series, we see:

$$k(\omega) = k_0 + \left.\frac{dk}{d\omega}\right|_{\omega_0} (\omega - \omega_0) + \frac{1}{2} \left.\frac{d^2 k}{d\omega^2}\right|_{\omega_0} (\omega - \omega_0)^2 + ...$$

$$= k_0 + k'(\omega - \omega_0) + \frac{1}{2} k''(\omega - \omega_0)^2 + ... \tag{7.39}$$

Of these coefficients, we recall that k_0 and k' are related to the phase and group velocities, respectively. We find that higher order dispersion, beginning with k'', begins to change the shape of the pulse, reducing the peak intensity, and is therefore a critical factor for many nonlinear experiments.

7.1.4.1 Group Velocity Dispersion

There is a simple way to think about the spreading of a pulse as it propagates in a material. Consider a transform limited pulse of light, consisting of a spectrum of colors. If we cut the spectrum in half, we will have a higher-energy "blue" pulse and a lower-energy "red" pulse. If we propagate these partial pulses in a media with only linear dispersion (k' is constant and $k'' = 0$), both will propagate with the same group velocity, and we can recombine the blue and red pulses to obtain the original pulse duration. If the medium has higher order dispersion, $k'' \neq 0$ and the group velocity changes as a function of frequency, causing the red and blue pulses to separate in time as they propagate. When we recombine them, there will be a delay between the red and blue pulses, and their combination will be of longer duration than the original pulse. This fixed delay is known as the *group delay dispersion* (GDD). An optical element, such as a fixed length of fiber or a microscope objective, will have a fixed amount of GDD.

If we care about the pulse duration as we propagate, we require the GDD per unit length, which is known as the *group velocity dispersion* (GVD). We define the group velocity dispersion in a material as:

$$\text{GVD} = \frac{\partial}{\partial \omega}\left(\frac{1}{v_g}\right) = \frac{\partial}{\partial \omega}\left(\frac{\partial k}{\partial \omega}\right) = \frac{\partial^2 k}{\partial \omega^2}, \tag{7.40}$$

GVD has units of time squared per length (often fs^2/mm).

We can clarify the difference between GDD and GVD by considering an experiment that consists of several optics (mirrors, lenses, etc.) leading up to a nonlinear pulse propagation experiment (for example, a fiber or a photonic chip). Each optical element before the fiber adds a fixed amount of GDD, broadening the pulse. However, we must consider the interplay between the nonlinearity and dispersion as the pulse propagates within the fiber and therefore, we consider the fiber's GVD.

Just as we had normal and anomalous dispersion previously, the group velocity dispersion can be normal or anomalous. Here, we consider positive values of the GVD as normal and negative values as anomalous. This labeling convention is because most materials at visible wavelengths show normal GVD. For example, the GVD of silica is normal (positive) in the visible, reaches zero around 1.3 μm, and becomes anomalous (negative) for longer wavelengths, such as 1.5 μm.

To make things slightly more confusing, the optical engineering community takes the derivative of the refractive index with respect to the wavelength, producing another term, known as the *dispersion parameter D* given by:

$$D = -\frac{\lambda}{c}\frac{d^2 n}{d\lambda^2} = -\frac{2\pi c}{\lambda^2}\text{GVD} = -\frac{2\pi c}{\lambda^2}\frac{\partial^2 k}{\partial \omega^2}. \tag{7.41}$$

The dispersion parameter has units of time per length squared, often specified in ps/nm/km. These units are convenient when we estimate strong pulse broadening. It is important to note that the sign of the dispersion parameter is opposite to that of GVD, and thus, a material with anomalous dispersion has a *positive* dispersion parameter. These are often used interchangeably, so one should avoid saying "positive" and "negative" dispersion and instead use "normal" and "anomalous" dispersion.

7.1.4.2 Dispersive Pulse Broadening

To observe dispersive broadening, we can consider the Gaussian pulse from Eq. (7.37) and apply the effects of group velocity dispersion given by k''. To simplify the analysis, we assume $k_0 = 0$ and $k' = 0$, both of which will not broaden our pulse, as we have shown. We take the Fourier transform of Eq. (7.37):

$$E(z = 0, \omega) = \frac{1}{\sqrt{2\pi}}\int_{-\infty}^{\infty} E_0 e^{\frac{-t^2}{2\tau^2}} e^{-i\omega_0 t} e^{i\omega t}\,dt = E_0 \tau e^{\frac{-\tau^2(\omega_0 - \omega)^2}{2}}. \tag{7.42}$$

From here, we can add the spectral phase and take the inverse Fourier transform:

$$E\left(z=L,t\right)=\frac{1}{\sqrt{2\pi}}\int_{-\infty}^{\infty}E_0\tau e^{\frac{-\tau^2(\omega_0-\omega)^2}{2}}e^{-i\frac{k''}{2}(\omega-\omega_0)^2L}e^{-i\omega t}d\omega$$

$$=\frac{\tau E_0}{\sqrt{\tau^2+ik''L}}e^{\frac{-t^2}{2\tau^2\left(1+\left(\frac{k''L}{\tau^2}\right)^2\right)}}e^{i\frac{k''Lt^2}{2\left((k''L)^2+\tau^4\right)}}e^{-i\omega_0 t}. \qquad (7.43)$$

We notice that the amplitude changes as the pulse broadens and there is additional phase from the propagation. We also observe that the middle term closely resembles the form of Eq. (7.42) if we let:

$$\tau'=\tau\sqrt{1+\left(\frac{k''L}{\tau^2}\right)^2}, \qquad (7.44)$$

thus, the pulse broadens in time by $\sqrt{1+(k''L/\tau^2)^2}$. We can write this expression in terms of the full-width at half-maximum to show:

$$\tau'_{FWHM}=\tau_{FWHM}\sqrt{1+\left(4\ln 2\frac{GVD}{\tau_{FWHM}^2}d\right)^2}\approx 4\ln 2\frac{GVD}{\tau_{FWHM}}d, \qquad (7.45)$$

as it propagates through a distance d. This approximation is valid for strong dispersive broadening. For silica fiber at 800 nm, GVD $= 36$ fs^2/mm, which corresponds to a dispersion parameter D of -106 ps/nm/km. Consider a 100 fs pulse at 800 nm; after propagating through 1 m of silica fiber, it will have a duration of 1 ps. As the broadening is very strong, we see that using the dispersion parameter is convenient to estimate the pulse duration. For this situation, a 100 fs pulse at 800 nm has a spectral bandwidth of $\Delta\lambda \approx 9.4$nm, thus $\Delta\tau \approx |-106\text{ps/nm/km}| (9.4\text{ nm} \times 1\text{m}) = 996\text{fs}$, which is approximately correct. However, this expression is invalid for small broadening, for example, from a 10-cm length of fiber. Recall that a short pulse has a wide bandwidth and is therefore more susceptible to dispersive broadening than a longer pulse with a reduced bandwidth. This phenomenon creates the counter-intuitive effect where a narrowed spectrum can produce a shorter pulse for a given amount of dispersion.

7.1.4.3 Group Velocity Dispersion Compensation

To facilitate strong nonlinear interactions with low pulse energies, we require very short pulses. As each optical element adds dispersion, potentially broadening the pulse, we address the practical concern of pulse compression here. As the change in pulse duration is a linear effect, we can counteract an amount of normal GDD with an equal amount of anomalous GDD to recover the original pulse duration. With sufficient GDD, we can pre-compensate additional optics to form the shortest pulse
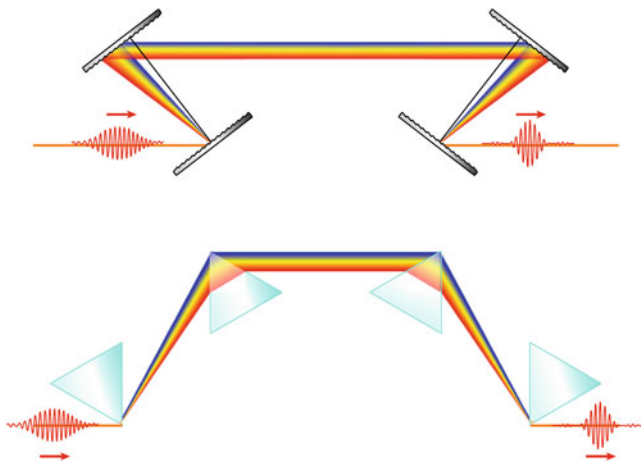
Fig. 7.5 Schematic of a two types of pulse compressors: a grating compressor (*top*) and a prism compressor (*bottom*)

somewhere later in the optical path. For visible and most NIR optical elements, the dispersion is normal. To compensate, we can use a device that has tunable anomalous GDD known as a pulse compressor.

Tunable anomalous group delay dispersion can be achieved using both gratings and prisms, as shown in Fig. 7.5 (top and bottom, respectively). These configurations consist of four elements (gratings or prisms) such that the first two provide half of the intended group delay dispersion starting with a collimated beam and ending with parallel, spatially dispersed colors. The second pair provides the second half of the GDD and reforms the collimated beam. Very often, we use a single grating or prism pair with a mirror that reflects the spatially dispersed colors backward to "fold" the compressor onto itself. This folding-mirror is angled slightly so that the compressed, retroreflected beam can be diverted by another mirror that is initially missed by the incoming beam.

To determine the GDD through a grating or prism pair, we determine the wavelength-dependent path length and the resulting phase through a single pair. From here, we calculate $d^2\varphi/d\omega^2$. For the case of a grating pair, the total GDD is [3]

$$\frac{d^2\varphi}{d\omega^2} = -\frac{\left(1/\omega^2\right)(\lambda/\Lambda)(2\pi L/\Lambda)}{\left[1 - (\sin\theta_i - \lambda/\Lambda)^2\right]^{3/2}}. \tag{7.46}$$

Here, ω is the angular frequency, λ is the wavelength, Λ is the spatial period, θ_i is the angle of incidence of the incoming light, and L is the separation of the gratings. We tune the amount of dispersion compensation by changing the separation of the gratings, L.

For the case of a prism pair, the situation is more complicated because of the additional material dispersion within the prism itself. We find the following approximation is useful for small amount of material dispersion when the prism pair is cut and aligned to the Brewster angle (for maximum efficiency) [4]:

$$\frac{d^2\varphi}{d\omega^2} \approx \frac{\lambda^3}{2\pi c^2} \left[-8L\left(\frac{dn}{d\lambda}\right)^2 + 8\left(\frac{d^2n}{d\lambda^2}\right)(D_{1/e^2}) \right]. \qquad (7.47)$$

Here, L is the separation of the prisms, D_{1/e^2} is the beam diameter (at the $1/e^2$ clipping level), n is the index of refraction, and c is the speed of light. The first term provides tunable anomalous dispersion and depends on the prism material and the separation of the prisms (similar to gratings). The second term is very often normal and depends on the propagation length in the prism material.

For a fixed separation L, the amount of dispersion compensation obtained using gratings is very large compared to prisms, making for shorter separation distances and potentially smaller footprints. For example, to compensate roughly 1,000 fs^2, fused silica prisms require separation of 77 cm and SF10 glass prisms only require 21 cm [4]. However, gratings compressors typically have high amounts of loss and cannot be used for all applications, such as intra-cavity dispersion compensation for a femtosecond laser.

7.2 Nonlinear Optics

The strong electric fields achievable in a laser can drive the motion of electrons and atoms to create a *nonlinear polarization*. This nonlinear polarization gives rise to many effects, from the generation of new frequencies to light-by-light modulation. In this section, we will explore these effects and establish a foundation to later explore all-optical devices.

7.2.1 Nonlinear Polarization

For weak electric fields, the polarization depends linearly on the material susceptibility (in SI units):

$$\vec{P} = \varepsilon_0 \chi \vec{E}, \qquad (7.48)$$

For stronger electric fields, we expand Eq. (7.48),

$$P = \varepsilon_0 \left(\chi^{(1)} E + \chi^{(2)} E^2 + \chi^{(3)} E^3 + \ldots \right), \qquad (7.49)$$

to produce a series of polarizations:

$$P = P^{(1)} + P^{(2)} + P^{(3)} + ..., \tag{7.50}$$

where $P^{(1)} \equiv \varepsilon_0 \chi^{(1)} E$ is the linear polarization, $P^{(2)} = \varepsilon_0 \chi^{(2)} E^2$ is the second-order nonlinear polarization, and so on. Although we have written this polarization in terms of scalars, the electric field is a vector quantity and therefore $\chi^{(1)}$ is a second rank tensor (with 9 elements), $\chi^{(2)}$ is a third rank tensor (27 elements), and $\chi^{(3)}$ is a fourth rank tensor (81 elements), to which we often apply symmetry arguments to isolate unique, non-zero terms [5].

These nonlinear polarization terms act as a driving field in the wave equation, forming the nonlinear wave equation:

$$\nabla^2 \vec{E} - \frac{n^2}{c^2} \frac{\partial^2 \vec{E}}{\partial t^2} = \frac{1}{\varepsilon_0 c^2} \frac{\partial^2 \vec{P}^{NL}}{\partial t^2}, \tag{7.51}$$

Here, n is the linear index of refraction and P^{NL} is the nonlinear polarization (excluding the linear term from Eq. (7.50) contained within n). This driving term acts as a source of new propagating waves.

7.2.1.1 Second-Order Nonlinear Polarization

The second order nonlinear polarization is responsible for several effects involving three photons. For example, two photons can combine to make a third photon. If the two initial photons are of the same (different) frequency, this effect is second harmonic generation (sum-frequency generation). Alternatively, one photon can split to make two photons through difference frequency generation.

Not all bulk crystals exhibit second-order nonlinearities. Let us consider the centrosymmetric case where a crystal has inversion symmetry. For the second order polarization, we find that

$$\vec{P}^{(2)} = \varepsilon_0 \chi^{(2)} \vec{E} \vec{E}. \tag{7.52}$$

If we invert the sign of the fields, we expect the same polarization, only with an opposite sign, therefore

$$-\vec{P}^{(2)} = \varepsilon_0 \chi^{(2)} \left(-\vec{E} \right) \left(-\vec{E} \right) = \varepsilon_0 \chi^{(2)} \vec{E} \vec{E}. \tag{7.53}$$

Both equations cannot be simultaneously true in a centrosymmetric crystal, unless $\chi^{(2)}$ vanishes. Therefore, materials possessing inversion symmetry do not exhibit second-order nonlinearities within the bulk material. Examples include many types of crystals, amorphous materials such as glasses, as well as liquids and gases. However, inversion symmetry is broken at an interface, leading to second-order nonlinearities even for materials with bulk inversion symmetry [6, 7].

Now, let us consider second-harmonic generation in a non-centrosymmetric crystal. Here, we have an electric field given by

$$\vec{E}\left(\vec{r},t\right) = \frac{1}{2}\left(E\left(\vec{r},t\right)e^{-i\omega_0 t} + \text{c.c.}\right)\hat{x}, \tag{7.54}$$

where we consider a single polarization in the *x*-direction. We use the slowly varying envelope approximation through the use of the scalar field $E\left(\vec{r},t\right)$, which we will refer to simply as *E*. The nonlinear polarization is given by

$$\vec{P}^{NL}\left(\vec{r},t\right) = \frac{1}{2}\left(P^{NL}\left(\vec{r},t\right)e^{-i\omega_{NL}t} + \text{c.c.}\right)\hat{x}, \tag{7.55}$$

which produces a second-order polarization:

$$\vec{P}^{(2)} = \varepsilon_0\chi^{(2)}\vec{E}\vec{E} = \varepsilon_0\chi^{(2)}\left[\frac{EE^*}{2} + \frac{1}{2}\left(\frac{E^2}{2}e^{-i2\omega_0 t} + c.c.\right)\right]\hat{x}\hat{x}. \tag{7.56}$$

From this expression, we see two terms. The first is at zero frequency, and is not responsible for generating a propagating wave as it vanishes when operated on by the time-derivative in the wave equation. The next term is at twice the initial frequency, known as the *second harmonic*. We can solve this expression for the slowly varying amplitude of the nonlinear polarization and the frequency to show:

$$P^{(2)}_{2\omega_0} = \frac{\varepsilon_0\chi^{(2)}E^2}{2} \text{ and } \omega_{NL} = 2\omega_0. \tag{7.57}$$

The process of generating second-harmonic signal efficiently requires additional considerations, known as phase matching, which is often achieved using birefringent crystals [8]. In a similar way, a field consisting of two different frequencies can generate terms at the second harmonic of each frequency, as well as for their summation and difference.

7.2.1.2 Third-Order Nonlinear Polarization

The majority of materials are centrosymmetric and therefore, the first non-zero nonlinear polarization is usually the third-order polarization. Writing this polarization out, we find:

$$\vec{P}^{(3)}(t) = \varepsilon_0\chi^{(3)}\vec{E}\vec{E}\vec{E} = \varepsilon_0\chi^{(3)}\left[\frac{1}{2}\left(\frac{E^3}{4}e^{-i3\omega_0 t} + c.c.\right)\right.$$
$$\left. + \frac{1}{2}\left(\frac{3}{4}|E|^2 E e^{-i\omega_0 t} + c.c.\right)\right]\hat{x}\hat{x}\hat{x}. \tag{7.58}$$

Two terms emerge, leading to distinct physical processes. As before, the slowly varying envelope amplitude and nonlinear frequency for the first term is:

$$P_{3\omega_0}^{(3)} = \frac{\varepsilon_0 \chi^{(3)} E^3}{4} \quad \text{and} \quad \omega_{NL} = 3\omega_0, \tag{7.59}$$

respectively. This term is responsible for third harmonic generation. This process is often not efficient unless we use phase-matching techniques.

Meanwhile, the second term is extremely relevant, as the polarization occurs at the original frequency. The slowly varying amplitude and nonlinear frequency are:

$$P_{\omega_0}^{(3)} = \frac{3\varepsilon_0 \chi^{(3)} |E|^2 E}{4} \quad and \quad \omega_{NL} = \omega_0. \tag{7.60}$$

This effect leads to a nonlinear index of refraction and is extremely important for devices. The nonlinear index is perhaps the most frequently observed nonlinearity. Not only do all materials exhibit third-order nonlinearities, but also, phase-matching is automatically satisfied as the polarization is *at the original frequency*. Therefore, we can observe this nonlinear effect without the specialized configurations required of other nonlinearities, such as second- and third-harmonic generation.

7.2.1.3 Anharmonic Oscillator Model

In the same way that we used the Drude-Lorentz model to gain physical insight into the linear dielectric function, we can use the classical anharmonic oscillator model to explore electronic nonlinearities. We base this nonlinear model on the same principles as before, but replace the binding force with an altered, nonlinear force. Just as the binding force for the Drude model is proportional to an electron's displacement from its equilibrium position (x), the second-order polarization requires a term proportional to x^2. For the (more applicable) third-order case, the binding force is:

$$F_{binding} = -m\omega_0^2 x + mbx^3, \tag{7.61}$$

where we have introduced a force term proportional to x^3 with a phenomenological proportionality constant of b. Typically, b is on the order of ω_0^2/d^2, where d is on the order of the Bohr radius [5]. The equation of motion becomes

$$m\frac{d^2x}{dt^2} + m\gamma\frac{dx}{dt} + m\omega_0^2 x - mbx^3 = -eE_0 e^{-i\omega t}. \tag{7.62}$$

We proceed in much the same way as before, which we will not show here. For the case of self-phase modulation, we arrive at [5]:

$$\chi^{(3)} = \frac{Nbe^4}{\varepsilon_0 m^3 D(\omega)^3 D(-\omega)}, \tag{7.63}$$

where $D(\omega) = \omega_0^2 - \omega^2 - i\gamma\omega$. This expression takes a very similar form as χ_e from Eq. (7.18), with additional factors of e^2 and m^{-2}, along with multiple degenerate resonances given by $D(\omega)$. We can approximate this expression if we are far from resonance using:

$$\chi^{(3)} \approx \frac{Ne^4}{\varepsilon_0 m^3 \omega_0^6 d^2}. \tag{7.64}$$

7.2.2 Nonlinear Index of Refraction

The third-order nonlinear polarization gives rise to a nonlinear index of refraction that we use to make all-optical devices. An intensity-dependent index leads to self-phase modulation (SPM) for coherent waves and cross-phase modulation for non-coherent waves. In addition, by allowing $\chi^{(3)}$ to take on complex values, we discover a new source of *nonlinear absorption*, analogous to the linear absorption caused by a complex $\chi^{(1)}$.

7.2.2.1 Intensity-Dependent Refractive Index

If we take the slowly varying envelope amplitudes for the linear polarization $P^{(1)} = \varepsilon_0 \chi^{(1)} E$ and add this new term, we can write an effective linear susceptibility:

$$P^{(1)} + P^{(3)}_{\omega_0} = \varepsilon_0 \chi^{(1)} E + \frac{3\varepsilon_0 \chi^{(3)} |E|^2}{4} E = \varepsilon_0 \left(\chi^{(1)} + \frac{3\chi^{(3)}}{4} |E|^2 \right) E = \varepsilon_0 \chi^{(1)}_{eff} E. \tag{7.65}$$

This effective susceptibility creates an effective index of refraction:

$$n = \sqrt{\mathrm{Re}(\varepsilon)} = \sqrt{\mathrm{Re}\left(1 + \chi^{(1)}_{eff}\right)} = \sqrt{1 + \mathrm{Re}\left(\chi^{(1)}\right) + \frac{3\mathrm{Re}\left(\chi^{(3)}\right)}{4} |E|^2}, \tag{7.66}$$

which we can simplify by expanding around small $|E|^2$:

$$n \approx \sqrt{1 + \mathrm{Re}\left(\chi^{(1)}\right)} + \frac{3\mathrm{Re}\left(\chi^{(3)}\right)}{8\sqrt{1 + \mathrm{Re}\left(\chi^{(1)}\right)}} |E|^2 = n + \frac{3}{8n}\mathrm{Re}\left(\chi^{(3)}\right) |E|^2 = n + \bar{n}_2 |E|^2. \tag{7.67}$$

This derivation produces our first definition of the nonlinear refractive index (in terms of $|E|^2$):

$$\bar{n}_2 = \frac{3}{8n_0}\text{Re}\left(\chi^{(3)}\right).$$ (7.68)

In terms of the intensity, Eq. (7.67) becomes:

$$n = n_0 + n_2 I = n_0 + \frac{3}{4n_0^2\varepsilon_0 c}\text{Re}\left[\chi^{(3)}\right] I.$$ (7.69)

The nonlinear index if often referred to as the *Kerr effect*. For a single wave propagating in a Kerr-medium, the wave's intensity modulates the index of refraction, which modulates the phase of the wave as it propagates. We refer to this process as *self-phase modulation*. A similar effect occurs across different, non-coherent waves, known as *cross-phase modulation* [5]. We note that n_2 can be either positive or negative, depending on the origin of the nonlinearity (electronic polarization, molecular orientation, thermal, etc.). For the electronic, non-resonant nonlinear polarization in silica, n_2 is positive and therefore, we will assume a positive value of n_2. For silica, the nonlinear index of refraction is $2.2\text{–}3.4 \times 10^{-20}$ m^2/W [9].

We have used SI units during this derivation, thus $\chi^{(3)}$ is in units of m^2/V^2. Often $\chi^{(3)}$ is often given in electrostatic units (cm^3/erg, or simply esu). Meanwhile, the nonlinear index is typically quoted in units of cm^2/W. The conversion is [5]:

$$n_2\left(\frac{cm^2}{W}\right) = \frac{12\pi^2}{n_0^2 c}10^7 \chi_{esu}^{(3)},$$ (7.70)

7.2.2.2 Two-Photon Absorption

Using a complex valued $\chi^{(3)}$, we see that the third-order nonlinear polarization implies a nonlinear extinction coefficient, given by:

$$\kappa = \kappa_0 + \kappa_2 I = \kappa_0 + \frac{3}{4n_0^2\varepsilon_0 c}\text{Im}\left[\chi^{(3)}\right] I.$$ (7.71)

Using $\alpha = 2\omega_0\kappa/c$, we can write this expression as the nonlinear absorption:

$$\alpha(I) = \alpha_0 + \alpha_2 I = \kappa_0 + \frac{3\omega_0}{2n_0^2\varepsilon_0 c^2}\text{Im}\left[\chi^{(3)}\right] I.$$ (7.72)

The new term is responsible for two-photon absorption and has units of length per power. For two-photon absorption to occur, the total energy of both photons must be large enough to promote an electron from the valence to the conduction band, and therefore $\chi^{(3)}$ must necessarily be frequency dependent. For degenerate (same frequency) two-photon absorption, the single-photon energy must be at least half of the band-gap energy.

We note that two-photon absorption is a *third-order process* and not a second-order process. We can see this distinction by observing Eq. (7.58), whereby the imaginary third-order nonlinear polarization produces a wave at the original frequency. This out-of-phase wave adds destructively with the original wave, resulting in attenuation.

7.2.3 *Self-Phase Modulation Effects*

Self-phase modulation gives rise to several effects that we can use in devices. Applying SPM in the spatial domain leads to self-focusing; and in the time domain, this effect is responsible for spectral broadening, supercontinuum generation, and four-wave mixing. These processes require high intensities to be efficient; therefore, all sources of loss are important for materials and devices. With losses in mind, we explore the nonlinear figures of merit to assess current and future materials for third-order nonlinear optical applications.

7.2.3.1 Nonlinear Phase

Understanding the accumulation of nonlinear phase is essential, as it forms the basis for many all-optical devices. Starting with Eq. (7.3), we realize that as the wave propagates, it accumulates a phase given by $\varphi = kL$, where L is the distance traveled. Adding the nonlinear index we see:

$$\varphi = k(I)L = \frac{2\pi}{\lambda}\left(n + n_2 I\right)L = \frac{2\pi n L}{\lambda} + \frac{2\pi n_2 L}{\lambda}I = \varphi_L + \varphi_{NL}, \quad (7.73)$$

the intensity alters the phase accumulated by a factor of:

$$\phi_{NL} = \frac{2\pi n_2 L}{\lambda}I, \quad (7.74)$$

through a process known as self-phase modulation. For a plane wave at a single frequency, the wave gains a fixed phase change per unit distance. As we will show later, we can use this nonlinear phase to modulate nonlinear interferometers.

7.2.3.2 Self-Focusing

If we make the intensity non-uniform in space or in time, these gradients results in self-focusing or spectral-broadening, respectively. To demonstrate the effects of a spatial non-uniformity, let us consider a Gaussian beam profile passing through a thin, flat, nonlinear-material. At the center of the beam, the intensity is higher than at the edges, therefore the center accumulates a larger amount of nonlinear phase. For a

material with a positive nonlinear index, the distribution of nonlinear phase shifts is analogous to a positive lens and causes the wave to focus. The Z-scan technique uses this intensity-dependent lens to measure the nonlinearity of bulk samples [10, 11].

7.2.3.3 Spectral Broadening

If we make the intensity non-uniform in time using a pulse, self-phase modulation broadens the pulse's spectrum. Consider a pulse at a fixed location in space that has an intensity that changes in time, $I(t)$. Using Eq. (7.73), we can take a derivative with respect to time, to find a change in frequency given by:

$$\Delta \omega = -\frac{d\varphi}{dt} = -\frac{2\pi}{\lambda} L n_2 \frac{d I(t)}{dt}. \qquad (7.75)$$

For the case of a Gaussian pulse, we remember that Eq. (7.38) can be converted to intensity by dividing by an area and replacing $P_p \rightarrow I_0$. With Eq. (7.75), we find the frequency shift for a Gaussian pulse is:

$$\Delta \omega = \frac{2\pi}{\lambda} L n_2 \frac{8 \ln(2)}{\tau^2} t I(t). \qquad (7.76)$$

From this equation, we realize that $I(t)$ is always positive and $t I(t)$ goes from negative to positive. At a fixed position, negative time is the front of the pulse and therefore, the front of the pulse experiences a negative frequency shift, creating longer, "red" wavelengths in the front. Oppositely, the back end of the pulse (positive time values) is frequency shifted positively and the wavelengths appear "blue-shifted". These are new frequencies that are not present in the original pulse. Alternatively, one can picture this process as the peak of a pulse traveling with a slower phase velocity and therefore, the carrier wave "stretches out" in the front and "bunches up" in the back, creating red and blue wavelengths in the front and back, respectively.

Group velocity dispersive effects are extremely important in a real system. For a positive nonlinearity and normal GVD, both effects cause the red to move toward the front of the pulse and the blue to the back, reducing the intensity, leading to a limited amount of spectral broadening. If GVD is low, the broadening can be very strong, forming a continuum of wavelengths, known as supercontinuum or "white light" generation. In the case of anomalous GVD, the effects of self-phase modulation and GVD are opposite and can lead to a situation where the two effects balance one another, creating stable packets of light, known as *solitons*.

7.2.3.4 Nonlinear Figures of Merit

Material losses limit the performance of SPM-based all-optical switches. Switches made using nonlinear interferometers, for example, require a specified total non-

linear phase for full modulation (i.e. 2π). Total losses (both intrinsic and from fabrication) limit the maximum amount of nonlinear phase by attenuating the wave as it propagates, making full modulation impossible for certain materials [12]. We quantify these limitations using dimensionless parameters known as the nonlinear figures of merit.

To proceed, we ask: for a given material, what is the maximum amount of nonlinear phase that we can accumulate? Let us consider the simplest case of a monochromatic plane-wave experiencing both linear and nonlinear attenuation. Our first step must be to determine the intensity as a function of distance using:

$$\frac{dI(z)}{dz} = -\left[\alpha_0 + \alpha_2 I(z)\right] I(z). \tag{7.77}$$

This differential equation has a solution of the form:

$$I(z) = I_0 e^{-\alpha_0 z} \left[1 + I_0 \alpha_2 \left(\frac{1 - e^{-\alpha_0 z}}{\alpha_0}\right)\right]^{-1}. \tag{7.78}$$

The total nonlinear phase accumulated over a distance L is therefore:

$$\text{total}\varphi_{NL} = \int_0^L \frac{2\pi n_2}{\lambda} I(z) dz = 2\pi \left(\frac{n_2}{\alpha_2 \lambda}\right) \ln\left[1 + I_0 \alpha_2 \left(\frac{1 - e^{-\alpha_0 L}}{\alpha_0}\right)\right]. \tag{7.79}$$

From this expression, we define the effective length for plane-waves and in waveguides as [11].

$$L_{eff} = \frac{1 - e^{-\alpha_0 L}}{\alpha_0}. \tag{7.80}$$

Taking $L \to \infty$, the effective length becomes $1/\alpha_0$ and the maximum nonlinear phase is given by:

$$\max\varphi_{NL} = 2\pi \left(\frac{n_2}{\alpha_2 \lambda}\right) \ln\left[1 + \left(\frac{n_2}{\alpha_2 \lambda}\right)^{-1} \left(\frac{n_2 I_0}{\alpha_0 \lambda}\right)\right]. \tag{7.81}$$

From this result, we can define two figures [13, 14]:

$$W \equiv \left(\frac{n_2 I_0}{\alpha_0 \lambda}\right) \quad \text{and} \quad T^{-1} \equiv \left(\frac{n_2}{\alpha_2 \lambda}\right), \tag{7.82}$$

and we can rewrite Eq. (7.81) as:

$$\max\varphi_{NL} = 2\pi T^{-1} \ln\left[1 + TW\right]. \tag{7.83}$$

The W and T^{-1} figures of merit are associated with linear losses and two-photon absorption, respectively.

Now, let us look at the simplest case, where we have only linear losses, by taking the limit of Eq. (7.83) as $T^{-1} \to \infty$. The maximum nonlinear phase amounts to $2\pi W$, and if we require $\max\varphi_{NL} > 2\pi$, we require that $W > 1$. This result suggests the need for a minimum operating intensity: for a given attenuation coefficient α_0 we require an intensity of $I_0 > \alpha_0\lambda/n_2$. The damage threshold of the material or additional nonlinear effects (particularly two- and three-photon absorption) pose limits for all-optical switching. Alternatively, for a given operating intensity, we must achieve total losses (absorption and scattering) less than $\alpha_0 < n_2 I_0/\lambda$.

Usually, we are only interested in materials with no intrinsic linear absorption and therefore, two-photon absorption and imperfections from the fabrication are limiting factors. For strong two-photon absorption, T^{-1} is small, and the wave is strongly absorbed at the start of propagation. After the intensity quickly drops, we will continue to accumulate nonlinear phase at a reduced rate, requiring very large devices for full modulation. For a fixed value of T^{-1}, we can determine the required value of $\max\varphi_{NL} > 2\pi$:

$$W_{req} > \frac{(e^T - 1)}{T} \approx 1 + \frac{1}{2}T + \frac{1}{6}T^2 + ... \qquad (7.84)$$

For reasonable values of W_{req} (near unity), we use the following guidelines [13, 14]:

$$W = \left(\frac{n_2 I_0}{\alpha_0\lambda}\right) > 1 \text{ and } T^{-1} = \left(\frac{2n_2}{\alpha_2\lambda}\right) > 1. \qquad (7.85)$$

These two figures of merit are a simple and effective way to evaluate a nonlinear material. Although the intrinsic nonlinearity of silica fiber is relatively low, it is a fantastic nonlinear material, having exceptionally low loss and low two-photon absorption. These factors become much more critical in new materials systems with high nonlinearity and serve as a check for applications. For example, silicon has a very strong intrinsic nonlinearity, 200–300 times silica glass. However, this high nonlinearity is accompanied by strong two-photon absorption, and thus the T^{-1} figure of merit is below unity for all telecommunications wavelengths and is only above unity for wavelengths longer than 1,800 nm [15]. Although low figures of merit make ultrafast interferometric switches impractical in silicon, other effects are used for switching [16].

7.3 Nanoscale Optics

In this section, we will explore sub-wavelength waveguides both theoretically and experimentally and use these in the next section to enhance nonlinear interactions. To motivate the use of waveguides for nonlinear optics, we observe that the total

accumulated nonlinear phase depends on the intensity and the effective length in Eq.
(7.79). We can reach high intensities by focusing a laser using a lens; however, the
beam will quickly diverge, leading to few accumulated nonlinearities. Considering
a Gaussian beam, the peak intensity is $I_0 = P_0/(\pi w_0^2)$, where P_0 is the power,
and w_0 is the beam waist. For a focused beam, the divergence limits the length of
nonlinear phase accumulation. If the effective length for a Gaussian beam is given
by the Rayleigh distance $z_R = \pi w_0^2/\lambda$, the intensity-length product for a focused
beam is [9]:

$$I_0 z_R = \left(\frac{P_0}{\pi w_0^2}\right)\left(\frac{\pi w_0^2}{\lambda}\right) = \frac{P_0}{\lambda}. \tag{7.86}$$

The intensity is inversely proportional to the square of the spot size, w_0;
meanwhile, the focused spot will diverge based on the Rayleigh distance, which
is directly proportional to the square of the spot size. These combined effects lead
to a situation whereby tight focusing, alone, does not change the accumulated
nonlinearity. We can achieve much stronger nonlinear interactions if we can
counteract the divergence by keeping the wave confined as it propagates. Such
confinement is precisely what we achieve using a waveguide. If the waveguide has
a loss of α_0, using Eq. (7.80), the intensity-length product is [9]:

$$I_0 L_{eff} = \left(\frac{P_0}{\pi w_0^2}\right)\left(\frac{1 - e^{-\alpha_0 L}}{\alpha_0}\right) \approx \frac{P_0}{\pi w_0^2 \alpha_0}. \tag{7.87}$$

The maximum intensity-length product (for a waveguide of infinite length)
depends completely on the loss of the waveguide and is far greater than for a
focused beam. This ability to accumulate a large amount of nonlinear phase in
a waveguide is an essential tool for nonlinear optics. In addition, we see that the
nonlinear interaction scales inversely with the area. Therefore, the highest nonlinear
interactions will occur for waveguides with the smallest effective area and thus, by
employing nano-scale waveguides, we can achieve very large nonlinear interactions
efficiently.

7.3.1 Waveguides

Waveguides use multiple reflections to confine light signals into discrete channels,
known as modes. By considering geometrical arguments, we will first develop an
intuitive understanding of the guiding condition using reflections from metallic
mirrors. Similarly, we will use total internal reflection to form waveguides in dielec-
tric materials. By observing the wavelength-dependence of the guiding condition,
we will demonstrate how waveguides can alter the effective propagation constant
and use it to engineer the effective dispersion within a waveguide. Lastly, we will
observe the field distributions within waveguides, which will enable us to create
enhanced nonlinearities using sub-wavelength structure.
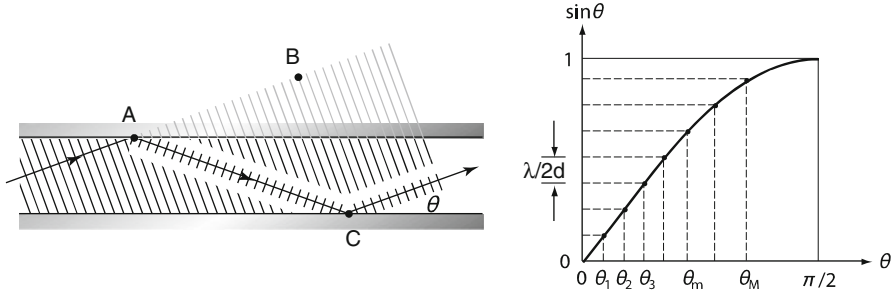
Fig. 7.6 A metallic mirror waveguide showing the periodicity condition requirement (*left*) and a graphical method to determine the solutions to Eq. (7.89) (*right*)

7.3.1.1 Metal Mirror Waveguide

We will start by considering the simplest waveguide formed by two parallel metallic mirrors. Considering the geometry of Fig. 7.6 (left), we see that for the wave to sustain itself, the phase accumulated from multiple bounces must add constructively with the original wave. Each bounce off a metal mirror adds a phase shift of π. Therefore, the total phase from the path length and from each bounce, must be an integer multiple of 2π. From the geometry in Fig. 7.6, this condition is [17]:

$$\frac{2\pi}{\lambda_0}(AC - AB) - 2\pi = \frac{2\pi}{\lambda_0}(AC - AC\cos(2\theta)) - 2\pi$$

$$= \frac{2\pi}{\lambda_0}2d\sin\theta - 2\pi = 2\pi m',$$
(7.88)

where m' is an integer (starting from zero). Simplifying this expression and using $m = m' + 1$, we obtain:

$$2d\sin\theta = m\lambda_0 \; m = 1,\, 2,\, ...$$
(7.89)

Therefore, we have a discrete number of propagating solutions, as shown in Fig. 7.6 (right). Each solution is known as a *mode* and acts like a channel for an electromagnetic wave. The number of guided modes for a single polarization is given by:

$$M = \frac{2d}{\lambda_0}.$$
(7.90)

We find that no guiding can occur when the distance becomes less than half of the wavelength.

Depending on the orientation of the electric field, two unique waves can propagate. If the electric field of the wave is transverse to the plane of the mirror, we find the *transverse-electric* polarization (TE) and there is no electric field in the direction of propagation. Swapping the electric and magnetic fields results in *transverse-magnetic* polarization (TM). These will become important when we consider dielectric waveguides, as the boundary conditions are slightly different for TE- versus TM-waves.

In the case of a metal mirror waveguide, this condition is identical for the both TE and TM polarizations, and therefore the total number of supported modes is twice this value. Alternatively, we can write down an equation for the cutoff frequency (the lowest frequency that is still guided), by setting $\sin\theta = 1$ and $m = 1$, then solving for the frequency to show:

$$\omega_c = \frac{\pi c}{d}.$$ (7.91)

7.3.1.2 Planar Dielectric Guiding

Alternatively, we can form a waveguide using dielectric materials. This case is very similar to the two-mirror case, except the wave is guided using total internal reflection. Therefore, we require a high index material surrounded on the top and bottom by lower index materials. The relative index difference is related to the index contrast and determines parameters including the number of modes, the phase and group velocities, GVD and the confinement.

For total internal reflection, the angle between the wavevector and the normal to the interface must be greater than the critical angle. The critical angle is given by $\sin\theta_c = n_2/n_1$, where n_1 is the index in the guiding layer and n_2 is the cladding index. We should note that our current waveguide discussion uses the *complimentary angle*. In our present notation, waves will be totally internally reflected if $\theta < (\pi/2 - \theta_c)$. Using these conditions, we modify Eq. (7.88) by scaling the length by the index of the guiding layer, n_1, and we replace the phase-shift upon reflection, previously π, with a new material- and polarization-dependent phase-shift, φ:

$$\frac{2\pi}{\lambda_0} n_1 (2d \sin\theta) - 2\varphi = 2\pi m'$$ (7.92)

If we use the convention that $\lambda = \lambda_0/n_1$, the condition becomes [17]:

$$\frac{2\pi}{\lambda} 2d \sin\theta - 2\varphi = 2\pi m.$$ (7.93)

Fig. 7.7 Graphical solutions to the waveguiding condition from Eq.(7.97)
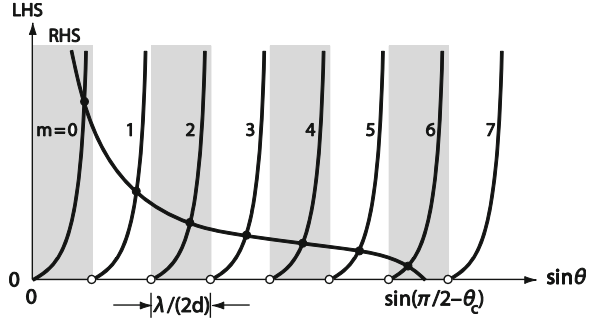
The phase change depends on the materials (through θ_c) and on the polarization [18]:

$$\varphi_{TE} = 2\tan^{-1}\left(\sqrt{\frac{\cos^2\theta_c}{\sin^2\theta} - 1}\right), \text{ and} \tag{7.94}$$

$$\varphi_{TM} = 2\tan^{-1}\left(\csc^2\theta_c\sqrt{\frac{\cos^2\theta_c}{\sin^2\theta} - 1}\right), \tag{7.95}$$

for TE- and TM-polarizations, respectively. Using these expressions, we determine the guiding condition to be:

$$\tan\left[\frac{\pi d}{\lambda}\sin\theta_{TE} - \frac{m\pi}{2}\right] = \sqrt{\frac{\sin^2(\pi/2 - \theta_c)}{\sin^2\theta_{TE}} - 1}, \text{ and} \tag{7.96}$$

$$\tan\left[\frac{\pi d}{\lambda}\sin\theta_{TM} - \frac{m\pi}{2}\right] = \csc^2\theta_c\sqrt{\frac{\sin^2(\pi/2 - \theta_c)}{\sin^2\theta_{TM}} - 1}. \tag{7.97}$$

To find the modes graphically, we can plot both the left- and right-hand sides in terms of $\sin\theta$, the solutions occur whenever the two curves intersect, as shown in Fig. 7.7.

In addition, we can calculate the number of modes by determining the number of crossings. We realize that the left-hand side is periodic in $\sin\theta$ and we can expect a solution for each of period until the right hand side goes to zero. Considering both even and odd values of m, the function has a periodicity of $\lambda/(2d)$ in terms of $\sin\theta$. We find that the right-hand side goes to zero when $\sin\theta = \sin(\pi/2 - \theta_c)$. Therefore, the number of modes, M, for TE-polarization is given by:

$$M \doteq \frac{\sin(\pi/2 - \theta_c)}{\lambda/(2d)}. \tag{7.98}$$

Note that we must round up in this case. Alternatively, we can write this expression in terms of the refractive indices use by using:

$$\sin(\pi/2 - \theta_c) = \cos\theta_c = \sqrt{1 - \sin^2\theta_c} = \sqrt{1 - n_2^2/n_1^2} = \frac{\sqrt{n_1^2 - n_2^2}}{n_1}, \quad (7.99)$$

to show:

$$M \doteq \frac{2d}{\lambda n_1}\sqrt{n_1^2 - n_2^2} = \frac{2d}{\lambda_0}\sqrt{n_1^2 - n_2^2}, \quad (7.100)$$

for TE-polarization [17]. (Note the substitution of the free-space wavelength.) This expression is not correct if we consider an asymmetric waveguide with a different upper and lower cladding. Similarly, we have a cutoff frequency of [17]:

$$\omega_c = \frac{\pi c}{d}\frac{1}{\sqrt{n_1^2 - n_2^2}}, \quad (7.101)$$

above which multiple modes of one polarization will propagate.

Multiple modes in a waveguide can make designing and fabricating devices difficult. Although modes are linearly independent, small perturbations in real systems can couple multiple modes to one another. Therefore, we often try to make waveguides *single-mode*. We consider a waveguide single-mode if it only supports a single guided mode for a particular polarization (TE or TM). We can obtain single-mode operation by adjusting the waveguide materials and geometry, as shown in Eqs. (7.90) and (7.100).

Comparing the single-mode condition for mirror versus dielectric guiding, we find that using 600-nm light, the single-mode thicknesses d for mirror guiding is in the range from 300 to 600 nm, below which, no modes are supported. On the other hand, for fused silica, we find single-mode guiding for thicknesses less than 283 nm, with no minimum thickness, in contrast to the mirror guided case. If we reduce the index contrast between the core and the cladding, we can increase the size of the waveguide, as is done for standard silica fiber.

7.3.1.3 Propagation Constants

A guided wave will propagate at a different speed due to the multiple bounces it must undergo. Therefore, it no longer makes sense to use the wavevector k to describe the rate of phase propagation and we define a new constant $\beta = 2\pi n_{eff}/\lambda_0$ known as the propagation constant. The wave travels in an analogous manner to a plane wave, however k is replaced by $\beta = 2\pi n_{eff}/\lambda_0$ and the wave propagates with an effective index of n_{eff}. We can illustrate the propagation constant by consider the mirror waveguide shown in Fig. 7.8. We see that [17]:
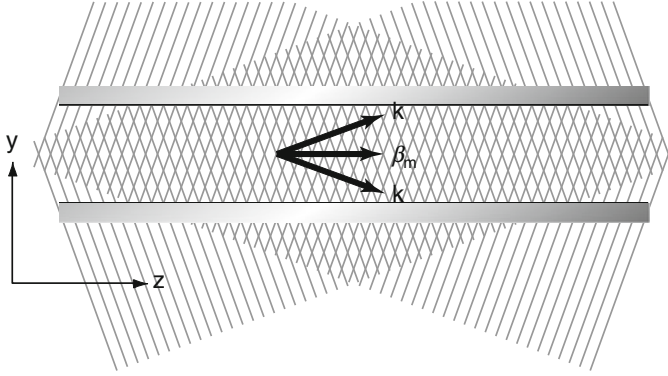
Fig. 7.8 Propagation constant for a metallic mirror waveguide

$$\beta^2 = k^2 - k_y^2 = k^2 \left(1 - \sin^2\theta_m\right) = k^2 \left(1 - \frac{m^2\lambda_0^2}{4d^2}\right) = k^2 - \frac{m^2\pi^2}{d^2}, \quad (7.102)$$

Which we write this expression in terms of the cutoff frequency to obtain:

$$\beta_m = \frac{\omega}{c}\sqrt{1 - m^2\frac{\omega_c^2}{\omega^2}} = \frac{\omega}{c}\cos\theta_m. \quad (7.103)$$

The propagation constant for a mirror waveguide is less than the free-space propagation constant, implying that the phase velocity is greater than the speed of light. We determine the group velocity for a mirror waveguide using:

$$v_g = \left[\frac{d\beta_m}{d\omega}\right]^{-1} = c\sqrt{1 - m^2\frac{\omega_c^2}{\omega^2}} = c\cos\theta_m. \quad (7.104)$$

showing that the group velocity is still slower than the speed of light. Similarly, we calculate the GVD for a mirror waveguide using:

$$GVD = \frac{d^2\beta_m}{d\omega^2} = -\left(\frac{m^2\omega}{c}\right)\left(\frac{\omega_c}{\omega^2 - m^2\omega_c^2}\right)^2\sqrt{1 - \left(\frac{m\omega_c}{\omega}\right)^2}. \quad (7.105)$$

This simple model provides two critical insights. First, we find that the dispersion for a metal waveguide is always negative (anomalous), contrary to many dielectric materials. Secondly, we find that the GVD depends heavily on the cutoff frequency of the waveguide $\omega_c = \pi c/d$ and becomes very strong as we approach the cutoff frequency. Therefore, the GVD is heavily dependent on the waveguide geometry. Thus, by changing the mirror separation d, we have the ability to tune the GVD, which we have seen is a critical parameter for pulse propagation.

In a similar way, we determine the propagation constant for a dielectric wave-guide starting with:

$$2d\sqrt{\frac{\omega^2}{c_1^2} - \beta^2} = 2\varphi_r + 2\pi m, \tag{7.106}$$

with integer values of m. Similar to the mirror waveguide, we can use this condition to derive the group velocity for a dielectric waveguide. The derivation is rather mathematical and is of limited use in the present context. Therefore, we refer the reader to the derivation presented in [17], and present the result here:

$$v_g = \frac{d\cot\theta + \Delta z}{n_1 d\csc\theta/c + \Delta\tau}. \tag{7.107}$$

Here, n_1 is the refractive index of the core, θ is the angle associated with the planar mode. In addition, we have introduced Δz, which corresponds to the additional distance that the wave propagates along the boundary in the form of an evanescent wave for each round trip. This additional propagation takes a time $\Delta\tau$. We can relate this result to our previous result, if we have no evanescent field by setting $\Delta z = \Delta\tau = 0$. Equation (7.107) reduces to $v_g = (c/n_1)\cos\theta$, which is identical to Eq. (7.104), with the addition of a dielectric between the two mirrors.

Just as for a metal mirror waveguide, the group velocity depends on the thickness of the dielectric waveguide. The dielectric's intrinsic GVD alters the total GVD, which is sometimes approximated as the sum of the material dispersion and the waveguide dispersion [19, 20]. We must also consider the penetration of the evanescent wave into the cladding. Because of these considerations, and the complications of a two-dimensional waveguide cross-section, we often use numerical simulations.

As many materials display normal GVD at optical frequencies, we are often interested in reducing the amount of normal dispersion by introducing anomalous waveguide dispersion. For this case, we see two general design considerations. First, we should design our waveguides with dimensions that are comparable to the wavelength of interest (near cutoff). Second, we should use core and cladding materials with high index-contrasts to reduce the penetration of the evanescent field and better approximate the strong anomalous dispersion found in the mirror waveguide.

7.3.1.4 Waveguide Equation

Light propagates differently in a waveguide than it does in free-space; however, it is similar to plane wave propagation. To reflect this similarity, we can rewrite the wave equation and look for solutions that take the same form as plane waves. We use a spatially varying dielectric constant $\varepsilon_r(x, y)$ that is infinite in the z-direction. We start with the equation for the time-harmonic vector and scalar potentials in a source-free, non-magnetic, non-uniform, dielectric medium [3]:

$$\nabla^2 \vec{A} + \omega^2 \frac{\varepsilon_r}{c^2} \vec{A} = -i \frac{\omega}{c^2} \nabla \varepsilon_r \Phi. \qquad (7.108)$$

The electric field is determined by $\vec{E} = -i\omega\vec{A} - \nabla\Phi$. We see that the right hand side of Eq. (7.108) couples the vector and scalar potential. If we assume that $\nabla\varepsilon_r$ is small and set it to zero, we can obtain:

$$\nabla^2 \vec{A} + \frac{\omega^2}{c^2} \varepsilon_r \vec{A} = 0. \qquad (7.109)$$

We can look for solutions that resemble plane waves of the form:

$$\vec{A} = \vec{y} F(x, y) e^{-i\beta z}, \qquad (7.110)$$

where we assume that all the of z dependence is in $e^{-i\beta z}$, and therefore $F(x, y)$ is the *modal distribution*, which describes the spatial profile of the mode. After substitution, the differential equation for $F(x, y)$ is:

$$\nabla_T^2 F + \left(-\beta^2 + \frac{\omega^2}{c^2} \varepsilon_r (x, y) \right) F = 0, \qquad (7.111)$$

where ∇_T^2 is the Laplacian in the transverse spatial direction. This equation has the same form as the time-dependent Schrodinger equation for a two-dimensional potential well with a potential of $-\omega^2\mu_0\varepsilon(x, y)$. Therefore, this equation's solutions are completely analogous to those for a quantum well and, as we've seen previously, requires specific values of the propagation constant β.

7.3.1.5 Waveguide Field Distributions

For the case of a metallic mirror waveguide, the electric field must necessarily be zero at the metallic boundary. However, for the case of dielectric waveguides, the field extends beyond the boundary as a decaying *evanescent* field. Solving Eq. (7.111), a TE mode has an internal field given by [17]:

$$F_m(y) \propto \begin{cases} \cos\left(2\pi \frac{\sin\theta_m}{\lambda} y \right), & m = 0, 2, 4, \ldots \\ \sin\left(2\pi \frac{\sin\theta_m}{\lambda} y \right), & m = 1, 3, 5, \ldots \end{cases} \quad -\frac{d}{2} \leq y \leq \frac{d}{2}, \qquad (7.112)$$

with $\lambda = \lambda_0/n_1$. Outside of the waveguide core, the evanescent field is given by:

$$F_m(y) \propto \begin{cases} \exp\left[-\left(n_2 k_0 \sqrt{\frac{\cos^2\theta_m}{\cos^2(\pi/2-\theta_c)} - 1} \right) y \right], & y > d/2 \\ \exp\left[\left(n_2 k_0 \sqrt{\frac{\cos^2\theta_m}{\cos^2(\pi/2-\theta_c)} - 1} \right) y \right], & y < -d/2 \,. \end{cases} \qquad (7.113)$$

Fig. 7.9 The
spatial-distribution for the
wave functions of a quantum
well have the same form as a
guided electromagnetic wave.
Here, we see the several wave
function for an infinite
quantum well (*far left*), a
mirror waveguide (*middle
left*), a finite potential
quantum well (*middle right*),
and a dielectric waveguide
(*far right*)
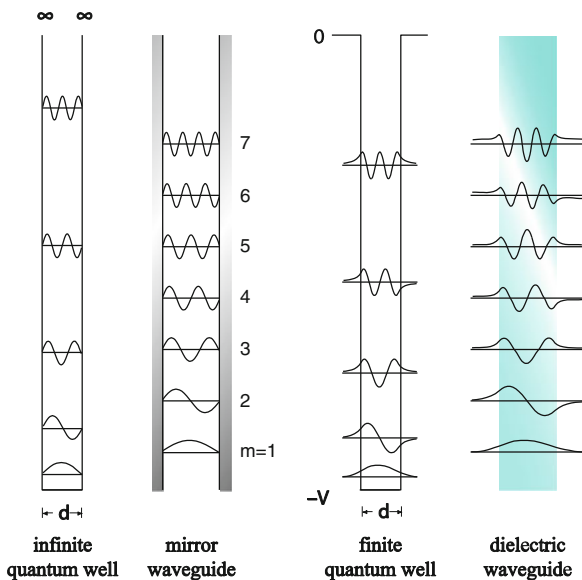
We see the evanescent field decays into the surrounding medium, as shown in
Eq. (7.113). The higher order modes, having larger angles, θ_m, will extend further
into the cladding [17].

Just as for quantum wells, there are analogous oscillatory solutions for waveg-
uides, as shown in Fig. 7.9. For mirror waveguides, the modes resemble an infinite
quantum well, with the wave going to zero at the boundaries (Fig. 7.9, left).
Alternatively, we see that waves guided by a dielectric extend beyond the boundaries
and propagate in the form of an evanescent wave, analogous to a finite quantum well
(Fig. 7.9, right).

We have only dealt with planar waveguides so far, for simplicity. We can confine
the wave in the other transverse dimension as well, which enables us to concentrate
light strongly in two-dimensions. Adding an additional degree of freedom leads to
many different type of waveguides including cylindrical waveguides, such as fibers,
as well as rectangular waveguides such as channel, strip, and ridge waveguides [2].

7.3.2 Silica Nanowires

We have seen that in dielectric waveguides, the thickness and refractive indices
determine the number of modes, their spatial distribution, propagation constants,
and GVD. High index contrasts enable stronger confinement, greater control over
the total GVD and can lead to bends with very small radii of curvature. However,
high index contrast waveguides require excellent uniformity. Abrupt tapers and
interfacial roughness causes scattering and can be large a source of optical loss.
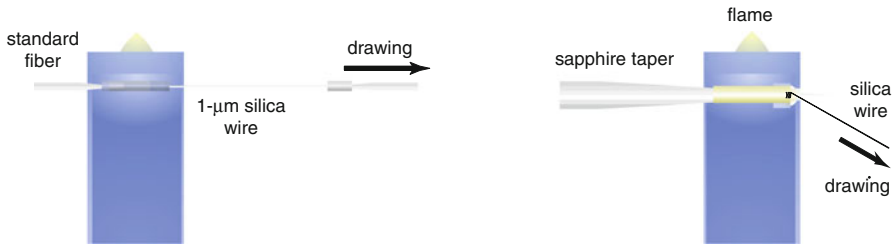
Fig. 7.10 Two-step drawing process for silica nanowires. First, we draw the standard fiber over a flame to form nanowires down to 1 μm (*left*). By attaching the fiber to a sapphire taper and drawing a second time, we fabricate nanowires down to 10's of nanometers [22]

Therefore, smooth, uniform waveguides are a necessity for operating in this high-index contrast regime. In this section, we will explore silica nanowires as a simple and effective waveguiding system for nano-scale optics.

7.3.2.1 Silica Nanowire Fabrication

Silica nanowires are easily fabricated using a fiber-pulling technique [21]. Starting with a standard silica fiber, we remove the protective coating to expose the cladding. We place the bare fiber within a flame until the silica softens and then the fiber is drawn until it breaks, Fig. 7.10 (left). This process creates a tapered region starting from a typical diameter of 125 μm that ends in a fiber that is 1–5 μm in diameter. We make smaller diameter nanowires, down to 20 nm, by attaching the free-end of the nanowire to a sapphire taper, placing the sapphire into the flame, and drawing a second time (Fig. 7.10, right) [21, 22]. Nanowires drawn this way are advantageous because one end is still attached to a standard optical fiber, facilitating simple coupling. Alternatively, we use a mechanical method for pulling nanowires, which results in slightly larger dimensions (down to 90 nm) with the advantage of having standard optical fiber on both ends [23].

The drawing process has several critical factors to achieve reliable results. First, the fiber must be extremely clean when being drawn to insure uniform heating. Second, the flame must be well controlled and well characterized to insure that the nanowire is at the optimum hot spot. Third, the flame must be very of high quality, such as hydrogen.

7.3.2.2 Mechanical Properties

Silica nanowires have extremely high quality mechanical properties [21, 24]. They can be made small (down to 20 nm) [22], with lengths up to tens of mm [21]. These are extremely uniform; for example, a 260-nm diameter fiber displays an 8-nm diameter variation over a total length of 4 mm, resulting in a uniformity of 10^6
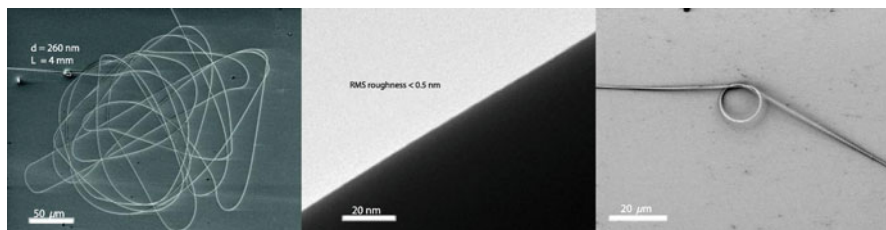
Fig. 7.11 Physical properties of silica nanowires. A coiled, 260-nm diameter silica nanowire that is 4-mm long (*left*). An SEM image of a silica nanowire, demonstrating smooth sidewall roughness (*middle*). We can bend can form these into devices such as this nano-knot (*right*)

with an aspect ratio of 7×10^{-5} [23]. Meanwhile, the surface roughness is less than 0.5 nm (Fig. 7.11, middle) [21, 22]. They are extremely strong with an estimated tensile strength of 5 GPa [21].

We can bend and twist silica nanowires to form devices (Fig. 7.11, right). The small diameter of the nanowires enables a strong Van Der Waals force that can hold devices in place. Nanowire bends are elastic and therefore straighten when stress is released; however, annealing nanowires enables such temporary bends to become permanent.

7.3.2.3 Optical Properties

The smoothness and uniformity of silica nanowires, combined with the high index-contrast between silica ($n = 1.45$) and air ($n = 1$), produces high quality sub-micrometer waveguides. We launch light into a nanowire by coupling into the macroscopic optical fiber using standard objective coupling techniques. Additionally, we collect the light exiting the nanowire using a similar method, thus creating a bi-directional link to the nanoscale.

Guiding losses display an interesting trend as a function of diameter. Figure 7.12 (left) shows the measured propagation loss as a function of diameter at two wavelengths, 633 and 1,550 nm. We see that losses are lower for longer wavelengths. In addition, larger diameter nanowires result in lower losses, typically below 0.1 dB/mm [23].

When guiding light in a nanowire, we observe scattering from microscopic dust particles (Fig. 7.12, right) and notice an interesting dependence on the diameter. For large fibers, we observe virtually no scatter (not shown). As we decrease the diameter below 1 μm, we find significant and uniform scattering. As we decrease the diameter below 450 nm, the scattering becomes restricted to increasingly fewer, brighter spots.

We can explain the peculiar scattering shown in Fig. 7.12 (right) intuitively if we observe the transverse shape of the mode. We calculate and plot the Poynting-vector profile for an 800-nm, 500-nm, and 200-nm diameter silica nanowire in Fig. 7.13
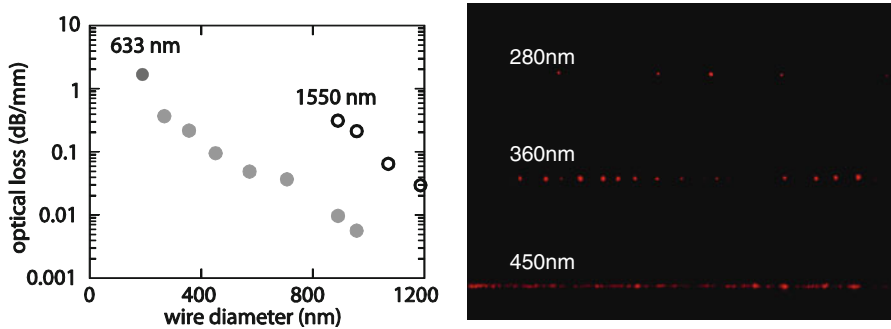
Fig. 7.12 Optical losses versus nanowire diameter for 633- and 1,550-nm light (*left*). Diameter dependent scattering of silica nanowires (*right*)
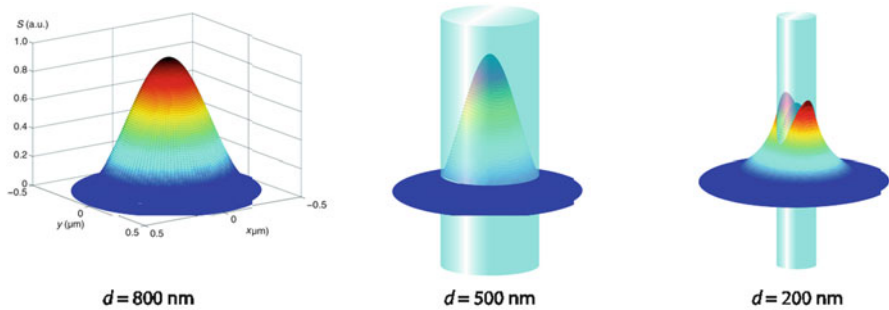
Fig. 7.13 Numerically simulated Poynting vector for 633-nm light in a silica nanowire for several diameters [23]

(left, middle, and right, respectively), with a wavelength of 633 nm. We find that for a waveguide with diameter of 800 nm and larger, the fraction of the wave guided within the core (which we refer to as the *confinement*) is very high, and there is little evanescent field. For smaller diameters (around 500 nm), a significant evanescent field develops, leading to more scattering. For even smaller diameters, the power is almost entirely guided on the outside of the fiber in the form of an evanescent wave. The large evanescent wave leads to very strong scattering. We might expect more scattering from smaller nanowires, but we actually observe fewer scattered particles. We can easily explain this trend when we realize that the surface area decreases in smaller nanowires, leading to less area for the dust particles to attach, reducing the total number of dust particles.

Quantitatively, Fig. 7.14 shows the confinement as a function of the diameter for silica nanowires guiding 633- and 1,550-nm light. For very large diameters, the light is confined completely within the core; however, the light is not very concentrated as it spreads across the total cross section of the waveguide. For diameters near or slightly smaller than the wavelength, the fraction of light within the core is over

Fig. 7.14 Calculated optical
confinement in a silica
nanowire for 633- and
1,550-nm light [23, 25]
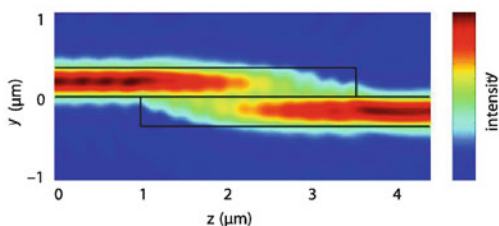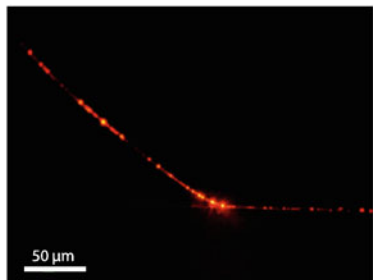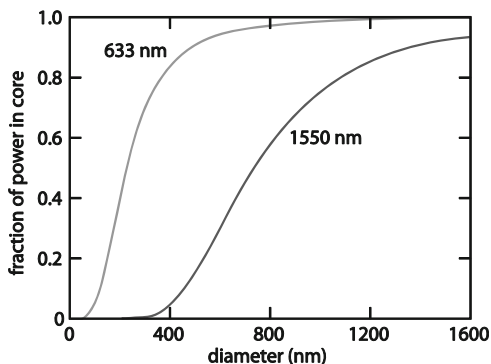
Fig. 7.15 Optical image of two silica-nanowires evanescently coupling (*left*) [21]. Numeric
simulation showing strong coupling over a distance of 3 μm (*right*) [26]

90 %, thus the light is tightly confined and well contained within the material, which
we refer to as *strong confinement*. Lastly, diameters less than one quarter of the
wavelength guide light almost completely in the evanescent field.

The substantial evanescent waves in silica nanowires are advantageous for
sensing. When a considerable fraction of the light is guided in the evanescent field,
the wave will strongly interact with nearby materials, enabling efficient coupling
over short distances [26]. In combination with the strong Van Der Waals force,
coupling is as simple as touching one nanowire to the other, as shown in Fig. 7.15
(left). Coupling can also happen on extremely short length-scales, down to a several
micron, as shown using simulation (Fig. 7.15, right) [26].

Just as we can bend, form, and cut silica nanowires mechanically, we can use
these techniques to form devices. So far, we have only considered devices that are
freely suspended in air. To make practical devices, we require a substrate with lower
index; otherwise, the wave will escape into the cladding below. Potential substrates
include MgF$_2$ ($n = 1.37$), mesoporous silica ($n = 1.18$) [23, 27], and silica aerogel
($n = 1.05$) [24]. Using such a substrate, we can form devices such as the directional
coupler shown in Fig. 7.16 (middle) [24]. We can achieve very small bending radii,
as low as 5 μm with losses around 1 dB per 90-degree turn, as shown Fig. 7.16
(left) [24]. In addition, we can use silica nanowires to couple into and out of other
nano-scale materials such as ZnO nanowires, shown in Fig. 7.16 (right) [27].
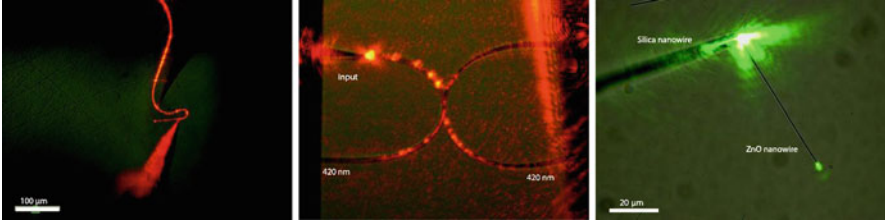
Fig. 7.16 The high index contrast between silica and air enables tight bends for devices (*left*) [21]. We can form micro-scale devices such as a directional coupler (*middle*) [24]. We can couple into other nano-scale devices such as this ZnO waveguide (*right*) [27]

7.4 Nonlinear Optics at the Nanoscale

We have explored both the linear and nonlinear propagation of plane waves in materials and in waveguides, developed an understanding of linear pulse propagation, and have identified how waveguides can enable high intensities in space (strong confinement) and time (short-pulse dispersion management). Now we will merge these concepts together to introduce nonlinear optics at the nanoscale and demonstrate several applications.

7.4.1 Nonlinear Schrodinger Equation

The generalized nonlinear Schrodinger equation (NLSE) is the workhorse of nonlinear fiber and integrated optics. It adds a third-order nonlinear response to the waveguide equation and describes the temporal evolution of a pulse in a nonlinear waveguide. Although we will discuss the simplest version here, we can extend this model to include wide-bandwidth pulses, a delayed nonlinearity, and two-photon absorption.

7.4.1.1 Nonlinear Schrodinger Equation

To develop the nonlinear Schrodinger equation, we will follow the derivation by Agrawal [9]. Let us consider the wave equation in terms of the linear and nonlinear polarization in the time domain:

$$\nabla^2 \vec{E} - \frac{1}{c^2} \frac{\partial^2 \vec{E}}{\partial t^2} = \mu_0 \frac{\partial^2 \vec{P}_L}{\partial t^2} + \mu_0 \frac{\partial^2 \vec{P}_{NL}}{\partial t^2}. \tag{7.114}$$

Our strategy for simplifying this differential equation starts by including the nonlinear polarization into an effective dielectric constant $\varepsilon_{eff}(\omega)$. Next, we use separation of variables to isolate a transverse-wave equation from the propagation

equation, as we did when analyzing the modes in a waveguide. We incorporate the nonlinear polarization by solving the transverse equation and using the nonlinear part of $\varepsilon_{eff}(\omega)$ as a perturbation. The lowest order perturbation alters the propagation constant, while keeping the distribution of the mode intact. We apply the resulting linear and nonlinear propagation constants to the propagation equation to arrive at the NLSE, which describes the temporal evolution of a pulse in a nonlinear waveguide.

As we have seen in previously, the effects of dispersion are easiest to handle in the frequency domain. For clarity, we will denote variables in frequency domain using a tilde above. Therefore, we take the Fourier transform of Eq. (7.114), to show:

$$\nabla^2 \tilde{E} - \varepsilon_{eff}(\omega) k_0^2 \tilde{E} = 0, \tag{7.115}$$

and we define an effective relative dielectric constant in the frequency domain:

$$\varepsilon_{eff}(\omega) = 1 + \tilde{\chi}_{xx}^{(1)}(\omega) + \varepsilon_{NL}. \tag{7.116}$$

Although not explicitly stated, the effective dielectric constant varies in the transverse direction to form the waveguide. By combining both the linear and nonlinear terms into an effective dielectric constant, we simplify the analysis.

Next, we combine the slowly varying amplitude approximation from Eq. (7.36) with the modal distribution from Eq. (7.110) in the time domain:

$$\vec{E} = F(x, y) A(z, t) \exp(i\beta_0 z - \omega_0 t) \hat{x}. \tag{7.117}$$

Here, we have a carrier wave given by $\exp(i\beta_0 z - \omega_0 t)$ that is slowly modulated by an envelope function, $A(z, t)$. Taking the Fourier transform of this expression, we substitute

$$\tilde{E} = F(x, y) \tilde{A}(z, \omega - \omega_0) \exp(i\beta_0 z), \tag{7.118}$$

into (7.115). Now, we perform a separation of variables to show:

$$\frac{\partial^2 F}{\partial x^2} + \frac{\partial^2 F}{\partial y^2} + \left[\varepsilon_{eff}(\omega) k_0^2 - \tilde{\beta}(\omega)^2 \right] F = 0, \tag{7.119}$$

and

$$2i\beta_0 \frac{\partial \tilde{A}}{\partial z} + \left(\tilde{\beta}^2(\omega) - \beta_0^2 \right) \tilde{A} = 0. \tag{7.120}$$

We have used the slowly varying amplitude approximation and assumed the term $\partial^2 \tilde{A}/\partial z^2$ is negligible compared to $\beta(\omega) \left(\partial \tilde{A}/\partial z \right)$. Equation (7.119) closely resembles (7.111), determines the modal distribution $F(x, y)$ and the propagation constant $\tilde{\beta}(\omega)$, and includes the nonlinear dielectric constant $\varepsilon_{eff}(\omega)$.

We incorporate the nonlinearity by using first-order perturbation theory. We replace ε with n^2 and approximate $\varepsilon = (n + \Delta n)^2 \approx n^2 + 2n\Delta n$. Next, we use

$$\Delta n = n_2 |E|^2 + \frac{i\alpha}{2k_0}, \tag{7.121}$$

where n_2 is the nonlinear index of refraction and α is the attenuation coefficient. Using perturbation theory results in a modal distribution $F(x, y)$ that is unaffected by the nonlinearity, to first order. Meanwhile, the nonlinearity comes into play through a perturbation of the propagation constant:

$$\tilde{\beta}(\omega) = \beta(\omega) + \Delta\beta(\omega), \tag{7.122}$$

where

$$\Delta\beta(\omega) = \frac{\omega^2 n(\omega)}{c^2 \beta(\omega)} \frac{\int \int_{-\infty}^{\infty} \Delta n(\omega) |F(x, y)|^2 dx dy}{\int \int_{-\infty}^{\infty} |F(x, y)|^2 dx dy}. \tag{7.123}$$

This expression is completely analogous to self-phase modulation using a nonlinear wavevector k from Eq. (7.73), except applied to the propagation constant. This situation is slightly more complicated because we must consider the modal distribution. However, we can use the waveguide geometry, through $F(x, y)$, to increase the rate of nonlinear phase accumulation.

Solving Eq. (7.119) and applying (7.123), we obtain the modal distribution and both the linear and nonlinear propagation constants. Now, we can apply these results to Eq. (7.120). To further simplify Eq. (7.120), we assume that the frequency-dependent propagation constant remains close to the propagation constant of the carrier wave $\tilde{\beta}(\omega) \approx \beta_0$, and we approximate $\tilde{\beta}^2(\omega) - \beta_0^2 \approx 2\beta_0 \left(\tilde{\beta}(\omega) - \beta_0\right)$. Now, the Fourier transform of the slowly varying envelope $\tilde{A}(z, \omega - \omega_0)$ satisfies:

$$\frac{\partial \tilde{A}}{\partial z} = i [\beta(\omega) + \Delta\beta(\omega) - \beta_0] \tilde{A}. \tag{7.124}$$

As we are only concerned with the spectral bandwidth around the carrier frequency of the pulse, we Taylor expand the propagation constant in the frequency domain:

$$\beta(\omega) = \beta_0 + (\omega - \omega_0)\beta_1 + \frac{1}{2}(\omega - \omega_0)^2\beta_2 + \frac{1}{6}(\omega - \omega_0)^3\beta_3 + \dots \tag{7.125}$$

where $\beta_0 = \beta(\omega_0)$ is the propagation constant of the carrier wave and

$$\beta_m \equiv \left(\frac{d^m \beta}{d\omega^m}\right)_{\omega=\omega_0}. \tag{7.126}$$

Similarly, we expand $\Delta\beta\left(\omega\right)$:

$$\Delta\beta\left(\omega\right) = \Delta\beta_0 + \left(\omega - \omega_0\right)\Delta\beta_1 + \frac{1}{2}\left(\omega - \omega_0\right)^2\Delta\beta_2 + ..., \qquad (7.127)$$

using a comparable definition of $\Delta\beta_m$ to Eq. (7.126). Using these definitions for the propagation constant to second order in $\beta\left(\omega\right)$, and first order in $\Delta\beta\left(\omega\right)$, we take the inverse Fourier transform of Eq. (7.124) to arrive at:

$$\frac{\partial A}{\partial z} + \beta_1\frac{\partial A}{\partial t} + \frac{i\beta_2}{2}\frac{\partial^2 A}{\partial t^2} = i\Delta\beta_0 A. \qquad (7.128)$$

We note that both the nonlinearity and the losses are contained in the $\Delta\beta_0$ term. Using the assumption that the modal distribution $F\left(x, y\right)$ does not vary considerably over the pulse bandwidth and $\beta\left(\omega\right) \approx n\left(\omega\right)\omega/c$, we can write:

$$\frac{\partial A}{\partial z} + \beta_1\frac{\partial A}{\partial t} + \frac{i\beta_2}{2}\frac{\partial^2 A}{\partial t^2} + \frac{\alpha}{2}A = i\gamma\left(\omega_0\right)|A|^2 A. \qquad (7.129)$$

This equation is related to the nonlinear Schrodinger equation from quantum mechanics if the loss term α is zero. We have also introduced the nonlinear parameter, or *effective nonlinearity* [9]:

$$\gamma\left(\omega_0\right) = \frac{2\pi}{\lambda}\frac{\int\int_{-\infty}^{\infty}n_2\left(x, y\right)|F\left(x, y\right)|^4 dxdy}{\left(\int\int_{-\infty}^{\infty}|F\left(x, y\right)|^2 dxdy\right)^2}. \qquad (7.130)$$

The effective nonlinearity has units of $W^{-1}\,m^{-1}$ when $|A|^2$ represents the optical power.

Equation (7.129) is approximately valid for pulses that are longer than 1 ps and does not include the effects of Raman or Brillouin scattering. Raman scattering requires the inclusion of a delayed (non-instantaneous) nonlinearity. Meanwhile, shorter pulses have a much larger bandwidth that requires several modifications. For short, large-bandwidth pulses propagating in the linear regime, $\beta\left(\omega\right)$ cannot be sufficiently modeled unless we include higher-order dispersive terms beyond β_2. Additionally, for short pulses in the nonlinear regime, the nonlinear parameter's frequency dependence must also be included, leading to an effect known as self-steepening [9]. These additional effects change the details of how a pulse evolves as it propagates; however, Eq. (7.129) describes many of the major features.

The NLSE is only solvable analytically under certain conditions using the inverse-scattering method [28]. However, an efficient method for numerically simulating the NLSE exists, which is known as the split-step Fourier method [29, 30]. The technique discretizes pulse propagation in the z-direction. We split each discrete step into two parts. We apply only the nonlinear phase in the time

domain during the first part. Subsequently, we Fourier transform and apply linear dispersion in the frequency domain, followed by second Fourier transform back to the time domain, which completes the z-step. This method is both efficient and straightforward to apply.

7.4.1.2 Effective Nonlinearity

The effective nonlinearity is the nonlinear phase per distance, per power, thus, large value of γ can enable smaller and more efficient devices. With the effective nonlinearity, we can rewrite Eq. (7.73) for the nonlinear phase within a waveguide by including the propagation constant β and the effective nonlinearity $\gamma(\omega)$:

$$\varphi = \beta L + \gamma(\omega) LP = \varphi_L + \varphi_{NL}. \tag{7.131}$$

We note that γ takes both the distribution of the mode into account and a location-dependent nonlinearity. The importance of the modal distribution is critical for silica nanowires because the only significant nonlinearity occurs within the silica and not the air cladding. The spatially dependent nonlinearity is also important for waveguides formed from multiple materials with different intrinsic nonlinearities.

If the field is contained within a single material, such as in optical fiber, we can write:

$$\gamma(\omega_0) = \frac{n_2(\omega_0)\,\omega_0}{c A_{eff}}, \tag{7.132}$$

where the *effective mode area* is:

$$A_{eff} = \frac{\left(\int\int_{-\infty}^{\infty} |F(x,y)|^2 dxdy\right)^2}{\int\int_{-\infty}^{\infty} |F(x,y)|^4 dxdy}. \tag{7.133}$$

Alternatively, we can write the effective area in terms of the *mode-field diameter* (MDF) d, related to the effective area by $A_{eff} = \pi(d/2)^2$.

7.4.1.3 Pulse Propagation Using the Nonlinear Wave Equation

Pulse propagation within a nonlinear waveguide is considerably different from the continuous-wave case. For large nonlinear interactions, high powers are necessary. This requirement benefits from restricting the wave spatially by reducing the effective area, and controlling the spreading of the pulse in time using dispersion. Therefore, there is an interplay between the nonlinearity and the group velocity dispersion.

To get a sense of which effects are dominant, we look to Eq. (7.129) and determine length scales on which these relative effects become important. The length associated with group velocity dispersion is:

$$L_D = \frac{T_0^2}{|\beta_2|},\qquad(7.134)$$

known simply as the dispersion length. Similarly,

$$L_{NL} = \frac{1}{\gamma P_0}.\qquad(7.135)$$

is known as the nonlinear length. When the physical length of the waveguide is comparable to these lengths scales, the associated effects become important.

There are four relevant combinations of these lengths scales [9]. For $L \ll L_D$ and $L \ll L_{NL}$, both the dispersion and the nonlinearity are minimal and the pulse passes through unaffected, ideal for transmission systems. When $L \geq L_D$ and $L \ll L_{NL}$, the pulse undergoes significant dispersive broadening, but the spectrum remains constant. If $L \ll L_D$ and $L \geq L_{NL}$, the pulse is affected primarily by the nonlinearity and the spectrum will change via self-phase modulation. This regime is important for wide spectral broadening because the pulse remains relatively short due to the minimal dispersive broadening.

The final combination requires special attention [9]. When both $L \geq L_D$ and $L \geq L_{NL}$, the interplay between the dispersion and the nonlinearity produces dramatically different results depending on relative signs of the two effects. If both effects are positive ($n_2 > 0$ and $\beta > 0$, dispersion in the normal regime), spectral broadening can occur and even temporal pulse compression can be achieved under certain conditions [9]. If the dispersion is anomalous with $\beta < 0$ and $n_2 > 0$, stable solutions, known as solitons, can form [9, 31]. Under these conditions, the group velocity dispersion causes the red to move toward the front and blue toward the back; however, the nonlinearity causes the opposite effect and the two effects balance one another. These solutions are quantized in the sense that the shape repeats itself after a regular, fixed distance. Solitons are extremely stable because they can shed excess energy in the form of a *dispersive wave* until a stable solution is formed [32].

The lowest order (fundamental) soliton is of particular interest for communications systems because the dispersion and nonlinearity are in constant balance ($L_D = L_{NL}$) and the pulse maintains its shape as it propagates [33, 34]. In addition, the spectral phase across the pulse is flat, which has two advantages for all-optical switching [35–37]. First, a fundamental soliton is intrinsically transform-limited, leading to efficient switching. Secondly, unlike other pulses, the flat-phase guarantees that the entire pulse will undergo switching, avoiding pulse distortions.
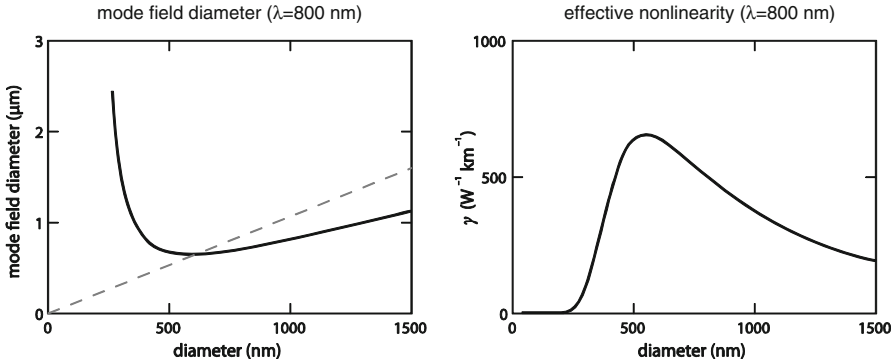
Fig. 7.17 Strong nonlinear-optical interaction in silica nanowires. The mode-field diameter versus the physical diameter (*left*). The effective nonlinearity as a function of the physical diameter (*right*) [25]

7.4.2 Nonlinear Properties of Silica Nanowires

We will theoretically explore the advantages of silica nanowires for nonlinear optics. This discussion will illustrate how high index-contrast sub-wavelength waveguides can achieve large effectively nonlinearities and tunable group velocity dispersion.

7.4.2.1 Effective Nonlinearities

The high index contrast between silica and air enables strong light confinement, facilitating large effective nonlinearities (γ). High confinement within a waveguide, alone, does not increase γ. Instead, we must consider both the effective mode area and the distribution of the mode, as shown in Eq. (7.130).

To study how we can maximize γ in silica nanowires, we will first consider the how the MFD changes as we change the physical diameter (PD) of the nanowire [25]. Figure 7.17 (left) shows the MFD versus the PD. For illustration, we also plot the PD versus itself (a dashed line with a slope of unity). We see that for large diameter fibers, the MFD is smaller than the PD [25]. As we reduce the PD, the MFD becomes equal to the PD. Then the evanescent field increases rapidly, causing the MFD to become much larger than the PD. Because the nonlinearity of air is negligible, we expect the largest γ when the MFD is smallest, while remaining in the core. This crossover occurs when the MFD is equal to the PD, which corresponds to a diameter around 550 nm for 800-nm light.

From the simple structure of silica nanowires, we expect the highest effective nonlinearity when the MFD coincides with the PD. We calculate and plot the effective nonlinearity for a silica nanowire as a function of the diameter (Fig. 7.17, right) [25]. As expected, the largest nonlinearity occurs for a diameter of 550 nm
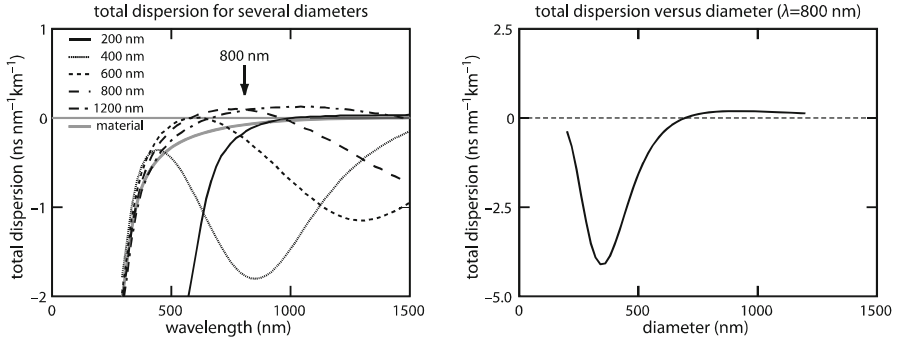
Fig. 7.18 Dispersion engineering in silica nanowires. The dispersion parameter *D* versus wavelength for several waveguide dimensions (*left*). The dispersion parameter *D* as a function of silica nanowire dimension for 800-nm light (*right*) [39]

for 800-nm light. The nonlinearity peaks at a value of 660 W^{-1} km^{-1}, which is over 300 times the effective nonlinearity of standard telecommunications fibers [9]. This result is impressive considering that we are using a material, silica, which has a comparatively low nonlinear index of refraction [38].

7.4.2.2   Group Velocity Dispersion

As we have seen previously, waveguide dispersion enables us to engineer the total dispersion, greatly influencing nonlinear pulse propagation. Figure 7.18 (left) shows the wavelength-dependent total dispersion for silica nanowires of varying diameters [39]. We see that the material dispersion in silica is normal for short wavelengths, reaches zero around 1,300 nm, and then becomes anomalous for longer wavelengths. If we operate around 800 nm, we are restricted to normal dispersion, unless we can counteract the normal dispersion with anomalous waveguide dispersion.

Figure 7.18 (right), shows the dispersion for 800-nm light as a function of nanowire diameter [39]. For diameters of 700–1,200 nm, strong anomalous waveguide dispersion overcomes the material dispersion and results in anomalous total dispersion. For diameters near 700 nm, total dispersion is very low. For even smaller dimensions, the dispersion becomes extremely normal. This ability to tune the total dispersion is a key element for engineering efficient nonlinear interactions.

7.4.3   Supercontinuum Generation in Silica Nanowires

We can achieve significant nonlinear effects if the nonlinear length is comparable to the waveguide length. To demonstrate these strong nonlinearities, we fabricate a series of silica nanowires with minimum diameters that vary from 360 to 1,200 nm [40]. For each nanowire, we launch 90-fs pulses at a central wavelength of 800 nm
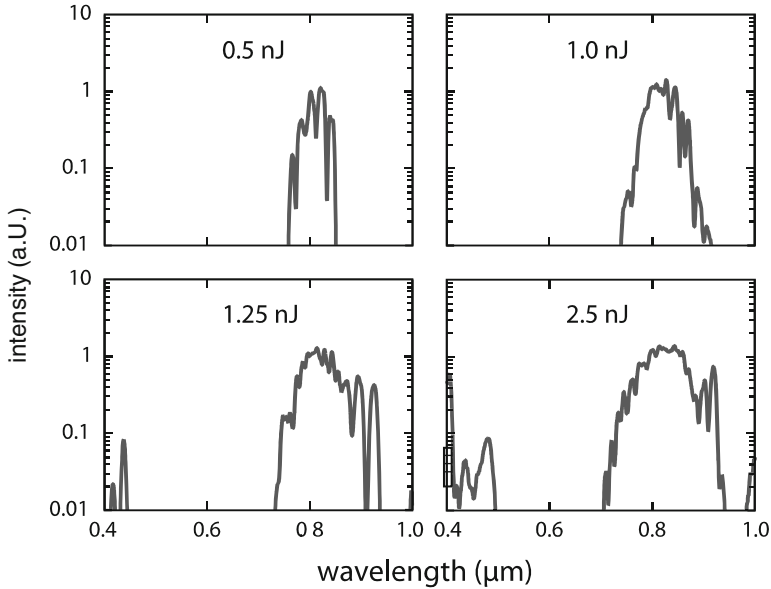
Fig. 7.19 Energy-dependent spectral broadening in a 1,200-nm diameter silica nanowire [40]

and observe the output spectrum. To understand the phenomena, we will first consider the energy-dependence of the spectral broadening in a single nanowire. Next, we will observe the diameter dependence of spectral broadening, which incorporates changes both the effective nonlinearity as well as the group velocity dispersion.

7.4.3.1   Energy-Dependent Spectral Broadening

Figure 7.19 shows the output spectra for a 1,200-nm diameter silica nanowire as we increase the input pulse energy. For an input pulse of 0.5 nJ, we observe no broadening and the output pulse spectrum is identical to the input pulse spectrum. Around 1 nJ, we reach the threshold for spectral broadening. For higher pulse energies, we see larger broadening and develop blue-peaks near 415 and 437 nm. These are not believed to be second-harmonic signal, as bulk amorphous silica is centrosymmetric [23]; instead, we attribute this phenomenon to higher-order soliton self-splitting, as has been observed previously [41–45].

7.4.3.2   Diameter-Dependent Spectral Broadening

Using similar pulse energies, we observe the diameter dependence of supercontinuum generation in Fig. 7.20 [40]. For a diameter of 360 nm, we find very
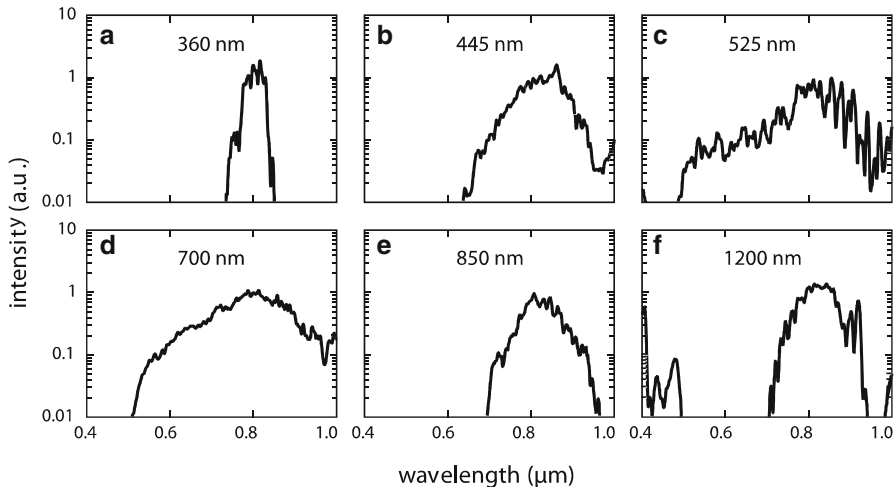
Fig. 7.20 Diameter-dependent supercontinuum generation in silica nanowires [40]

little spectral broadening. The absense of broadening for a 360-nm nanowire is consistent with a significant evanescent field reducing the nonlinear parameter, as shown in Fig. 7.17. As we increase the diameter to 445 nm, we begin to observe broadening due to a larger nonlinear parameter, however the broadening is limited by the strong normal dispersion (Fig. 7.18). For a 525-nm diameter fiber, the near-maximal nonlinear parameter is responsible for the large broadening observed; meanwhile, the 700-nm nanowire's spectrum can be partially attributed to the near-zero dispersion. For the 850-nm diameter fibers, we enter the anomalous dispersive regime and reduced broadening may be related to soliton formation. Lastly, the 1,200-nm nanowire shows additional structure in the blue-part of the visible spectrum which can be attributed to dispersive waves [41–45].

We see that by combining strong confinement and dispersion engineering in sub-wavelength nanowires, we can achieve significant spectral broadening using nJ pulse energies. These compact, integratable supercontinuum sources open the door to more advanced devices such as all-optical modulators.

7.4.4   All-Optical Modulation, Switching, and Logic

Now that we have come to understand nonlinear optics and the advantages of using nano-scale waveguides, we will explore light-by-light modulation, switching, and logic. All-optical modulation requires an optical device whose output depends nonlinearly on its input. Strong all-optical modulation leads to all-optical switching, whereby light-signals turn other light-signals on and off. Finally, these all-optical switches form the basis for all-optical logic devices. Logic devices have the

Fig. 7.21 Diagram of a
Sagnac interferometer
showing the input pulse, the
coupling region, the
clockwise and
counter-clockwise paths as
well as the transmitted pulse
[23, 31]
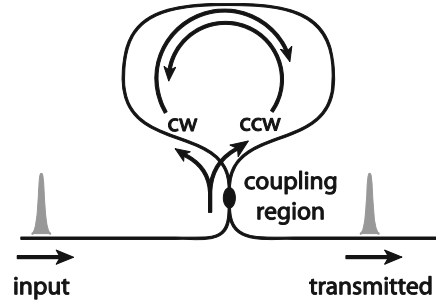
additional requirement that predefined input bits (logical 0's and 1's, determined by power or energy ranges) must undergo a Boolean logic operation to produce an output bit(s).

In this section, we will look at Sagnac interferometers as a prototype for all-optical modulation, switching, and logic. Our analysis will be restricted to self-switching that utilizes the self-phase modulation for simplicity. Similar results can be derived for cross-phase modulation [31]. We will demonstrate all-optical modulation in a Sagnac interferometer made using a silica nanowire. Lastly, we will end on a discussion on how to form all-optical logic gates using Sagnac interferometers.

7.4.4.1 Sagnac Interferometers

A Sagnac interferometer, as shown in Fig. 7.21, is an excellent configuration to demonstrate all-optical modulation, switching, and logic. These interferometers are perhaps the simplest nonlinear interferometer configuration achievable in a silica nanowire. These symmetric, self-balancing interferometers utilize counter-propagating waves and are therefore stable, immune to temperature gradients, and easy to work with [36, 46–48]. Sagnac interferometers provide a tunable balance between switching energy and device size simply by changing path lengths. These devices are non-resonant and therefore can sustain extremely high bit-rates [49]. Although we will only consider all-optical switching and logic as a final application, Sagnac interferometers are versatile, enabling operations including multiplexing/demultiplexing, switching and logic [50] and signal regeneration [51].

To understand how a Sagnac interferometer works, we can consider a nonlinear interferometer using a quasi-continuous-wave pulse in an interferometer. We form these by making a loop as shown in Fig. 7.21, then input light into the waveguide on the left of the loop and observe the output in the waveguide to the right.

The linear version of a Sagnac interferometer acts as a mirror [31]. A pulse enters the input in Fig. 7.21, and then encounters a directional coupler. A fraction of the pulse energy couples into the adjacent waveguide, adding a $\pi/2$ phase-shift, then it propagates around the loop in the counter-clockwise direction. The other fraction

remains within the same waveguide (no phase-shift), and proceeds in the clockwise direction. These two pulses collect identical amounts of phase as they traverse the loop and then recombine at the directional coupler. The output is a summation of the counter-clockwise pulse and the clockwise pulse. The counter-clockwise pulse picks up a second $\pi/2$ phase-shift at the directional coupler, resulting in a total phase shift of π relative to the clockwise pulse at the output. This phase-shift results in destructive interference at the output. Meanwhile, constructive interference occurs on the input-side and the pulse is reflected back toward input, creating a mirror. For a 50–50 directional coupler, the Sagnac interferometer acts as a "perfect mirror". If the ratio is different from 50 to 50, part of the light will reach the output.

A Sagnac interferometer can be made nonlinear, sometimes referred to as a *nonlinear optical loop mirror* (NOLM) [37, 47, 48, 50, 52–60], by forming the loop using a nonlinear optical material. When traversing the loop, the clockwise and counter-clockwise pulses collect both linear and nonlinear phase. Both pulses collect identical linear phase. If the coupling ratio is anything other than 50–50, there will be a nonlinear phase difference between the pulses, causing power-dependent interference at the output. Just as we observe fringes in a Michelson interferometer when we change one of the path lengths, we observe power-dependent fringes in a Sagnac interferometer. These fringes form a basic, all-optical modulator that we can extend to perform all-optical switching and logic applications. The speed of these devices is only limited by the response time of the nonlinearity, although a delay in the device will occur as the pulses propagate. For a pure electronic nonlinearity, this response is on the order of several femtoseconds [5], making such a device compatible with Tb/s operations [49].

7.4.4.2   Analysis of a Sagnac Interferometer

The operation of a nonlinear Sagnac interferometer can be quite complex if we include all possible effects to correctly model pulse propagation; however, we can get a very good sense of how one works if we consider a quasi-continuous-wave pulse [31]. Essentially, we modulate a carrier wave with a square envelope, simplifying the analysis by using a continuous-wave approximation using peak-powers, (not pulse energies). For this approximation, we ignore dispersion and temporal phenomena, such as spectral broadening. For simplicity, we will also ignore cross-phase modulation between the counter-propagating pulses. This effect is negligible if the pulse durations are much shorter the loop-propagation time. In the continuous-wave regime, cross-phase modulation is the dominant source of nonlinear phase, however the results are identical [31].

Analysis in the quasi-continuous-wave regime first requires us to determine the power that is traveling in the clockwise versus the counter-clockwise directions. We define a coupling parameter ρ that represents the fraction of the power that stays within the input leg of the directional coupler and traverses the loop in the clockwise-direction. Thus, ρP_{in} is the clockwise power in the loop, corresponding

to an electric field of magnitude $\sqrt{\rho}E_{in}$, for an input power of P_{in} and input electric field of E_{in}. Similarly, in the counter-clockwise direction, the power and electric field magnitudes are $(1 - \rho) P_{in}$ and $\sqrt{1 - \rho}E_{in}$, respectively. When we build our devices, we can change ρ within the directional coupler by adjusting the separation between the two-waveguides and/or adjusting the distance of the parallel section (described using coupled-mode theory [3]).

Now, we determine the total phase accumulated in both directions, which requires that we define the length of the loop, L. We consider three sources of phase: from the directional coupler, linear propagation, and nonlinear propagation. Within the directional coupler, the power transferred from the input pulse to the counter-clockwise pulse receives a phase shift of $\pi/2$. This phase shift occurs a second time when the counter-clockwise pulse is transferred to the output, leading to total phase shift of π for the counter-clockwise pulse only (the clockwise pulse remains in the original waveguide). Combining this phase-shift with the linear and nonlinear phase from Eq. (7.131), we obtain the total phase at the output for the clockwise and counter-clockwise pulses:

$$\varphi_{CW} = \varphi_L + \varphi_{CWNL} = \beta L + \gamma(\omega) L \rho P_{in}, \tag{7.136}$$

$$\varphi_{CCW} = \varphi_L + \varphi_{CCWNL} + \varphi_{DC} = \beta L + \gamma(\omega) L (1 - \rho) P_{in} + 2(\pi/2). \tag{7.137}$$

Here, φ_{CW} is the total phase in the clockwise direction at the output, made up of a linear and a nonlinear contributions, φ_L and φ_{CWNL}, respectively. In the counter-clockwise direction, these terms are φ_{CCW}, φ_L, and φ_{CCWNL}, respectively. Additionally, there is a phase shit φ_{DC} from the directional coupler in the counter-clockwise direction.

Lastly, we sum the electric fields at the output to determine the transmission. The magnitude of the electric field for the clockwise pulse becomes ρE_{in} at the output, having picked up an additional factor of $\sqrt{\rho}$ from the directional coupler. Similarly, the magnitude of the electric field for the counter-clockwise pulse is $(1 - \rho) E_{in}$ at the output. The electric field at the output is:

$$E_{out} = \rho E_{in} e^{i\varphi_{CW}} + (1-\rho) E_{in} e^{i\varphi_{CCW}} = \left(\rho E_{in} e^{i\varphi_{CWNL}} - (1 - \rho) E_{in} e^{i\varphi_{CCWNL}} \right) e^{i\varphi_L}. \tag{7.138}$$

We can solve this equation for the transmission to show:

$$T = \frac{|E_{out}|^2}{|E_{in}|^2} = 1 - 2\rho(1 - \rho)\{1 + \cos[(1 - 2\rho)\gamma P_{in}L]\}. \tag{7.139}$$

From this equation, we see that if ρ is 0.5, the transmission is zero and therefore, we require that $\rho \neq 0.5$ to achieve modulation.

Fig. 7.22 Transmitted power
as a function of input power
for a typical nonlinear Sagnac
interferometer [23, 31]
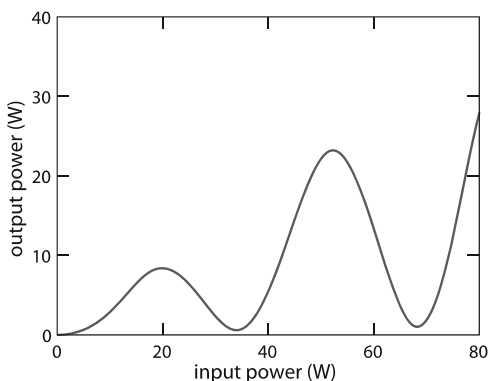
We can understand the nature of this device by plotting the output power, $P_{in}T$, as a function of the input power, as shown in Fig. 7.22. We also note that we can change the spacing of the fringes relative to the input power, using the coupling parameter. For small values of ρ, the fringes are closely spaced in power and the modulation is minimal. As the coupling parameter ρ approaches 0.5, the first minimum requires higher powers while the modulation increases.

Although changing the coupling parameters is straightforward experimentally, simply making longer devices is not always possible and requires that we consider both linear and nonlinear losses. Linear losses, as we have seen in previously, effectively limit the amount of nonlinear phase that we can accumulate. Similarly, two-photon absorption limits the highest power that we can effectively use.

In addition to losses, a real device must include the effects of the pulse shape as well as dispersion. When moving to pulsed operation without dispersion, the phase accumulated will be different across the pulse. The non-uniform phase will cause the peak of the pulse to switch before the front and back, creating pulse distortions, and lowering the modulation. With normal dispersion, a similar effect will occur. Even with all of these complications, by exploiting nonlinear optics in nano-scale waveguides, significant modulation with minimal pulse distortion is possible using solitons, as has been shown in fiber [36].

7.4.4.3 All-Optical Modulation Using Silica Nanowires

We have fabricated silica nanowires and formed Sagnac interferometers to demonstrate all-optical modulation. Using a 500-nm silica nanowire, we have observed all-optical modulation of femtosecond-pulses at a wavelength of 800 nm, as shown in Fig. 7.23 [23]. The approximate interaction length for this device is 500 μm and we modulate it using pulse energies up to 2 nJ.

We can fit this data to the model in Eq. (7.139) and estimate a coupling parameter of 0.08. Although we have achieved light-on-light modulation, our data shows that it is necessary to increase the coupling ratio in order to obtain stronger modulation.

Fig. 7.23 Experimental data for a silica nanowire-based Sagnac interferometer (*triangles*) and theoretical fit (*solid line*) [23]
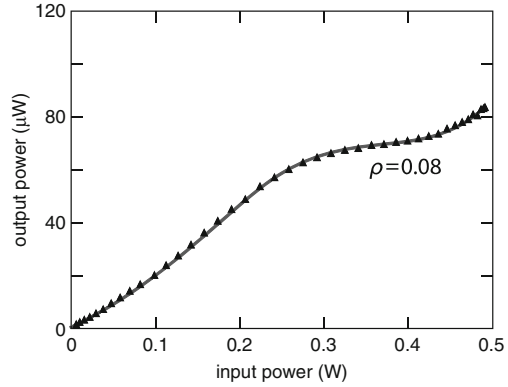
7.4.4.4 All-Optical Switching

In all-optical switching devices, the power ratio between "on" and "off" states, as well as the power required for full modulation, are important design considerations. The ratio of the "off" to the "on" power is the *depth of modulation* or *extinction coefficient* [2]. We can approximate the depth of modulation for our Sagnac interferometer by evaluating Eq. (7.139) when the argument of the cosine function is equal to π (the approximate location of the first maximum) and 2π (the approximate location of the first minimum). The extinction ratio is approximately given by:

$$\frac{P_{\max}}{P_{\min}} \approx \frac{1}{2(1-2\rho)^2}. \tag{7.140}$$

For example, we find that the extinction ratio reaches 3 dB when $\rho = 0.25$ and 17 dB when $\rho = 0.45$.

Stronger modulation requires higher input powers or longer length devices; therefore, we consider this trade-off by observing the power required to reach the first minimum, given by:

$$P_{switch} \approx \frac{2\pi}{(1-2\rho)\,L\gamma}. \tag{7.141}$$

As we approach a coupling ratio of 0.5, the required power for full switching increases as $(1-2\rho)^{-1}$. Comparing this expression to Eq. (7.140), as ρ approaches 0.5, the extinction ratio improves as $(1-2\rho)^{-2}$. Therefore, we can achieve a substantially increased extinction ratio for only a moderate operational power increase. In addition, we can design a longer device to offset the additional power requirements.
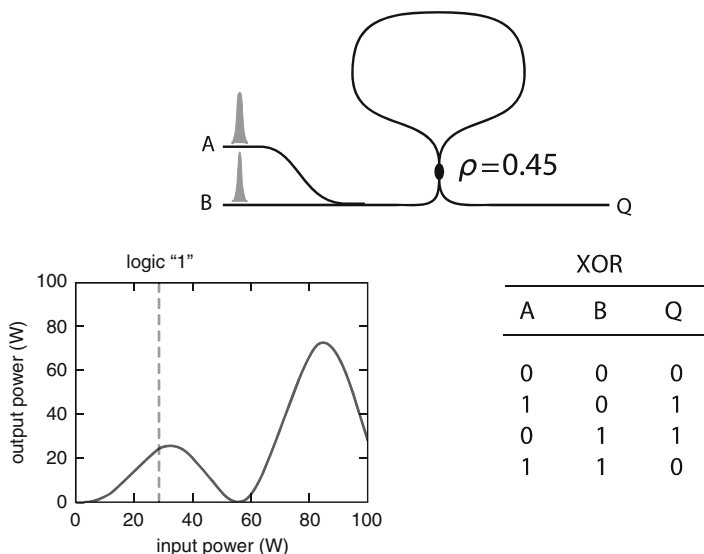
Fig. 7.24 All-optical XOR logic gate. Physical layout (*top*), input versus output for the Sagnac interferometer, showing logical 0's and 1's (*bottom left*), truth table for the resulting XOR gate (*bottom right*) [23]

7.4.4.5 All-Optical Logic

Now we show how to form all-optical logic gates using a nonlinear Sagnac interferometer. The nonlinear optical loop mirror serves as a prototypical all-optical logic-gate for future communications systems. These and similar devices have been shown using bulk fiber [49, 50, 61, 62] as well as using active nonlinear devices [51]. Our configuration begins by adding two (or more) inputs before our Sagnac interferometer, as showing in Fig. 7.24 (top). For each logical operation, we must define logical 1's and 0's for both the input and the output.

As a first example, we will explore an exclusive-OR gate, having the truth table shown in Fig. 7.24 (bottom right). We observe the power-dependent transmission plot in Fig. 7.24 (bottom left), using a coupling ratio of 0.45 to define our logical 1's and 0's. On the input, a logical 1 has an input power greater of 28 W. On the output, we define a logical 1 as an output power greater than 18 W. Using the Sagnac's transmission function, we can construct the truth table. If neither A nor B is present at the input, the device produces a logical 0. If only input A or input B is present, the output is close to the first maximum, resulting in a logical 1. If both A and B are present at the input, the device produces a logical 0. This demonstrates the truth table for an XOR gate.

We can construct other gates by adjusting the coupling coefficient, and possibly adding a clock signal. We are particularly interested in constructing a "universal" logic gate. These gates can be configured together to form the entire set of Boolean
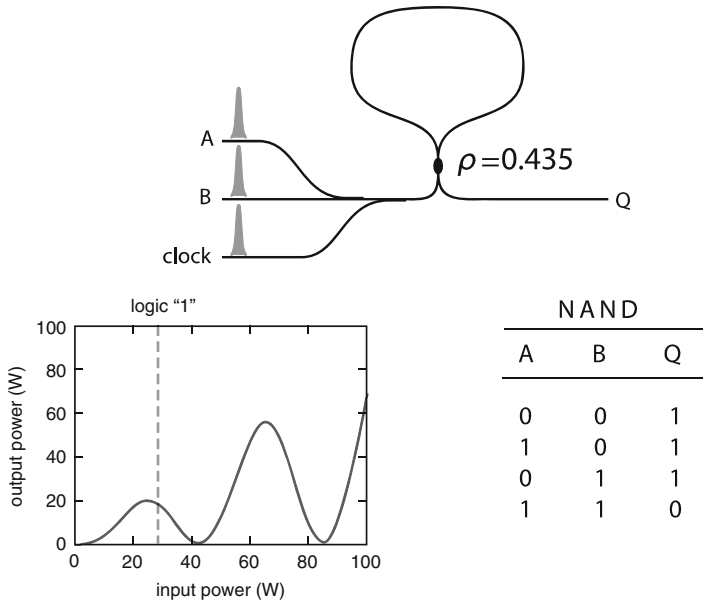
Fig. 7.25 All-optical NAND logic gate. Physical layout (*top*), input versus output for the Sagnac interferometer, showing logical 0's and 1's (*bottom left*), truth table for the resulting NAND gate (*bottom right*) [23]

logic operations. One particular universal logic gate we can construct using a Sagnac interferometer is a NAND gate. A NAND gate has the truth table shown in Fig. 7.25 (bottom right). As we can see, this gate is more difficult to create than an XOR-gate because we require a logical 1 when there is no input. Therefore, we add an additional input to our Sagnac interferometer and deliver a clock pulse with every set of input pulses. By adjusting our coupling parameter to 0.435, we find that for no inputs in either A nor B, the clock pulse produces a logical 1 at the output. For an input in either A or B, the output of the device is around 15 W, constituting a logical 1 at the output. Now, if both A and B are present, the devices reaches the second minimum, resulting in a logical 0. This prototypical device shows how we can construct an all-optical NAND gate and thereby create all other Boolean logic gates.

7.5 Summary

We have shown the advantages of using sub-wavelength dielectric waveguides for nonlinear optics. We have developed a theoretical basis for linear and nonlinear propagation of continuous-wave and pulsed optical signals in free-space, within materials, and using waveguides. We have seen how nano-scale, high-index contrast

waveguides are capable of enhancing nonlinear interactions spatially, using strong confinement, and in time, using tunable dispersion. To demonstrate these effects in a physical system, we have fabricated silica nanowires, explored their mechanical properties, and observed their linear and nonlinear optical properties. Lastly, we have developed two devices, a supercontinuum source, and an all-optical modulator, which serve as the foundation for more advanced nonlinear devices, including all-optical logic devices, both in silica and in future material systems.

References

1. Griffiths DJ (1999) Introduction to electrodynamics, 3rd edn. Prentice Hall, Upper Saddler River, p xv, 576 p
2. Hunsperger RG (2009) Integrated optics: theory and technology, 6th edn, Advanced texts in physics. Springer, New York, p xxviii, 513 p
3. Haus HA (1984) Waves and fields in optoelectronics, Prentice-Hall series in solid state physical electronics. Prentice-Hall, Englewood Cliffs, p xii, 402 p
4. Application note: prism compressor for ultrashort laser pulses (Newport Corporation, 2006). Retrieved 21 May 2012. http://assets.newport.com/webDocuments-EN/images/12243.pdf
5. Boyd RW (2008) Nonlinear optics, 3rd edn. Academic, Amsterdam/Boston, p xix, 613 p
6. Chen JM, Bower JR, Wang CS, Lee CH (1973) Optical second-harmonic generation from submonolayer Na-covered Ge surfaces. Opt Commun 9:132–134
7. Shen YR (1989) Surface properties probed by second-harmonic and sum-frequency generation. Nature 337:519–525
8. Boyd RW (2003) Nonlinear optics, 2nd edn. Academic, San Diego, p xvii, 578 p
9. Agrawal GP (2007) Nonlinear fiber optics, 4th edn, Quantum electronics–principles and applications. Elsevier/Academic Press, Amsterdam/Boston, p xvi, 529 p
10. Sheik-Bahae M, Said AA, Wei TH, Hagan DJ, Van Stryland EW (1990) Sensitive measurement of optical nonlinearities using a single beam. Quantum Electron IEEE J 26:760–769
11. Stryland EWV, Sheik-Bahae M (1998) Z-scan measurements of optical nonlinearities. In: Kuzyk MG, Dirk CW (eds) Characterization techniques and tabulations for organic nonlinear optical materials. Marcel Dekker, New York
12. Stegeman GI, Wright EM, Finlayson N, Zanoni R, Seaton CT (1988) Third order nonlinear integrated optics. Lightwave Technol J 6:953–970
13. Stegeman GI (1993) Material figures of merit and implications to all-optical waveguide switching. SPIE 1852:75–89
14. Stegeman GI, Torruellas WE (1996) Nonlinear materials for information processing and communications. Philos Trans Math Phys Eng Sci 354:745–756
15. Lin Q, Zhang J, Piredda G, Boyd RW, Fauchet PM, Agrawal GP (2007) Dispersion of silicon nonlinearities in the near infrared region. Appl Phys Lett 91:021111
16. Vilson RA, Carlos AB, Roberto RP, Michal L, Mark AF, Dimitre GO, Alexander LG (2004) All-optical switch on a Silicon chip. In: Proceedings of the Conference on lasers and electro-optics/international quantum electronics conference and photonic applications systems technologies, technical digest (CD), Optical Society of America, CTuFF3
17. Saleh BEA, Teich MC (2007) Fundamentals of photonics, 2nd edn, Wiley series in pure and applied optics. Wiley-Interscience, Hoboken, p xix, 1177 p
18. Jackson JD (1999) Classical electrodynamics, 3rd edn. Wiley, New York, p xxi, 808 p

19. Gloge D (1971) Dispersion in weakly guiding fibers. Appl Opt 10:2442–2445
20. Marcuse D (1979) Interdependence of waveguide and material dispersion. Appl Opt 18:2930–2932
21. Tong L, Gattass RR, Ashcom JB, He S, Lou J, Shen M, Maxwell I, Mazur E (2003) Subwavelength-diameter silica wires for low-loss optical wave guiding. Nature 426:816–819
22. Tong LM, Lou JY, Ye ZZ, Svacha GT, Mazur E (2005) Self-modulated taper drawing of silica nanowires. Nanotechnology 16:1445–1448
23. Svacha G (2008) Nanoscale nonlinear optics using silica nanowires. Harvard University, Cambridge, MA
24. Tong L, Lou J, Gattass RR, He S, Chen X, Liu L, Mazur E (2005) Assembly of silica nanowires on silica aerogels for microphotonic devices. Nano Lett 5:259–262
25. Foster MA, Moll KD, Gaeta AL (2004) Optimal waveguide dimensions for nonlinear interactions. Opt Expr 12:2880–2887
26. Huang KJ, Yang SY, Tong LM (2007) Modeling of evanescent coupling between two parallel optical nanowires. Appl Opt 46:1429–1434
27. Voss T, Svacha GT, Mazur E, Müller S, Ronning C, Konjhodzic D, Marlow F (2007) High-order waveguide modes in ZnO nanowires. Nano Lett 7:3675–3680
28. Zakharov VE, Shabat AB (1972) Exact theory of two-dimensional self-focussing and one-dimensional self-modulating waves in nonlinear media. Sov Phys JETP 34:62
29. Hardin RH, Tappert FD (1973) Numerical solutions of the Korteweg-de Vries equation and its generalizations by the split-step Fourier method. SIAM Rev Chron 15:423
30. Fisher RA, Bischel W (1973) The role of linear dispersion in plane-wave self-phase modulation. Appl Phys Lett 23:661–663
31. Agrawal GP (2001) Applications of nonlinear fiber optics, Optics and photonics. Academic, San Diego, p xiv, 458 p
32. Paschotta R (2008) Encyclopedia of laser physics and technology. Wiley-VCH, Weinheim
33. Hasegawa A, Kodama Y (1981) Signal transmission by optical solitons in monomode fiber. Proc IEEE 69:1145–1150
34. Blow KJ, Doran NJ (1983) Bandwidth limits of nonlinear (soliton) optical communication systems. Electron Lett 19:429–430
35. Trillo S, Wabnitz S, Wright EM, Stegeman GI (1988) Soliton switching in fiber nonlinear directional couplers. Opt Lett 13:672
36. Blow KJ, Doran NJ, Nayar BK (1989) Experimental demonstration of optical soliton switching in an all-fiber nonlinear Sagnac interferometer. Opt Lett 14:754–756
37. Islam MN, Sunderman ER, Stolen RH, Pleibel W, Simpson JR (1989) Soliton switching in a fiber nonlinear loop mirror. Opt Lett 14:811–813
38. Adair R, Chase LL, Payne SA (1989) Nonlinear refractive index of optical crystals. Phys Rev B 39:3337
39. Leon-Saval S, Birks T, Wadsworth W, Russell PSJ, Mason M (2004) Supercontinuum generation in submicron fibre waveguides. Opt Expr 12:2864–2869
40. Gattass RR, Svacha GT, Tong LM, Mazur E (2006) Supercontinuum generation in submicrometer diameter silica fibers. Opt Expr 14:9408–9414
41. Sakamaki K, Nakao M, Naganuma M, Izutsu M (2004) Soliton induced supercontinuum generation in photonic crystal fiber. Sel Top Quantum Electron IEEE J 10:876–884
42. Herrmann J, Griebner U, Zhavoronkov N, Husakou A, Nickel D, Knight JC, Wadsworth WJ, Russell PSJ, Korn G (2002) Experimental evidence for supercontinuum generation by fission of higher-order solitons in photonic fibers. Phys Rev Lett 88:173901
43. Cristiani I, Tediosi R, Tartara L, Degiorgio V (2004) Dispersive wave generation by solitons in microstructured optical fibers. Opt Expr 12:124–135
44. Tartara L, Cristiani I, Degiorgio V (2003) Blue light and infrared continuum generation by soliton fission in a microstructured fiber. Appl Phys B Laser Opt 77:307–311
45. Teipel J, Franke K, Türke D, Warken F, Meiser D, Leuschner M, Giessen H (2003) Characteristics of supercontinuum generation in tapered fibers using femtosecond laser pulses. Appl Phys B Laser Opt 77:245–251

46. Otsuka K (1983) Nonlinear antiresonant ring interferometer. Opt Lett 8:471–473
47. Mortimore DB (1988) Fiber loop reflectors. Lightwave Technol J 6:1217–1224
48. Doran NJ, Forrester DS, Nayar BK (1989) Experimental investigation of all-optical switching in fibre loop mirror device. Electron Lett 25:267–269
49. Huang A, Whitaker N, Avramopoulos H, French P, Houh H, Chuang I (1994) Sagnac fiber logic gates and their possible applications: a system perspective. Appl Opt 33:6254–6267
50. Jinno M, Matsumoto T (1992) Nonlinear Sagnac interferometer switch and its applications. Quantum Electron IEEE J 28:875–882
51. Cotter D, Manning RJ, Blow KJ, Ellis AD, Kelly AE, Nesset D, Phillips ID, Poustie AJ, Rogers DC (1999) Nonlinear optics for high-speed digital information processing. Science 286:1523–1528
52. Doran NJ, Wood D (1988) Nonlinear-optical loop mirror. Opt Lett 13:56–58
53. Uchiyama K, Takara H, Kawanishi S, Morioka T, Saruwatari M, Kitoh T (1993) 100 Gbit/s all-optical demultiplexing using nonlinear optical loop mirror with gating-width control. Electron Lett 29:1870–1871
54. Asobe M, Ohara T, Yokohama I, Kaino T (1996) Low power all-optical switching in a nonlinear optical loop mirror using chalcogenide glass fibre. Electron Lett 32:1396–1397
55. Jiun-Haw L, Ding-An W, Hsin-Jiun C, Ding-Wei H, Gurtler S, Yang CC, Yean-Woei K, Chen BC, Shih MC, Chuang TJ (1999) Nonlinear switching in an all-semiconductor-optical-amplifier loop device. Photon Technol Lett IEEE 11:236–238
56. Pelusi MD, Matsui Y, Suzuki A (1999) Pedestal suppression from compressed femtosecond pulses using a nonlinear fiber loop mirror. Quantum Electron IEEE J 35:867–874
57. Bogoni A, Scaffardi M, Ghelfi P, Poti L (2004) Nonlinear optical loop mirrors: investigation solution and experimental validation for undesirable counterpropagating effects in all-optical signal processing. Sel Top Quantum Electron IEEE J 10:1115–1123
58. Pottiez O, Kuzin EA, Ibarra-Escamilla B, Camas-Anzueto JT, Gutierrez-Zainos F (2004) Experimental demonstration of NOLM switching based on nonlinear polarisation rotation. Electron Lett 40:892–894
59. Simova E, Golub I, Picard M-J (2005) Ring resonator in a Sagnac loop. J Opt Soc Am B 22:1723–1730
60. Sumetsky M (2005) Optical microfiber loop resonator. Appl Phys Lett 86:161108
61. Jinno M, Matsumoto T (1991) Ultrafast all-optical logic operations in a nonlinear Sagnac interferometer with two control beams. Opt Lett 16:220–222
62. Miyoshi Y, Ikeda K, Tobioka H, Inoue T, Namiki S, Kitayama K- (2008) Ultrafast all-optical logic gate using a nonlinear optical loop mirror based multi-periodic transfer function. Opt Expr 16:2570–2577

8
Synthesis and Spectroscopy of Nanoparticles

Alexander P. Voitovich, G.E. Malashkevich, and N.V. Tarasenko

8.1 Introduction

A lattice period of crystalline inorganic solids lies typically in the range 0.5–1.0 nm. The processes involved in the electron subsystem of solids determine their optical and other characteristics. The quantum dimensional effects are caused, when even one of the geometrical sizes of solids becomes commensurable with the de Broglie wavelength of an electron, a hole or an exciton. In this case the spatial confinement of these waves in solids takes place. For instance, in CdSe crystal at room temperature, de Broglie wavelengths are equal 5.3, 4.35 and 1.25 nm for an exciton, an electron and a hole accordingly. As we see, the lengths of de Broglie waves for particles in crystals lay in a nanometers range. Therefore, the objects, for which quantum dimensional effects are typical, should have sizes of the nanometers order. In this connection, about such objects they usually speak as about nanostructures or nanomaterials. The electron confinement results in size-dependent absorption spectra, emission spectra and transition probabilities in solids. In recent years, in view of the prospects of practical applications, increasing attention is paid to the development of methods for synthesizing nanostructures and studying their physicochemical properties.

At present, the methods for the nanostructures production are based on chemical deposition, molecular epitaxy, and deposition from the gas phase upon thermal, laser, or magnetron sputtering. A wide range of structures has been obtained, including nanowires, nanotubes, nanobelts, nanorings, nanosprings, etc. In this paper we generalize the results of the studies devoted to the formation of nanoparticles of controlled composition, structure, and size under discharge sputtering and

A.P. Voitovich (✉) • G.E. Malashkevich • N.V. Tarasenko
Institute of Physics, National Academy of Sciences, 68 Nezalezhnosci Ave,
Minsk 220072, Belarus
e-mail: voitovich@imaph.bas-net.by

laser ablation of solid targets in liquid media. The application of liquids has a certain flexibility in controlling their properties with a corresponding choice of liquid type, in particular, by combining different solid targets and liquids to obtain nanostructures of new composition (for example, immiscible alloys and metastable phases). We also demonstrate that the formation of the $[Ce^{4+}O_8]_n{:}(Ln^{3+})_m$ oxide nanoparticles with nanocrystalline nature is possible in a process of the sol–gel synthesis of optical materials coactivated by Ce together with another rare earth elements. The spectroscopic properties of produced nanoscale particles are considered.

8.2 Synthesis of Nanoparticles by Discharge Sputtering in Liquid Media

In this work, the results of investigation into zinc oxide structures formed by the methods of discharge sputtering in liquid media will be presented. Although ZnO is not a "new" material for microelectronics and has been investigated for several decades, the interest in the research and production of ZnO structures, including nanostructures, has increased significantly in recent years. This is due to the fact that ZnO is a multifunctional compound with piezoelectric, ferroelectric, and ferromagnetic properties [1].

8.2.1 Morphology and Structure of Zinc Oxide Nanoparticles

Figure 8.1 shows a schematic diagram of the setup for nanoparticle synthesis under the conditions of electric discharge submerged into a liquid. The device consists
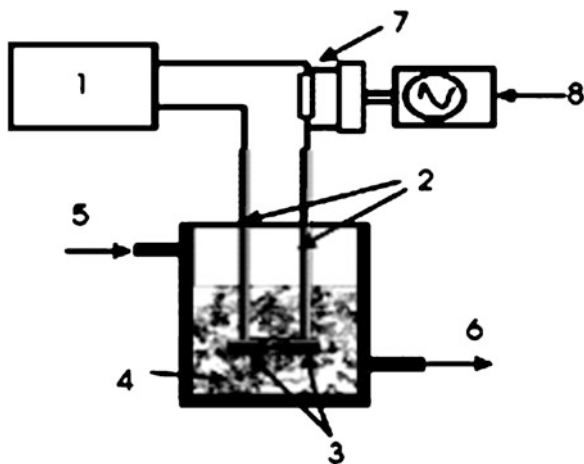
Fig. 8.1 Schematic diagram of electric discharge setup: *1*–discharge power supply, *2*–metal racks with electrode supports, *3*–electrodes, *4*–liquid, *5*–inlet and *6*–outlet of the cooling liquid, *7*–measuring circuit, and *8*–oscilloscope [2]
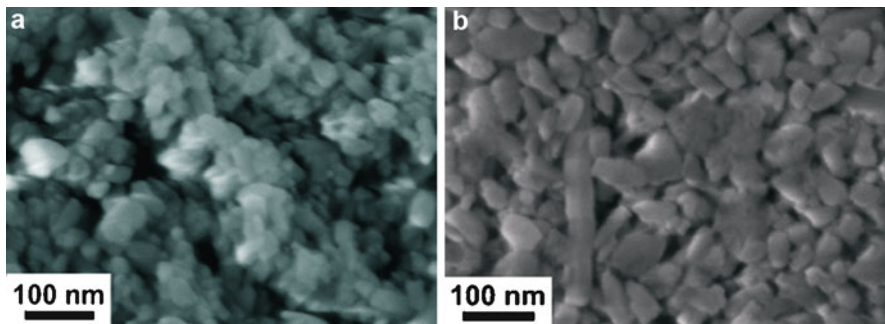
Fig. 8.2 SEM-images of the powders obtained by electric discharge synthesis in water under the conditions of (**a**) arc and (**b**) spark discharge [2]

Table 8.1 Conditions for ZnO electric discharge synthesis

Discharge mode	Electrodes	Liquid	Synthesis rate, mg/min	Particles shape and size, nm
Arc	Zn:Zn	Distilled water	31.8	Wires (rods): diameter 10–15, length 150–200
Spark	The same	The same	40.8	Wires (rods): diameter 10, length 150

of four major elements: a discharge power supply, a glass vessel with a liquid, electrodes, and a water cooling system. The discharge was generated between two electrodes submerged into distilled water to a depth of 3 cm. Zinc rods, 6 mm in diameter, were used as the electrodes. The power supply made it possible to initiate ac or dc discharges in the "spark" and "arc" modes. To form nanocomposite particles during the electric discharge in liquids, it is possible to use electrodes made of different metals and alloys, as well as liquids containing elements necessary for doping the final product.

The colloidal solutions prepared by the electric discharge technique were evaporated in the electric furnace. The powders obtained in this way were analyzed using electron microscopy, X-ray diffraction analysis, absorption and luminescent spectroscopy. The scanning electron microscope images (SEM-images) of the powders obtained are shown in Fig. 8.2. The conditions of discharge synthesis and the data on the rate of synthesis, shape, and size of the particles are given in Table 8.1.

Figure 8.2 and data from Table 8.1 show that the material produced mainly consists of the particles in the shape of wires (rods). According to the estimates, separate particles can be 150–200 nm long and 10–15 nm wide. It should be noted that nanowires are formed in the spark, as well as in the arc discharge. The efficiency of nanoparticle synthesis in the ac spark discharge is higher than in the arc discharge.

The results of X-ray diffraction analysis of the synthesized material show the presence only the peaks that correspond to ZnO and Zn lattices. The component composition of the samples remains almost the same upon the change in the

Fig. 8.3 Luminescence
spectra of commercial zinc
oxide powder (*1*), and of zinc
oxide synthesized in the
electric discharge in water
(*2*). Luminescence was
excited by radiation at a
wavelength of 310 nm [2]
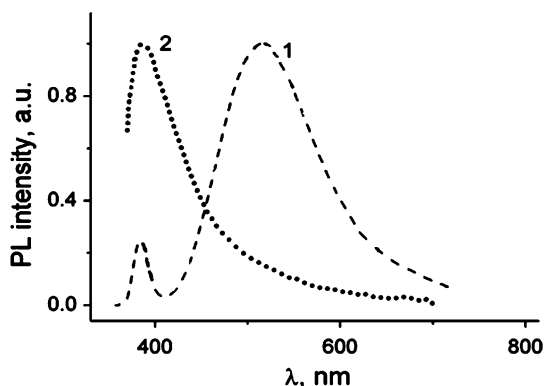
discharge mode (arc, spark), and the ZnO : Zn ratio is approximately 2 : 1. The
lattice parameters of hexagonal ZnO correspond to $a = 0.325$ nm and $c = 0.521$ nm,
which correlate well with the base data for ZnO. The measured ratio $c/a = 1.60$ is in
a good agreement with that for ideal close-packed hexagonal structures ($c/a = 1.63$).
We can assume that zinc atoms and clusters were formed in the discharge, which,
while reacting with the oxygen dissolved in water, produced zinc oxide. This
reaction can also take place after evaporation of the working fluid between zinc
unoxidized nanoparticles and atmospheric oxygen.

8.2.2 Optical Properties of Synthesized Nanopowders

Measuring photoluminescence spectra can be useful for determining structural
defects and impurities in zinc oxide structures. According to the literature [3, 4],
when zinc oxide nanostructures are excited at room temperature, an ultraviolet
luminescent band with a maximum near 380 nm and one or more bands in the
visible spectrum are observed. The luminescence spectra of ZnO structures at room
temperature are shown in Fig. 8.3. The most intense glow of powder was observed
under the action of radiation at wavelengths of 270 and 330 nm. It is clear from
the figure that the spectrum consists of two bands: the ultraviolet band with the
maximum at 380 nm and the green band with the maximum at about 520 nm. For
the sample made of ZnO commercial powder, the spectrum displays a relatively
weak ultraviolet band (383 nm) and a wide green band with the maximum at
approximately 515 nm. The luminescence spectrum of the ZnO samples synthesized
in electric discharge has an intense ultraviolet band at 380 nm and a relatively weak
violet emission.

Recombination emission of electron–hole pairs can be responsible for the
luminescence band in the UV spectral range. It is known that the bands appear in
the visible range due to various point defects of the zinc oxide structure, caused by
the introduced impurities or internal defects of the crystal lattice [3, 4].

Thus, the results considered show that the methods of discharge synthesis make it possible to form low-dimensional zinc oxide structures in liquid media with, as well as without, dopants. The processes that occur in the colloidal solution after the discharge termination have a decisive influence on the morphology and optical properties of the synthesized material. The results may be of interest for the development of technological bases for synthesis of zinc oxide nanostructures with reproducible properties, as well as oxides and carbides of other metals, in order to produce novel efficient materials.

8.3 Laser Synthesis of Nanoparticles in Liquids

Among the new methods for fabricating nanoparticles, the ones based on laser ablation in liquids [5, 6] are of great interest. In contrast to chemically synthesized nanoparticles, the nanoparticles formed by laser ablation in liquids do not content foreign ions and surface-active materials, which is an undoubted advantage for a number of applications (for example, in medicine). Other advantages of laser ablation are universality (it can be used for metals, semiconductors, and insulators of different composition) and possibility of controlling the characteristics of synthesized particles by changing the plasma parameters.

During laser ablation small clusters and particles are either directly emitted from the target surface or formed as a result of condensation in the decaying plume [7]. Particles begin to grow after a decrease in temperature during adiabatic expansion of the plasma plume. Particles of complex composition are formed during laser ablation due to the chemical reactions of target atoms with each other and with the environmental molecules [8]. The concentrations of components in the laser plume and its temperature directly affect the processes leading to particle synthesis. Therefore, it is important to know the dynamics of plume composition evolution to optimize the conditions of pulsed laser ablation in liquids (PLAL) for fabricating nanoparticles. We consider the results of the studies devoted to the formation of composite nanoparticles of controlled composition, structure, and size under laser ablation of solid targets in liquid media [9].

8.3.1 Experimental Setup and Some Characteristics of Plasma

Experiments on obtaining nanoparticles and diagnostics of laser plasma in liquids were performed on the setup schematically shown in Fig. 8.4. The radiation sources were two Nd:YAG lasers with pulse duration of 10 ns and a pulse repetition rate of 10 Hz, operating at the first (1,064 nm) and second (532 nm) harmonics. The laser radiation was focused on the surfaces of a target. The target was placed in a cell with a liquid. The power density on the target surface could be varied from 10^8 to 5×10^9 W cm^{-2}.
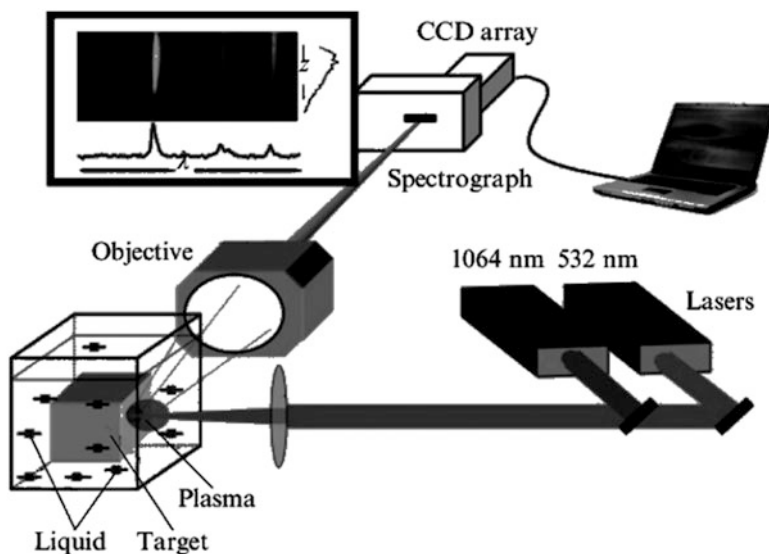
Fig. 8.4 Experimental setup for obtaining nanoparticles [9]

Two regimes of laser ablation were applied: the single-pulse regime, where plasma was formed by irradiating a target with a 532-nm laser pulse, and the double-pulse regime, where the second 532-nm laser pulse followed with some delay ($\tau \leq 100$ μs) the first 1,064-nm pulse. The laser beams were aligned on the target surface. The data on the laser plume size and shape were obtained using the technique of time-resolved image detection [10]. Typical images and intensity distributions for the luminous region of the plasma plume are shown in Fig. 8.5.

The shock wave generated by the expanding plasma plume in the presence of a liquid increases the temperature and pressure of the initial laser-induced plasma [11]. The high-temperature and high-density state of the plasma is favorable for endothermic chemical reactions, and the short lifetimes of these states facilitate the formation of metastable phases of the structures synthesized [8]. When decaying in a liquid, laser plasma is cooled and ablation products are condensed. The rapid decay of the laser-induced plasma in the liquid limits the growth of the formed particles [12]. Most condensation products are dispersed in the liquid to form nanoparticles, whose parameters are eventually determined by the thermodynamic state of decaying plasma (its temperature and atomic and ionic densities). On the assumption that the mass of the ejected target material depends linearly on the number of laser pulses and that the evaporated material is completely atomized, the concentration of copper atoms in the plasma was 1.4×10^{19} cm^{-3}. The electron temperature of the plasma in the double-pulse regime was found to range from 0.8 eV (at the plume periphery) to 1.4 eV (in its central part). The electron concentration was determined (from the experimental line widths) to vary from 2×10^{18} cm^{-3} in the central part of the plume to 1×10^{18} cm^{-3} at its periphery.
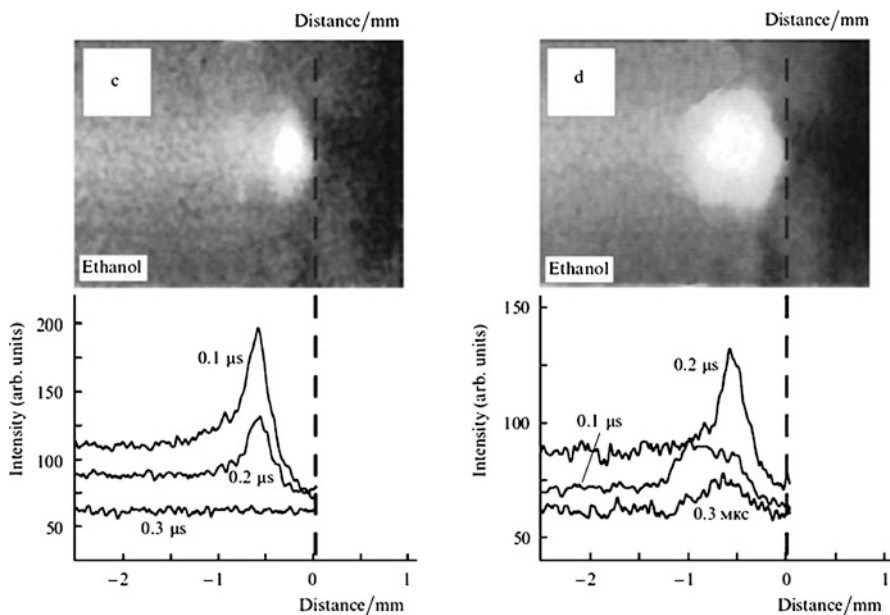
Fig. 8.5 Plasma plume images recorded 200 ns after laser irradiation and the corresponding radiation intensity distributions (at different instants) for the plasma formed in the (**c**) single-pulse and (**d**) double-pulse (1,064 and 532 nm) regimes of ablation of a copper plate in ethanol, recorded along the normal to the target surface. The position of the target surface is shown by the *dashed lines*. The time window for image detection is 100 ns [9]

As it was shown in [13], the double-pulse ablation in liquids is more efficient than the single-pulse one. The micrographs show that the particles formed by double-pulse ablation are smaller than those produced in the single-pulse regime by a factor of 2–3 [13]. The particles are most likely to decrease in size as a result of their heating and fragmentation by the second laser pulse (if appropriate time delays are chosen). The metal particles formed by laser ablation have typical sizes of 3–20 nm. In this range there is no strong dependence of the absorption spectra on the particle size. The absorption spectra of silver, gold, and copper nanoparticles, for example, have characteristic absorption bands peaking at about 400, 520, and 570 nm respectively. These bands are known to be due to the collective excitation of conduction electrons of the metal (the so-called surface plasmon resonances) [14].

8.3.2 Laser Synthesis of Bimetallic Nanoparticles

Pulsed laser ablation in liquids was used to obtain composite particles with metal – metal, semiconductor – metal, and semiconductor – semiconductor structures [15–17], including nanoparticles with a metal core and oxide shell, for example,
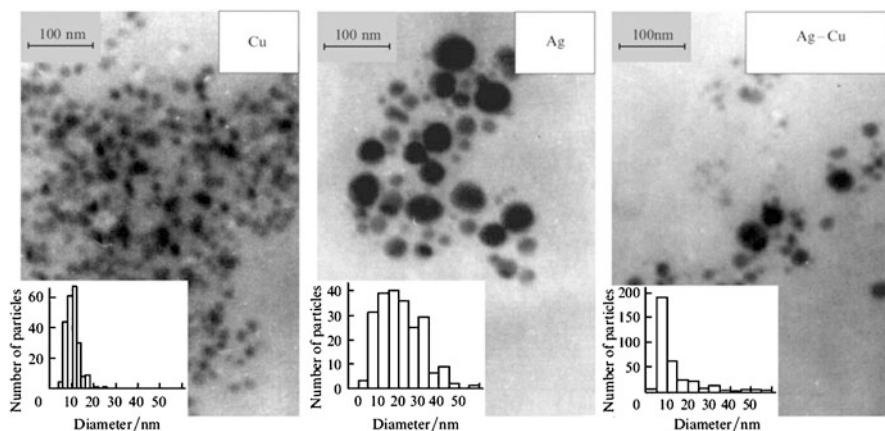
Fig. 8.6 TEM images of copper and silver nanoparticles and bimetallic Ag – Cu particles obtained by laser ablation of the corresponding targets in ethanol for 3 min and the histograms of particle size distributions [9]

Zn – ZnO and Sn – SnO_2 [17, 18]. It was recently reported [19] about the use of laser ablation of a metal target (Sn) in a solution of particles of another metal (Au) to form shell Au – SnO_2 nanoparticles. The formation of a thin shell around a nanoparticle was considered to occur as a result of deposition of the ablation products of the other metal.

The formation of bimetallic Ag – Cu and Ag – Au nanoparticles will be considered. They were synthesized by laser ablation of a combined target, composed of two plates of the corresponding metals, for example, silver – copper or silver – gold. The target was placed in a cell with a liquid (acetone or ethanol), and ablation was performed by the second harmonic of yttrium aluminium laser (532 nm). The laser beam was focused at the interface between the two metals into a spot 0.5 mm in diameter; the laser fluence on the target surface was 15 J cm^{-2}. Single-metal silver and copper nanoparticles were also produced. Transmission electron microscopy (TEM) images of single-metal particles and the particles formed by laser ablation of a two-metal (Ag – Cu) joint are shown in Fig. 8.6. According to the presented data, ablation of a combined Ag – Cu target leads to the formation of particles with an average diameter of 5–7 nm. The average size of silver and copper particles is about 15 and 10 ± 2 nm respectively.

The TEM image of the silver – gold particles formed by laser ablation in ethanol is shown in Fig. 8.7. In absorption spectra, two pronounced bands, peaking at 405 and 540 nm, were observed for the solutions prepared by separate ablation of silver and gold targets (Fig. 8.7, curves 1, 2). Absorption bands with single maxima at about 430 and 445 nm were observed in the case of ablation of a two-sample joint (curves 3, 4). These peaks are located between the maxima of the plasmon bands of single-metal silver and gold particles; therefore, the spectra recorded correspond
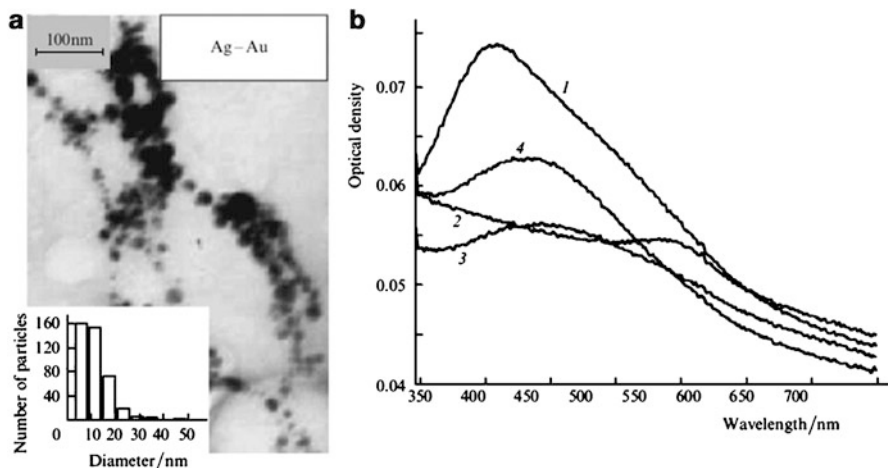
Fig. 8.7 TEM image (**a**) and the optical absorption spectra (**b**) of colloidal nanoparticle solutions obtained under laser ablation ($\lambda = 532$ nm) of silver (*1*), gold (*2*), and combined Ag – Au (**a**, and **b**, curves *3*, *4*) targets in ethanol [9]

to the plasmon absorption of alloy particles. The plasmon absorption maxima of bimetallic Ag – Au particles shift away from the maximum of single-metal silver particles, proportionally to the increase in the gold content in the particles. These spectral features indicate that the Ag – Au particles formed by the above-described method are homogeneously alloyed nanoparticles. As ideal solid solutions are formed at any concentration ratio of Ag and Au, alloying of these two metals is thermodynamically favorable, and the material of the nanoparticles formed is a homogeneous alloy.

The diffraction pattern of the powder of particles obtained by laser ablation of an Ag – Cu joint contains reflections of both silver and copper of cubic structure, with the lattice constants a = 0.409 and 0.362 nm, respectively. This finding, as was suggested above, agrees with the formation of bimetallic particles composed of crystalline silver and copper clusters. In the case of formation of alloyed nanoparticles the diffraction pattern should contain alloy reflections. The presence of a single band in the optical absorption spectrum, with a position dependent on the concentration of a particular metal, may indicate the alloy formation. However, since silver and copper are characterized by low mutual solubility, particles composed of nuclei of silver and copper crystalline phases are more likely to be formed.

Thus, laser ablation of a combined target in the liquid yields Ag – Cu and Ag – Au nanocomposite particles. The optical absorption spectra showed that the particles synthesised by laser ablation of combined samples are not a mixture single-metal nanoparticles, but each particle has a mixed composition. The technique developed is expected to be useful to produce other two-component systems.

8.3.3   Formation of Nanoparticles Under Laser Ablation of Complex Composition Targets in Liquids

Pulsed laser ablation in liquids makes it possible to obtain nanostructures of different composition using combinations of different solid targets and liquids. In particular, PLAL was used to form nanoparticles of chalcopyrite ($CuFeS_2$) and cadmium selenide (CdSe) under laser ablation of corresponding targets and gadolinium carbide nanoparticles under ablation of metallic gadolinium target in carbon-containing media (ethanol and acetone) [20, 21].

Chalcopyrite nanoparticles were synthesised by laser sputtering of a sample of the original mineral in water. The phase and elemental compositions of the particles formed were analysed by XRD and energy-dispersive X-ray (EDX) methods. A chalcopyrite target was placed in a cell with distilled water and irradiated by a Nd:YAG laser ($\lambda = 1,064$ nm, energy per pulse 60 mJ, pulse repetition rate 10 Hz, and pulse duration 12 ns). The particles synthesized formed a colloidal solution. The relative contents of Fe, Cu, and S atomic components in the formed particles, determined from the EDX spectrum, corresponded to the stoichiometric ratio for the $CuFeS_2$ phase. X-ray diffraction pattern shows that the synthesized powder consists of tetragonal chalcopyrite $CuFeS_2$. Note that there are few diffraction small peaks from the $CuFe_2S_3$ and $Cu_2Fe_4S_7$ phases near the diffraction peaks of $CuFeS_2$. Thus, the formation of metastable copper- and iron-containing compounds is not excluded. However, oxide phases were not observed. The atomic force micrographs of the chalcopyrite particles deposited on a mica substrate showed agglomerates of nanoparticles, which were most likely formed during deposition. The initial particles were of approximately the same size (50–100 nm). It is noteworthy that the formation of stoichiometric nanoparticles under laser ablation of chalcopyrite in water is rather unexpected.

It should be noted that, according to the experimental data [9], laser ablation of cadmium selenide single crystals in ethanol by the second harmonic of Nd:YAG laser also leads to the formation of particles with the corresponding stoichiometry. The typical shape of the CdSe nanoparticles obtained by laser ablation is spherical. The particles with an average diameter of 25 nm are formed at a laser fluence of $0.2 \, J \, cm^{-2}$.

Oxide particles can be obtained either by direct laser ablation of a solid oxide target or using ablation of the corresponding metals in reactive liquids. Synthesis of nanocrystals of different oxides, including TiO_2, SnO_2, ZnO, etc., was reported in a number of studies [9, 12, 18, 22, 23]. In particular, very small (3–5 nm in diameter) TiO_2 nanoparticles were formed by pulsed laser ablation of a titanium target immersed in an aqueous solution of sodium dodecyl sulfate $C_{12}H_{25}SO_4Na$ and in deionised water [12]. The use of this solution prevents aggregation of the obtained particles.

The possibility of using laser ablation in liquids to obtain stable gadolinium nanoparticles was investigated for the first time in [21]. A metallic gadolinium target was fixed in a vessel filled with a liquid. Micrographs of the nanoparticles obtained

Fig. 8.8 Luminescence spectrum of the nanoparticles formed by laser ablation of a gadolinium target with 3.5 % terbium in water. Luminescence was excited at a wavelength of 276 nm [9]
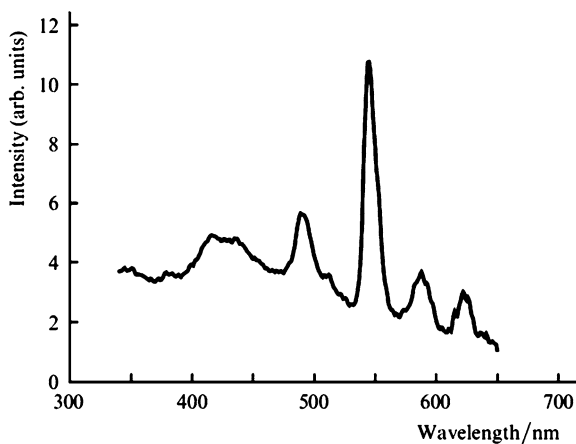
by laser ablation of gadolinium showed that spherical particles with an average size from 10 to 12 nm (ablation in water) and from 6 to 10 nm (ablation in ethanol) are dominant. The EDX and XRD analyses were used to determine the composition and phase of the nanoparticles formed. In the case of laser ablation in distilled water, the results were obtained which showed the formation of nanocrystalline gadolinium oxide particles (Gd_2O_3) in the monoclinic phase. No other phases were found [21]. The XRD patterns for the powder produced in ethanol demonstrated a more complex phase composition. This powder was a mixture of gadolinium carbide GdC_2 and gadolinium hydride GdH_3; reflections of metallic Gd were also recorded.

Laser ablation of a gadolinium target containing 3.5 % terbium in water yielded gadolinium oxide nanocrystals doped with terbium ions, which have luminescent properties. The luminescence spectra of these nanocrystals contain several single peaks, which are due to the electronic transitions of Tb^{3+} in the Gd_2O_3 lattice (Fig. 8.8). Particles of gadolinium oxide doped with rare earth ions can be used as effective luminescent labels in bioanalysis due to their optical properties (emission spectra, luminescence lifetime), as well as photostability and possibility of inexpensive synthesis.

Lanthanides and their alloys are promising magnetic materials for a number of technological and biomedical applications [24]. In particular, gadolinium and its compounds are used as contrast materials in magnetic resonance tomography, as a therapeutic agent for hyperthermia of tumors, and as drug carriers.

Now we say shortly about laser modification of nanoparticles in solutions. Currently, the interaction of laser radiation with nanostructures is intensively investigated to develop methods for deliberately changing the nanoparticle structure and morphology [25–29]. It was demonstrated that laser radiation can be used to fragment gold and silver nanoparticles [25, 26, 28] and aggregate them [30]. Laser-induced transformation of nanowires into nanospheres [31] or, vice versa, spherical particles into nanowires [27] was also observed. Laser irradiation may change not only the morphology of particles but also their composition and structure.

Laser synthesis and modification of nanoparticles in liquids is relatively young but rapidly developing field of research, which has a wide range of practical applications.

8.4 Nanocrystals in Silica Gel Glasses

8.4.1 The Formation of Nanocrystallites in Gel Glasses

The formation of high-symmetry Ln(III) complexes is possible in silica gel glasses coactivated by Ce^{4+} and Ln^{3+} ions [32, 33]. Here the investigation results of such complexes are presented. Samples were prepared using the direct sol–gel–glass transition according to the procedure described in [34]. The glasses were activated by impregnating porous xerogels with cerium and europium chloride solutions. The xerogels were sintered until the formation of transparent glasses in air at $T = 1240^{\circ}$ C.

The presence of crystalline phases in glasses was controlled on a DRON-2.0 X-ray diffractometer. Figure 8.9 presents the X-ray diffraction pattern of glasses containing cerium and europium. As can be seen from Fig. 8.9, the pattern exhibits peaks at the angles $2\theta \approx 28°$, $33°$, $47°$, and $56°$ and also more weak peaks with $2\theta > 56°$ which are not shown in Fig. 8.9. The X-ray diffraction patterns of nonactivated glasses do not exhibit any indications of crystalline phases. According to the data available in the JCPDS-1998 Powder Diffraction File, the Bragg reflections at the specified angles with observed relative intensities correspond to the CeO_2 cubic lattice with space group of symmetry O^5_h–$Fm3m$, in which the coordination number of the cations is 8. These results confirm the presence of the CeO_2 nanoparticles in the glass samples and support the assumption that the high-symmetry Eu^{3+} local environment is formed through the replacement of cerium by europium in CeO_2 nanoparticles.
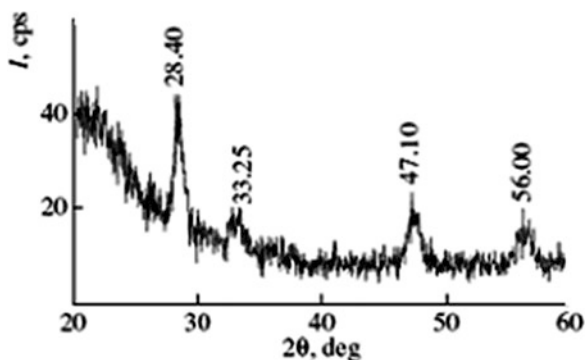
Fig. 8.9 X-ray diffraction pattern of silica gel glasses containing cerium and europium (6 wt.% and 0.6 wt.% of corresponding chlorides in the ingrained solution) [35]

Fig. 8.10 The scattering
vector dependences of the
small-angle neutron
scattering intensity for (*1*)
nonactivated silica gel glass
and (*2*) glass containing
cerium and europium (2 wt.%
for CeCl$_3$ and 1 wt.% for
EuCl$_3$ in the ingrained
solution) [35]
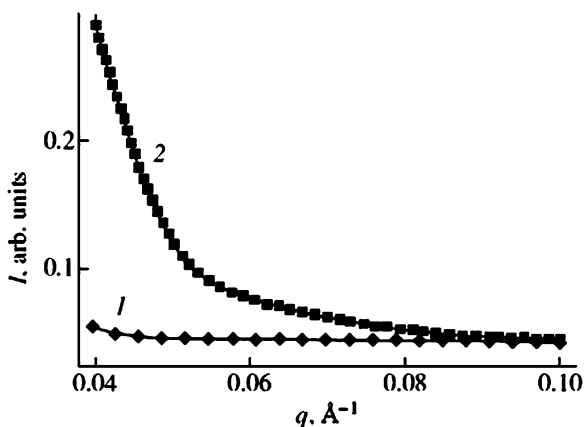
Figure 8.10 shows the small-angle neutron scattering (SANS) intensity curves for the nonactivated silica gel glass (curve 1) and the glass containing cerium and europium (curve 2). It can be seen that the SANS intensity I for the nonactivated glass does not depend on the scattering vector q (the glass is homogeneous on a nanometer scale), whereas the coactivated glass contains nanoinhomogeneities. The diameter of these inhomogeneities was determined in the Guinier approximation [36]. It was approximately equal to 10 nm for the case with curve 2 data. It should be noted that variations in the temperature–time conditions of synthesis, the doping procedure, and the activator concentration lead to appreciable changes in the nanoparticle diameters.

8.4.2 Spectral Properties of Nanostructured Ce–Ln-Containing Silica Gel Glasses

Figure 8.11 depicts the luminescence (a) and luminescence excitation (b) spectra of low-symmetry (curves 1, 3) and high-symmetry (curves 2, 4) Ce^{4+}–Eu^{3+} centers in the range of the $^5D_0 \rightarrow ^7F_j$ transitions in glasses containing cerium and europium. It can be seen from Fig. 8.11 that, compared to the low-symmetry centers excited into the f–f bands of Eu^{3+} ions (curve 1, $\lambda_{exc} = 395$ nm), the high-symmetry centers excited through a sensitizer (curve 2, $\lambda_{exc} = 320$ nm) are characterized not only by a considerably smaller luminescence branching ratio for the electric dipole transitions but also by a multiple narrowing of the $^5D_0 \rightarrow ^7F_0$ band. The half-width of this band for high-symmetry centers is equal to 1.0 nm ($\Delta\nu$ 30 cm^{-1}). This value is close to the half-width of the same name band for the dominant type of centers for oxides CeO_2 (30 cm^{-1} at $T = 298$ K) [37] and is three times less than the half-width characteristic of europium-containing glasses upon selective laser excitation at $T = 77$ K [38]. These findings can be a weighty argument in support of the nanocrystalline nature of the high-symmetry centers.
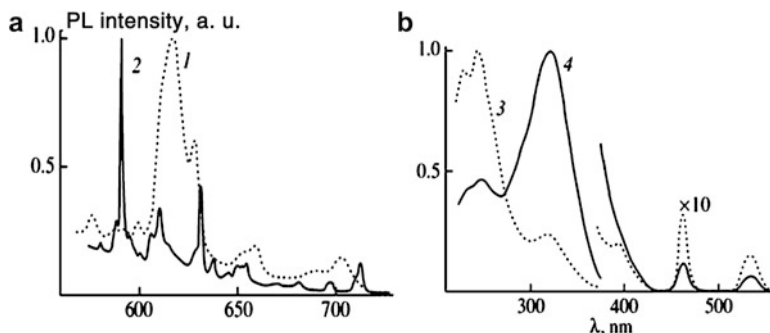
Fig. 8.11 Luminescence spectra (**a**) and luminescence excitation spectra (**b**) of Ce^{4+}–Eu^{3+} centers in silica glasses containing cerium and europium (2 wt.% for $CeCl_3$ and 1 wt.% for $EuCl_3$ in the ingrained solution) [35]
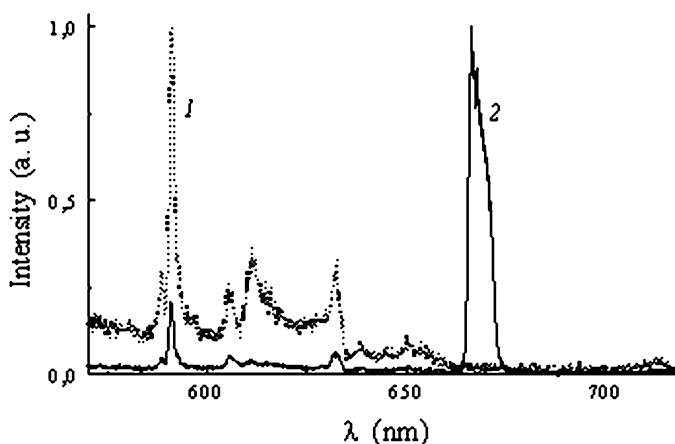
Fig. 8.12 The luminescence spectra of silica gel glasses containing Ce-Eu (*1*) and Ce-Eu-Mg (*2*); $\lambda_{exc} = 266$ nm, $T = 30$ K

The spectra of silica gel glasses activated with the $[Ce^{4+}O_8]_n$:$(Ln^{3+})_m$ nanoparticles, where Ln = Sm, Nd, Ho, Er, Tb, Yb, were also investigated. All of them are characterized by intense absorption at $\lambda < 400$ nm, by luminescence spectra of the Ln^{3+} ions similar to spectra in cubic crystalline matrixes, by an effective sensitization of the Ln^{3+} ions luminescence with labile photoreduced $(Ce^{4+})^-$ ions and by weak vibronic interaction of the Ln^{3+} ions with the glassy host-matrix. The luminescence sensitization may be realized by means of energy transfer or transfer of electron. In the latter case, the excited photoreduced $[(Ln^{3+})^-]^*$ ion, as a rule, converts into $(Ln^{3+})^*$ ion giving up an electron to the ligand from its ground state. It have been discovered that the use of some extrinsic local charge compensators at the nanoparticles formation can leads to stabilization of the $[(Ln^{3+})^-]^*$ ions and to observation of their luminescence. Such situation confirms by the Fig. 8.12 where

luminescence spectrum of glass activated by the $[Ce^{4+}O_8]_n$:Eu^{3+} nanoparticles without the local charge compensator is typical for the cubic centers of Eu^{3+} ions (curve 1) whereas the spectrum of the activated glass with the use of Mg as the compensator possesses additional band ($\lambda \approx 666$ nm) which is caused by transitions from the lowest $f^6 d$-state of the $(Eu^{3+})^-$ cubic centers (curve 2).

So, the silica gel glasses coactivated by cerium or cerium and one more lanthanide contain nanoinhomogeneities 10 nm in size. The lattice of these inhomogeneities is identical to that of the CeO_2 with space group of symmetry $O^5_h - Fm3m$, in which the coordination number of the cations is 8. The Ln^{3+} ions included in the nanoparticles are characterized by the following features: (a) sufficiently effective sensitization of their luminescence with labile photoreduced $(Ce^{4+})^-$ ions by means of excitations transfer through the exchange mechanism or/and by transfer of electron; (b) a weak vibronic interaction of the Ln^{3+} ions with the glassy host-matrix; (c) a high relative intensity of magnetic dipole transitions and similarity of the Ln^{3+} luminescence spectra to spectra of the same ions with coordination number 8 located in cubic crystalline matrixes.

References

1. Klingshirn C (2007) ZnO: from basics towards applications. Phys Status Solidi B 244:3027–3073
2. Burakov VS, Tarasenko NV, Nevar EA, Nedelko MI (2011) Morphology and optical properties of zinc oxide nanostructures synthesized by the methods of thermal and discharge sputtering. Tech Phys 56:245–253
3. Umar A, Kim SH, Suh E-K, Hahn YB (2007) Ultraviolet-emitting javelin-like ZnO nanorods by thermal evaporation: growth mechanism, structural and optical properties. Chem Phys Lett 440:110–115
4. Ho GW, Wong ASW, Kang DJ, Welland ME (2007) One step solution synthesis towards ultra-thin and uniform single-crystalline ZnO nanowires. J Appl Phys A 86:457–462
5. Shafeev GA (2008) Laser-based formation of nanoparticles. In: Lackner M (ed) Lasers in chemistry, vol 1: probing matter. Wiley VCH Verlag, Wienheim, pp 713–741
6. Kabashin AV, Meunier M (2006) Laser ablation-based synthesis of nanomaterials. In: Perriere J, Millon E, Fogarassi E (eds) Recent advances in laser processing of advanced materials. Elsevier, Amsterdam, pp 1–36
7. Bogaerts A, Chen Z, Gijbels R, Vertes A (2003) Laser ablation for analytical sampling: what can we learn from modeling? Spectrochim Acta B 58:1867–1893
8. Yang GW (2007) Laser ablation in liquids: applications in the synthesis of nanocrystals. Prog Mater Sci 52:648–698
9. Tarasenko NV, Butsen AV (2010) Laser synthesis and modification of composite nanoparticles in liquids. Quantum Electron 40:986–1003
10. Burakov VS, Tarasenko NV, Nedelko MI, Isakov SN (2008) Time-resolved spectroscopy and imaging diagnostics of single pulse and collinear double pulse laser induced plasma from a glass sample. Spectrochim Acta B 63:19–26
11. Sakka T, Saito K, Ogata YH (2005) Confinement effect of laser ablation plume in liquids probed by self-absorption of C_2 Swan band emission. J Appl Phys 97:014902
12. Liang CH, Shimizu Y, Sasaki T, Koshizaki N (2005) Preparation of ultrafine TiO_2 nanocrystals via pulsed-laser ablation of titanium metal in surfactant solution. J Appl Phys A 80:819–822

13. Burakov VS, Tarasenko NV, Butsen AV, Rozantsev VA, Nedelko MI (2005) Formation of nanoparticles during double-pulse laser ablation of metals in liquids. Eur Phys J Appl Phys 30:107–113

14. Boren CF, Huffman DR (1983) Absorption and scattering of light by small particles. Wiley, New York

15. Compagnini G, Messina E, Puglisi O, Nicolosi V (2007) Laser synthesis of Au/Ag colloidal nano-alloys: exploring the optical properties for an accurate analysis. Appl Surf Sci 254:1007–1011

16. Kamat PV (2002) Photophysical, photochemical and photocatalytic aspects of metal nanoparticles. J Phys Chem B 106:7729–7744

17. Zeng HB, Cai WP, Li Y (2005) Composition/structural evolution and optical properties of ZnO/Zn nanoparticles by laser ablation in liquid media. J Phys Chem B 109:18260–18266

18. Liang CY, Shimizu T, Sasaki N, Koshizaki M (2003) Synthesis of ultrafine SnO_{2-x} nanocrystals by pulsed laser-induced reactive quenching in liquid medium. J Phys Chem B 107:9220–9225

19. Bajaj G, Soni RK (2010) Synthesis of composite gold/tin-oxide nanoparticles by nano-soldering. J Nanoparticle Res 12:2597–2603

20. Nevar EA, Savastenko NA, Bryuzer V, Lopatik DA, May F, Butsen AV, Tarasenko NV, Burakov VS (2010) Plasma synthesis and treatment of nanosized chalcopyrite particles. J Appl Spectrosc 77:136–141

21. Tarasenko NV, Butsen AV, Nevar EA (2008) Laser ablation of gadolinium targets in liquids for nanoparticle preparation. J Appl Phys A 93:837–841

22. Li Y, Xu G, Zhu YL, Ma XL, Cheng HM (2007) SnO_2/In_2O_3 one-dimensional nano-core-shell structures: synthesis, characterization and photoluminescence properties. Solid State Commun 142:441–444

23. Usui H, Shimizu Y, Sasaki T (2005) Photoluminescence of ZnO nanoparticles prepared by laser ablation in different surfactant solutions. J Phys Chem B 109:120–124

24. Bohigas X, Molins E, Roig A, Tegada J, Zhang XX (2000) Room-temperature magnetic refrigerator using permanent magnets. IEEE Trans Magn 36:538–544

25. Henglein A (1993) Physicochemical properties of small metal particles in solution: "microelectrode" reactions, chemisorption, composite metal particles, and the atom-to-metal transition. J Phys Chem 97:5457–5471

26. Mafune F, Kohno J, Takeda Y, Kondow T, Sawabe H (2002) Growth of gold clusters into nanoparticles in a solution following laser-induced fragmentation. J Phys Chem B 106:8555–8561

27. Tsuji T, Okazaki Y, Higuchi T, Tsuji M (2003) Laser induced morphology change of silver colloids: formation of nano-size wires. Appl Surf Sci 211:189–193

28. Takami A, Kurita H, Koda S (1999) Laser-induced size reduction of noble metal particles. J Phys Chem B 103:1226–1232

29. Tarasenko NV, Butsen AV, Nevar EA, Savastenko NA (2006) Synthesis of nanosized particles during laser ablation of gold in water. Appl Surf Sci 252:4439–4444

30. Burda C (2000) Optical spectroscopy of nanophase material. In: Wang ZL (ed) Characterization of nanophase materials. Wiley-VCH Verlag, Wienheim, p 197

31. Link S, Burda C, Nikoobakht B, El-Sayed MA (2000) Laser-induced shape changes of colloidal gold nanorods using femtosecond and nanosecond laser pulses. J Phys Chem B 104:6152–6163

32. Malashkevich GE, Poddenezhny EN, Melnichenko IM, Semchenko AV (1998) Luminescence spectral properties of Sm- and (Ce, Sm)-containing silica gel glasses. Phys Solid State 40:420–426

33. Malashkevich GE, Makhanek AG, Semchenko AV, Gaishun VE, Melnichenko IM, Poddenezhny EN (1999) Luminescence-spectral properties and structure of optical centers in Eu- and Ce–Eu-containing quartz gel-glasses. Phys Solid State 41:202–207

34. Malashkevich GE, Poddenezhny EN, Melnichenko IM, Boiko AA (1995) Optical centers of cerium in silica glasses obtained by the sol–gel process. J Non-Cryst Solid 188:107–117

35. Malashkevich GE, Sigaev VN, Semkova GI, Champagnon B (2004) Nanocrystalline nature of high-symmetry Ce^{4+}–Eu^{3+} centers in silica gel glasses. Phys Solid State 46:552–556
36. Guinier A, Fournet G (1955) Small-angle scattering of X-rays. Wiley, New York
37. Malashkevich GE, Lapina VA, Semkova GI, Pershukevich PP, Shevchenko GP (2003) Luminescence of Eu^{3+} ions in ultra disperse diamond powders. JETP Lett 77:291–294
38. Hayakawa T, Nogami M (2001) Energy migration of the local excitation at the Eu^{3+} site in a Eu-O chemical cluster in sol–gel derived SiO_2:Eu^{3+} glasses. J Appl Phys 90:2200–2205

9
Photonic-Crystal Fiber Platform for Ultrafast Optical Science

Aleksei M. Zheltikov

Abstract The latest breakthroughs in photonic-crystal-fiber (PCF) technologies open new horizons in photonics and optical science. The frequency profile of dispersion and the spatial profile of electromagnetic field distribution in waveguide modes of microstructure fibers can be tailored by modifying the core and cladding design on a micro- and nanoscale, suggesting the ways of creating novel fiber-optic components and devices. Recently developed new types of PCFs provide highly efficient spectral and temporal transformation of laser pulses with pulse widths ranging from tens of nanoseconds to a few optical cycles (several femtoseconds) within a broad range of peak powers from hundreds of watts to several gigawatts. Enhanced nonlinear-optical processes in waveguide modes of these novel optical fibers will offer unique opportunities for ultrafast optical science and lightwave technologies.

9.1 Introduction

Over the past few years, photonic-crystal fibers (PCFs) [1–3] – new optical fibers (Fig. 9.1) with tailored dispersion and nonlinearity [7, 8] – have been providing a constantly growing platform (Fig. 9.2) for the development of advanced fiber-format devices and components for optical metrology [9, 10], ultrashort-pulse

A.M. Zheltikov (✉)
Physics Department, International Laser Center, M.V. Lomonosov Moscow State University, Moscow 119992, Russia

Department of Physics and Astronomy, Texas A&M University, College Station, TX 77843-4242, USA

Laboratory of Neurophotonics, Department of Neuroscience, Kurchatov National Research Center, pl. Akad. Kurchatova 1, Moscow 123098, Russia
e-mail: zheltikov@phys.msu.ru

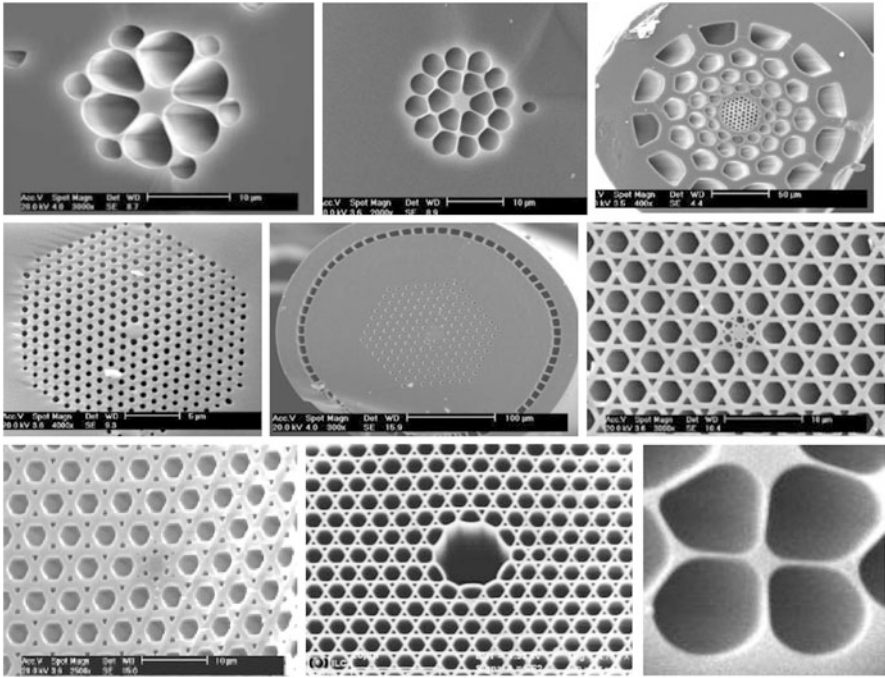**Fig. 9.1** SEM images of photonic-crystal fibers [3–6]: (**a**, **b**) solid-core high-index-step silica PCFs, (**c**) solid-core silica PCF with a dual microstructure cladding, (**d**) periodic-cladding PCF, (**e**) YAG-doped PCF, (**f**, **g**) soft-glass PCF with a nanohole-array-modified core, (**h**) hollow-core PCF, and (i) nanowaveguide PCF
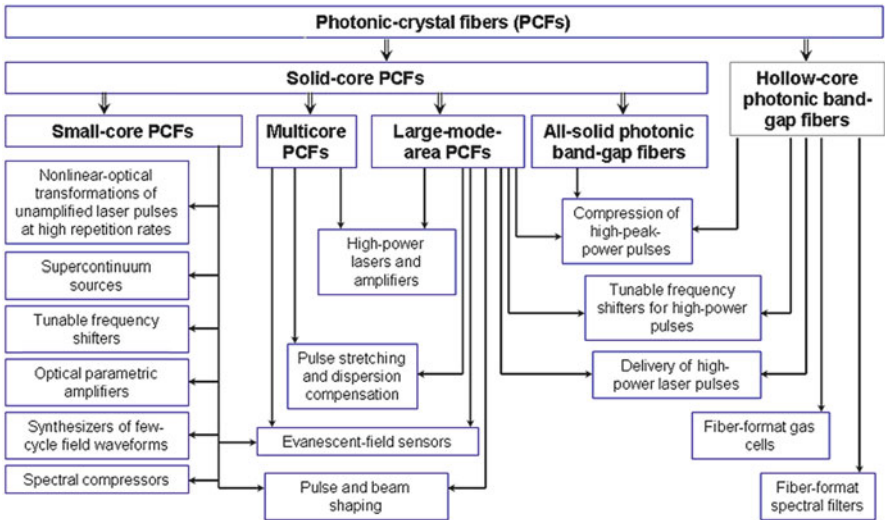
Fig. 9.2 Photonic-crystal fiber platform for ultrafast optical science

laser technologies [11, 12], biomedicine [13], quantum optics [14], spectroscopy [15–17], microscopy [18], and neurophotonics [19–21]. Unique options offered by photonic-crystal fiber technology [22], such as dispersion management through fiber structure engineering [7] and enhancement of optical nonlinearity due to a strong field confinement in a small-size fiber core [23], have been pushing the frontiers of fiber optics, allowing the creation of efficient sources of supercontinuum radiation [24–26], novel compact fiber lasers [27–29], as well as frequency converters [4], pulse compressors [30], fiber components for biomedical optics [31, 32], and optical sensors [33–35].

In the rapidly expanding field of nonlinear microscopy and spectroscopy, PCFs have been shown to possess a tremendous potential for making laser microscopes and spectrometers simpler and much more compact through the replacement of wavelength-tunable laser sources, such as optical parametric amplifiers and dye lasers, by a specifically designed segment of fiber. Efficient frequency conversion and supercontinuum generation in PCFs have been shown to enhance the capabilities of chirped-pulse CARS [36] and coherent inverse Raman spectroscopy [37, 38]. Efficient spectral broadening of ultrashort pulses in PCFs with carefully engineered dispersion profiles makes these fibers ideal light sources for pump–supercontinuum probe time- and frequency-resolved nonlinear-optical measurements [25] and offer interesting new options for multiplex CARS microscopy [38, 39]. In experiments [40], a single-beam CARS approach [41] has been implemented in a new and elegant way through the generation of supercontinuum in a PCF followed by a compression and pulse shaping of this supercontinuum with the help of a pulse shaper based on a spatial light modulator.

Light sources based on photonic-crystal fibers have been recently shown to offer attractive fiber-optic solutions for simplification and compactization of CARS microscopes [18] and spectrometers [15]. Fibers of this type can provide high efficiencies of nonlinear-optical spectral transformations of ultrashort laser pulses due to the strong confinement of the light field in a small-area fiber core and tailored dispersion of guided modes, which can be optimized for a given type of nonlinear-optical interaction by modifying the fiber structure. Specially designed PCF frequency converters for ultrashort laser pulses have been used to demonstrate frequency-resolved optically gated CARS [36], where a blue-shifted output of PCFs pumped with femtosecond Cr: forsterite laser pulses was used as a Stokes field and the second harmonic of the Cr: forsterite laser was employed as a pump field. Supercontinuum-generating PCFs have been shown to provide a broad range of wavelength tunability, offering new interesting options for multiplex CARS microscopy [36, 38].

In what follows, we provide a brief overview of what appears to be some of the most promising and interesting applications of photonic-crystal fibers in ultrafast optical science and technology.

9.2 Photonic-Crystal Fiber Ultrafast Lightwave Synthesizers

Generation of ultrashort light pulses with a high contrast and a high quality of temporal envelope requires not only a broad spectrum, but also an appropriate profile of the spectral phase of electromagnetic field [42]. Self- and cross-phase modulation processes [43], as well as high-order stimulated Raman scattering [44] are known to induce spectral profiles of the nonlinear phase suitable for the generation of few-cycle light pulses, while the generation of properly phased high-order harmonics has been demonstrated to allow the generation of attosecond pulses [45]. The richest spectral content is, however, often achieved in the regimes that involve a combination of several nonlinear-optical processes [46]. Supercontinuum generation in filaments [47, 48] or highly nonlinear fibers [24–26] is, perhaps, the most notable example of this type of nonlinear-optical interactions. Special regimes of filamentation-assisted spectral broadening have been shown to be remarkably well suited for the generation of few-cycle pulses [49]. On the other hand, adaptive techniques enhanced by blind-optimum-search algorithms have been applied to compress supercontinua generated in highly nonlinear fibers to few-cycle field waveforms [50]. In a more general situation, however, spectral phase profiles of multioctave supercontinua tend to be prohibitively complicated for a straightforward pulse compression to transform-limited pulse widths.

The interplay of various nonlinear-optical processes involved in the spectral broadening of a laser pulse becomes especially complicated in the regime of anomalous dispersion. Here, the nonlinear phase shift can be balanced by a dispersion-induced phase shift, giving rise to solitonic features in the temporal structure of the laser field. As the retarded part of optical nonlinearity induces a continuous red shift of such solitons [51], the long-wavelength part of supercontinuum is often dominated by overlapping spectra of frequency-shifted solitons [25, 26]. With the balance between dispersion and nonlinearity tending to isolate the phase of each individual soliton from the phase of other solitons and the nonsolitonic part of the field, this type of dynamics is usually viewed as unfavorable for efficient pulse compression.

Experiments [52] show that frequency-shifted solitons in a highly nonlinear photonic-crystal fiber (PCF) can give rise to high-visibility interference fringes in PCF output spectra, indicating flat spectral phase profiles of individual solitons in the PCF output. This experimental finding, supported by numerical simulations, suggests a promising method of fiber-format pulse shaping and an attractive technology for few-cycle field synthesis through a coherent addition of frequency-shifted solitons generated in a highly nonlinear fiber.

In experiments [52], we used a laser source based on a femtosecond Ti: sapphire laser system, consisting of a master oscillator pumped by the second-harmonic output of a Nd: YLF laser, a stretcher, a multipass amplifier pumped by the second harmonic of a Nd: YAG laser, and a compressor. The master oscillator delivered laser pulses with a central wavelength of 800 nm, a typical pulse width of 40–50 fs, and an average power of 500 mW at a repetition rate of 90 MHz. The amplified
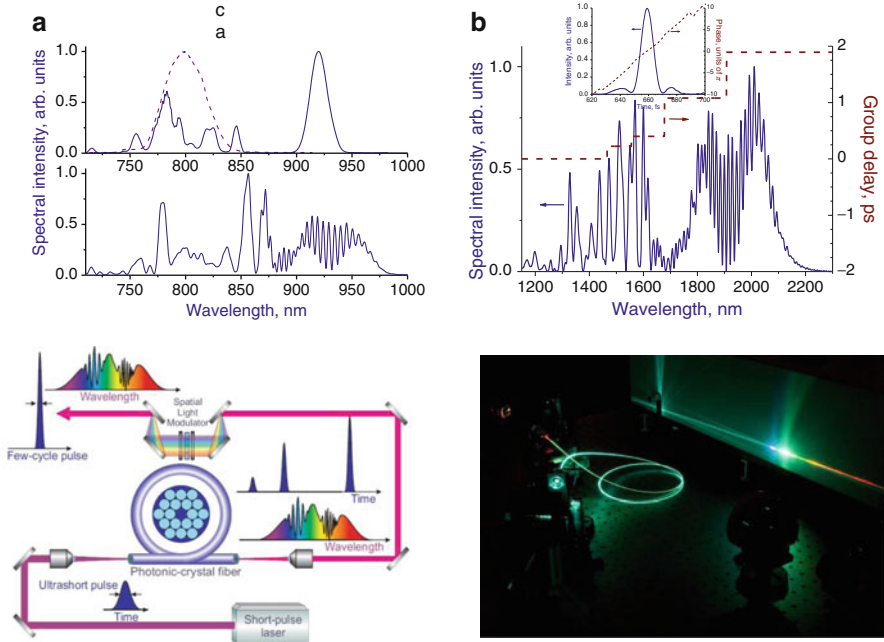
Fig. 9.3 (**a**) The spectra of the input Ti: sapphire laser pulses (*dashed line*) and pulses transmitted through a 1.5-m piece of a photonic-crystal fiber (*solid line*) with the cross-section structure shown in the *inset* [53]. The energy of input laser pulses is 0.6 nJ (*upper panel*) and 7 nJ (*lower panel*). (**b**) The spectrum of laser pulses with an initial central wavelength of 1,250 nm, a pulse width of 100 fs, and an energy of 30 nJ transmitted through a 5-cm piece of nonlinear fiber with parameters specified in the text. The *dashed line* shows the profile of the group delay used to transform the five-soliton PCF output into a few-cycle light pulse. The *inset* shows the temporal envelope (*solid line*) and the phase (*dashed line*) of the pulse synthesized upon such a group-delay compensation. (**c**) Sketch of a PCF-based few-cycle pulse synthesizer. A highly nonlinear PCF transforms input laser pulses into multiple solitons. Coherent addition of these solitons leads to a synthesis of few-cycle pulses. (**d**) Supercontinuum generation in a photonic-crystal fiber

10-Hz, 800-nm output of the laser system was launched into a 1.5-m-long piece of a highly nonlinear PCF with an effective mode area of 2.5 μm^2 (the inset in Fig. 9.3), zero-group-velocity-dispersion (zero-GVD) wavelength $\lambda_0 \approx 770$ nm, and nonlinear coefficient $\gamma \approx 100$ W^{-1} km^{-1} at a wavelength of 0.8 μm. As the entire spectrum of input laser pulses (shown by the dashed line in Fig. 9.3) falls within the range of anomalous dispersion, laser pulses tend to evolve toward solitons as they propagate through the fiber. These solitons undergo a continuous frequency downshift due to the Raman effect [51], giving rise, at moderate input pulse peak powers, to well-resolved features in the long-wavelength part of PCF output spectra (Fig. 9.3).

As the input laser power is increased, shorter solitons with broader spectra are generated inside the fiber. For 50-fs input pulses with an energy above 3 nJ,

the spectra of frequency-shifted solitons in the PCF output start to overlap. In this regime, high-visibility interference fringes are observed within the wavelength range of 800–970 nm in the PCF output spectrum (Fig. 9.3). These fringes display two characteristic beat frequencies, 1.65 and 1.78 THz, indicating an interference of three soliton pulses with different central frequencies and flat spectral phase profiles across each individual soliton spectrum.

To give more quantitative insights into the origin of fringes observed in Fig. 9.1, we represent the PCF output as a superposition of M soliton pulses,

$$E\left(\theta\right) = \sum_{m=1}^{M} A_m \sec h \left(\frac{\theta - \Delta_m}{\tau_m}\right) \exp\left[i\left(\varphi_m - 2\pi \nu_m \theta\right)\right], \tag{9.1}$$

where A_m, τ_m, Δ_m, φ_m, and ν_m are the amplitudes, pulse widths, delay times, phases and central frequencies of individual solitons ($\tau_m = T_m/1.763$, where T_m is the FWHM soliton pulse width). In agreement with our intuitive expectations, the best fit of the PCF output spectrum presented in Fig. 9.3 is achieved by assuming the interference of three solitons ($M = 3$) with different carrier frequencies ($\nu_1 \approx 338$ THz, $\nu_2 \approx 329$ THz, $\nu_3 \approx 316$ THz), pulse widths ($T_1 \approx 70$ fs, $T_2 \approx 34$ fs, $T_3 \approx 32$ fs), and amplitudes ($A_2/A_1 \approx 3.8$, $A_3/A_1 \approx 4.0$) whose phases remain constant over the spectrum of each individual soliton ($\varphi_2 - \varphi_1 \approx 0.97\pi$, $\varphi_3 - \varphi_2 \approx 0.22\pi$). The delay times Δ_m between the solitons calculated from the fringes in the PCF output spectra in Fig. 9.3, $\Delta_2 - \Delta_1 \approx 610$ fs and $\Delta_3 - \Delta_2 \approx 560$ fs, agree very well with the delay times dictated for solitons with given ν_m by the fiber dispersion.

The invariance of the spectral phase φ_m of each individual soliton over its spectrum is the key finding of our experiments. The beat frequency of the fringes observed in the PCF output spectra can be tuned by changing the length of the nonlinear fiber, offering an attractive solution for all-fiber pulse shaping for a coherent excitation of molecular vibrations and coherent Raman microspectroscopy, including single-beam microscopy based on coherent anti-Stokes Raman scattering [18]. Furthermore, due to the constancy of φ_m over the spectrum of mth soliton, the total spectral bandwidth of M solitons ($M = 3$ in our experiments) can be employed to synthesize light pulses with pulse widths shorter than the pulse width T_m of any of the solitons generated at the fiber output. Indeed, a light modulator introducing a stepwise group-delay profile would transform a three-soliton PCF output with the spectrum shown by the solid line in Fig. 9.2 into a light pulse with an FWHM pulse width $T_\Sigma \approx 24$ fs.

To demonstrate the suitability of frequency-shifted solitons generated in a highly nonlinear fiber for the synthesis of few-cycle light pulses, we numerically solve the generalized nonlinear Schrödinger equation (GNSE) [51] modeling the evolution of Gaussian light pulses with an input central wavelength of 1,250 nm and an initial pulse width of 100 fs in a fused silica fiber with an effective mode area of 20 μm², zero-GVD wavelength $\lambda_0 \approx 1,000$ nm, and high-order dispersion coefficients $\beta_m = \left(\partial^m \beta / \partial \omega^m\right)|_{\lambda_0}$ chosen in such a way as to mimic a typical

dispersion profile of a large-mode-area PCF suitable for the generation of high-power solitons: $\beta_3 = 7.6 \cdot 10^{-5}$ ps³/m, $\beta_4 = -9.4 \cdot 10^{-8}$ ps⁴/m, $\beta_5 = 2.5 \cdot 10^{-10}$ ps⁵/m, $\beta_6 = -1.2 \cdot 10^{-12}$ ps⁶/m. These numerical simulations fully support our main conclusions based on the analysis of experimental data. A laser pulse with a sufficiently high input peak power tends to split into multiple red-shifting solitons as it propagates through the fiber. At a sufficiently high level of input peak powers, the soliton spectra overlap, giving rise to interference fringes in the output spectrum. The solid line in Fig. 9.3 shows the spectrum of a light pulse with an input energy of 30 nJ transmitted through a 5-cm piece of fiber. The fringes observed in this spectrum result from the spectral interference of five ($M = 5$) red-shifted solitons, readily seen in the simulated time-domain structure of the fiber output. The simulated spectral and temporal field structure at the fiber output is accurately approximated by Eq. (9.1) with $\nu_1 \approx 211$ THz, $\nu_2 \approx 198$ THz, $\nu_3 \approx 191$ THz, $\nu_4 \approx 164$ THz, $\nu_5 \approx 149$ THz, pulse widths $T_1 \approx 22$ fs, $T_2 \approx 27$ fs, $T_3 \approx 29$ fs, $T_4 \approx 30$ fs, $T_5 \approx 35$ fs, energies 1.6, 2.6, 2.9, 4.6, and 5.5 nJ, and delay times $\Delta_2 - \Delta_1 \approx 220$ fs, $\Delta_3 - \Delta_1 \approx 400$ fs, $\Delta_4 - \Delta_1 \approx 1{,}080$ fs, $\Delta_5 - \Delta_1 \approx 1{,}890$ fs. With a light modulator generating a five-step group-delay profile shown by the dashed line in Fig. 9.3, the solitons add up to synthesize a light pulse (the inset in Fig. 9.3) with a pulse width $T_\Sigma \approx 10$ fs. The total radiation energy of the compressed PCF output is 26.6 nJ, with the central, 10-fs part of the compressed pulse in the inset to Fig. 9.3 carrying an energy of 11.7 nJ. Experiments [52] thus show that frequency-shifted solitons generated in a highly nonlinear fiber can coherently add up, with an appropriate group-delay compensation, to synthesize few-cycle light pulses (Fig. 9.3). The proposed method of short-pulse synthesis can be scaled up to light fields with higher energies through the use of soliton self-frequency shift in hollow-core PCFs [16, 54]. Of special interest in this context is to explore the soliton dynamics of high-peak-power ultrashort pulses in kagome-lattice hollow PCFs, which provide an ultrabroad transmission band in the visible and infrared spectral ranges [55].

9.3 Photonic-Crystal Fibers for Nonlinear-Optical Microspectroscopy

Ultrafast nonlinear optics offers a unique arsenal of methods and instruments for high-resolution bioimaging, helping to confront the most challenging problems in the vast area of biosciences. Two-photon imaging [56–58] is one of the most broadly established nonlinear-optical imaging techniques, which has recently been extended to fiber-based *in vivo* neuroimaging and endoscopy [19–21]. Microscopy based on second- and third-harmonic generation [59–63] has been shown to suggest new ways to explore the structural properties of biotissues, allowing fine details in the morphology of biotissues to be visualized with a high spatial resolution. In neuroimaging, second-harmonic generation (SHG) provides a powerful tool.

Coherent anti-Stokes Raman scattering (CARS) [64] has long been established as a powerful tool for time-resolved studies of ultrafast molecular dynamics and diagnostics of excited gases, combustion, flames and plasmas [64–67]. Because of the nonlinear nature of this type of scattering, CARS field-interaction region is strongly confined to the beam-waist area, suggesting an attractive approach for microscopy and high-spatial-resolution imaging [68]. Recent advances in femtosecond laser technologies, as well as the development of high-speed scanning and imaging systems, have given a powerful momentum to the development of CARS imaging techniques, making CARS a practical and convenient instrument for biomedical imaging and visualization of processes inside living cells [69].

In the early days of CARS, stimulated Raman scattering has been successfully used to generate the Stokes field for time-resolved measurements [70] of vibrational lifetimes of molecules in liquids and phonons in solids. Dye lasers and optical parametric sources have later proved to be convenient sources of wavelength-tunable Stokes radiation [71, 72], giving a powerful momentum to CARS as a practical spectroscopic tool. A rapid progress of femtosecond lasers and the advent of novel highly nonlinear fibers put a new twist on the strategy of Stokes-field generation in CARS, enabling the creation of compact and convenient wavelength-tunable fiber-format ultrashort-pulse Stokes sources for a new generation of CARS spectrometers and microscopes [17, 18, 36–38, 73, 74]. Below in this section, we provide an overview of a new platform for nonlinear-optical microspectroscopy integrating the new PCF components with cutting-edge methods and technologies optical science. As recently shown by Lanin et al., this new PCF-based platform enables an ultrafast three-dimensional readout of coherent optical-phonon oscillations from a diamond film using temporally and spectrally shaped ultrashort laser pulses, delivered by a compact, oscillator-only laser system. This system integrates a long-cavity ytterbium-fiber-laser-pumped 30-fs Cr: forsterite oscillator with a photonic-crystal-fiber (PCF) soliton frequency shifter and a periodically poled lithium niobate (PPLN) spectrum compressor. The spectrally and temporally shaped two-color output of this system provides coherent Raman excitation and time-delayed probing of optical phonons in diamond at a 20-MHz repetition rate with a submicron spatial resolution.

Due to a unique combination of its properties, including a wide band gap, biocompatibility, chemical robustness, high thermal conductivity, and high breakdown voltage, diamond is especially promising for a broad range of advanced optical technologies, including nanoprobe-based biosensing [75], ultrafast nonlinear optics [74, 76], quantum information processing [77–80], and extreme-intensity physics [81]. Diamond has two atoms per primitive cell and falls into the O_h^7 group of spatial symmetry, featuring one triply degenerate zone-center $\Gamma^{(25+)}$ (F_{2g}) symmetry optical phonon that is active in Raman scattering [53]. Due to the long lifetime of this phonon, ultrashort laser pulses can efficiently control the optical response of diamond [82]. In the Raman spectrum, this phonon mode of diamond is manifested as a well-resolved peak at 1,332-cm^{-1}. Since this peak is well separated from the most intense typical Raman features in biotissues, it enables a high-contrast
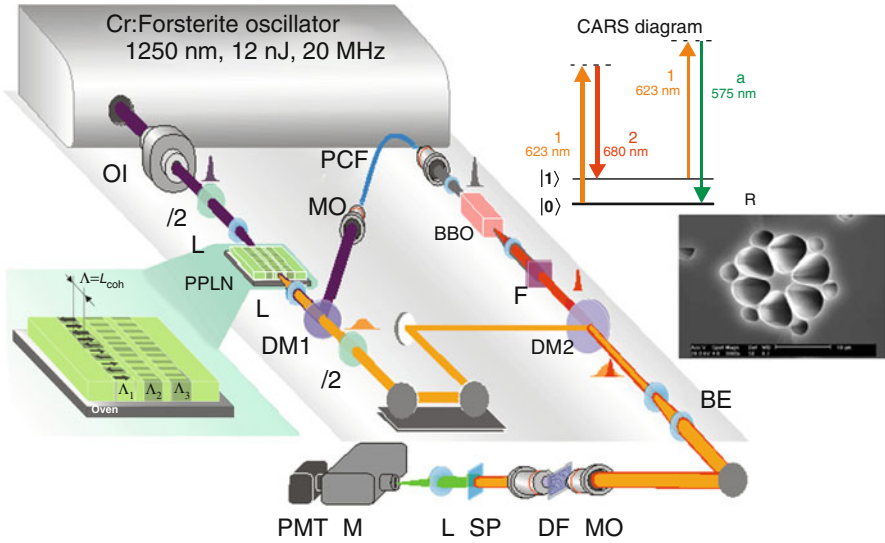
Fig. 9.4 Diagram of the experimental setup: *OI* optical isolator, *λ/2* half-wave plate, *L* lens, *PPLN* periodically poled LiNbO$_3$ crystal, *DM1, DM2* dichroic mirrors, *MO* microscope objective, *PCF* photonic crystal fiber, *F* optical filter *BE* beam expander, *SP* shortpass filter, *DF* diamond film, *M* monochromator, *PMT* photomultiplier. The *insets* show a quantum diagram of the CARS process and an SEM image of the cross section of the PCF

bioimaging technique using diamond nanoparticles [83]. Coherent Raman scattering by optical phonons in diamond has been shown to be ideally suited for measuring the key parameters of optical phonons in diamond crystals [72] and synthetic diamonds [74], as well as for *in situ* diagnostics of diamond film growth [84].

The method of ultrafast three-dimensional interrogation of optical phonons implemented by Lanin et al. is based on coherent anti-Stokes Raman scattering (CARS). This process involves a coherent excitation of Raman-active modes with a frequency Ω_p by pump and Stokes fields, whose central frequencies, ω_1 and ω_2, are chosen in such a way (inset 1 in Fig. 9.4) as to meet the condition of a two-photon, Raman-type resonance, $\omega_1 - \omega_2 \approx \Omega_p$. The third (probe, or interrogating) field with a central frequency ω_3 is then scattered off the coherence induced by the pump and Stokes fields to give rise to the anti-Stokes signal at the central frequency $\omega_a = \omega_1 - \omega_2 + \omega_3$ (inset 1 in Fig. 9.4), thus reading out the information stored in optical-photon oscillations.

In our experiments, we employ a two-color version of CARS with the pump and probe fields delivered by the same light source, implying that $\omega_1 = \omega_3$ and $\omega_a = 2\omega_1 - \omega_2$. Our laser system is based on a home-built ytterbium-fiber-laser-pumped mode-locked Cr: forsterite laser oscillator [85], which delivers laser pulses with a central wavelength of 1.25 μm and a pulse width of 40 fs. The extended-cavity design of the Cr: forsterite laser allows the output laser energy to be increased

up to 18 nJ at a pulse repetition rate of 20 MHz. Such a combination of the laser pulse energy and repetition rate makes the extended-cavity mode-locked Cr: Forsterite laser an ideal source for high-repetition-rate coherent excitation and interrogation of optical phonon modes in solids.

The Cr: forsterite laser output is launched into a waveguide channel in a PPLN crystal (Fig. 9.4), which delivers a spectrally compressed second-harmonic output [86, 87], needed as a probe pulse for high-sensitivity coherent Raman interrogation of optical phonon oscillations with reduced nonresonant background in the readout signal. Typically, for input laser pulses with an energy of 10 nJ and a bandwidth of 300 cm^{-1}, the a waveguide channel with a pitch of 10.9 µm provides the efficiency of second-harmonic generation (SHG) at the level of 30 %, yielding second-harmonic pulses with a central wavelength of 623 nm and a bandwidth of 60 cm^{-1}. These pulses are used as pump and probe fields in the CARS scheme. The fundamental-wavelength output of the PPLN crystal (nonconverted 1.25-µm radiation) is separated from its second harmonic with a beam splitter (Fig. 9.4) and is launched into a photonic-crystal fiber with a cross section structure as shown in inset 2 to Fig. 9.4. This PCF was designed to provide efficient wavelength conversion of 1.25-µm laser pulses through soliton self-frequency shift (SSFS), delivering tunable ultrashort light pulses within a wavelength range of 1.35–1.80 µm, used as Stokes pulses in CARS microscopy. For coherent Raman excitation of the 1,332-cm^{-1} optical-phonon mode of diamond, the PCF wavelength shifter was adjusted to generate a red-shifted solitonic output with a central wavelength tunable within the range of 1,300–1,500 nm and a pulse energy of about 0.5 nJ. These pulses were frequency-doubled in a 2-mm-thick BBO crystal, yielding 120−150-fs, 50-pJ pulses of 650−750-nm radiation, providing a Stokes field for the coherent Raman excitation of the 1,332-cm^{-1} optical-phonon mode in diamond.

Envelope shaping of pump and probe pulses in our experimental scheme is based on the sensitivity of SHG phase matching to the nonlinear-phase shift induced in a nonlinear crystal by the fundamental field. Due to the self-phase modulation of the fundamental field and cross-phase modulation of the second harmonic, the phase mismatch between the fundamental field and its second harmonic become nonuniform over the fundamental pulse [88, 89], giving rise to a double-pulse structure of the second-harmonic output of the PPLN crystal. In experiments, the temporal structure of light pulses was characterized by measuring the 311-nm second-harmonic output of a 0.5-mm-thick BBO crystal as a function of the delay time between two replicas of the waveform of interest produced in two arms of a Michelson interferometer. The increase in the peak power of fundamental pulses tends to modify the temporal envelope of the second-harmonic output toward a clearly resolved double-pulse waveform. The best fit for the experimental autocorrelation traces of the second-harmonic PPLN output measured with 8.5-nJ, 1.25-µm pulses at PPLN input is achieved with a double-spike pulse shape of the second-harmonic PPLN output where each individual spike has a Gaussian envelope with an individual pulse width of 180 fs, a time interval between the spikes $\tau_p \approx 400$ fs, and the first-to-second-spike intensity ratio of 1:7. The autocorrelation
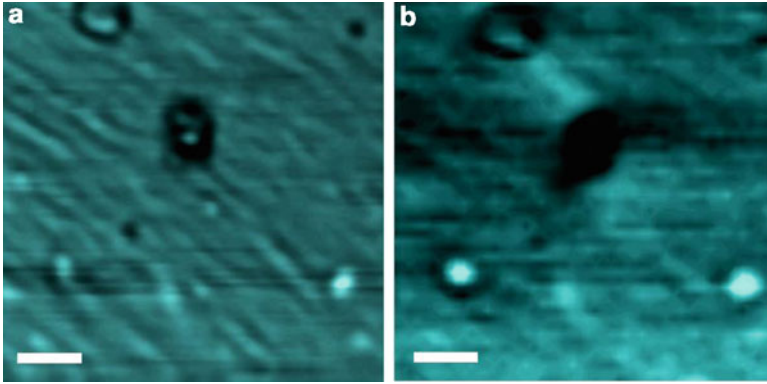
Fig. 9.5 CARS images of a diamond film with laser beams focused (**a**) on the surface of the film and (**b**) 10 μm below the surface. The scale bar is 5 μm

trace of the 680-nm second harmonic of the wavelength-shifted soliton PCF output, used as the Stokes pulse in coherent Raman excitation of optical phonons, visualizes a hyperbolic secant pulse shape with a pulse width of 120 fs.

Coherent Raman excitation of the 1,332-cm^{-1} zone-center $\Gamma^{(25+)}$ (F_{2g}) symmetry optical phonon in our scheme is provided by the 680-nm, 120-fs pulses and one of the two 623-nm, 180-fs pulses generated by PPLN crystal. The second pulse of the PPLN output serves as a time-delayed probe, providing optical interrogation of coherent phonon oscillations through the generation of the anti-Stokes field centered at 575 nm (inset 1 in Fig. 9.4). The anti-Stokes signal at ω_a is generated by the interfering fields produced through the $\omega_a = 2\omega_1 - \omega_2$ CARS by Raman-resonant modes and a nonresonant coherent signal originating from the $\omega_a = 2\omega_1 - \omega_2$ four-wave mixing process, which does not involve any Raman resonance.

The nondispersive nonlinear-optical susceptibility responsible for the nonresonant component of the CARS signal translates into a fast decaying nonlinear-optical response function in the time domain. A time-delayed probe is therefore known to efficiently discriminate the resonant part of the CARS signal, strongly suppressing its nonresonant component. The pulse shaped second-harmonic PPLN output in our scheme enables such time-delayed probing of coherently excited optical phonons. The first pulse in the pair of pulses at the output of the PPLN crystal serves as a pump field, while the second pulse provides a time-delayed probe.

Due to the nonlinear nature of the coherent Raman process used in our scheme to excite and interrogate optical phonon modes, the optical-field–phonon coupling region is tightly confined to the laser-beam-waist area. Due to this feature, coherent Raman scattering is receiving wide applications as a powerful tool for three-dimensional bioimaging [68, 69]. Here, we show that coherent Raman scattering offers unique solutions for a three-dimensional selective interrogation of coherent phonon modes in the bulk of solids with a submicron resolution in the transverse plane. In Fig. 9.5, we present the maps of the CARS signal measured by scanning a
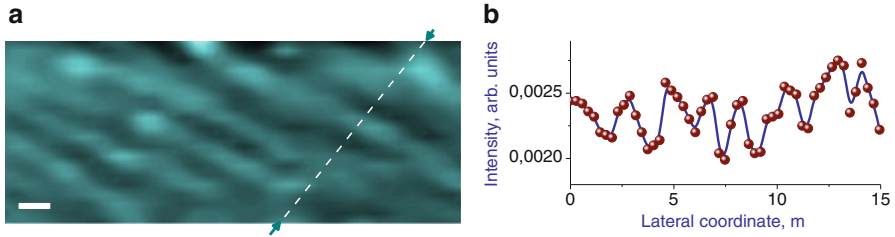
Fig. 9.6 A two-dimensional CARS image (**a**) and one-dimensional profile of the CARS signal along the direction shown by the *dashed line* in Fig. 9.4 for the surface of a diamond film with small-scale surface corrugation. The scale bar is 2 μm

diamond film in the *xy*-plane perpendicular (Fig. 9.4) to the light beams (the *z*-axis) focused on the film surface (Fig. 9.5) and 10 μm below the film surface (Fig. 9.5) with $\tau_d = 0$. As can be seen from these images, local variations in film density in three dimensions can be visualized by scanning the light beams with respect to a sample along the *x*-, *y*, and *z*-axes. In Fig. 9.5, such local density variations are observed as bright spots at $x = 5.1$ μm, $y = 8.3$ μm, and $z = 10$ μm, illustrating the capability of coherent Raman scattering of locally reading out the excitation stored in optical phonon modes, converting the data stored in these phonon modes into an optical signal.

The spatial resolution of the coherent Raman technique of optical phonon interrogation was assessed in an experiment on a synthetic diamond film sample with submicron surface corrugation, induced by thermal instabilities building up at the stage of diamond film synthesis. As can be seen from the map of the CARS signal (Fig. 9.6) and a one-dimensional profile (Fig. 9.6) of the CARS signal along the direction shown by the dashed line in Fig. 9.6, measured with $\tau_d = 0$, the coherent Raman technique can resolve submicron features on the film surface. The scale of the finest feature resolved in these experiments (the feature centered at $\xi \approx 8$ μm in Fig. 9.6) is estimated as 0.7 μm.

9.4 Hollow-Core PCFs for the Delivery of High-Peak-Power Ultrashort Light Pulses

Rapidly developing ultrafast laser technologies offer a vast arsenal of solutions and instruments for life sciences. Femtosecond light pulses are showing their utility as a powerful tool for high-resolution bioimaging [56–58], intracellular nanosurgery [90], laser ophthalmology [91, 92], targeted cell transfection [93], axotomy [94], all-optical histology [95], targeted action on subsurface cortical blood vessels [96], and cell fusion [97]. While experiments with free-beam ultrashort laser pulses interacting with bio-objects show much promise for diversified life-science applications, such as multiphoton spectroscopy on slices of biotissues

[56–58], implementation of these approaches in the endoscopic mode, which is often needed for *in vivo* work, faces several fundamental challenges. Standard optical fibers, used for the delivery of ultrashort pulses in the endoscopic mode, tend to give rise to dispersion-induced pulse stretching and impose severe limitations on the laser fluence, which needs to be kept below the fiber damage threshold. In the nano- and picosecond ranges of pulse widths, several attractive solutions have been demonstrated using hollow-core photonic-crystal fibers (PCFs) [1–3, 98], enabling the fiber delivery of high-energy nanosecond [99] and picosecond [100] laser pulses for a variety of biophotonic and biomedical applications [101]. For femtosecond pulses with relatively low peak powers, typically employed for multiphoton absorption and coherent Raman imaging, the fiber-delivery problem for the endoscopic format of *in vivo* work can often be resolved by using soliton regimes of pulse propagation in hollow- [16] and solid-core [19] PCFs, as well as low-dispersion, low-nonlinearity air-guided modes in this class of fibers [20, 31, 102]. Femtosecond laser surgery, however, requires an adequate level of laser energy, posing additional serious problems for fiber delivery related to fiber damage by laser radiation.

Recent experiments show that large-core hollow PCFs operating in the pulse-compression mode can enable a fiber-format air-guided delivery of ultrashort infrared laser pulses for neurosurgery applications. We demonstrate that, with an appropriate dispersion precompensation, a 15-μm-core hollow PCF can compress stretched 510-fs, 1,070-nm laser pulses to a pulse width of about 110 fs, providing a peak power in excess of 5 MW. In the experiments presented here, the compressed PCF output is employed to induce a local photodisruption of corpus callosum tissues in mouse brain and is used to generate the third harmonic in brain tissues with backward third-harmonic delivery through the PCF cladding.

Doronina-Amitonova et al. [20] have recently demonstrated that a hollow-core PCF can serve as an ideal fiber-format spectral filter for an all-PCF platform for multicolor nonlinear-optical spectroscopy, microscopy, and imaging. Such fiber filters are especially efficient and useful when integrated on the proposed PCF platform with PCF supercontinuum sources [8], providing spectral selectivity of optical excitation, enhancing the detection sensitivity, and protecting detectors from powerful laser radiation (Fig. 9.7). Hollow-core PCFs [34] can guide light in a low-index hollow core due to the high reflectivity of their periodically structured cladding within its photonic band gaps (PBGs). Within the PBGs, the periodic structure of the cladding serves as an antiresonance reflector, making the elementary waves reflected from its periodic refractive-index inhomogeneities interfere constructively in the hollow core, thus producing air-guided PCF modes. Hollow PCFs for multicolor neuroimaging are designed in such a way as to meet two goals: (i) to support PBG-assisted guidance within the frequency bands where parts of the supercontinuum spectrum can selectively interact with the system under study through molecular vibrations, phonons, or electronic excitation, generating an optical response, and (ii) to induce a high leakage loss within the bands where powerful laser radiation or unwanted fluorescence needs to be blocked for a better protection and a higher sensitivity of detection.
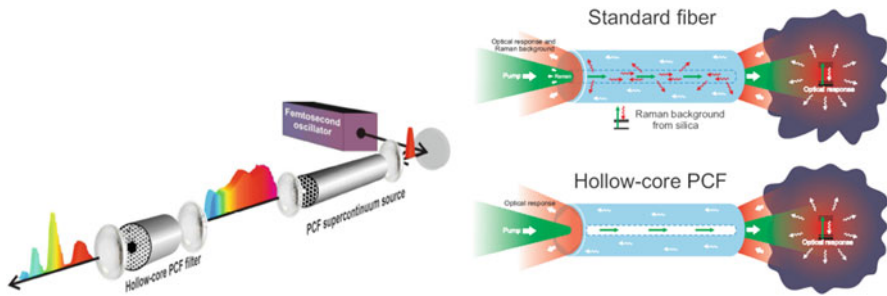
Fig. 9.7 (**a**) A hollow-core PCF spectral filter integrated with a PCF-based source of super-continuum radiation. (**b**) A hollow-core PCF probe (*lower panel*) versus a standard fiber probe (*upper panel*). The hollow-core design helps suppress an intense background related to the Raman scattering in silica

The PCF architecture is instrumental in addressing the problem of the Raman background, which is inevitably generated by the optical pump inside the fiber, making it one of the key issues of fiber components intended for the delivery of low-intensity optical signals (Fig. 9.7, upper panel).

In the PCF format (Fig. 9.7, lower panel), the level of the Raman background can be radically reduced by decreasing the content of silica in the fiber, i.e., by increasing the air-filling fraction in the PCF. For a hollow PCF used experiments [103], the high air-filling fraction of the cladding helps keep the Raman background well below 10 % of the photoluminescence response from NV centers, which infiltrate the fiber.

9.5   Conclusion

We have shown in this chapter that PCFs offer an attractive platform for the development of the key components for nonlinear-optical microspectroscopy. Enhanced nonlinear-optical processes in solid- and hollow-core PCFs enable the generation of frequency-tunable radiation within the wavelength range stretching from the ultraviolet to the near-infrared with output pulse widths ranging from tens of femtoseconds to a few picoseconds and peak powers from a few watts to several megawatts, suggesting a convenient, efficient, and compact fiber format of short-pulse sources for time-resolved nonlinear spectroscopy and microscopy. Frequency-shifted solitons generated in properly designed PCFs can coherently add up, with an appropriate group-delay compensation, to synthesize few-cycle light pulses. Large-core hollow PCFs enable a fiber-format air-guided delivery of ultrashort infrared laser pulses for neurosurgery applications.

References

1. Russell PSJ (2003) Photonic crystal fibers. Science 299:358–362
2. Knight JC (2003) Photonic crystal fibers. Nature 424:847–851
3. Zheltikov AM (2000) Holey fibers. Phys Uspekhi 43:1125–1136
4. Akimov DA, Serebryannikov EE, Zheltikov AM, Schmitt M, Maksimenka R, Kiefer W, Dukel'skii KV, Shevandin VS, Kondrat'ev YN (2003) Efficient anti-Stokes generation through phase-matched four-wave mixing in higher-order modes of a microstructure fiber. Opt Lett 28:1948–1950
5. Zheltikov AM (2006) Nanoscale nonlinear optics in photonic-crystal fibres. J Opt A Pure Appl Opt 8:S47–S72
6. Serebryannikov EE, Fedotov AB, Zheltikov AM, Ivanov AA, Alfimov MV, Beloglazov VI, Skibina NB, Skryabin DV, Yulin AV, Knight JC (2006) Third-harmonic generation by Raman-shifted solitons in a photonic-crystal fiber. J Opt Soc Am B 23:1975–1980
7. Reeves WH, Skryabin DV, Biancalana F, Knight JC, Russell PSJ, Omenetto FG, Efimov A, Taylor AJ (2003) Transformation and control of ultra-short pulses in dispersion-engineered photonic crystal fibres. Nature 424:511–515
8. Serebryannikov EE, Zheltikov AM (2006) Nanomanagement of dispersion, nonlinearity, and gain of photonic-crystal fibers: qualitative arguments of the Gaussian-mode theory and nonperturbative numerical analysis. J Opt Soc Am B 23:1700–1707
9. Jones DJ, Diddams SA, Ranka JK, Stentz A, Windeler RS, Hall JL, Cundiff ST (2000) Carrier-envelope phase control of femtosecond mode-locked lasers and direct optical frequency synthesis. Science 288:635–639
10. Udem T, Holzwarth R, Hänsch TW (2002) Optical frequency metrology. Nature 416:233–237
11. Zheltikov AM (2005) The friendly gas phase. Nature Mater 4:265–267
12. Zheltikov AM (2007) Photonic-crystal fibers for a new generation of light sources and frequency converters. Phys Uspekhi 50:705–727
13. Hartl I, Li XD, Chudoba C, Ghanta RK, Ko TH, Fujimoto JG, Ranka JK, Windeler RS (2001) Ultrahigh-resolution optical coherence tomography using continuum generation in an air–silica microstructure optical fiber. Opt Lett 26:608–610
14. Rarity J, Fulconis J, Duligall J, Wadsworth W, Russell P (2005) Photonic crystal fiber source of correlated photon pairs. Opt Expr 13:534–544
15. Sidorov-Biryukov DA, Serebryannikov EE, Zheltikov AM (2006) Time-resolved coherent anti-Stokes Raman scattering with a femtosecond soliton output of a photonic-crystal fiber. Opt Lett 31:2323–2325
16. Ivanov AA, Podshivalov AA, Zheltikov AM (2006) Frequency-shifted megawatt soliton output of a hollow photonic-crystal fiber for time-resolved coherent anti-Stokes Raman scattering microspectroscopy. Opt Lett 31:3318–3320
17. Ivanov AA, Alfimov MV, Zheltikov AM (2006) Wavelength-tunable ultrashort-pulse output of a photonic-crystal fiber designed to resolve ultrafast molecular dynamics. Opt Lett 31:3330–3332
18. Paulsen HN, Hilligsøe KM, Thøgersen J, Keiding SR, Larsen JJ (2003) Coherent anti-Stokes Raman scattering microscopy with a photonic crystal fiber based light source. Opt Lett 28:1123–1125
19. Doronina LV, Fedotov IV, Voronin AA, Ivashkina OI, Zots MA, Anokhin KV, Rostova E, Fedotov AB, Zheltikov AM (2009) Tailoring the soliton output of a photonic crystal fiber for enhanced two-photon excited luminescence response from fluorescent protein biomarkers and neuron activity reporters. Opt Lett 34:3373–3375
20. Doronina-Amitonova LV, Fedotov IV, Ivashkina OI, Zots MA, Fedotov AB, Anokhin KV, Zheltikov AM (2011) Photonic-crystal-fiber platform for multicolor multilabel neurophotonic studies. Appl Phys Lett 98:253706

21. Doronina-Amitonova LV, Fedotov IV, Ivashkina OI, Zots MA, Fedotov AB, Anokhin KV, Zheltikov AM (2010) Fiber-optic probes for in vivo depth-resolved neuron-activity mapping. J Biophoton 3:660–669
22. Russell PSJ (1006) Photonic-crystal fibers. J Lightwave Technol 24:4729–4749
23. Fedotov AB, Zheltikov AM, Tarasevitch AP, von der Linde D (2001) Enhanced spectral broadening of short laser pulses in high-numerical-aperture holey fibers. Appl Phys B 73:181–184
24. Ranka JK, Windeler RS, Stentz AJ (2000) Visible continuum generation in air-silica microstructure optical fibers with anomalous dispersion at 800 nm. Opt Lett 25:25–27
25. Zheltikov AM (2006) Let there be white light: supercontinuum generation by ultrashort laser pulses. Phys Uspekhi 49:605–628
26. Dudley JM, Genty G, Coen S (2006) Supercontinuum generation in photonic crystal fiber. Rev Mod Phys 78:1135–1176
27. Limpert J, Roser F, Schreiber T, Tunnermann A (2006) High-power ultrafast fiber laser systems. IEEE J Sel Top Quantum Electron 12:233–244
28. Fang X-H, Hu M-L, Liu B-W, Chai L, Wang C-Y, Zheltikov AM (2010) Generation of 150-MW, 110-fs pulses by phase-locked amplification in multicore photonic crystal fiber. Opt Lett 35:2326–2328
29. Liu H, Hu M, Liu B, Song Y, Chai L, Zheltikov AM, Wang C (2010) Compact high-power multiwavelength photonic-crystal-fiber-based laser source of femtosecond pulses in the infrared–visible–ultraviolet range. J Opt Soc Am B 27:2284–2289
30. Südmeyer T, Brunner F, Innerhofer E, Paschotta R, Furusawa K, Baggett JC, Monro TM, Richardson DJ, Keller U (2003) Nonlinear femtosecond pulse compression at high average power levels by use of a large-mode-area holey fiber. Opt Lett 28:1951–1953
31. Flusberg BA, Jung JC, Cocker ED, Anderson EP, Schnitzer MJ (2005) In vivo brain imaging using a portable 3.9 gram two-photon fluorescence microendoscope. Opt Lett 30:2272–2274
32. Flusberg BA, Nimmerjahn A, Cocker ED, Mukamel EA, Barretto RPJ, Ko TH, Burns LD, Jung JC, Schnitzer MJ (2008) High-speed, miniaturized fluorescence microscopy in freely moving mice. Nat Methods 5:935–938
33. Monro TM, Belardi W, Furusawa K, Baggett JC, Broderick NGR, Richardson DJ (2001) Sensing with microstructured optical fibres. Meas Sci Technol 12:854–858
34. Jensen JB, Pedersen LH, Hoiby PE, Nielsen LB, Hansen TP, Folkenberg JR, Riishede J, Noordegraaf D, Nielsen K, Carlsen A, Bjarklev A (2004) Photonic crystal fiber based evanescent-wave sensor for detection of biomolecules in aqueous solutions. Opt Lett 29:1974–1976
35. Konorov S, Zheltikov A, Scalora M (2005) Photonic-crystal fiber as a multifunctional optical sensor and sample collector. Opt Expr 13:3454–3459
36. Konorov SO, Akimov DA, Serebryannikov EE, Ivanov AA, Alfimov MV, Zheltikov AM (2004) Cross-correlation FROG CARS with frequency-converting photonic-crystal fibers. Phys Rev E 70:057601
37. Kano H, Hamaguchi H (2003) Characterization of a supercontinuum generated from a photonic crystal fiber and its application to coherent Raman spectroscopy. Opt Lett 28:2360–2362
38. Kano H, Hamaguchi H (2005) Vibrationally resonant imaging of a single living cell by supercontinuum-based multiplex coherent anti-Stokes Raman scattering microspectroscopy. Opt Expr 13:1322–1327
39. Andresen ER, Paulsen HN, Birkedal V, Thøgersen J, Keiding SR (2005) Broadband multiplex coherent anti-Stokes Raman scattering microscopy employing photonic-crystal fibers. J Opt Soc Am B 22:1934–1938
40. von Vacano B, Wohlleben W, Motzkus M (2006) Actively shaped supercontinuum from a photonic crystal fiber for nonlinear coherent microspectroscopy. Opt Lett 31:413–415
41. Dudovich N, Oron D, Silberberg Y (2002) Single-pulse coherently controlled nonlinear Raman spectroscopy and microscopy. Nature 418:512–514
42. Brabec T, Krausz F (2000) Intense few-cycle laser fields: frontiers of nonlinear optics. Rev Mod Phys 72:545–591

43. Shen YR (1984) The principles of nonlinear optics. Wiley, New York
44. Zhavoronkov N, Korn G (2002) Generation of single intense short optical pulses by ultrafast molecular phase modulation. Phys Rev Lett 88:203901
45. Corkum PB, Krausz F (2007) Attosecond science. Nat Phys 3:381–387
46. Zheltikov AM, L'Huillier A, Krausz F (2007) Nonlinear optics. In: Träger F (ed) Handbook of lasers and optics. Springer, New York, pp 157–248
47. Bergé L, Skupin S, Nuter R, Kasparian J, Wolf J-P (2007) Ultrashort filaments of light in weakly ionized, optically transparent media. Rep Prog Phys 70:1633–1713
48. Couairon A, Mysyrowicz A (2007) Femtosecond filamentation in transparent media. Phys Rep 441:47–189
49. Hauri CP, Kornelis W, Helbing FW, Heinrich A, Couairon A, Mysyrowicz A, Biegert J, Keller U (2004) Generation of intense, carrier-envelope phase-locked few-cycle laser pulses through filamentation. Appl Phys B 79:673–677
50. Schenkel B, Paschotta R, Keller U (2005) Pulse compression with supercontinuum generation in microstructure fibers. J Opt Soc Am B 22:687–693
51. Agrawal GP (2001) Nonlinear fiber optics. Academic, San Diego
52. Voronin AA, Fedotov IV, Fedotov AB, Zheltikov AM (2009) Spectral interference of frequency-shifted solitons in a photonic-crystal fiber. Opt Lett 34:569–571
53. Solin SA, Ramdas AK (1970) Raman spectrum of diamond. Phys Rev B 1:1687–1698
54. Ouzounov DG, Ahmad FR, Müller D, Venkataraman N, Gallagher MT, Thomas MG, Silcox J, Koch KW, Gaeta AL (2003) Generation of megawatt optical solitons in hollow-core photonic band-gap fibers. Science 301:1702–1704
55. Couny F, Benabid F, Roberts PJ, Light PS, Raymer MG (2007) Generation and photonic guidance of multi-octave optical frequency combs. Science 318:1118–1121
56. Denk W, Strickler JH, Webb WW (1990) Two-photon laser scanning fluorescence microscopy. Science 248:73–76
57. Zipfel WR, Williams RM, Webb WW (2003) Nonlinear magic: multiphoton microscopy in biosciences. Nat Biotechnol 21:1369–1377
58. Helmchen F, Denk W (2005) Deep tissue two-photon microscopy. Nat Methods 2:932–940
59. Campagnola PJ, Loew LM (2003) Second-harmonic imaging microscopy for visualizing biomolecular arrays in cells, tissues and organisms. Nat Biotechnol 21:1356–1360
60. Dombeck DA, Sacconi L, Blanchard-Desce M, Webb WW (2005) Optical recording of fast neuronal membrane potential transients in acute mammalian brain slices by second-harmonic generation microscopy. J Neurophysiol 94:3628–3636
61. Squier JA, Müller M, Brakenhoff GJ, Wilson KR (1998) Third harmonic generation microscopy. Opt Expr 3:315–324
62. Sidorov-Biryukov DA, Naumov AN, Konorov SO, Fedotov AB, Zheltikov AM (2000) Three-dimensional microscopy of laser-produced plasmas using third-harmonic generation. Quantum Electron 30:1080–1083
63. Débarre D, Supatto W, Pena A-M, Fabre A, Tordjmann T, Combettes L, Schanne-Klein M-C, Beaurepaire E (2006) Imaging lipid bodies in cells and tissues using third-harmonic generation microscopy. Nat Methods 3:47–53
64. Eesley GL (1981) Coherent Raman spectroscopy. Pergamon, Oxford
65. Eckbreth AC (1988) Laser diagnostics for combustion temperature and species. Abacus, Cambridge
66. Zheltikov AM, Koroteev NI (1999) Coherent four-wave mixing in excited and ionized gas media. Phys Uspekhi 42:321–351
67. Zheltikov AM (2000) Coherent anti-Stokes Raman scattering: from proof-of-the-principle experiments to femtosecond CARS and higher order wave-mixing generalizations. J Raman Spectrosc 31:653–667
68. Zumbusch A, Holtom GR, Xie XS (1999) Three-dimensional vibrational imaging by coherent anti-stokes Raman scattering. Phys Rev Lett 82:4142–4145

69. Evans CL, Potma EO, Puoris'haag M, Côté D, Lin CP, Xie XS (2005) Chemical imaging of tissue in vivo with video-rate coherent anti-Stokes Raman scattering microscopy. Proc Natl Acad Sci 102:16807–16812

70. Laubereau A, von der Linde D, Kaiser W (1971) Decay time of hot TO phonons in diamond. Phys Rev Lett 27:802–805

71. Akhmanov SA, Dmitriev VG, Kovrigin AI, Koroteev NI, Tunkin VG, Kholodnykh AI (1972) Active spectroscopy of Raman scattering using an optical parametric oscillator. JETP Lett 15:425–428

72. Levenson MD, Flytzanis C, Bloembergen N (1972) Interference of resonant and nonresonant three-wave mixing in diamond. Phys Rev B 6:3962–3965

73. Mitrokhin VP, Fedotov AB, Ivanov AA, Alfimov MV, Zheltikov AM (2007) Coherent anti-Stokes Raman scattering microspectroscopy of silicon components with a photonic-crystal fiber frequency shifter. Opt Lett 32:3471–3473

74. Savvin AD, Lanin AA, Voronin AA, Fedotov AB, Zheltikov AM (2010) Coherent anti-Stokes Raman metrology of phonons powered by photonic-crystal fibers. Opt Lett 35:919–921

75. McGuinness LP, Yan Y, Stacey A, Simpson DA, Hall LT, Maclaurin D, Prawer S, Mulvaney P, Wrachtrup J, Caruso F, Scholten RE, Hollenberg LCL (2011) Quantum measurement and orientation tracking of fluorescent nanodiamonds inside living cells. Nat Nanotechnol 6:358–363

76. Zhi M, Wang X, Sokolov AV (2008) Broadband coherent light generation in diamond driven by femtosecond pulses. Opt Expr 16:12139–12147

77. Wrachtrup J, Jelezko F (2006) Processing quantum information in diamond. J Phys Condens Matter 18:S807–S824

78. Gaebel T, Domhan M, Popa I, Wittmann C, Neumann P, Jelezko F, Rabeau JR, Stravrias N, Greentree AD, Prawer S, Meijer J, Twamley J, Hemmer PR, Wrachtrup J (2006) Room-temperature coherent coupling of single spins in diamond. Nat Phys 2:408–413

79. Dutt MVG, Childress L, Jiang L, Togan E, Maze J, Jelezko F, Zibrov AS, Hemmer PR, Lukin MD (2007) Science 316:1312

80. Aharonovich I, Greentree AD, Prawer S (2011) Diamond photonics. Nat Photon 5:397–405

81. Steinke S, Henig A, Schnürer M, Sokollik T, Nickles PV, Jung D, Kiefer D, Hörlein R, Schreiber J, Tajima T, Yan X, Hegelich M, Meyer-ter-Vehn J, Sandner W, Habs D (2010) Laser Part Beams 28:215

82. Ishioka K, Hase M, Kitajima M, Petek H (2006) Coherent optical phonons in diamond. Appl Phys Lett 89:231916

83. Chao J-I, Perevedentseva E, Chung P-H, Liu K-K, Cheng C-Y, Chang C-C, Cheng C-L (2007) Nanometer-sized diamond particle as a probe for biolabeling. Biophys J 93:2199–2208

84. Bühler J, Prior Y (1999) Back-scattering CARS diagnostics on CVD diamond. Diam Relat Mater 8:673–676

85. Fedotov AB, Voronin AA, Fedotov IV, Ivanov AA, Zheltikov AM (2009) Opt Lett 34:851

86. Marangoni M, Gambetta A, Manzoni C, Kumar V, Ramponi R, Cerullo G (2009) Opt Lett 34:3262

87. Krauss G, Hanke T, Sell A, Träutlein D, Leitenstorfer A, Selm R, Winterhalder M, Zumbusch A (2009) Opt Lett 34:2847

88. Koroteev NI, Zheltikov AM (1998) Chirp control in third-harmonic generation due to cross-phase modulation. Appl Phys B 67:53–57

89. Naumov AN, Zheltikov AM (2002) Asymmetric spectral broadening and temporal evolution of cross-phase-modulated third harmonic pulses. Opt Expr 10:122–127

90. Koenig K, Riemann I, Fischer P, Halbhuber KH (1999) Intracellular nanosurgery with near infrared femtosecond laser pulses. Cell Mol Biol 45:195–201

91. Juhasz T, Frieder H, Kurtz RM, Horvath C, Bille JF, Mourou G (1999) Corneal refractive surgery with femtosecond lasers. IEEE J Sel Top Quantum Electron 5:902–909

92. König K, Riemann I, Fritzsche W (2001) Nanodissection of human chromosomes with near-infrared femtosecond laser pulses. Opt Lett 26:819–821

93. Tirlapur UK, Konig K (2002) Cell biology – targeted transfection by femtosecond laser. Nature 418:290–291
94. Yanik MF, Cinar H, Cinar HN, Chisholm AD, Jin YS, Ben-Yakar A (2004) Neurosurgery – functional regeneration after laser axotomy. Nature 432:822–822
95. Tsai PS, Friedman B, Ifarraguerri AI, Thompson BD, Lev-Ram V, Schaffer CB, Xiong C, Tsien RY, Squier JA, Kleinfeld D (2003) All-optical histology using ultrashort laser pulses. Neuron 39:27–41
96. Nishimura N, Schaffer CB, Friedman B, Tsai PS, Lyden PD, Kleinfeld D (2006) Targeted insult to subsurface cortical blood vessels using ultrashort laser pulses: three models of stroke. Nat Methods 3:99–108
97. Gong JX, Zhao XM, Xing QR, Li F, Li HY, Li YF, Chai L, Wang QY, Zheltikov AM (2008) Femtosecond laser-induced cell fusion. Appl Phys Lett 92:093901
98. Zheltikov AM (2004) Isolated waveguide modes of high-intensity light fields. Phys Uspekhi 47:1205–1220
99. Tauer J, Orban F, Kofler H, Fedotov AB, Fedotov IV, Mitrokhin VP, Zheltikov AM, Wintner E (2007) High throughput of single high-power laser pulses by hollow photonic band gap fibers. Laser Phys Lett 4:444–448
100. Konorov SO, Fedotov AB, Kolevatova OA, Beloglazov VI, Skibina NB, Shcherbakov AV, Wintner E, Zheltikov AM (2003) Laser breakdown with millijoule trains of picosecond pulses transmitted through a hollow-core photonic-crystal fibre. J Phys D Appl Phys 36:1375–1381
101. Konorov SO, Fedotov AB, Mitrokhin VP, Beloglazov VI, Skibina NB, Shcherbakov AV, Wintner E, Scalora M, Zheltikov AM (2004) Appl Opt 43:2251
102. Tai S-P, Chan M-C, Tsai T-H, Guol S-H, Chen L-J, Sun C-K (2004) Two-photon fluorescence microscope with a hollow-core photonic crystal fiber. Opt Expr 12:6122–6128
103. Fedotov IV, Safronov NA, Shandarov YA, Tashchilina AY, Fedotov AB, Nizovtsev AP, Pustakhod DI, Chizevski VN, Sakoda K, Kilin SY, Zheltikov AM (2012) Photonic-crystal-fiber-coupled photoluminescence interrogation of nitrogen vacancies in diamond nanoparticles. Laser Phys Lett 9:151–154
104. Evans CL, Xie XS (2008) Coherent anti-stokes Raman scattering microscopy: chemical imaging for biology and medicine. Annu Rev Anal Chem 1:883–909
105. Pezacki JP, Blake JA, Danielson DC, Kennedy DC, Lyn RK, Singaravelu R (2011) Chemical contrast for imaging living systems: molecular vibrations drive CARS microscopy. Nat Chem Biol 7:137–145
106. Freudiger CW, Min W, Saar BG, Lu S, Holtom GR, He C, Tsai JC, Kang JX, Sunney Xie X (2008) Label-free biomedical imaging with high sensitivity by stimulated Raman scattering microscopy. Science 322:1857–1861
107. Evans CL, Xu X, Kesari S, Sunney Xie X, Wong STC, Young GS (2007) Chemically selective imaging of brain structures with CARS microscopy. Opt Expr 15:12076–12087
108. Voronin AA, Fedotov IV, Doronina-Amitonova LV, Ivashkina OI, Zots MA, Fedotov AB, Anokhin KV, Zheltikov AM (2011) Ionization penalty in nonlinear Raman neuroimaging. Opt Lett 36:508–510
109. Hell SW (2008) Microscopy and its focal switch. Nat Methods 6:24–32
110. Eggeling C, Ringemann C, Medda R, Schwarzmann G, Sandhoff K, Polyakova S, Belov VN, Hein B, von Middendorff C, Schönle A, Hell SW (2009) Direct observation of the nanoscale dynamics of membrane lipids in a living cell. Nature 457:1159–1162

10
Structure Property Relationships for Exciton Transfer in Conjugated Polymers

Trisha L. Andrew and T.M. Swager

10.1   Introduction

Conjugated polymers (CPs) are useful materials that combine the optoelectronic properties of semiconductors with the mechanical properties and processing advantages of plastics. In general, CPs in their neutral state are wide band-gap semiconductors with direct band gaps [1]. Many CPs have an extremely large absorption cross section ($\sigma \approx 10^{-15}$ cm^2) because the $\pi \rightarrow \pi^*$ transition is allowed and the quasi one-dimensional electronic wavefunctions have a high density of states at the band edge [2]. Additionally, a CP can exhibit strong luminescence depending on the system. The luminescence efficiency is primarily related to the delocalization and polarization of the electronic structure of the CP [1].

A vast number of studies on oligomers confirm that the electronic states in a CP have limited delocalization, and the electronic structure of a given CP is often determined by 7–13 repeating units. This is particularly prevalent in systems containing aromatic rings since the aromatic character localizes the electronic wave functions. As a result of this localization, a CP's band gap is largely determined by its local electronic structure [1].

The emission of CPs is dominated by energy migration to local minima in their band structures. For example, the emission from electroluminescent devices occurs from regions with greatest conjugation [3] and the emission from complex ladder polymers can be dominated by defect sites present in low concentration [4]. However, a fundamental understanding of the relative mechanisms of energy migration in these systems remains elusive. This inherent difficulty is a result of the fact that CPs have disordered dynamic conformations that produce variable

T.L. Andrew • T.M. Swager (✉)
Department of Chemistry, Massachusetts Institute of Technology, 77 Massachusetts Avenue, Cambridge, MA 02139, USA
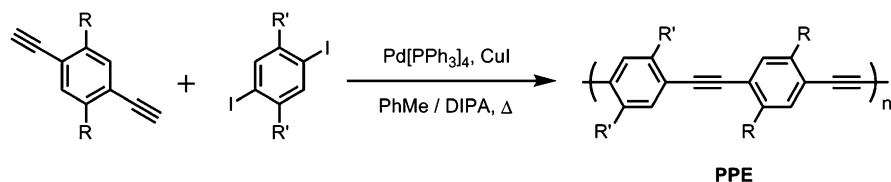e-mail: trishala@mit.edu; tswager@mit.edu

Fig. 10.1

electronic delocalization, both within a given polymer and between neighboring polymer chains [5]. To improve this situation, it is necessary to design polymers with specific structures and properties intended to test proposed mechanisms of energy migration.

In this chapter, we review the photophysical properties of and exciton transport in a series of poly(p-phenyl ethynylene)s (PPEs, see Fig. 10.1). First, the use of energy migration in PPEs to create signal gain in chemical sensors is discussed. Next, we detail the importance of dimensionality and molecular design in directing excitations and the effect of excited-state lifetime modulation on energy migration in PPEs. The ability to extend electronic delocalization and induce well-defined CP conformations in liquid crystal solutions is also discussed. We restrict our analysis to primarily poly(p-phenyl ethynylene)s (PPEs), as details relating to energy migration in other common luminescent polymers, such as poly(phenylene)s and poly(p-phenylene vinylene)s, will be addressed in later chapters.

10.2 Signal Gain in Amplifying Fluorescent Polymers

Rigid rod CPs, such as PPEs (Fig. 10.1), may be thought of as "molecular wires" with well-defined lengths proportional to molecular weight. Therefore, PPEs can be used to interconnect, i.e. wire in series, receptors to produce fluorescent chemosensory systems with sensitivity enhancements over single receptor analogues [6]. In a PPE with a receptor attached to every repeat unit, the degree of polymerization defines the number of receptor sites, n. If energy migration is rapid with respect to the fluorescence lifetime, then the excited state can sample every receptor in the polymer, thereby allowing the occupation of a single binding site to dramatically change the entire emission of the PPE. In the event that a receptor site is occupied by a quencher, the result is an enhanced deactivation of the excited state [6]. For isolated polymer chains in solution, the sensitivity may be enhanced by as much as n times over single-molecule receptors; however, larger effects may occur in the solid state wherein interpolymer energy transfer may also occur (Fig. 10.2).

This concept is demonstrated by studying the fluorescence quenching responses of model compounds **1**-**2** and their corresponding PPEs, **P1**-**2** (see Fig. 10.3). The operative interaction that leads to quenching of fluorescence in these systems is
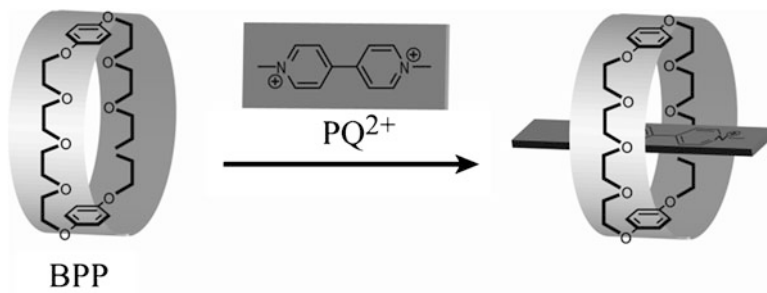
Fig. 10.2

the formation of a pseudorotaxane between a bis(*p*-phenylene)-34-crown-10 (BPP) moiety and paraquat, PQ^{2+}, a well-known electron transfer quenching agent (see Fig. 10.2) [7].

Electron transfer fluorescence quenching by PQ^{2+} can occur by either dynamic (collisional) or static (associated complex) processes. The dependence of the fluorescence intensity on the quencher concentration follows the Stern-Volmer relationship, whose general form is shown in Eq. 10.1 [8].

$$\frac{F_0}{F} = 1 + K_D[Q]e^{V[Q]} \tag{10.1}$$

In this equation, F_0 and F are the fluorescence intensities in the absence and presence of the quencher, respectively, K_D denotes the dynamic quenching constant, and V represents the static quenching constant. When $[Q]$ or V is very small, the contribution from static quenching can be approximated by a linear function of quencher concentration and Eq. 10.1 simplifies to:

$$\frac{F_0}{F} = (1 + K_D[Q])(1 + K_S[Q]) \tag{10.2}$$

where K_S now denotes the static quenching constant. Furthermore, if either a static or dynamic process dominates the quenching response, Eq. 10.2 can be further simplified to include only one linear term:

$$\frac{F_0}{F} = (1 + K_{SV}[Q]) \tag{10.3}$$

where K_{SV} is either the dynamic (K_D) or static (K_S) quenching constant. When the fluorophore and the quencher form a simple one-to-one dark complex, K_{SV} is equivalent to the association constant, K_a. However, for systems with more complex species, the quenching profile may deviate from the linear function and the more general form of the Stern-Volmer relationship (i.e., Eq. 10.1) must be used [8].
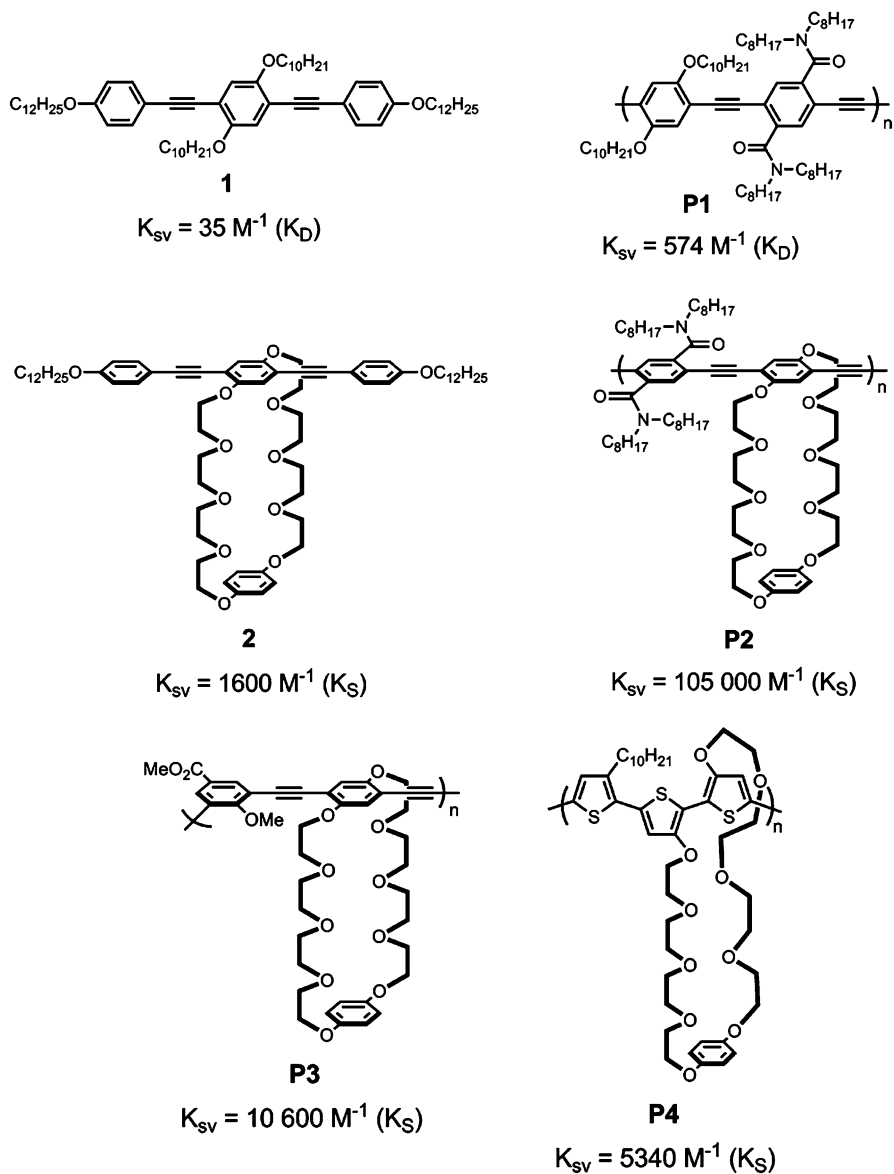
Fig. 10.3

In static quenching, diffusion rate of the quencher is not a factor and the fluorescence lifetime of the fluorophore, τ, is independent of [Q]. However, for purely dynamic quenching, the excited state is quenched by a collision with the quencher and thus the lifetime is truncated with added quencher [8]. As a result,

Monomeric Chemosensor: Sensitivity determined by the equilibrium constant

$K_a = 1630$

Receptor Wired in Series: Amplification due to a collective system response

Exciton diffusion length ca. 140 (Ph-CC-) Units

$K_{SV} = K_a \cdot$ (Number of Receptor Sites Visited by the Exciton)
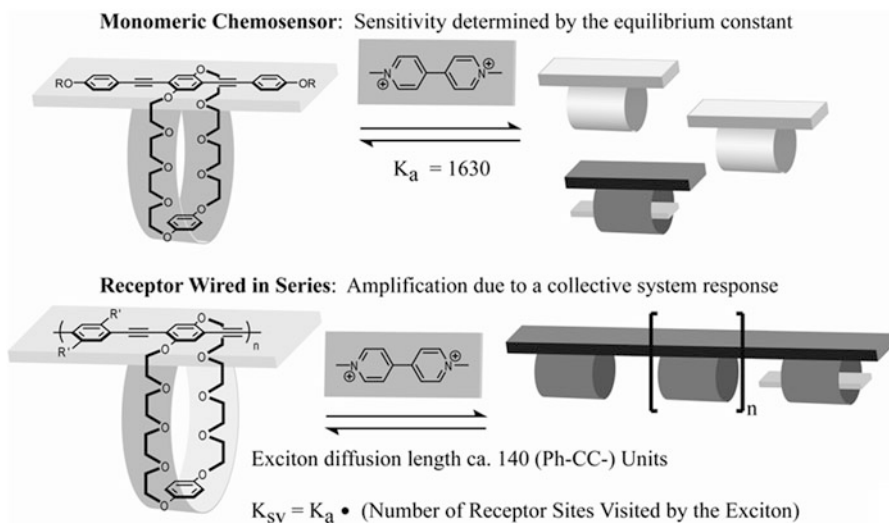
Fig. 10.4

monitoring the changes in the lifetime of the fluorophore with added quencher represents the conventional practice for determining the dynamic quenching constant independent of the static quenching process. The correlation of lifetime with quencher concentration can be expressed as:

$$\frac{\tau_0}{\tau} = 1 + K_D[Q] \tag{10.4}$$

The structures of the model compounds and polymers used to investigate amplified fluorescence quenching are shown in Fig. 10.3, along with their quenching constants with PQ^{2+} [9]. Comparing **1** and **P1**, a 16-fold enhancement in the dynamic quenching constant is observed upon transitioning from a small molecule to a conjugated polymer (35 vs. 574 M^{-1}, respectively), even in a system lacking the BPP receptor. This enhancement results from the extended electronic structure of the polymer, which produces a mobile delocalized excited state and a larger effective size. It is important to note that this enhancement occurs in spite of the fact that the lifetime of **P1** (0.5 ns) is shorter than that of **1** (1.2 ns). When the BPP receptor is introduced, addition of PQ^{2+} results in the formation of a charge transfer (CT) complex with either an associated red-shifted absorption onset or the growth of a new CT band and static quenching dominates. A 66-fold increase in K_S value is observed for conjugated polymer **P2** relative to small molecule **2**, in agreement with our model for signal amplification due to a collective system response (see Fig. 10.4).

The degree of enhancement resulting from energy migration is determined by the radiative lifetime and the mobility of the excitations in the polymer. Longer lifetimes

and higher mobilities will produce longer average diffusion lengths. For isolated polymers in solution, if this diffusion length exceeds the length of the polymer, then an increase in molecular weight will produce greater enhancements. Accordingly, lower molecular weight analogs of **P2** display smaller values of K_S than higher molecular weight analogs: $K_S = 105,000 \, M^{-1}$ for M_n 122,500 but $K_S = 75,000 \, M^{-1}$ for M_n 31,100. However, it must be noted that the value of K_S remains largely unaffected after the molecular weight of the polymer exceeds ca. 65,000. This result reveals that the exciton was not able to visit the entire length of the higher molecular weight polymers because of its limited mobility and finite lifetime (there is always competitive relaxation to the ground state). Therefore, one can conclude that the exciton diffusion length in a PPE is approximately 140 (Ph-CC-) units [9].

Additionally, the *para*-linked polymer **P2** is observed to be more effective at energy migration than both its *meta*-linked analog, **P3**, and a poly(thiophene) analog, **P4**. This difference exists in spite of the fact that the lifetime of **P3** (1.88 ns) is about a factor of 3 longer than that of **P2** (0.64 ns). The observation that excitations in **P3** have longer lifetimes indicates that energy migration is slower in this system relative to **P2**.

It can be argued that the greater tendency for energy migration in *para*-linked **P2** over *meta*-linked **P3** might be expected based on delocalization; however, greater delocalization is not a guarantee of superior performance. This fact is illustrated by polymer **P4**, which displays a K_S value of only 5,340 M^{-1}. This result indicates that **P4** is less effective at energy migration than **P2**, even though poly(thiophene)s display much greater bandwidths (delocalization) relative to PPEs.

10.3 Directing Energy Transfer Within CPs: Dimensionality and Molecular Design

10.3.1 Solutions vs. Thin Films

As stated before, the emission of conjugated polymers is often dominated by energy migration to local minima in their band structures. For example, selective emission from states associated with anthracene end groups has been demonstrated in solutions of PPEs (see Fig. 10.5) [10]. As is characteristic for most PPEs, **P5** displays a broad absorption band centered at 446 nm and a relatively sharp emission spectrum with vibronically-resolved (0,0) and (0,1) bands centered at 478 and 510 nm, respectively. In the case of **P6**, however, where terminal anthracene units are present, the solution emission spectrum is dominated by a single band at 524 nm, which corresponds to emission from the anthracene end-group. The fluorescence quantum yields of **P5** and **P6** are roughly comparable (0.35 and 0.28, respectively), the emission spectra of both polymers are insensitive to the excitation wavelength and their corrected excitation spectra match the absorption spectra, thus confirming that the 524 nm band of **P6** results from excitation of the bulk material

$n_{ave} = 23.6$
$\lambda_{abs} = 446$ nm
$\lambda_{em} = 478$ nm

P5

$n_{ave} = 22$
$\lambda_{abs} = 446$ nm
$\lambda_{em} = 524$ nm

P6
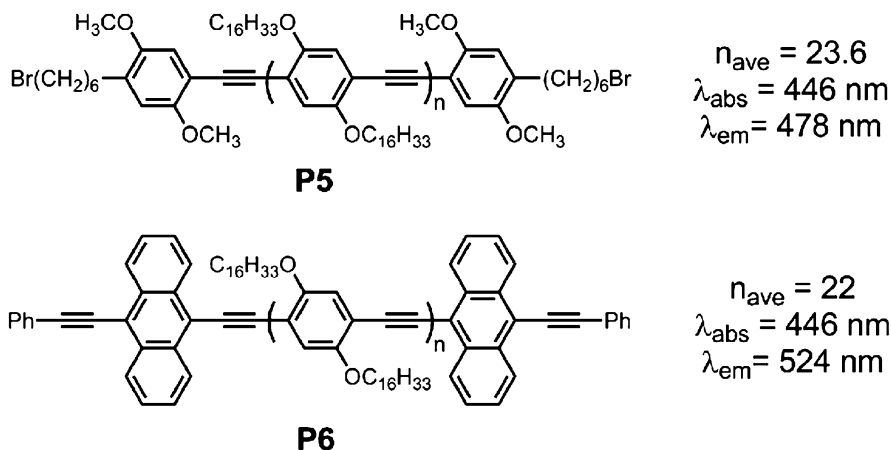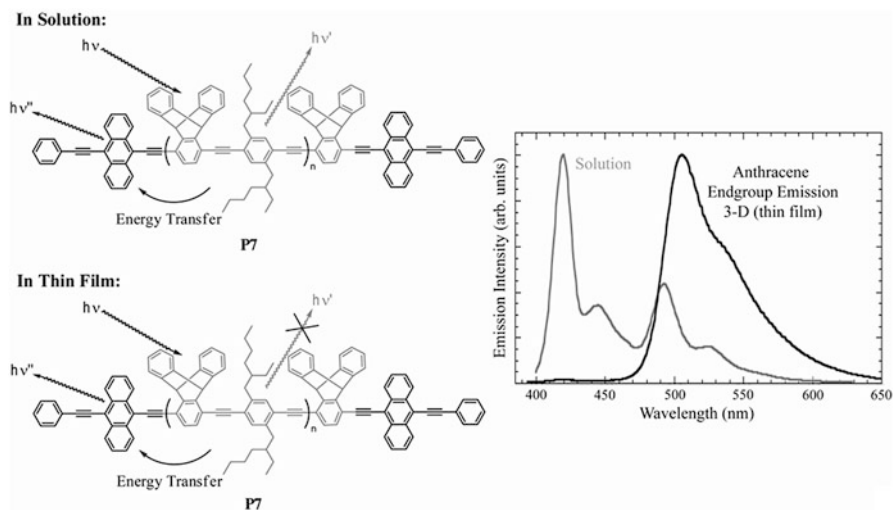
Fig. 10.5

Fig. 10.6

and subsequent energy migration to the lower energy end-groups. By comparison of the emission intensities of the 524 nm band and a residual 474 nm band (that corresponds to fluorescence from the PPE backbone) in the emission spectrum of **P6**, it was concluded that the energy transfer from the polymer backbone to the anthracene end-groups proceeded with >95 % efficiency in solution.

Energy transfer in a related PPE, **P7**, (see Fig. 10.6) however, was found to be more sensitive to the physical state of the system. In solutions of **P7**, emission from both the polymer backbone and anthracene end-group can be observed in an approximately 2:1 ratio. On the other hand, thin films of **P7** *exclusively* display

Exciton Diffusion Length (L) = v • τ
v ~ energy transfer rate (effective mass, delocalization, ε, solid state structure, energy surface topology)
τ ~ lifetime (electronic structure, chain-chain interactions, quenchers)

Fig. 10.7

emission from the anthracene end groups at 492 nm. Therefore, transitioning from a 1-D solution system to 3-D thin films enables intra- and interpolymer energy transfer, which results in more extensive exciton migration to energy minima.

Although PPEs superficially appear to have rigid-rod structures, materials with higher degrees of polymerization exhibit coiled solution structures with persistence lengths of approximately 15 nm [11]. For isolated polymer chains in dilute solutions, the migration of excitations along the polymer backbone follows the random walk statistics of 1-D diffusion. Therefore, given that the exciton diffusion length in PPEs is ca. 140 (Ph-CC-) units, one-dimensional exciton transport requires $(140)^2$ hops to travel 140 linear hops. Although this means that the exciton can theoretically sample approximately 20,000 phenylethynyl repeat units, 1-D random walks do not provide the optimal pathway for energy migration (and thus signal amplification) because an excitation necessarily retraces portions of the polymer backbone multiple times. Hence, it is necessary to enable 2-D and 3-D random walks of the excitations. This increased dimensionality decreases the probability of an excitation retracing a given segment of the polymer and thereby produces a larger amplification in sensory schemes.

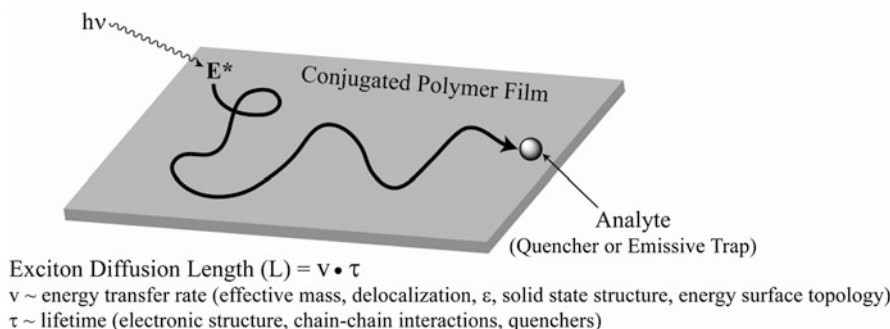It is for this reason that thin films of conjugated polymers can serve as unparalled, highly-sensitive chemosensors (exemplarily for TNT [12]). In general, increases in the diffusion length of the exciton within the CP thin film will enhance the sensitivity of the chemosensor. As shown in Fig. 10.7, the exciton diffusion length (L) is provided by the product of the energy transfer rate (v) and lifetime (τ) of the exciton. The energy transfer rate, v, is dependent in part, on the extent of delocalization in the polymer, the effective mass of the exciton, and the energy surface topology of the CP thin film. The lifetime of the exciton is largely defined by the photophysics of the polymer repeat unit and can be further influenced by the presence of interchain interactions and quenchers.

Within thin films, individual polymer chains electronically couple, thus encouraging interpolymer energy transfer. The efficiency of intermolecular energy migration depends on facile dipolar Forster-type processes, which are optimal when
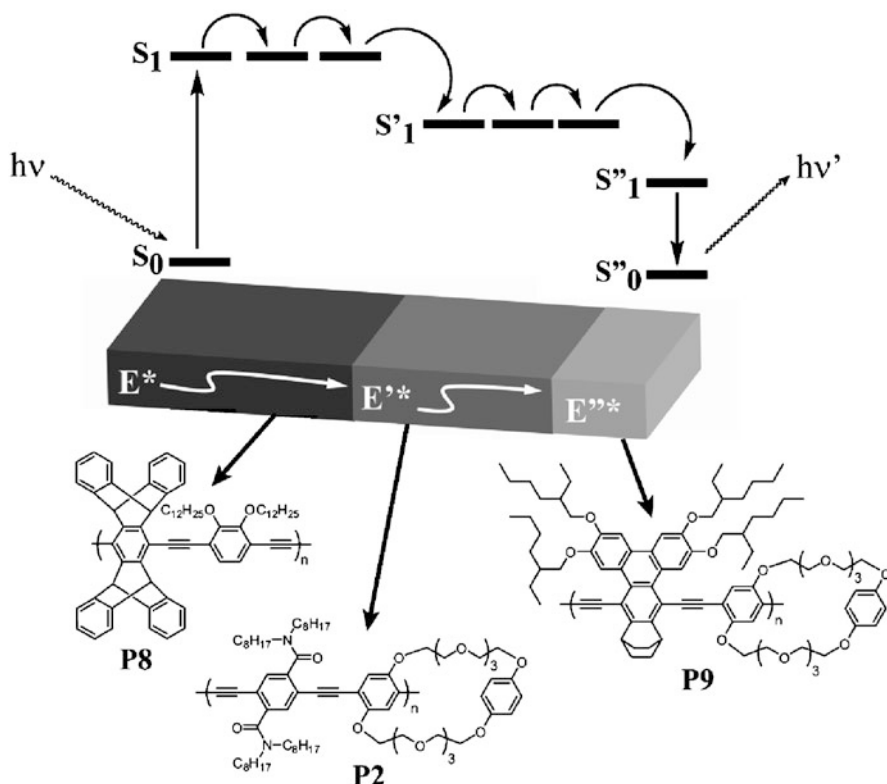
Fig. 10.8

the transition dipoles of the donor and acceptor groups are aligned. As a result, films of aligned polymers with extended chain conformations provide an ideal situation for energy migration. Such optimal polymer conformations are best achieved by forming monolayer or multilayer films of PPEs prepared by the Langmuir-Blodgett (LB) deposition technique [13].

For example, a striated multipolymer system composed of three different PPEs with tailored absorption and emission maxima designed to have large spectral overlap between a donor emission and an acceptor absorption can be precisely fabricated using the Langmuir-Blodgett technique (see Fig. 10.8) [14]. In this system, spectral overlap encourages energy transfer from **P8** to **P2** and from **P2** to **P9**. Polymers **P2** and **P9** are also non-aggregating and ampiphilic, thus allowing manipulations at the air-water interface. The trilayer assembly was created by first spin-coating the shortest-wavelength polymer, **P8**, on a glass substrate. Next, 16 LB layers of **P2** were coated over this spin-cast film and finally a single monolayer of **P9** was coated, thus providing a composite film where the band gap decreases directionally from the substrate to the polymer-air interface. Excitation of the
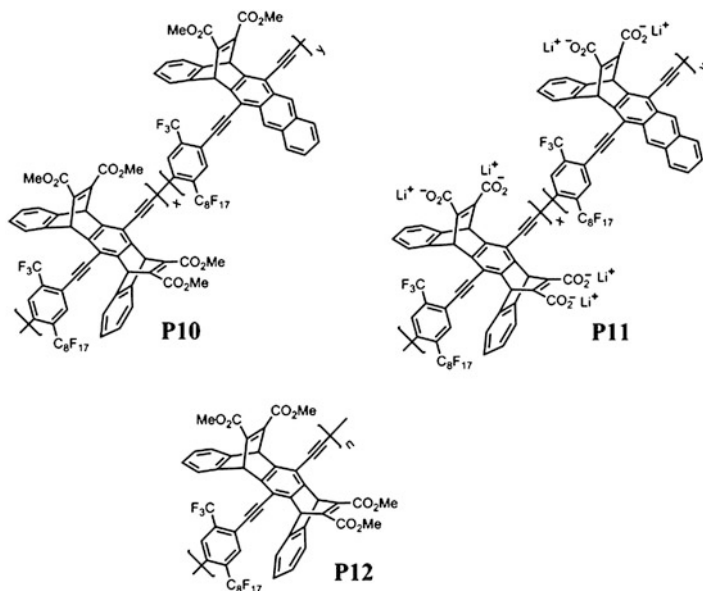
Fig. 10.9

three-component film at 390 nm (λ_{max} of **P8**) resulted in an emission spectrum consisting of three peaks: two small peaks at 423 and 465 nm, which are attributed to emission from **P8** and **P2**, respectively, and a third, dominant peak at 512 nm that is a result of energy transfer from **P8** and **P2** to **P9** and subsequent emission from **P9**. The observation that most of the excitation energy is transferred from **P8** through 16 layers of **P2** to **P9** demonstrates that energy can be efficiently moved in the *z*-direction, thereby concentrating the energy at the film-air interface. Direct excitation of **P9** at 490 nm resulted in a peak at 512 nm of much lower fluorescence intensity than the peak resulting from excitation at 390 nm; the difference in fluorescence intensity is directly proportional to the difference in optical density at 390 nm versus 490 nm, again confirming the efficiency of energy transfer.

10.3.2 Aggregates

Continuing with the aforementioned practice of using anthracene moieties as low energy emissive traps, PPEs **P10** and **P11** (see Fig. 10.9) incorporating anthryl units were synthesized and investigated (polymer **P11** is simply a polyelectrolytic analog of **P10**) [15, 16]. In contrast to polymers **P6** and **P7**, which contained anthracene moieties as end groups, polymers **P10** and **P11** are random copolymers containing small concentrations (1–9 %) of an anthryl comonomer. However, the optical effects of incorporating anthryl moieties into the polymer backbone are largely similar

to those observed with **P6** and **P7**: new, intense, long-wavelength emission bands that are sensitive to the dimensionality of the system are observed. For example, the effect of anthracene incorporation can best be appreciated upon comparing the emission spectra of **P10** with that of **P12**, which is an anthryl-free analog of **P10**. PPE **P12** displays the characteristic two-band emission spectrum of PPEs, with an emission maximum at 433 nm in solutions and in thin films. Solution emission spectra of **P10** exhibit these same two bands, but also display a third, green emission band centered between 500 and 520 nm (depending on the percent of anthryl comonomer) that greatly increases in intensity in thin films of **P10**. Furthermore, **P10** has a long (1.5–1.9 ns) excited-state lifetime, as compared to **P12** (0.44 ns).

As discussed before, the green band emission from **P10** is much more pronounced when the polymer is in its film state than when it is dissolved in dilute solutions because of the enhanced exciton migration present in CP films (3-D) relative to that present in dilute polymer solutions (1-D). In dilute solutions only *intra*chain exciton migration is possible because individual polymer chains are isolated from one another. However, in the film state, chains of **P10** are aggregated within close proximity to each other such that *inter*chain exciton migration becomes possible. If the low-energy exciton trap sites are emissive, such as the anthryl defect sites in **P10** and **P11**, then they can dramatically alter the emission spectra of CPs in their film state.

To further investigate the effects of exciton migration on luminescence properties, absorption and fluorescence spectroscopy were conducted on PPE solutions in various degrees of aggregation. By adding a poor solvent (i.e., a solvent in which **P10** is in a collapsed or aggregated state) to a PPE solution dissolved in a good solvent (i.e., a solvent in which the polymer is in an expanded and well-dissolved state), one can study the polymers in various degrees of aggregation. In dilute THF solution, **P10** was well-dissolved and individual polymer chains were isolated; therefore, only *intra*chain exciton migration is possible and the small concentration of emissive exciton traps was not noticeable in the fluorescence spectra. Thus, THF solutions of **P10** appear fluorescent blue, as characterized by the sharp emission band around 432–434 nm. However, in a 50:50 THF:H_2O cosolvent mixture, **P10** was present in the aggregated state, held together by hydrophobic and π-π interactions. Upon aggregation, *inter*chain exciton migration became significant, so the emissive exciton traps noticeably altered the fluorescence spectra, exhibiting a dominant green emission band around 513 nm. If the ratio of the anthryl comonomer in **P10** is increased, the ratio of green to blue emission (I_{green}/I_{blue}) in the aggregated state also increases.

Furthermore, the fluorescence color change of **P10** dispersed in a solid poly(vinyl alcohol) (PVA) matrix was investigated. PVA is a water soluble polymer that has been widely used to make water-permeable hydrogels. In order to disperse **P10** in PVA, a THF solution of **P10** was quickly added into an aqueous solution of PVA and the resulting, precipitated polymer blend was crosslinked with glutaric dialdehyde before isolation. Upon washing the **P10**/PVA blend with THF, it became fluorescent blue and remained so even after drying. Subsequently, submerging this blend into pure water for 2 min causes it to become fluorescent green.
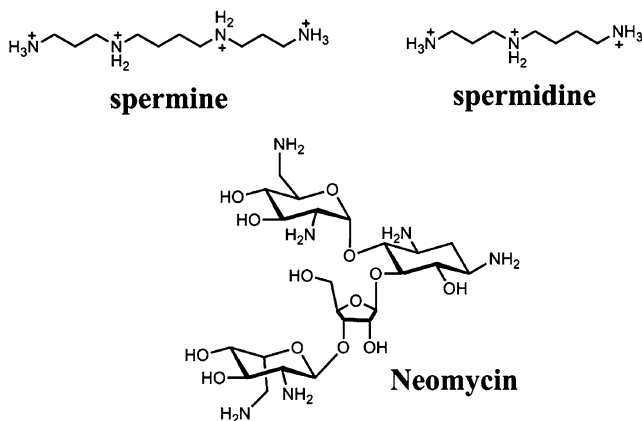
Fig. 10.10

The observed blue-to-green fluorescence color change was attributed to the water-induced aggregation of the PPE chains within the PVA matrix. Surprisingly, re-washing this fluorescent green blend in THF did not restore blue fluorescence—this was probably due to the difficulty of separating individual PPE chains once they become strongly aggregated in 100 % water.

The phenomenon of enhanced exciton trapping in PPE aggregates was exploited to make aggregation-based sensors for nonquenching multicationic analytes [16]. Nonquenching analytes are described as analytes that cannot participate in direct quenching of the inherent fluorescence intensity of a CP via electron transfer or energy transfer due to incompatible redox and spectral properties, relative to the photoexcited CP. Examples of such analytes are biologically-relevant small-molecules, such as multicationic spermine and spermidine, and neomycin (see Fig. 10.10). It was found that spermine, spermidine, and neomycin induced the formation of tightly associated aggregates in ethanol solutions of the polyelectrolyte **P11**, which was accompanied by a visually noticeable blue-to-green fluorescence color change (Fig. 10.11). Dicationic and monocationic amines were not observed to affect this change, thus demonstrating that a conjugated polyelectrolyte sensor relying on nonspecific, electrostatic interactions may still attain a certain level of selectivity.

Although CP aggregates represent another option to enable 3D exciton migration (other than thin films), it must be noted that, with few exceptions, the strong electronic interactions between chains of conjugated polymers that accompany aggregation dramatically lower their quantum efficiency. This is due to the phenomenon of self-quenching, which can be generally described as any interaction between an excited molecule, $M*$, and a ground-state molecule of the same type, M, that leads to fluorescence quenching of $M*$[17]. Therefore, it is generally true that the design principles for maintaining high quantum yields in conjugated polymers have been diametrically opposed to those for the optimization of charge and exciton transport, which encourage greater interpolymer contact [18, 19].

Fig. 10.11

| **Parallel** | **Oblique** | **Orthogonal** |
| Efficient exciton transport but dipole-dipole cancellation leads to fluorescence quenching | Compromise between efficient exciton transport and luminescence | High luminescence but minimal interchain exciton migration |
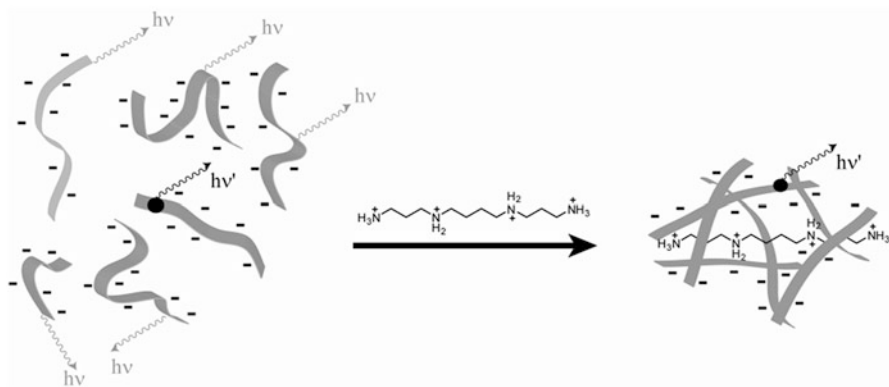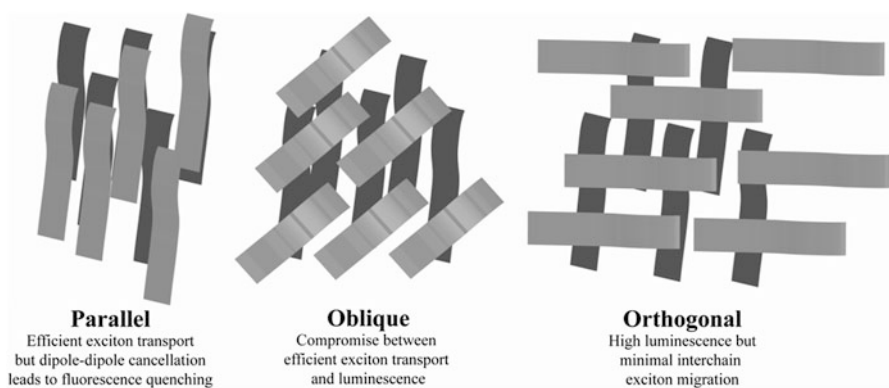
Fig. 10.12

However, it *is* possible to produce strongly interacting polymer chains with 3D electronic interactions while maintaining high luminescence efficiency (Fig. 10.12). Specifically, it has been proposed that an oblique orientation between neighboring transition dipole moments of conjugated polymers will prevent self-quenching [20]. Based on an exciton-coupling model, a parallel orientation of polymer chains is expected to result in cancellation of transition dipoles to give a forbidden S_0-S_1 transition, but coupled chromophores with oblique organizations should exhibit an allowed S_0-S_1 transition [21]. Therefore, by incorporating specific chemical structures within the repeat unit of a CP that enforce an oblique arrangement of chain segments, highly luminescent CP aggregates can be accessed. Following this concept, we will describe two PPE systems that exhibit a highly emissive aggregated phase and discuss the role of specific chemical structures in enabling oblique packing of chromophores.

Fig. 10.13
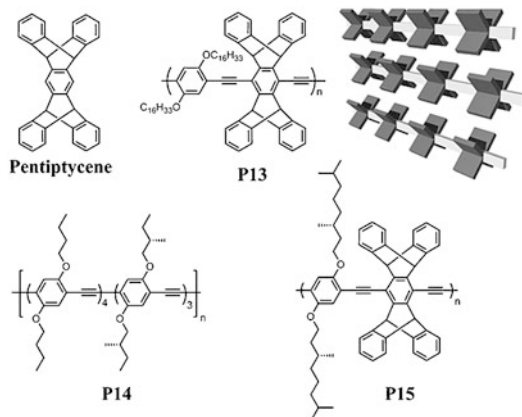
Pentiptycene (see Fig. 10.13) displays a rigid, three-dimensional structure, which, upon inclusion within a CP backbone, effectively prevents π-stacking or excimer formation between individual chains [18]. In comparison with analogous PPEs lacking a pentiptycene comonomer, thin films of **P13** display enhanced fluorescence quantum yield and stability. Moreover, thin films of **P13** exhibit exceptionally high sensitivity as an artificial fluorescent chemosensor for the vapors of nitroaromatic compounds, such as TNT and 2,4-dinitrotoluene (DNT) [12]. Essentially, the pentiptycene moiety imparts a porosity to solid-state structures (Fig. 10.13, top right) that prevents direct electronic interaction between polymer chains (thus inhibiting self-quenching) while still allowing for strong dipole-dipole interactions (thus enabling 3D exciton migration).

Given the rigid structure of pentiptycene-incorporated PPEs, however, it was not initially anticipated that oblique aggregates of such polymers could be formed. Therefore initial investigations [22] into fabricating obliquely-aligned PPE aggregates were carried out with **P14**. Chiral side chains were introduced into the repeat unit with the expectation that chirality, coupled with the normal twisting of polymer backbones will yield self-assembled, ordered aggregates. Although enantiomerically-pure **P14** was found to initially form chiral aggregates in 40 % methanol/chloroform (see Fig. 10.14), the fluorescence intensity of these aggregates was strongly decreased relative to isolated polymer chains in dilute chloroform solutions. Moreover, the preliminary chiral structures thus formed ultimately rearranged to favor a stronger aggregate with coincident alignment of polymer chains at methanol concentrations higher than 50 %. The resultant organization gave a low or nonexistent dihedral angle between polymer chains and, as expected, the fluorescence quantum yield dropped to <5 % of its original value.

Therefore, in order to stabilize a strongly aggregated chiral and emissive organization of polymers while preventing aggregated chains from achieving a collinear structure, pentiptycene-containing structures were investigated [22]. Although pentiptycene-containing PPEs were not expected to form aggregates, it was initially found that addition of methanol (30 %) to solutions of **P13** yielded
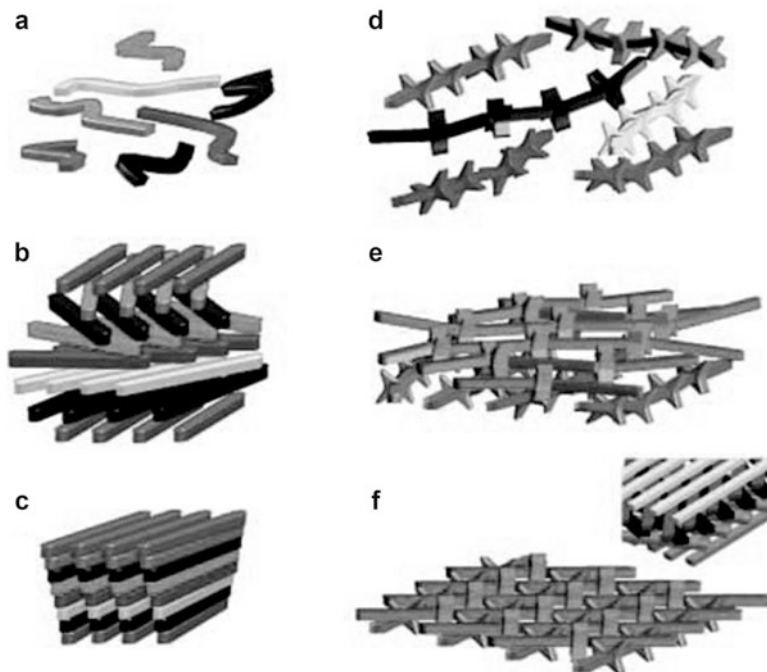
Fig. 10.14

aggregates with significantly quenched emission ($\Phi = 0.21$). These aggregates were much slower to assemble than those of **P14** and it was hypothesized that the polymer chains assemble into an interlocking structure, in which the polymer chains are constrained in the clefts between the pentiptycene groups (see Fig. 10.14). Considering that such an interlocking structure would prevent a coincidence of strongly interacting polymer chains, the aggregation behavior of an enantiomerically-pure, pentiptycene-containing PPE, **P15**, was investigated. On the basis of solvent-dependent circular dichroism and absorbance spectroscopy, **P15** was indeed found to form restricted chiral aggregates in a poor solvent (methanol) yet still retain the majority of its fluorescence intensity ($\Phi = 0.61$).

This unique aggregated state of **P15** also showed sensitivity enhancements toward nitroaromatics. In solutions, fully aggregated **P15** was 15-fold more sensitive to fluorescence quenching by TNT and DNT than fully-solvated **P13**. In addition, spun-cast films of aggregated **P15** displayed a fourfold increase in sensitivity toward TNT vapor (75 % fluorescence quenching within 10 s) over optimized thin films of **P13**. The increased sensitivity of the fluorescent, chiral aggregates is proposed to derive from both an improved exciton diffusion length in the 3D-coupled chiral grids and an extension of the polymer conjugation length in the highly organized aggregated structure.

Fig. 10.15

P16
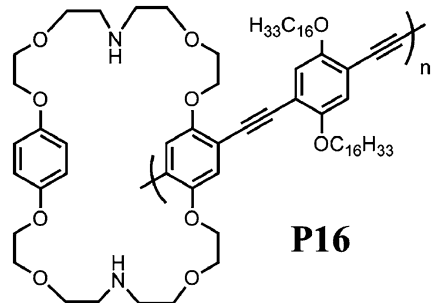
In addition to pentiptycene moieties encouraging an oblique packing of PPE chains, other three-dimensional structures, such as cyclophanes, were also found to yield emissive PPE aggregates.[23] Specifically, spun-cast samples of polymer **P16** (Fig. 10.15) displayed a visible, strong yellow emission that could be assigned to fluorescence from aggregated main chains. Notably, **P16** has a very low solution fluorescence quantum yield ($\Phi = 0.06$) due to electron transfer quenching of the polymer excited state by the amine residues. However, the aggregated phase of **P16** has a quantum yield 350 % ($\Phi = 0.21$) of its solution value. This observation is unique because most other examples of conjugated polymer aggregates display fluorescence quantum yields that either match (at best), or are only a few percent of the solution values. In this case it is likely that the system displays a disordered structure and that isolated oblique aggregates are a minority species. The strong emission is a result of the fact that these aggregates are low energy species and that energy migration results in a disproportionate emission intensity.

10.3.3   Kinetics of Energy Migration in Thin Films

In order to ascertain the photophysical and energy transport properties of PPEs, highly aligned Langmuir-Blodgett (LB) multilayers of **P2** that were surface modified with luminescent traps (acridine orange, **AO**) were fabricated and investigated [24]. The LB deposition technique produced highly anisotropic films of **P2** with a well-defined thickness. The film thickness increases linearly with the number of layers transferred, thereby producing a well-defined geometry and distance for which to study energy migration processes.

The fact that energy migration is present in **P2** could be readily seen in wavelength-dependent lifetime measurements on spin-cast films. The excited state lifetime was observed to increase when monitored at progressively longer wavelengths ($\lambda = 460$, 475, and 495 nm). These lifetime characteristics are consistent with a model that describes the polymer as a continuous distribution (usually Gaussian) of site energies. In this model, each state corresponds to a conjugated polymer segment that is interrupted by chain defects (conformational or chemical),

with the longer segments having lower energy, and energy migration is described as incoherent hopping of excitations to lower energy states. Emission from high-energy states (i.e. shorter wavelength of emission) should exhibit a faster decay rate due to energy transfer to lower energy chromophores within the system, consistent with what was observed for spin-cast films of **P2**. Evidence for intrachain energy migration in **P2** is likewise provided by fluorescence depolarization measurements, which will be discussed in a later section.

Emissive trapping sites were deposited selectively on the film surfaces by dipping LB films into methanol solutions of **AO**, which was chosen because its emission and absorption spectra are well separated from those of **P2** and its absorption spectrum has good overlap with the emission of **P2**. Additionally, the solubility of **AO** was almost orthogonal to that of **P2**, which allowed LB films of **P2** to be dip-coated in solution of **AO** with varying concentrations. **AO** was found to selectively localize at the film's surface, as evidenced by the fact that the ratio of **AO** fluorescence intensity between films of different thicknesses examined immediately after dipping or after extended periods of time remained constant. Polarization measurements showed that the **AO** transition dipole was principally aligned parallel to the polymer chain.

In the simplest case of energy transfer to **AO** from a monolayer of **P2**, the average lifetime of an excitation (τ) in an infinite one-dimensional chain with randomly distributed efficient quenching traps should be $\tau = 1/(2WC^2)$, where C is the trap concentration and W is the hopping rate between neighboring sites. Therefore, the steady-state transfer rate should be proportional to C^2. In contrast, it was found that the degree of energy transfer to **AO** traps from a monolayer of **P2** was linearly dependent on the concentration of AO. This observation can be explained by either one-dimensional energy migration with inefficient trapping or two-dimensional transport. Considering that monolayer films of **P2** organize into highly aligned structures that could potentially allow excitations to undergo efficient interpolymer energy transport, the latter explanation of two-dimensional transport is more likely.

If the number of LB layers was varied, an increase in the **AO** emission with increasing polymer layers was observed, up to 16 layers. At low concentrations of the **AO** trap, the **AO** fluorescence had a linear dependence on **AO** concentration, similar to the monolayer system described above. This last point leads to the conclusion that, at low **AO** concentration, the steady-state energy transfer rate in a monolayer film is less than $1/\tau$, where τ is the polymer's excitation lifetime. Moreover, the fact that the relative fluorescence of **AO** increases with increasing numbers of polymer layers is a direct indication of a transition to a three-dimensional energy migration topology. The observation of saturation behavior in films with higher numbers of layers is a manifestation of the diffusion length for energy migration. The increase in the efficiency of energy migration to surface traps with increasing film thickness may, at first glance, seem counterintuitive since the concentration of **AO** relative to that of **P2** is actually smaller in thick films. However, this increased trapping efficiency is a direct result of the fact that three-dimensional exciton migration necessarily creates a more efficient trapping process.
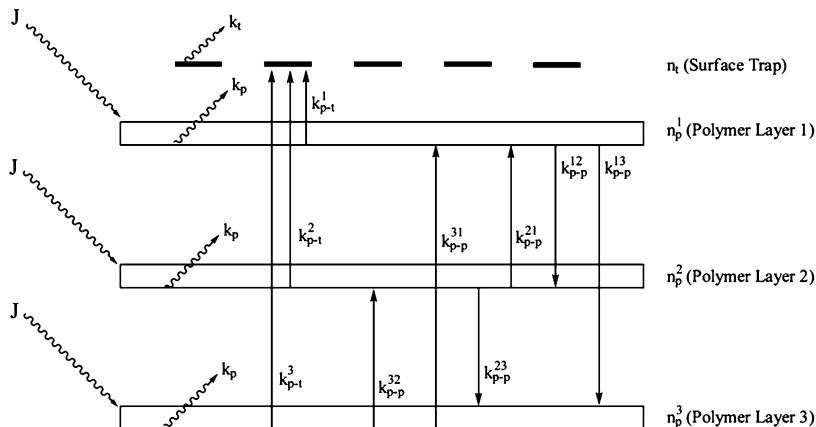
J : Intensity of steady state excitation

$n_{p,t}$: Excitation population in polymer layers and traps

$k_{p,t}$: Decay rates of polymer and trap. $k_P = 1/\tau_p$, $k_t = 1/\tau_t$

$k_{p\text{-}t}^1$: Rate constant for energy migration from polymer layer 1 to the trap. $k_{p\text{-}t}^1 \sim C$, where C is the concentration of traps.

$k_{p\text{-}t}^{2,3}$: Rate constant for direct energy transfer to the trap from polymer layers 2 and 3. $k_{p\text{-}t}^2 \sim \dfrac{C}{\ell^6}$, $k_{p\text{-}t}^3 \sim \dfrac{C}{(2\ell)^6}$
ℓ is the thickness of the layer

$k_{p\text{-}p}^{ij}$: Rate constant for energy transfer between polymer layers i and j $\quad k_{p\text{-}p}^{ij} \sim \dfrac{1}{(\ell(i\text{-}j))^6}$

A steady state assumption for n_t, n_p^1, n_p^2, and n_p^3 gives:

$$-n_t k_t + n_p^1 k_{p\text{-}t}^1 + n_p^2 k_{p\text{-}t}^2 + n_p^3 k_{p\text{-}t}^3 = 0$$

$$-n_p^1 k_p - n_p^1 k_{p\text{-}t}^1 - n_p^1 k_{p\text{-}p}^{12} - n_p^1 k_{p\text{-}p}^{13} + n_p k_{p\text{-}p}^{21} + n_p^3 k_{p\text{-}p}^{31} + J = 0$$

$$-n_p^2 k_p - n_p^2 k_{p\text{-}t}^2 - n_p^2 k_{p\text{-}p}^{21} - n_p^2 k_{p\text{-}p}^{23} + n_p^1 k_{p\text{-}p}^{12} + n_p^3 k_{p\text{-}p}^{32} + J = 0$$

$$-n_p^3 k_p - n_p^3 k_{p\text{-}t}^3 - n_p^3 k_{p\text{-}p}^{32} - n_p^3 k_{p\text{-}p}^{31} + n_p^1 k_{p\text{-}p}^{13} + n_p^2 k_{p\text{-}p}^{12} + J = 0$$

Fig. 10.16

X-ray measurements on the monolayer and multilayer films revealed that the thickness per layer is 11 Å. Since the bimolecular Förster radius for most organic compounds is 20–60 Å, dipole- dipole excitation transfer between polymers must be involved as part of the mechanism for energy transfer to the **AO** trap.

In order to model the various energy transfer processes in LB films of **P2** surface modified with **AO**, rate constants for each possible energy transfer and decay process for an *N*-layer system were assigned. Figure 10.16 outlines these rate constants and their associated processes for a three-layer system. Since PPEs have a relatively large band gap and a narrow bandwidth, excitations were assumed to exist as strongly bound excitons. Assuming a steady-state population of all excited species, a set of balanced equations can be formulated (see Fig. 10.16) and, ultimately, the relative intensity of **AO** fluorescence versus number of LB layers

can be modeled. Such modeling has determined, firstly, that the rate of energy transfer between layers exceeds 6×10^{11} s^{-1}. This high rate results in a uniform excitation population throughout all the layers of the LB films. Additionally, the model confirms the saturation of **AO** fluorescence intensity with increasing LB layers.

Therefore, it is clear that an optimal thickness will exist in sensor schemes requiring exciton trapping at the polymer surface. However, it must be pointed out that additional enhancements in energy migration may be possible by creating multilayer structures that provide vectorial energy transport in a specific direction. For example, in the striated, three-component film depicted in Fig. 10.8, energy was preferentially transferred to the surface by utilizing layers of sequentially decreasing band gap and, in this way, the 16-layer energy transfer limitation for PPEs was overcome.

10.4   Lifetime Modulation

As discussed above, a thorough understanding of the mechanisms underlying energy migration in CPs is necessary to design its enhancement. The high efficiency of energy transfer in most conjugated systems relative to systems with pendant chromophores suggests that strongly coupled electronic intrachain (Dexter-type) processes may increase transport in these systems over those provided solely by the dipole-dipole (Forster-type) interactions that govern weakly interacting chromophores. Discrepancies between the two mechanisms allow the determination of which process dominates in a given system. [25]

As derived by Forster, the dipole-dipole approximation yields a transition probability (k_{ET}):

$$k_{ET} = \frac{\kappa^2 J \, 8.8 * 10^{-28} mol}{n^4 \tau_0 R_{DA}^6} \tag{10.5}$$

where κ is an orientation factor; n is the refractive index of the medium, τ_0 is the radiative lifetime of the donor; R_{DA} is the distance (cm) between donor (D) and acceptor (A); and J is the spectral overlap (in coherent units cm^6 mol^{-1}) between the absorption spectrum of the acceptor and the fluorescence spectrum of the donor. Therefore, a weakly allowed transition, as manifest in a long radiative lifetime, should discourage purely coulombic energy transfer.

Electron exchange effects contributing to energy transfer described by Dexter account for shorter-range processes that result from direct wave function overlap of interacting molecules. In this case, the transition probability is described by

$$k_{ET} = K J e^{\frac{2R_{DA}}{L}} \tag{10.6}$$

Where K is related to specific orbital interactions; J is the spectral overlap; R_{DA} is the donor-acceptor distance; and L is the van der Waals radii distance between donor and acceptor. This process is often termed electron exchange because molecule must be almost within the van der Waals radii of each other to interact. In the specific case of CPs, chromophores are directly conjugated, and therefore, one might expect the Dexter mechanism to dictate the overall efficiency of energy migration, at least within the polymer backbone.

To determine the dominant *intra*chain energy migration mechanism in PPEs, the unique oscillator strength independence of the Dexter mechanism was invoked to guide the design of polymers with long radiative lifetimes. Long radiative lifetimes translate into reduced oscillator strengths of D* to D and A to A* transitions, which, according to the Forster mechanism (Eq. 10.5), would result in a severely truncated rate of energy transfer. However, because the Dexter electron exchange mechanism does not depend on the oscillator strength, longer lifetimes affected by less allowed transitions can serve to increase energy transfer by providing more time for the excitation to migrate before radiative decay [25].

10.4.1 Triphenylene-Incorporated PPEs

Long-lifetime PPEs can be accessed by incorporating structures with extended aromatic cores, such as triphenylene, dibenzo[*g,p*]chrysene and benzothiophene, into the backbone of the polymer. Triphenylene has a well-known symmetrically forbidden ground state transition and therefore exhibits a long excited state lifetime. Although incorporation into a CP will decrease the triphenylene's symmetry, it was hypothesized that the strong aromatic structure would dominate the photophysics of the resulting polymer. In order to determine the general effect of triphenylene incorporation, a family of triphenylene-based PPEs (TPPEs) was synthesized along with chemically similar phenylene analogs (see Fig. 10.17) [26]. Polymers were size-selected by gel permeation chromatography to ensure comparison of similar chain lengths and the excited state lifetimes were measured in the frequency domain in methylene chloride solutions. It was found that triphenylene incorporation universally extended the excited state lifetime of targeted PPEs without severely compromising quantum yield. The combination of Φ and τ data demonstrate that the enhanced lifetimes are principally due to differences in radiative rates and not differences in non-radiative rates.

In PPEs where the excitation is more localized, the lifetime enhancing effect of the triphenylene moiety was more pronounced. An example is **P23**, consisting of a triphenylene monomer and a biphenyl monomer. Because biphenyl planarizes in the excited state, a large Stokes shift is observed in the resulting polymer. This process serves to localize the excitation and the radiative decay rate becomes more competitive with energy transfer. Consequentially, the lifetime of **P23** is about three times longer than its phenylene analog, **P24**. This effect is also observed in *meta*-linked PPE, P27: the *meta* linkage disrupts conjugation, thus localizing
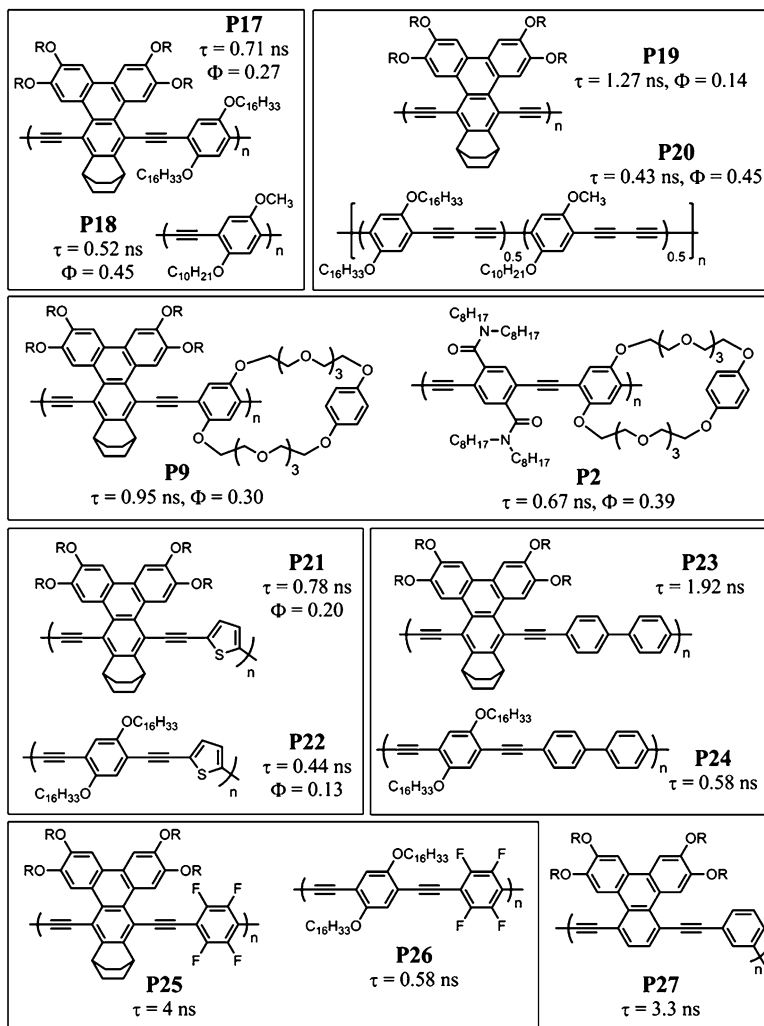
Fig. 10.17

the excitation and resulting in one of the longest lifetimes observed for TPPEs. As expected, PPEs with a larger triphenylene component demonstrated more pronounced lifetime enhancement relative to their phenylene analogs (**P19** vs. **P20**).

In addition, electrostatic variation in TPPEs was found to lead to excited state interactions. The long lifetime (4 ns) observed for **P25** most probably arises from an exciplex that is formed between the triphenylene moiety and its electron deficient tetrafluorinated comonomer. This proposal is also supported by the broad, red-shifted emission spectra recorded for **P25**. Notably, these features were not observed for the phenylene analog, **P26**, thus suggesting that the flat, electron-rich nature of the triphenylene is necessary to induce exciplex formation.
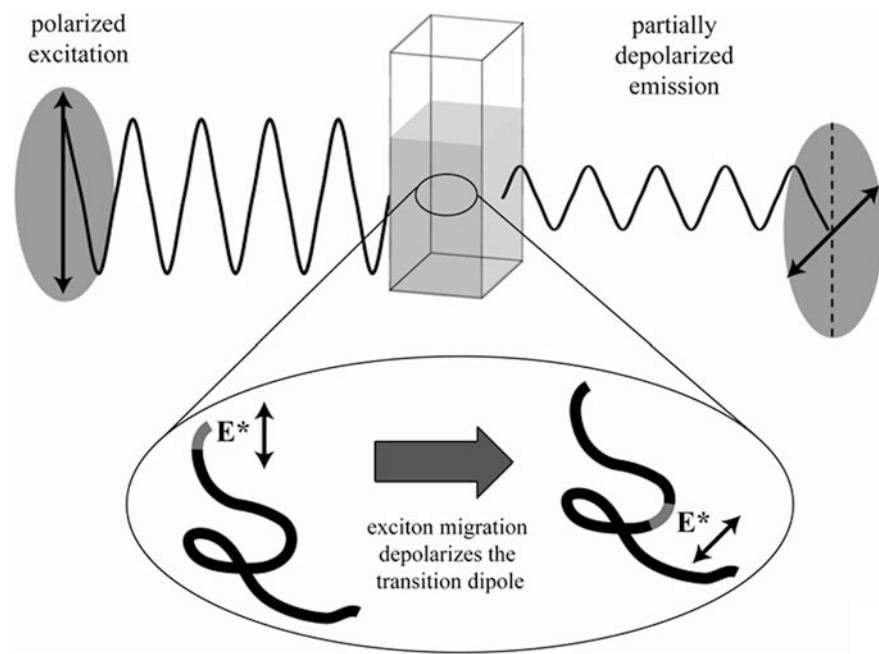
Fig. 10.18

The relationship between excited-state lifetime and energy migration can be investigated through fluorescence depolarization measurements [25]. A simplified pictorial depiction of depolarization due to energy migration in conjugated polymers is shown in Fig. 10.18. The excitation beam is vertically polarized and therefore only vertical transition dipoles are initially excited on the CP chain. Vertically polarized excitons on the polymer chain can migrate and, as they move over a disordered polymer chain, can lose their initial polarization. The emission of the CP is thus depolarized relative to the excitation beam. Therefore, the amount of measured depolarization directly indicates the extent of energy migration in the conjugated polymer.

Since all polymers studied were high molecular-weight materials, they can be considered rotationally static over the emission lifetime of the polymer. Therefore, energy migration is the major contributor to the fluorescence depolarization in conjugated polymers, and the exciton loses more of its initial polarization as it diffuses along a disordered polymer chain. The polarization value, P, was determined from the standard equation

$$P = \frac{I_\parallel - GI_\perp}{I_\parallel + GI_\perp} \tag{10.7}$$
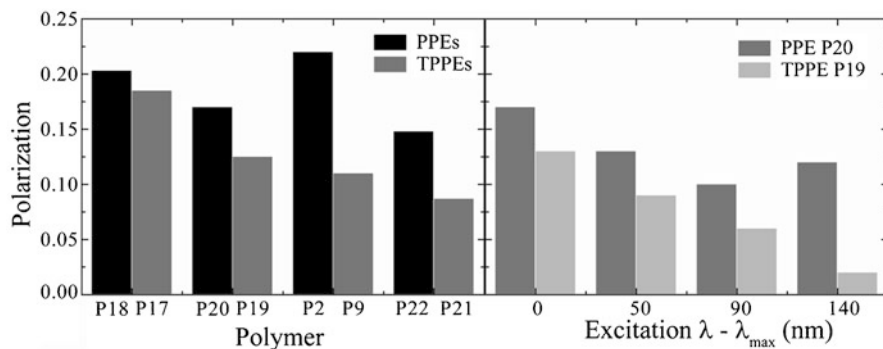
Fig. 10.19

where $I_{\parallel}$ and $I_{\perp}$ are the intensities of emissions detected parallel and perpendicular to the polarization vector of the incident light, respectively, and G is an instrumental correction factor. Theoretically, the highest value of P for a randomly-oriented, isolated, fixed chromophore with coincident transition dipoles for absorption and emission is 0.5.

Concurring with lifetime data, depolarization was found to be universally more pronounced in TPPEs than their phenylene analogs (Fig. 10.19, left). In the case of polymers **P21** and **P22**, the kinked thiophene linkage resulted in a much greater depolarization than in other polymers studied. Greater polarization loss per migration step is expected in a kinked structure. Polymer **P27**, with its localizing biphenyl monomer, retained one of the highest polarization values. Polymer **P25**, however, displayed the highest polarization value among the TPPEs. The energy minimum formed by its exciplex probably quickly traps the wandering excitation, thus reducing energy migration.

Additionally, the fluorescence depolarization of a subset of polymers as a function of excitation energy was studied in order to separate depolarization owing to energy migration from that due to absorption/emission dipole alignment (Fig. 10.19, right). If energy migration is indeed present, then polarization values should decrease as excitations move to shorter wavelengths. Measurements were performed on materials selected for similar chain length, all above the small molecular weight regime. As excitation energy is increased, it was found that both the TPPEs and their phenylene analogs display lower P values, consistent with population of higher energy excitons that readily lower their energy by migration to lower energy states. However, polarization continued to significantly decrease with shorter wavelengths of excitation in TPPEs but only leveled off in PPEs, indicating that radiative rates of emission are not competitive with energy migration in TPPEs as they are in PPEs. If the Forster mechanism dominated, then the enhanced radiative rates in PPEs would encourage more extensive energy migration (and therefore greater fluorescence depolarization) as compared to the TPPEs; however,

Fig. 10.20

lower persistence length
(i.e. highly coiled structure)
leads to greater depolarization
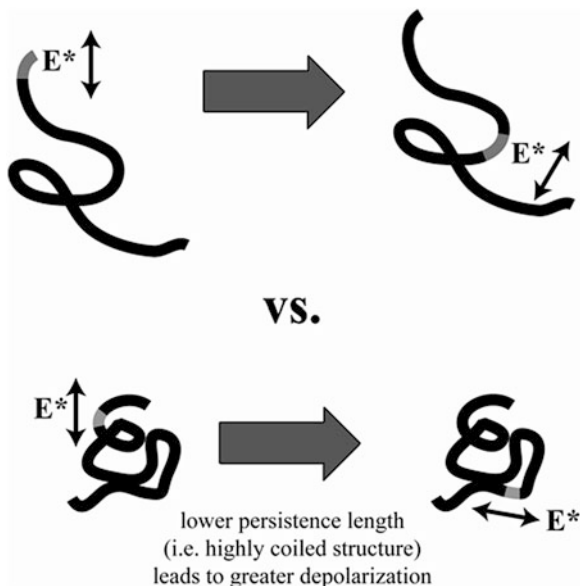
the opposite phenomenon is observed, thus lending credence to the claim that the Dexter mechanism is the dominant intramolecular energy transport process in these systems.

10.4.2 Chrysene-Incorporated PPEs

It was also possible that the increased fluorescence depolarization observed for the TPPEs is due to a reduced persistence length as compared to analogous PPEs (see Fig. 10.20). Steric interactions between the ethynylenes and proximate CH bonds of the TPPEs could conceivably result in a more coiled structure that could be responsible for the more rapid fluorescence depolarization in the TPPEs. To address this concern, polycyclic dibenzo[*g*,*p*]chrysene-based PPEs (CPPEs) were investigated (Fig. 10.21) [27]. CPPEs lack any complicating steric factors and have a more rigid structure that should increase the persistence length and yield less coiled polymers compared to PPEs.

The photophysical properties of the CPPEs were found to be similar to those observed in TPPEs: i.e., longer excited state lifetimes and more extensive energy migration. Polymers **P29** and **P31** displayed lifetimes greater than 2 ns, while most PPEs have sub-nanosecond lifetimes. Polarization studies confirmed the presence of enhanced exciton migration in CPPEs [25]. For all chain lengths and at all excitation wavelengths, the polarization values of CPPEs were about half of those in the corresponding PPEs. Additionally, polarization data as a function of excitation

P28
$\tau = 0.51$ ns
$\Phi = 0.50$

P29
$\tau = 2.5$ ns
$\Phi = 0.29$

P30
$\tau = 1.4$ ns
$\Phi = 0.35$

P31
$\tau = 2.6$ ns
$\Phi = 0.25$
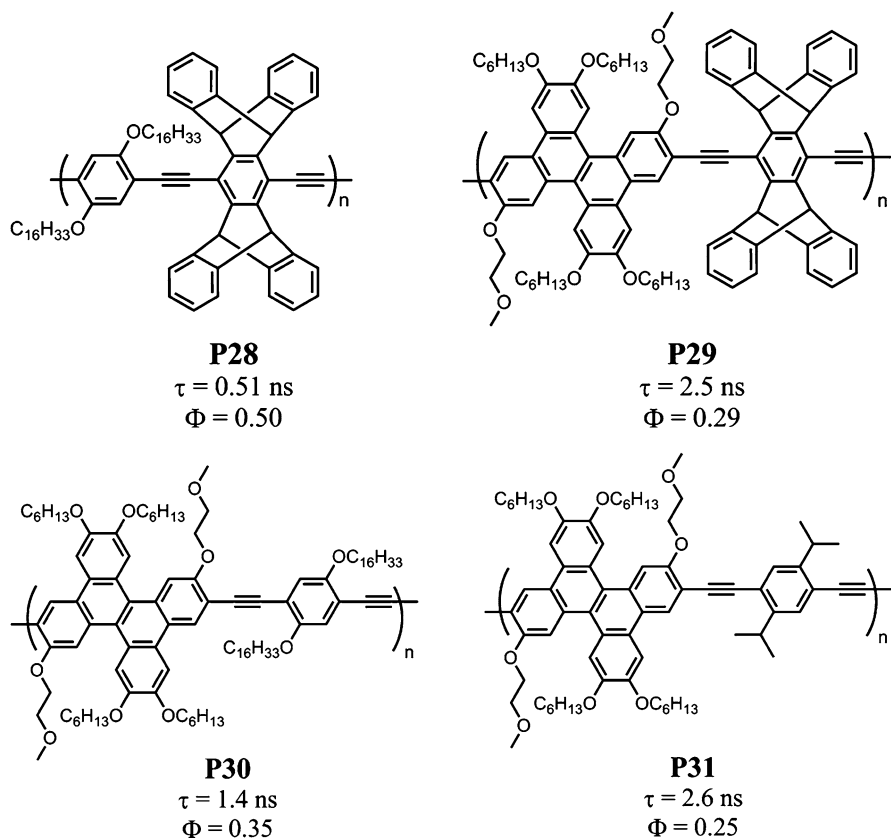
Fig. 10.21

wavelength discounted dipole displacement as a main contributor to depolarization. Chain length-dependent studies on **P29** revealed that radiative decay did not supersede energy migration even for the longest chain lengths (n 220). Therefore, the CPPEs, similar to the TPPEs, allowed for greater intrachain exciton migration than PPEs because of the fact that energy migration is not truncated by radiative deactivation of the excited state.

10.4.3 Thiophene-Based Model Compounds and PPEs

Lastly, polymers with pendant thiophenes further illuminate lifetime extension (Fig. 10.22) [28]. Sulfur incorporation benefits materials properties in part owing to the larger radial extension of its bonding. This promotes cofacial electronic interactions between stacked molecules that could enhance energy transfer. Cyclized

MC1
"para pendant"

MC2
"para cyclized"

P32
"para pendant"

P33
"para cyclized"

MC3
"meta pendant"

MC4
"meta cyclized"

P34
"meta pendant"

P35
"meta cyclized"

Fig. 10.22

and non-cyclized versions of each model compound and polymer were investigated to assess the effects of imposed symmetry and rigidity on the photophysics of the material. With both *meta* and *para* linkages represented, the family of polymers investigated allowed for exploration of the effects of different degrees of aromatization as well as changes in conjugation pathways.

To predict the behavior of such thiophene containing polymers, model compounds, **MC1**-**4** provided systems with precisely defined conjugation lengths, allowing separation of planarization effects from effective conjugation length variations. The cyclized compounds **MC2** and **MC4** showed a sharpening of vibronic structure concomitant with a decrease in Stokes shift as degrees of freedom were reduced. The oscillator strength of the (0,0) transition was significantly reduced in the *meta* system **MC4** (log $\varepsilon = 3.63$) when compared with the *para* isomer **MC2** (log $\varepsilon = 4.69$). Accordingly, *meta* **MC4** had a longer excited state lifetime (5.00 ns) than the *para* **MC2** (1.12 ns).
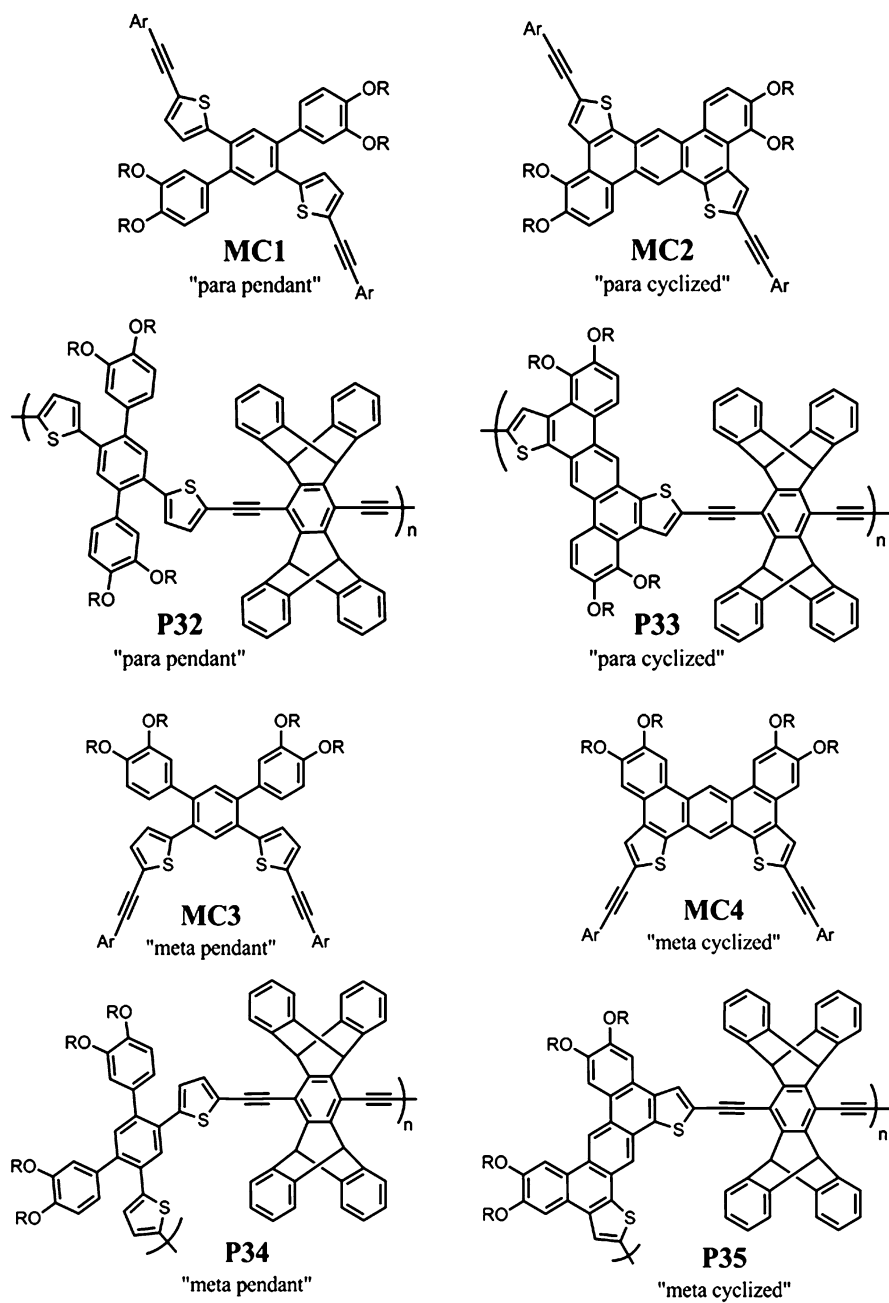
While a sharpening of emission spectra was observed, no significant wavelength shift in either system occurred upon cyclizing (aromatizing) either **MC1** to **MC2** or **MC3** to **MC4**. This suggested that there is planarization in the excited state of **MC1** and **MC3** to allow for greater delocalization. Additionally, the lifetime of the both systems was found to increase upon cyclization: the *meta* system displayed a ninefold increase in excited state lifetime upon cyclization (0.58 ns for **MC3** to 5.0 ns for **MC4**) while the *para* system showed a more modest increase (0.8 ns for **MC1** to 1.12 ns for **MC2**).

Consistent with other conjugated polymers, the photophysical properties of the model compounds **MC1**-**4** were reflected in the corresponding polymers. The absorption spectra of rigid, aromatized **P33** and **P35** displayed sharper vibronic structure and a decrease in Stokes shift when compared with the non-cyclized **P32** and **P34**. The *meta* cyclized polymer **P35** displayed much lower oscillator strength at the band edge than its *para* analog, **P33**—which was predicted by the corresponding model compounds. Aromatization effects only slightly shifted the emission maxima of both the *meta* and *para* systems. As in **MC1** and **MC3**, this may attest to excited state planarization in the flexible systems.

Lifetime trends in the model compounds were also consistent with the related polymers. In accordance with the diminished oscillator strength, the *meta* polymers **P34** and **P35** displayed a lifetime discrepancy (0.30 versus 1.06 ns, respectively) similar to that of their model compounds, **MC3** and **MC4** (0.58 versus 5.00 ns, respectively). The *para* polymers also mimicked the model systems. However, in this case, the model compounds **MC1** and **MC2** exhibited comparable lifetimes (0.80 versus 1.12 ns, respectively) before and after cyclization. As a result, the *para* polymers shared almost identical lifetimes (**P32**: 0.57 ns, **P33**: 0.61 ns). Both these examples correspond to the previously observed trend which suggests that monomer photophysics critically influences the photophysics of the resulting polymers.

Polarization experiments revealed that energy migration is not enhanced without lifetime enhancement [25]. In other words, the *meta* cyclized polymer **P35** displayed the greatest fluorescence depolarization, with polarization values reaching near zero. This was due to both the enhanced lifetime of the polymer and the curved

architecture of the polymer chain, which causes significant depolarization even when energy has migrated through a single hop. In contrast, since a large lifetime enhancement was not obtained upon aromatizing the *para* pendant polymer **P32** to its cyclized analog, **P33**, a large depolarization was not observed for either of the two *para* polymers. Together, the polarization measurements on these thiophene systems underscore an important distinction: simply rigidifying the polymer backbone is not enough to extend lifetime and enhance energy migrations. One must carefully consider chromophore photophysics when attempting to impart these properties into CPs because the excited state behavior of polymers is essentially encoded by the choice of monomers.

10.5 Conformational Dependence on Energy Migration: Conjugated Polymer—Liquid Crystal Solutions

The achievement of complete control over the conformation of conjugated polymer single chains and their assembly into functional structures is paramount to the thorough understanding and optimization of energy transfer and conductivity in conjugated polymers. Inconveniently, high molecular weights PPEs have finite persistence lengths and exist as flexible coils (as opposed to rigid rods) in solution [11]. Consequently, the disorder displayed in solution is often transferred to the solid state structures of PPEs, and there is a general lack of long-range molecular order due to conformational disorder in the polymer main chain. The many structural defects in the solid state ultimately result in diminished electronic delocalization and limit the ability to study the intrinsic properties of these materials.

As one potential solution to this conundrum, liquid crystals (LCs) represent an ideal means to produce ordered arrays of molecular wires. Columnar LCs with extended aromatic cores have long been considered one-dimensional conductors; however, there is limited electronic coupling between aromatic cores due to limited overlap of the π-orbitals, particularly in the liquid crystalline state [29]. An alternate strategy to exploit the long-range order of liquid crystals and assemble electronic materials is to dissolve conjugated polymers into a liquid crystal host. In this way, the strong intramolecular electronic coupling of the CP and the organizational ability of the LC host can work together to form a highly organized electronic material.

Revisiting the rigid, 3D pentiptycene scaffold mentioned earlier, it is worth noting that the three-dimensional nature of pentiptycene and its analog triptycene (Fig. 10.23) also has important organizational influences. Specifically, the addition of triptycene moieties into the backbone of a polymer can either be used to redirect [30] or enhance [31] molecular alignment in liquid crystals and stretched polymers. This property results from the natural tendency of host-guest mixtures to lower their energy by minimizing the amount of free volume. Therefore, fluorescent dyes, PPEs and PPVs containing triptycene groups can theoretically be aligned along the nematic director in LCs and thus achieve significant ordering with high order parameters (S) and dichroic ratios (D) [31].

Fig. 10.23

Triptycene

Pentiptycene

Fig. 10.24

6CHBT

5PCH
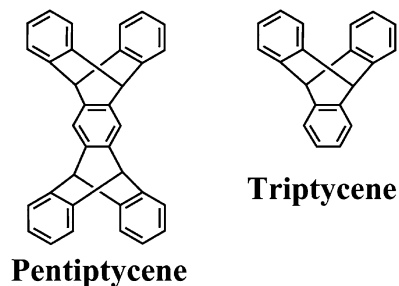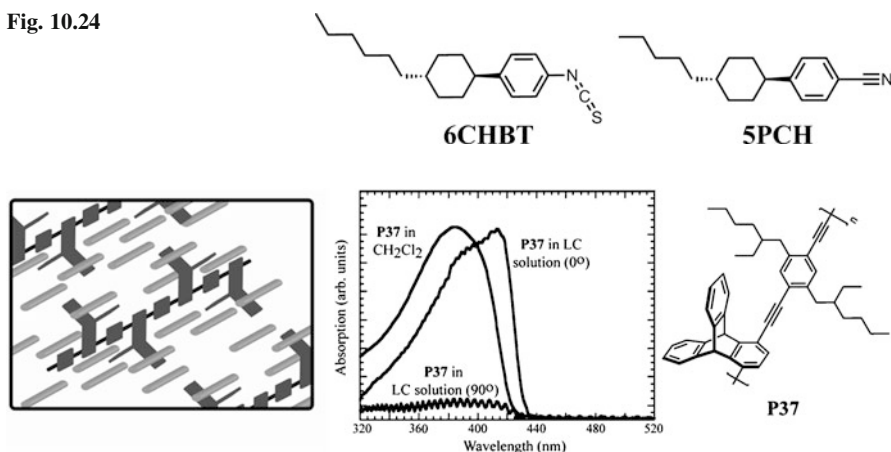
Fig. 10.25

Accordingly, nematic liquid crystalline solutions of the highly-emissive, triptycene-incorporated PPV, **P36** and the triptycene-incorporated PPE, **P37** (Fig. 10.24) were investigated [32]. Solutions of **P36** and **P37** in **6CHBT** (Fig. 10.25) were loaded into liquid crystal cells with rubbed internal polyimide surfaces that gave a homogenous alignment of the nematic LC. Polarized absorption spectroscopy of these test cells with the polarizers aligned parallel (0°) or perpendicular (90°) to the nematic director were used to calculate the order parameters, S. The liquid crystalline solvent (a wide variety of nematics were acceptable, but **6CHBT** and **5PCH** were primarily used) had the important feature that it created an extended CP chain conformation that was highly aligned (S ranged between 0.7 and above 0.8). Additionally, the polymers were found to have greatly enhanced conjugation lengths in nematic LC solutions. This could readily be observed by comparing the absorption spectra of **P37** in a CH_2Cl_2 solution and an LC solution: **P37** in a liquid crystal solvent displayed an absorption spectrum that was red shifted and had a comparatively abrupt band edge relative to its absorption spectrum in a CH_2Cl_2 solution (Fig. 10.24). Both these features suggest that the
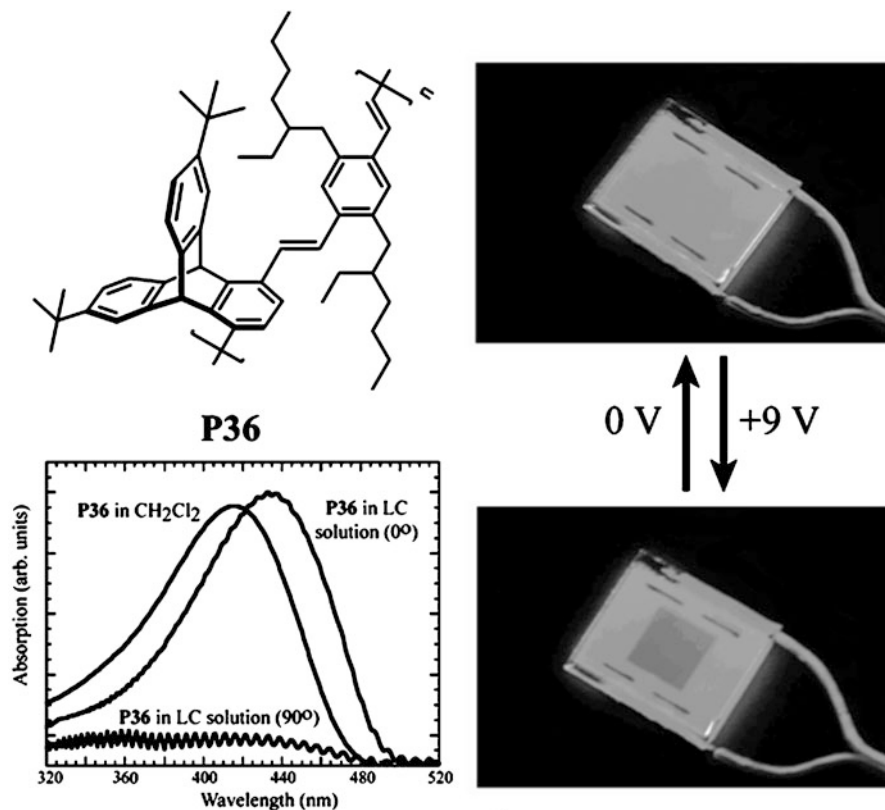
Fig. 10.26

CPs' long axes aligned with the director of the nematic LC and that the polymer chains were in a highly extended conformation as opposed to the typical random coil present in isotropic solutions.

Further proof that the polymers formed true solutions in nematic LCs was provided by demonstrating that the polymers could be reoriented with the nematic host by application of electric fields (Fig. 10.26). Under an applied field (9 V) the nematic director and the polymer backboned aligned normal to surface of the LC test cells. This resulted in a dramatic reduction (75–80 %) in the polymer absorption and complete loss of polarization. These results are due to the realignment of the CP's transition dipole (that is coincident with the polymer's long axis) to match the direction of the electric field (normal to the surface of the test cell), which minimized the projection of the transition dipole along the electric vector of the incident light beam. The reorientation of the CPs was also readily apparent by visualizing the polymer's fluorescence in the presence (fluorescence OFF) and absence (fluorescence ON) of an applied voltage (Fig. 10.26). In all cases the polarized fluorescence was rapidly recovered upon removal of the voltage.
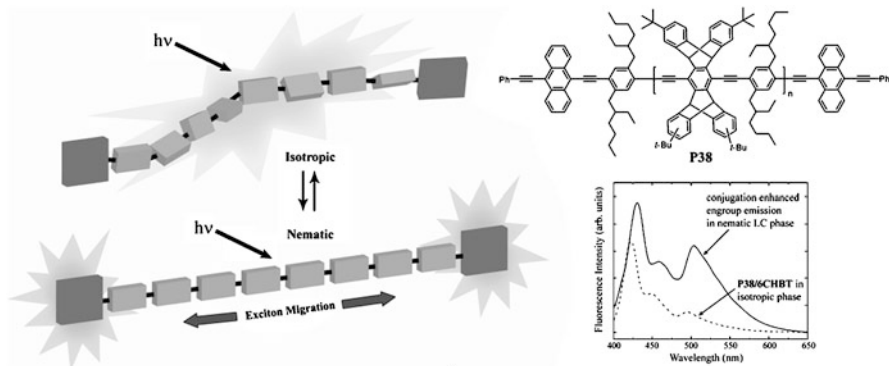
Fig. 10.27

To better illustrate the conformational dependence of energy migration in CPs, LC solutions of **P38**, which is a pentiptycene-incorporated PPE endcapped with low-energy anthracene trapping sites, were investigated (Fig. 10.27) [33]. As explained earlier, the introduction of anthracene endgroups solicits efficient energy transfer from the polymer backbone to these trapping sites and thus, site-selective, green emission from the polymer termini can be observed if significant exciton migration is operative. Therefore, dissolving **P38** in **6CHBT** allowed for the study of the rate of intrachain exciton migration under conditions of increased conjugation length and high alignment. These studies revealed that the order imposed by the nematic LC solvent increased the energy transfer efficiency to the low-energy anthracene termini. This process was accompanied by a significant increase in the fluorescence quantum yield. The liquid crystalline phase was found to be a necessary requirement for this phenomenon, as when the temperature of the system was increased above the nematic–isotropic transition temperature of the LC host, a dramatic reduction of the energy transfer efficiency and fluorescence quantum yield was observed.

Structure-property relationships that govern the extent of conformational enhancement achievable in PPE-LCs mixtures were investigated using PPEs **P39**-**41** (Fig. 10.28) [34]. These PPEs contain more elaborate iptycene scaffolds introduced to create polymers displaying greater order and enhanced solubility in LCs at high molecular weights (high molecular weight versions of **P36** and **P37** were found to be poorly soluble in nematic LCs). As expected, **P39** and **P40** displayed higher order parameters ($S_A = 0.86$ and 0.81, respectively) than both **P36** and **P37** ($S_A = 0.69$ and 0.73, respectively). Similar to observations made with **P36** and **P37**, mixtures of **P39** and **P40** in MLC-6884 (which has a negative dielectric anisotropy and a nematic phase at room temperature) displayed the same absorption red shift and band-sharpening relative to isotropic solutions, thus indicating conjugation length enhancement in LC solutions. However, **P41** did not exhibit any signs of conjugation length enhancement and hence, it appears that steric crowding in this material
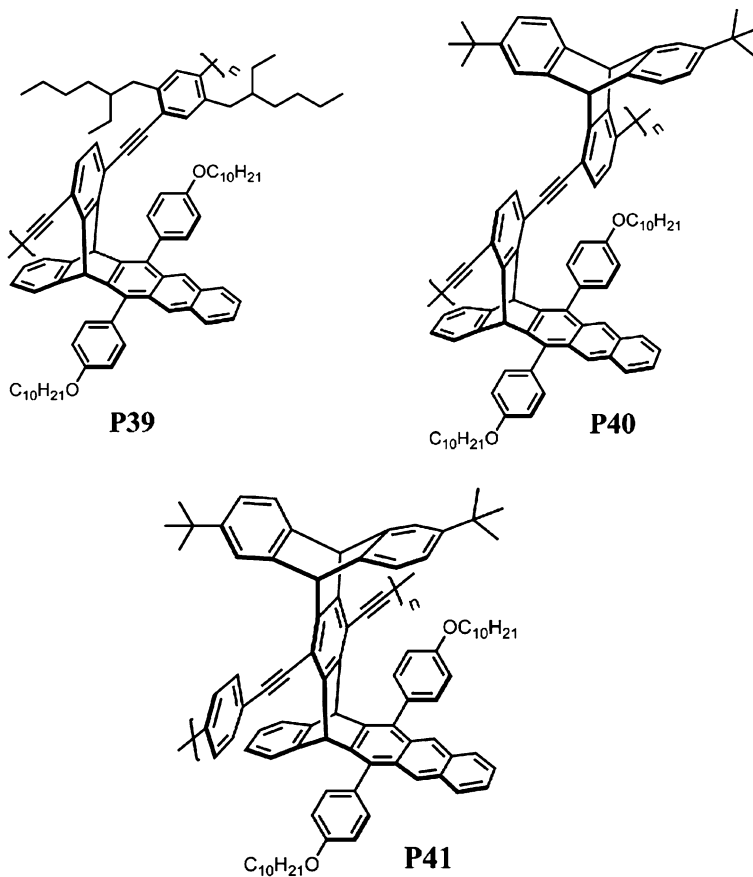
Fig. 10.28

restricts the large degree of interaction with the LC solvent necessary to promote planarization. Consistently, only low molecular weight versions of **P41** were soluble in the LC. In contrast, **P39**, with the least amount of steric congestion, showed the greatest amount of conjugation length enhancement and the highest order parameter. Therefore, it is reasonable to conclude that the role of steric congestion about the polymer mainchain plays an important role in determining the order parameter and conjugation length enhancement in PPE-LC mixtures. Additionally, molecular weight-dependent studies with **P39** revealed that order parameters as high as $S = 0.90$ can be achieved using samples with M_n greater than ca. 20,000.

Lastly, conformational and conjugation length enhancements in PPEs are not only restricted to nematic LC solvents. Lyotropic liquid crystals composed of water-potassium dodecanoate-decanol were also found to effect the same changes in PPEs (e.g., **P42**, Fig. 10.29), provided the repeat unit of the polymer contained ampiphilic side chains [35].

Fig. 10.29

P42

10.6 Conclusions

The ability of conjugated polymers to function as electronic materials is dependent on the efficient transport of excited states (excitons) along the polymer chain. Facile exciton migration in poly(*p*-phenylene ethynylene)s (PPEs) allows energy absorbed over large areas to be funneled into traps created by the binding of analytes, resulting in signal amplification in sensory devices. The energy migration in conjugated polymers can occur both *intra*molecularly and *inter*molecularly. In the case of dilute solutions, the *intra*molecular process dominates in the form of a one-dimensional exciton random walk along isolated chains. Much higher efficiency can be reached in polymer aggregates and in solid films, where the energy migration occurs as a three-dimensional process by both *intra*molecular and *inter*molecular pathways. The interplay between these two pathways has been a topic of contention, with intrachain migration being sometimes considered slow and inefficient as compared to its interchain counterpart. However, based on signal amplification of fluorescence quenching and efficient energy transfer to low-energy emissive traps in solution, we have shown that the intramolecular exciton migration in isolated polymer chains may indeed be very efficient.

A detailed understanding of intramolecular energy transfer in conjugated polymers can be elusive and is complicated by the conformational complexities that are typically associated with conjugated polymers in solutions and in thin films. Langmuir-Blodgett monolayers constitute exceptions, as the rate of energy transfer can be investigated in PPEs assembled into discrete multilayers with precise control of polymer conformation and alignment. Kinetic analyses on LB multilayers surface modified with emissive traps indicated that energy transfer was much faster in the plane defined by each layer of the polymer chains as compared to the direction normal to the chains, thereby suggesting that *intra*molecular energy transfer is faster than the *inter*molecular process.

Fluorescence depolarization studies conducted on a family of triphenylene-incorporated PPEs with long lifetimes point to the through-bond Dexter energy transfer mechanism as being the dominant energy transfer pathway for *intra*molecular exciton diffusion. Extending the lifetime of a CP was universally found to increase the degree of *intra*molecular energy migration. Inclusion of structures with extended aromatic cores into the repeat unit of a PPE generally leads to an increase in the excited state lifetime of PPEs. In addition, introduction of features that tend to localize excitations—such as biphenyl moieties, kinked polymer backbones or exciplexes—into the polymer backbone also causes dramatic increases in excited state lifetime. Generally, the photophysics of the chromophore monomer dictate the excited state behavior of the corresponding conjugated polymers.

Emissive polymer films with modest to high quantum yields of fluorescence usually have limited electronic interaction between polymer chains, and in this case interchain energy migration is generally accepted to occur through the dipole-induced dipole mechanisms. The three-dimensional nature of energy migration in films usually leads to longer exciton diffusion lengths, but often is accompanied by formation of low-emissive intermolecular species, resulting in diminished emission quantum yields. However, incorporation of rigid, three-dimensional scaffolds, such as iptycenes and cyclophanes, can encourage an oblique packing of the chromophore units of a conjugated polymer, thus allowing the formation of electronically-coupled aggregates that retain high quantum yields of emission.

The rigid iptycene scaffolds also act as excellent structural directors that encourage complete solvation of PPEs in a liquid crystal solvent. LC-PPE mixtures display both an enhanced conformational alignment of polymer chains and extended effective conjugation lengths relative to isotropic solutions.

References

1. McQuade DT, Pullen AE, Swager TM (2000) Conjugated polymer-based chemical sensors. Chem Rev 100:2537–2574
2. McGehee MD, Heeger AJ (2000) Semiconducting (conjugated) polymers as materials for solid-state lasers. Adv Mater 12:1655–1668
3. Samuel IDW, Crystall B, Rumbles G, Burn PL, Holmes AB, Friend RH (1993) The efficiency and time-dependence of luminescence from poly(*p*-phenylene vinylene) and derivatives. Chem Phys Lett 213:472–478
4. Goldfinger MB, Swager TM (1994) Fused polycyclic aromatics via electrophile-induced cyclization reactions: application to the synthesis of graphite ribbons. J Am Chem Soc 116:7895–7896
5. Schwartz BJ (2003) Conjugated polymers as molecular materials: how chain conformation and film morphology influence energy transfer and interchain interactions. Annu Rev Phys Chem 54:141–172
6. Zhou Q, Swager TM (1995) Methodology for enhancing the sensitivity of fluorescent chemosensors: energy migration in conjugated polymers. J Am Chem Soc 117:7017–7018
7. Allwood BL, Spencer N, Shahriari-Zavareh H, Stoddart JF, Williams DJ (1987) Complexation of paraquat by a bisparaphenylene-34-crown-10 derivative. J Chem Soc Chem Comm 14:1064–1066

8. Lakowicz JR (2006) Principles of fluorescence spectroscopy, 3rd edn. Springer, New York, pp 9–12
9. Zhou Q, Swager TM (1995) Fluorescent chemosensors based on energy migration in conjugated polymers: the molecular wire approach to increased sensitivity. J Am Chem Soc 117:12593–12602
10. Swager TM, Gil CJ, Wrighton MS (1995) Fluorescence studies of poly(*p*-phenyleneethynylene)s: the effect of anthracene substitution. J Phys Chem 99:4886–4893
11. Cotts PM, Swager TM, Zhou Q (1996) Equilibrium flexibility of a rigid linear conjugated polymer. Macromolecules 29:7323–7328
12. Yang J-S, Swager TM (1998) Fluorescent porous polymer films as TNT chemosensors: electronic and structural effects. J Am Chem Soc 120:11864–11873
13. Wegner G (1992) Ultrathin films of polymers: architecture, characterization and properties. Thin Solid Films 216:105–116
14. Kim J, McQuade DT, Rose A, Zhu Z, Swager TM (2001) Directing energy transfer within conjugated polymer thin films. J Am Chem Soc 123:11488–11489
15. Satrijo A, Kooi SE, Swager TM (2007) Enhanced luminescence from emissive defects in aggregated conjugated polymers. Macromolecules 40:8833–8841
16. Satrijo A, Swager TM (2007) Anthryl-doped conjugated polyelectrolytes as aggregation-based sensors for nonquenching multicationic analytes. J Am Chem Soc 129:16020–16028
17. Turro NJ (1991) Modern molecular photochemistry. University Science, California, pp 357–359
18. Yang J-S, Swager TM (1998) Porous shape persistent fluorescent polymer films: an approach to TNT sensory materials. J Am Chem Soc 120:5321–5322
19. Sato T, Jiang D-L, Aida T (1999) A blue-luminescent dendritic rod: poly(phenyleneethynylene) within a light-harvesting dendritic envelope. J Am Chem Soc 121:10658–10659
20. Bredas J-L, Cornil J, Beljonne D, dos Santos DA, Shuai Z (1999) Excited-state electronic structure of conjugated oligomers and polymers: a quantum chemical approach to optical phenomena. Acc Chem Res 32:267–276
21. Kasha M (1976) In: Di Bartollo B (ed) Spectroscopy of the excited state. Plenum, New York, pp 337–363
22. Zahn S, Swager TM (2002) Three-dimensional electronic delocalization in chiral conjugated polymers. Angew Chem Int Ed 41:4226–4230
23. Deans R, Kim J, Machacek MR, Swager TM (2000) A poly(*p*-phenyleneethynylene) with a highly emissive aggregated phase. J Am Chem Soc 122:8565–8566
24. Levitsky IA, Kim J, Swager TM (1999) Energy migration in a poly(phenylene ethynylene): determination of interpolymer transport in anisotropic Langmuir-Blodgett films. J Am Chem Soc 121:1466–1472
25. Rose A, Tovar JD, Yamaguchi S, Nesterov EE, Zhu Z, Swager TM (2007) Energy migration in conjugated polymers: the role of molecular structure. Phil Trans R Soc A 365:1589–1606
26. Rose A, Lugmair CG, Swager TM (2001) Excited-state lifetime modulation in triphenylene-based conjugated polymers. J Am Chem Soc 123:11298–11299
27. Yamaguchi S, Swager TM (2001) Oxidative cyclization of Bis(biaryl)acetylenes: synthesis and photophysics of dibenzo[g, p]chrysene-based fluorescent polymers. J Am Chem Soc 123:12087–12088
28. Tovar JD, Rose A, Swager TM (2002) Functionalizable polycyclic aromatics through oxidative cyclization of pendant thiophenes. J Am Chem Soc 124:7762–7769
29. Boden N, Movaghar B (1998) In: Demus D, Goodby J, Gray GW, Spies HW, Will V (eds) Hand book of liquid crystals: low molecular weight liquid crystals, Vol. 2b, Chapter IX. Wiley, New York, p. 781
30. Long TM, Swager TM (2001) Minimization of free volume: alignment of triptycenes in liquid crystals and stretched polymers. Adv Mater 13:601–604
31. Long TM, Swager TM (2002) Using 'internal free volume' to increase chromophore alignment. J Am Chem Soc 124:3826–3827

32. Zhu Z, Swager TM (2002) Conjugated polymer liquid crystal solutions: control of conformation and alignment. J Am Chem Soc 124:9670–9671
33. Nesterov EE, Zhu Z, Swager TM (2005) Conjugation enhancement of intramolecular exciton migration in poly(*p*-phenylene ethynylene)s. J Am Chem Soc 127:10083–10088
34. Ohira A, Swager TM (2007) Ordering of poly(*p*-phenylene ethynylene)s in liquid crystals. Macromolecules 40:19–25
35. Bouffard J, Swager TM (2008) Self-assembly of amphiphilic poly(phenylene ethynylene)s in water-potassium dodecanoate-decanol lyotropic liquid crystals. Chem Commun 42:5387–5389

11
Coherent Control of Biomolecules and Imaging Using Nanodoublers

L. Bonacina and Jean-Pierre Wolf

11.1 Introduction

In the quest for the next generation of imaging bio-markers, successful probes have to prove to be non toxic, bright, stable against long term excitation, and able to generate a sharp contrast against background fluorescence. In all these respects, Harmonic Nanoparticles (HNPs, "nanodoublers") are receiving an increasing attention as they also open a series of alternative detection possibilities simply not accessible with the present generation of fluorescent dyes and quantum dots. In the first part of the chapter, we report on this novel labelling method with unprecedented wavelength flexibility, enabled by the non-resonant nature of the second harmonic process. The possibility of employing infrared excitation and the consequent deeper tissue penetration is especially promising for their in vivo applications [1]. The phase-coherent optical response of HNPs can also be exploited to fully characterize the excitation laser pulse in the focal spot of a high-NA objective with nanometric resolution. This proof-of-principle "nano-FROG" experiment [2] sets the ground for further phase-sensitive self-referenced applications, after the recent demonstration of harmonic holography and heterodyne detection with external references.

Although significant progress has been achieved in the quest for better bio-markers, such as the above mentioned HNPs, the ultimate goal would be the use of no external probe for achieving "label-free" imaging. In the last decade coherent control with optimally tailored ultrashort laser pulses revolutionized molecular spectroscopy. It allowed not only observing with unprecedented detail the atomic

L. Bonacina (✉) • J.-P. Wolf
GAP-Biophotonics, University of Geneva, 22, chemin de Pinchat, 1211 Geneva, Switzerland
e-mail: jean-pierre.wolf@unige.ch

motion within molecules but also controlling it. In the second part of this chapter, we present how coherent control might significantly contribute towards the goal of label-free imaging using only endogenous molecular processes.

After an introduction of the basic processes and techniques used in coherent control, we concentrate on recent achievements in the field of coherent manipulation of biological objects. Particular interest will be dedicated to the discrimination of biological molecules that exhibit almost identical linear spectra and the wealth of related applications, such as fluorescent label free microscopy, and specific detection of pathogens in air and water. Recent experiments indeed demonstrated that discrimination between amino acids and similar organic moiety lacking the peptidic backbone was possible using sequences of multicolour pulses. Similar approaches allowed discriminating bacteria from non-biological organic particles such as soot [3, 4]. But the most striking feature of coherent control schemes based on optimally tailored UV pulses was recently the demonstration of its ability to discriminate nearly identical cellular vitamins (riboflavin (RBF) vs. its phosphated counterpart flavin mononucleotide (FMN))[5–7], which exhibit identical (linear) spectroscopic signatures. This latter demonstration opens therefore very attractive perspectives for label free imaging of cellular metabolism (e.g. quantification of NAD's concentration in mitochondria) and early cancer detection.

11.2 Harmonic Nanodoublers as Inherent Nonlinear Probes for Multi-photon Imaging

The development of imaging labels for microscopy has followed some unexpected routes in the last decade. Superresolution techniques based on stochastic intensity fluctuations have redefined the very requirements on fluorophores, shifting the focus on the possibility of photo-activation and of tailoring dark states lifetimes rather than increasing stability against bleaching. On the other hand, the growing availability of nonlinear microscopy systems based on tunable Ti:Sapphire lasers, thanks to their intrinsic three dimensional sectioning capability, has raised the demand for photo-stable fluorophores with two-photon absorption bands in the near infrared (to limit sample degradation and increase image depth) and narrow emission bands (to be better distinguished from autofluorescence background). In parallel to these efforts committed to improving fluorescent labels, since 2005, a completely different approach has appeared promoting the use of a novel family of inherently nonlinear harmonic nanoparticles (HNPs), such as nanodoublers, expressly conceived for multi-photon microscopy. These labels, based on inorganic noncentrosymmetric crystals, possess a series of attractive properties as compared to fluorescent dyes, including: (i) complete absence of bleaching and blinking, (ii) narrow emission bands, (iii) excitation-wavelength tunability, (iv) orientation retrieval capability, and (v) coherent optical response. So far, only a few of the possibilities opened by these nanoprobes have been shown by a very restrict number of research groups beyond ours, but it is clear that their outreach is significantly greater than what these proof-of-principle experiments have demonstrated (Fig. 11.1).

Fig. 11.1 Multi-photon image of breast cancer cells (MDA-MB-436) stained with a membrane dye and treated with KNbO3HNPs
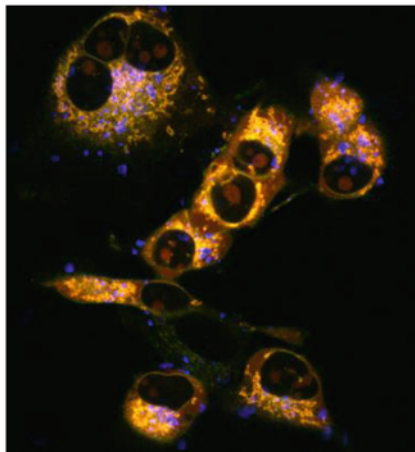
The principal results we obtained in this field in the last 5 years are summarized in Fig. 11.2. The noncentrosymmetric crystal structure is at the origin of the second-order nonlinear properties of this family of particles. So far, a series of nanomaterials including: $LiNbO_3$, $KNbO_3$, $BaTiO_3$, $Fe(IO_3)_3$, ZnO, KTP have been studied. From their common lack of crystal inversion symmetry, it follows that the second order susceptibility tensor, $\chi^{(2)}$, presents not vanishing elements, sustaining a nonlinear polarization at frequency 2ω when excited by an electromagnetic field E^ω at frequency ω

$$P_i^{(2\omega)} = \varepsilon_0 \sum_{jk} \chi_{ijk}^{(2)} E_j^\omega E_k^\omega$$

The different materials tested belong to different symmetry point groups with characteristic $\chi^{(2)}$ tensor elements, thus they yield different responses in polarization-resolved nonlinear microscopy. Being function of individual nanoparticles orientation, these responses can be exploited for optical orientation retrieval and electric field probing at microscopic scale (see refs. [8] and [9] for details).

Because harmonic generation is a nonresonant process, no absorption occurs. As a consequence, no energy is converted into heat, preventing sample photo-degradation. Moreover signal bleaching and blinking observed with fluorescent dyes and quantum dots are completely absent, as one can appreciate from the comparison in Fig. 11.2, showing the signal decay as a function of irradiation time for HNPs and a cell staining dye simultaneously imaged for several consecutive hours.

Interestingly, given that the coherent length of the nonlinear excitation process is longer than the typical dimensions of the nanoparticles (<100 nm), no phase-matching constraints apply and any wavelength can be used for excitation [1, 10]. We have demonstrated such broad excitation tunability under different experimental
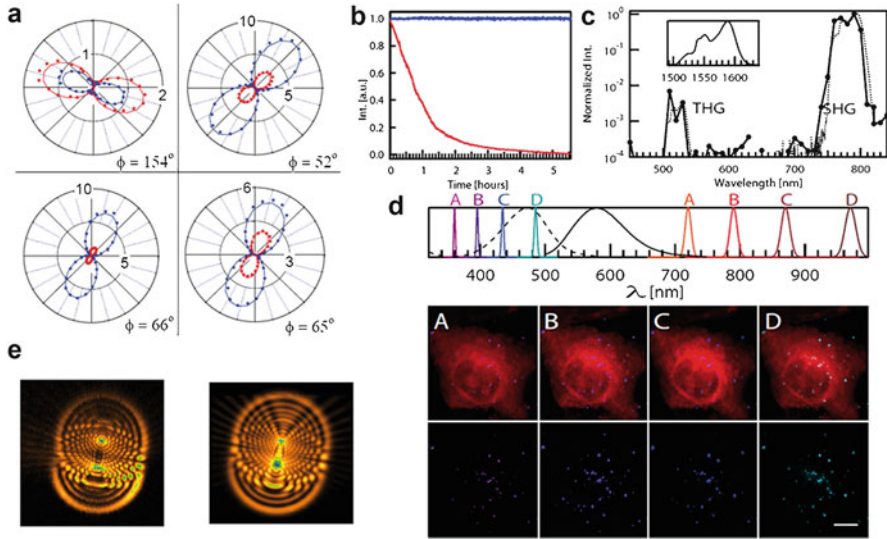
Fig. 11.2 (**a**) The polarized emissions of individual HNPs bear information about their local three-dimensional orientation, in the plots Φ corresponds to the HNP in-plane angle [8]. (**b**) The excellent photostability upon continuous laser irradiation for several hours of HNPs is compared with the decreasing signal of a fluorescent dye imaged simultaneously. (**c**) The absence of phase-matching constraints allows complete doubling of any input pulse bandwidth. A single HNP up-converts the spectrum of a Erbium ion laser at 1,550 nm (*inset*) generating simultaneously SH and TH. The experimental spectral bandwidths are compared with the calculated ones (*dotted lines*). (**d**) A dye-stained cells treated with HNPs is imaged at different wavelengths within the range of a Ti:Sapphire laser. *Upper plots*: all detection channels overlaid, *lower plots*: single detection channels *A*,*B*, *C*, and *D*. The frequency-doubled signal from the HNPs appear each time uniquely in a narrow spectral detection region. (**e**) *Left image*. Coherent interference pattern between the emissions of two nanoparticles adjacently lying on a waveguide nonlinearly excited by an evanescent wave. *Right image*. Numerical simulations (in collaboration with J. Enderlein, University of Goettingen)

conditions, with laser pulses ranging from vis–UV (400 nm) to IR (1.5 um). As an example, Fig. 11.1 shows the responses of Polyethylene Glycol (PEG)-coated LiNbO3 HNPs attached to breast cells membranes stained with FM 1-43FX membrane dye. The response of the nanoparticles can be excited at any wavelength within the Ti:Sapphire spectrum (700–1,100 nm). The optimal contrast obtained with respect to this standard fluorescent dye, widely used for biological assays, testifies the appeal of this approach for in vitro cell imaging. Longer wavelength excitation, due to the reduced tissue scattering, is indeed very promising for extending the penetration depth of imaging techniques and decreasing sample photo-damage. In Fig. 11.1, as a demonstration, the second and third harmonic spectra generated by a single HNP excited by a 1.55 μm laser show the complete up-conversion of the original laser bandwidth (dotted line).

Finally, Fig. 11.1, shows the most clearly, the coherent nature of the emission of HNPs as opposed to fluorescence. Two neighbouring KTP nanoparticles lying on

a waveguide are excited at the second harmonic (SH) by the evanescent mode of a laser pulse propagating through the guide. The two emission patterns interfere coherently at the CCD detector [9]. The accompanying image is a numerical simulation of this observation. So far, what we believe is the immense imaging potential of this coherent response has not been fully exploited, just a series of demonstration measurements have been published on especially conceived set-ups: heterodyne detection[11] of nanoparticles for sensitivity increase, harmonic holography[12], digital phase conjugation[13, 14], and our work on spatially resolved pulse phase-retrieval for microscopy (nano-FROG)[2].

The motivations of the nano-FROG procedure reside on the demand for a versatile and reliable pulse phase-sensitive characterization technique, more and more critical as a number of nonlinear approaches have recently been bridged from spectroscopy to imaging. Just to mention a few examples, pulse-shaping has been applied to temporally recompress femtosecond pulses at the measuring site, to improve spatial resolution, and to increase fluorescence excitation and harmonic generation yield [15]. Intra-pulse micro-CARS [16, 17] and coherent control microscopy have demonstrated successful for obtaining higher selectivity in the imaging of structures in very diverse samples[18]. Furthermore, interest has been focused on the effects of pulse polarization, and the related capability to achieve control of optical near field [19]. To fully exploit the potential of these techniques, equally developed pulse diagnostics capabilities are necessary. In particular, considering that femtosecond pulses are prone to undergo modifications during their propagation (temporal stretching by group velocity dispersion, higher order distortions in the spectral-phase induced by microscope objectives [20], spectral amplitudes modulation by sample scattering [21] and absorption) an in situ measurement of the excitation pulse is customary for any advanced application. Since the early work of Muller et al. [22], several techniques, largely based on Frequency Resolved Optical Gating (FROG), have been proposed, but until present none of them incorporates the spatial resolution necessary to resolve features inside the focal region of a high numerical aperture (NA) objective [23]. The starch-based FROG approach proposed by Amat et al. [24] and the scanning SEA TADPOLE technique by the group of Trebino [25] represented a clear progress in this direction, but unfortunately both techniques are limited to a spatial resolution of a few micrometers. We have proposed a technique to achieve unprecedented spatial resolution, without renouncing at the tenability of the FROG technique.

The approach, which can be implemented on a conventional or an inverted laser scanning microscope, is based on the use of individual HNPs as nonlinear medium. An exemplary FROG trace, like the one presented in Fig. 11.3 can be obtained by spectrally resolving the autocorrelation trace of a single HNP and then by filtering out the modulation components in the Fourier space. Successively, the inverse Fourier transform can be applied to return back to the time/wavelength space. The so treated data can successively be fed into a commercial FROG-inversion program [22] to determine the actual pulse characteristics. The typical retrieval error corresponds to $2.50 = 00$. The retrieved FROG trace is shown in Fig. 11.3 (lower plots series), along with pulse electric field intensity temporal profile and spectrum
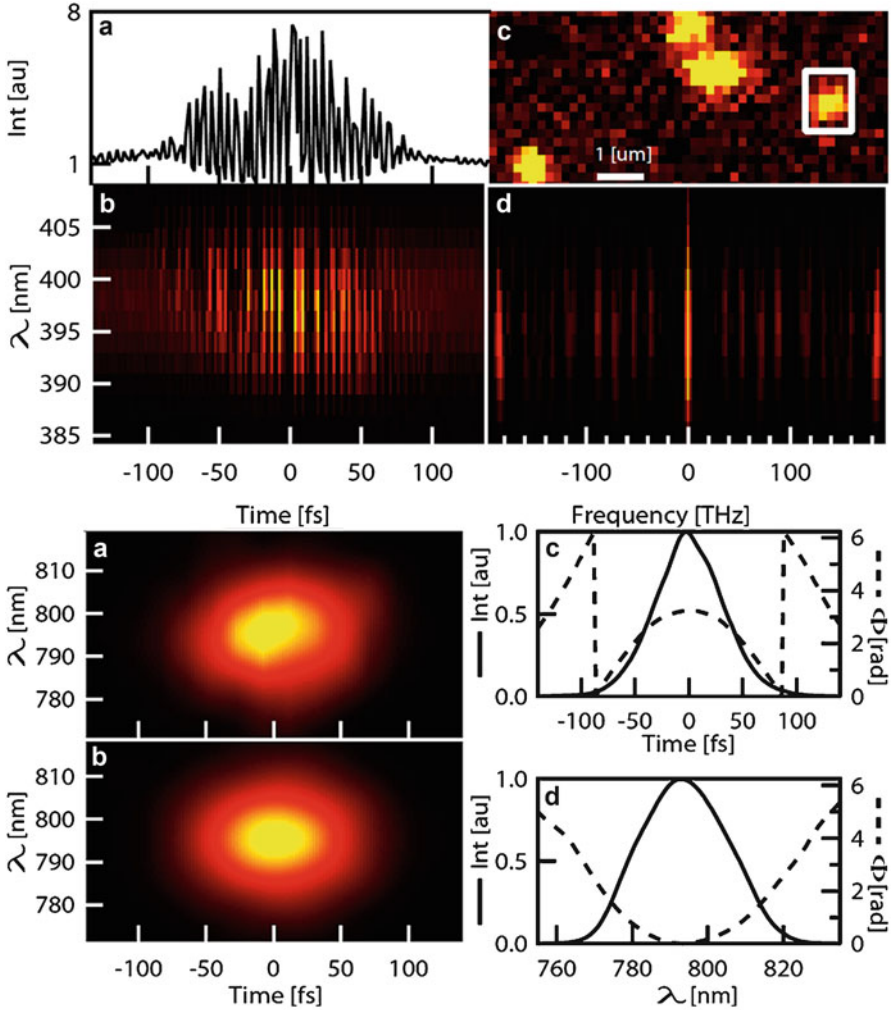
Fig. 11.3 *Upper plots.* (**a**). Interferometric autocorrelation trace. (**b**). cFROG trace. (**c**). Image of the nanoparticles dispersed on a microscopic glass slide. The particle highlighted by the 1 mm square was used as nonlinear medium for acquiring the autocorrelation and the cFROG trace. (**d**). Result of the Fourier transform along the time axis of the cFROG trace in **b**. *Lower plots.* Experimental FROG trace. (**b**). Retrieved FROG trace. Electric field intensity (*solid line*) and phase (*dashed line*) as a function of time (**c**) and of wavelength (**d**) (From Ref. [2])

reported in (c) and (d). The corresponding phase-functions are also shown. The latter indicate the presence of a residual quadratic chirp on the pulse due to group velocity dispersion accumulated during propagation through the microscope optics, which is not fully corrected by the grating compressor.

11.3 Basics of Coherent Control

Coherent control has induced a revolution in photochemistry. Not only can the atomic motion be observed within molecules by snapshots of a few femtoseconds duration, it can now also be controlled. The basic idea of this revolution is the use of quantum interference between different states that are in coherent superposition so that a target state is reached with maximum probability. A key element for achieving this control is the transfer of coherence from the exciting light field to the atomic or molecular system via the electric dipole operator. A tailored coherent laser pulse is used to excite a molecule in a superposition of states, which drives the molecule along a specific path to obtain a targeted result.

A famous example of coherent control is the Tannor, Koslov and Rice [26, 27] "pump-dump" method, in which many vibrational states of a molecule ABC are coherently excited for generating a vibrational wavepacket. This wavepacket explores, as a function of time, a large fraction of the electronically excited hypersurface. By shining a second laser at convenient times t1 or t2, the molecule is brought back to its ground state onto different dissociation paths, resulting in different species $AB + C$ or $A + BC$. The system can thus be driven to a specific daughter fragment by using the quantum control of the photodissociation process.

In 1992, H. Rabitz at Princeton University introduced [28, 29] the concept of "optimal control", in which a feedback loop optimizes the laser pulse characteristics in order to most efficiently reach the desired target. For this, a large number of parameters (corresponding to the amplitude and phase of each spectral component within the exciting laser spectrum) have to be controlled. This "pulse shaping" technique is usually performed by introducing a liquid crystal array in the Fourier plane between 2 gratings (4f arrangement) [30]. Excellent results in terms of efficiency have been obtained using genetic-type optimization algorithms [31–33].

Besides the above mentioned "pump-dump" scheme, other successful control methods have been extensively applied, including stimulated Raman scattering (STIRAP), Four Wave Mixing like CARS (Coherent AntiStokes Raman Scattering), multiphoton absorption and multiphoton ionization. The controlled targets can be, for instance, specific fragments, specific isomers or specific isotopes, but also the enhancement or reduction of the fluorescence of a specific molecule (by driving it preferentially into other relaxation pathways). In this respect, a pioneering work has been performed by the group of G. Gerber [34, 35], in which the capability of distinguishing two different dyes using two-photon absorption control was demonstrated, although the dyes had similar linear absorption and fluorescence spectra.

An attractive application is the ability of discriminating different biological systems that are usually undistinguishable with standard linear spectroscopic approaches. This is the approach that is followed in this chapter in order to reach label-free imaging of biological structures or the detection and identification of harmful bacteria.

11.4 Detection of Airborne Bacteria

11.4.1 Multi-photon-Excited Fluorescence (Mpef)
and Discrimination of Bioaerosols

We recently demonstrated that manipulating the excited states dynamics of biomolecules allows for distinguishing biological microparticles from nonbiological PAH (Polycyclic Aromatic Hydrocarbons)-containing ones. More precisely, we could distinguish amino acids (Tryptophan, Trp) and flavins (riboflavin RBF, FMN and FAD) from PAHs (naphthalene) and diesel fuel in the liquid phase using a "Pump-Probe Deletion" (PPD) technique. We also showed that the non-linear properties of aerosols and droplets produce a strong backward enhancement of the emitted light, which is most favorable for remote sensing applications.

The most prominent feature of non-linear processes in aerosol particles using femtosecond laser pulses is a strong localization of the emitting molecules within the particle, and subsequent backward enhancement of the emitted light [36–39]. This unexpected behavior is very attractive for remote detection schemes, such as Lidar applications.

As already mentioned, a major drawback inherent in LIF instruments is the lack of selectivity because UV–vis fluorescence is incapable of discriminating different molecules with similar absorption and fluorescence signatures. While mineral and carbon black particles do not fluoresce significantly, aromatics and polycyclic aromatic hydrocarbons from organic particles and diesel soot strongly interfere with biological fluorophors such as amino acids. The similarity between the spectral signatures of PAHs and biological molecules under UV excitation lies in the fact that similar π-electrons from carbonic rings are involved. Therefore, PAHs (from Diesel soot for instance) exhibit absorption and emission bands similar to those of amino acids like Tryptophan (Fig. 11.4). Some shifts are present because of differences in specific bonds and the number of aromatic rings, but the broad featureless nature of the bands renders them almost indistinguishable.
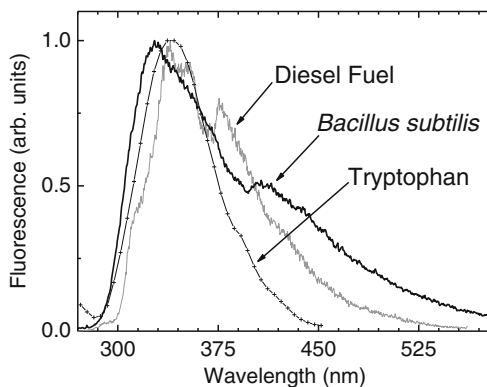

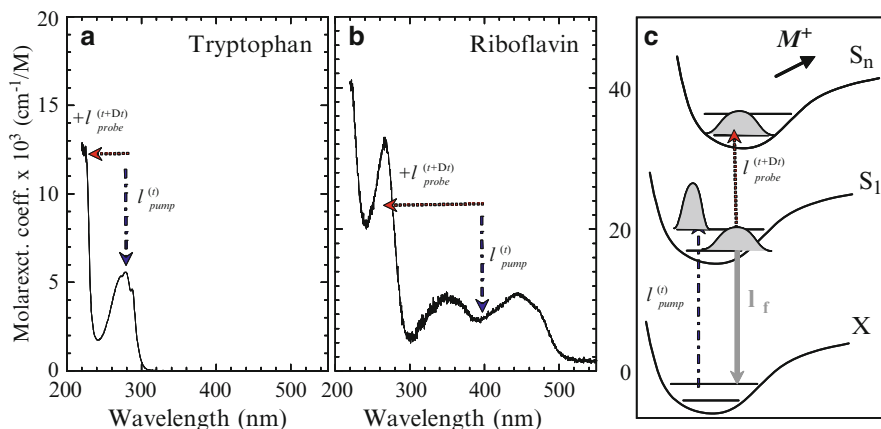**Fig. 11.4** Comparison of the fluorescence spectra of Tryptophan, *B. Subtilis* and Diesel fuel (From Ref. [3])

Fig. 11.5 Absorption spectra of Tryptophan (**a**) and Riboflavin (**b**). (**c**) PPD scheme in Trp, flavins and polycyclic aromatics. The pump pulse brings the molecules in their first excited state S1. The S1 population (and therefore the fluorescence) is depleted by the second probe pulse (From Ref. [40])

In order to discriminate these fluorescing molecules we applied a novel femtosecond pump-probe depletion (PPD) concept. It is based on the time-resolved observation of the competition between excited state absorption (ESA) into higher lying excited states and fluorescence into the ground state. This approach makes use of two physical processes beyond that available in the usual linear fluorescence spectroscopy: (1) the dynamics in the intermediate pumped state (S1) and (2) the coupling efficiency to higher lying excited states (Sn).

As shown in Fig. 11.5, a first femtosecond pump pulse (at 270 nm for Trp and PAHs, 405 nm for flavins), resonant with the first absorption band of the fluorophores, coherently excites them from the ground state S0 to a set of vibronic levels S1{v'}. The vibronic excitation relaxes by internal energy redistribution to lower {v} modes. Fluorescence relaxation to the ground state occurs within a lifetime of several nanoseconds. Meanwhile, a second 810 nm femtosecond probe pulse is used to transfer part of the S1{v'} population to higher lying electronic states Sn.

The depletion of the S1 population under investigation depends on both the molecular dynamics in this intermediate state and the transition probability to Sn. The relaxation from the intermediate excited state may be associated with different processes, including charge transfer, conformational relaxation(52, 53) and intersystem crossing with repulsive $\pi\sigma^*$ states [41].

Sn states are both autoionizing and relaxing radiationless into S0. By varying the temporal delay Δt between the UV–vis and the IR pulses, the dynamics of the internal energy redistribution within the intermediate excited potential hypersurface S1 is explored. The S1 population and the fluorescence signal are therefore depleted as a function of Δt. As different species have distinct S1 hypersurfaces, discriminating signals can be obtained [3, 4].
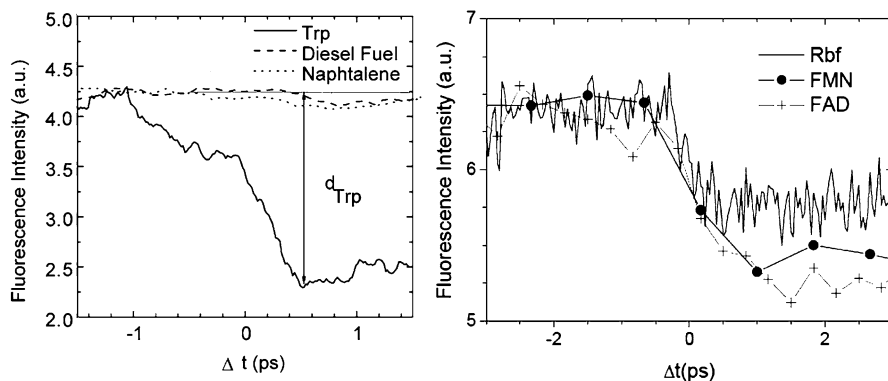
Fig. 11.6 *Left*: PPD experiment on Trp and PAHs, demonstrating discrimination capability between the amino acid and other aromatic molecules. *Right*: Similar results obtained in flavins (From Ref. [40])

Figure 11.6 (left) shows the PPD dynamics of S1 in Trp as compared to diesel fuel and naphthalene in cyclohexane, one of the most abundant fluorescing PAHs in diesel. While depletion reaches as much as 50 % in Trp, diesel fuel and naphthalene appear almost unaffected (within a few percent), at least on these timescales [3, 4].

The depletion factor δ is defined as $\delta = (P_{undepleted} - P_{depleted})/P_{undepleted}$ (where P is the fluorescence power). This remarkable difference allows for efficient discrimination between Trp and organic species, although they exhibit very similar linear excitation/fluorescence spectra.

Two reasons might be invoked to understand this difference: (1) the intermediate state dynamics are predominantly influenced by the NH- and CO- groups of the amino acid backbone and (2) the ionization efficiency is lower for the PAHs. Further electronic structure calculations are required to better understand the process, especially on the higher lying Sn potential surfaces.

Fluorescence depletion has been obtained as well for RBF, FMN, and FAD (Fig. 11.6, right). However, the depletion in this case is only about 15 % (with a maximum intensity of 5×10^{11} W/cm2 at 810 nm).

In order to more closely approach the application of detecting and discriminating bioagents from organic particles, we applied PPD spectroscopy to live bacteria ($\lambda_1 = 270$ nm and $\lambda_2 = 810$ nm), such as *Escherichia coli*, *Enterococcus* and *Bacillus subtilis*. Artefacts due to preparation methods have been discarded by using a variety of samples, i.e. lyophilized cells and spores, suspended either in pure or in biologically buffered water (i.e. typically 10^7–10^9 bacteria per cc). The bacteria containing solutions replaced the Trp or flavin containing solutions of the formerly described experiment. The observed pump-probe depletion results are remarkably robust (Fig. 11.7), with similar depletion values for all the considered bacteria (results for *Enterococcus*, not shown in the figure, are identical), although the Trp microenvironment within the bacteria proteins is very different from water.
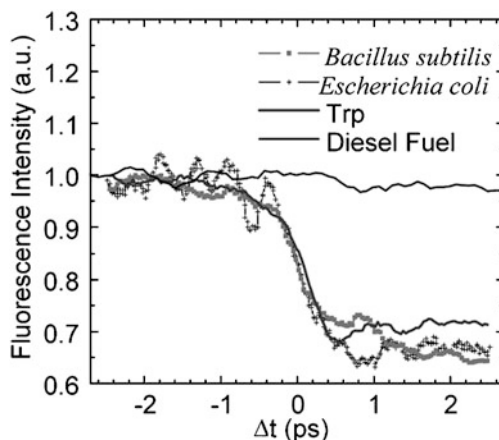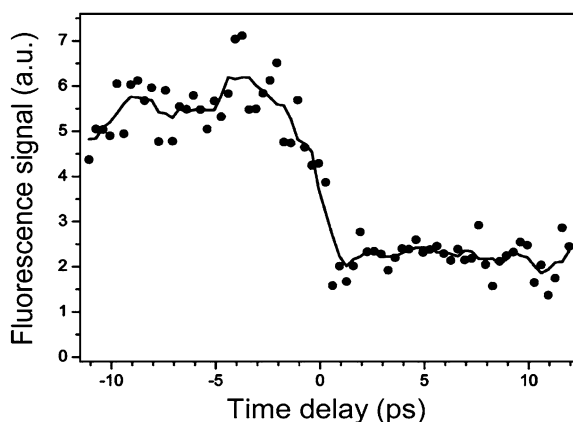
On the other hand the very similar depletion behaviour for all bacteria and Trp also shows the limitations of PPD spectroscopy in the present configuration. Biomolecules can be distinguished from other aromatics but PPD is unable to discriminate two different bacteria in solution.

We finally investigated bacteria embedded in microdroplets, as it usually occurs in nature. Saliva drops (coughing, breathing, speaking, etc.) are indeed the most current infectious vectors.

The most impressive result of these experiments is the very high PPD efficiency as compared to depletion ratios in liquids. In particular, we used PPD on 20 μm water droplets containing typically 100 live bacteria (*Escherichia coli*). As shown in Fig. 11.8, the depletion factor δ is enhanced as compared to bacteria in bulk water: 60 % depletion in the microdroplet and 20 % in solution ($\lambda_1 = 270$ nm, $\lambda_2 = 810$ nm).
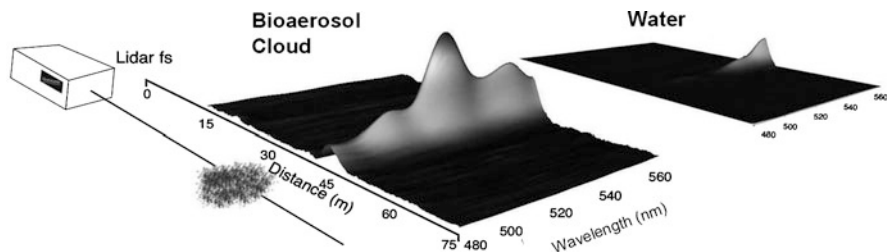
Fig. 11.9 2-Photon Excited Fluorescence Lidar detection of bioaerosols (From Ref. [43])

Some tentative explanations could be (1) The spatial overlap between pump and probe pulses might be enhanced by the shape of the droplet, or (2) The spherical shape induces hot spots inside the droplet where intensities are up to 100 times higher than the incident one, but the total hot spot volume is rather small.

11.4.2 Remote Discrimination of Bioaerosols

The first multiphoton excited fluorescence Lidar detection of biological aerosols was performed using the "Teramobile" system. The Teramobile (http://www.teramobile.org) is the first femtosecond-terawatt laser based Lidar [42, 43], and was developed by a French-Swiss-German consortium.

The bioaerosol particles, consisting of 1 μm size water droplets containing 0.03 g/l Riboflavin (typical for bacteria), were generated at a distance of 50 m from the Teramobile system. Riboflavin was excited by two photons at 800 nm and emitted a broad fluorescence around 540 nm. This experiment [42, 43] is the first demonstration of the remote detection of bioaerosols using a 2-PEF-femtosecond Lidar. The broad fluorescence signature is clearly observed from the particle cloud (typ. 10^4 p/cm^3), with a range resolution of a few meters (Fig. 11.9). As a comparison, droplets of pure water do not exhibit any parasitic fluorescence in this spectral range. However, a background is observed for both types of particles, arising from the scattering of white light generated by filaments in air.

Primarily, MPEF might be advantageous as compared to linear LIF for the following reasons: (1) MPEF is enhanced in the backward direction as seen above and (2) the transmission of the atmosphere is much higher for longer wavelengths. For example, if we consider the detection of tryptophan (which can be excited with three photons of 810 nm), the transmission of the atmosphere is typically 0.6 km^{-1} at 270 nm, whereas it is 3×103 km^{-1} at 810 nm (for a clear atmosphere, depending on the background ozone concentration). This compensates the lower 3-PEF cross-section compared to the 1-PEF cross-section at distances larger than a couple of kilometers [43]. The most attractive feature of MPEF is, however, the possibility of using pump-probe techniques, as described hereafter in order to discriminate bioaerosols from background interferents such as traffic related soot and PAHs.

It is interesting to notice that at these high intensities, competing processes occur such as LIBS (Laser Induced Breakdown Spectroscopy). The ionization potential of water molecules is 6.5 eV, so that five photons are required at a laser wavelength of 800 nm to initiate the process of plasma formation. Both localization and backward enhancement strongly increase with the order n of the multiphoton process, exceeding $Rf = 35$ for $n = 5$ (38). As for MPEF, LIBS has the potential of providing information about the aerosols composition, as was demonstrated for bacteria.

Although nanosecond-laser LIBS (nano-LIBS) has already been applied to the study of bacteria [44, 45], femtosecond lasers open new perspectives in this respect. The plasma temperature is indeed, much lower in the case of femtosecond excitation, which strongly reduces the blackbody radiation background and interfering lines from excited N2 and O2. This allows performing time gated detection with very short delays, and thus observing much richer and cleaner spectra from biological samples [46–48].

11.5 Use of Optimal Control for Discriminating Almost Identical Bio-Systems

The identification or discrimination of molecules and quantum systems that are nearly identical (proteins, bacteria, etc..) is normally an exceedingly difficult task. The conventional means of addressing this common need is through various static spectroscopic techniques, which can be especially difficult in complex remote environments. However, recent theoretical work showed that two or more quantum systems, even if they differ only infinitesimally, may be drawn apart to have distinct signatures through tailored control of their dynamics. Ultrafast broad bandwidth lasers with adaptive pulse shaping provide a means to implement this theoretical concept through controlled quantum optimal dynamic discrimination (ODD) [49]. In collaboration with the group of H. Rabitz at Princeton University, we demonstrated the capabilities of ODD by discriminating between two almost identical molecules of riboflavin (RBF) and flavin mononucleotide (FMN) in water solution, which have virtually identical linear absorption and fluorescence spectra (see Fig. 11.10) [7]. The successful implementation of ODD opens up numerous applications including in fluorescence microscopy, protein identification, as well as possible remote discrimination of different bacteria. A key component of ODD is operation with shaped laser pulses, which can nonlinearly interact with the molecules to fully exploit their dynamical capabilities and create discriminating signatures. The similar optical spectra of RBF and FMN arise from the common isoalloxazine ring with the only distinguishing feature being changes at the end of the side chain tail (Fig. 11.10).

The present application of ODD utilizes a control field consisting of a shaped ultraviolet (UV) portion at 400 nm and a near infrared (IR) component at 800 nm,
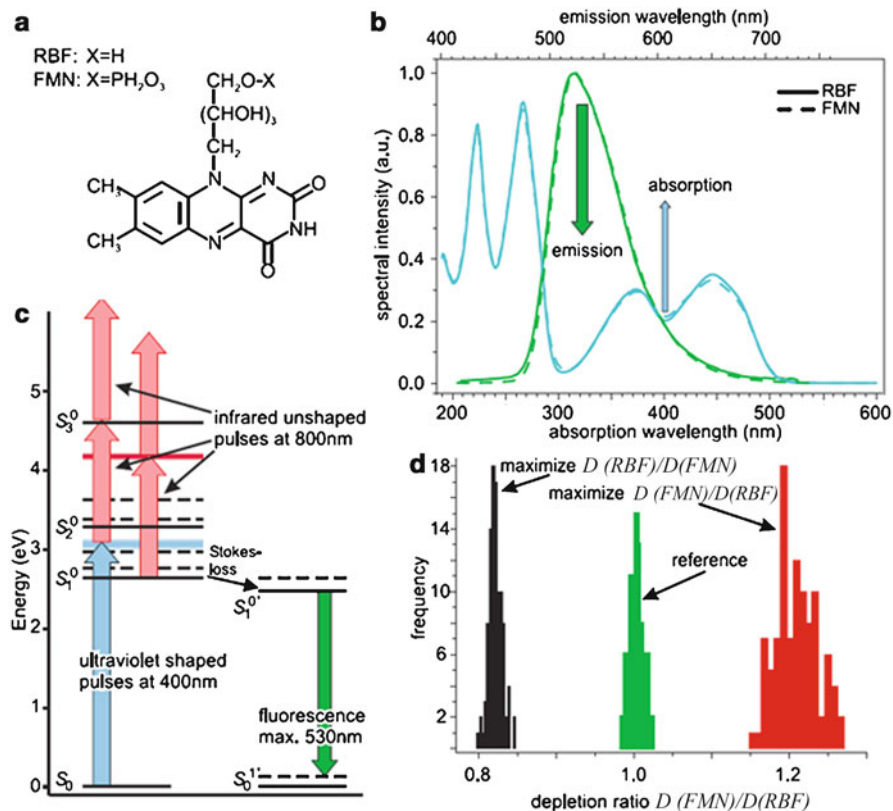
Fig. 11.10 The RBF and FMN molecules in (**a**) are very similar exhibiting nearly identical linear absorption and emission spectra in (**b**). The shaped UV control is centred at 400 nm and the flavin fluorescence signals are recorded over a window around 530 nm indicated by the respective *arrows*. The controlled optimal dynamic discrimination (*ODD*) of the flavins operates as indicated in (**c**) with a shaped UV pulse coordinated with a time delayed unshaped IR pulse to draw apart the vibronic dynamics of the flavins in the S1 or S2 excited states. The unshaped IR pulse serves to selectively disrupt the subsequent fluorescence signals from the two flavins and the *red arrows* indicate various possible means of action for the IR pulses. A typical outcome is shown in (**d**) where the ratio of flavin depletion signals, either D(RBF)/D(FMN) or D(FMN)/D(RBF), is maximized. The reference case corresponds to the application of transform limited pulses (From Ref. [7])

which is Fourier transform limited. The unshaped IR pulse follows the shaped UV pulse by a time delay π, and the structure of the shaped UV pulse is deduced optimally under adaptive control to achieve ODD in the fluorescence signals from RBF and FMN. The primary operation of ODD relies on the shaped UV pulse coherently transferring ground state population into the flavin S1 or S2 excited states with the IR component likely creating further excitation of the molecules to higher lying Sn states. The IR field disrupts the vibronic excitation in S1 or S2 created by the UV pulse in order to make a discriminating difference in the fluorescence

spectra of RBF and FMN from S1 recorded in the window 525–535 nm after a relaxation period of 5 ns. Fluorescence is therefore depleted, and this fluorescence depletion value is used as measure of the molecular response to the field. The overall mechanism also may take advantage of any beneficial intra- and inter-molecular dynamical processes, and the ODD discrimination can draw on suitable coherent and incoherent aspects of the molecular dynamics.

In the first series of experiments the RBF and FMN solutions are in separate identical flow cells exposed to the same trial shaped UV pulse and time delayed unshaped IR pulse. An acousto-optic modulator is used to shape the UV pulses. A sequence of experiments $n = 1, 2, ...$ was performed to record the relative depletion signal D_n

$$D_n(RBF) = [F_n^{und}(RBF) - F_n^d(RBF)]/F_n^{und}(RBF),$$

where $F_n^{und}(RBF)$ is the undepleted fluorescence signal from the RBF cell (i.e., without application of the time delayed IR pulse) and $F_n^d(RBF)$ is the depleted signal in the presence of the IR pulse. An analogous expression applies to $D_n(FMN)$ for data collected from the FMN cell exposed to the same laser pulses.

The pulse shaper operated through phase modulation with 50 pixels, each on the range 0-2π over the bandwidth of the UV pulse (only 3–4 nm) A genetic algorithm of 30 individuals was used to optimize the UV pulse phases with convergence typically occurring in 100 300 generations.

Figure 11.10 demonstrates the ability of ODD to significantly draw apart the RBF and FMN fluorescence signatures in spite of their nearly identical linear optical spectra in Fig. 11.10 (57). For a given time delay τ, a specific optimal UV pulse is determined in the adaptive control experiment. The best discrimination was found for τ 250–500 fs and the procedure was not able to find significant discrimination for $\tau \geqslant 1ps$ indicating a loss of coherence and/or insufficient overlap between the UV and IR pulses.

With a delay time τ typically around 250–500 fs, optimal pulse shapes found in different runs were very complex and showed considerable difference. They however produced exactly the same discrimination ratio when applying them, even weeks after the initial experiment. The underlying mechanisms are currently investigated, in order to identify whether this behaviour is generic or particular to this RBF/FMN system.

The assembled set of optimally discriminating laser pulses and their long-term stable performance permits exploiting ODD as a novel means for detection of nearly identical molecules when they are simultaneously present in a sample. In this work the recorded fluorescence depletion signals F_n^d are utilized, as they are proportional to their respective flavin concentrations. Thus, the fluorescence signal $F_n(mix)$ from a mixture of flavins generated with the n-th control UV-IR pulse pair is related to its individual counterparts by

$$F_n(mix) = c(RBF)F_n^d(RBF) + c(FMN)F_n^d(FMN),$$

where $c(RBF)$ is the fraction of RBF present and $c(RBF) + c(FMN) = 1$. The reference signals $F_n^d(RBF)$ and $F_n^d(FMN)$ are normalized to their respective concentrations deduced in learning the n-th control field, and similarly F_n is normalized to the total sum of the two flavins present. Two distinct ODD laser pulses could **successfully determine the fractional content of the two flavins** (the constrained relation between the fractions was not used in order to test the capabilities of ODD). Increasing the number of interrogating optimal pulses improves the standard deviation of the extracted component concentration fractions and a typical result using six pulses was $c(RBF) = 0.35 \pm 0.04$ and $c(FMN) = 0.68 \pm 0.05$ where the exact values were 0.33 and 0.66, respectively (57).

11.6 Conclusion

Quantum control and femtosecond spectroscopy shine a new light onto the detection and identification of biological systems, such as biochromophores but also highly complex systems like cells or bacteria. These applications are only at their beginning, and there is a reasonable hope for widely spread applications in the future, such as label-free microscopy or discrimination of pathogen from non-pathogen bacteria in air. Major technical improvements required for reaching these goals lie in the spectral range and the spectral bandwidth accessible by future femtosecond coherent sources. For instance the access to the deep UV (230–300 nm) will open up applications to proteins and DNA, which constitute major biological targets. Recent developments showed the way in this respect, with first deep-UV pulse shaping devices [50, 51]. The other aspect, namely broad spectral bandwidth, will provide a better controllability, as more states within the excited potential sheets will be coherently superposed. It is remarkable, that even with a very limited bandwidth (4 nm), ODD was able to draw apart the fluorescence signatures of quasi identical molecules such as RBF and its phosphated counterpart. This might constitute an example of the capability of molecular complexity helping discrimination rather than preventing it. Complexity indeed increases the local density of states, which is favorable in the case of relatively narrowband pumping. However, broadband UV pulses would allow a far more efficient discrimination capability. A novel and very attractive approach for producing UV supercontinuua is filamentation in rare gases, as reported recently [43, 52–56].

References

1. Extermann J, Bonacina L, Cuna E, Kasparian C, Mugnier Y, Feurer T, Wolf JP (2009) Nanodoublers as deep imaging markers for multi-photon microscopy. Opt Express 17:15342–15349
2. Extermann J, Bonacina L, Courvoisier F, Kiselev D, Mugnier Y, Le Dantec R, Galez C, Wolf JP (2008) Nano-FROG: frequency resolved optical gating by a nanometric object. Opt Express 16:10405–10411
3. Courvoisier F, Boutou V, Guyon L, Roth M, Rabitz H, Wolf JP (2006) Discriminating bacteria from other atmospheric particles using femtosecond molecular dynamics. J Photochem Photobiol A-Chem 180:300–306
4. Courvoisier F, Boutou V, Wood V, Bartelt A, Roth M, Rabitz H, Wolf JP (2005) Femtosecond laser pulses distinguish bacteria from background urban aerosols. Appl Phys Lett 87:063901
5. Petersen J, Mitric R, Bonacic-Koutecky V, Wolf JP, Roslund J, Rabitz H (2010) How shaped light discriminates nearly identical biochromophores. Phys Rev Lett 105:073003
6. Roslund J, Roth M, Guyon L, Boutou V, Courvoisier F, Wolf JP, Rabitz H (2011) Resolution of strongly competitive product channels with optimal dynamic discrimination: application to flavins. J Chem Phys 134(3):034511
7. Roth M, Guyon L, Roslund J, Boutou V, Courvoisier F, Wolf JP, Rabitz H (2009) Quantum control of tightly competitive product channels. Phys Rev Lett 102:253001
8. Bonacina L, Mugnier Y, Courvoisier F, Le Dantec R, Extermann J, Lambert Y, Boutou V, Galez C, Wolf JP (2007) Polar Fe(IO3)(3) nanocrystals as local probes for nonlinear microscopy. Appl Phys B-Lasers Opt 87:399–403
9. Baumner R, Bonacina L, Enderlein J, Extermann J, Fricke-Begemann T, Marowsky G, Wolf JP (2010) Evanescent-field-induced second harmonic generation by noncentrosymmetric nanoparticles. Opt Express 18:23218–23225
10. Extermann J, Béjot P, Bonacina L, Mugnier Y, Le Dantec R, Mazingue T, Galez C, Wolf JP (2009) An inexpensive nonlinear medium for intense ultrabroadband pulse characterization. Appl Phys B 97:537–540
11. Le Xuan L, Brasselet S, Treussart F, Roch JF, Marquier F, Chauvat D, Perruchas S, Tard C, Gacoin T (2006) Balanced homodyne detection of second-harmonic generation from isolated subwavelength emitters. Appl Phys Lett 89:121118
12. Pu Y, Centurion M, Psaltis D (2008) Harmonic holography: a new holographic principle. Appl Opt 47:A103–A110
13. Hsieh CL, Pu Y, Grange R, Laporte G, Psaltis D (2010) Imaging through turbid layers by scanning the phase conjugated second harmonic radiation from a nanoparticle. Opt Express 18:20723–20731
14. Hsieh CL, Pu Y, Grange R, Psaltis D (2010) Digital phase conjugation of second harmonic radiation emitted by nanoparticles in turbid media. Opt Express 18:12283–12290
15. Squier JA, Muller M, Brakenhoff GJ, Wilson KR (1998) Third harmonic generation microscopy. Opt Express 3:315–324
16. Dudovich N, Oron D, Silberberg Y (2002) Single-pulse coherently controlled nonlinear Raman spectroscopy and microscopy. Nature 418:512–514
17. von Vacano B, Wohlleben W, Motzkus M (2006) Actively shaped supercontinuum from a photonic crystal fiber for nonlinear coherent microspectroscopy. Opt Lett 31:413–415
18. Ogilvie JP, Debarre D, Solinas X, Martin JL, Beaurepaire E, Joffre M (2006) Use of coherent control for selective two-photon fluorescence microscopy in live organisms. Opt Express 14:759–766
19. Aeschlimann M, Bauer M, Bayer D, Brixner T, Cunovic S, Dimler F, Fischer A, Pfeiffer W, Rohmer M, Schneider C, Steeb F, Struber C, Voronine DV (2010) Spatiotemporal control of nanooptical excitations. Proc Natl Acad Sci USA 107:5329–5333
20. Fuchs U, Zeitner UD, Tunnermann A (2005) Ultra-short pulse propagation in complex optical systems. Opt Express 13:3852–3861

21. Tal E, Oron D, Silberberg Y (2005) Improved depth resolution in video-rate line-scanning multiphoton microscopy using temporal focusing. Opt Lett 30:1686–1688
22. Muller M, Squier J, Brakenhoff GJ (1995) Measurement of femtosecond pulses in the focal point of a high-numerical-aperture lens by 2-photon absorption. Opt Lett 20:1038–1040
23. Brixner T, De Abajo FJG, Spindler C, Pfeiffer W (2006) Adaptive ultrafast nano-optics in a tight focus. Appl Phys B-Lasers Opt 84:89–95
24. Amat-Roldan I, Cormack IG, Loza-Alvarez P, Artigas D (2004) Starch-based second-harmonic-generated collinear frequency-resolved optical gating pulse characterization at the focal plane of a high-numerical-aperture lens. Opt Lett 29:2282–2284
25. Bowlan P, Gabolde P, Trebino R (2007) Directly measuring the spatio-temporal electric field of focusing ultrashort pulses. Opt Express 15:10219–10230
26. Tannor DJ, Kosloff R, Rice SA (1986) Coherent pulse sequence induced control of selectivity of reactions – exact quantum-mechanical calculations. J Chem Phys 85:5805–5820
27. Tannor DJ, Rice SA (1985) Control of selectivity of chemical-reaction via control of wave packet evolution. J Chem Phys 83:5013–5018
28. Judson RS, Rabitz H (1992) Teaching lasers to control molecules. Phys Rev Lett 68:1500–1503
29. Warren WS, Rabitz H, Dahleh M (1993) Coherent control of quantum dynamics – the dream is alive. Science 259:1581–1589
30. Weiner AM (2000) Femtosecond pulse shaping using spatial light modulators. Rev Sci Instrum 71:1929–1960
31. Bonacina L, Extermann J, Rondi A, Boutou V, Wolf JP (2007) Multiobjective genetic approach for optimal control of photoinduced processes. Phys Rev A 76:023408
32. Dantus M, Lozovoy VV (2004) Experimental coherent laser control of physicochemical processes. Chem Rev 104:1813–1859
33. Levis RJ, Menkir GM, Rabitz H (2001) Selective bond dissociation and rearrangement with optimally tailored, strong-field laser pulses. Science 292:709–713
34. Brixner T, Damrauer NH, Niklaus P, Gerber G (2001) Photoselective adaptive femtosecond quantum control in the liquid phase. Nature 414:57–60
35. Brixner T, Gerber G (2003) Quantum control of gas-phase and liquid-phase femtochemistry. Chemphyschem 4:418–438
36. Boutou V, Favre C, Hill SC, Pan YL, Chang RK, Wolf JP (2002) Backward enhanced emission from multiphoton processes in aerosols. Appl Phys B-Lasers Opt 75:145–152
37. Favre C, Boutou V, Hill SC, Zimmer W, Krenz M, Lambrecht H, Yu J, Chang RK, Woeste L, Wolf JP (2002) White-light nanosource with directional emission. Phys Rev Lett 89:035002
38. Hill SC, Boutou V, Yu J, Ramstein S, Wolf JP, Pan YL, Holler S, Chang RK (2000) Enhanced backward-directed multiphoton-excited fluorescence from dielectric microcavities. Phys Rev Lett 85:54–57
39. Pan YL, Hill SC, Wolf JP, Holler S, Chang RK, Bottiger JR (2002) Backward-enhanced fluorescence from clusters of microspheres and particles of tryptophan. Appl Opt 41:2994–2999
40. Courvoisier F, Bonacina L, Boutou V, Guyon L, Bonnet C, Thuillier B, Extermann J, Roth M, Rabitz H, Wolf JP (2008) Identification of biological microparticles using ultrafast depletion spectroscopy. Faraday Discuss 137:37–49
41. Iketaki Y, Watanabe T, Ishiuchi S, Sakai M, Omatsu T, Yamamoto K, Fujii M, Watanabe T (2003) Investigation of the fluorescence depletion process in the condensed phase; application to a tryptophan aqueous solution. Chem Phys Lett 372:773–778
42. Kasparian J, Rodriguez M, Mejean G, Yu J, Salmon E, Wille H, Bourayou R, Frey S, Andre YB, Mysyrowicz A, Sauerbrey R, Wolf JP, Woste L (2003) White-light filaments for atmospheric analysis. Science 301:61–64
43. Mejean G, Kasparian J, Yu J, Frey S, Salmon E, Wolf JP (2004) Remote detection and identification of biological aerosols using a femtosecond terawatt lidar system. Appl Phys B-Lasers Opt 78:535–537
44. Dixon PB, Hahn DW (2004) Feasibility of detection and identification of individual bioaerosols using laser-induced breakdown spectroscopy. Anal Chem 77:631–638

45. Morel S, Leone N, Adam P, Amouroux J (2003) Detection of bacteria by time-resolved laser-induced breakdown spectroscopy. Appl Opt 42:6184–6191
46. Baudelet M, Guyon L, Yu J, Wolf JP, Amodeo T, Frejafon E, Laloi P (2006) Spectral signature of native CN bonds for bacterium detection and identification using femtosecond laser-induced breakdown spectroscopy. App Phys Lett 88(6):63901
47. Baudelet M, Guyon L, Yu J, Wolf JP, Amodeo T, Frejafon E, Laloi P (2006) Femtosecond time-resolved laser-induced breakdown spectroscopy for detection and identification of bacteria: a comparison to the nanosecond regime. J Appl Phys 99:084701
48. Baudelet M, Yu J, Bossu M, Jovelet J, Wolf JP, Amodeo T, Frejafon E, Laloi P (2006) Discrimination of microbiological samples using femtosecond laser-induced breakdown spectroscopy. Appl Phys Lett 89:163903
49. Li BQ, Rabitz H, Wolf JP (2005) Optimal dynamic discrimination of similar quantum systems with time series data. J Chem Phys 122:154103
50. Rondi A, Extermann J, Bonacina L, Weber SM, Wolf JP (2009) Characterization of a MEMS-based pulse-shaping device in the deep ultraviolet. Appl Phys B-Lasers Opt 96:757–761
51. Weber S, Barthelemy M, Chatel B (2010) Direct shaping of tunable UV ultra-short pulses. Appl Phys B-Lasers Opt 98:323–326
52. Berge L, Skupin S, Mejean G, Kasparian J, Yu J, Frey S, Salmon E, Wolf JP (2005) Supercontinuum emission and enhanced self-guiding of infrared femtosecond filaments sustained by third-harmonic generation in air. Phys Rev E 71:016602
53. Berge L, Skupin S, Nuter R, Kasparian J, Wolf JP (2007) Ultrashort filaments of light in weakly ionized, optically transparent media. Rep Prog Phys 70:1633–1713
54. Chin SL, Hosseini SA, Liu W, Luo Q, Theberge F, Akozbek N, Becker A, Kandidov VP, Kosareva OG, Schroeder H (2005) The propagation of powerful femtosecond laser pulses in optical media: physics, applications, and new challenges. Can J Phys 83:863–905
55. Couairon A, Mysyrowicz A (2007) Femtosecond filamentation in transparent media. Phys Rep-Rev Sect Phys Lett 441:47–189
56. Kasparian J, Wolf JP (2008) Physics and applications of atmospheric nonlinear optics and filamentation. Opt Express 16:466–493

12
Taking Whispering Gallery Mode Biosensing to the Single Protein Limit

Steve Arnold, V.R. Dantham, N. Rivilis, and S. Holler

12.1 Introduction

Finding a method for label-free sensing of individual protein is considered the "Holy Grail" in the bio-sensing field. An ideal technology that could do this would be able to follow the sensing of biological antigen-antibody interactions in their native form and in real-time without interfering tags. The challenge is great, however the rewards are likely greater. To date the most sensitive photonic label-free transducer is a resonant biosensor in the form of a Ring Resonator or Whispering Gallery Mode (WGM) resonator for which there have been a number of recent reviews [1, 2].

The WGM biosensor utilizes a resonator in which light trapped by total internal reflection orbits within a dielectric gallery such as a microsphere (Fig. 12.1).

At resonance a light wave is wrapped around the sphere "equator", returning in phase after each revolution (Fig. 12.1). A tunable laser drives a light guide that in turn drives the WGM resonance through evanescent coupling. Light coupled back into this guide from the WGM is 180°out of phase with the guide's uncoupled light leading to a dip in the detected spectrum. Nanoparticle adsorption to the outer surface of the ring leads to a local phase shift requiring a change in the resonator's frequency (Fig. 12.1). From its inception theory indicated that although single protein detection was out of the question with a bare silica resonator due to intrinsic baseline noise and cavity leakage, human virus with a mass more than 1000× larger should be detectable [3]. Indeed individual virus particles were detected [4] under previously prescribed conditions [5]. The beauty of bio-nanoparticle detection in

S. Arnold (✉) • V.R. Dantham • N. Rivilis • S. Holler
MicroParticle PhotoPhysics Laboratory (MP3L), Polytechnic Institute of NYU, 6 Metroteck Center, Brooklyn, NY 11201, USA
e-mail: arnold@photon.poly.edu; sarnold935@aol.com

S. Holler
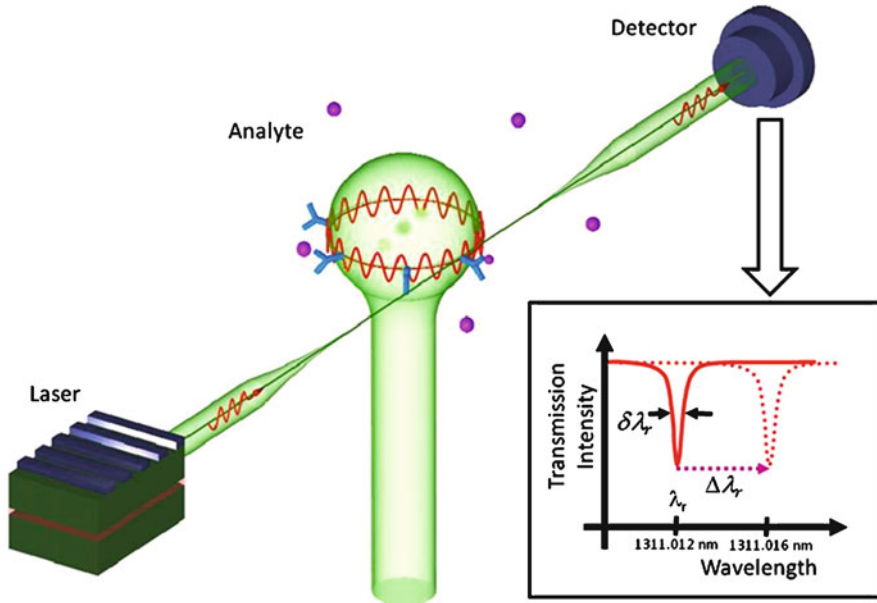Department of Physics, Fordham University, Bronx, NY, USA

Fig. 12.1 Whispering Gallery Mode Biosensor (microsphere) stimulated by a fiber waveguide driven by a tunable laser. In use the surface is functionalized, and adsorption produces a shift of the resonant dip (lower rt.) to longer wavelength (i.e. lower frequency)

this way is that it is fully analytical; an accurate determination of the nanoparticle size is possible for particles pulled to the WGM's ring of light [6] by optical gradient forces [7]. In what follows we (1) review the mechanism responsible for single virus detection, (2) design a signal enhancement scheme based on adding a plasmonic nano-structure on the sensing ring, and (3) show that this approach should put single protein detection within reach.

12.2 Reactive Sensing Principle

What happens when a nanoscopic particle adsorbs on the surface of a WGM microcavity? What nanoparticle size and position would produce a detectable shift? We knew in 2003 that formal theory would be extremely difficult since the particle would alter the beautiful cylindrical or spherical symmetry. One approach that seemed easiest was to keep the existing WGM shape (1st order perturbation) and invoke adiabatic invariance. This principle involves holding a parameter in the problem constant while varying other parts. We decided to try a thought experiment. It involved "photon thinking". We supposed that the cavity was in quasi-stationary state with one invariant photon. Classically, energy in a WGM means oscillating electromagnetic fields. A WGM's energy is mostly inside, but a small part is outside

in the form of an exponentially decaying evanescent field. This field polarizes a particle which enters it and that requires energy. The photonic state has to pay a price to do this. A photon's energy is proportional to its frequency; more precisely it is equal to Planck's constant h times the frequency, hf. If we suppose that the time-averaged work (over one cycle) to polarize a nanoparticle is W_p, then to account for this energy payment the photonic state would have to lose energy, causing a change in frequency Δf;

$$h\Delta f = -W_p \tag{12.1}$$

Equation 12.1 is beautifully simple, not only applicable to WGMs but also to any resonant optical cavity such as a Photonic Crystal or Fabry Perot device. It also predicts that frequency fluctuations will be seen for a particle moving just outside the cavity since the evanescent field exponentially decays into the environment from the cavity-environment interface, and the energy to polarize the nanoparticle is proportional to the square of the field. The next step is to figure out how to use this svelte equation.

The first thing that comes to mind when looking at Eq. 12.1 is that the result should be classical; h should not be necessary. That is quite correct because the energy needed to polarize the nanoparticle as represented by a quantum calculation will also contain h and so there will be a cancellation. We can more easily get h out of the equation by dividing by the energy of the photonic state hf on the left hand side of Eq. 12.1 and its time averaged classical equivalent W_c on the right;

$$\frac{\Delta f}{f} = -\frac{W_p}{W_c}. \tag{12.2}$$

Now we have a rather beautiful dimensionless result. To use it we must flesh out the right-hand side so that the properties of the particle and resonator are revealed. First, some assumptions about the nanoparticle must be made. Let's say it is round, homogeneous, and has a radius, a, much smaller than the light wavelength, λ; a Rayleigh particle. With these choices $W_{p,R} = \left(\frac{1}{4}\right)\alpha E_0(r_p)^2$ where α is the real part of the excess polarizability, and $E_0(r_p)$ the amplitude of the oscillating electric field at the position of the center of the particle, r_p. The denominator on the right can also be expressed in terms of classical fields by recognizing that a high Q cavity contains equal amounts of electric and magnetic energy; $W_c = (1/2)\int \varepsilon(r_c)E_0(r_c)^2 dV_c$. Equation 12.2 now becomes [3]

$$\frac{\Delta f}{f} = -\frac{\alpha E_0(r_p)^2}{2\int \varepsilon(r_c)E_0(r_c)^2 dV_c}. \tag{12.3}$$

The discussion that led to Eq. 12.1 was based on a single photon, however Eq. 12.3 would be no different if N invariant photons had been chosen since both the square of the field in the numerator and that in the denominator are each proportional to the photon number. Equation 12.3 tells us a great deal optical resonant sensing.

First the fact that the shift is proportional to the polarizability means that it is proportional to the volume of the nanoparticle. So a measurement of the shift can give the nanoparticle size. Since the density of most protein are fairly constant the protein mass can also be estimated. Such a measurement is most certain if the landing point of the nanoparticle is known [6, 8]. Next, the denominator is intimately related to the volume of the microcavity, suggesting that sensitivity can be enhanced as the cavity volume is decreased in inverse proportion.

Because the resonance frequency is shifted in reaction to the polarization of the nanoparticle, Eq. 12.2 has been called a "reactive sensing principle (*RSP*)" [6]. For label-free detection with a microcavity, this is the primary principle that can be turned to for estimating the amplitude of frequency shift signals.

The energy argument used to arrive at Eq. 12.1 may be substituted for one that utilizes light forces [9]. In the absence of dissipative processes, consistent with photon number Adiabatic Invariance, the nanoparticle is drawn to the surface by a time-averaged gradient force $\mathbf{F} = \nabla(W_{p,R})$ [10]. By doing work on the nanoparticle to draw it from a distance at which the polarization energy is negligible, the energy of the photonic state is reduced by an equivalent amount;

$$h\Delta f = -\int F \bullet dr = -\int_{\infty}^{r} \nabla W_{p,R} \bullet dr = -W_{p,R}(r). \qquad (12.4)$$

This is a rather satisfying result. It not only agrees with Eq. 12.1, but also shows the intimate connection between the gradient force and the frequency shift.

Before discussing the validity of the RSP, it should be noted that a ring resonator is intrinsically degenerate. By thinking of the sphere in Fig. 12.1 as an Earth-like globe we can say with certainty that a photon circulating clockwise (eastward) in Fig. 12.1 has the same frequency as one that circulates counter-clockwise (westward). A nanoparticle adsorbing to the ring splits this degeneracy into two new states [11]. These states are standing waves in which the particle either sits at a node or anti-node. With the particle sitting at a node the field in the numerator of Eq. 12.3 is zero and thereby has no shift, whereas at the anti-node the numerator is twice what it would be for a traveling wave and the mode shifts by twice the degenerate shift. Mode splitting has been used to advantage in producing a nanoparticle sensing technique that is "zero referencing"; instead of having to detect a real time step as evidence of adsorption, mode splitting produces a memory of the event in as much as two dips are in appearance after the event is over. Most ring resonators do not display mode splitting because the linewidth of the resonant dips is considerably broader than the average shift [12]. Under this circumstance the split modes superpose to reproduce a travelling wave, and the degenerate state reappears. Discussion of mode splitting may be academic for single protein detection since protein are expected to produce less than one-thousandth of the shift in comparison with virus, and virus in aqueous media are already difficult to detect using the mode splitting technique.

12.3 Validation of RSP

The Rayleigh particle *RSP* (Eq. 12.3) can be evaluated either numerically or analytically for sizing particles in a way that includes WGM devices of all shapes whether sphere, cylinder, disk, ring, capillary, or toroid. The classic case is that of the sphere for which an analytical closed form expression can be worked out simply for transverse electric polarization (TE) for the mode for which the angular momentum quantum number *l* and its z-projection *m* are equal (equatorial mode) [3];

$$\frac{\Delta f}{f} = -\frac{\alpha E_0(r_p)^2}{2 \int \varepsilon(r_c) E_0(r_c)^2 dV_c} = -\frac{(\alpha/\varepsilon_0)|Y_{i,i}(\theta,\varphi)|^2 e^{-a/L}}{(n_s^2 - n_e^2) R^3} \qquad (12.5)$$

where n_s and n_e are the refractive index of the micro-sphere and external environment respectively, and a, R, and L are the nano-sphere and microsphere radii and characteristic decay length of the evanescent intensity, respectively. The absolute square of the spherical harmonic displayed in Eq. 12.5 is independent of the azimuthal angle φ, but has distinct polar angle dependence as shown in Fig. 12.2. Gradient forces operating in solution draw particles to the equator where the intensity is greatest, and where the largest frequency shift is produced [6]. Since most protein and virus are charged it is possible to condition the surface with like charges so that other parts of the sphere are avoided. It is also possible to move antibodies to the equator where they can be bound. We call this approach "Light Force Functionalization". Equation 12.5 provides a direction for obtaining
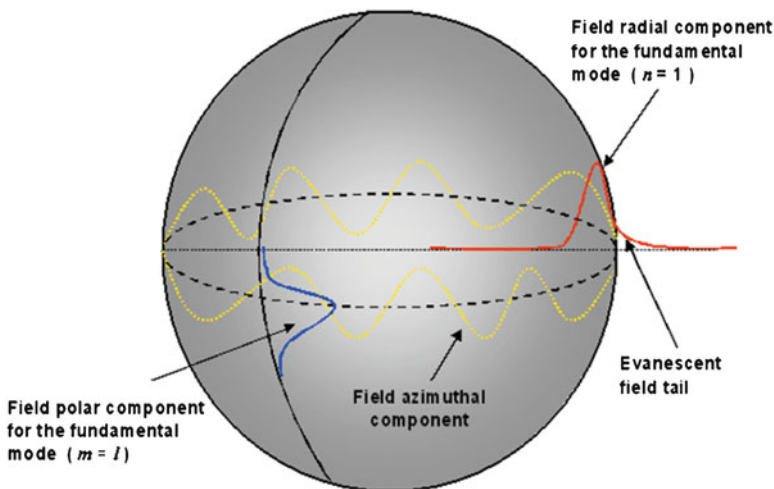

Fig. 12.2 Radial and polar intensity distributions for the fundamental WGM in a microsphere as adapted from [2]

the polarizability of a nanoparticle from the frequency or free space wavelength shift. In inverting Eq. 12.5 to obtain a particle's polarizability we will suppose that the particle binds to the equator ($\theta = \pi/2$).

The solution to Eq. 12.5 for the polarizability from the free-space wavelength shift is displayed in Eq. 12.6, and this is related in turn to the Rayleigh polarizability equation for a homogeneous spherical particle,

$$(\alpha/\varepsilon_0) = \frac{(n_s^2 - n_e^2)\, R^3 e^{a/L}}{|Y_{i,i}(\pi/2, \varphi)|^2}\left(\frac{\Delta\lambda}{\lambda}\right)_{max} = 4\pi n_e^2 \left(\frac{n_{np}^2 - n_e^2}{n_{np}^2 + 2\,n_e^2}\right)a^3, \qquad (12.6)$$

where n_{np} is the refractive index of the nanoparticle. Equation (12.6) may be solved for the nanoparticle size in the limit of large l,

$$a_{RSP} \approx a_0\left[1 + \xi + (3/2)\xi^2 + (3/8)\xi^3 + O(\xi^3)\dots\dots\right] \qquad (12.7a)$$

$$a_0 = \frac{R^{5/6}\lambda^{1/6}}{D^{1/3}}\left(\frac{\Delta\lambda}{\lambda}\right)_{max}^{1/3} \qquad (12.7b)$$

$$\xi = \frac{a_0}{3\,L} \qquad (12.7c)$$

Since the evanescent length L for grazing incidence at the glass-water interface is greater than the nanoparticle radius for nanoparticles below 50 nm (e.g. Influenza A virus) for all of the particle-laser wavelength combinations that we will consider, ξ is a small fraction. Consequently Eq. 12.7b is all that is normally necessary for size evaluation. Figure 12.3 shows results for particle sizes evaluated using the *RSP* in comparison to the mean size reported by manufacturers or in the case of Influenza from Scanning Electron Microscopy (SEM). The *RSP* appears to work independent of the laser wavelength that is used. Although the data used in evaluating a_{RSP} came from the largest steps recorded, due to light forces drawing particles to the equator, the distribution of steps in each case was fairly narrow. Figure 12.3 says a lot about the limits of measurement for a WGM cavity that is bare (i.e. no local enhancement mechanism).

12.4   Limit of Detection of a Bare WGM Microcavity

Some notes about Fig. 12.3. Agreement is good for all radii from 375 to 12.5 nm; the RSP is displayed as working over a range of 27,000 in mass. All points except the smallest at 12.5 nm (9 atto-gram) used spherical WGM microcavities [4, 6, 13]. This smallest detected polystyrene (PS) nano-sphere was measured with a micro-toroid by using a reference interferometer for beating down wavelength shift noise from laser frequency fluctuations [14]. Its free space wavelength shift
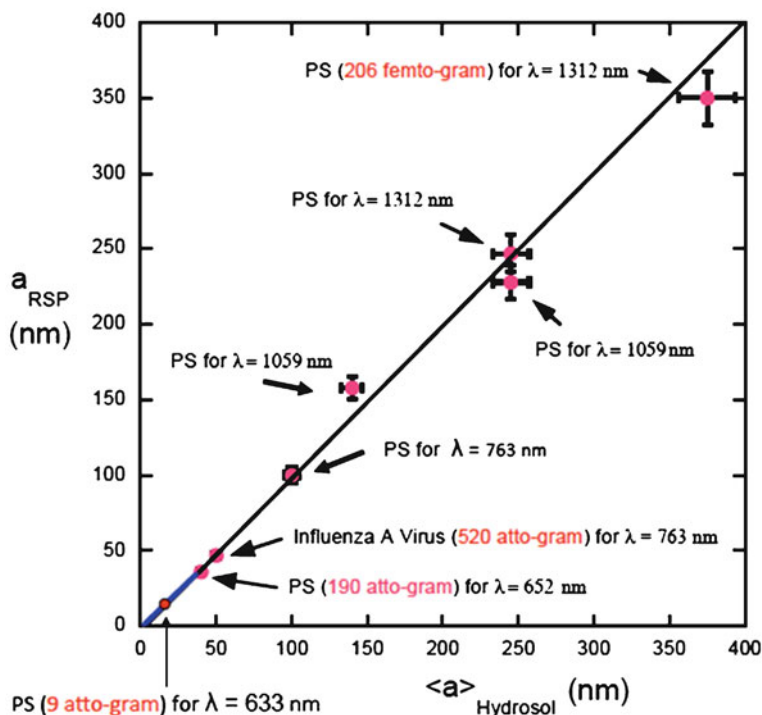
Fig. 12.3 Comparison of the nanoparticle sizes arrived at from the RSP with the sizes either obtained from manufacturer's mean sizes in the case of polystyrene (PS) and from SEM in the case of InfA virus

of 0.5 fm is very close to the rms noise. Unfortunately a 12.5 nm PS microsphere (25 nm diameter) has a lot larger mass than an intermediately sized protein such as streptavidin or bovine serum albumin (BSA). The researchers in [13] minimized the noise while maximizing the wavelength shift signal but fell short of streptavidin or BSA detection by a factor of 15. With little more that can be done to lower the noise, the only reasonable approach is to boost the signal. A nano-plasmonic hybrid microcavity will likely be the solution.

12.5   Nano-Plasmonic Microcavity Hybrid

The first paper dealing with this subject was published 2 weeks before our NATO Advanced Study Institute [15]. The next came 2 months after [16]. A couple of other papers have followed. I will recount the research that came from our laboratory (MP^3L) [14].
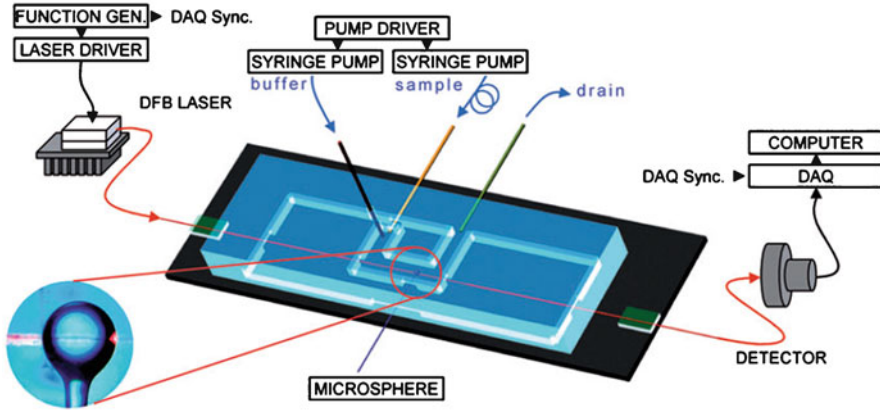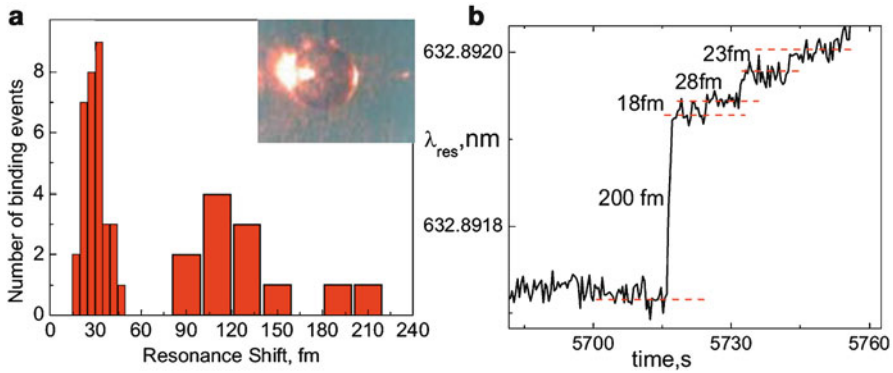
Fig. 12.4 Microfluidic sensing system

Fig. 12.5 (**a**) Shift statistics after injecting PS particles into a cell with a WGM resonator having gold nanoshells bound to its equator; inset: a typical image showing scattering from a Au shell on the surface; (**b**) wavelength shift data showing steps from the two groups

The plasmonic enhancement mechanism came from a discovery made in the lab using a microfluidic system (Fig. 12.4) [5].

The distributed feedback laser (DFB) that we would ordinarily be using was replaced by a tunable external cavity laser (ECL) operating near 633nm. When gold nano-shells about 70nm in radius were injected into the cell some were seen to attach (3 or less) to the equator of the installed microcavity (R = 33.5 μm). The sphere was washed in buffer but the nano-shells remained. Next dielectric polystyrene particles 55nm in radius were injected into the cell revealing steps in the free space resonant wavelength of the silica microsphere (R = 33.5 μm). Unlike all of the experiments we had done in the past the distribution of steps was not in one group (Fig. 12.5). There were two distinct groups in evidence. One group had a distribution centered around 30 fm consistent with what we would predict from the RSP for 55 nm

beads attaching to the equator of a bare silica microsphere. The other group were considerably larger with one of the steps as large as 216 fm. Figure 12.5 shows a small section of the data showing a "giant step" along with the more usual smaller steps. We associated this second group of giant steps in Fig. 12.5 with the presence of the gold nano-shells on the surface. The ratio between the average step height in the second group to that in the first was 4. This odd occurance was attributed to a hot spot plasmonic resonance stimulated by the WGM.

A theoretical effort ensued to try to describe and understand the apparent enhancement. The first realization was that calculating the fields for the microsphere-Au-nanoshell system at a single frequency by employing a Finite Element Method (FEM) numerical simulation would take weeks. The problem needed to be broken up into parts. A simple question was asked: if the particle was solid gold and much smaller than the evanescent length L, would an enhancement be expected? A mechanism materialized and once again it involved the *RSP*.

To estimate the enhancement we suppose that the WGM is the lowest order transverse electric (TE) mode with an approximately Gaussian shaped intensity profile having a breadth of a few microns around the equator, thereby bathing the plasmonic nanoparticle in a nearly uniform field. Excitation of this particle with modal field amplitude E_0 generates hot spots in intensity. Enhanced gradient forces capture a dielectric nanoparticle at one of these spots [17]. Since the hot spots are part of the local field of the plasmonically modified microresonator, the resonance frequency undergoes an enhanced shift by comparison with binding to the bare resonator in proportion to the increase in the polarization energy (Eq. 12.2), which is in turn proportional to the increase in local intensity (Eq. 12.3). The enhancement R_E when an infinitesimally small particle lands on the plasmonic particle at r_{hs} is

$$R_{E,\max} = \frac{|E_T|^2}{E_0^2} = \left| \frac{E_0 + E_{ind}(r_{hs})}{E_0} \right|^2, \tag{12.8}$$

where $E_{ind}(r_{hs})$ is the induced field at the hot spot of the plasmonic particle. Next we will calculate $R_{E,\max}$ for the simplest case, a solid gold nanoparticle.

We will assume a simple dipole mode is induced in the bound gold nanoparticle and that an infinitesimally small dielectric particle landing at the top gives rise to an enhanced shift (Fig. 12.6). The experimental situation that led to Fig. 12.5 is more complicated, however for now the solid gold model should be instructive. The field on the top of the solid gold particle (at T in Fig. 12.6) is that of the induced dipole at the plasmonic particle's radius a_p; $E_{ind} = 2 k \alpha_p E_0 \hat{Z} / a_p^3$, where α_p is the polarizability of the plasmonic particle, $k = (4\pi\varepsilon_0\varepsilon_e)^{-1}$, and $\hat{Z}$ is a unit vector in the z-direction. Using this expression in Eq. 12.8 we arrive at [18]

$$R_{E,\max} = \frac{|E_T|^2}{E_0^2} = \left| 1 + 2 k \alpha_p / a_p^3 \right|^2. \tag{12.9}$$
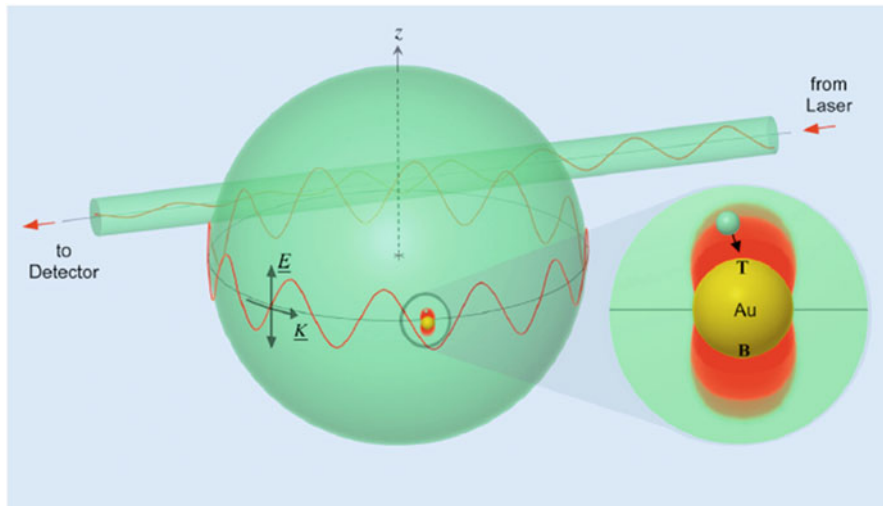
Fig. 12.6 Illustrates a traveling WGM interacting with a stationary gold nanoparticle stimulated into a plasmonically resonant dipole mode. This generates hot spots north and south of the equator that capture smaller dielectric nanoparticles as the WGM's Carousel forces are transporting them. The effect is an enhanced resonant shift of the microcavity's frequency

For a nanosphere we have already written polarizability in terms of refractive indices (Eq. 12.6), however here it is more useful to use permittivity; $\alpha_p = k^{-1}\alpha_p{}^3(\varepsilon_p - \varepsilon_e)/(\varepsilon_p + 2\varepsilon_e)$ With this express Eq. 12.9 becomes

$$R_{E,\max} = \frac{|E_T|^2}{E_0^2} = \left|1 + 2\frac{(\varepsilon_p - \varepsilon_e)}{(\varepsilon_p + 2\varepsilon_e)}\right|^2 = \left|\frac{3\,\varepsilon_p}{\varepsilon_p + 2\,\varepsilon_e}\right|^2. \qquad (12.10)$$

Equation 12.10 is quite reasonable. If we set $\varepsilon_p = \varepsilon_e$ the enhancement should disappear and indeed it becomes 1. If we are dealing with a perfect metal (i.e. infinite conductivity) then $\varepsilon_p = -\infty$, and the enhancement is 9, a text book result [19]. More interestingly, at a dipole plasmonic resonance frequency ω_1 where the real part of the metallic permittivity is controlled by the environment (i.e. $\text{Re}[\varepsilon_p(\omega_1)] = -2\varepsilon_e = -3.5$ for water) the enhancement is limited principally by the $\text{Im}[\varepsilon_p(\omega_1)]$. For a gold nanoparticle in water [20] at resonance $\text{Im}[\varepsilon_{pg}(\omega_1)] \approx 2$, which gives an enhancement $R_{Eg} \approx 37$, occurring at 530 nm. To a large extent the enhancement although large is not nearly as large as it could be if the resonance occurred in the near IR where the imaginary part of the dielectric function of gold is smaller. A system that can go there and maintain spherical symmetry is a gold nanoshell because its dipole mode is tunable by simply altering the thickness of the shell.

The approach we have taken thus far is quasistatic. It assumes that the structure size is much smaller than the wavelength. In this limit equations for the fields and

polarizability can be obtained to a good approximation from electrostatics, and realistic optical responses can be calculated by using complex optical dielectric functions.

The gold nanoshell consists of a spherical core of radius r^1, usually of silica or polystyrene with permittivity ε_1, surrounded by a thin layer of gold with permittivity ε_2, for an overall radius r^2. For our purpose its environment is water with permittivity ε_3. One of its amazing properties is its tunability. For a given outer radius, as the shell thickness is reduced the dipole resonance of the structure shifts to the red. It is straightforward to work out the electrostatics of this structure [21]. The enhancement in field at the top of the structure can be written, as before using Eq. 12.9, however the polarizability is different due to the internal structure of the nanoshell. Instead of working through all of the electrostatics we present an analytical equation for the enhancement

$$R_{E,\text{max}} = \frac{|E_T|^2}{E_0^2} = \left| \frac{3\,\varepsilon_2}{\varepsilon_2 + 2\,\varepsilon_3\,g} \right|^2 . \tag{12.11}$$

By comparing Eq. 12.11 to the right most expression in Eq. 12.10 we see that the only difference is the factor g since clearly ε_2 is the gold permittivity ε_p, and ε_3 is the permittivity of the environment ε_e. The factor g is in a strategic location with respect to the tuning of the resonance. With g equal to 1 we return to a solid gold particle and the resonance occurs at 530 nm; this corresponds to RE $[\varepsilon_2(\omega_1)] = -2\varepsilon_3 = -3.5$ for water. The parameter g is a measure of the strength of interaction between a dipole that forms from charges on the gold silica interface with one that forms on the gold water interface. As the shell thickness is reduced these dipoles form both symmetric and anti-symmetric hybrids (Fig. 12.7). In particular the lower energy symmetric state is responsible for pronouncing bio-sensing enhancements as the interaction between the two dipoles grows. The Re[g] grows from zero on a positive trajectory as the shell thickness decreases and the interaction increases. As a result we can expect the dipole resonance to shift to the red where the Im[ε_2] decreases, thereby enabling huge wavelength shift enhancements for a particle adsorbing to T (Fig. 12.7).The promise that Fig. 12.7 offers is much greater than the enhancement first discovered (Fig. 12.5). As we will show, the mechanism for both effects is the same and the smaller signal is a direct consequence of the experimental conditions.

The enhancement R_E is the ratio of the wavelength shift for a particle adsorbing to a hot spot on a gold nanoshell to that for a particle adsorbing on the silica equator. The dielectric particles used in obtaining Fig. 12.5 had an average radius of 55nm. This allows the evanescent field of the WGM to easily interact with the particle since L 88 nm. On the other hand, the near field of a gold nanoshell only extends over a characteristic length of a couple of nanometers, allowing a small portion of the 100 nm particle to be polarized. Fortunately the mathematical machinery for using the *RSP* in such a situation has been presented [23]. It involves a volume integral over the adsorbed particle. On that basis the enhancement R_E is
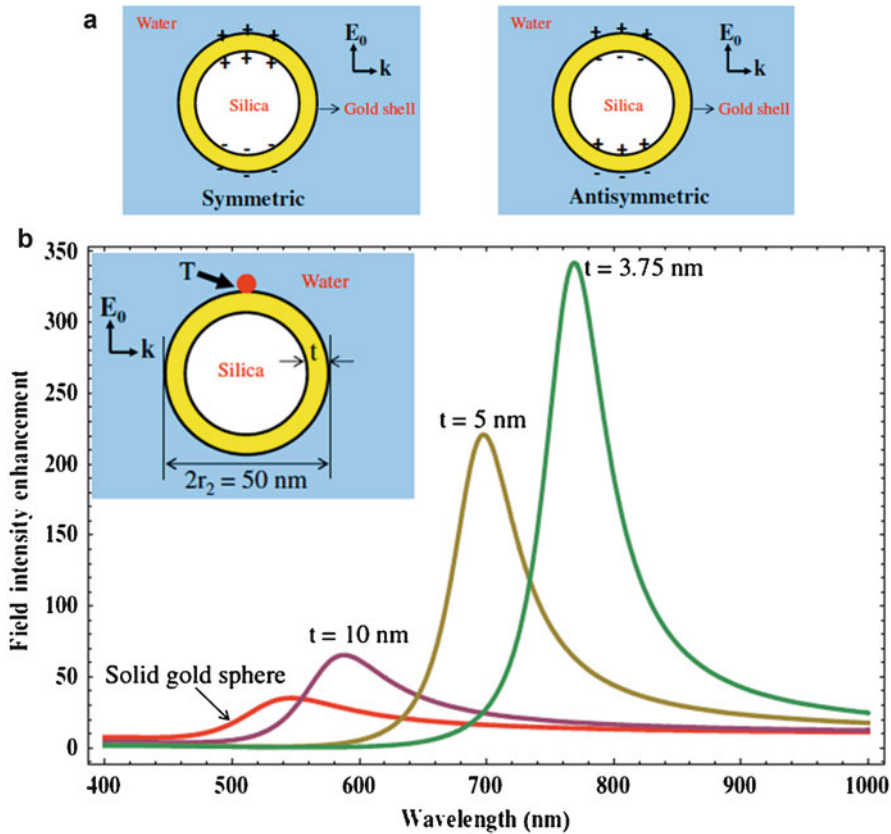
Fig. 12.7 (**a**) The symmetric and antisymmetric hybrid modes of a gold nanoshell. (**b**) Enhancement in the wavelength shift of the symmetric mode for an infinitesimally small particle binding at T on a gold nanoshell 50 nm in diameter having thicknesses ranging from the full radius (i.e. solid gold) down to 3.75nm For these calculations, the dielectric constant values of gold are taken analytical fits to recent experimental data [22]. Note the large wavelength shift and the enhancement that grows to 340×

$$R_E = \frac{\int \Delta\varepsilon \, E_b \, E_a^* \, dV}{\alpha_d \, E_0(r_p)^2}, \qquad (12.12)$$

where $\Delta\varepsilon = \varepsilon_d - \varepsilon_e$ with ε_d being with relative permittivity of the dielectric particle, $E_b E_a^*$ is the product of the field before the particle insertion with that after the particle insertion, and α_d is the polarizability of dielectric particle.

Figure 12.8 shows the nanoshell absorption spectrum obtained from Mie theory [24], and Fig. 12.8 shows the calculated fields using a Finite Element Method (*FEM*). The gold nanoshell is actually stimulated into a quadrupole mode. The particle is positioned at one of the four hot spots of this mode. As one can see the
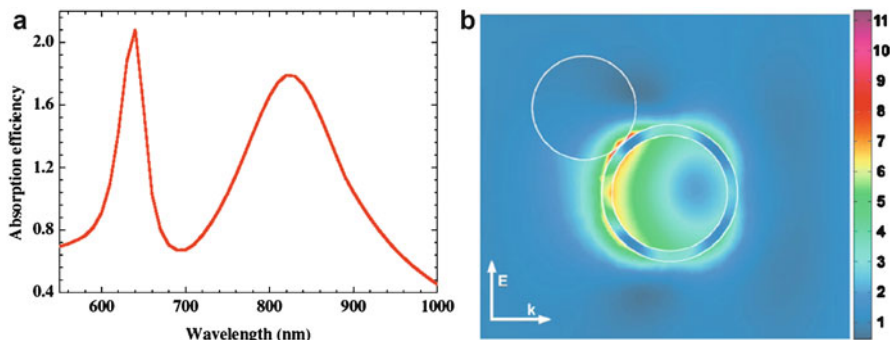
Fig. 12.8 (**a**). The theoretical absorption spectrum of a nanoshell with inner and outer radii of 60 and 70 nm. The dimensions were employed in acquiring the data in Fig. 12.5. The peak at 633nm corresponds to the excitation of the quadrupole mode. (**b**) The absolute field strengths arrived at by using *FEM.* At the position of the dielectric nanoparticle the absolute field rises to 11× the incident field (increase of 121× in intensity)

field from the nanoshell only slightly penetrates into the dielectric particle, however where it does the field is elevated by a factor of 11 (i.e. the intensity is increased by a factor of 121). Upon evaluating Eq. 12.12 we find that the overall enhancement is 3.4, in good agreement.

12.6 Conclusions

The question that remains is whether the nanoshell enhancement is large enough to see protein one at a time. Our answer is decidedly yes. An enhancement of 300× lowers the detectable polarizability by a factor of 300, which in turn lowers the detectable size by the cube root of 300, a factor of 6.7. Since individual nanoparticles with radii of 12.5nm have already been detected in aqueous solution, the enhancement afforded by gold nanoshells should reduce this to 1.9 nm, which is well below the effective radius of BSA, 3nm.

Since publishing Shopova et al. [15] there has been a flurry of activity in which a variety of nanoparticle shapes for the enhancement toward single protein detection have been proposed. In particular, Bowen's group in Australia [25] has concentrated on nanorods and predicted an overall enhancement of over 800x for BSA. In practice such rods would attach at random angles relative to the equatorial if light force were the only means for functionalization. However, lithography is probably not far behind, and we are liable to see rods along meridional (North-South) directions on the equator. In the future we hope there will be many novel designs for nanoplasmonic microcavity hybrid sensors that push the limit of detection farther than ever before.

References

1. Sun Y, Fan X (2011) Optical ring resonators for biochemical and chemical sensing. Anal Bioanal Chem 399:205–211
2. Soria S et al (2011) Optical microspherical resonators for biomedical sensing. Sensors 11:785–805
3. Arnold S, Khoshsima M, Teraoka I, Holler S, Vollmer F (2003) Shift of whispering-gallery modes in microspheres by protein adsorption. Opt Lett 28:272–274
4. Vollmer F, Arnold S, Keng D (2008) Single virus detection from the reactive shift of a whispering-gallery mode. Proc Natl Acad Sci USA 105:20701–20704
5. Arnold S, Ramjit R, Keng D, Kolchenko V, Teraoka I (2008) Microparticle photophysics illuminates viral biosensing. Faraday Discuss 137:65–83
6. Arnold S, Keng D, Shopova SI, Holler S, Zurawsky W, Vollmer F (2009) Whispering gallery mode carousel. Opt Express 17:6230–6238
7. Ashkin A, Dziedzic JM, Bjorkholm JE, Chu S (1986) Observation of a single-beam gradient force optical trap for dielectric particles. Opt Lett 11:288–290
8. Zhu J et al (2010) On-chip nanoparticle detection and sizing by mode splitting in an ultrahigh-Q microresonator. Nat Photonics 4:46–49
9. Hu J, Lin S, Kimerling LC, Crozier K (2010) Optical trapping of dielectric nanoparticles in resonant cavities. Phys Rev A 82:053819
10. This is the negative gradient of the potential energy since the potential energy is $-W_p$; the force is conservative
11. Teraoka I, Arnold S (2009) Resonance shifts of counter-propagating whispering-gallery modes: degenerate perturbation theory and application to resonator sensors with axial symmetry. J Opt Soc B 26:1321–1329
12. Kim W, Ozdemir AK, Zhu J, Yang L (2011) Observation and characterization of mode splitting in microsphere resonators in aquatic environment. Appl Phys Lett 98:141106
13. Shopova SI, Rajmangal R, Nishida Y, Arnold S (2010) Ultrasensitive nanoparticle detection using a portable whispering gallery mode biosensor driven by a periodically poled lithium-niobate frequency doubled distributed feedback laser. Rev Sci Inst 81:103110
14. Lu T et al (2011) High sensitivity nanoparticle detection using optical microcavities. Proc Natl Acad Sci USA 108:5976–5979
15. Shopova SI, Rajmangal R, Holler S, Arnold S (2011) Plasmonic enhancement of a whispering gallery mode biosensor for single nanoparticle detection. Appl Phys Lett 98:243104
16. Santiago-Cordoba MA, Boriskina SV, Vollmer F, Demirel MC (2011) Nanoparticle-based protein detection by optical shift of a resonant microcavity. Appl Phys Lett 99:073701
17. Novotny L, Bian RX, Xie XS (1997) Theory of nanometric optical tweezers. Phys Rev Lett 79:645–648
18. One warning- the trick of adding the dipole contribution to the field inducing the dipole for obtaining the field at T works for plasmonic structures having spherical symmetry. This will not work for the enhancement from a nanorod for example
19. Reitz JR, Milford FJ, Christy RW (1980) Foundations of electromagnetic theory, 3rd edn. Addison-Wesley, Reading

20. Stoller P, Jacobsen V, Sandoghdar V (2006) Measurement of the complex dielectric constant of a single gold nanoparticle. Opt Lett 31:2474–2476
21. Averitt RD, Westcott SL, Halas NJ (1999) Linear optical properties of gold nanoshells. J Opt Soc B 16:1824–1832
22. Rakić AD, Djurišić AB, Elazar JM, Majewski ML (1998) Optical properties of metallic films for vertical- cavity optoelectronic devices. Appl Opt 37:5271–5283
23. Teraoka I, Arnold S (2006) Theory of resonance shifts in TE and TM whispering gallery modes by nonradial perturbations for sensing applications. J Opt Soc Am B 23:1381–1389
24. Bohren CF, Huffman DR (1983) Absorption and scattering of light by small particles. Wiley, New York
25. Swaim JD, Knittel J, Bowen WP (2011) Detection limits in whispering gallery biosensors with plasmonic enhancement. Appl Phys Lett 99:243109

13
Terahertz Spectroscopy and Imaging at the Nanoscale for Biological and Security Applications

John W. Bowen

Abstract The chemical specificity of terahertz spectroscopy, when combined with techniques for sub-wavelength sensing, is giving new understanding of processes occurring at the nanometre scale in biological systems and offers the potential for single molecule detection of chemical and biological agents and explosives. In addition, terahertz techniques are enabling the exploration of the fundamental behaviour of light when it interacts with nanoscale optical structures, and are being used to measure ultrafast carrier dynamics, transport and localisation in nanostructures.

This chapter will explain how terahertz scale modelling can be used to explore the fundamental physics of nano-optics, it will discuss the terahertz spectroscopy of nanomaterials, terahertz near-field microscopy and other sub-wavelength techniques, and summarise recent developments in the terahertz spectroscopy and imaging of biological systems at the nanoscale. The potential of using these techniques for security applications will be considered.

13.1 Introduction

The terahertz part of the electromagnetic spectrum lies between the infrared and microwave regions, covering frequencies between 100 GHz and 10 THz. This frequency range corresponds to wavelengths between 3 mm and 30 μm. It may therefore seem surprising, given the relatively large size of the wavelengths involved, that terahertz radiation can be used to probe processes occurring at the nanometer scale, providing information that is not easily obtainable using other

J.W. Bowen (✉)
Terahertz Laboratory, School of Systems Engineering, University of Reading, Whiteknights, Reading, RG6 6AY UK
e-mail: j.bowen@reading.ac.uk; cybjb@cyber.reading.ac.uk

wavelengths. This state of affairs is due to three factors. Firstly, a frequency of 1 THz corresponds to a period of 1 ps. Consequently, terahertz frequencies interact strongly with phenomena that fluctuate on a picosecond or sub-picosecond timescale. The continual breaking and re-forming of the hydrogen bonds between the water molecules in liquid water occur on just this timescale, and so water is a very strong absorber of terahertz radiation. This makes terahertz spectroscopy extremely sensitive to small changes in the volume of water present in biological systems as well as to changes in the dynamic behaviour of the water molecules. This timescale also corresponds to the collective vibrational modes of biomolecules, including those of DNA. In typical biological systems these biomolecules are in solution, surrounded by water molecules. Therefore, conformational changes in biomolecules can be sensed using terahertz spectroscopy due to the combined effect of changes to the vibrational modes of the biomolecule and associated changes in the dynamics of the surrounding network of water molecules. The collective motion of the charge carriers in nanostructures also happens on this picosecond or subpicosecond timescale, and so terahertz spectroscopy can, in addition, be used to characterise the dynamic behaviour of charge carriers in nanomaterials.

Secondly, the fundamental behaviour of light as it interacts with nanoscale objects, such as the extraordinary transmission of light through sub-wavelength apertures, or the scattering of light by small particles, is difficult to explore directly at the nanoscale using visible light, precisely because of the small dimensions involved. However, these phenomena can be brought within reach by scaling the test objects in proportion to the wavelength and operating in the terahertz regime. These larger test objects are much more easily fabricated to a given tolerance than their nanoscale counterparts, while terahertz imaging can be used to map the three-dimensional, wavelength-dependent, time evolution of the electromagnetic fields in the vicinity of the object. While this approach has to be treated with some caution because not all electromagnetic phenomena, such as surface plasmons, scale directly with the wavelength, it can be used very successfully to test whether theoretical treatments hold in the terahertz range, giving some confidence that the same theory is then applicable in the visible part of the spectrum.

Finally, using near-field microscopy techniques, it proves possible to concentrate terahertz radiation to allow very deep sub-wavelength resolution imaging at the nanoscale. All of these approaches to nanoscale sensing using terahertz radiation will be discussed in more detail later in this chapter. However, as many of these techniques are based on terahertz time-domain spectroscopy (TDS), it will be helpful to start by considering the operation of a basic TDS system.

Figure 13.1 illustrates the layout of a typical TDS system operating in transmission geometry; that is, it is setup to measure the terahertz transmission spectrum of a sample. With some modification of the optical layout, it is possible to use a similar approach to measure the spectrum of the terahertz signal reflected from the sample (see [1] for a typical example). For the purposes of this discussion, the sample will be considered to be a slab of solid material, however, it is also possible to measure the spectra of liquid and gaseous samples given a suitable sample cell. The system relies on an ultrafast pulsed laser (typically a Ti:sapphire laser) both
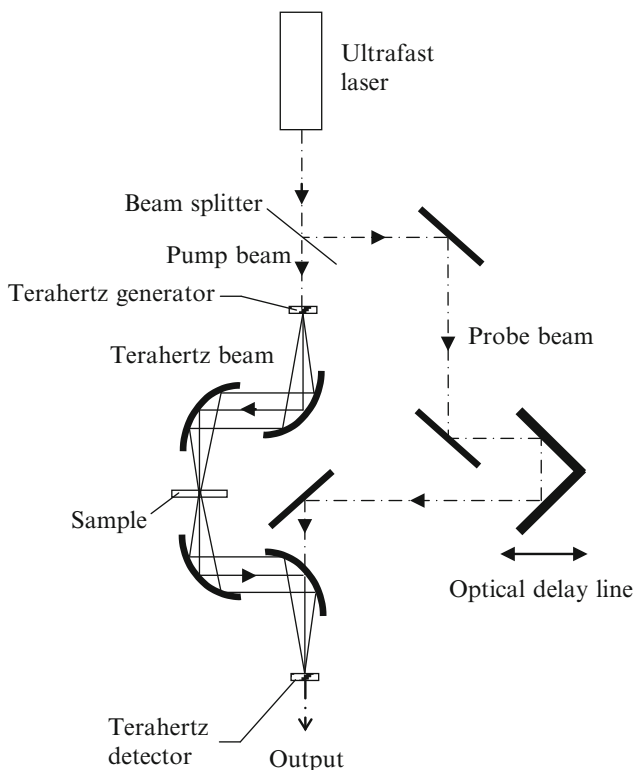
Fig. 13.1 Terahertz time-domain spectroscopy system

to generate the terahertz pulse that is incident on the sample, and to provide a
gating pulse for the detection system, enabling time-resolved measurement of the
terahertz pulse transmitted through the sample. The laser beam is split into two
beams using a beam-splitter: a pump beam used to generate the terahertz pulse, and
a probe beam for gating the detection. The pump beam falls on a terahertz generator,
which converts the incident near-infrared pulse from the laser into a terahertz pulse.
The resulting terahertz pulse will have a somewhat longer pulse-width than the
incident laser pulse, typically being of the order of a few hundred femtoseconds,
but will be still be short enough to contain spectral components which typically
give continual coverage from at least 100 GHz to 3 THz. The terahertz beam is
propagated via a system of focusing reflectors, through the sample and on to the
detector. The probe beam from the laser also falls on the detector, although it does
so via a scanning optical delay line, which enables the relative time of arrival of
the terahertz pulse and probe pulse to be adjusted. The detection system is gated
by the probe pulse so that it can detect any incident terahertz radiation only for
the length of time that the probe pulse is present. Therefore, as the probe pulse is
shorter than the terahertz pulse, being only a few tens of femtoseconds in length,

the detection system will provide a snapshot of the field amplitude in the terahertz pulse at a time corresponding to the arrival of the probe pulse. As the laser produces a train of pulses, one after the other, the optical delay line can be adjusted so that field amplitude of the series of terahertz pulses is sampled at different time points, thereby mapping out the detected terahertz waveform. The resulting time domain waveform can be Fourier transformed into the frequency domain to obtain the spectrum of the detected pulse. Recording a second waveform in the same way but without the sample in the beam, so that the beam passes unimpeded through the instrument provides a reference pulse, which may be Fourier transformed to provide a reference spectrum. Dividing the spectrum recorded with the sample in situ by the reference spectrum, point by point, yields the transmission spectrum of the sample. As the detection process is coherent, if complex fast Fourier transforms are used to obtain the spectra, the resulting ratio also yields the frequency dependent phase delay introduced by the sample. The frequency dependent amplitude and phase can then be used to determine the frequency dependent refractive index and absorption coefficient of the sample.

If the sample is not a simple slab of material, but is a more complex object with regions made from different materials, it can be raster scanned on a translation stage through the focus of the beam, in the plane orthogonal to the beam axis, to construct a terahertz image of the object. The spatial resolution that can be obtained will be limited by how small a spot the beam can be focused to, this ultimately being limited by diffraction as a result of the terahertz optical components typically being only a few tens of wavelengths across. A direct result of this is that higher spatial resolutions are possible for the shorter wavelengths corresponding to the higher frequencies within the incident pulse. A variety of imaging parameters can be used to construct an image from the recorded data. For example, with respect to the reference pulse, the relative amplitude of the time domain pulse, its time delay, the relative amplitude at a particular frequency or over a range of frequencies can all be used to form an image, some imaging parameters giving better contrast in a given circumstance than others. The data recorded to obtain an image also contains the full spectral information for each pixel in the image, and so spatially resolved spectral characterization of the materials constituting the object is possible.

If instead of operating in transmission the system is configured to detect the terahertz time domain signal reflected from an object consisting of different layers of material at different depths, the resulting recorded waveform will consist of a series of pulse-like signatures corresponding to the boundaries between the different layers within the object. The times at which these signatures occur within the waveform will depend on the round-trip time for the pulse reflected from each particular boundary, and so can be used to provide depth information or to reconstruct a three-dimensional image of the object. By selecting just one of these signatures and gating out the others, it is possible to record a two-dimensional image of the selected layer, or to Fourier transform the signature for spectroscopic analysis of the layer material.

There are two main approaches to generating the terahertz pulse that is incident on the sample. In photoconductive generation, the pump beam from the ultrafast pulsed laser is incident on a semiconductor material that bridges the gap between

the two halves of a dipole antenna, which is formed as a metallized pattern on a dielectric substrate. The two halves of the dipole are electrically biased so that a potential difference exists across the gap. When the laser pulse is incident on the semiconductor, it photo-excites carriers into the conduction band allowing a current to flow through the antenna, resulting in radiation of the terahertz pulse.

Alternatively, in optoelectronic generation, the terahertz radiation is generated by allowing the different frequency components of the incident laser pump pulse to mix together in a non-linear crystal. The resulting difference frequencies result in an emergent pulse in the terahertz range.

Similarly, there are two approaches to the gated detection of the terahertz pulse after it has interacted with the sample. In photoconductive detection, the terahertz pulse is incident on an antenna which, although unbiased, is similar to that used for photoconductive generation. However, no current flows until photo-excited carriers are generated in the semiconductor material by the incident probe pulse from the ultrafast laser, thus gating the detection. The average current flow resulting from a train of incident terahertz pulses can be measured using conventional electronics and is proportional to the terahertz field amplitude.

In the second approach, electro-optic detection, the terahertz pulse and laser probe pulse are both incident on a crystal of a material displaying the linear Pockels effect. Both the terahertz pulse and laser pulse are linearly polarized in the same direction when they are incident on the crystal. The emergent laser probe beam is split into two orthogonally polarized components using a quarter-wave plate and Wollaston prism, and the difference between these two components is measured using a balanced pair of photodetectors. The degree of ellipticity of the elliptically polarised laser beam that emerges from the crystal depends on the amplitude of the terahertz pulse at that instant, so that the difference signal from the photodetectors is directly proportional to the terahertz amplitude. Again, the detection is gated by the probe beam, as there can only be a signal present on the photodetectors for the duration of the probe pulse.

13.2 Terahertz Scale Modelling

Terahertz scale modelling provides a convenient technique for studying fundamental optical phenomena that are difficult to observe at shorter wavelengths. As a result of the scale invariance of Maxwell's equations, light scattering by small particles can be explored by replacing the incident light with terahertz radiation and scaling up the dimensions of the scattering particles in proportion to the wavelength. Operating in the terahertz range has a number of advantages [2, 3]. Firstly, the wavelengths involved are approximately 500 times those of visible light, greatly aiding in the fabrication of test samples with well controlled and well characterized properties. Secondly, the bandwidth of terahertz TDS systems is sufficiently large to enable the complete range from Rayleigh scattering to Mie scattering to be covered in a single experiment. Furthermore, TDS directly measures both the amplitude and phase of

the scattered field. Finally, the ability to conduct time-resolved measurements of the scattered field allows different scattering centres and scattering mechanisms to be identified, as well as enabling standing waves and reflections from the surroundings to be time-gated out of the signal. This section describes terahertz scale model experiments that have been conducted to explore scattering from small particles, starting with an investigation of the optical phenomenon known as the glory.

13.2.1 Glory Scattering

In the visible part of the spectrum, the glory is seen by air passengers as a rainbow-coloured halo surrounding the shadow thrown by their aircraft on a cloud below them. It may also be seen by mountaineers about the shadow thrown by the mountain top on lower level cloud, and even in the clouds of steam rising from hot springs and geysers, encircling the shadow of the observer's head. The effect is caused by the back-scattering of sunlight from water droplets in clouds, mist or steam, and so requires the sun to be behind the observer. While theoretical treatments describing the origin of the rainbow-banded halo have existed since the 1940s, they have, until recently, been very difficult to verify experimentally, as there has been no means of separating components of the scattered field that have been scattered through different mechanisms. In fact the first measurements to test the validity of the theoretical models were carried out not at visible wavelengths, but in the terahertz range.

In their experiments, Cheville et al. [4] used a terahertz TDS system, modified to transmit a terahertz beam approximating a plane wave at a test target and to collect the back-scattered terahertz radiation over a narrow range of angles centred on an angle of 11° to the incident beam. Their system covered a frequency range of 100 GHz to 2 THz. They used a 6.35 mm diameter alumina sphere as their target. The capability of TDS to time resolve components of the scattered pulse that had taken different paths, and therefore arrived at different times at the detector, enabled scattered signals with three different origins to be identified. Firstly, there was a component that was specularly reflected from the front surface of the sphere. Secondly, there were components arriving at glancing incidence at the sides of the sphere, travelling as surface waves for a short distance around the circumference of the sphere, before taking a short-cut through the sphere, and then becoming another surface wave on the opposite side of the sphere, to finally be re-radiated. These surface wave components took two different paths dependent on whether they were incident on left side of the sphere and travelled in a clockwise direction around the sphere, or were incident on the right side and travelled in an anti-clockwise direction. They could be separately identified in the scattered signal because they suffered different time delays. Finally, there was a component transmitted through the sphere to be reflected from its back surface. Analysing the spectra of these components, it was found that the surface wave components had an oscillatory character in the frequency domain due to frequency-dependent constructive and

deconstructive interference between surface waves travelling in opposite directions around the sphere. This result was in good agreement with theoretical predictions. As the constructive and deconstructive interference shows an angular dependence as well as a frequency dependence, this effect will give rise to a rainbow-like halo with unpolarized incident radiation. Although the refractive index of the alumina sphere in the terahertz range was greater than that of water at visible wavelengths, simplifying the paths taken by the surface waves, this experiment still provided the first validation of the theoretical models and confirmed the role played by surface waves in glory scattering. Subsequently, the behavior of light circulating near the surface of dielectric microcavities has been explored using time-resolved measurements with ultrafast lasers in the visible and infrared parts of the spectrum [5].

13.2.2   Multiple Scattering in Random Media

Mittleman's group at Rice University in Texas have used terahertz TDS to study multiple scattering in random media. Again, the results they have gained are difficult to measure in other parts of the spectrum. The results are relevant to the imaging of buried objects in scattering media at shorter wavelengths, particularly in the context of biomedical imaging.

In all of their experiments, their experimental samples have consisted of large numbers of PTFE spheres of diameter 0.794 ± 0.025 mm poured into sample cells of various sizes and dimensions, the cells being made from PTFE or having PTFE windows. PTFE has low absorption and dispersion in the terahertz range, making it well suited to this application. The corresponding volume fraction of the samples was 0.56 ± 0.04. Because of the relatively large size of the scattering spheres, enabling them to be produced with greater uniformity, the sample size distribution and density is better characterized than for samples in optical scattering experiments, which commonly consist of a suspension of latex spheres in water.

Experiments were performed to explore both ballistic scattering, in which the properties of the undeviated beam passing through the scattering medium were characterized, and on diffusive scattering, where the field scattered to different angles was measured. In the ballistic case, although that portion of the beam is undeviated, the radiation will still be scattered between the individual spheres as it propagates through the sample, modifying the amplitude and time delay of the received terahertz pulse. By measuring the transmission through a range of samples of different thickness, Pearce and Mittleman [2] were able to extract the frequency-dependent mean free path. In addition, an effective refractive index can be determined from the measured phase, this differing markedly to a simple volume-weighted average refractive index due to interference between the multiply scattered waves. They found that the measured group velocity showed very good agreement with that predicted by the quasi-crystalline approximation theoretical model, but that this overestimated the mean free path and the phase velocity, although similar

trends and resonant features were seen in the measurements. However, the range of validity for the quasi-crystalline approximation is usually considered limited to volume fractions of less than about 0.4, so it is not surprising that some deviation is seen for the higher volume fractions used in the experiments.

In the diffusive scattering experiments, correlations between the field scattered to different angles and at different time delays made it possible to identify specific scattering events inside the sample [3]. These events vary for different random arrangements of the scattering medium, but the experiments allowed the probability distributions for the amplitude and phase of the scattered radiation to be determined [6].

13.3 Terahertz Near-Field Microscopy

The preceding section explained how terahertz TDS can be used with scale model samples to explore the interaction between light and small scattering particles. However, it proves possible to concentrate terahertz radiation down to sub-wavelength dimensions, enabling the interaction between terahertz radiation and small objects to be measured directly. This is valuable, as observing objects with terahertz radiation can provide information that is not available to other wavelengths. Moreover, it proves possible to form terahertz images of objects on this scale, in other words to perform microscopy, but with the added advantages of spectroscopy and ultrafast time resolution. Although some of the techniques to be described in this section reach spatial resolutions of the order of a few microns rather than nanometers, they can still be used via scale modelling to test theories of the interaction of light with nanoscale objects in the visible part of the spectrum. However, these techniques are gradually being pushed towards finer resolutions. Already, one technique has achieved a spatial resolution of 40 nm, corresponding to 1/3,000 of the wavelength, and is capable of imaging regions of different carrier density in semiconductor devices at this scale. Four methods for terahertz microscopy will be described in this section: aperture-based techniques, plasmonic focusing using parallel plate waveguides, terahertz aperture-less near-field scanning optical microscopy (ANSOM), and laser terahertz emission microscopy. Because of the sub-wavelength dimensions involved, all are concerned with the interaction between the object and the terahertz beam in its near-field region.

13.3.1 Aperture-Based Techniques

One way to achieve sub-wavelength resolution images at terahertz frequencies is to place the object in the beam from a terahertz source and raster scan it in front of a sub-wavelength aperture in a metal sheet or film, detecting the evanescent field coupled through the aperture. The object needs to be placed immediately in

front of the aperture. Mitrofanov et al. [7] have described an integrated aperture and photoconductive detector with dipole antenna that can be used in a terahertz TDS system. Because the field amplitude of the radiation coupled through a sub-wavelength aperture decreases as the third power of the aperture size, the aperture was limited to 5 μm across, giving a spatial resolution of 7 μm over a 200 GHz to 2.5 THz frequency range. Kawano [8] has presented a different integrated aperture and detector structure, incorporating a near-field probe which enhances the coupling of evanescent modes to the detector. In this case, the detector was a two-dimensional electron gas detector and the spatial resolution was 9 μm.

Rather than sampling the terahertz radiation with a physical aperture in a metal sheet, the portion of the beam that is sampled can be defined by the width of the probe beam if electro-optic detection is used with TDS. This approach is known as dynamic aperture near-field imaging. The technique has been used by the group at TU Delft to explore the transmission of terahertz radiation through sub-wavelength slits and holes [9, 10]. For these experiments, the slit or hole to be characterized was formed in a gold layer on the top of a gallium phosphide substrate. This gallium phosphide substrate acts as both the electro-optic detection crystal and the substrate for the test sample. A thin layer of germanium separates the gold layer from the gallium phosphide substrate. The terahertz field is incident on the gold surface of the structure, so that some of it is coupled through the hole in the metal, passing through the germanium layer and into the gallium phosphide, in which it induces optical birefringence through the Pockels effect. This birefringence is sampled by focusing the probe beam from the near-infrared ultrafast laser under the sample, so that it is incident on the opposite side of the substrate to the metal layer. The probe beam will be reflected from the germanium layer, while its polarization will be modified by the terahertz-induced birefringence of the gallium phosphide. The polarization of the reflected probe beam can then be analysed as in conventional electro-optic detection to measure the terahertz field amplitude. Raster scanning the substrate relative to the probe beam produces an image of the terahertz electric field transmitted through the hole or slot under test. By appropriate choice of the gallium phosphide crystal orientation, it is possible to measure different Cartesian components of the terahertz field. It should be stressed that although the hole being tested is quite small, having sub-wavelength dimensions, it is the significantly smaller width of the probe beam focus that defines the effective aperture. A spatial resolution of better than 10 μm has been achieved using this technique.

Experiments using the dynamic aperture technique can provide information on the transmission of electromagnetic radiation through narrow slits and holes that is also relevant to other wavelengths. Seo et al. [9] found that the terahertz radiation is funnelled through narrow slits, so that the field amplitude increased as the slit got narrower, although the overall integrated amplitude through the slit remained constant. The maximum field amplitude was achieved when the slit was half a wavelength long and as narrow as possible. Adam et al. [10] compared measurements of the time evolution of the near-field of the axial component of the electric field transmitted through a sub-wavelength hole with theoretical and numerical models, providing considerable insight into what actually happens when

light is transmitted through small holes. The authors point out that a comparable measurement in the visible part of the spectrum on a 200 nm hole would require measurement of the E-field of a 1 fs long, single-cycle pulse, with a temporal resolution of 100 attoseconds, in a bandwidth extending from 250 to 3,000 nm, and that such a measurement is currently not feasible.

13.3.2 Plasmonic Parallel-Plate Waveguides

Adiabatic tapering of the width and separation of parallel plate waveguides provides another method for confining terahertz radiation to sub-wavelength dimensions, and could form the basis of a scanning probe for imaging and spectroscopy. Zhan et al. [11] have demonstrated focusing down to 10 µm by 18 µm using this technique. As their peak frequency was 0.115 THz, this corresponds to a mode area of $2.6 \times 10^{-5}\lambda^2$, which they claim is the smallest fractional mode area ever experimentally demonstrated with any waveguide at any wavelength. From their experiments it is clear that for maximum confinement, it is important to taper the waveguide in both dimensions. As they observed a field enhancement at the edge of the waveguide, they attribute the strong field confinement at the open sides of the waveguide to the coupling of plasmonic edge modes across the air gap. They found that the radiation was funnelled along the waveguide, with the amplitude increasing as the dimensions were reduced. Propagation along the waveguide was dispersion-free and showed no reduction in bandwidth of the transmitted radiation. Rusina et al. [12] have presented the theoretical limits for terahertz focusing in plasmonic waveguides. They find that a funnel shaped taper at the end of the waveguide would give the best performance, but that losses will limit the smallest spot size that can be achieved to the region of 100–250 nm.

13.3.3 Terahertz Ansom

Terahertz apertureless near-field scanning optical microscopy (ANSOM) relies on the interaction between the sample to be imaged and the evanescent fields generated at the tip of a sharply pointed conductive probe placed in an incident terahertz beam. The probe tip can be scanned across the object to build up an image. A major advantage of this approach over aperture-based techniques is that it is not prone to the rapid fall-off of transmission that occurs as the size of the aperture is decreased.

In order to detect the resulting signal, it is necessary to separate that due to the near-field interaction with the probe from the background signal produced by the incident terahertz beam, which would otherwise completely swamp the signal of interest. Two schemes have been used to detect the near-field signal. In one method, the sample is placed on the surface of a gallium phosphide crystal, just

below the probe tip [13]. When a linearly polarized terahertz pulse is incident on the crystal and probe, a terahertz near-field is developed below the probe tip, with the E-field lines oriented perpendicularly to the crystal surface. Now, if a probe pulse from a near-infrared ultrafast laser is incident on the reverse side of the gallium phosphide crystal, its polarization will be modified by birefringence induced in the crystal through the linear Pockels effect. Because the crystal has a (100) orientation, the polarization of the probe pulse is only affected by the terahertz E-field that is perpendicular to the crystal surface. As the incident terahertz pulse is polarized parallel to the crystal surface, it has no effect on the polarization of the probe pulse, making the method background free. Where the perpendicular component of the terahertz field is strong, in the near-field of the tip, it elliptically polarizes the probe pulse with an ellipticity proportional to the E-field. The polarization of the resultant reflected probe pulse is then analysed as in conventional terahertz TDS electro-optic detection to measure the amplitude of the terahertz near-field after it has interacted with the sample. The spatial resolution scales with the tip apex diameter and is independent of frequency. A spatial resolution of about 10 μm has been achieved using this technique. By growing caesium iodide crystals on top of the gallium phosphide crystal, Planken et al. [14] have used this technique to demonstrate terahertz spectroscopy on the sub-wavelength scale by measuring the spectra of regions with and without caesium iodide crystals separated by about 20 μm. By comparing the resulting spectra, they could identify the caesium iodide phonon absorption resonance at 1.8 THz. However, a potential disadvantage of this approach is that it is limited to measuring thin objects in transmission, which have to be placed on the gallium phosphide crystal surface.

In a second approach, the terahertz signal back-scattered by the interaction between the probe tip and the sample surface is measured using a terahertz detector. In this case, the scattered signal is separated from the background signal due to the incident terahertz beam by vibrating the probe tip and using lock-in detection. Astley et al. [15] have demonstrated that the scattered field can be enhanced if the vibrating probe is placed above a thin metallic film due to contributions from surface plasmon states on both sides of the film. Their experiment was conducted using a 0.5 μm probe tip, with a 750 Hz, 750 nm vibration and a 500 nm thick gold film. Huber et al. [16] have built a terahertz nanoscope, operating at 2.54 THz, based around lightening-rod field enhancement at the apex of an atomic force microscope probe tip. They use a continuous-wave incident beam and interferometric detection to amplify the scattered signal. Using this instrument they have demonstrated terahertz images of single nano-transistors, with a spatial resolution of 40 nm, corresponding to 1/3,000 of the wavelength. The image contrast makes it possible to differentiate between the different materials in the transistor. Furthermore, it is possible to spatially resolve regions of different carrier density within the semiconductor materials in the important 10^{16}–10^{19} carrier cm^{-3} range, where visible and infrared methods lack sensitivity. Calculations show that as few as 100 electrons are all that are needed to generate significant contrast within the terahertz images.

13.3.4 Laser Terahertz Emission Microscopy

Yamashita et al. [17] have demonstrated a technique known as laser terahertz emission microscopy (LTEM), which is capable of non-contact, non-destructive testing for failures in integrated circuits. In this technique, a pump pulse from a near-infrared ultrafast laser is scanned across the surface of the integrated circuit, which may be under applied electrical bias. In response to this pump pulse, terahertz radiation is emitted from various areas of the integrated circuit due to regions acting as biased photoconductive switches, unbiased interfaces with built-in electric fields such as pn junctions and Schottky diodes, or from the surface of the semiconductor. The emitted terahertz pulses are detected using photoconductive detection, as in conventional terahertz TDS, to form the terahertz image. The spatial resolution is dependent on the spot size of the probe beam and has been demonstrated to be better than 3 μm. The resulting amplitude and phase distribution in the terahertz image is characteristic of the integrated circuit and can be used to identify failures within the circuit, which will show up as unexpected differences in the image.

13.4   Terahertz Spectroscopy of Nanomaterials

Terahertz spectroscopy is ideal for studying conductivity in materials because the 0.1–2 THz range covered by typical TDS systems is a good match to typical carrier scattering rates of 10^{12}–10^{14} s^{-1}. Other techniques cannot provide information about charge transport in materials on sub-picosecond to nanosecond time scales and nanometre length scales. This makes it a very powerful technique for studying nanomaterials.

Measurements of this sort are carried out using time-resolved terahertz spectroscopy (TRTS), which is also known as optical pump terahertz probe (OPTP) spectroscopy. This is an adaptation of the TDS technique in which the beam from the femtosecond laser is split three ways, so that one beam can provide an optical pump beam to photo-excite carriers in the sample, which is then probed using the terahertz beam as in conventional TDS. A typical set-up is shown in Fig. 13.2. An optical delay line in the pump beam allows the relative time of arrival of the optical pump and terahertz probe pulses at the sample to be adjusted.

The relaxation dynamics of transient photoconductivity in nanomaterials can be probed by scanning the pump beam delay while holding the terahertz gating delay at the peak of the terahertz waveform. Typically, $-\Delta T/T_0$ is plotted against the probe time delay, showing the change in the difference of transmission on photo-excitation divided by the transmission of the sample before photo-excitation. Example plots comparing silicon nanocrystal films with a silicon on sapphire film are presented in [18]. The photoconductive lifetime can be determined from the rate of decay in plots of this kind.
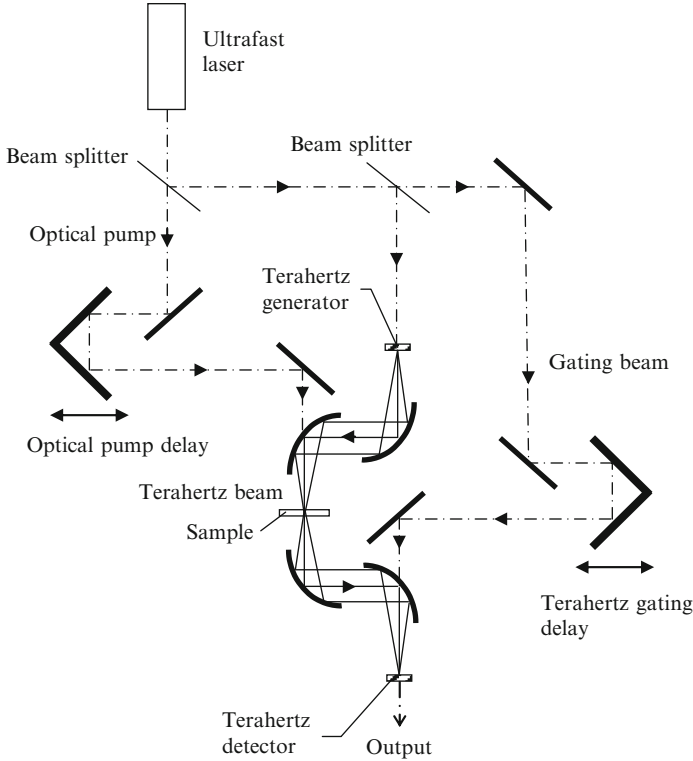
Fig. 13.2 Time-resolved terahertz spectroscopy system

The conductivity of a sample can be determined from measurements made by holding the pump beam delay constant while the terahertz gating delay is scanned to record the full terahertz waveform at a fixed time after photo-excitation. The conductivity is found by firstly Fourier transforming the recorded waveform to the frequency domain to yield the spectrum, from which the frequency dependent absorption coefficient α and refractive index n can be found. For nano-structures, it may be necessary to make use of an effective medium approximation to determine α and n [19]. The frequency dependent complex conductivity can then be determined from α and n.

The carrier scattering time τ, the plasma frequency ω_p and the persistence of velocity parameter c_1 can all be found by fitting the Drude-Smith model to the complex conductivity as a function of angular frequency ω:

$$\tilde{\sigma}(\omega) = \frac{\varepsilon_0 \omega_p^2 \tau}{1 - i\omega\tau} \left[1 + \frac{c_1}{1 - i\omega\tau} \right] \tag{13.1}$$

The mobility for the Drude-Smith model can then be determined from:

$$\eta = (1 + c_1) \frac{e\tau}{m^*} \qquad (13.2)$$

where e is the electronic charge and m^* is effective mass. The parameter c_1 is related to carrier backscatter and indicates how localized the carriers are [20].

The carrier dynamics of a variety of nanostructures have been characterised by terahertz spectroscopy. A few examples include: ZnO nanowires, nanoparticles and thin films [19]; nanocrystal-carbon nanotubes and nanocrystal-graphene oxide hybrid nanostructures [21]; GaAs nanowires [22]; and Ge nanowires [23].

13.5 Biological Systems at the Nanoscale

The terahertz spectroscopy of biological systems in general has been covered in detail in an earlier book in this series [24], and so this section will concentrate on summarising those aspects that are relevant to sensing biological phenomena at the nanoscale. Terahertz spectroscopy is sensitive to both the collective vibrational modes of large biomolecules and to dynamic fluctuations in the water networks that surround such biomolecules in their functional state inside biological cells. Characteristic spectral features of biomolecules, such as DNA nucleobases, have been measured with samples in the form of pellets of polycrystalline powder mixed with polyethylene [25] or in the form of polycrystalline thin films [26]. However, these sharp spectral features disappear when the molecules are in solution, as the spectra become dominated by strong absorption due to water. Nevertheless, the spectra contain useful information about the dynamics of the water surrounding the biomolecules, and because the water dynamics influence and are influenced by the biomolecules they are surrounding, information about the conformational state of the biomolecules themselves. By measuring the concentration dependence of the terahertz absorption spectra of biomolecules in solution, it has proven possible to determine the size of the dynamical hydration shell of water with modified physical properties that surrounds each biomolecule [27]. This dynamical hydration shell can extend to greater than 1 nm away from the surface of a protein molecule, which is much further than the static hydration radius inferred using other techniques. Within this hydration shell, the fluctuations in the water hydrogen bond network are slowed down such that the water dynamics are different from those of bulk water, leading to a distinct terahertz absorbance. Similar terahertz measurements indicate that the introduction of sugar molecules slows the hydration dynamics, leading to reduced biological activity of proteins [27]. As a result of these measurements, it is thought that this is the mechanism behind anhydrobiosis, whereby plants that can survive extreme conditions produce sugars which have a stabilising and protective effect on their proteins and cell membranes. Further measurements have indicated that the change of water dynamics is much less for partially unfolded proteins than for the

wild type, and that large changes are seen due to site-specific mutants. Furthermore, as proteins fold to a new state, terahertz measurements indicate the surrounding water molecules have rearranged themselves long before the protein has settled into its new shape. Therefore, it is not surprising that conformational changes lead to distinct terahertz absorption spectra, for example in light induced conformational change in photoactive yellow protein in solution [28].

Groma et al. [29] have used light induced terahertz radiation to explore the fundamental primary charge translocation phenomena in bacteriorhodopsin. In their experiment, they effectively used the bacteriorhodopsin sample as the terahertz generator in a TDS-like system and analysed the emitted terahertz radiation.

Terahertz biochips enabling label-free DNA sequencing have been developed which allow femtomolar sensitivity levels and single-base mutation detection capability [30, 31]. These rely on shifts of the resonant frequency of a terahertz resonator on the biochip due to differences in the refractive index and absorption coefficient of hybridized and denatured DNA.

Because of the extreme sensitivity of terahertz radiation to water, a modification of TDS, referred to as terahertz differential time domain spectroscopy (DTDS), is capable of sensing a 1 nm thickness change in a layer of liquid water. As a result, changes in living cell monolayers are more readily detected using DTDS than with optical phase contrast microscopy [32].

13.6   Security Applications

Explosives [33–35], chemical [36] and biological threats [37] all have unique spectral signatures in the terahertz range. There is considerable potential for sensing these substances at the nanoscale because, while the spectral detail becomes indistinct in large ensembles of molecules, single molecules should have distinct spectral lines, allowing them to be identified from terahertz fingerprint spectra. Terahertz near-field techniques, as described in Sect. 13.3 above, are developing rapidly and offer the potential to identify very small quantities of substances. Although there is still much work to be done, Terahertz nano-spectroscopy may ultimately provide the necessary specificity and sensitivity to provide instant early warning of threats at the single molecule level.

13.7   Conclusions

This chapter has shown that, despite the relatively large size of the wavelengths involved, terahertz spectroscopy and imaging can provide information on processes occurring at the nanoscale that is difficult or impossible to acquire using techniques operating in other regions of the electromagnetic spectrum. Terahertz scale modelling can be used to test theories of the fundamental behaviour of light that are

also applicable to the visible part of the spectrum. Terahertz near-field techniques with extreme sub-wavelength spatial resolution are capable of mapping regions of different carrier density within semiconductor devices. Terahertz spectroscopy of nanomaterials enables their ultrafast carrier dynamics to be characterized. Terahertz spectroscopy of biomolecules may lead to greater understanding of biological function at the molecular level. Finally, these recent developments give some hope that terahertz techniques will ultimately be developed that are capable of detecting single molecules of explosives and of chemical and biological agents.

References

1. Huang S, Ashworth PC, Kan KWC, Chen Y, Wallace VP, Zhang Y, Pickwell-MacPherson E (2009) Improved sample characterization in terahertz reflection imaging and spectroscopy. Opt Express 17:3848–3854
2. Pearce J, Mittleman DM (2003) Using terahertz pulses to study light scattering. Phys B 338:92–96
3. Jian Z, Pearce J, Mittleman DM (2003) Characterizing individual scattering events by measuring the amplitude and phase of the electric field diffusing through a random medium. Phys Rev Lett 91: 033903-1-4
4. Cheville RA, McGowan RW, Grischkowsky D (1998) Time resolved measurements which isolate the mechanisms responsible for terahertz glory scattering from dielectric spheres. Phys Rev Lett 80:269–272
5. Wolf JP, Pan YP, Turner GM, Beard MC, Schmuttenmaer CA, Holler S, Chang RK (2001) Ballistic trajectories of optical wave packets within microcavities. Phys Rev A 64: 023808-1-5
6. Pearce J, Jian Z, Mittleman DM (2003) Statistics of multiply scattered broadband terahertz pulses. Phys Rev Lett 91: 043903-1-4
7. Mitrofanov O, Lee M, Hsu JWP, Brener I, Harel R, Fredereci JF, Wynn JD, Pfeiffer LN, West KW (2001) Collection-mode near-field imaging with 0.5-THz pulses. IEEE J Sel Top Quantum Electron 7:600–607
8. Kawano Y (2011) Collection-mode near-field imaging with 0.5-THz pulses. IEEE J Sel Top Quantum Electron 17:67–78
9. Seo MA, Adam AJL, Kang JH, Lee JW, Ahn KJ, Park QH, Planken PCM, Kim DS (2008) Near field imaging of terahertz focusing onto rectangular apertures. Opt Express 16:20484–20489
10. Adam AJL, Brok JM, Seo MA, Ahn KJ, Kim DS, Kang JH, Park QH, Nagel M, Planken PCM (2008) Advanced terahertz electric near-field measurements at sub-wavelength diameter metallic apertures. Opt Express 16:7407–7417
11. Zhan H, Mendis R, Mittleman DM (2010) Superfocusing terahertz waves below λ/250 using plasmonic parallel-plate waveguides. Opt Express 18:9643–9650
12. Rusina A, Durach M, Nelson KA, Stockman MI (2008) Nanoconcentration of terahertz radiation in plasmonic waveguides. Opt Express 16:18576–18589
13. van der Valk NCJ, Planken PCM (2004) Towards terahertz near-field microscopy. Phil Trans R Soc Lond A 362:315–321
14. Planken PCM, van Rijmenam CEWM, Schouten RN (2005) Opto-electronic pulsed THz systems. Semicond Sci Technol 20:S121–S127
15. Astley V, Zhan H, Mittleman DM, Hao F, Nordlander P (2007) Plasmon-enhanced terahertz near-field microscopy. CLEO 2007, CTuJJ5.pdf
16. Huber AJ, Keilmann F, Wittborn J, Aizpurua J, Hillenbrand R (2008) Terahertz near-field nanoscopy of mobile carriers in single semiconductor nanodevices. Nano Lett 8:3766–3770

17. Yamashita M, Kawase K, Otani C, Kiwa T, Tonouchi M (2005) Imaging of large-scale integrated circuits using laser terahertz emission microscopy. Opt Express 13:115–120
18. Cooke DG, MacDonald AN, Hryciw A, Wang J, Li Q, Meldrum A, Hegmann FA (2006) Transient terahertz conductivity in photoexcited silicon nanocrystal films. Phys Rev B 73: 193311-1-4
19. Baxter JB, Schmuttenmaer CA (2006) Conductivity of ZnO nanowires, nanoparticles, and thin films using time-resolved terahertz spectroscopy. J Phys Chem B 110:25229–25239
20. Hegmann FA, Cooke DG, Walther M, Baillie DMJ, Sydora RD, Marsiglio F (2008) Terahertz dynamics of localized carriers. EOS Annual Meeting 2008, Paris, TOM 2, Session 12
21. Jung BJ, Myung Y, Cho YJ, Sohn YJ, Jang DM, Kim HS, Lee CW, Park J, Maeng I, Son JH, Kang C (2010) Terahertz spectroscopy of nanocrystal-carbon nanotube and –graphene oxide hybrid nanostructures. J Phys Chem C 114:11258–11265
22. Parkinson P, Joyce HJ, Gao Q, Tan HH, Zhang X, Zou J, Jagadish C, Herz LM, Johnston MB (2009) Carrier lifetime and mobility enhancement in nearly defect-free core-shell nanowires measured using time-resolved terahertz spectroscopy. Nano Lett 9:3349–3353
23. Strait JH, George PA, Levendorf M, Blood-Forsythe M, Rana F, Park J (2009) Measurements of the carrier dynamics and terahertz response of oriented germanium nanowires using optical-pump terahertz-probe spectroscopy. Nano Lett 9:2967–2972
24. Bowen JW (2011) Terahertz spectroscopy of biological systems. In: Di Bartolo B, Collins J (eds) Biophotonics: spectroscopy, imaging, sensing, and manipulation. Springer, Dordrecht, pp 287–303
25. Fischer BM, Walther M, Uhd Jepsen P (2002) Far-infrared vibrational modes of DNA components studied by terahertz time-domain spectroscopy. Phys Med Biol 47:3807–3814
26. Laman N, Sree Harsha S, Grischkowsky D, Melinger JS (2008) High-resolution waveguide THz spectroscopy of biological molecules. Biophys J 94:1010–1020
27. Leitner DM, Gruebele M, Havenith M (2008) Solvation dynamics of biomolecules: modeling and terahertz experiments. HFSP J 2:314–323
28. Castro-Camus E, Johnston MB (2008) Conformational changes of photoactive yellow protein monitored by terahertz spectroscopy. Chem Phys Lett 455:289–292
29. Groma GI, Hebling J, Kozma IZ, Váró G, Hauer J, Kuhl J, Riedle E (2008) Terahertz radiation from bacteriorhodopsin reveals correlated primary electron and proton transfer processes. PNAS 105:6888–6893
30. Haring Bolivar P, Nagel M, Richter F, Brucherseifer M, Kurz H, Bosserhoff A, Büttner R (2004) Label-free THz sensing of genetic sequences: towards 'THz biochips'. Phil Trans R Soc Lond A 362:323–335
31. Nagel M, Först M, Kurz H (2006) THz biosensing devices: fundamentals and technology. J Phys Condens Matter 18:S601–S618
32. Liu H-B, Plopper G, Earley S, Chen Y, Ferguson B, Zhang X-C (2007) Sensing minute changes in biological cell monolayers with THz differential time-domain spectroscopy. Biosens Bioelectron 22:1075–1080
33. Leahy-Hoppa MR, Fitch MJ, Zheng X, Hayden LM, Osiander R (2007) Wideband terahertz spectroscopy of explosives. Chem Phys Lett 434:227–230
34. Laman N, Sree Harsha S, Grischkowsky D, Melinger JS (2008) 7 GHz resolution waveguide THz spectroscopy of explosives related solids showing new features. Opt Express 16:4094–4105
35. Liu H-B, Zhong H, Karpowicz N, Chen Y, Zhang X-C (2007) Terahertz spectroscopy and imaging for defense and security applications. Proc IEEE 95:1514–1527
36. Kawase K, Ogawa Y, Watanabe Y (2003) Non-destructive terahertz imaging of illicit drugs using spectral fingerprints. Opt Express 11:2549–2554
37. Brown ER, Khromova TB, Globus T, Woolard DL, Jensen J, Majewski A (2006) Terahertz-regime attenuation signatures in *Bacillus subtilis* and a model based on surface polariton effects. IEEE Sens J 6:1076–1083

14
Application of Plasmonics in Biophotonics: Laser and Nanostructures for Cell Manipulation

Alexander Heisterkamp, M. Schomaker, and D. Heinemann

Abstract In cell biology and regenerative medicine, there is a certain need to modify or manipulate cells, for example within the field of tissue engineering or gene therapy.

Laser radiation allows the precise manipulation and imaging of cells with subcellular resolution. However, high numerical aperture objectives have to be used, to achieve spatial localization and confinement of the laser radiation. Thereby, cell throughput is limited. A possible technology to achieve a similar confinement of laser radiation can be the employment of plasmonic resonances. Using noble metals so-called surface plasmons, being collective electron oscillations at the surface of nanostructures or nanoparticles, can be excited by the laser radiation. Within the near field of these plasmons, the high field intensities can be used to achieve manipulation or characterization of biological processes within a cell.

A. Heisterkamp (✉)
Institute of Applied Optics, Friedrich-Schiller University Jena, Froebelstieg 1,
Jena 07743, Germany

Excellence Cluster REBIRTH, Hannover, Germany

Department of Biomedical Optics, Biophotonics Group, D-30419 Hannover, Germany
e-mail: a.heisterkamp@lzh.de

M. Schomaker • D. Heinemann
Excellence Cluster REBIRTH, Hannover, Germany

Laser Zentrum Hannover e.V., Hannover, Germany

14.1 Introduction

The selective manipulation of cells or tissues is of very high interest in the fields of tissue engineering or regenerative medicine. Especially the introduction of foreign materials, such as DNA, RNA or other foreign molecules into a cell is a key method in cell biology. The so-called transfection, introduction and expression of foreign genetic material into a cell, is usually performed by conventional techniques, like viral transfer, lipofection, nucleofection, electroporation, each of these techniques having its special advantages and disadvantages.

Tightly focused ultrashort laser pulses allow the manipulation of cells and tissues on the subcellular scale with nearly negligible side effects. Due to the nonlinear absorption of near-infrared laser pulses, the induced effects, like generation of a microplasma, shockwave generation and photodissociation, are limited to a sub-femtoliter volume, allowing the ablation of subcellular components, like parts of the nucleus, the cytoskeleton or puncturing the cell membrane. However, in order to achieve this nonlinear absorption, usually very tightly laser light has to be applied, calling for the use of microscope objectives with high numerical apertures around NA = 1.4. The cell throughput of these laser-based cell manipulation is therefore limited.

Using plasmonic resonances in noble metals, the laser intensities at certain frequencies can be amplified near the surface of sub-micron structures. Using these collective electron oscillation in noble metals, the nonlinear effects can be achieved in the near field of nanostructures like gold nanoparticles, allowing the manipulation of high cell numbers using only mildly focused laser light.

In the following we will present the fs-laser based cell and tissue manipulation, based on tight focusing. Following exemplary applications in cell manipulation are shown.

In another section, the fundamentals of plasmonics on noble metals are very briefly introduced, leading the use of these resonances in the field of cell manipulation.

14.2 Nonlinear Ionization of Biological Substances

In order to achieve a manipulation or processing of biological substances like cells or cell organelles, the energy of the laser pulses has to be coupled to the media. In case of fs-laser pulses, this process is dominated by the generation of free electrons [1], [2]. As sketched in Fig. 14.1 the simultaneous absorption of several photons leads to the excitation of electrons into a quasi free band [3]. As the main constituent of tissue and cells is water, most of the models deal with the absorption properties of water. Within the exciton band the quasi-free electrons can further be accelerated by the laser radiation and lead to generation of more free electrons, a microplasma. Within the laser pulse of usually 100–200 femtoseconds, free electron densities around 10^{21}–10^{22} cm^{-3} are generated.
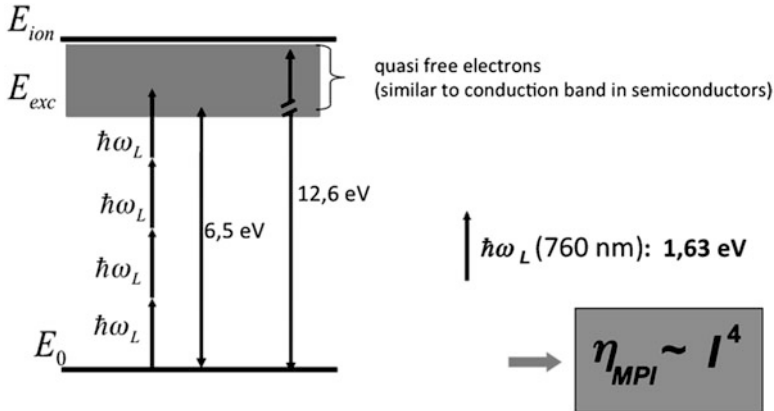
Fig. 14.1 Multiphoton ionization of water by simultaneous absorption of near-infrared photons (here at 760 nm), the probability η_{MPI} for this process is thus proportional number of photons (in this case four)
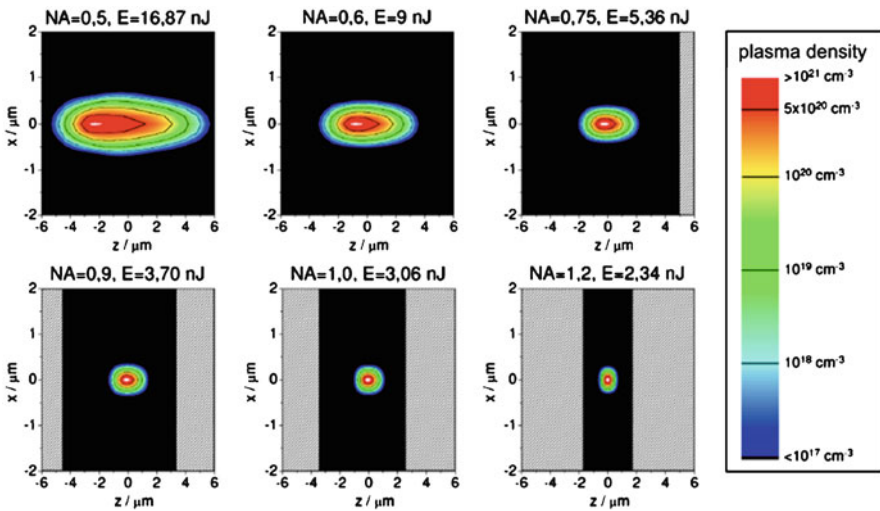

Fig. 14.2 Plasma densities calculated by Arnold et al. [2] for different numerical apertures

The extension of the laser manipulated areas, especially the spatial distribution of the microplasma generated by the fs-laser pulses can be calculated using numerical modeling of the multiphoton and cascade ionization in combination with the propagation integrals for the laser beam propagation at the focus, see Fig. 14.2.

At very high apertures, the manipulated area can be of submicron dimensions, allowing the cutting or ablation of subcellular organelles or structures, as demonstrated first by Koenig et al. [4]. An example of subcellular ablation is depicted in Fig. 14.3., showing the ablation of the cytoskeleton of a living cell, using a numerical
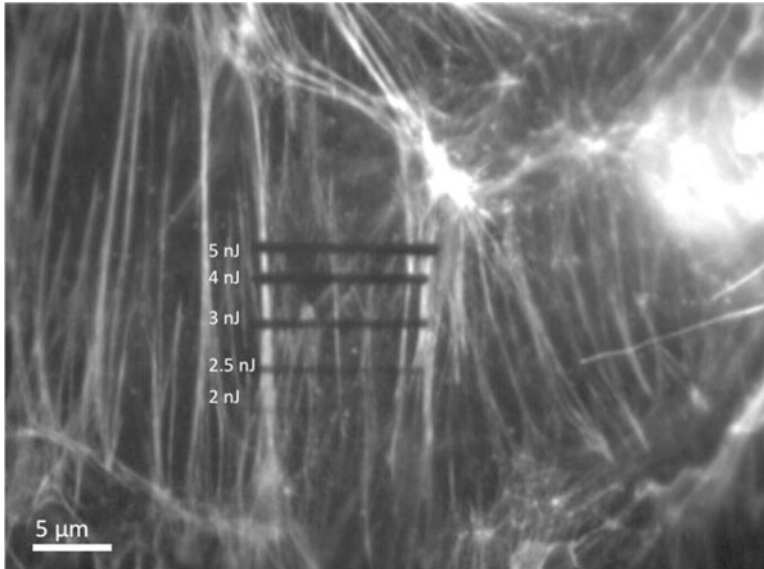
Fig. 14.3 fs-laser cuts within the cytoskeleton of a fixed bovine capillary endothelial cell. The cytoskeleton is stained for actin, the laser cutting width increases with increasing pulse duration (between 2 and 5 nJ.) [5]

aperture of 1.4 and 200 fs laser pulses at a few nanojoule energy and 1 kHz repetition rate [5]. The highly selective ablation of the subcellular structures can even be used to open the cellular membrane with very high spatial selectivity, allowing highly efficient DNA or RNA delivery into the target cell, so-called fs-laser transfection or optoperforation [6], [7], [8].

However, this method depends on the tight focusing using high numerical objectives to achieve the nonlinear effects in the confined volume at the cell membrane. Thereby, only one cell at a time is usually perforated, leading to very low throughput and thus limiting the applicability of this procedure.

14.3 Plasmon Resonances at Gold Nanoparticles

A possible way to overcome this limitation of single cell targeting can be the use of plasmonic resonances in gold nanoparticles. When noble metals are illuminated with optical fields, especially with dimensions smaller than the wavelength of the light, so-called surface plasmon resonance (SPR) can be excited. Metals like Ag, Au and Cu have plasmon resonances in the visible, meaning that the surface electrons of these particles oscillate at the corresponding frequencies, driven by the irradiating optical field. The effect was first theoretically explained and described already a
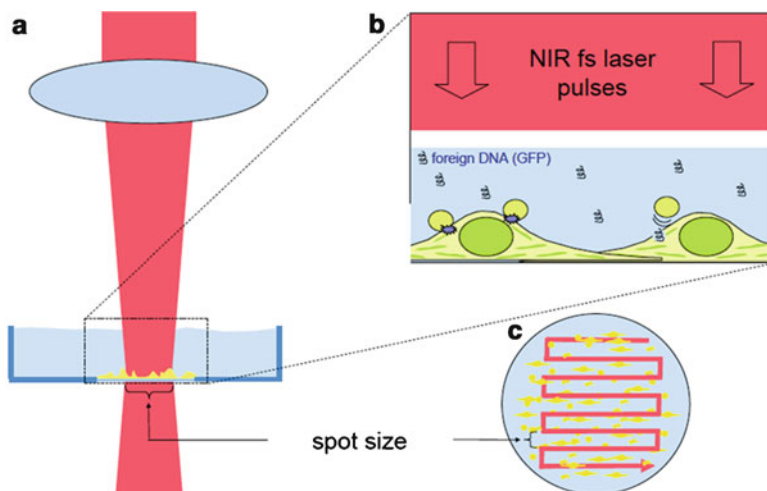
Fig. 14.4 Setup and principle of the nanoparticle mediated laser perforation of cells : (**a**) The laser radiation is moderately focused onto the cells resting in a Petri dish containing cell medium and the DNA or other molecules to be introduced into cell. (**b**) Due to the plasmon resonance at the particles, the laser intensity near the particle exceeds the threshold for optical breakdown and thereby perforates the cell membrane. (**c**) High throughput is achieved by scanning the laser spot over the whole Petri dish

century ago by Mie [9]. With respect to the application in cell manipulation, the key factor of this effect is the field enhancement in the near field of the particles, see for example Kelly et al. [9] or Nedyalkov et al. [10].

Like Nedyalkov has shown in his publication, these increased field intensities in the near field of the particle can be employed for material processing. As depicted in Fig. 14.4 a large number of cells can be addressed with the laser radiation, when gold nanoparticles are bound to the cell membrane. Scanning a moderately focused fs-laser beam over the cell dish, optical perforation by near field enhancement can be achieved in the vicinity of the nanoparticles, allowing the introduction of foreign molecules into the cells.

14.4 Materials and Methods

14.4.1 Cell Preparation

The cells used in this study were cultivated in glass-bottom-dishes (ibidi) or glass bottom well plates. The canine cell line (ZMTH3) was cultivated in RPMI-1640 medium, supplemented with 10 % FCS, penicillin and streptomycin. The cells were seeded onto the glass-bottom-dishes 254 prior to treatment. Apart from

the canine cell line, additional cells like primary cells from 12 week old albino mice (DRG neurons) and different human stem cells (embryonic and iPS cells) were used.

14.4.2 Nanopartcile Mediated Laser Cell Perforation

For the study of nanoparticle mediated laser perforation, different nanoparticle sizes and materials were used. Here we show the results concerning the gold nanoparticles with sizes between 80 and 250 nm (Kisker GmbH). The cells were incubated with the nanoparticles of the respective size at a particle concentration of 5.66–11.33 µg/ml for 3 h and washed with PBS afterwards.

The perforation efficiency was studied by using the membrane impermeable dye Lucifer yellow (LY). After the laser perforation, the dye was washed of the cell sample and the perforation efficiency was studied by optical microscopy. Cell viability was controlled by staining the cells with Propidium Iodide (PI).

14.4.3 Experimental Setup

The laser system used in this study consisted of a Ti:Sapphire laser (Thales, Bright laser), delivering 120 fs laser pulses at a repetition rate of 5 kHz and a wavelength of 780 nm. The laser was weakly focused by a 140 mm lens onto the samples, see Fig. 14.4. By moving the sample in a serpentine pattern at a constant velocity of 15 mm/s and constant pulse overlap, covering an area within the sample of approximately 3 mm^2.

14.5 Results

14.5.1 Nanoparticle-Cell Interaction

To verify the accumulation of nanoparticles at the cell membrane, environmental scanning electron microscope images of cells co-incubated with Au-nanoparticles have been performed. The ESEM images show that after incubating the cells with the goldparticle suspension several particles are bound to the cell membrane. With increasing incubation time both, the number of particles and the amount of particle clusters, increased. Figure 14.5 shows a representative ESEM image of ZMTH3 cells incubated with 200 nm goldparticles for 3 h.
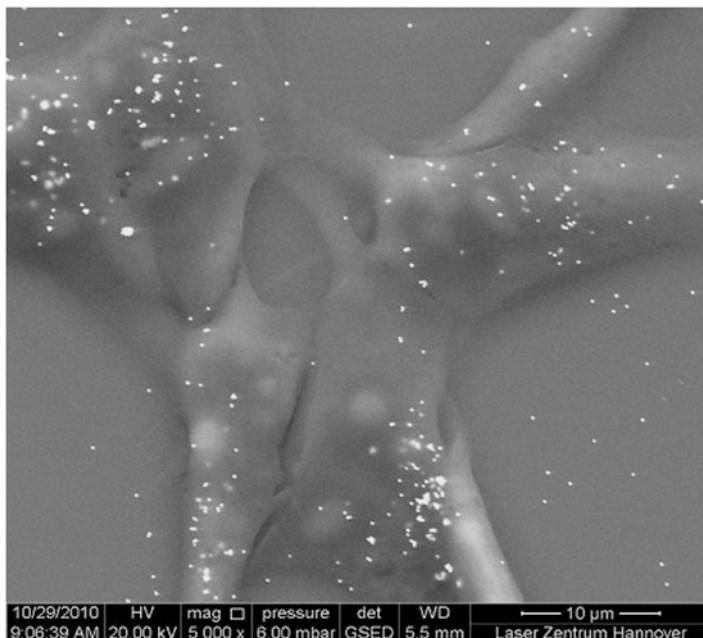
Fig. 14.5 ESEM image of nanoparticles (200 nm size) accumulating at the membrane of ZMTH3 cells after co-incubation for 3 h. Cells were fixed using 4 % PFA before imaging under wet conditions

14.5.2 Nanoparticle Mediated Laser Perforation

To perforate the cell membrane we incubated the cells with spherical GNP of different sizes for 3 h as described before. The cells were treated with fs laser pulses while scanning an area of 3 mm². A membrane impermeable fluorescent dye (Lucifer yellow) was used as an indicator for successfully perforated cells. The viability of the cells was checked with Propidium Iodide.

Perforation experiments were performed with different cell lines. The results show a successful perforation for human stem cells, human IPS cells and mouse DRG neurons using laser induced effects in 150 nm GNP, results are plotted for ZMTH3 cells in Fig. 14.6. The highest perforation rate of 79.3 % was achieved using ZMTH3 cells, 200 nm GNP with a cell viability of 83.3 %. That means nearly every vital cell was perforated. Reason for the loss of ca. 20 % of the cells could be the temperature fluctuation during the preparation and laser treatment procedure. The parameters for the best rate of perforation were a GNP incubation concentration of 11.33 μg/ml, a laser fluence of 0.1 J/cm² and a scanning velocity of 15 mm/s.

Since impermeable dye molecules, with a molecular weight of 457 Da, diffuse into the cells, transfection experiments with pEGFP-C1 vectors were performed. These plasmid vectors have a size of 4.7 kbp and are therefore much bigger than the
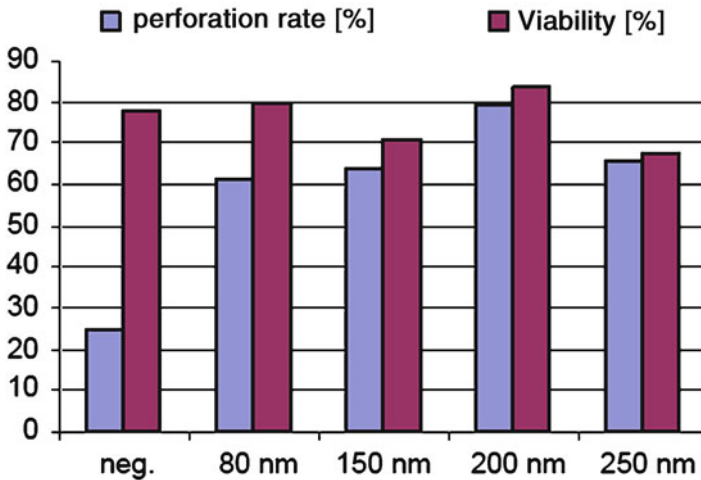
Fig. 14.6 Cell viability and efficiency of optical perforation by plasmonic enhancement for different nanoparticle sizes. Cell viability is very high for nearly all nanoparticle sizes, whereas the efficiency is increasing with increasing particle size. Above 250 nm, the efficiency starts to decrease again. (Nanoparticle concentration 11μml/ml, laser fluence 0.1 J/cm2 and scanning velocity 15 mm/s)

LY molecules. Even though, these GFP plasmids diffused into the cells after laser treatment but compared to the Ly molecule with a lower efficiency. The transfection was verified with a fluorescent microscope 48 h after laser treatment. In case of successful GFP expression the whole cell got fluorescent. To demonstrate successful transfection for primary cells, mouse DRG neurons were successfully transfected, using a pEGFP-C1-HMGA2 vector, a laser fluence of 0.37 J/cm2 and a scan velocity of 50 mm/.

14.6   Conclusion

The plasmon-mediated laser cell manipulation is suitable for highly efficient cell perforation, accompanied by very low side effects and thus high cell viability. The method relies on the interaction of nanoparticles with the cell membrane and following with the applied laser radiation, leading to a near field enhancement of the laser radiation, leading to the precise perforation of the cell membrane in a large number of cells. Instead of a tight focusing by high numerical aperture objectives, this method can employ weakly focused femtosecond radiation, leading to the optical perforation of the cells at large numbers. Once the membrane is perforated, membrane-impermeable dyes or molecules, like Lucifer yellow, DNA or RNA and siRNA can enter the cell.

Lucifer Yellow molecules with a molecular weight of 457 Da enter the cells with a higher efficiency than 4.7 kbp plasmid vectors. However, the possibility to transfer genes into living cells using GNP mediated laser cell perforation is very promising for high throughput cell transfection. Furthermore, this method is suitable for primary and stem cells permeabilization.

References

1. Vogel A, Venugopalan V (2003) Mechanisms of pulsed laser ablation of biological tissues. Chem Rev 103(2):577–644
2. Arnold CL, Heisterkamp A, Ertmer W, Lubatschowski H (2008) Computational model for nonlinear plasma formation in high NA micromachining of transparent materials and biological cells. Opt Express 15(16):10304–10317
3. Williams F, Varma S, Hillenius S (1976) Liquid water as a lone-pair amorphous semiconductor. J Chem Phys 64(4):1549–1554
4. Koenig K, Riemann I, Fischer P, Halbhuber K (1999) Intracellular nanosurgery with near infrared femtosecond laser pulses. Cell Mol Biol 45:192–201
5. Kumar S, Maxwell IZ, Heisterkamp A, Polte TR, Lele T, Salanga M, Mazur E, Ingber DE (2006) Viscoelastic retraction of single living stress fibers and its impact on cell shape, cytoskeletal organization and extracellular matrix mechanics. Biophys J 90:3762–3773
6. Tirlapur UK, Koenig K (2002) Targeted transfection by femtosecond laser. Nature 418:290–291
7. Stevenson D, Agate B, Tsampoula X, Fischer P, Brown CTA, Sibbet W, Riches A, Gunn-Moore F, Dholakia K (2006) Femtosecond optical transfection of cells: viability and efficiency. Opt Express 14:7125–7133
8. Baumgart J, Bintig W, Ngezahayo A, Willenbrock S, Murua Escobar H, Ertmer W, Lubatschowski H, Heisterkamp A (2008) Quantified femtosecond laser based opto-perforation of living GFSHR-17 and MTH53a cells. Opt Express 16(5):3021–3031
9. Mie G (1908) Optical properties of colloidal gold solutions. Ann Phys 25:329
10. Kelly KL, Coronado E, Zhao L, Schatz GC (2003) The optical properties of metal nanoparticles: the influence of size, shape, and dielectric environment. J Phys Chem B 107:668–677

15
Principles and Applications of Rare Earth Ion-Doped Nanoparticles

John Collins

Abstract This article presents some fundamental properties of nanoparticles of insulating materials doped with rare earth ions as optically active centers. In the nano-regime, the effects of confinement can affect the optical properties. These affects are well known in semiconductors such as CdS or CdSe, where the particle size dictates the band gap, and hence the particle's absorption and emission properties. In the case of insulators, such affects are less important. For insulators, the optical properties are affected by the particle size mainly through (1) the reduced phonon density of states and (2) the role of the surface and near-surface sites occupied by the rare earth ion. In this article we examine the fundamental physics of these systems, and call attention to various experiments in which these affects have been observed.

15.1 Introduction to Rare Earth Ions in Solids

For those readers not familiar with the optical properties of rare earth ions in solids, we summarize in this section some of their fundamental properties and the physical reasons behind them. Given our concern in this article for confinement effects, we pay particular attention to those properties that may (or may not) be affected by such a system when placed in a nano-particle.

The rare earth elements range from lanthanum (atomic number 57) to lutetium (atomic number 71). When placed in a solid, the rare earths usually substitute in the trivalent state. The ground state configuration of the trivalent rare earth ions is $[Xe]4f^n$. It is important to note that Xe (atomic number 54) has filled shells, including the $5s^2$ and $5p^6$. Because the wavefunctions of the 4f electrons lie

J. Collins (✉)

Department of Physics and Astronomy, Wheaton College, Norton, MA 02766, USA
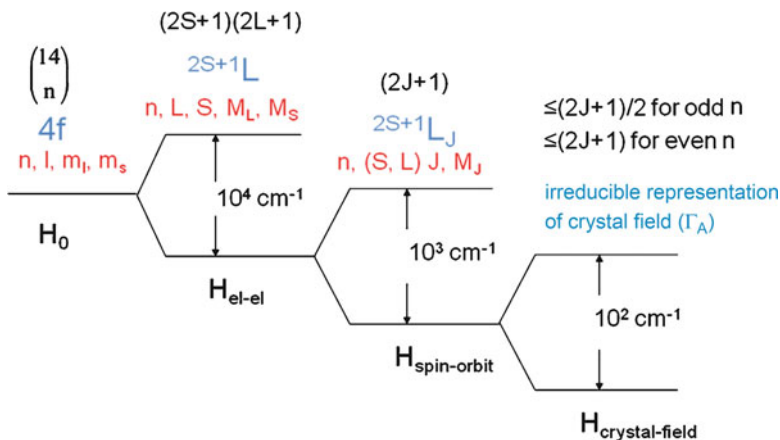e-mail: jcollins@wheatonma.edu

Fig. 15.1 The interactions experienced by the 4f electrons (of decreasing importance *left-to-right*), the labels of the states, the "good" quantum numbers, and the degeneracies. The diagram also shows the order of magnitude of the splitting that result from each interaction

generally closer to the nucleus than those of the 5s and 5p electrons, the 4f electrons are shielded from the crystalline field by the 5s and 5p electrons. This limits the interaction between the ion and the crystalline field to a small perturbation.

15.1.1 States of Rare Earth Ions in Solids

The optical activity of the rare earth ions in solids occurs mainly between electronic states within the 4f configuration. In this section we give a brief introduction to the nature of the states associated with the 4f electrons, their labeling, and how they vary from one crystal to another.

The Hamiltonian of an atomic system can be written as follows:

$$H = H_0 + H_{el-el} + H_{SO} + H_{CF} \qquad (15.1)$$

In Eq. 15.1, H_0 is the Hamiltonian in the central field approximation, H_{el-el} is the electron-electron interaction, H_{SO} is the spin orbit interaction, and H_{CF} is the crystal field interaction. We briefly discuss each of these separately. Their affects are summarized in Fig. 15.1.

In a perturbative approach, the most important term in the Hamiltonian, H_0, is considered first. It contains the kinetic energies of the electrons, the electrostatic interaction of the electrons with the nucleus, as well as those interactions with the electrons that contribute to a central field. The eigenstates of H_0 lead to all the 4f electrons being degenerate, because each 4f electron experiences the same central field. The total orbital angular momentum (l) of *each* electron and its z-component (m_l) is conserved separately, as is the z-component of the spin of each electron

(m$_s$). Thus, n, l, m$_l$, and m$_s$ are all good quantum numbers. The degeneracy is given by the number of ways that the spins of the n electrons can be arranged in the 4f shell, constrained, of course, by the Pauli Exclusion Principle. Such a set of states is known as a configuration.

H$_{e-el}$ is the electrostatic interaction between the 4f electrons. This interaction reduces the symmetry so that the total and z-components of orbital angular momentum of the *system of 4f electrons* and their total spin angular momentum are good quantum numbers. The configuration is accordingly split into different spectral terms, each term having a specific total angular momentum L, and a total spin S, and designated by $^{2S+1}$L.

The spin-orbit interaction, H_{SO}, couples the spin to the orbital motion. Assuming that Russell Saunders coupling is valid, the allowed total angular momentum, designated by J, runs from J = L + S to J = L−S. Thus, good quantum numbers are J and its z-component, M$_J$. The degeneracy of each level is determined by the number of possible values of M$_J$, that is 2 J + 1. The states are labeled as $^{2S+1}$L$_J$. Note that the labeling scheme retains the S and L designations, as if they were good quantum numbers. This is because to a large extent the states retain their S and L character.

Finally, the last interaction to be considered is the electrostatic interaction between the ion and the static crystalline field due to the ion's nearest neighbors. At this point, spherical symmetry is lost, so that angular momentum as we normally envision it is no longer a good quantum number. Instead the quantum numbers are associated with the symmetry of the crystalline field. Generally speaking, the higher the local symmetry, the higher will be the degeneracies of the states. The degeneracy of these crystal field levels is less than or equal to 2 J + 1 for an ion with an even number of electrons. For systems with an odd number of electrons, Kramer's degeneracy demands that the degeneracy of the levels must be less than or equal to (2 J + 1)/2. (In this case, a full splitting of the 2 J + 1 levels can only be done with a magnetic field.) These crystal field levels should be labeled, strictly speaking, according to the irreducible representations of the crystalline field. However, the crystal field splitting of the J-manifolds is usually much smaller than the spin-orbit splitting, and so the $^{2S+1}$L$_J$ notation is often retained.

Because of the small crystal field splitting, the 4f energy levels of the rare earth ions relative to the ground state are not very sensitive to the host crystal. Thus, it is possible to develop an energy level diagram that is mainly valid for the trivalent rare earth ions in any host material. Such a diagram is often referred to as the Dieke diagram [1] (Fig. 15.2).

15.1.2   Radiative Transitions Among 4f Levels

The purely radiative transitions among these 4f states are given by Fermi's golden rule, and so the matrix elements responsible for the transitions have the form $\left\langle \psi_f^* \left| er \right| \psi_i \right\rangle$, where the ψ_f and ψ_i are the final and initial 4f electronic
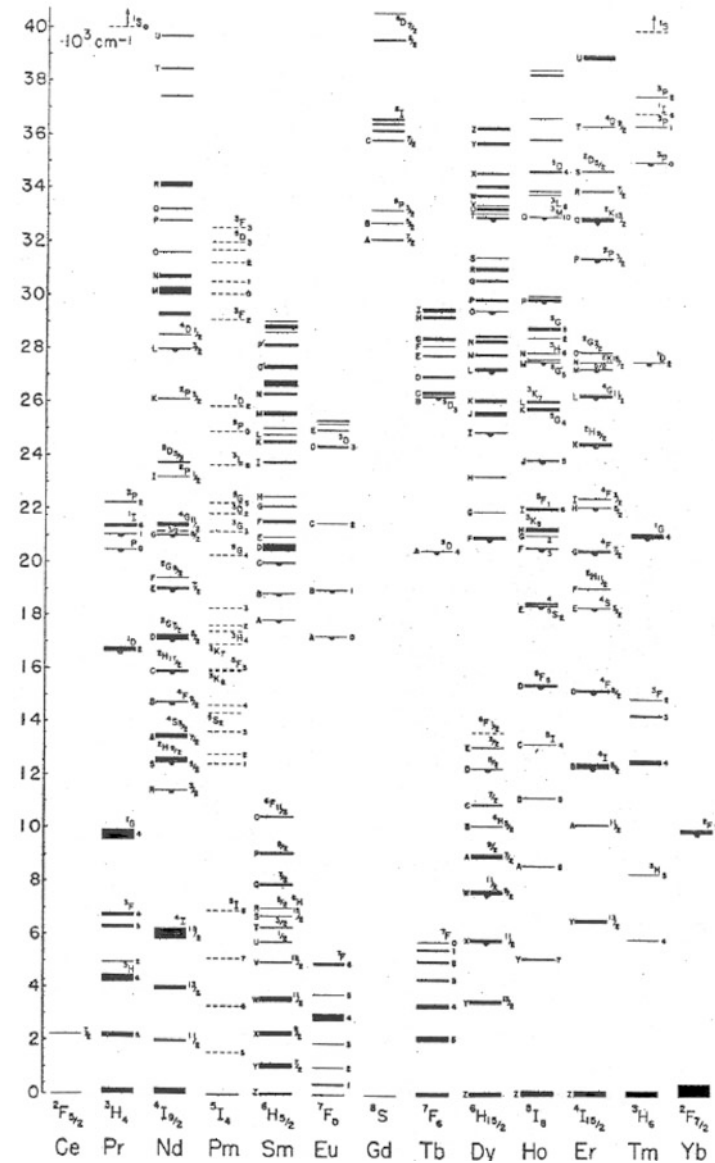
Fig. 15.2 The energy levels of the trivalent rare earth (lanthanide) ions in solids [1]

wavefunctions, respectively, and er is the electric dipole operator. The wavefunction of the 4f levels of the free ion have a definite parity defined by the following:

$$\text{parity} = (-1)\sum_i l_i = -1^{3n} \tag{15.2}$$

where l is the angular momentum of the sum is over all 4f electrons. (Note $l = 3$ for an electron in an f-shell.) This definite parity of the states and the odd nature of the leads to the Laporte selection rule: an electric dipole transition is forbidden between two states of the same parity.

When placed in a crystal, the mixing of the 4f states with those from other configurations of opposite parity (e.g. the 5d configuration) relaxes this selection rule somewhat. The result is that the transitions between 4f states are weak, with f-numbers on the order of 10^{-6}, and radiative lifetimes in the microsecond and millisecond regimes. The absorption and emission lines are sharp, and the Stokes shifts are very small.

These qualities of rare earth ions in solids (sharp lines, weak transitions, small Stokes shifts) are all related to the fact that the electronic charge distribution of the 4f states are shielded from the nearby ligands, and so ion retains much of the character of the free ion. Due to the weak effects of the neighboring ions on the 4f states, non-radiative decay from many excited states is generally weak. Thus, in spite of the weak radiative rates, radiative emission may still be the dominant decay process, so that these systems can be efficient emitters. Applications of rare earth ions to optical systems (e.g. lasers, lamp phosphors, biological markers, solar cell downconverters) are numerous, and usually capitalize on this high radiative efficiency.

15.2 Confinement in Nanoparticles

It is well known that when the size of the particle is reduced into the nano-regime, effects of confinement may be observed. This effect is most common in semiconductors, where tuning the bandgap of the material, and hence the emission wavelength, can be altered by changing the particle size. The goal of this section is to discuss what will be the prominent features of confinement in rare earth ion doped insulators. We shall discover that the confinement effect observed in semiconductors will be less important in rare earth doped systems, and that the main affect of particle on the luminescence properties of these systems will be related to the surface states and to the phonon density of states.

15.2.1 Effects of Confinement on Electronic States

In semiconductor materials (e.g. CdS and CdSe), reducing the size of the particles to tens of nanometers or less results in a widening of the bandgap. To understand whether this effect occurs in insulating systems, we review the basic physics of the bandgap dependence on the particle size.

For simplicity, we consider a crystal as a three-dimensional cube with sides L with infinite potential at the walls. A free charge carrier occupies a state of the entire crystal, and obeys the following relationships:
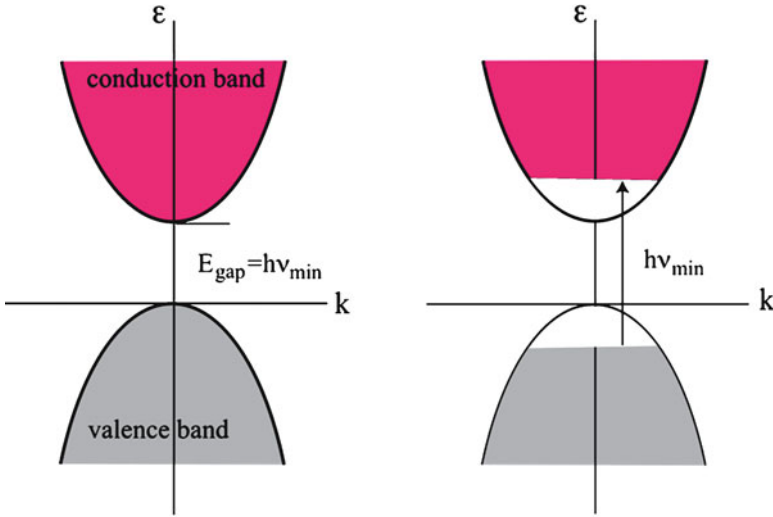
Fig. 15.3 The energy-wavevector diagram for a direct gap semiconductor for (**a**) bulk crystal and (**b**) a nanoparticle. The *shaded* regions represent accessible kinetic energy states within each band. For the nanoparticle, the low kinetic energy states are not accessible to the electron (or hole), and so the minimum energy required to excite an electron from the valence band to the conduction band is larger than in a bulk crystal

$$E = \frac{p^2}{2m^*} = \frac{\hbar^2}{2m^*}k^2 \text{ dispersion relation} \tag{15.3}$$

$$E_n = \left(\frac{\hbar^2}{8m^*L^2}\right)n^2 \text{ allowed energies} \tag{15.4}$$

where $n^2 = n_x^2 + n_y^2 + n_z^2$ and L is the characteristic size of the crystal. m^* is the effective mass of the charge carrier, and is given by

$$m^* = \hbar\frac{d^2k}{d\omega^2} \tag{15.5}$$

Note that the effective mass of a hole is negative, due to the fact that the parabola for the valence band is concave down.

A schematic of a direct gap semiconductor is shown in Fig. 15.3. For charge carriers in solids, it is customary to use the top of the valence band as the zero energy. For an electron in the conduction band, the energy in Eq. (15.4) must be shifted up by the bandgap energy, E_{gap}. With these adjustments, the energies of the particles are:

$$E = E_{gap} + \left(\frac{\pi^2\hbar^2}{2m_e^*L^2}\right)n^2 \text{ (electron in conduction band)} \tag{15.6}$$

$$E = -\left(\frac{\pi^2\hbar^2}{2m_h^*L^2}\right)n^2 \text{ (hole in valence band)} \tag{15.7}$$
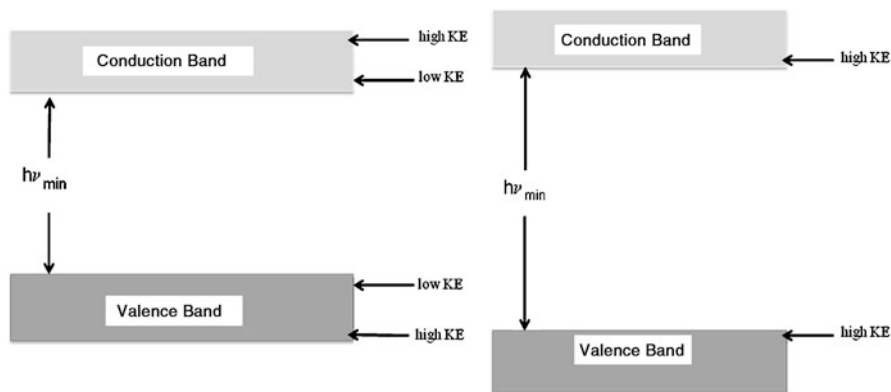
Fig. 15.4 The energies of electrons in the conduction band and holes in the valence band for large crystals (*left* diagram) and nanoparticles (*right* diagram). Note that in this representation, the *bottom* of the conduction band and the *top* of the valence band are located where the particles have lowest available values of the kinetic energy. In nanoparticles, the lowest allowed kinetic energies are substantial, and to the minimum energy required to bridge the gap is higher

This equation says that the energy of the transition depends on the bandgap and on the kinetic energy of the electron and the hole. (Note that the interaction between an electron and a hole is neglected here.) A transition across the bandgap in a direct semiconductor can be visualized on an energy-wavevector diagram, as shown in Fig. 15.3. The transition takes an electron of wavevector **k** in the valence band and brings it to a state in with wavevector **k** in the conduction band, thus conserving both energy and momentum.

For large crystals (i.e.) large values of L in Eqs. (15.7) and (15.8), the lowest translational states have kinetic energies close to zero. As the size of the particle is reduced, the value of L decreases, and so the energy required to bridge the gap increases. Essentially, states in the valence band and conduction bands that are accessible in large crystals are no longer accessible in nanoparticles. Figures 15.3 and 15.4 show two different representations of this effect.

Note that this analysis of the increase in the bandgap as the particle size decreases is predicated on the fact that the electrons are free, and so can be described by highly non-localized states of the entire crystal. We make the following observations:

1. In insulators and large gap semiconductors, it is not unreasonable to expect a similar effect. It is usually the case, however, that the effective mass can be much larger in these systems. (The parabolas on the E vs. k diagrams, are much flatter.) This will make the effect much smaller than in small gap semiconductors.
2. The states of the rare earth ions in solids that lie within the $4f^n$ configuration are highly localized, and so will not exhibit confinement effects.
3. States of the excited configurations of the rare earth ion may exhibit some effect of confinement since they often lie within the conduction band. Any confinement effects on these states are likely to be small.

4. For REI doped semiconductors, the REI states in the vicinity of the conduction band could be affected by particle confinement if the shift in the bandgap caused a substantial change in the position of the REI level relative to the bad edge. For example, if the conduction band is raised while the REI level remains fixed, thermal excitation from the excited REI level into the conduction band could be decrease with decreasing particle size.

With the exception of point 4 above, we expect that the effects of confinement will not be noticeable on the electronic and translational states of rare earth ion-doped insulators. The main reason for this is that the electronic states in these materials are much more localized than those in semiconductors.

15.2.2   Effects of Confinement on the Density of Phonon States

Though the electronic states of the rare earth ion doped insulators are highly localized, the phonon states of the solid are extended states of the entire solid. Thus they are highly delocalized and should experience effects of confinement. In this section we consider the behavior of phonon states when the particle size is reduced.

The wavelengths of the phonons vary from roughly twice the atomic spacing to twice the diameter of the particle. The energy of a phonon is

$$E_{ph} = \frac{hc_s}{\lambda} = \frac{hc_s}{2d}n \tag{15.8}$$

where $n = \left(n_x^2 + n_y^2 + n_z^2 \right)^{1/2}$ and d is a characteristic length. The speed of sound in the solid is represented by c_s, and is on the order of a few thousand meters per second. For particle of diameter $\sim 10^{-2}$ m and a speed of sound of 3,000 m s^{-1}, the minimum energy (longest wavelength) phonons have energies on the order of

$$E_{\min} = h\frac{c_s}{\lambda} = h\frac{c_s}{2d} \approx 6 \times 10^{-10} \text{eV} \tag{15.9}$$

and the maximum energy phonon is on the order of

$$E_{\max} = h\frac{c_s}{\lambda} = h\frac{c_s}{2a} \approx 0.03 \text{eV} \tag{15.10}$$

where we estimated the atomic spacing, a, to be 0.2 nm. A simplified phonon density of states as given by the Debye approximation:

$$\rho_{ph}(v) = \frac{3\pi}{2} \left(\frac{2d}{c_s} \right)^3 v^2, \tag{15.11}$$

where the maximum phonon cutoff frequency is given by Eq. (15.10). This cutoff frequency is determined by the interatomic spacing, and so is independent of the particle size.

The low frequency phonons, however, are determined by the size of the particle: as the particle size decreases, the energy of the lowest frequency phonons decreases. Thus, as the particle size decreases, the low frequency phonons can no longer be supported. Given the prominent role of phonons in the relaxation of an atomic system from an excited electronic state, this effect may be of some importance to the luminescence of rare earth ions in solids.

There is another important way in which the nanoparticle's phonon spectrum differs from that of the bulk crystal; instead of being treated as a continuous function, as in the Debye approximation, the density of states becomes a discrete function. To see why this happens, we note that the total number of phonon modes is given by 3 N, where N is the total number of particles in the crystal. As one moves form the bulk to the nano, N decreases as the cube of the diameter, and the number of phonon modes can be estimated as:

$$3N \sim \left(\frac{d}{a}\right)^3 \qquad (15.12)$$

For a bulk crystal with $d = 0.25$ cm and $a = 0.25$ nm, $3N \sim 3 \times 10^{21}$, whereas when d is deceased to 2.5 nm, $3N \sim 3 \times 10^3$, a decrease by 18 orders of magnitude! The result is that the phonon spectrum can no longer be treated as a continuous function of frequency. This is especially true at the lower frequencies.

Figure 15.5 shows the results of calculations by Liu et al. who modeled the nanoparticle as a sphere and calculated all the spherical and torsional modes [2]. The speed of sound was assumed to be 3,500 m s^{-1}, and the calculations were carried out for nanoparticles of diameters 20 and 10 nm. The spectra show the two effects of decreasing the particle size; (1) the disappearance of the low frequency phonons, and (2) the movement from the continuous to the discrete. We note that these effects become very pronounced for nanoparticles less than 10 nm. For particle size increases to 100 nm or larger, these effects are likely not to play an important role in the luminescence from the rare earth ions in solids.

Finally, it is instructive to look at the actual number of phonons in a crystal. Treating the phonon density of states as a spectrum as a discrete function of frequency, we let the function $\phi_{nano}(\nu_i)$ represent the number of phonon modes at frequency ν_i. The number of phonons at this frequency is given by the number of modes at frequency ν_i weighted by the occupancy of that mode.

$$n(\nu_i) = \phi_{nano}(\nu_i)\frac{1}{e^{h\nu/kT} - 1} \qquad (15.13)$$

$\phi_{nano}(\nu)$ must be calculated (e.g. see [2]), and the phonon occupancy of each mode is given by the Bose-Einstein distribution (see Fig. 15.6). Figure 15.5 clearly shows that the highest occupancy numbers are for those phonon modes with low phonon frequencies. Given that these low phonon frequency modes do not exist in the nanoparticle, then the total number of phonons per unit volume in a nanoparticle is much less than that in the bulk.
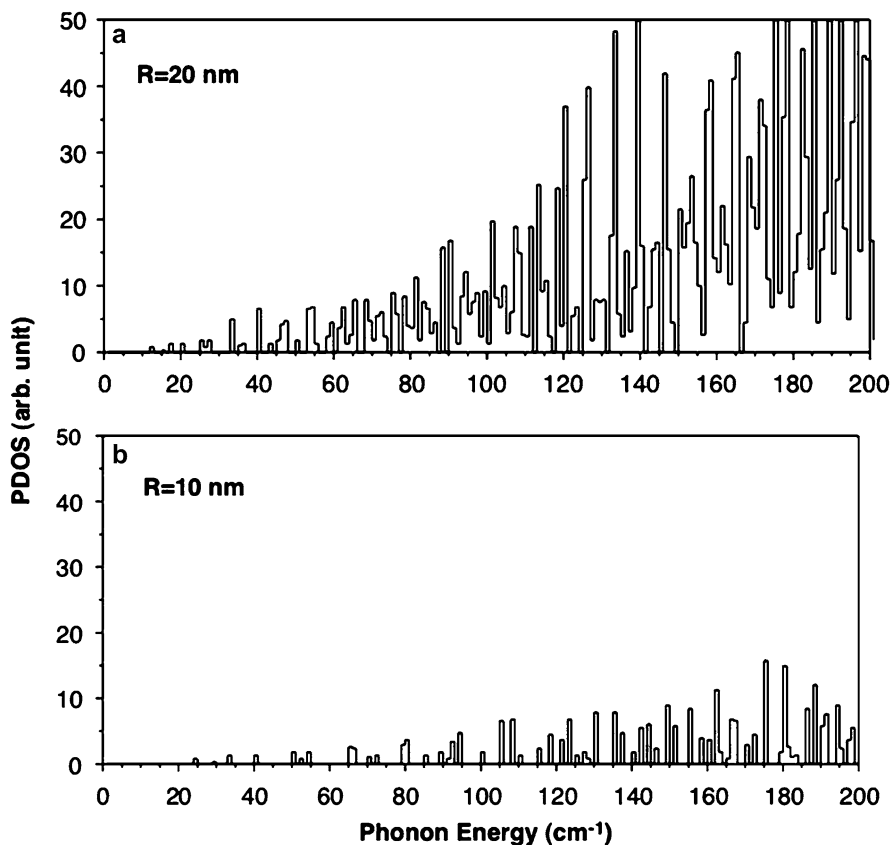
Fig. 15.5 The phonon density of states of the spherical and torsional modes of spherical nanoparticles of radius (**a**) 20 nm and (**b**) 10 nm. The velocity of sound was assumed to be 3,500 m s^{-1} [2]

15.2.3 Placement of Rare Earth Ions and Surface States

In bulk crystals, the placement of the rare earth ion in the lattice during crystal growth is usually assumed to be randomly distributed among the allowed sites. Though this not always the case, it is largely true that in a bulk crystal any variations in "equivalent" sites in bulk crystal is very small. These small site-to-site variations manifest themselves in the generally narrow linewidths for the transitions within the $4f^n$ configuration. The contribution of these site-to-site variations to the linewidth are best determined by measuring the linewidths at low temperature, where the thermal broadening is negligible.

In nanocrystals, the linewidths of the $4f^n$ transitions at low temperature are much broader than in bulk crystals, indicating a larger variety of sites (i.e. local crystalline fields) at which the rare earth ion is located. In the literature, this large variety of

$$f(v) = \frac{1}{e^{hv/kT} - 1}$$
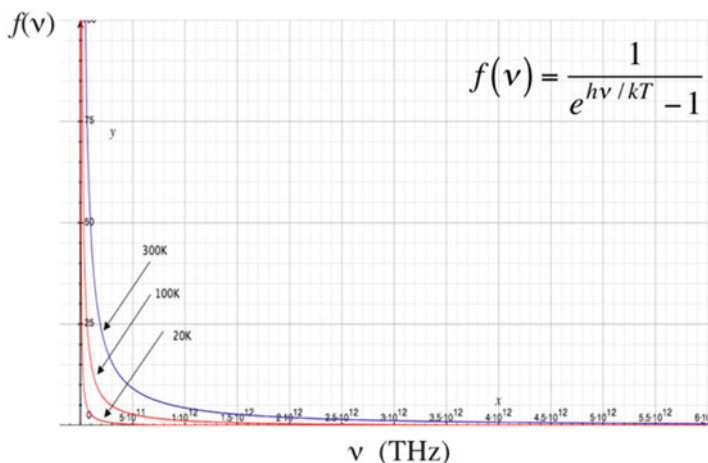
Fig. 15.6 The phonon occupancy as a function of frequency at different temperatures. We see that as those modes with the highest occupancy are always the low frequency modes

sites is often explained as being due to the surface-to-volume ratio as the particle size decreases or, differently stated, to the proximity of surface states. The idea is that the rare earth ions located at the surface will experience a significantly different crystalline field as those in the bulk, and this will cause the energy levels to be shifted resulting in a broader spectral line.

The explanation is, of course, very plausible. However, it is qualitative, and so does not explain any details of the observed linewidth. Unresolved questions regarding the placement of rare earth ions in nanoparticles include the following. Does the rare earth ion have to be at the surface to experience a different crystalline field, or will it experience different fields from the bulk even at a distance of several lattice parameters in from the surface? Exactly how do the local fields vary as one moves from the center of the nanoparticle to the surface? Where is the rare earth ion most likely to be situated, closer to the center of the nanoparticle or closer to its surface? Despite the vast amount of work that has been done on these systems, these questions remain open.

Luminescence Spectroscopy can help answer these questions. For example, one may conduct site-selective spectroscopy experiments, examining one (or more) subsets of sites at any time. One may also excite all sites, and look at the statistical distribution of sites. Linewidth and lineshift studies under these conditions will give information on the variety of sites in the crystal. Also, examining the response of these systems under pulsed excitation can reveal information on these sites, since the lifetimes will vary site-to-site. Another useful way to probe these questions is to do energy transfer studies. The variation in the energy levels may affect energy transfer processes in the nanoparticles, where presumably it would be less likely to find ions in resonance and reduce the energy transfer. If the energy levels are far enough form resonance, on may expect less diffusion among like ions, different transfer rates between unlike ions, and reduced concentration quenching affects.

In the next section, we present only two examples of experimental results that demonstrate some of the spectral features that can be observed in nanoparticles as compared to analogous results in bulk crystals.

15.3 Spectroscopy of Rare Earth Ion Doped Systems

In this section we provide experimental results on Pr-doped YAG and on Er-doped Y_2O_2S. The data on the Pr:YAG system show some general spectroscopic features (e.g. linewidth and lifetime) of single crystals and of nanoparticles of various sizes. In the Er-doped Y_2O_2S system, we shall see direct evidence of the how the confinement, through the density of phonon states, can affect the luminescence from these systems.

15.3.1 *Spectroscopy of Pr-Doped YAG – Bulk vs. Nano*

As an example of comparing the spectroscopic properties of rare earth ions in bulk vs. nanoparticles, we present in this section on some luminescence features of praseodymium-doped Yttrium Aluminum Garnet. Figure 15.7 shows time-resolved luminescence spectra at 29 K of the $^3P_0$ and $^1D_2$ emission lines from Praseodymium (Pr) (a) in nanocrystals (average d = 58 nm) and (b) in a large single crystal ($\sim$0.5 cm^3). The samples were excited at 460 nm into the $^3P_2$ level, which is followed by a fast relaxation to the $^3P_0$ level. The small line near 611 nm is from the $^1D_2$ to $^3H_4$, while the main lines above 615 nm originate from the $^3P_0$ level.

In comparing the two spectra, it is clear that the linewidths are much greater in the nanocrystals than in the bulk. This is related to the large variety of environments for the Pr ion in nanocrystals compared with the bulk. We also notice that some of the lines (near 627 nm, for example) change width and shape as the delay between the laser pulse and detection time is changed. This may be explained by the variety of environments, and the fact that ions in different environments decay at different rates.

Figure 15.8 shows the decay patters of the $^3P_0$ following the excitation at 460 nm. In these decay patterns, no attempt was made to isolate the different sites, so the decay pattern represents a sum of exponentials from the various sites. We note that in the bulk Pr-YAG single crystal, the lifetime is very close to a pure exponential.

The lifetime data show evidence, consistent with the spectral data in Fig. 15.7, of the multiple sites for Pr to be situated in the nanocrystals. Each site will generally have its own lifetime, but all sites emit close in energy to one another. Thus the observed decay pattern is the sum of decays patterns of ions from the various sites. We note also that the decay times are shorter for nanoparticles than for bulk crystals. This result seems to be generally true in all rare earth ion doped insulators. It is speculated, reasonably so, that the shorter lifetime is due to the surface effects.
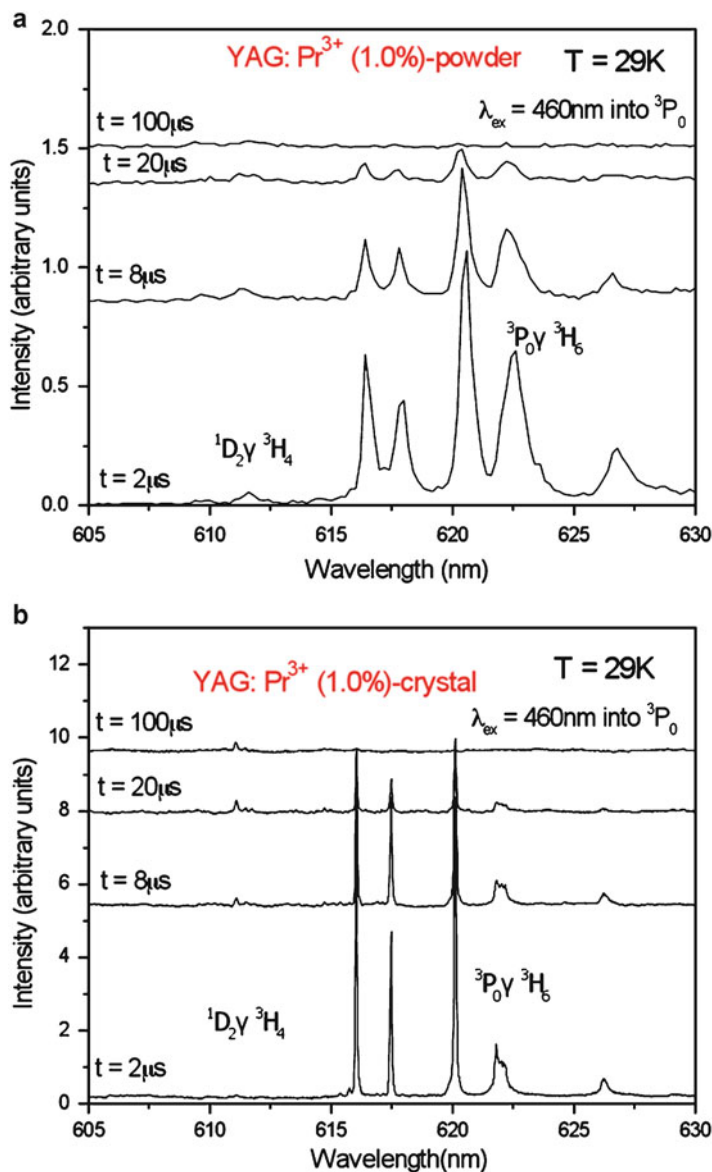
Fig. 15.7 Time resolved luminescence spectra of the nanocrystalline YAG:Pr^{3+} (**a**) and bulk YAG:Pr^{3+} (**b**) with the time delays 2, 8, 20, and 100 μs in the 605 and 630 nm wavelength range at 29 K (The excitation was into the $^3P_0$ level with the dye laser tuned at 460 nm) (Ozen et al. private communications)

Those to the surface will have a greater chance to decay non-radiatively. Given that, and the fact that electronic energy may migrate throughout the nanocrystal, then as the particle size decreases a shorter lifetime is expected.
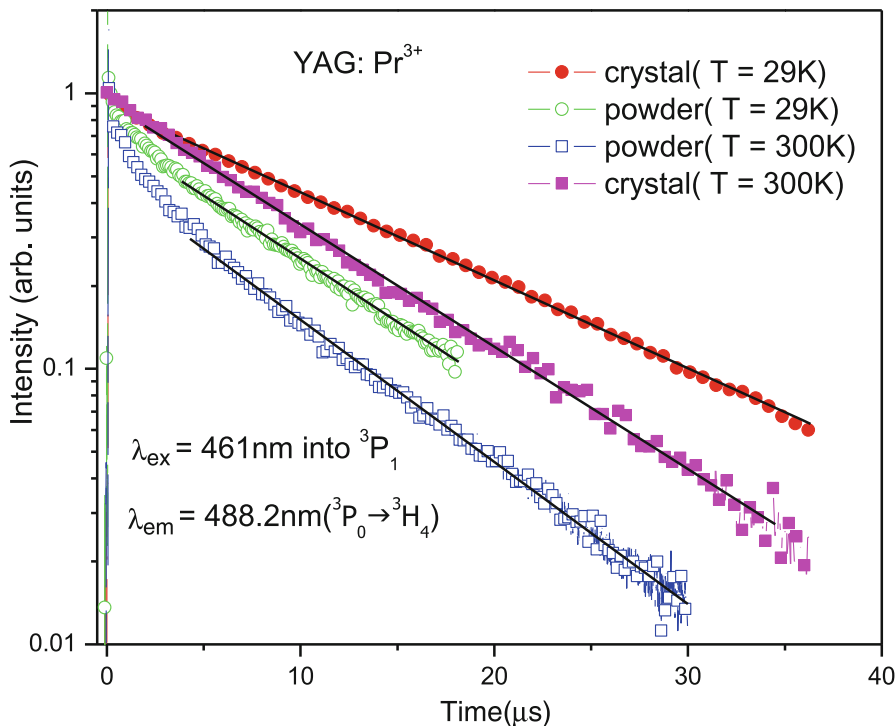
Fig. 15.8 Decay curves of the $^3P_0$ level of YAG:Pr^{3+} in bulk crystal and in the 58 nm particles. While the decay patterns in the nanoparticles exhibit a strong non-exponential decay, in the single crystal the patterns are nearly pure exponential

15.3.2   Affect of Phonon Density of States on the Luminescence of Er-Doped Y$_2$O$_2$S Nanoparticles

In the previous section, we gave an example of some of the general affects observed when rare earth ions are doped into nanoparticles. These features can be explained by the number and variety of different sites present in nanoparticles in comparison with the bulk. In this section we give experimental evidence of the reduced density of phonon states (see Sect. 15.2.2) due to confinement.

The work presented here was conducted by G. Liu at Argonne National Laboratories, and to this author's knowledge is the only data of its kind, and represents perhaps the clearest evidence to date indicating the phonon density of states is indeed reduced in nanoparticles. The excitation and emission spectra were obtained using a tunable pulsed laser as a source. This laser was operated at 10 Hz and had a pulsewidth of 5 ns. Acquisition of the data was done with a boxcar integrator set a delay of 5 μs after the pulse and a gate width of 1 μs. Figure 15.9 shows the excitation spectrum of Er-doped Y$_2$O$_2$S at low temperature (2.6 K) in particles of diameter of ∼400 nm (bulk) and of diameter ∼25 ± 15 nm [3]. We first assume
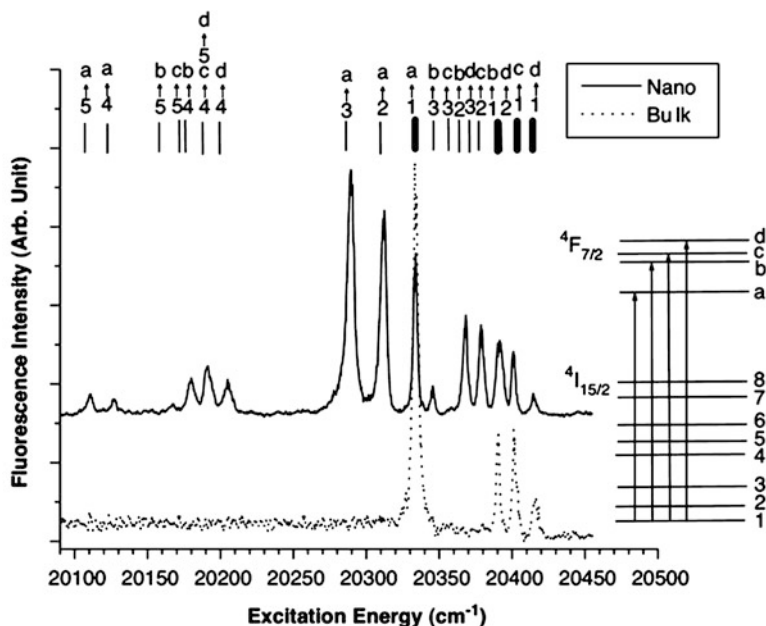
Fig. 15.9 Excitation spectrum of the $^7F_2$ to $^4I_{15/2}$ emission in bulk (*dotted line*) and in 10–40 nm diameter nanocrystals (*solid line*) of Er:Y_2O_2S at 2.6 K [3]

that before the experiment starts the energy levels of the system are in thermal equilibrium, so that at 2.6 K all the ions are in their ground state. That is, all ions are in the crystal field level labeled "1" in Fig. 15.9.

In the larger particles (dotted line) the excitation spectrum shows four absorption transitions (1 → a, b, c, d) that lead to emission. This behavior is completely unsurprising, and is consistent with the assumption of thermal equilibrium among the energy levels of the system.

In the nanocrystals (solid line), however, the excitation spectrum shows numerous lines in addition to the four lines observed in the bulk spectrum. An analysis of the energies of these lines shows that they represent transitions from crystal field levels 1–5 of the ground $^4I_{15/2}$ manifold to the crystal field levels a–d of the excited $^4F_{7/2}$ manifold. This is rather surprising, since thermal equilibrium demands that only the lowest energy level be occupied at T = 2.6 K. The data clearly indicate, however, that the upper crystal field levels of the ground state manifold have are occupied. Evidently, thermal equilibrium among the various energy levels is not readily achieved in these nanoparticles These spectral lines that result from the occupation of levels not in thermal equilibrium with the phonon bath are sometimes called "hot bands".

The results shown in Fig. 15.9 can be explained as follows. In the excitation experiment, absorption of the exciting laser light into the $^4F_{7/2}$ level is followed by a fast relaxation to the lower $^4S_{3/2}$ level. This relaxation, which is accompanied by the emission of phonons, can be fast enough to occur before the laser pulse has ended.

Fig. 15.10 Energy level diagram of the $^4I_{15/2}$ and $^4F_{7/2}$ manifolds of Er in Y_2O_2S. The energies of each level are given in cm^{-1}
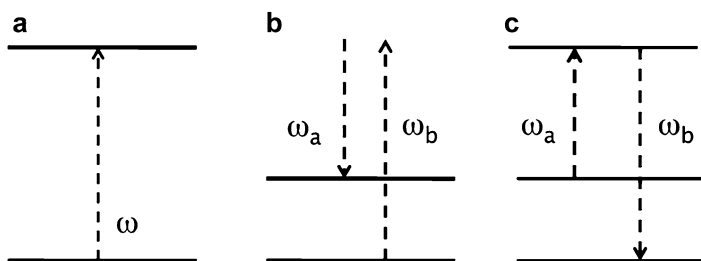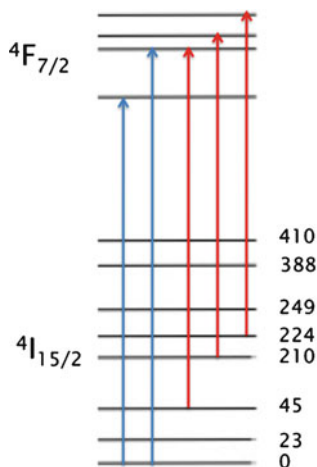

Fig. 15.11 Phonon processes that can cause the ion to transition between energy levels: (**a**) Direct (one phonon) process, (**b**) Raman (two-phonon) process, and (**c**) Orbach (two-phonon) process

These phonons can be absorbed by a nearby Er ion in its ground state, causing that Er ion to become excited to one of the excited levels in its ground state manifold.

To understand how this happens, it is useful to refer to Fig. 15.10, which gives the energy levels of the ground state $^4I_{15/2}$ manifold, and also to Fig. 15.11, which shows three phonon process that can cause some of the upper levels of the $^4I_{15/2}$ manifold to become occupied. These processes include the absorption of a single phonon, known as a direct process. Also shown in Fig. 15.11 are two two-phonon processes that involve the emission and absorption of phonons. These are the Raman process and the Orbach process, the difference between them being that the Orbach process proceeds through a real intermediate state, whereas the Raman process involves a virtual intermediate state.

We must also recall that the phonon density of states is different in nanoparticles than the bulk, and is characterized by a low phonon cutoff frequency, a discrete spectrum, and a drastic reduction in low energy phonons. For the sake of this argument, we shall pretend that the low phonon energy cutoff frequency is 50 cm^{-1}. In this scenario, the energy levels at 23 and 45 cm^{-1} cannot become occupied by absorbing a single phonon because the required phonon energies are below the cutoff energy, and hence do not exist in the nanoparticle.

We make the following points.

1. At low temperatures, only those energy levels of the $^4I_{11/2}$ manifold above 50 cm^{-1} can become occupied by a direct process.
2. The energy levels at 23 and 45 cm^{-1} will require two phonon processes to become excited, since phonons of those frequencies are not available due to the small particle size. Both Orbach and Raman processes are possible, providing the appropriate phonon energies are available.
3. Following excitation with a photon, the ion can produce phonons of several different frequencies, so that many frequencies are likely available. The phonons at a particular frequency can be produced during the relaxation process or afterward in some scattering process if anharmonic terms are present in the vibrational potential energy curves.
4. The radiative decay from the excited electronic states (e.g. $^4F_{7/2}$) to the upper levels of the $^4I_{15/2}$ manifold can populate direction these levels without involving any phonon participation.

The points outlined above can lead to the population of the upper levels of the $^4I_{15/2}$ manifold. To explain the spectrum in Fig. 15.9, all this must happen before the end of the laser pump pulse (5ns FWHM). Also, the system must remain in that state for a significant period of time (on the order of ns). This may occur for ions in nanoparticles, since the low energy phonons would not be available and the phonon density of states is drastically reduced. Assuming these conditions are met, there is time for the ion to absorb a photon before the laser pulse ends. In the bulk, the phonon density of states is such that thermal equilibrium is established on the picosecond time scale, and so there is very little time to absorb a photon from the laser pulse before its return to the ground state.

Exactly which process or processes are mainly responsible for the population of the upper levels of the $^4I_{15/2}$ manifold in unknown, but the observation of excitation lines from these levels at low temperature clearly indicates the effect of confinement on the density of phonon states in nanoparticles. We note that once the temperature is raised above 7 K in this system, the hot bands disappear. Apparently, even at such low temperatures the two-phonon processes are fast enough so the thermal equilibrium can be established on a sub-ns timescale.

Further evidence of this non-equilibrium condition in nanoparticles is shown in the emission representing the $^4S_{3/2}$ to $^4I_{15/2}$ transition (Fig. 15.12) of $Y_2O_2S:Er^{3+}$. At 2.6 K in the bulk, the emission originates from only the lowest energy level of the $^4S_{3/2}$ manifold. In the nanoparticles, however, hot emission bands are observed. Pumping into the upper $^4F_{7/2}$ level, the creation of phonons that accompany the decay to the $^4S_{3/2}$, resulting in the population of the upper crystal field level of that manifold. As with the excitation spectrum, no hot bands were observed above $\sim$7 K.

In principle, the confinement effects on the phonon density of states can be observed in several ways other than a system's inability to rapidly attain thermal equilibrium. Essentially all luminescent-related phenomena are affected by phonons, including multiphonon relaxation, thermal broadening and shifting of spectral lines, and energy transfer, including diffusion (energy migration through a lattice) and upconversion processes.
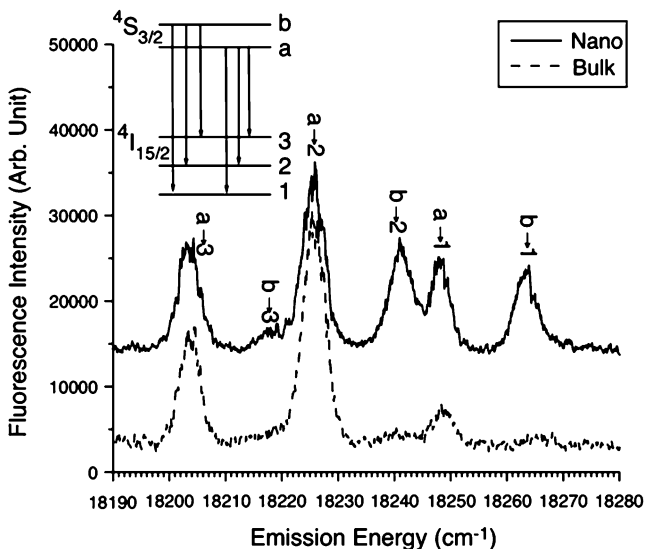
Fig. 15.12 The luminescence of the $^4S_{3/2}$ to $^4I_{15/2}$ transition of bulk (*dotted line*) and of 10–40 nm diameter nanocrystals (*solid line*) of Er:Y_2O_2S at 2.6 K [3]

Many observations have been made of these processes that are not discussed in detail here. Meltzer et al. for example, have studied the thermal line broadening by conducting spectral hole burning experiments in Eu_2O_3 and found a $\sim T^3$ dependence in nanoparticles as opposed to a T^7 dependence in crystals [4]. This was explained by the elimination of the low frequency phonons in the crystal and the associated reduction in the Raman scattering process, which is responsible for the broadening [5]. Also, upconversion has been studied in nanoparticles of Er-doped oxides. These results indicate a substantial difference in the dynamics of the upconversion process under 980 nm pumping between the bulk and the nanoparticles. In the nanoparticles, the red emission is enhanced relative to the green emission as the particle size decreases. The reader is referred to [6] for details. A review article by Tanner contains many more references for the different aspects of rare earth ion doped nanoparticles [7].

References

1. Dieke GH (1968) In: Crosswhite HM, Crosswhite H (eds) Spectra and energy levels of rare earth ions in crystals. Interscience, New York
2. Liu GK et al (2003) J Solid State Chem 123
3. Liu GK, Zhuang HZ, Chen XY (2002) Nano Lett 2:535
4. Meltzer RS, Hong KS (2000) Phys Rev B 61:3396
5. Di Bartolo B (1968) Optical interactions in solids. Wiley, New York
6. Vetrone F, Boyer JC, Capobianco JA, Speghini A, Bettinelli M (2003) Chem Mater 15:2737
7. Tanner PA (2005) J Nanosci Nanotechnol 5:1455–1464

16
Is There Segregation of Rare Earth Ions in Garnet Optical Ceramics?

Georges Boulon, T. Epicier, W. Zhao, M. Guzik, Y. Pan, and B. Jiang

16.1   Optical Materials: From Single Crystals to Ceramics

Research on advanced optical materials for a large variety of applications is always increasing. As an example, we can note high progress in solid-state laser sources like laser-diode (LD) – pumped solid-state lasers (DPSSL) including developments of new materials and high-power laser diode led to high-power and tuneable solid-state lasers. A wide variety of materials has been studied to develop more efficient and high power microchip lasers [1]. In end-pumping schemes, in particular, materials with a short absorption length for the LD pump beam are strongly anticipated for highly efficient operations because of the excellent match between the mode and pump beam profiles. High Nd^{3+} concentrations were so considered such as NdP_5O14, $LiNdP_4O_{12}$ (LNP), and $NdAl_3(BO_3)O_4$. However, crystal growths of these compositions are not so easy. Cubic crystals are much more researched. When looking at the literature for actual applications, we see immediately the importance

G. Boulon (✉) • W. Zhao • M. Guzik
Physico Chimie des Matériaux Luminescents (LPCML), Université Claude Bernard/Lyon 1, UMR 5620 CNRS, Bât. Kastler, La Doua, 69622 Villeurbanne, France
e-mail: boulon@pcml.univ-lyon1.fr

T. Epicier
Matériaux, Ingénierie et Sciences (MATEIS), UMR 5510 CNRS, Université de Lyon, INSA-Lyon, 7 Avenue Jean Capelle, 69621 Villeurbanne, France

W. Zhao
University of Science and Technology of China (USTC), Hefei, Anhui 230026, China

M. Guzik
Faculty of Chemistry, University of Wrocław, Joliot-Curie 14, PL-50-383 Wrocław, Poland

Y. Pan • B. Jiang
Key Laboratory of Transparent Opto-Functional Inorganic Materials, Chinese Academy of Sciences, Shanghai Institute of Ceramics, Shanghai 200050, China

of cubic garnet crystals for which dodecahedral (Y^{3+}), octahedral (Al^{3+}) and tetrahedral (Al^{3+}) sites are considered as a reservoir for many activators like: Ce^{3+}, Nd^{3+}, Er^{3+}, Tm^{3+}, Ho^{3+}, Yb^{3+} rare earth ions in dodecahedral symmetry sites and transition metal ions like Cr^{3+} in the octahedral symmetry sites or Cr^{4+} in the tetrahedral symmetry sites. Among garnet crystals, $Y_3Al_5O_{12}$ (YAG) host is the most used, commercially produced by the Czochralski method. However, in the case of the most used Nd^{3+}: YAG laser crystal, the Nd^{3+} concentration that affects the performance in laser applications, is strongly limited to 0.2–1.4 Nd^{3+} at. % as a result of the segregation distribution coefficient [1].

Consequently, the technique of sintering mono-crystalline grains to large optically transparent ceramics was developed. Ceramics have advantages in their sizes, mechanical strengths and manufacturing costs. New chemical compositions, which cannot be achieved with single crystals, may be also achieved, because the laser sintering method works in high-temperature (2,000 K) environment. Ikesue et al. [2, 3]. first demonstrated the possibility of fabricating transparent Nd^{3+}:YAG ceramics of sufficient quality for solid-state lasers with reasonable efficiency. More recently, a number of studies have shown that transparent polycrystalline Nd^{3+}: YAG is equivalent or better than single crystals grown by the Czochralski method [4–6]. In the polycrystalline Nd^{3+}: YAG ceramics, the doping concentration can be increased to as much as 9 at. %. Such high concentration of Nd^{3+} ions into the YAG ceramics has been successfully attained to overcome the short absorption length in Nd^{3+}: YAG single crystals and 2.3 times higher output power than a 0.9 at. % Nd^{3+}: YAG single crystal laser has been reported in a 3.4 at. % Nd^{3+}: YAG ceramic laser [7], thus providing the possibility to develop more efficient and higher power microchip lasers. Systematic studies of Nd^{3+}: YAG ceramic lasers for different doping levels such as fabrication process, optical properties and thermal properties have been reported [2, 3, 8–10]. It has been shown that if we dope Nd^{3+}-ions higher than 4 at. %, it is difficult to keep the large grain size, although the thermal conductivity is unchanged. Then, the number of grain boundaries will increase within the same path length and the cavity loss increases accordingly. Although high efficiencies have been demonstrated, one limitation seems due to Nd^{3+} segregation at grain boundaries in transparent Nd^{3+}: YAG ceramics lasers [11].

The second important application within this scientific area is the development of inorganic crystals for scintillators which are playing a major role in many fields of radiation detection, including medical imaging, astrophysics, and exploring resources like oil [12]. Garnet crystals also play an important role like Ce^{3+}-doped YAG crystals and the higher density analogue Ce^{3+}-doped LuAG crystals proposed as fast and efficient scintillator materials. Naturally, Ce^{3+}-doped YAG ceramic scintillators have already been manufactured, and their gamma-ray responses evaluated [13] as well as temperature dependences as a scintillator [14].

The third recent application of Ce^{3+}-doped YAG luminescence to be mentioned is the use under single-crystalline disks to monitor and control the dose of VUV radiation in wafer steppers.

Another known application of Ce^{3+}-doped YAG crystal has received renewed interest related to the use as colour converter in (In,Ga)N-based phosphor-converted LEDs (pc-LEDs). At present, Ce^{3+} doped YAG is the most widely applied phosphor

in white light LEDs. Part of the blue light from the (In,Ga)N LED is absorbed by a thin layer of Ce^{3+}-doped YAG and is converted into yellow light. The combination of blue and yellow gives a bright white light source with an overall energy efficiency that is approaching that of the compact fluorescent lamp [15]. Lastly, active-tip based near-field optics is realized by coating a standard tips with Ce^{3+}-doped YAG particles [16].

In front of such development of new rare earth ions-doped crystals, there is also a need to know if rare earth ions-doped ceramics would provide better optical performances. Among parameters playing a role in efficiency, especially, rare earth ion distribution is important for quenching processes. Then, we should know on the rare earth ion distribution inside grains and across grain boundaries.

We have chosen Ce^{3+} rare earth ions from the beginning of the lanthanide family and Yb^{3+} at the end of this family to see any difference concerning the segregation behaviour as it was analysed previously in crystals [17–19]. We have found good optical quality samples with both Ce^{3+}-doped YAG at the Shanghai Institute of Ceramics [20] and Ce^{3+}-doped ceramic from a new chemical composition scintillator, Ce^{3+}-doped $(Gd,Y)_3Al_5O_{12}$, namely Ce^{3+}-doped GYAG, at the Japanese Konoshima Company, in which heavy Gd^{3+} ions allow to achieve a higher stopping power to gamma-rays [12]. Ce^{3+} has also been selected due to high intensity in visible range under blue or UV excitations, by using complementary tool as Imaging Confocal Microscopy [21]. Yb^{3+}, the last active luminescent of the rare earth family, has been also obtained from the Shanghai Institute of Ceramics [22] in YAG laser ceramic.

In this report, we present our successful approach in characterizing by Transmission Electronic Microscopy (TEM), rare earth ion distribution in Ce^{3+} and Yb^{3+}-doped garnet ceramics [20, 22], the first and the last active ions among rare earth family.

16.2 Experimental Procedures

16.2.1 Elaboration of Samples at the Shanghai Institute of Ceramics

The raw materials, α-Al_2O_3, Y_2O_3, and CeO_2 (or Yb_2O_3) were commercial powders with high purity (99.99%), they were weighed according to the stoichiometric ratio of Ce^{3+}-doped $Y_3Al_5O_{12}$, (or Yb^{3+}-doped $Y_3Al_5O_{12}$), and 0.5 wt. % tetraethyl orthosilicate (TEOS) was added as a sintering aid. The starting powders were mixed and ball milled for 10–12 h using a high energy ball milling apparatus. Anhydrous alcohol was used as ball milling medium. The slurry was dried, sieved, and finally pressed to biscuits of 20mm by a cold isostatic pressing (CIP) under 200 MPa. All biscuits were sintered at 1,750°C for 10–40 h under vacuum of 10-3 Pa. After sintering, they were annealed at 1,450°C for 10–20 h in air to remove the possible existed oxygen vacancies introduced during the sintering process.

Fig. 16.1 Photograph of Ce^{3+}−doped YAG transparent ceramics with different doping concentrations: 0.1 at. %, 0.3 at. %, 0.5 at. %, and 1.0 at. %.(double face polished, $\varnothing$14 mm × 1.0 mm). *Yellow color* characterizes Ce^{3+} ions
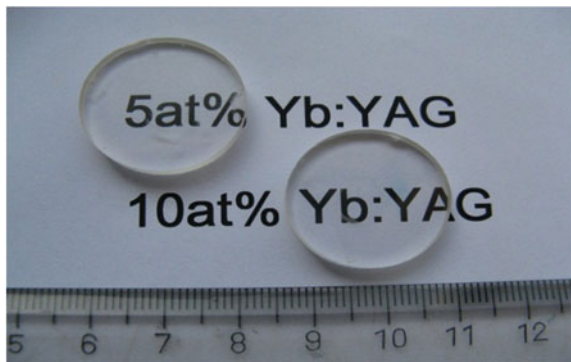

Fig. 16.2 Photographs of Yb^{3+}−doped YAG transparent optical ceramics with different doping concentration of Yb^{3+}: 5 at. % Yb: YAG, double face polished, size:$\varnothing$23 mm × 3.9 mm and 10% Yb: YAG, double face polished, size: $\varnothing$23 mm × 3.9 mm. They are completely transparent since Yb^{3+} ions don't absorb within visible range

The YAG phase was identified by X-ray diffraction (XRD, Model D/MAX-2550 V, Rigaku Co., Japan) [22].

Photographs of two YAG transparent ceramic samples can be seen in Figs. 16.1 and 16.2.

16.2.2 Transmission Electronic Microscopy Technique (Tem)

TEM Experiments were conducted at the CLYM (Centre Lyonnais de Microscopie) and the laboratory "Matériaux, Ingénierie et Sciences (MATEIS)", CNRS UMR
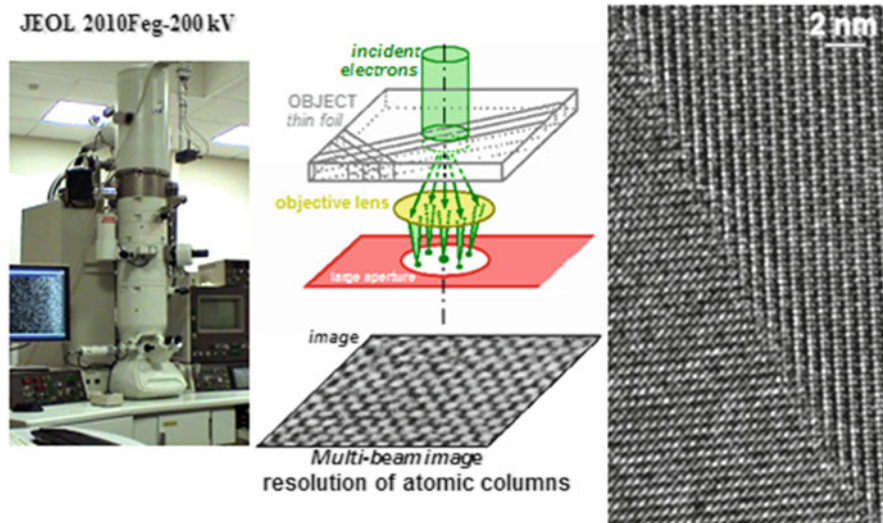
Fig. 16.3

5510, Université de Lyon, INSA-Lyon, France", on thin foils classically prepared by ion beam thinning (PIPS Gatan), using a JEOL2010F field emission gun transmission electron microscope operating at 200 kV (Fig. 16.3). The microscope is fitted with an Oxford EDX (energy dispersive X-ray) analyser which was used for all elemental chemical analysis (Fig. 16.4). The microscope was fitted with an Oxford EDX (energy dispersive X-ray) analyser and a Gatan DigiPEELS spectrometer with a standard photodiode array detector. EELS spectra were acquired according to the following conditions (unless otherwise specified): probe convergent half-angle of 11 mrad, probe size of 2.4 nm, collection half-angle of 9.4 mrad, energy resolution (FWHM of the zero-loss peak) of 1.2 C/K0.2 eV, acquisition times of individual core loss EELS spectra of 30 s.

16.3 Characterization of the Distribution of Ce^{3+} and Yb^{3+} Rare Earth Ions by TEM

16.3.1 Ce^{3+}-Doped Yag Ceramic

In order to improve the spatial segregation characteristic with respect of our former results on Imaging Confocal Technique [20, 21], we have used the EDX measurements in a Transmission Electronic Microscopy (TEM), which is more
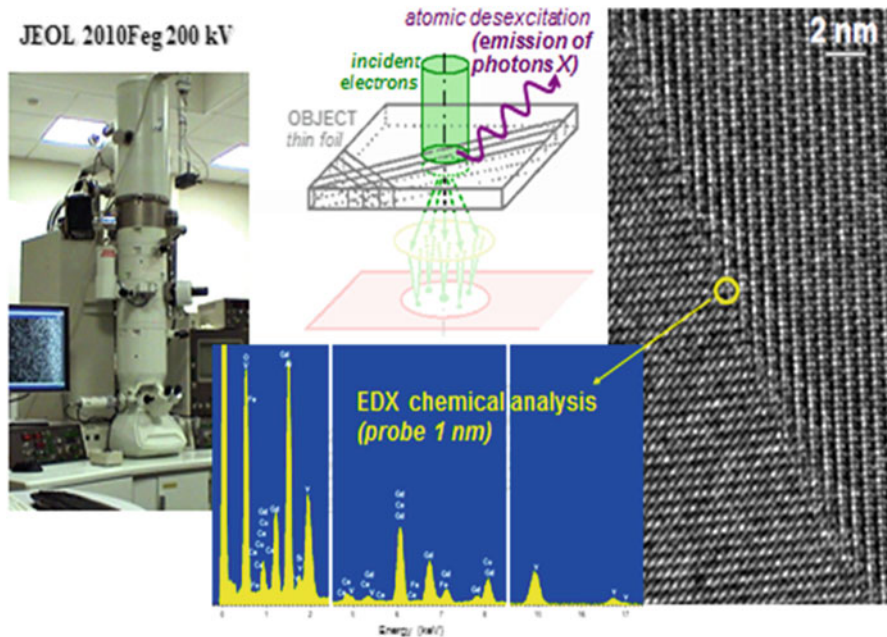
Fig. 16.4

resolved system at the nanometric size. Visualization of grains and grain boundaries based on spatially resolved techniques can be seen in Fig. 16.5. According to EDX measurements, most of the Ce^{3+} cations were sited on the grain boundaries with concentrations of about 0.07 at. % in the grain bodies and about 0.32 at. % on the grain boundaries. Thus, about four times difference was detected when concentrations of the Ce^{3+} were compared.

Details of mean chemical composition analysis for the left and right grains and for the grain boundary are illustrated in Table 16.1. The normalization of the as measured results to the garnet formula unit (with 12 oxygen anions) confirmed authenticity of the obtained experimental data. It is noted that Fe and Co elements belong only to the sample holder of the TEM apparatus. From these measurements, the accuracy is estimated to be better than 0.05 at. % for the Ce^{3+} cations. All EDX measurements with 1–2.4 nominal nano-probe were done with a 1 min acquisition time. This leads to a very high Signal-to-noise (SNR) ratio of about 30–50 for the major elements (Al, Y), and a SNR of 5 for a Ce^{3+} content of about 0.3 at. %. Several grain-boundaries have been simultaneously studied by EDX and HRTEM imaging, but only one example has been detailed here for sake of brevity.
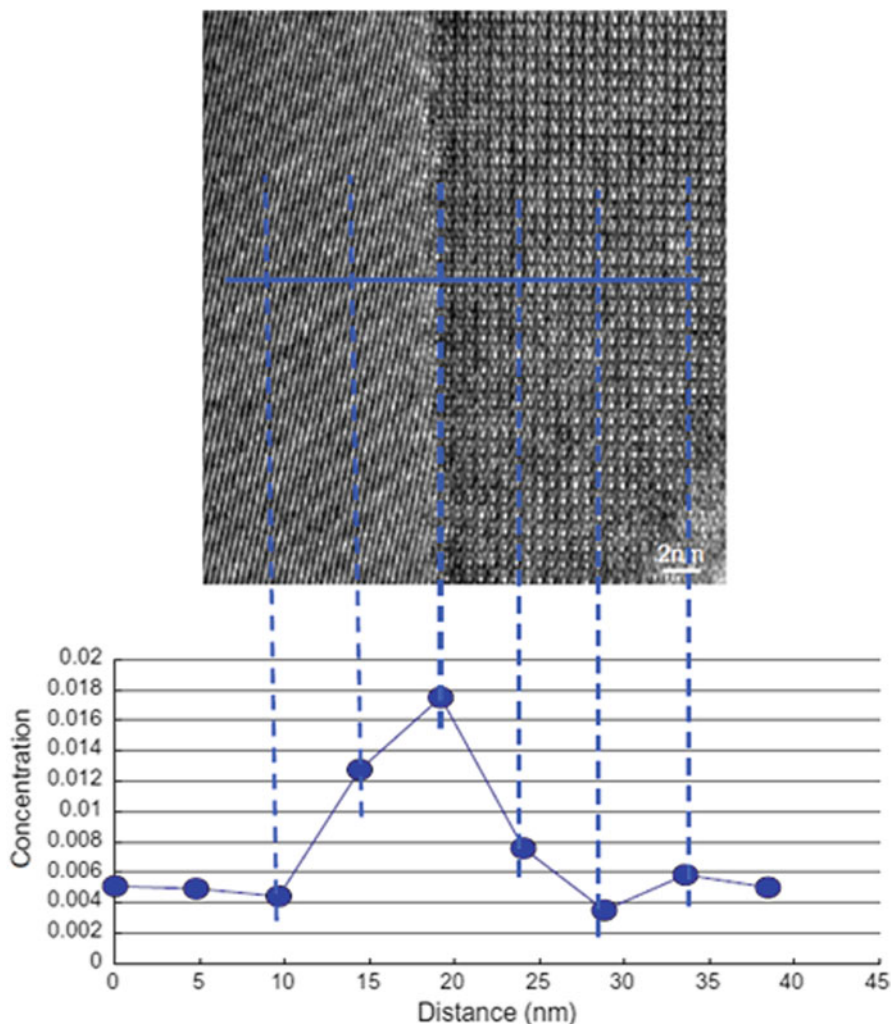
Fig. 16.5 High Resolution TEM image of a typical grain boundary in Ce^{3+}-doped YAG ceramic. Length of the white marker (*right-bottom* side of the image) is 2 nm. Results of chemical analysis in the vicinity ($+/-10$ nm) of the grain boundary are shown. Three sections are distinguishable from left to right: (i) 10–15 nm long part of the left grain with constant Ce/Y value of approximately 0.005, (ii) 10–20 nm thick grain boundary with maximum Ce/Y value of about 0.018, and (iii) 10–15 long part of the right grain with again constant Ce/Y value of approximately 0.005. Linescan with a probe of "2.4 nm" (measured FWHM = 2.6 nm). Lateral step across the boundary = 4.8 [20]

Like in Confocal Microscopy Technique [20], a clear tendency of higher Ce^{3+} concentration is unambiguously evidenced in the grain boundaries by EDX. We can conclude to a clear trend of increasing spatial inhomogeneities in Ce^{3+} concentration between grains and grain boundaries at the nanometric probe size, with much higher concentration in the grain boundaries.

Table 16.1

Location atom	L-grain		R-grain		Boundary	
	Measured	Normalized	Measured	Normalized	Measured	Normalized
Y	1.267	3.055	1.263	3.007	1.265	2.998
Al	2.042	4.924	2.033	4.840	1.950	4.622
Ce	0.006	0.014	0.008	0.019	0.027	0.064
Fe	0.022	0.053	0.021	0.050	0.021	0.050
Co	0.021	0.051	0.022	0.052	0.020	0.047
O	4.976	12.000	5.040	12.000	5.063	12.000
Total	8.334	20.098	8.387	19.969	8.346	19.781

16.3.2 Comparison With Nd^{3+}-Doped Yag Ceramic

These observations make sense with two recent works. The first observation involved on micro-structuration induced differences in the thermo-optical and luminescence properties as seen in Nd^{3+}-doped YAG fine grain ceramics and crystals where it has been shown that grain boundary diffusion in the presence of impurities involves a complex interplay between grain boundary and bulk regions that is dictated, at least in part, by the impurity concentration [23]. The second observation is connected with the role of segregating impurities in grain-boundary diffusion in which the results are interpreted in the variation of the grain-boundary diffusivity in un-doped and doped ceramic oxides. The retardation of diffusion in doped ceramics is the result from segregation of the impurity concentration in the grain boundaries [10, 23].

Recent experimental studies performed on Nd^{3+}-doped YAG ceramics by using Confocal Imaging and TEM techniques demonstrated also that Nd^{3+} rare earth doping ions in ceramic garnets are mostly sited in the vicinity of the grain boundaries [10]. Such results show that spatial distribution of these dopants correlates well with low segregation coefficients of Nd^{3+} and Ce^{3+} in the garnet crystals grown from the melt and/or flux [17–19]. These cations (Nd^{3+} and Ce^{3+}) are both too large for the dodecahedral sites of unit (with 12 oxygen anions) confirmed authenticity of the obtained experimental data.

16.3.3 Yb^{3+}-Doped Yag Ceramic

We have applied to this sample the same procedure as for Ce^{3+}-doped YAG ceramic in order to evaluate the segregation phenomenon of Yb^{3+} cations located at the opposite side of the rare earth family. Visualization of grains and grain boundaries based on spatially resolved techniques can be seen in Fig. 16.6. First of all, we observe from several analyses in different positions of the sample that the average composition has been found as: $Y_{2.49}$ $Al_{5.29}$ $O_{12.00}$ $Yb_{0.16}$ $Fe_{0.03}$ $Co_{0.03}$. It means after normalization at 100%:
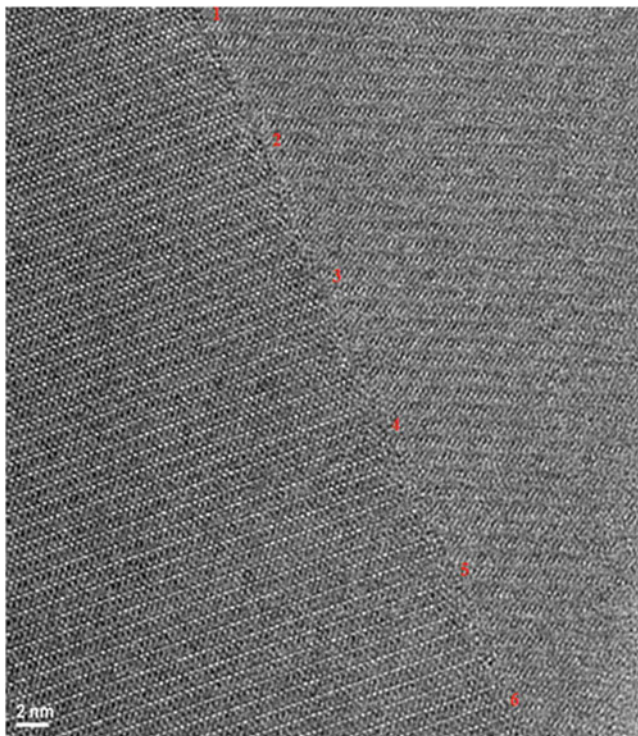
Fig. 16.6 High Resolution TEM image of a typical grain boundary in Yb^{3+}-doped YAG ceramic. Length of the white marker (*right-bottom* side of the image) is 2 nm. Results of chemical analysis in the vicinity ($+/-25$ nm) of the grain boundary are shown in Table 16.2. Linescan with a probe of "2.4 nm" (measured FWHM $= 2.6$ nm). Lateral step across the boundary $= 4.8$

$Y_{0.125 \pm 0.001} Al_{0.264 \pm 0.002} O_{0.600} Yb_{0.008 \pm 0.001} Fe_{0.002 \pm 0.001} Co_{0.002 \pm 0.001}$

So that there is a contamination by Fe and Co transition metal ions belonging only to the sample holder of the TEM apparatus like in the case of Ce^{3+}-doped YAG ceramic sample.

We also have noted that the amount of Yb^{3+} cations is much less (0.73 at. %) than the 5 at. % announced by elaboration.

The most striking feature according to EDX measurements and to our main purpose of this study is connected with much more uniform distribution of Yb^{3+} cations between grains and grain boundaries than for Ce^{3+} cations. Yb^{3+} cations were not detected concentrated on the grain boundaries contrary to Ce^{3+} cations as it can be seen from the values measured in six zones of the grain boundary in Fig. 16.6. For each zone equally distributed between the zone 1 and the zone 6 in Fig. 16.6, we have measured and indicated Yb^{3+} % concentrations in Table 16.2, systematically on the three positions of the grain boundary, below and above the grain boundary respectively at $+/-25$ nm. So that we can easily compare with

Table 16.2 Yb^{3+} % concentrations for the 6 positions along the grain boundary in Fig. 16.6.

Zones	1	2	3	4	5	6
Grain Boundary	0.69%	1.17%	0.89%	0.9%	0.85%	0.81%
Grain at 25 nm below GB	0.74%	0.94%	0.77%	0.78%	0.82%	0.78%
Grain at 25 nm above GB	0.73%	0.92%	0.70%	0.89%	0.70%	0.76%

Ce^{3+}-doped YAG ceramic in Fig. 16.5 where about four times difference of the Ce^{3+} concentrations between grain boundary and grains was detected on the similar nanometric size variation of $+/- 20$ nm.

Due to near infrared emission of Yb^{3+} rare earth ions, it was not possible to observe segregation by using Confocal Microscopy Technique and then we have only analysed TEM measurements in the evaluation of the Yb^{3+} ion distribution. However this is the most precise technique for such quantitative goal and we can conclude here a clear tendency of uniform Yb^{3+} distribution unambiguously evidenced by EDX between grains and grain boundaries at the nanometric probe size.

TEM analysis at nanometric scale was also recently performed with the same equipment (HRTEM and EDX) on new samples of Yb^{3+}-doped YAG ceramic provided by the Institute of Science and Technology for Ceramic, National Research Council, Faenza in Italy, prepared by reactive sintering of commercial oxides and using polyethylene glycol (PEG) as dispersant [24]. Our previous predictions on the absence of the phenomenon of segregation of Yb^{3+} rare earth element in YAG have been confirmed.

16.4 Correlation Between Segregation of Rare Earth Dopants in Melt Crystal Growth and Ceramic Processing for Optical Applications

These experimental results correlate well with low segregation coefficients of Ce^{3+} and Nd^{3+} large rare earth cations and the higher segregation coefficient for small rare earth cations like Yb^{3+} in the garnet structure observed in the melt crystal growth and thin film liquid phase epitaxy from flux [17, 25–27]. Indeed, previous essays had been done to understand the nature of rare earth segregation by growing enormously multi-component garnet films [17] by liquid phase epitaxy (LPE) from the fluxes that contained equal atomic fraction of ten or over ten different rare-earth elements. The growth rates in these experiments were set to be extremely low (about 1 μm/min) to ensure practically equilibrium segregation of rare-earth cations. This way, it was possible to compare segregation coefficients of various rare-earth cations introduced into the garnet structure in the same unique process.

We think that the segregation in solid-state grain growth might be qualitatively similar to that observed in melt/flux growth of garnet single crystals. The data

on segregation in melt/flux crystal growth are widely available and can be used for preliminary estimation of the dopant distribution in the solid-state ceramic processing. The lower is the segregation coefficient of the dopant in the melt growth, the greater amount of dopant will be collected on the grain boundaries of the ceramic material. This could help to predict uniform distribution of doping [28].

This suggests that, although acceptable optical properties have been reported for Nd^{3+}-doped YAG ceramics up to the several % of dopant level, the material quality is in fact reduced at high Nd^{3+} concentrations, at least regarding its spectroscopic properties. This inhomogeneity may also be responsible for the higher passive losses inferred from laser experiments on Nd^{3+} high-concentration ceramics [1, 29].

In this way, the higher homogeneity of rare earth ions in YAG laser ceramics positioned at the end of the lanthanide family like Yb^{3+} ion is another important advantage to get higher quality of the optical properties, especially for laser applications where the profile of the beam plays an important role. In [28] we have shown the dependencies of the segregation coefficients of various rare earth ionic radii for the following garnets of iron and gallium:

(Yb,Tm,Er,Ho,Y,Dy,Tb,Gd,Eu,Sm)3Fe5O12 and

(Lu,Yb,Tm,Er,Ho,Y,Dy,Tb,Gd,Eu,Sm,Nd,Pr)3Ga5O12.

The case of $Y_3Al_5O_{12}$ an Al garnet, had been only estimated and a very low segregation coefficient for Ce^{3+} and much higher for Yb^{3+} were expected. This is well in coincidence with the experimental values measured recently in this garnet at the Shanghai Institute of Ceramics [30]: 0.08 for Ce^{3+} and 1.09 for Yb^{3+}. The large difference of values of segregation coefficient between Ce^{3+} and Yb^{3+} explains the respective behavior of the distribution of luminescent cations inside ceramic materials.

16.5   Conclusion

The present TEM analyses confirm previous predictions on the phenomenon of segregation in the grain boundaries of rare earth elements in YAG optical ceramics depending on their position in the lanthanide family. For the first elements like Ce^{3+} and also Nd^{3+} ions, strong segregation and spatial variations of content between grains and grain boundaries have been visualized by quantitative data obtained from EDX spectroscopy, whereas no significant segregation in the grain boundaries has been detected for Yb^{3+}ion, the last active element one.

Qualitative suggestions have been made by considering the variation of rare earth dopants segregation coefficients in solid-state grain growth of YAG ceramics from previous observations in melt/flux growth of garnet single crystals.

References

1. Kawai R, Miyasaka Y, Otsuka K, Ohtomo T, Narita T, Ko JY, Shoji I, Taira T (2004) Opt Express 12(10):2293
2. Ikesue A, Furusato I, Kamata K (1995) J Am Ceram Soc 78:225–228
3. Ikesue A, Kinoshita T, Kamata K, Yoshida K (1995) J Am Ceram Soc 78:1033–1040
4. Lu JR, Ueda K, Yagi H, Yanagitani T, Akiyama T, Kaminskii AA (2002) J Alloys Comp 341:220–225
5. Rabinovitch Y, Tetard D, Faucher MD, Pham-Thi M (2003) Opt Mater 24(1, 2):345–351
6. Dubinskiy M, Merkle LD, Goff JR, Quarles GJ, Castillo VK, Schepler KL, Zelmon D, Guha S, Gonzalez LP, Rickey MR, Lee JJ, Hegde SM, Dumm JQ, Messing GL, Lee S-H (2005) SPIE 5792:1–9
7. Shoji I, Kurimura S, Sato Y, Taira T, Ikesue A, Yoshida K (2000) Appl Phys Lett 77:939–941
8. Shoji I, Sato Y, Kurimura S, Lupei V, Taira T, Ikesue A, Yoshida K (2002) Opt Lett 27:234–236
9. Taira T, Ikesue A, Yoshida K (1998) Diode-pumped Nd:YAG ceramic lasers. OSA TOPS 19:430–432
10. Ramirez MO, Wisdom J, Li H, Aung YL, Stitt J, Messing GL, Dierolf V, Liu Z, Ikesue A, Byer RL, Gopalan V (2008) Opt Express 16(9):5965
11. Yanagida T, Itoh T, Takahashi H, Hirakuri S, Kokubun M, Makishima K, Sato M, Enoto T, Yanagitani T, Yagi H, Shigetad T, Ito T (2007) Nucl Instrum Methods Phys Res A 21:23–26
12. Yanagida T et al (2005) IEEE Trans Nucl Sci NS-52 (5) part 3: 1836
13. Takahashi H, Yanagida T et al (2006) IEEE Trans Nucl Sci 53:2404
14. Bachmann V, Ronda C, Meijerink A (2009) Chem Mater 21(10):2077–2084
15. Cuche A, Masenelli B, Ledoux G, Amans D, Dujardin C, Sonnefraud Y, Mélinon P, Huant S (2009) Nanotechnology 20:015603
16. Jacinto C, Benayas A, Catunda T, García-Solé J, Kaminskii AA, Jaque D (2008) J Chem Phys 129:104705
17. Chani VI, Yoshikawa A, Kuwano Y, Hasegawa K, Fukuda T (1999) J Cryst Growth 204:155
18. Chani VI, Tschudi TT (ed.) (1990) Thin films in optics. In: Proceedings of the SPIE 1125. SPIE, Bellingham, Washington, DC, 107
19. Chani VI, Fukuda T, Rudolph P, Uda S (eds) (2004) Fiber crystal growth from the melt. Springer, Berlin/Heidelberg/New York, pp 129–130
20. Zhao W, Anghel S, Mancini C, Amans D, Boulon G, Epicier T, Shi Y, Feng XQ, Pan YB, Chani V, Yoshikawa A (2011) Opt Mater 33:684–687
21. Zhao W, Mancini C, Amans D, Boulon G, Epicier T, Min Y, Yagi H, Yanagitani T, Yanagida T, Yoshikawa A (2010) Jpn J Appl Phys 49:022602
22. Shi Y, Pan YB, Feng XQ, Li J, Guo J-K (2012) J Inorg Mater (China) 25(2):125–128
23. Kansuwan P, Rickman JM (2007) J Chem Phys 126:094707
24. Esposito L, Epicier T, Serantoni M, Piancastelli A, Alderighi D, Pirri A, Toci G, Vannini M, Anghel S, Boulon G (2012) J Eur Ceram Soc. Accepted on 27 February
25. Chani VI (1990) Thin films in optics. In: Tschudi TT (ed) Proceedings of the SPIE 1125 SPIE, Bellingham, Washington, DC, 107

26. Chani VI (2004) In: Fukuda T, Rudolph P, Uda S (eds) Fiber crystal growth from the melt. Springer, Berlin/Heidelberg/New York, p 129
27. Simura R, Yoshikawa A, Uda S (2009) J Cryst Growth 311(23–24):4763
28. Chani VI, Boulon G, Zhao W, Yanagida T, Yoshikawa A (2010) Jpn J Appl Phys 49(7 part 1):0756011–0756016
29. Merkle LD, Dubinskii M, Schlepler KL, Hedge SM (2006) Opt. Express 14:3893
30. Jiang B, Li J, Liu W, Pan Y (2012) to appear in Optical Materials

17
Random Lasing in Solid State Materials

J. Fernández, R. Balda, S. García-Revilla, J. Azkargorta, and I. Iparraguirre

17.1 Introduction

In 1967, Letokhov theoretically predicted the possibility of generating laser-like emission starting from scattering particles with negative absorption, the so-called *random* or *powder laser*. Random lasers are the simplest sources of stimulated emission without cavity, with the feedback provided by disordered-induced light scattering due to spatial inhomogeneity of the medium [1]. The specific feedback mechanism and behaviour of a given system depends on its particular nature and morphology. A detailed discussion about the latest results and theories concerning the mechanisms responsible for random lasing and the precise nature of the random laser modes can be found in Refs. [2–6].

Since 1986 when Markushev et al. demonstrated laser-like behaviour in a powder of $Na_5La_{1-x}Nd_x(MoO_4)_4$ at liquid nitrogen temperature [7], similar random laser experiments have been conducted at room temperature in numerous Nd-doped pulverized materials and highly scattering Nd-doped ceramics. The history and the state of the art of these neodymium-activated random lasers are reviewed by Noginov in Ref. [3]. Among these materials, the stoichiometric $NdAl_3(BO_3)_4$ powder was regarded as a promising room temperature solid-state random laser material [8] because it presents many desirable features, such as a low laser threshold, a high gain, high Nd^{3+} concentration, and excellent physical and chemical properties [9, 10].

J. Fernández (✉) • R. Balda • S. García-Revilla • J. Azkargorta • I. Iparraguirre
Dpto. Física Aplicada I, Escuela Superior de Ingenieria, Universidad del País Vasco UPV/EHU, Alda. Urquijo s/n, Bilbao 48013, Spain

J. Fernández • R. Balda
Materials Physics Center CSIC-UPV/EHU and Donostia International Physics Center, San Sebastian 20080, Spain
e-mail: joaquin.fernandez@ehu.es

We present here the random laser performance of ground powders of the yttrium borate family, $Nd_xY_{1-x}Al_3(BO_3)_4$ (x = 0.5–1). In particular, the dependence of their random laser threshold, slope efficiency, and emission kinetics on the Nd^{3+} concentration. Although the obtained results are qualitatively similar in all the explored powders, our findings show a reduction of the onset of laser-like emission and an increase of the slope efficiency when increasing the Nd^{3+} content [11]. At a first glance this behaviour seems to be unexpected due to the luminescence quenching at high concentrations; however, account taken of the short build up time of the random laser pulses, the lifetime shortening of the excited state, as concentration increases, does not affect the random laser process. It is therefore clear that for a random laser material high effective gain within the build up time scale of the pulse construction is the important issue. Following these results, we have looked for alternative crystal laser materials having higher stimulated emission cross-sections than borates and which could allow using low rare-earth concentration doping but keeping the effective gain still optimal for random laser operation. Among those possible candidates Nd-doped orthovanadate crystals have been proved to be efficient laser materials for diode-pumped solid state lasers due to their large absorption and emission cross sections, high chemical stability, and high damage threshold. Among vanadates Nd^{3+}:LuVO$_4$ has attracted much attention since it has the highest absorption and emission cross-sections, 6.9×10^{-19} cm^2 at 808 nm and 14.6×10^{-19} cm^2 at 1.06 μm respectively. Moreover, the relevance of Nd^{3+}:LuVO$_4$ crystal has been recently confirmed by the demonstration of passively Q-switched laser-diode pumped nanosecond self-Raman laser operating at cascade downconverted frequency [12].

Here we show the most relevant features of the random lasing action both in the spectral and temporal domains of a low concentrated Nd^{3+}-doped lutetium vanadate powder [13]. Laser threshold and emission efficiency were comparable to those obtained in stoichiometric borate crystal powders obtained under the same focusing and measuring conditions.

17.2 Experimental

17.2.1 Synthesis and Characterization of the Powder Laser Samples

Polycrystalline powders of $Nd_xY_{1-x}Al_3(BO_3)_4$ (x = 0.5, 0.6, 0.7, 0.8, 0.9, and 1) have been prepared at the Materials Science Institute of Madrid by Prof. Cascales group. The laser materials were ground afterwards by using a mixer mill. The polydispersity of the resulting powder was evaluated from scanning electron microscope photographs. The average particle size was 4 ± 2 μm, similar for all samples. All the ground powder samples were compacted in quartz cells without

a front window for handling ease and optical characterization. The volume filling factor of the powder materials ($f = 0.39$) was calculated by measuring sample volume and weight.

The Nd^{3+}-doped lutetium vanadate single crystals utilized in the random laser experiments presented in this work were grown at the University of Verona by Prof. M. Bettinelli group by using spontaneous nucleation in a $Pb_2V_2O_7$ flux [14]. The Nd^{3+} concentration in the sample used for random laser experiments was 3 mol%. The polydispersity of the measured powders was also evaluated from SEM photographs. The average particle size was $3 \pm 2 \, \mu m$.

17.2.2 Experimental Techniques

The random laser experiments were performed at room temperature in a backscattering arrangement by using a Ti-sapphire laser pumped by a pulsed frequency doubled Nd: YAG laser (9 ns pulse width) as the excitation source. The pump beam diameter on the sample surface was varied from 0.3 to 4 mm. The emission from the front face of the samples was collected with an optical fiber by use of two lenses. A long-pass filter was used to remove light at the pump wavelength. In the spectral measurements, the emitted light was dispersed by a 0.25 m monochromator and detected with a photomultiplier coupled to a boxcar integrator. The emission kinetics traces were recorded by using a fast photodiode connected to a digital oscilloscope (temporal resolution of 400 ps).

17.3 Random Laser Performance of $Nd_xY_{1-x}Al_3(BO_3)_4$ Laser Crystal Powders

In this section, the optimum neodymium concentration and focusing conditions in order to reduce the random lasing threshold pumping density in yttrium borate compounds are presented. Moreover, the dependence of the output slope efficiency on the Nd^{3+} concentration is investigated.

We experimentally analyzed the spectra and emission dynamics of $Nd_xY_{1-x}Al_3$ $(BO_3)_4$ ground powders when increasing the excitation energy. At low pumping energies, these laser crystal powders show only regular spontaneous emission with a single exponential emission kinetics. Figure 17.1 shows the normalized spontaneous emission spectrum (dashed line) of the $NdAl_3(BO_3)_4$ powder at the $^4F_{3/2} \rightarrow {}^4I_{11/2}$ transition. This spectrum was measured at 4 mJ/pulse, with a pump beam diameter on the sample of 1.87 mm. The lifetime of the Nd^{3+} upper laser level $^4F_{3/2}$ (determined by its spontaneous emission decay) is reduced from 15.6 μs in the less concentrated sample ($x = 0.5$) to 12.7 μs for the stoichiometric sample. Similar concentration quenching of the Nd^{3+} lifetime is observed in other

Fig. 17.1 Normalized emission spectra of the NdAl$_3$(BO$_3$)$_4$ powder obtained pumping at 802 nm with a pump spot size of 1.87 mm. The *dashed* and *solid lines* correspond to the fluorescence and laser-like emission spectra measured below and above the threshold at 4 mJ/pulse and 20 mJ/pulse, respectively
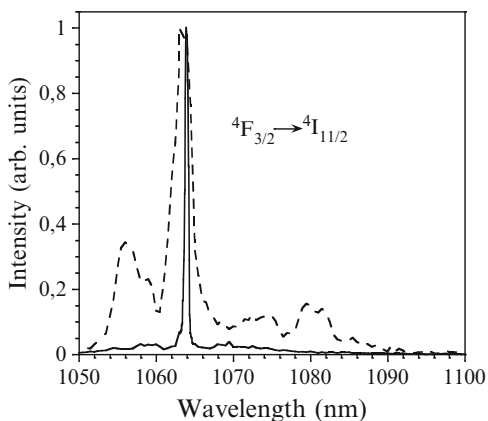
neodymium-doped laser materials. On the other hand, with the increase of the pumping energy, the amplified spontaneous emission of the laser crystal powders increases causing an enhancement of the emission intensity and a non exponential nature of the emission dynamics. In particular, above a certain critical threshold value both the spectra and the kinetics of Nd^{3+} luminescence change dramatically. The intensity of the strongest line in the spontaneous emission spectrum increases several orders of magnitude and its width becomes smaller. As evidenced in Fig. 17.1, the spectrum obtained at 20 mJ/pulse collapses to a narrow single line with a linewidth of 0.4 nm. It is worthy to remark that no spikes were observed in the laser-like emission spectra of our powder samples which suggests a nonresonant feedback mechanism of the explored random laser effect.

As mentioned before, just above the threshold energy the emission kinetics changes to a very short and intense emission pulse with a duration in the nanosecond time-scale ($\sim$1 ns). At stronger pumping, a second emission pulse emerges in the kinetics, and as the pumping energy is increased, the number of stimulated emission pulses increases manifesting the typical laser relaxation behaviour. Notice that relaxation oscillations in random lasers have been theoretically predicted by Letokhov in 1968 [1] and studied more recently in detail [15 and references therein]. In neodymium random lasers, they occur in a highly nonlinear regime showing narrow stimulated emission pulses ($\sim$1 ns) occurring during a much longer pumping pulse ($\sim$10 ns) [10]. These oscillations are strong in the beginning of the lasing process and are damped at longer times. Moreover, the study of the kinetics of relaxation oscillations in random lasers reveals information about the photon residence time in the scattering medium [16]. Figure 17.2 shows the temporal evolution of the NdAl$_3$(BO$_3$)$_4$ powder emission recorded below the lasing threshold (2 mJ/pulse solid line), just above the lasing threshold (5 mJ/pulse dashed-dotted line), and well above the lasing threshold (15 mJ/pulse dashed line) with the same pump spot size used to measure the emission spectra. As can be observed, the delay time between the first emission pulse and the onset of the fluorescence becomes shorter as the excitation energy increases. The other laser crystal powders exhibited a qualitative similar behaviour.

Fig. 17.2 Temporal
evolution of the emission
intensity of the NdAl$_3$(BO$_3$)$_4$
powder obtained at
2 mJ/pulse (*solid line*),
5 mJ/pulse (*dashed-dotted
line*) and 15 mJ/pulse (*dashed
line*) with a pump spot size of
1.87 mm ($\lambda_{exc} = 802$ nm)

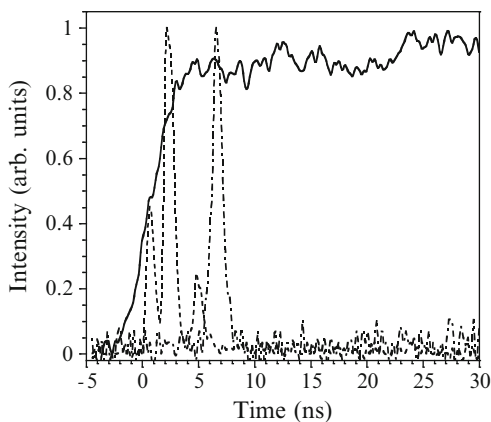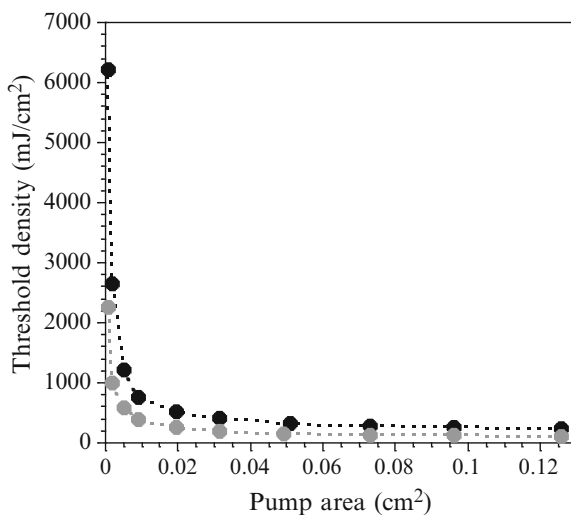**Fig. 17.3** Threshold
pumping density of the
NdAl$_3$(BO$_3$)$_4$ (*grey dots*) and
Nd$_{0.5}$Y$_{0.5}$Al$_3$(BO$_3$)$_4$ (*black
dots*) powder as a function of
the pumped spot area
($\lambda_{exc} = 802$ nm)

We also explored the dependence of the random laser threshold energy of the
NdAl$_3$(BO$_3$)$_4$ and Nd$_{0.5}$Y$_{0.5}$Al$_3$(BO$_3$)$_4$ laser crystal powders on the size of the
pumped spot. Figure 17.3 depicts the threshold pumping density of both samples
as a function of the pumped area. Both curves show the same behaviour but larger
threshold values are found in the non-stoichiometric borate powder. As can be
observed, the threshold pumping density sharply increases at rather small areas
of the pumped spot (where damage of the powder laser material can also occur
at high pumping energies). In order to explain this result, one should take into
account that (1) gain spatial distribution is governed by the spreading of pump light
in the powder, and (2) light is emitted in the pumped region of the powder from
where it starts to diffuse. For small excitation beam sizes, the light paths will very
probably leave the amplifying or pumped volume after a short time, with a small
chance to return. This implies that the threshold pumping density should be high

as a large gain is needed to compensate losses. With the increase of the size of the pumped spot, the amplifying volume increases. Therefore, photon walk paths elongate as light can travel longer inside the gain volume and can be more strongly amplified. Furthermore, if the photon leaves the gain volume and reaches the passive (unexcited) part of the powder, it could have a higher chance to return back to the amplifying region because of the larger excited volume. Consequently, a reduction of the random laser threshold density is expected in such a case. Nevertheless, as evidenced from Fig. 17.3, the threshold pumping density is almost independent of the pump spot area at large diameters. This behaviour can be explained regarding the flat-disk geometry of our pumping (the pump beam diameter, d, is larger than the penetration depth, which is typically less than 60 μm in neodymium random lasers at 532 nm [16]). Note that as $d \rightarrow \infty$ the number of paths per unit area of the pumped spot with a greater enough length to produce laser-like emission does not increase infinitely, but rather it will saturate at some constant value accounting for the saturation behaviour presented in Fig. 17.3 [17]. The same threshold trend with the pump beam size was experimentally observed in other neodymium doped materials [17]. It is worthy mentioning that the condition for the diffusion approximation ($\lambda << l_t << L$, where λ is the pump wavelength and L is the scattering sample thickness) is satisfied in the explored powder samples as l_t was estimated to be around 9.3 μm in the $NdAl_3(BO_3)_4$ and nonstoichiometric powders at the excitation wavelength ($\lambda = 802$ nm).

It is also clear from Fig. 17.3 that the Nd^{3+} concentration strongly influences the onset of laser-like emission. By measuring the input-output curves of the $Nd_xY_{1-x}Al_3(BO_3)_4$ laser crystal powders, we studied the Nd^{3+} concentration effect on the random laser performance of this yttrium borate family. Figure 17.4 shows the time integrated output intensity of the random laser pulses versus pump pulse energy for Nd^{3+} concentrations between x = 0.5 and 1. A pump spot size of 2 mm was employed. As already mentioned, just above the threshold the emission intensity undergoes a dramatic increase which is linear with pump fluence making the threshold sharp and well defined. As in regular lasers, the linear fit of these curves provides not only the threshold value but also the slope efficiency of stimulated emission. The fits corresponding to each powder sample are also displayed in Fig. 17.4. Figure 17.5 shows the random laser threshold energies (black squares) and slopes (black diamonds) inferred from the linear fits of the experimental data depicted in Fig. 17.4. The grey points of Fig. 17.5 represent the critical energy value at which the emission kinetics of the different powder samples is shortened to one short pulse. The error bars of these data are due to the energy fluctuations of the Ti-sapphire pump laser. As expected, there is a good agreement between these energies and the threshold values obtained from the linear fit of the input-output curves (black squares). It is clear from Fig. 17.5 that despite the existence of some lifetime concentration quenching, the increase of the Nd^{3+} content in the yttrium borate family leads to a reduction of the random laser threshold and to an enhancement of the relative slope of the random laser emission. Note that under the focusing conditions described above, the threshold energy of the $Nd_{0.5}Y_{0.5}Al_3(BO_3)_4$ powder
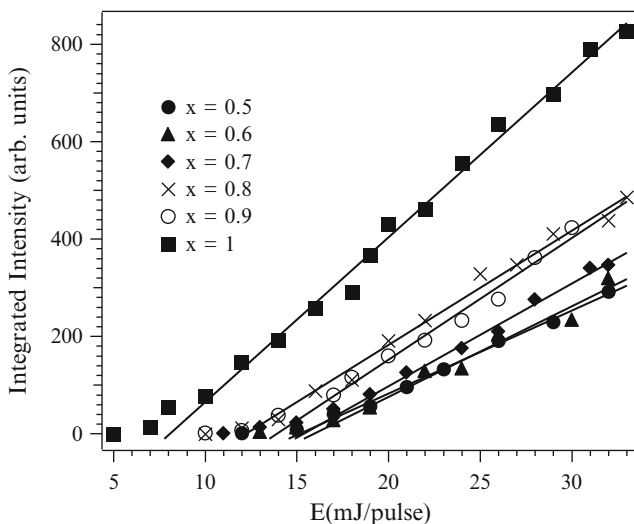
Fig. 17.4 Integrated area under the emission kinetics trace of the $Nd_xY_{1-x}Al_3(BO_3)_4$ (x = 0.5–1) powder as a function of the pump energy. *Dots, triangles, diamonds, crosses, circles*, and *squares* correspond to powder compositions with x = 0.5, 0.6, 0.7, 0.8, 0.9, and 1, respectively. *Solid lines* represent the linear fits of the experimental data. The diameter of the pump spot is 2 mm (λ_{exc} = 802 nm)
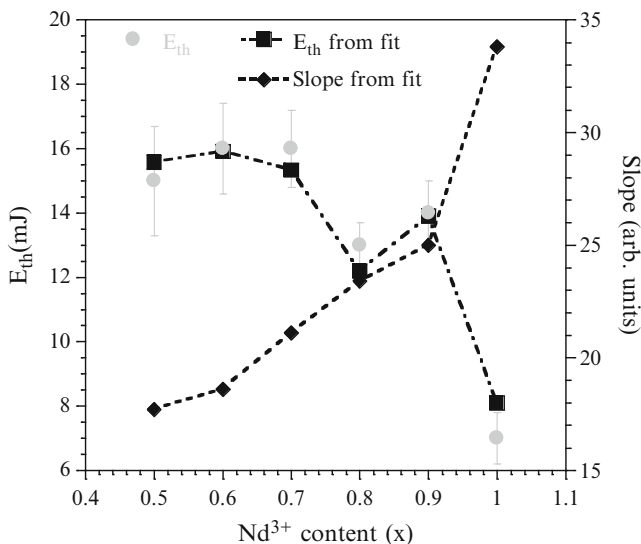

Fig. 17.5 Random laser threshold energy (*black squares*) and slope (*black diamonds*) values obtained from the linear fits of the input-output curves of the $Nd_xY_{1-x}Al_3(BO_3)_4$ powders as a function of the Nd^{3+} content. *Grey dots* correspond to the energy values at which their emission dynamics is shortened to one short pulse. The error bars represent the energy fluctuations of the pump laser

is about 15 mJ/pulse whereas the onset of laser-like emission in the NdAl$_3$(BO$_3$)$_4$ powder is around 7 mJ/pulse. Moreover, the stoichiometric powder has twice a larger slope efficiency than the former one.

17.4 Random Laser Performance of Nd^{3+}:LuVO$_4$ Crystal Powders

Figure 17.6 shows the emission spectra of the ^{4}F$_{3/2}$ →^{4}I$_{11/2}$ transition of Nd^{3+} in the Nd^{3+}:LuVO$_4$ powder sample obtained at low (5 mJ) and high (24 mJ) pumping energies. At low pump energy the spectrum presents the typical spontaneous emission features with a main peak around 1,065.6 nm and some additional structures spreading over 10 nm. When increasing the pump energy, there is a threshold value of 9 mJ above which the emission peak intensity suddenly increases whereas the emission spectrum collapses to a narrow single line at 1,065.6 nm and 0.3 nm HWHM, our spectral resolution limit.

The emission kinetics parallels the spectral behaviour; at low pumping energy the spontaneous emission is single exponential with a decay time of 60 μs whereas above threshold the time profile shortens up and gives a fast emission pulse with a duration of about 800 ps. As pumping increases well above the threshold energy, more pulses appear in the emission temporal profile showing the typical laser relaxation oscillation behaviour. As can be seen in Fig. 17.7, we recorded, at maximum pump energy, up to six oscillations. As is common in conventional solid state lasers, the build-up time (time delay between the output pulses and the pumping pulse) of the random laser pulse decreases gradually as pumping energy increases. As its duration is about 10 ns, this figure clearly shows that the relaxation oscillations remain until the pump pulse is over.
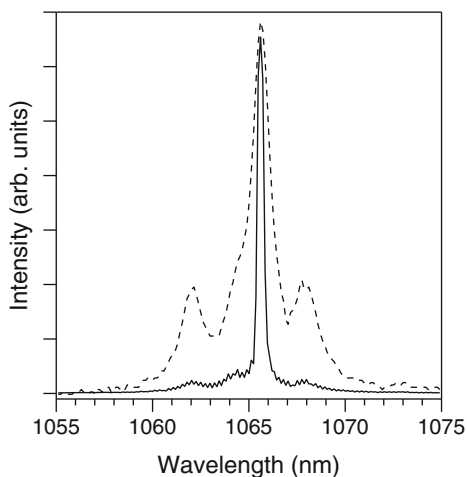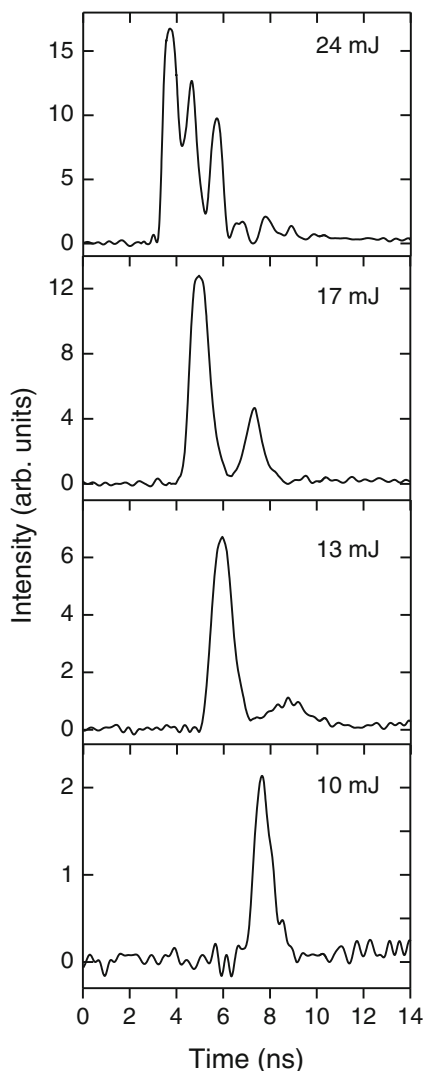

Fig. 17.6 Normalized emission spectra from Nd^{3+}(3%) LuVO$_4$ powder crystal obtained at pumping energies below (5 mJ *dashed line*) and above (24 mJ *solid line*) the laser threshold

Fig. 17.7 Stimulated emission intensity pulses of Nd^{3+} (3%) :LuVO$_4$ powder crystal as function of time at some different pump energies. The zero time marks the start of the pump pulse

We have compared the random laser performance of this material with the one obtained in a ground laser powder of NdAl$_3$(BO$_3$)$_4$ under the same focusing and measuring conditions. To avoid damage in the vanadate sample surface the maximum pump energy used was 25 mJ (about 300 mJ/cm^2). The damage threshold in borate is at least one magnitude order higher.

Figure 17.8 shows the time integrated intensity of the output pulses from these powders as a function of the pumping energy. The laser threshold was obtained with pump pulses of about 9 mJ for both samples being the slope efficiencies similar but slightly higher for the vanadate sample. The origin of this similar random lasing behaviour relies on the different Nd^{3+} concentrations of both compounds.

Fig. 17.8 Laser output energy as a function of the pumping energy for Nd^{3+} (3%):$LuVO_4$ (*dots*) and $NdAl_3(BO_3)_4$ (*crosses*) powders
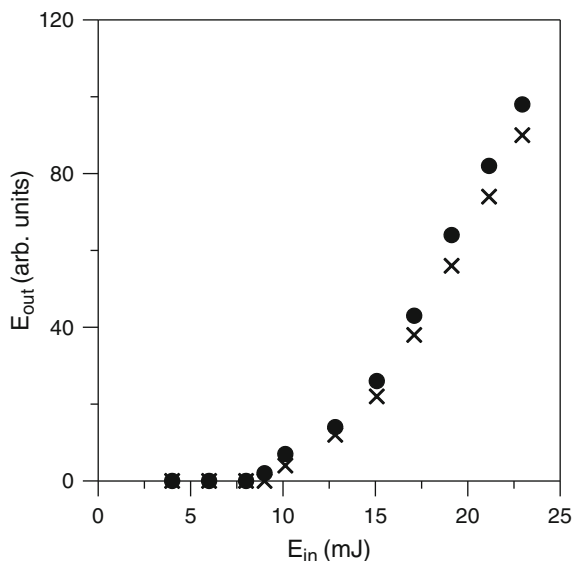
Although the emission cross section in Nd-doped lutetium vanadate is higher than in the aluminium borate compound, $NdAl_3(BO_3)_4$ is a stoichiometric compound with higher Nd^{3+} concentration (around 20 times) than the 3% Nd^{3+}-doped $LuVO_4$ and therefore it is possible to obtain an "accidental" equalized gain for the random lasing emission. Moreover, although the focussing conditions were the same for both compounds, the pumped volume, and therefore gain, may be different due to the different neodymium concentrations and refractive indices of both compounds. These results therefore suggest that better random laser performances of the vanadate could be achieved with more concentrated powders as has already been demonstrated in Nd-doped borate crystal powders.

17.5 Conclusions

We have obtained random laser action in Nd^{3+}-doped yttrium borate and lutetium vanadate crystal powders. We have compared their random laser performances, under similar experimental conditions. Account taken of the similar performances obtained and the very different dopant concentration of both powders, the results open up the possibility of using these Nd-doped vanadates as efficient random laser sources.

References

1. Letokhov VS (1967) Stimulated emission of an ensemble of scattering particles with negative absorption. JETP Lett 5:212–215
2. Wiersma DS (2008) The physics and applications of random lasers. Nat Phys 4:359–367
3. Noginov MA (2005) Solid-state random lasers. Springer, Berlin
4. Cao H (2003) Lasing in random media. Waves Random Media 13:R1–R39
5. Wiersma DS, Noginov MA (2010) Nano and random lasers. J Opt 12:020201
6. Andreasen J, Asatryan AA, Boten LC, Byrne MA, Cao H, Ge L, Labonté L, Sebbah P, Stone AD, Türeci HE, Vanneste C (2011) Modes of random lasers. Adv Opt Photon 3:88–127
7. Markushev VM, Zolin VF, Briskinia CM (1986) Luminescence and stimulated emission of neodymium in sodium lanthanum molybdate powders. Sov J Quantum Electron 16:281–283
8. Bahoura M, Noginov MA (2003) Determination of the transport mean free path in a solid-state random laser. J Opt Soc Am B 20:2389–2394
9. Xue D, Zhang S (1996) Calculation of the nonlinear optical coefficient of $NdAl_3(BO_3)_4$ crystal. J Phys Condens Matter 8:1949–1956
10. Noginov MA, Noginova NE, Caulfield HJ, Venkateswarlu P, Thompson T, Mahdi M, Ostroumov V (1996) Short-pulsed emission in the powders of $NdAl_3(BO_3)_4$, $NdSc_3(BO_3)_4$, and $Nd:Sr_5(PO_4)_3$ laser crystals. J Opt Soc Am B 13:2024–2033
11. García-Revilla S, Iparraguirre I, Cascales C, Azkargorta J, Balda R, Illarramendi MA, Al-Saleh M, Fernández J (2011) Random laser performance of $Nd_xY_{1-x}Al_3(BO_3)_4$ laser crystal powders. Opt Mater 34:461–464
12. Kaminskii AA, Bettinelli M, Dong J, Jaque D, Ueda K (2009) Nanosecond $Nd^{3+}:LuVO_4$ self-Raman laser. Laser Phys Lett 6:374–379
13. Azkargorta J, Bettinelli M, Iparraguirre I, Garcia-Revilla S, Balda R, Fernández J (2011) Random lasing in $Nd:LuVO_4$ crystal powder. Opt Express 19:19591–19599
14. Garton G, Smith SH, Wanklyn BM (1972) Crystal growth from the flux systems $PbO–V_2O_5$ and $Bi_2O_3–V_2O_5$. J Cryst Growth 13–14:588–592
15. Zhu G, Tumkur T, Noginov MA (2010) Anomalously delayed stimulated emission in random lasers. Phys Rev A 81:065801
16. Bahoura M, Morris KJ, Zhu G, Noginov MA (2005) Dependence of the neodymium random laser threshold on the diameter of the pumped spot. J Quantum Electron 41:677–685
17. Bahoura M, Morris KJ, Noginov MA (2002) Threshold and slope efficiency of $Nd_{0.5}La_{0.5}Al_3(BO_3)_4$ ceramic random laser: effect of the pumped spot size. Opt Commun 201:405–411

18

Imprint-Templated Nanocoax Array Architecture: Fabrication and Utilization

B. Rizal, F. Ye, P. Dhakal, T.C. Chiles, S. Shepard, G. McMahon, M.J. Burns, and Michael J. Naughton

18.1 Introduction

Arrays of vertically-oriented cylindrical, coaxial and triaxial nanostructures are fabricated from polymer nanopillar arrays prepared by nanoimprint lithography. With particular process modifications, these arrays have wide potential utility, including as molecular-scale biological (biomarker, pathogen, etc.) and chemical (explosives, environmental agents, etc.) sensors, high density neuroelectronic interfaces and retinal prostheses, radial junction photovoltaic solar cells, ultracapacitors, and optical metastructures. We report on their fabrication and example utilizations in the latter of these areas, with arrays of typical area density 10^6 mm^{-2}.

Vertically-oriented metallic nanowire and semiconducting or insulating nanopillar arrays are finding increasing use for a wide range of novel and enabling applications in, for example, electronics [1], photovoltaics [2, 3], optics [4, 5], and biochemical sensing [6–9]. Metal nanowire arrays are usually formed by electrodepositing metal in the pores of a nanoporous template, such as anodized aluminum oxide (AAO) or polycarbonate track-etch membranes, and removing/dissolving the template. Semiconducting nanowire arrays can be formed by etching a crystalline semiconductor such as silicon, or by epitaxially growing wires on a crystalline substrate. AAO-based nanowire arrays are quasi-ordered in the plane, while semiconductor nanopillar arrays can be random or well-ordered.

B. Rizal • F. Ye • P. Dhakal • M.J. Burns • M.J. Naughton (✉)
Department of Physics, Boston College, Chestnut Hill, MA 02467, USA
e-mail: naughton@bc.edu

T.C. Chiles
Department of Biology, Boston College, Chestnut Hill, MA 02467, USA

S. Shepard • G. McMahon
Nanofabrication Clean Room, Boston College, Chestnut Hill, MA 02467, USA

Nanoimprint lithography (NIL) is a useful technique for rapid and inexpensive replication of nanostructures [10], including those with 3D features such as the nanowire/pillar arrays of interest here. NIL involves coating a prepared "master" nanostructure with an elastomer to form a mold that serves as the negative of the master. A common elastomer is polydimethyl-siloxane (PDMS). After separation from the master, this mold is used to stamp imprint its shape onto a another resist atop a substrate [11], forming a nearly exact replica of the master. Due to the properties of the stamp, even nontrivial 3D structures can be accurately replicated with NIL. Aside from its nanoscale fidelity, perhaps the greatest advantage of the NIL technique is its ability to produce a large number of replicas from a single master.

One structure in which these virtues are manifest is a nanocoaxial array. That is, NIN-prepared nanopillar arrays can be used as starting points for the fabrication of vertically-oriented mono-axial (solid or hollow cylinders), coaxial, triaxial, *etc.* arrays, which have a number of potential technological uses. Here, we describe the NIL-initiated fabrication of variants of such arrays, and their potential utilization as optical waveguides and metamedia.

18.2   Fabrication

18.2.1   *Nil Replication of Nanopillar Arrays*

As mentioned, NIL utilizes an elastomer to make a flexible mold from a robust master and a photopolymer, such as a photoresist (PR), to make polymeric replicas of the master. As NIL masters in this report, silicon nanopillar (Si-NP) arrays were prepared by a combination of thermal oxidation and reactive ion etching of silicon substrates that were photolithographically patterned. Typical Si-NP dimensions were 2 µm height and 200 nm diameter, in hexagonal close-packed arrays with periodicity/pitch between 0.8 and 1.5 µm, on substrates containing 10×20 mm^2 areas of Si-NP arrays. In addition to vertical pillars, conical and sloped cross-section pillars were prepared with similar average dimensions. These latter ones can facilitate improved step coverage (conformality) of subsequent coatings, relative to that achievable with strictly vertical pillars. PDMS molds were prepared by NIL using a custom clamp apparatus that also facilitated subsequent thermal and/or photopolymerization of resist for replicas. We used SU-8 [12] resist for the NP replicas, chosen for its relatively low glass transition temperature, low volume shrinkage coefficient, and wide range of operating temperatures. Application of heat and pressure between the mold and the substrate coated with SU-8 helps to transfer the pattern from mold to substrate. A single mold can be used to make many replicas without requiring cleaning, and many replicas can be made from a single master. Figure 18.1 shows scanning electron microscope (SEM) images of a representative Si-NP master/PDMS stamp/SU-8 replica set. Note the high fidelity of the replicant
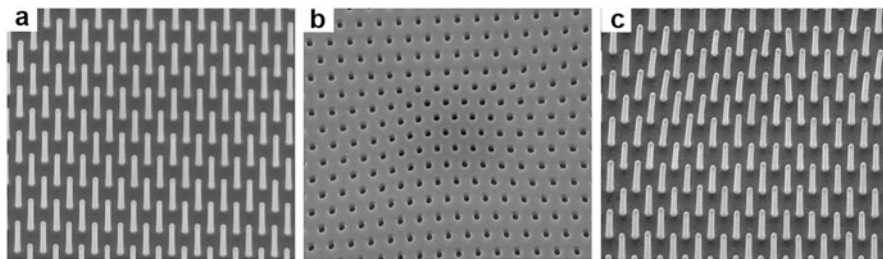
Fig. 18.1 SEM images of the SUV-NIL process. (**a**) Arrays of vertical 2 μm-tall Si nanopillars of period 1.5 μm used as master. (**b**) PDMS mold of the master. (**c**) SU-8 replica of the master

features with respect to the master. Below, we describe the fabrication and potential applications of vertically-oriented arrays of metallic nano-cylinder, coax, and triax arrays of SU-8 nanopillars made by the NIL process.

18.2.2 Fabrication of Hollow Metal Nanocylinders

The simplest nanopillar array-based structure to fabricate via NIL, aside from nanopillar replicas themselves, is a metal cylinder. To make this structure, we metallized the surfaces of SU-8 nanopillar arrays using a PVD system (usually sputter deposition, though thermal and electron beam evaporation can be employed, albeit with reduced conformality) followed by mechanical polishing to remove metal from the top of the nanopillar, and reactive ion etching (RIE) to remove the polymer from the core of the pillar. To avoid SU-8 nanopillar shape degradation due to plastic flow, this metallization needs, as do all subsequent process steps, to be performed at the lower of the glass transition or polymerization temperature of SU-8. Figure 18.2 shows an illustration of the fabrication scheme for nanocylinder arrays. We used 20–100 nm thick Au, Ag, Cr, Ti and combinations thereof for the metallization step, deposited by sputter deposition, as well as Pt by atomic layer deposition (ALD). The thickness of the sputtered metal coating in vertical nanostructures was not always uniform, being typically 10–20% thicker (measured radially) at the top than at the bottom. Not surprisingly, we found improved conformality of coating on conical, compared to strictly vertical structures.

Typically, and depending on pillar height, the radial thickness of the metal on the wall of the conical pillar was one third to one half that of the vertical thickness of the metal on the "floor" between pillars. Before polishing, support for each nanopillar was provided by coating the array with a second SU-8 stabilizing layer, filling the space between the pillars to a thickness comparable to or greater than the height of the pillars. Mechanical polishing is then done by using suspensions of 50 nm alumina nanoparticles on a vibratory polisher, typically for several hours per run. Polishing/inspection cycles continue until the metal on the top of the pillars

Fig. 18.2 Summary of the procedure used to fabricate arrays of hollow metallic nanocylinder from the polymer pillars. (**a**) Polymer nanopillar array. (**b**) Inner metal coating. (**c**) Polymer coating; (**d**) Etching of polymer
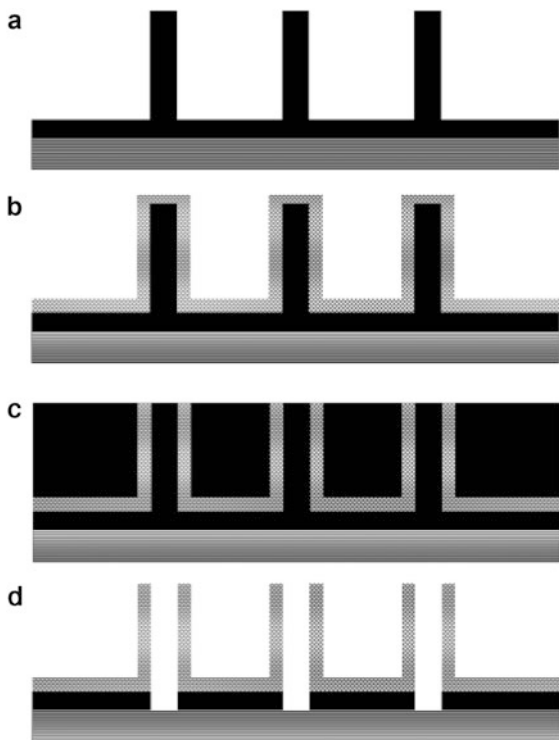
has been either exposed or fully removed, thus exposing the SU-8 centers. RIE is performed in a Plasma-Therm Versaline inductively-coupled reactive ion etch (ICP-RIE) system with 20 SCCM flow of CF_4 at 0.5 Pa pressure, 200 W power and 355 V self-bias conditions, which produces an etch rate $\sim$5 nm/s for SU-8. Figure 18.3 shows SEM images at different stages of fabrication of arrays of hollow metallic (Au) nanocylinders of 1.3 μm pitch, 300 nm inner diameter, 450 nm outer diameter and 1.8 μm height. We have made similar arrays with pitches between 800 nm and 1.5 μm. In addition, inner diameter tuning is facilitated by isotropic or anisotropic etching of the master Si-NP arrays or of the replicated SU-8 arrays, outer diameter by metal film deposition time, height by polishing time, and depth (inside the metal cylinder) by etch time and/or process (*i.e.* wet or dry etch).

As such, this fabrication method has been used to make arrays of different metals, pitch, radius, and height of hollow metallic nanocylinders. The pitch of the arrays always matches that of the master used to make the replica. Our template method may be an improvement over a previously reported method [13], especially to make arrays of nanocylinders of hard metals like Cr and W without artifacts and defects. Figure 18.4 shows two examples with Cr.

Fig. 18.3 SEM images of a
hollow gold cylinder array at
different stages of fabrication.
(**a**) Metallized SU-8
nanopillar array of pitch
1.3 μm. (**b**) Polished
nanopillar array embedded in
SU-8 film. (**c**) Hollow
metallic nanocylinder array
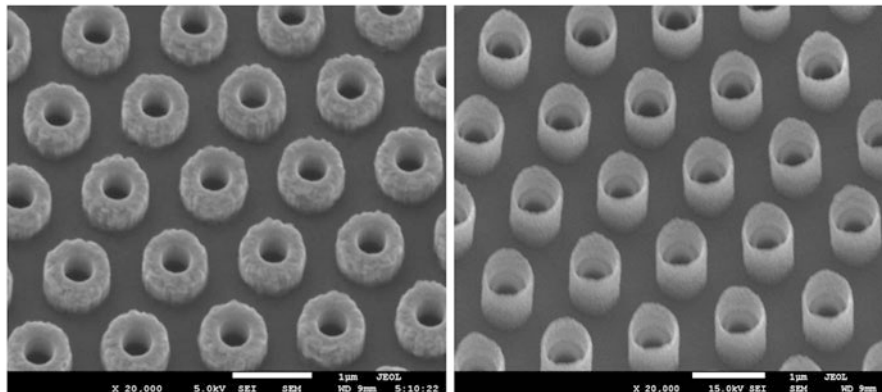with 300 nm inner radii and
1.8 μm height
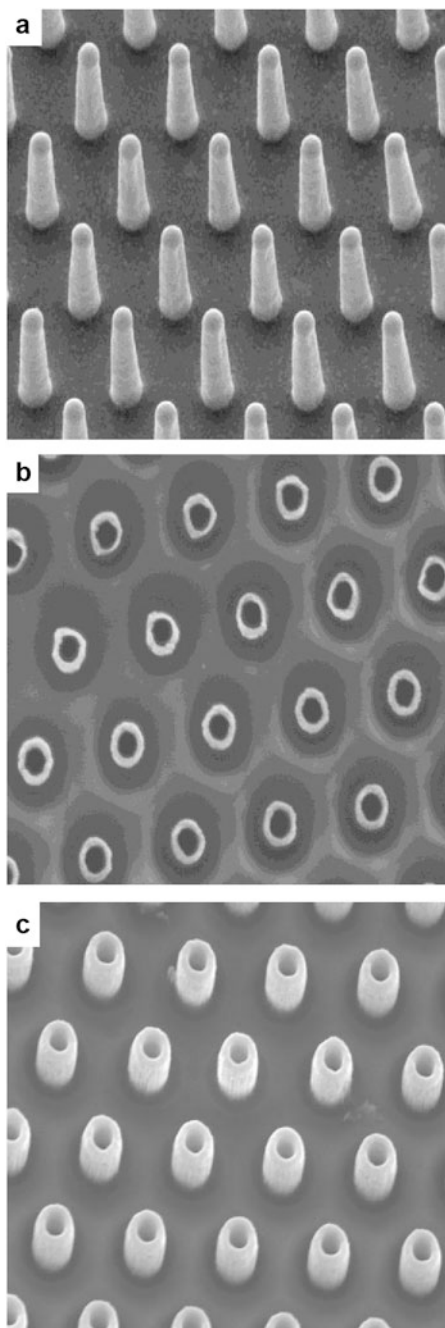
Fig. 18.4 Hollow metallic (Cr) cylinder arrays of various dimensions. Scale bars = 1 μm

18.2.3 Fabrication of Nanocoaxes

To form nanocoaxes, the first steps are as stated above through NP metallization (*i.e.* Figs. 18.2b and 18.3a). Figure 18.5 depicts the steps involved to fabricate arrays picking up from this point. After the initial metallization, we deposit a dielectric layer. We have deposited different kinds of dielectrics using different methods, including ALD, plasma enhanced chemical vapor deposition (PECVD), sputtering, and spin-coating, to deposit films anywhere between 10 and 200 nm thick (measured radially) of porous or nonporous dielectrics such as Al_2O_3, SiO_2, Si_3N_4, polymer, *a*-Si, *etc*. For ALD of Al_2O_3, we used trimethylaluminum (TMA) as precursor, whereas for PECVD SiO_2, and Si_3N_4, a gas mixture with ratio SiH_4/N_2O : 2/9 has been used at 200 °C. Reactively-sputtered Al_2O_3 deposition is done by introducing O_2 gas in ratio 1:6 to Ar during deposition of Al at room temperature. Of the three deposition methods, ALD and spin-coating yield the most conformal and dense coatings of dielectrics, especially on strictly vertical structures. In an early nanocoax application, the dielectric annulus was prepared as a radial *p-i-n* junction with amorphous silicon (*a*-Si), so that the array functioned as a photovoltaic solar cell [2].

Next, an outer metal film is deposited, of typical thickness 20–100 nm to form a nanocoaxial structure. For many applications, such as biological, chemical and neurological sensing, and for the study of nanoscopic effects of light propagation, the top ends of coax structures are removed ("decapitated" by mechanical polishing), forming open-ended nanocoaxes, as depicted in Fig. 18.5. In some cases, the arrays are processed further by etching the annuli and/or the cores inside the inner coax metal, by processes similar to those employed in the fabrication of hollow nanocylinder arrays, Figs. 18.2, 18.3, and 18.4 above. Such examples are shown in Fig. 18.6 (including full process steps) and Fig. 18.7 below.
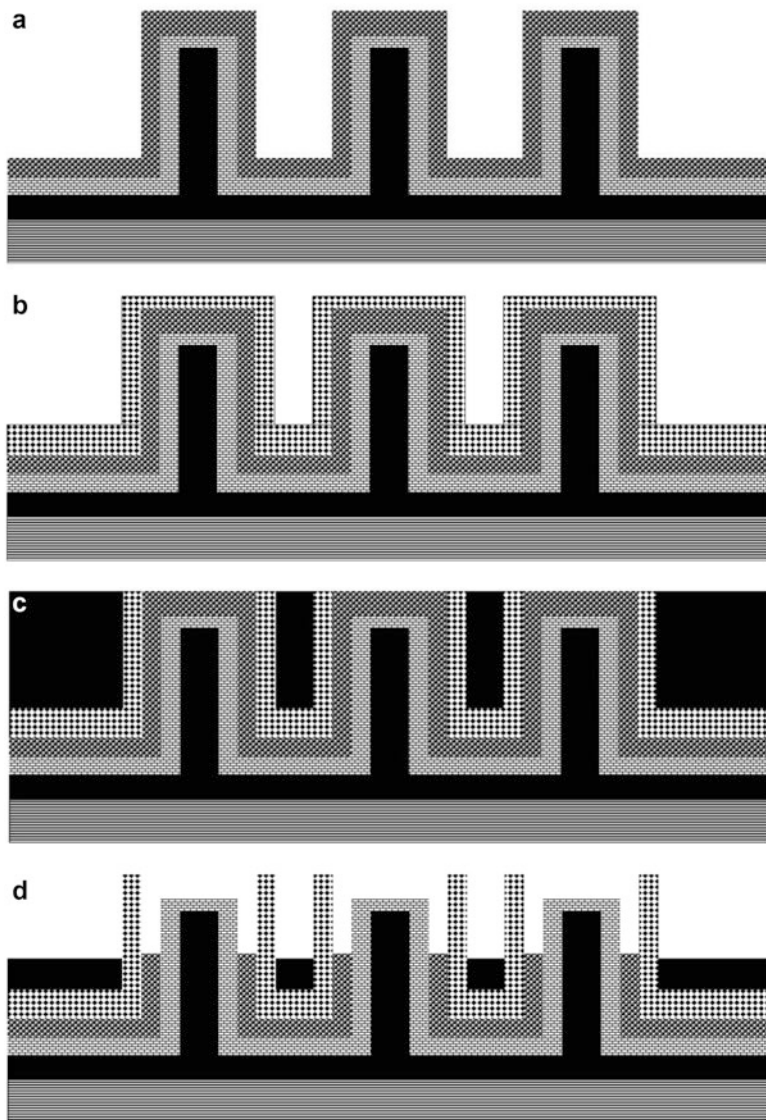
Fig. 18.5 Schematic representations of fabrication process for nanocoax arrays. (**a**) Dielectric coating. (**b**) Outer metal coating. (**c**) Polymer coating. (**d**) Etching of dielectric
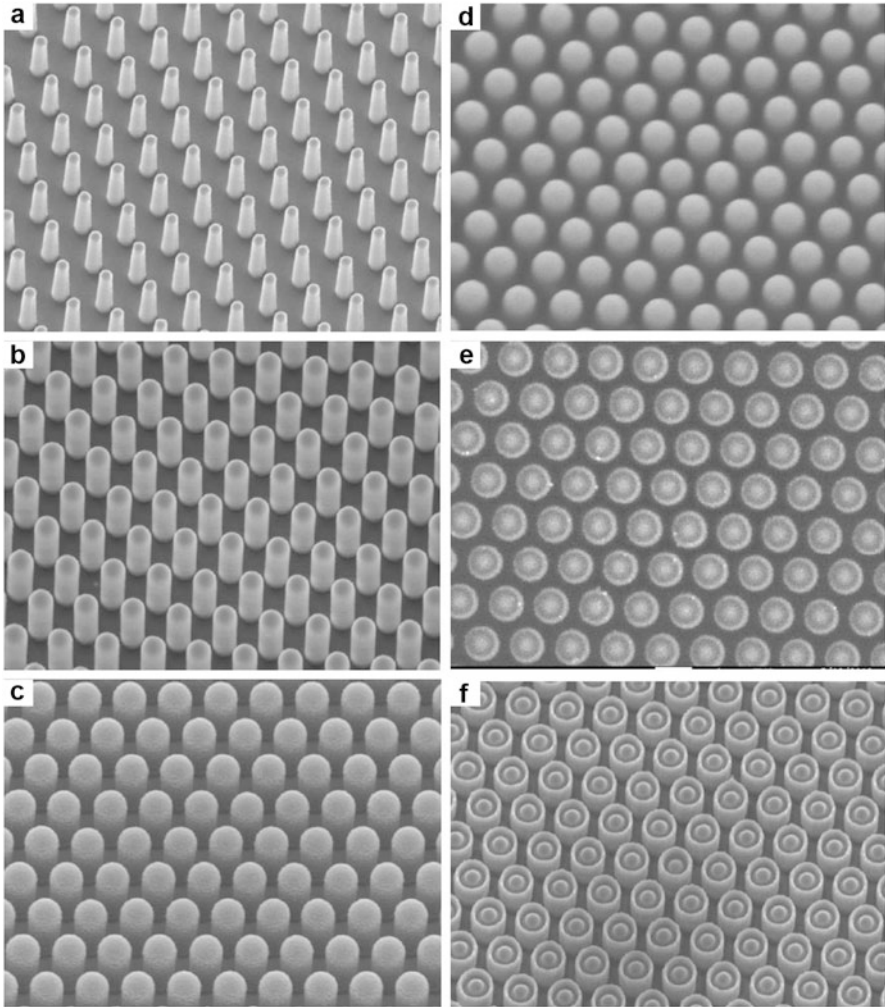
Fig. 18.6 SEM images of the fabrication process for open ended nanocoax structure of 1.3 μm pitch and 2 μm height. (**a**) Inner metal coating. (**b**) Dielectric coating. (**c**) Outer metal coating. (**d**) SU-8 coating. (**e**) Mechanical polishing. (**f**) Etching of dielectric

18.3 Optical Utilization

18.3.1 Light Transmisson Through Hollow Metallic Nanocylinders

Hollow metallic nanostructures have interesting optical properties. The top panel of Fig. 18.8 shows the results of finite-difference time-domain (FDTD) simulation of 500 nm light through an array of conical Au nanocylinders of 1.3 μm pitch, 1.8 μm
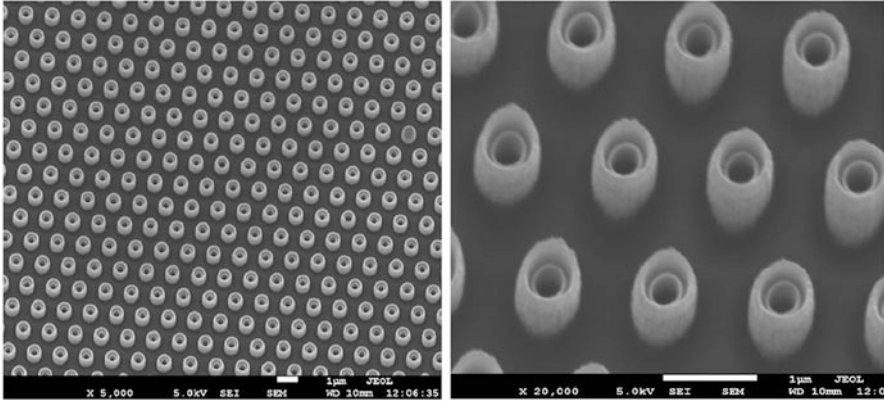
Fig. 18.7   Nanocoax array with hollow core and hollow annulus. Scale bars $= 1\ \mu$m

height, and 300 nm base diameter. Despite the nanocylinders dimensions being subwavelength in diameter, the simulations indicate that light should be able to propagate through them. This is confirmed in the center panel of Fig. 18.8, in a near-field scanning optical microscope (NSOM/SNOM) image of a sample illuminated from below with $\lambda = 500$ nm light. The bottom panel is an optical micrograph of the sample, illuminated from below with white light, clearly showing light not just emerging from the subwavelength holes, but the mere fact that the microscope formed an image illustrates that the emerging light was able to launch into the far-field. The transmission is dominated by light in the 600–700 nm wavelength range (bright spots are red in color), significantly larger than the inner radius, such that some degree of subwavelength propagation into the far field occurs. This transmission may be associated with resonant coupling of local surface plasmons in the cylindrical cores with incident light [14]. Thus, arrays of such nanocylinders could serve as a basic tool to study and characterize nanoscale manipulation of light.

18.3.2   *Light Transmisson Through Nanocoaxes*

The coaxial cable is known to be an ideal geometry for the efficient propagation of electromagnetic waves, being one of only two configurations (the other being a semi-infinite parallel plate) that propagates a transverse electromagnetic mode (TEM). For perfect electrical conductors, this mode has no cutoff free, while the TE_{mn} modes cut off at wavelengths larger than the average of the circumferences of the inner and outer conductors [15]. A nanoscale version of a coax, a nanocoax, operates similarly [16], with the exception that, for high enough frequency (*i.e.* visible), the radiation can interact with the metals comprising the waveguide. Transmission in a nanoscale coax as been shown theoretically to propagate in a
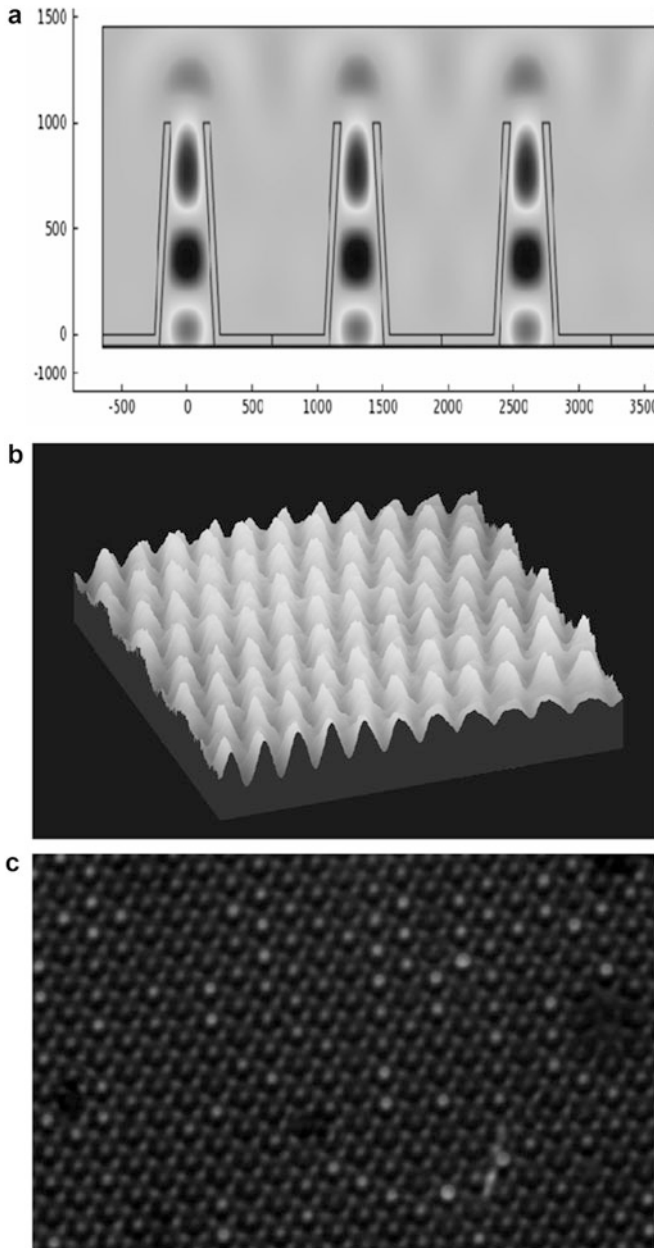
Fig. 18.8 (**a**) Simulation of light passing through an array of subwavelength nanocylinders as described in the text. (**b**) NSOM micrograph of 500 nm light passing through an array of subwavelength nanocylinders. (**c**) Optical micrograph of an array of subwavelength nanocylinders illuminated with light from below, showing transmission peaked in the bright spots
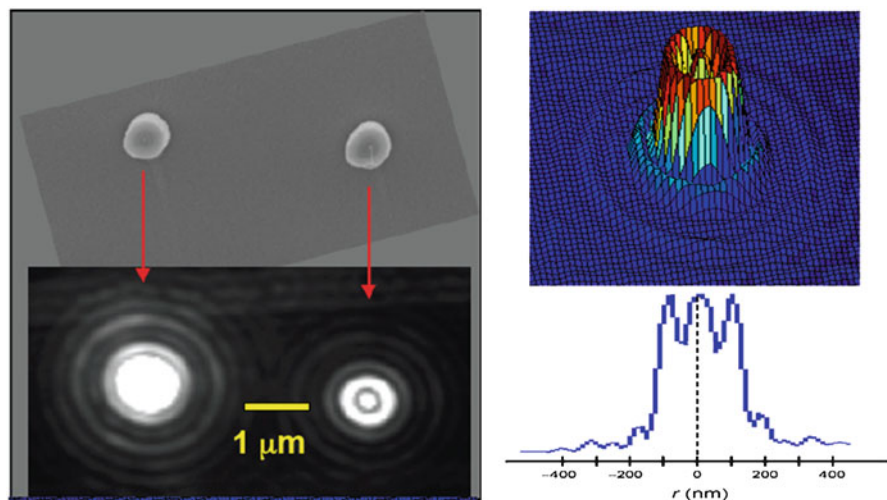
Fig. 18.9 (**a**) SEM top view of two isolated nanocoaxes with 150 nm diameter core and 100 nm thick annulus. (**b**) Optical micrograph of light emanating out the tops of the two coaxes, illuminated from below. (**c**) Light intensity map of right coax. (**d**) Line cut along a radial direction of transmitted light intensity

TM_{00} mode, which reduces to the TEM in the appropriate wavelength regime [17]. Nanocoaxes fabricated for optical purposes at Boston College indeed have been shown to transmit light for wavelengths larger than the nanocoax [5].

In Fig. 18.9, we show a scanning electron micrograph of two vertically-oriented nanocoaxes surrounded by an optically-opaque (150 nm thick W) film. The dielectric in the annuli of these coaxes is 100 nm thick ALD-deposited Al_2O_3, and the tops were exposed by focused ion beam milling. Immediately below this SEM is an optical micrograph of the same two nanocoaxes while illuminated by white light from below the opaque film. One can see in the optical image the transmission of the light, including Airy's rings [18] due to the diffraction-limited detection of the optical microscope that is observing the far field radiation emanating from the ends of the nanocoaxes. In the right panels, we show a 3D intensity map of the right nanocoax's emission pattern, and a line cut though the center of that pattern. This latter graph also shows Airy rings as spatial oscillations with a spacing of about 100 nm in the image.

In summary, we used imprint-templated lithography to replicate arrays of silicon nanopillars in SU-8 polymer, and used those replicated arrays to form arrays of metal nanocylinders and nanocoaxes (as well as nanotriaxes, *etc*., not discussed here). These structures can be employed in a variety of sensing applications, and for the nanoscale manipulation of light, including as radial-junction solar cells and nanophotonic waveguides. Examples of the latter were presented herein.

References

1. Duan X, Huang Y, Cui Y, Wang J, Lieber CM (2001) Indium phosphide nanowires as building blocks for nanoscale electronic and optoelectronic devices. Nature 409:66–69
2. Naughton MJ, Kempa K, Ren ZF, Gao Y, Rybczynski J, Argenti N, Gao W, Wang Y, Peng Y, Naughton JR, McMahon G, Paudel T, Lan YC, Burns MJ, Shepard A, Clary M, Ballif C, Haug F-J, Söderström T, Cubero O, Eminian C (2010) Efficient nanocoax-based solar cells. Phys Status Solidi Rapid Res Lett 4:181–183
3. Paudel T, Rybczynski J, Gao YT, Lan YC, Peng Y, Kempa K, Naughton MJ, Ren ZF (2011) Nanocoax solar cells based on aligned multiwalled carbon nanotube arrays. Phys Status Solidi A 208:924–927
4. Sirbuly DJ, Law M, Yan J, Yang P (2005) Semiconductor nanowires for subwavelength photonics integration. J Phys Chem B 109:1519–15213
5. Rybczynski J, Kempa K, Herczenski A, Wang Y, Naughton MJ, Ren ZF, Haung ZP, Cai D, Giersig M (2007) Subwavelength waveguide for visible light. Appl Phys Lett 90:021104
6. Zhao HZ, Rizal B, McMahon G, Wang H, Dhakal P, Kirkpatrick T, Ren ZF, Chiles TC, Naughton MJ, Cai D (2012) Ultrasensitive chemical detection using nanocoax sensor. ACS Nano 6:3171–3178
7. Kabashin AV, Evans P, Pastkovsky S, Hendren W, Wurtz GA, Atkinson R, Pollard R, Podolskiy VA, Zayats AV (2009) Plasmonic nanorod metamaterials for biosensing. Nat Mater 8:867–871
8. Holgado M, Barrios CA, Ortega FJ, Sanza FJ, Casquel R, Laguna MF, Banuls MJ, Lopez-romero D, Puchades R, Maquaieira A (2010) Label-free biosensing by means of periodic lattices of high aspect ratio SU-8 nanopillars. Biosens Bioelectron 25:2553–2558
9. Kubo W, Fujikawa S (2011) Au double nanopillars with nanogap for plasmonic sensor. Nano Lett 11:8–15
10. Chou SY, Krauss PR, Renstrom PJ (1996) Imprint lithography with 25-nanometer resolution. Science 272:85–87
11. Gates BD, Xu Q, Stewart M, Ryan D, Willson CG, Whitesides GM (2005) New approaches to nanofabrication: molding, printing, and other techniques. Chem Rev 105:1171–1196
12. Microchem Corporation, Newton, MA
13. Xu Q, Perez-Castillejos R, Li ZF, Whitesides GM (2006) Fabrication of high-aspect-ratio metallic nanostructures using nanoskiving. Nano Lett 6:2163–2165
14. Krishnan A, Thio T, Kim TJ, Lezec HJ, Ebbesen TW, Wolff PA, Pendry J, Martin-Moreno L, Garcia-Vidal FJ (2001) Evanescently coupled resonance in surface plasmon enhanced transmission. Opt Commun 200:1–7
15. Pozar D (2012) Microwave engineering, 4th edn. Wiley, New York
16. Kempa K, Wang X, Ren ZF, Naughton MJ (2008) Discretely guided electromagnetic effective medium. Appl Phys Lett 92:043114
17. Peng Y, Wang X, Kempa K (2008) TEM-like optical mode of a coaxial nanowaveguide. Opt Express 16:1758–1763
18. Airy GB (1835) On the diffraction of an object-glass with circular aperture. Trans Camb Philos Soc 5:283–291

Part II
Short Seminars

19
Metallic Nanoclusters in Layered Crystals: Spectroscopy and Computer Simulations

Ivan Karbovnyk, I. Bolesta, S. Velgosh, I. Rovetsky, and I. Kolych

Abstract Clusters are essentially the aggregations of countable number of atoms and may range in sizes from nanometers to microns, thus exhibiting many specific features of fundamental and practical importance. Isolation of metallic clusters within the dielectric environment leads to a variety of different effects which can be used in the fabrication of modern electronic devices.

Herewith, clusters which are embedded in the matrices of layered structures are considered. It has been shown that during crystal growth process and/or further treatment non-stoichiometric atoms of metals (e. g. silver) in the matrices of layered crystals tend to arrange in microsized and nanosized formations. According to rough estimates, such aggregates contain from 10^5 up to 10^{11} atoms. The essential difference between the properties of the pure host material and the material with embedded matrix-isolated clusters follows from the fact that surface atoms play a key role in the optical response of an individual cluster.

One can outline several important cluster-induced effects affecting optical properties of the host dielectric environment.

Firstly, due to the quantum confinement of electrons small clusters have discrete energy levels, which may be observed in the luminescence from the material. Scattering and absorption of light inside metallic clusters changes the extinction spectra profile with respect to that of the pure crystal. More interesting features appear as the cluster concentration in the host matrix increases. Secondly, for systems with clusters, the energy can be concentrated in a few degrees of freedom (especially at low temperatures). Consequently, the temperature dependencies of such characteristics as specific heat and thermal expansion, as well as non-linear optical properties exhibit anomalies at certain temperatures. And finally, several

I. Karbovnyk (✉) • I. Bolesta • S. Velgosh • I. Rovetsky • I. Kolych
Department of Electronics, Ivan Franko National University of Lviv, 107 Tarnavskogo str, Lviv 79017, Ukraine
e-mail: ivan_karbovnyck@yahoo.com

factors may have influence on the vibrational modes of the host medium. Surface plasmon resonance due to collective movement of electrons in a single cluster may results in the modification of infrared spectra. Additional vibrational modes might develop because of neighboring clusters interaction.

Summarizing, the matrix-isolated cluster formations at the nanoscale have interesting properties, which can be probed by complementary experimental methods and computational techniques. The interaction of electromagnetic wave with small metallic particles aggregating in clusters is reflected in the optical response of the material in UV, near-IR, medium-IR and far-IR ranges. Thus, it is a challenging task to combine the appropriate experiments with ab initio calculations for deeper understanding of the fundamental light emission/absorption processes at the microscopic level.

20
Optical Antennas for Single Emitter Fluorescence Enhancement

Palash Bharadwaj and Lukas Novotny

Abstract Colloidal metal nanoparticles offer a convenient realization of optical antennas for visible light frequencies. They serve to spatially enhance and localize fields, and modify the excitation rate (Γ_{exc}) and the radiative decay rate (Γ_r) when placed close to single emitters (molecules, quantum dots, etc.). In addition, they can also cause undesirable losses leading to an increase in the non-radiative decay rate (Γ_{nr}). This interplay of rates can lead to a strong modification of the emission characteristics over the intrinsic behavior [1].

Using Au nanoparticle antennas of different geometries, we demonstrate enhancements of fluorescence from single quantum emitters by a factor 10–100, with the highest enhancements resulting for molecules with very low intrinsic quantum yields [2]. Such enhancements afford an improvement in imaging resolution down to λ/30.

We also investigate changes to fluorescence blinking of a single colloidal quantum dot (QD) coupled to an antenna, as a function of antenna-QD distance. We find that power-law blinking is preserved unaltered even as the antenna drastically modifies the excitonic decay rate in the QD, and reduces the blinking probability. This resilience of the power-law to change provides evidence that blinking statistics are not swayed by environment-induced variations in kinetics.

P. Bharadwaj (✉) • L. Novotny
The Institute of Optics, University of Rochester, Wilmot Annex 101, 275 Hutchison Avenue, Rochester, NY 14627, USA
e-mail: palash@pas.rochester.edu; novotny@optics.rochester.edu

References

1. Anger P, Bharadwaj P, Novotny L (2006) Enhancement and quenching of single molecule fluorescence. Phys Rev Lett 96:113002
2. Bharadwaj P, Novotny L (2010) Plasmon enhanced photoemission from a single $Y_3N@C_{80}$ fullerene. J Phys Chem C 114:7444
3. Bharadwaj P, Beams R, Novotny L (2011) Nanoscale spectroscopy with optical antennas. Chem Sci 2:136
4. Bharadwaj P, Novotny L (2011) Robustness of quantum dot power-law blinking. Nano Lett 11:213

21
Ultrafast All-Optical Switching in TiO$_2$

Christopher C. Evans, J. Bradley, O. Reshef, E. Marti-Pameño, and Eric Mazur

Abstract Titanium dioxide (TiO$_2$) is a promising yet unexplored material for ultrafast, on-chip nonlinear optical devices. Here, we explore TiO$_2$'s capacity for nonlinear applications and then fabricate linear on-chip devices using this material. We measure TiO$_2$'s Kerr nonlinearity to be 30 times that found in silica glass by using the *Z*-scan technique with a bulk sample. During the same experiment, the low two-photon absorption observed can enable all-optical applications around 800 nm. To realize devices, we require waveguides made from thin films of TiO$_2$. We deposit our thin films on oxidized silicon wafers using reactive sputtering of titanium metal in an oxygen environment. This method produces thin films with a high refractive index (2.4) and low planar waveguiding losses (<0.4 dB/cm). Using these films, we define structures with electron-beam lithography. Next, we form waveguides using reactive-ion etching to achieve feature sizes in TiO$_2$ down to 100 nm. We show both visible and 780-nm light propagation in 300-nm wide waveguides. Lastly, we test simple linear devices such as bends, directional couplers, and Sagnac interferometers. From our observations of the nonlinear optical properties in bulk samples and our demonstration of basic on-chip devices, we conclude that TiO$_2$ is a viable material for all-optical applications.

C.C. Evans (✉) • J. Bradley • O. Reshef • E. Mazur
Department of Physics, Harvard University, 9 Oxford Street, Cambridge, MA 02138, USA
e-mail: evans@fas.harvard.edu

E. Marti-Pameño
Universidad Autónoma de Puebla, Av. San Claudio y Rio Verde, Puebla, Puebla C.P. 72000, Mexico

E. Mazur
Division of Applied Sciences, Harvard University, Pierce Hall 225, Cambridge, MA 02138, USA

22
Coherent Manipulation of Motional States of a Single Trapped Ion

Alessandro S. Villar

Abstract The ability to precisely manipulate an isolated quantum system opens new avenues in the simulation of more complicated quantum systems, using the tools of quantum computation. While the paradigm of quantum computation nowadays considers a collection of two-level systems known as qubits, it is also possible to generalize the basic logic quantum units to multi-level or even continuous systems.

Our proposal, under development in the Max Planck Institute for the Science of Light, in Erlangen, Germany, aims to coherent manipulate the motion of a single trapped ion – i.e. its position and momentum – with pulses of light. Those continuous observables are better visualized in phase space, with the aid of the Wigner function, from which wave properties of the quantum system, such as interference in phase space, are evident. In this case, universality of the computation is guaranteed when a minimum set of operations can be realized.

Gaussian operations, which maintain as Gaussian an originally Gaussian Wigner function, are realized by displacements and squeezers. Non-Gaussian operations require higher order nonlinearities to be available in the quantum system, such as the Kerr effect [1], and are essential for the universality of operations in continuous systems.

We show how to realize all the necessary operations with a trapped ion [2]. We present a brief overview on the current status of our experiment.

A.S. Villar (✉)
Max Planck Institute for the Science of Light, University of Erlangen-Nuremberg, Günther-Scharowsky-str. 1/Bau 24, 91058 Erlangen Germany
e-mail: Alessandro.Villar@mpl.mpg.de

References

1. Stobinska M, Villar AS, Leuchs G (2011) Generation of Kerr non-Gaussian motional states of trapped ions. Europhys Lett 94:54002
2. Villar AS, Stobinska M (2011) Universal toolbox for quantum computation over the motion of a trapped ion (in preparation)

23
Thermalization of an Open Quantum System Via Full Diagonalization

K. Jacobs and Luciano Silvestri

Abstract Thermalization, the irreversible relaxation of a system to thermodynamic equilibrium, ultimately arises from the reversible dynamics of many-body quantum systems. Weakly coupling a small system to a large many-body quantum system (heat bath) results in the equilibration of the small system to the Boltzmann distribution. We solve numerically, using full diagonalization, a model in which a small system is coupled to a large quantum system, and retrieve the thermodynamic behavior from the underlying quantum mechanics. We discuss the mechanism of thermalization, and the applications of our simulation for exploring the behavior of damped quantum systems.

K. Jacobs (✉) • L. Silvestri
Department of Physics, University of Massachusetts Boston, 100 Morrissey Blvd, Boston, MA 02125, USA
e-mail: lucianosilvetri88@gmail.com

24

The Role of Localized and Propagating Surface Plasmons in Periodically-Arrayed Nanopillars

Francisco J. Bezares, Joshua D. Caldwell, O.J. Glembocki, R.W. Rendell, M. Feygelson, M. Ukaegbu, R. Kasica, L. Shirey, N.D. Bassim, and C. Hosten

Abstract Periodic arrays of plasmonic nanopillars have been shown to provide large, uniform surface-enhanced Raman scattering (SERS) enhancements. We show that these enhancements are the result of the combined impact of localized and propagating surface plasmon modes within the plasmonic architecture. Here, arrays of periodically-arranged silicon nanopillars of varying sizes and interpillar gaps were fabricated to enable the exploration of the SERS response from two different structures; one featuring only localized surface plasmon (LSP) modes and the other featuring LSP and propagating (PSP) modes. It is shown that the LSP modes determine the optimal architecture, and thereby determine the optimum diameter for the structures at a given incident. However, the increase in the SERS enhancement factor for a system in which LSP and PSP cooperatively interact was measured to be over an order of magnitude higher and the peak in the diameter dependence was significantly broadened, thus, such structures not only provide larger enhancement factors but are also more forgiving of lithographic variations.

F.J. Bezares • J.D. Caldwell (✉) • O.J. Glembocki • R.W. Rendell • M. Feygelson • L. Shirey • N.D. Bassim
U.S. Naval Research Laboratory, 4555 Overlook Ave, S.W, Washington, DC 20375, USA
e-mail: francisco.bezares.ctr@nrl.navy.mil; joshua.caldwell@nrl.navy.mil

M. Ukaegbu • C. Hosten
Department of Chemistry, Howard University, Washington, DC 20059, USA

R. Kasica
Center for Nanoscale Science and Technology, NIST, Gaithersburg, MD 20899, USA

25
Optical and Structural Properties of Noble Metal Island Films

M. Lončarić, H. Zorc, and J. Sancho-Parramon

Abstract Ultrathin layers of noble metals obtained by deposition to dielectric substrate during evaporation in high vacuum represent nanostructured matter – noble metal island films (MIFs). Nanoparticles showing interesting optical properties due to the localized surface plasmons (LSP) are formed instead of homogenous layer. Optical properties of noble metal nanoparticles are closely related to their size, shape, distribution and dielectric environment. LSP properties may be tailored by changing deposition parameters (amount of material and substrate temperature) or by changing dielectric environment (dielectric layers below and/or above metal nanoparticles).

The optical properties of noble MIFs were investigated using variable angle spectroscopic ellipsometry and structural characterisation was performed by atomic force microscopy (AFM) and grazing incidence small angle X-ray scattering (GISAXS) measurements [1, 2]. Modelling of optical properties of noble MIFs using oscillators provided detailed description of optical constants in wide spectral range. Various physical phenomena resulting from structural properties of the samples were explicitly accounted for: LSP (due to existence of metallic nanoparticles) and metal-like behaviour in the infrared (in case of percolation). This approach gave description of noble MIFs which was not possible with the use of standard effective medium theories.

The availability of effective optical constants for noble MIFs enables to incorporate these films in the design of complex multilayer structures, combining dielectric layers and noble MIFs that may offer advantages with respect to classical coatings. This application potential is clearly shown in the design of high luminosity reflectors [3].

M. Lončarić (✉) • H. Zorc • J. Sancho-Parramon
Ruđer Bošković Institute, Bijenička cesta 54, 10000 Zagreb, Croatia
e-mail: mloncaric@irb.hr

References

1. Lončarić M, Sancho-Parramon J, Zorc H (2011) Optical properties of gold island films – a spectroscopic ellipsometry study. Thin Solid Films 519:2946–2950
2. Lončarić M, Sancho-Paramon J, Pavlović M, Zorc H, Dubček P, Turković A, Bernstorff S, Jakopic G, Haase A (2009) Optical and structural characterization of silver islands films on glass substrates. Vacuum 84(1):188–192
3. Zorc H, Lončarić M, Sancho-Parramon J (2011) Use of gold island films in design of reflectors with high luminosity. Appl Opt 50(9):C364–C367

26
Localized Photonic States in Two Dimensional Quasicrystalline Waveguides

G. Benedek and Andrea Trabattoni

Abstract The introduction of defects in photonic lattices generally allows to control the localization and the propagation of light. While point defects are conventionally used in order to obtain localized photonic states, linear defects are introduced for waveguiding EM waves. In this work we demonstrate the possibility of obtaining localized states also in a waveguiding configuration, by using quasicrystalline lattices. This result opens a new range of possibilities in designing optical circuits, in which the localization-propagation switch is easily obtainable by mechanical or opto-electric methods.

G. Benedek (✉)
Dipartimento di Scienza dei Materiali, Università Milano-Bicocca, Via Roberto Cozzi 53, Milan 20125, Italy

A. Trabattoni
Department of Physics, University of Milan-Bicocca, Piazza della Scienza 3, Milan 20126, Italy
e-mail: sebach.traba@gmail.com

27

Unified Theoretical Model of Loss Compensation and Energy Transfer for Plasmonic Nanoparticles Coated with a Shell of Active Gain Molecules

Vitaliy Pustovit, F. Capolino, and A. Aradian

Abstract One issue in using metallic nanostructures for metamaterial applications at optical frequencies is their high level of losses. A most promising strategy to circumvent this obstacle is loss compensation, where the structures are coupled to active compounds enabled to transfer energy and therefore amplify the desired response. We here present the first unified theory of the response of plasmonic nanoparticles assisted by optical gain media, in the case of a nanoparticle coated with a shell of optically active dipoles (fluorescent molecules or dyes). The mechanism of the losses compensation is based on nonradiative energy transfer (ET) or quenching between the layer of gain elements and nanoparticle [1, 2]. We establish a complete description of the optical response of the system based on Green's functions, which allows us to investigate high molecular coverage of nanoparticle with either regular or random distribution of dye molecules, taking into account not only the interactions between NP (treated in a multipolar approach) and dye dipoles, but also between dyes molecules, either directly or via the nanoparticle [3–5]. We then obtain the optical response of the core-shell aggregate in terms of its equivalent polarizability composed of the direct response from the nanoparticle and the contribution rising from the energy transfer mechanism. Our numerical calculations reveals that cooperative plasmon-mediated coupling between optically active dyes and metal nanostructure leads to the compensation of plasmon losses and some instability that is resolved either by surface plasmon amplification of stimulated emission (spasing states) or by enhanced absorption in the system.

V. Pustovit (✉) • A. Aradian
Centre de Recherche Paul Pascal, CNRS & University of Bordeaux, 115enue Schweitzer, 33600 Pessac, France
e-mail: pustovit@crpp-bordeaux.cnrs.fr

F. Capolino
Department of Electrical Engineering and Computer Science, University of California Irvine, Irvine, CA, USA

References

1. Lakowicz R (2006) Principles of fluorescence spectroscopy. Springer, NY
2. Dulkeith E et al (2005) Gold nanoparticles quench fluorescence by phase induced radiative rate suppression. Nano Lett 5:585–589
3. Pustovit VN, Shahbazyan TV (2010) Plasmon-mediated superradiance near metal nanostructures. Phys Rev B 82:075429
4. Pustovit VN, Shahbazyan TV (2009) Plasmonic Dicke effect: cooperative emission of light by an ensemble of dipoles near a metal nanoparticle. Phys Rev Lett 102:077401
5. Pustovit VN, Shahbazyan TV (2011) Resonance energy transfer near metal nanostructures mediated by surface plasmons. Phys Rev B 83:085427

Part III
Poster Presentations

28
Deep UV Strategy for Discriminating Biomolecules

Svetlana Afonina, O. Nenadl, A. Rondi, S. Weber, L. Bonacina, D. Kiselev, J. Extermann, M. Roth, J. Roslund, H. Rabitz, and Jean-Pierre Wolf

Abstract Label-free selective discrimination of spectrally similar biomolecules, such as peptides and proteins using Optimal Control strategies is a challenge in a variety of practical applications such as label-free fluorescence imaging and protein identification. The principle of Optimal Control is based on the fact that a suitably shaped laser field can differently drive the dynamics of almost identical quantum systems [1, 2].

Most of the biomolecules (including DNA) have absorption bands in the deep UV, a spectral region that is hardly accessible by transmissive devices. MEMS pulse-shapers using Reflective -Electro-Mechanical Systems (MEMS) have proven their broadband applicability for femtosecond pulse shaping [3, 4], even in deep UV and are capable of re-compressing spectrally broadened UV pulses with a closed-loop approach based on a genetic algorithm.

Recent experiments demonstrate that discriminating between nearly identical flavin molecules is possible using a reflective pulse shaping technique. We demonstrate that discrimination is possible between amino-acids, so the Optimal Control of complex systems such as proteins is envisioned as an all-optical method for identification of biomolecules.

S. Afonina (✉) • O. Nenadl • A. Rondi • L. Bonacina • D. Kiselev • J. Extermann • J.-P. Wolf
GAP-Biophotonics, University of Geneva, 20 rue de l'Ecole de Medecine,
CH 1211 Genève, Switzerland
e-mail: Svetlana.Afonina@unige.ch; jean-pierre.wolf@unige.ch

S. Weber
EPFL/STI/IMT-NE/SAMLAB, Rue Jaquet-Droz 1, 2002 Neuchâtel, Switzerland

M. Roth • J. Roslund • H. Rabitz
Department of Chemistry, Princeton University, Princeton, NJ 08544, USA

References

1. Roth M, Guyon L, Roslund J, Boutou V, Courvoisier F, Wolf J-P, Rabitz H (2009) Quantum control of tightly competitive product channels. Phys Rev Lett 102:253001
2. Petersen J, Mitric R, Bonacic-Koutecky V, Wolf J-P, Roslund J, Rabitz H (2010) How shaped light discriminates nearly identical biochromophores. Phys Rev Lett 105:073003
3. Weber S, Extermann J, Bonacina L, Noell W, Kiselev D, Waldis S, de Rooij N, Wolf J-P (2010) Ultraviolet and near-infrared femtosecond temporal pulse shaping with a new high-aspect-ratio one-dimensional micromirror array. Opt Lett 35:3102–3104
4. Extermann J, Weber SM, Kiselev D, Bonacina L, Lani S, Jutzi F, Noell W, de Rooij NF, Wolf J-P (2011) Spectral phase, amplitude, and spatial modulation from ultraviolet to infrared with a reflective MEMS pulse shaper. Opt Express 19:7580

29
Silicon Nanowires Light Emitting Devices at Room Temperature

Pietro Artoni, A. Irrera, G. Franzò', B. Fazio, M. Galli, E. Pecora, F. Iacona, and F. Priolo

Abstract Group-IV semiconductor nanowires (NWs) are attracting interest among the scientific community as building blocks for a wide range of future nanoscaled devices. Vapor-liquid-Solid (VLS) is the most used technique for semiconductor NWs growth. Si NWs are promising as building blocks for photovoltaic elements, sensors and high-performance batteries; however, Si NWs are less explored for photonic applications, probably since there are many drawbacks due to the NW structure obtained by VLS. In fact, there is a minimum obtainable size which reduces the possibility to have quantum confinement effects without high temperature oxidation processes; metal used as a catalyst may be incorporated inside the NW thus affecting its electrical and optical properties. Moreover, by VLS method the doping is no easily controllable because of the segregation of the dopants at the NWs interface. Indeed, the possibility of obtaining light from silicon at room temperature under optical and electrical pumping is strategic for the communication technology.

Metal-assisted chemical etching (MacEtch) is a powerful technique to obtain high density and low-cost Si NWs with high and controllable aspect ratio. NWs obtained by this technique have exactly the same structure and doping properties of the substrate; their main size is less than 10 nm allowing quantum confinement effects.

P. Artoni (✉) • G. Franzò' • E. Pecora • F. Iacona • F. Priolo
Department of Physics and Astronomy, MATIS CNR IMM & University of Catania, via Santa Sofia 64, 95121 Catania, Italy

P. Artoni • F. Priolo
Dipartimento di Fisica e Astronomia, Università di Catania, via Santa Sofia 64, 95121 Catania, Italy
e-mail: pietro.artoni@ct.infn.it

A. Irrera • B. Fazio
IPCF CNR MESSINA, Viale Ferdinando Stagno d'Alcontres, 37, 98158 Messina, Italy

M. Galli
Department of Physics "A. Volta", University of Pavia, Via Bassi 6, 27100 Pavia, Italy

We will show that Si NWs made by MacEtch are suitable for photonic applications. Although some evidence of luminescence properties of axial nanostructures have been reported in literature, there are no detailed studies on PL properties of Si NWs. In this work we will show a detailed and complete study of the excitation and de-excitation properties as a function of the temperature and of the pump power, determining the excitation cross section and the presence and the origin of possible non-radiative phenomena. Moreover, this detailed study shows the influence of the structural properties on the mechanisms of light emission, in such a way to optimize the emission properties. Based on these results, we performed a further investigation and we designed a light emitting device based on Si NWs, showing the EL emission at room temperature under low voltage pumping. These results have a great impact on the possibility to use Si NWs for photonic applications.

Furthermore, we investigated size-scaling in optical trapping of ultrathin silicon nanowires showing how length influences their Brownian dynamics, since optical trapping is fundamental for the characterization and manipulation of the single Si NW (e.g. for the Photonic Force Microscopy technique). Force and torque constants have been measured on Si NWs of different lengths through correlation function analysis of their tracking signals. Results are compared with a full electromagnetic theory of optical trapping developed in the transition matrix framework, finding good agreement [1].

Reference

1. Irrera A, Artoni P, Saija R, Gucciardi PG, Iatì MA, Borghese F, Denti P, Iacona F, Priolo F, Maragò OM (2011) Size-scaling in optical trapping of silicon nanowires. Nano Lett 11(11):4879–4884

30
Optical and Structural Properties of Europium Oxide Thin Films on Silicon Substrates

Gabriele Bellocchi, G. Franzò, F. Iacona, S. Boninelli, M. Miritello, A. Terrasi, C. Spinella, and F. Priolo

Abstract Europium-based materials are known for their intense and stable emission in the visible region. Moreover Eu is stable in both its divalent and trivalent oxidation states. In particular, emission of Eu^{2+} is much stronger, being allowed for electric dipole transition rules and is characterized by a broad peak, centered in the wavelength range 400–600 nm, while that of Eu^{3+} presents several sharp lines at around 600 nm. These peculiar optical properties make Eu-based systems an interesting material for photonic applications. The optical and structural properties of Eu_2O_3 thin films grown by RF magnetron sputtering on Si substrates have been studied. PL emission has been observed at room temperature and it is strongly dependent on the thermal process. In particular, annealing in O_2 atmosphere leads to an enhancement of the Eu^{3+} emission, while films annealed in N_2 ambient exhibit a very intense PL signal due to Eu^{2+}. The chemical and structural characterization of the films, performed by TEM and XPS, reveals that a massive mixing at the Eu_2O_3-Si interface occurs in N_2-annealed samples, leading to the formation of Eu (II) silicates, while in the case of O_2-annealed samples we observe the formation of a SiO_x layer at the interface, that minimize the diffusion of Si into the Eu_2O_3 layer.

G. Bellocchi • G. Franzò • F. Iacona • S. Boninelli • M. Miritello • A. Terrasi • F. Priolo
MATIS CNR IMM, via Santa Sofia 64, Catania, 95121 Italy

G. Bellocchi (✉) • A. Terrasi
Dipartimento di Fisica e Astronomia, Università di Catania,
via Santa Sofia 64, Catania 95121, Italy
e-mail: gabriele.bellocchi@ct.infn.it

C. Spinella
CNR IMM, Sezione di Catania, Stradale Primosole 50, Catania 95121, Italy

G. Bellocchi
Department of Physics and Astronomy, MATIS, IMM-CNR & University of Catania,
via S. Sofia, 64, I-95123 Catania, Italy
e-mail: gabriele.bellocchi@ct.infn.it

31

Experimental Indication of Quantum Mechanical Effects in Surface Enhanced IR-Spectroscopy?

Jorg Bochterle, F. Neubrech, D. Enders, T. Nagao, and A. Pucci

Abstract The conduction electrons of metal nanoparticles can be collectively excited by incident electromagnetic radiation. Their resonance frequency strongly depends on the geometric dimensions of the particles and can be tuned from the classical radio frequencies up to the visible range. Such resonantly excited localized surface plasmon resonances (LSPR) are accompanied by an electromagnetic nearfield enhancement which is concentrated at the surface. In the infrared (IR) spectral range these huge local fields can be applied to the enhancement of infrared vibrations of molecules. Using this technique, which is called surface enhanced infrared spectroscopy (SEIRS), with gold nanostripes, attomol sensitivity has been achieved [1].

In this contribution we show first results of the resonant signal enhancement of the carbon monoxide (CO) stretching vibration of physisorbed CO multilayers on micrometer-long gold nanoantennas on silicon substrates under ultrahigh vacuum (UHV) conditions. We cooled the sample to about 18 K to allow multilayer adsorption of CO gas.

The preliminary results show signal changes with increasing CO layer thickness which exhibit a behavior differing from classical expectations and are in accord to recent quantum mechanical predictions [2]. In the near future we will conduct systematic experiments to prove the origin of these deviations.

J. Bochterle (✉) • F. Neubrech • A. Pucci
Kirchhoff-Institute for Physics, Universität Heidelberg, Im Neuenheimer Feld 227, Heidelberg, Germany
e-mail: jboch@kip.uni-heidelberg.de

D. Enders • T. Nagao
International Center for Materials Nanoarchitectonics (MANA), National Institute for Materials Science (NIMS), 1-1 Namiki, Tsukuba, Ibaraki 305-0044, Japan

References

1. Neubrech F, Pucci A, Cornelius TW, Karim S, Garcia-Etxarri A, Aizpurua J (2008) Resonant plasmonic and vibrational coupling in a tailored nanoantenna for infrared detection. Phys Rev Lett 101:157403
2. Zuloaga J, Prodan E, Nordlander P (2010) Quantum plasmonics: optical properties and tunability of metallic nanorods. ACS Nano 4:5269–5276

32

Spectral Dependence of the Amplification Factor in Surface Enhanced Raman Scattering

**Cristiano D'Andrea, B. Fazio, A. Irrera, O.M. Marago', A.M. Iati',
G. Calogero, P.G. Gucciardi, and Pietro Artoni**

Abstract Surface Enhanced Raman Scattering (SERS) is characterized by a strong signal amplification (up to 10^{8-10}) when both the excitation and the Raman photons frequencies match the localized plasmon resonances (LSPR) of the nanoparticles (NPs). In order to understand if the effective LSPR profile refers to the bare NPs or to the resonance of NPs "dressed" with the probe molecules, we perform multiwavelength (514 nm, 633 nm and 785 nm) SERS experiments using both evaporate gold NPs and gold Nanoantennas produced by electron beam lithography (EBL) as SERS-active substrate on which we deposited Methylene Blue molecules (MB) that yields a resonance energy red-shift and a broadening of LSPR profile.

The SERS spectra at the investigated excitation wavelengths display a different intensity ratio of the characteristic MB band (peaks at 450 cm^{-1} and 1620 cm^{-1}) with respect to the Raman counterpart. We observed that:

- *Au NPs*: the LSPR in presence of MB molecules is 50 nm red shifted. The enhancement of the Raman modes at the different excitation wavelengths follows a trend similar to the LSPR profile of the "dressed" NPs, although the maximum enhancement is found at 785 nm excitation, in spite of a LSPR peak at 600 nm.
- *Au Nanoantennas*: The LSPR in presence of MB is not shifted. The enhancement of the Raman modes follows the LSPR profile, with maximum enhancement at 633 nm excitation and enhancement of the 1620 cm^{-1} peak a 20% smaller than that of the 440 cm^{-1} one.

C. D'Andrea (✉) • B. Fazio • A. Irrera • O.M. Marago' • A.M. Iati' • G. Calogero • P.G. Gucciardi
CNR – Institute for Chemical-Physics Process (IPCF), Viale F. Stagno D'Alconters 37, Messina
I-98158, Italy
e-mail: dandrea@its.me.cnr.it

P. Artoni
MATIS – Institute for Microelectronics and Microsystems (IMM), Via S. Sofia 64, Catania
I-95123, Italy

Department of Physics and Astronomy, MATIS, IMM-CNR & University of Catania,
via S. Sofia, 64, I-95123 Catania, Italy
e-mail: pietro.artoni@ct.infn.it

33

Investigation of the Metal – Semiconductor Hybrid Nanostructure as an Active Medium for Laser

Alaa EL-din Eid Abd EL-Aziz Ragab, A. Gadallah, M.B. Mohamed, and I.M. Azzouz

Abstract Recently, many efforts have been focused on the metal or surface plasmon induced local field enhancements. The enhanced local field occurring in hot spots is particularly important to trigger low-threshold lasing resonance since it can locally enhance the pump rate of gain media.

It is believed that as the surface plasmon (SP) energy of metals matches with the emitted photon energy of the surrounding materials, the resulting resonance can lead to an energy transfer from the metal surface to the surrounding or vice versa. Amplification of SPs can be considered analogous to photon amplification in a laser, thereby suggesting novel approaches in the field of nano-optics.

In the present work, we design metallic-dielectric core-shell nanoparticles dispersed in organic dye. In this case the SPs and the resonant cavity are represented by a nanoparticle, which supports the plasmonic modes. The energy source for the spasing mechanism is an active (gain) medium that is excited externally. So we prepare $Au@SiO_2$ (source of plasmonic modes) suspended in fluorescein dye (gain medium) which optically pumped at different powers to excite their molecules which coupled with SP modes of Au nanoparticles and then transfer its energy to it, So narrowing in dye emission is observed. Resonant energy transfer from excited dye molecules to surface plasmon oscillations is reported and emission narrowing is observed. This narrowing may be referred to spasing mechanism.

A. EL-din Eid Abd EL-Aziz Ragab (✉) • A. Gadallah • M.B. Mohamed • I.M. Azzouz
Laser Science and Interactions Department, National Institute of Laser Enhanced Science (NILES), Cairo University, Cairo, Egypt
e-mail: alaadin85@yahoo.com; alaadin85@niles.edu.eg

34
TiO₂ for Nonlinear Optical Devices

Christopher C. Evans, O. Reshef, J. Bradley, F. Parsy, J. Choy, P. Deotare, E. Martí-Panameño, M. Loncar, and Eric Mazur

Abstract As the demand for computational and telecommunication bandwidth continues to increase solutions are required to overcome the inherent speed limitations of electronic devices. In particular, there is a need for all-optical devices, with their potential for superior bandwidth and transmission rate, to replace various electronic functions. We have identified TiO_2 as a promising yet unexplored material platform for ultrafast, on-chip nonlinear optical devices. TiO_2's large nonlinear index of refraction is 30 times that of standard silica optical fiber. This nonlinearity can enable such operations as all-optical switching, logic, and wavelength conversion. The material's transparency throughout the visible spectrum makes it compatible with all telecommunications windows. In addition, its high linear index of refraction can enhance optical confinement down to nano-scale dimensions and facilitate the tight waveguide bends necessary for dense on-chip integration. We demonstrate several steps in this process including the evaluation of the material's nonlinearity, deposition and structuring results as well as visible light propagation. By exploring this material, we seek to demonstrate its viability as a novel on-chip nonlinear optics platform.

C.C. Evans (✉) • O. Reshef • J. Bradley • F. Parsy • J. Choy • P. Deotare • M. Loncar • E. Mazur
School of Engineering and Applied Sciences, Harvard University, 9 Oxford Street, Cambridge, MA, 02138 USA
e-mail: mazur@physics.harvard.edu

E. Martí-Panameño
Universidad Autónoma de Puebla, Av. San Claudio y Rio Verde, Puebla, C.P. 72000 Puebla, Mexico

C.C. Evans
Department of Physics, Harvard University, 9 Cambridge St. McKay 321, Cambridge, 02138 MA, USA

35

Atomic Layer Deposition of Lanthanide Oxides: Exemplified by Europium Oxide

Per-Anders Hansen, T. Finstad, H. Fjellvåg, and O. Nilsen

Abstract Lanthanide oxides are important components in a range of optoelectronical materials such as lasers, diodes and light conversion materials. We have investigated the possibilities to use atomic layer deposition (ALD) for deposition of thin films of of the Ln_2O_3 (Ln = Pr, Nd, Sm, Eu, Tb, Dy, Ho, Er, Tm, Yb) systems using the precursor combinations $Ln(thd)_3 + O_3$ (thd = 2,2,6,6-tetramethyl-3,5-dionato). The advantage of ALD is the possibilities of mixing different materials at the atomic level and at relatively low temperatures. This opens for synthesis of many new materials where controlled intermixing of elements is important. The results from this work have been used to deposit down conversion films based on europium doped titanium oxide.

P.-A. Hansen (✉) • H. Fjellvåg • O. Nilsen
Centre for Materials Science and Nanotechnology, Department of Chemistry, University of Oslo, Blindern, P.O.Box 1033, Oslo 0315, Norway
e-mail: p.a.hansen@kjemi.uio.no

T. Finstad
Department of Physics, University of Oslo, Blindern, P.O.Box 1033, Oslo 0315, Norway

36

Tip-Enhanced Raman Scattering from Bridged Metal Nanocones

**Mikko J. Huttunen, S. Rao, J.M. Kontio, J. Mäkitalo, M.R. Viljanen,
J. Simonen, M. Kauranen, and D. Petrov**

Abstract Tip-enhanced Raman scattering (TERS) is a powerful near-field spectroscopic tool to measure Raman spectra of materials with nanometer spatial resolution and even with sensitivity down to single-molecule level [1]. The optical enhancement in TERS relies on lightning-rod effect and plasmonic coupling of input electric field into sharp metal tips. In general, the presence of strong electric field component along the tip axis (i.e., longitudinal field) is required for efficient coupling and several coupling schemes (e.g., use of radial polarization) have been suggested to enhance the interaction [1, 2].

We propose a new approach for coupling light efficiently into the tip structures, which relies on coupling two metal tips together with a metal bridge. Due to the bridge, no strong longitudinal field is anymore needed for efficient coupling. The structures are manufactured using UV-nanoimprint lithography (UV-NIL)

M.J. Huttunen (✉)
Department of Physics, Tampere University of Technology, 33101 Tampere, Finland

Optics Laboratory Korkeakoulunkatu, Tampere University of Technology, 33720 Tampere,
P. O. Box 692, 3FI-33101 Tampere, Finland
e-mail: mikko.j.huttunen@tut.fi

S. Rao
ICFO – The Institute of Photonic Sciences, 08860 Castelldefels, Spain

J.M. Kontio • M.R. Viljanen • J. Simonen
Optoelectronics Research Centre, Tampere University of Technology, 33101 Tampere, Finland

J.Mäkitalo • M. Kauranen
Department of Physics, Tampere University of Technology, 33101 Tampere, Finland

D. Petrov
ICFO – The Institute of Photonic Sciences, 08860 Castelldefels, Spain

ICREA– Catalan Institution for Research and Advanced Studies, 08010 Barcelona, Spain

combined with electron-beam evaporation, which makes the technique fast, simple and relatively cheap [3]. In addition, large arrays of structures can be manufactured e.g. for lab-on-a-chip or optical tweezing applications.

We measured Raman spectra from aqueous solution of crystal violet molecules using arrays of bridged and single gold and silver nanocones [4]. Almost tenfold increase in the Raman signal for the bridged nanocones was observed, demonstrating the enhanced coupling of light.

References

1. Neacsu CC, Berweger S, Raschke MB (2007) Tip-enhanced Raman imaging and nanospectroscopy: sensitivity, symmetry, and selection rules. Nanobiotechnol 3:172–196
2. Cançado LG, Hartschuh A, Novotny L (2009) Tip-enhanced Raman spectroscopy of carbon nanotubes. J Raman Spectrosc 40:1420–1426
3. Kontio JM, Husu H, Simonen J, Huttunen MJ, Tommila J, Pessa M, Kauranen M (2009) Nanoimprint fabrication of gold nanocones with 10 nm tips for enhanced optical interactions. Opt Lett 34:1979–1981
4. Rao S, Huttunen MJ, Kontio JM, Mäkitalo J, Viljanen M-R, Simonen J, Kauranen M, Petrov D (2010) Tip-enhanced Raman scattering from bridged nanocones. Opt Express 18:23790–23795

37

Femtosecond Laser Nanofabrication of Metal Structures Through Multiphoton Photoreduction

Seung Yeon Kang, K. Vora, S. Shukla, and Eric Mazur

Abstract Metal mirco- and nano-structures play important role in various areas such as catalysts or in plasmonics field. A recent application with growing interest that also incorporates metal nanostructures is metamaterials. Metamaterials are artificial materials that have unique structures engineered to have extraordinary electric and magnetic response. To generate these structures, most fabrication techniques can allow mass production but are non-controllable or are limited in two dimensions. Electron beam and nanoimprint lithography and focused ion beam milling are well known for making two dimensional arrays of structures. However these techniques suffer from high cost, low throughput and are only limited to two dimensions.

Here we present a facile ultrafast laser technique for the direct-writing of silver structures of tunable dimensions (hundreds of nanometers to micrometers). By utilizing nonlinear optical interactions between chemical precursors and femtosecond pulses, we can limit the metal-ion photo-reduction process to a focused spot smaller than that of the diffraction-limit. This creates metal nanostructures in a focal volume that can be scanned rapidly in three dimensions by means of a computer-controlled translation stage to produce complex patterns. We study the chemistry that effects the photo induced metal growth. By varying types of solvent, the concentration ratio

S.Y. Kang (✉)
School of Engineering and Applied Sciences, Harvard University, 9 Oxford Street, Cambridge, MA 02138, USA

Department of Physics, Harvard University, 9 Cambridge St. McKay 321, Cambridge, MA 02138, USA
e-mail: kang5@fas.harvard.edu

K. Vora • S. Shukla • E. Mazur
School of Engineering and Applied Sciences, Harvard University, 9 Oxford Street, Cambridge, MA 02138, USA
e-mail: mazur@physics.harvard.edu

411

between metal ion precursors and a polymer capping agent, as well as laser pulse parameters, we demonstrate our control over the morphology of the resulting metal structures. We show that this process is scalable over macroscopic volumes and suggest the fabricated structures can be used for metamaterials or surfaced enhanced Raman spectroscopy applications.

38
Nanostructured Thick-Film Spinel Ceramic Materials for Sensor Device Applications

H. Klym and Ivan Karbovnyk

Abstract Nanostructured spinel ceramics based on mixed transition-metal manganites and/or magnesium aluminates are known to be widely used for temperature measurements, in-rush current limiting, liquid and gas sensing, flow rate monitoring and indication, etc. But their sensing functionality is sufficiently restricted because of bulk performance allowing, as a rule, no more than one kind of application. To fabricate the integrated temperature-humidity thick-film sensors, only two principal approaches have been utilized, they being grounded on temperature dependence of electrical resistance for humidity-sensitive thick films and/or on humidity dependence of electrical resistance for temperature-sensitive thick films.

Thick-film form of mixed spinel manganites restricted by $NiMn_2O_4$-$CuMn_2O_4$-$MnCo_2O_4$ concentration triangle has a number of essential advantages, non-available for other ceramic composites. Within the above system, one can prepare fine-grained semiconductor materials with p^+-type ($Cu_{0.1}Ni_{0.1}Co_{1.6}Mn_{1.2}O_4$) and p-type of conductivity ($Cu_{0.1}Ni_{0.8}Co_{0.2}Mn_{1.9}O_4$). This opens a real possibility of preparing multilayer thick-film spinel-type structures for new device application. In addition, the prepared multilayer thick-film structures involving semiconductor $NiMn_2O_4$-$CuMn_2O_4$-$MnCo_2O_4$ and insulating (i-type) $MgAl_2O_4$ spinels can be used as simultaneous thermistors and integrated temperature-humidity sensors.

H. Klym
Lviv Polytechnic National University, 12 Bandera str., Lviv 79013, Ukraine

Lviv Scientific Research Institute of Materials of SRC "Carat", 202 Stryjska str., Lviv 79031, Ukraine
e-mail: klymha@yahoo.com

I. Karbovnyk (✉)
Department of Electronics, Ivan Franko National University of Lviv, 107 Tarnavskogo str., 79017 Lviv, Ukraine
e-mail: ivan_karbovnyck@yahoo.com

Temperature sensitive $Cu_{0.1}Ni_{0.1}Co_{1.6}Mn_{1.2}O_4/Cu_{0.1}Ni_{0.8}Co_{0.2}Mn_{1.9}O_4$-based and humidity sensitive $MgAl_2O_4$-based pastes were prepared by mixing powders of basic with ecological glass powders (without PbO), inorganic binder Bi_2O_3 and organic vehicle. Prepared paste were printed on alumina substrates (Rubalit 708 S) with Ag-Pt electrodes using a using a manual screen-printing device equipped with the steel screen. Then, thick films were annealed in the PEO-601-084 furnace.

All obtained separate temperature sensitive thick-film elements based on spinel-type $NiMn_2O_4$-$CuMn_2O_4$-$MnCo_2O_4$ ceramics have excellent electrophysical characteristics. Both thick films exhibit good temperature sensitivity in the region from 298 to 368 K. The studied thick-film elements based on i-type $MgAl_2O_4$ ceramics possess linear dependence of electrical resistance from relative humidity (RH) in semilogarithmic scale without hysteresis effects in desorption cycle in the range of RH $\sim$40–99%.

39
Realization of a Two-Dimensional Isotropic Metamaterial: Fabrication of Metallic Structures Based on Stimulated Emission Depletion (STED) Direct Laser Writing (DLW)

Johannes Kaschke, J. Fischer, and Martin Wegener

Abstract Negative index metamaterials have given rise to a wide range of possible new applications, such as ultrahigh-resolution imaging or cloaking. Simultaneous negative effective permeability and negative electric permittivity have been realized, using two-dimensional fabrication techniques. However, these designs are one-dimensional (1D), as they are operational only in a one-dimensional k-space.

Recently two-dimensional isotropic negative index metamaterials have been designed at communication wavelength [1]. Due to the inherently connected nature with the next-unit-cell neighbors of this design, Direct Laser Writing (DLW) offers great solution to the challenge of manufacturability of these complex structures. Direct Laser Writing has proven to be a versatile lithography tool over the past decade. The possibility of creating nearly arbitrary three-dimensional structures has found many applications in photonics and biology. Its major drawback, however, is the resolution, which is limited to $\lambda/10$ by diffraction laws. The resolution of stimulated emission depletion (STED) microscopy [2] is conceptually diffraction-unlimited and features down to $\lambda/90$ can be resolved [3]. The purpose of STED-inspired Direct Laser Writing (STED-DLW) is to translate this improvement to three-dimensional lithography [4].

J. Kaschke • J. Fischer
Institute of Applied Physics, DFG-Center for Functional Nanostructures (CFN), Karlsruhe Institute of Technology (KIT), D-76128 Karlsruhe, Germany
e-mail: johannes.kaschke@student.kit.edu

M. Wegener (✉)
Institute of Applied Physics, DFG-Center for Functional Nanostructures (CFN), Karlsruhe Institute of Technology (KIT), D-76128 Karlsruhe, Germany

Institut für Nanotechnologie, Karlsruhe Institute of Technology (KIT), 76021 Karlsruhe, Germany
e-mail: martin.wegener@physik.uni-karlsruhe.de

References

1. Güney DÖ, Koschny T, Kafesaki M, Soukoulis CM (2009) Opt Lett 34:506
2. Klar TA, Jakobs S, Dyba M, Egner A, Hell SW (2000) Proc Natl Acad Sci 97:8206–8210
3. Rittweger E, Han KY, Irvine SE, Eggeling C, Hell SW (2009) Nat Photon 3:144–147
4. Fischer J, von Freymann G, Wegener M (2010) Adv Mat 22:3578. doi:10.1002/adma.201000892

40
Nanoscale Semiconductor Optical Devices

Nadezda Kuznetsova, E. Semenova, S. Kadkhodazadeh, and K. Yvind

Abstract We are doing research on nanoscale patterned growth of quantum wells, wires and dots for application in photonics crystal devices for terabit communication operating in the 1.55 μm wavelength region. Fabricating devices that allow complete control of the optical fields and electrical wave functions are the ultimate goals of this work which will allow fully tailored interaction of photons and materials. This will enable very efficient devices with low power consumption and precise wavelength control. Also, all-optical functionality like switching and routing can possibly be done economically.

Selective area growth is necessary for realization of independent control of the position and amount of active material. This method gives us quantum dots (QD) and wires in certain places with identical properties. Arrays of identical QDs with desired size, shape and position on the wafer can in principle be fabricated. This allows integrating the active material with the photonic crystal platform with the very precise e-beam resolution. We are looking for growth parameters to obtain QDs with high optical and crystalline quality and with desired properties.

This is performed using metalorganic vapour phase epitaxial (MOVPE) growth of quantum dots on InP substrates. E-beam lithography and high resolution hydrogen silsesquioxane (HSQ) resist are used for pattern realization. Active epitaxial material is deposited in the nano-openings in the resist. After the fabrication steps we carry out investigations of the optical and crystalline properties of the grown materials. The optical properties are characterized using photoluminescence (PL) and μPL and compared for the different structures and growth parameters.

N. Kuznetsova (✉) • E. Semenova • S. Kadkhodazadeh • K. Yvind
DTU Fotonik, Nanophotonic Devices, Department of Photonics Engineering, Technical University of Denmark, Ørsteds Plads, Building 343, Kgs. Lyngby DK-2800, Denmark
e-mail: naku@fotonik.dtu.dk

The optical properties are dependent on the shape of the QDs and surrounding matrix. Since the patterned dots are sparsely distribution across the wafer we are currently preparing special needle-shaped specimens that contain several QDs and can be used for high-resolution transmission electron microscopy (HRTEM) and atom probe tomography (APT).

41
Optical Properties of Thermochromic VO$_2$ Nanoparticles

Katri Laaksonen, S.-Y. Li, S.R. Puisto, G.A. Niklasson, T. Ala-Nissilä, and R.M. Nieminen

Abstract Thermochromic VO$_2$ undergoes metal-insulator transition at temperatures relatively near room temperature. The transition affects its optical properties especially at the near infrared (NIR) wavelengths. Consequently, thin films of VO$_2$ have been proposed for energy-saving applications such as window coatings. At high temperatures, metal VO$_2$ has high reflectivity of NIR light which is absorbed or transmitted at low temperatures. However, if used as nanoparticles instead of thin films, the optical properties of the high-temperature metal VO$_2$ are significantly different. Metal nanoparticles show strong surface plasmon resonance absorption which for VO$_2$ is at NIR wavelengths changing the high reflectivity of NIR light in thin films to absorption in nanoparticles.

We have studied the optical spectrum of VO$_2$ nanoparticles using two different methods suitable for the calculation of optical properties of nanoparticles embedded in a dielectric coating layer. Effective medium theory (EMT), in this case in the form of Maxwell Garnett theory, can describe the absorption properties of nanoparticles but does not consider scattering of light. It can be taken into account by using the

K. Laaksonen (✉) • T. Ala-Nissilä • R.M. Nieminen
Department of Applied Physics, Aalto University, Aalto, P.O.B. 11100 FI-00076, Finland

S.-Y. Li • G.A. Niklasson
Department of Engineering Sciences, The Ångström Laboratory, Uppsala University, Uppsala, P.O.B. 534 SE-75121, Sweden

S.R. Puisto
Matox Ltd, Pembroke House, 36-37 Pembroke Street, Oxford OX11BP, UK

K. Laaksonen
Department of Applied Physics, Aalto University School of Science, Espoo, Finland
e-mail: katri.laaksonen@tkk.fi

four-flux method with scattering and absorption efficiencies calculated with the Mie theory. The results from the two methods agree well at both low and high temperatures for small VO_2 nanoparticles where the scattering contribution to the spectrum is small.

42
Lithium Niobate: The Silicon of Photonics!

Michele Manzo, F. Laurell, V. Pasiskevicius, and K. Gallo

Abstract Lithium Niobate and its isomorphs (e.g. $LiTaO_3$) is an artificial ferroelectric crystal belonging to the 3 m crystallografic group [1]. It is characterised by large pyroelectric, piezoelectric, acusto-optic, nonlinear and electro-optic coefficients features and is one of the key materials for the fabrication of integrated optical devices [2]. $LiNbO_3$ is one of the most versatile and widely used material in photonics, with a broad range of applications ranging from acoustic-wave transducers and filters in mobile telephones, to optical modulators and wavelength converters in fibre telecommunication systems, to name just a few. Recent advances in linear and nonlinear microstructuring technologies on the $LiNbO_3$ material platform, involving domain engineering by electric field poling techniques as well as ion-exchange processes and etching techniques, enable the fabrication of both linear and nonlinear photonic crystals as showed in Fig. 42.1.

The possibility of periodically engineering the nonlinearity ($\chi^{(2)}$) of $LiNbO_3$ in one, two dimensions or also in quasi-periodic manner by mean of electric field poling enables high conversion efficiencies in nonlinear optical interactions employing the Quasi-Phase-Matching (QPM) technique [5]. Moreover, by employing common micro fabrication or UV writing techniques is possible to fabricate surface waveguides (Fig. 42.1d) for more compact and efficient surface photonic devices.

M. Manzo (✉) • F. Laurell • V. Pasiskevicius • K. Gallo
Laser Physics, Department of Applied Physics, Royal Institute of Technology (KTH), AlbaNova Universitetscentrum, Roslagstullsbacken 21, SE-106 91 Stockholm, Sweden
e-mail: mmanzo@laserphysics.kth.se
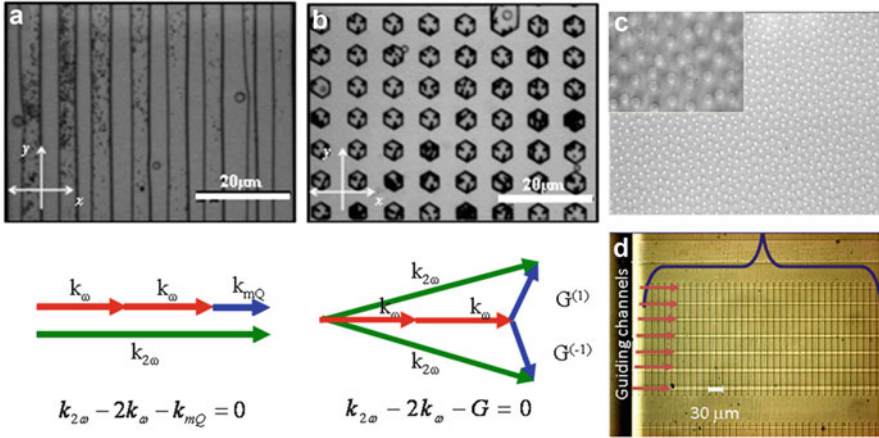
Fig. 42.1 View of structures for photonic applications in Lithium Niobate.(**a**) 1D and (**b**) 2D are bulk nonlinear photonic crystals for frequency doubling [3,4]; the quasi phase matching configuration is showed below.(**c**) and (**d**) show a bulk nonlinear photonic quasi-crystal and a group waveguides

References

1. Kösters M, Sturman B, Werheit P, Haertle D, Buse K (2009) Optical cleaning of congruent lithium niobate crystals. Nat Photonics 3:510–513
2. Weis RS, Gaylord TK (1985) Lithium niobate: summary of physical properties and crystal structure. Appl Phys A 37:191–203
3. Manzo M, Laurell F, Pasiskevicius V, Gallo K (2011) Electrostatic control of the domain switching dynamics in congruent LiNbO$_3$ via periodic proton-exchange. Appl Phys Lett 98:122910
4. Manzo M, Laurell F, Pasiskevicius V, Gallo K (2011) Two-dimensional domain engineering in LiNbO$_3$ via a hybrid patterning technique. Opt Mater Express 1(3):365–371
5. Myers LE, Eckardt RC, Fejer MM, Byer RL, Bosenberg WR, Pierce JW (1995) Quasi-phase-matched optical parametric oscillators in bulk periodically poled LiNbO$_3$. J Opt Soc Am B 12:2102

43
Infrared Induced White Anti-stokes Emission of LiYbP$_4$O$_{12}$ Nanocrystals

Łukasz Marciniak, W. Strek, A. Lukowiak, A. Bednarkiewicz, R. Wiglusz, and D. Hreniak

Abstract Upconversion properties of lithium ytterbium tetraphosphate (LiYbP$_4$O$_{12}$) nanocrystals under infrared excitation (976 nm) have been investigated. It has been found that the white color anti-Stokes emission intensity increased over two orders of magnitude with lowering the pressure from atmospheric (10^3 mbar) to vacuum (10^{-6} mbar). The dependence of emission intensity on excitation power was characterized by a sigmoidal shape characteristic to avalanche process (see Fig. 43.1b) The anti-Stokes white emission was accompanied with long build up times (see Fig. 43.1a). Moreover significant increase of photocurrent under excitation has been observed. The mechanism of white light generation has been discussed in terms of Yb^{2+}- CT luminescence

Ł. Marciniak (✉) • W. Strek • A. Lukowiak • A. Bednarkiewicz • R. Wiglusz • D. Hreniak
Department of Excited States Spectroscopy, Institute of Low Temperature and Structure
Research, Polish Academy of Sciences, Ul. Okolna 2, 50-422 Wroclaw, Poland
e-mail: L.Marciniak@int.pan.wroc.pl

© Springer Science+Business Media Dordrecht 2013

423
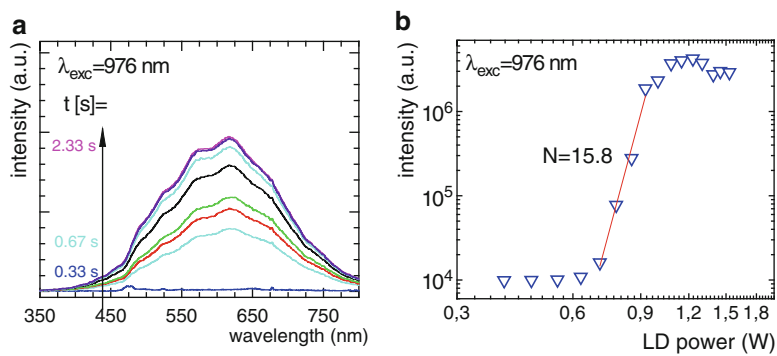
Fig. 43.1 Upconversion emission of LiYbP$_4$O$_{12}$ nanocrystals under 976 nm excitation: (**a**) time evolution of emission spectra, (**b**) and power dependence of emission intensity

44

Enhanced Light Emission from Si Nanocrystals Coupled to Plasmonics Structures

Enrico Massa, T. Roshuk, S. Maier, D. Kovalev, I. Crowe, M. Halsal, and R. Gwillian

Abstract Silicon (Si) is the material of choice for microelectronics but, as it happens to be an indirect band gap semiconductor, is also a poor light emitter. A great interest is arising on technologies able to integrate microelectronics and photonic devices on a single chip, in order for example to solve the technological problem known as the "interconnect bottleneck" on current microprocessors. In the last few years Si nano-crystals (NCs) have emerged as a promising technologies to increase the light emission of silicon. The study of the coupling between NCs and nano-antennas in order to further enhance the photoluminescence (PL) emission of the NCs is presented. Theoretically, it is important to shape the plasmonic nano-antennas, which sustain localized surface plasmons (LSPs) that increase the light matter interaction by several orders of magnitude, in order to produce the highest light emission from the NCs or the emitters. The experimental work consisted of the fabrication of the nano-antennas, such as nanostructures made via electron beam lithography (EBL) or colloidal nano-particles and their coupling to NCs, either directly under the surface of the substrate or placed from colloidal solution near them. PL and lifetime measurements via an optical microscope enabled us to measure the enhancement of the emission using a variety of parameters, depending both on the geometry of the nano-antennas and on the NCs′ fabrication

E. Massa (✉) • T. Roshuk • S. Maier
Department of Physics, Centre for Plasmonics and Metamaterials, Imperial College London, South Kensigton Campus, London SW7 2AZ, UK
e-mail: enrico.massa08@imperial.ac.uk

D. Kovalev
Department of Physics, University of Bath, Bath BA2 7AY, UK

I. Crowe • M. Halsal
Photon Science Research Institute, University of Manchester, Manchester M13 9PL, UK

R. Gwillian
Advanced Technology Institute, University of Surrey, Guildford GU2 7XH, UK

process. Results obtained for the coupling of Si NCs and gold NPs formed by annealing a thin Au film showed an enhancement factor in the lifetime of three. The measurements done on nanocrystals embedded on a silica matrix which interacts with nanoantennas fabricated on top of the surface via EBL showed an increased PL emission of around 20.

45

A Spintronic Single Photon Source and Spin Manipulation in Spininjection-LEDs

Andreas Merz

Abstract We present a spintronic single photon source which emits circularly polarized light, where the helicity is determined by an applied magnetic field. Photons are emitted from an electrically operated spin light-emitting diode consisting of the diluted magnetic semiconductor ZnMnSe and an InGaAs quantum dot as single photon source. The circular polarization degree of the emitted light is high (96 % at 6 T). Autocorrelation traces recorded with a Hanbury Brown-Twiss setup in pulsed operation mode prove the emitted light to be antibunched. The two circular polarization states of the emitted photons could be used for representing quantum states | 0 > and | 1 > in quantum cryptography implementations.

First results of the high frequency electron spin resonance experiment are presented, where a microwave resonator was adopted to be integrated into the spectroscopy setup in the magneto cryostat. Resonances of the Mn spins at 53 GHz and 2 T magnetic field with spin relaxation measurements were done on the way to spin manipulation of electrons in semiconductor quantum dots.

A. Merz (✉)

Institut für Angewandte Physik, DFG Center for Functional Nanostructures (CFN), Karlsruhe Institute of Technology (KIT), Wolfgang-Gaede-Strasse 1, 76131 Karlsruhe, Germany
e-mail: andreas.merz@student.kit.edu

46
Polarizing Beam Splitter: A New Approach Based on Transformation Optics

Jonhatan Mueller and Martin Wegener

Abstract Standard optical elements (e.g. lenses, prisms) are mostly designed of piecewise homogeneous and isotropic dielectrics. However, in theory one has far more possibilities to influence electromagnetic waves, namely all the components of the permittivity and permeability tensors. In the past few years, on the one hand, new micro fabrication methods allowed for new freedom in controlling of the optical parameters using so called artificial metamaterials. On the other hand, the theory of transformation optics has given a somewhat intuitive approach for the design of such structures. The most popular feature of this kind is certainly optical cloaking (i.e. [1, 2]). However, the full capabilities of other transformation optical devices are far from being fully explored. In my work, I focused on pure dielectric structures in a non-resonant and therefore non-lossy regime. Although the relative permittivity one can achieve this way is limited by the available natural dielectrics, a broad spectrum of features can be realized.

A polarizing beam splitter was chosen as the object of study since the use of transformation optics in this case provides some features that may be of interest for applications. Namely, the deviation angle does not vary as a function of tilts or shifts of the structure with respect to the incoming beam. Similar concepts have been proposed previously [3, 4], but none of them has been realized so far. Finite element

J. Mueller • M. Wegener (✉)
Institut für Angewandte Physik, DFG-Center for Functional Nanostructures (CFN), Karlsruhe Institute of Technology (KIT), 76128 Karlsruhe, Germany

Institute of Applied Physics, Karlsruhe Institute of Technology, Wolfgang-Gaede-Strasse 1, D-76128 Karlsruhe, Germany
e-mail: jonathan.mueller@student.kit.edu

M. Wegener
Institut für Nanotechnologie, Karlsruhe Institute of Technology (KIT), 76021 Karlsruhe, Germany
e-mail: martin.wegener@physik.uni-karlsruhe.de

simulations of a full metamaterial structure have been carried out and a practical method for the fabrication of the device using direct laser writing [5] is proposed.

References

1. Schurig D, Mock JJ, Justice BJ, Cummer SA, Pendry JB, Starr AF, Smith DR (2006) Metamaterial electromagnetic cloak at microwave frequencies. Science 314:977–980
2. Ergin T, Stenger N, Brenner P, Pendry JB, Wegener M (2010) Three-dimensional invisibility cloak at optical wavelengths. Science 328:337–339
3. Kwon D-H, Werner DH (2008) Polarization splitter and polarization rotator designs based on transformation optics. Opt Express 16:18731–18738
4. Zhai T, Zhou Y, Zhou J, Liu D (2009) Polarization controller based on embedded optical transformation. Opt Express 17:17206–17213
5. Maruo S, Nakamura O, Kawata S (1997) Three-dimensional microfabrication with two-photon-absorbed photopolymerization. Opt Lett 22:132–134

47

Point Defects Aggregation in Lithium Fluoride Crystals After Irradiation

Alexander P. Voitovich, V.S. Kalinov, A.N. Novikov, and A.P. Stupak

Abstract Lithium fluoride crystals (LiF) with radiation-induced color centers are widely used and studied. These crystals are well known materials for ionizing radiation dosimetry. LiF crystal is a model crystal to study radiation influence on solids.

Samples were irradiated at liquid nitrogen temperature, which is below the temperature of anion vacancy mobility (T_v). We measured the aggregation kinetics for the color centers at different annealing temperatures T which are above the temperature of anion vacancy mobility $T > T_v$.

We determine time constants and activation energies for the various processes involving growth and fall in the concentrations of aggregate color centers. The values of the lifetimes were found for vacancies and F_2^+ centers for different doses of irradiation. We show that a lifetime of vacancies decreases while that of F_2^+ centers rises with radiation doses increasing. We demonstrate that vacancies on the long-term stage of aggregation are created in the result of a reaction $F_2^+ + H \rightarrow \upsilon_a +$ fluoride ion at lattice site, in which F_2^+ centers participate. Therefore on the long-term stage vacancies υ_a and F_2^+ centers are involved in complicated process, consisting of two reactions, which lead to maintenance of vacancies in crystal during annealing until F_2^+ centers exist in crystal.

Both vacancies and F_2^+ centers take part in process of F_3^+ formation at the long-term stage. The vacancies take part in formation of F_2^+, F_2 and F_3^+ centers at the initial stage of the aggregation kinetic. The fast stage of growth in the concentrations

A.P. Voitovich • V.S. Kalinov • A.N. Novikov (✉) • A.P. Stupak
B.I. Stepanov Institute of Physics, National Academy of Sciences of Belarus, 68 Nezavisimosti Ave., Minsk, 22072 Belarus

A.P. Voitovich
National Academy of Sciences of Belarus, 66 Skaryna Av., Minsk, 220072, Belarus
e-mail: voitovich@imaph.bas-net.by

of F_2^+, F_2 and F_3^+ centers are characterized by different time constants. This is due to different time, required by vacancies to reach their partners in reactions to form these centers. The presence of F_1^- centers in samples after irradiation is proved by comparison of the vacancy activation energy with the activation energy of process, which describes the initial stage of the F_2 center concentration growth.

48
Diamond Photonic Crystal Slab with Enhanced Photoluminescence Extraction Efficiency

Lukas Ondič and I. Pelant

Abstract Diamond-based materials exhibit many unique properties, one of them being a broad-band visible photoluminescence (PL) due to a variety of color centers. However, the PL extraction from the diamond layer is inefficient due to high material refractive index. One possibility of increasing the extraction efficiency is by employing a shallow two-dimensional photonic crystal (2D-PhC) at the top of the layer. Then light generated inside the layer and coupled to guided modes can interact with the periodic index modulation and can be Bragg scattered into surrounding air in case that the phase matching condition is fulfilled [1].

Here we report on enhanced extraction efficiency of intrinsic PL from a nanocrystalline diamond (NCD) layer achieved by introducing the 2D-PhC consisting of NCD columns ordered into the square lattice. A 420 nm thick NCD layer was grown on silica substrate by microwave plasma assisted CVD process [2]. Its surface was then patterned employing electron beam lithography into the form of 2D-PhC, the dimensions of which were chosen carefully such they allow effective light extraction within the whole visible region.

Spectrally resolved micro-PL measurements, detected within a broad angle from the top of the structure, revealed up to 6-fold enhancement of PL from the PhC compared to the uncorrugated layer [3]. Angle and spectrally resolved measurements of PL and optical transmittance allow us to map the photonic band diagram of our sample [4]. The results show good agreement with the computed photonic band diagram suggesting that mainly the PhC effect contributes to the PL enhancement.

L. Ondič (✉) • I. Pelant

Institute of Physics, Academy of Sciences of the Czech Republic, v.v.i. Cukrovarnická 10, CZ-162 53 Prague 6, Czech Republic

L. Ondič
Faculty of Mathematics and Physics, Charles University, Ke Karlovu 3, 121 16 Prague 2, Czech Republic
e-mail: ondic@fzu.cz

To the best of our knowledge, this is the first observation of an effect of this kind in NCD and is promising for taking advantage of the diamond PL in optical, optoelectronic, and biological applications.

References

1. Boroditsky M et al (1999) Light extraction from optically pumped light-emitting diode by thin-slab photonic crystals. Appl Phys Lett 75:1036–1038
2. Kromka A et al (2008) Formation of continuous nanocrystalline diamond layers on glass and silicon at low temperatures. Chem Vap Depos 14:181–186
3. Ondič L et al (2011) Effective extraction of photoluminescence from a diamond layer with a photonic crystal. ACS Nano 5:346–350
4. Ondič L et al (2011) Enhanced photoluminescence extraction efficiency from a diamond photonic crystal via leaky modes. New J Phys 13:063005

49

Spectral Markers of Erythrocytes on Solid Substrate

Adkhamjon A. Paiziev and V.A. Krakhmalev

Abstract Proposed in previous paper [1, 2] the new nondestructive method of optical microscopy allows to examine the structures of living cells (human erythrocytes) in their natural colors without its staining by using a specially designed substrate for deposition of biological sample and observing a native blood smears in reflected light. Color interference contrast image is achieved due to special condition of experiment is connected with chose of angle of incidental light, wave length of light of reflected ray, chemical composition of sample, thickness of sample, refractive index of sample, refractive index of substrate, chemical composition of substrate [1, 2]. We can identify chemical compounds of erythrocytes after calibration color scale by alternative methods. For comparison we used Synchrotron Radiation based Fourier Transformed Infrared (SR-FTIR) microspectroscopy. By focusing of infrared beam of FTIR microscope on cell surface we can screen and distinguish difference erythrocytes by its color. For example on Fig. 49.1 we can see two neighbored erythrocytes where one of them have red color (point 1) and other-green (point 5). To identify their spectral markers we measured IR absorption spectra of cells at different points (1,2,3,4 and 5). Intermediated area (points 3 and 4) correspond to substrate spectra (silicon substrate) and their spectra are same. The peaks at 2,850 and 2,920 cm^{-1} correspond mainly to the CH$_2$ stretching modes of the methylene chains in membrane lipids. At 1,650 cm^{-1} the amide I band is observed, which results, principally, from the n(CO) stretching vibrations of the protein amide bonds; the amide II band, near 1,550 cm^{-1}, is a combination of the d(N–H) bending and n(C–N) stretching vibrations of the amide bonds. The peaks at 2,850 and 2,920 cm^{-1} correspond mainly to the CH$_2$ stretching modes of the methylene chains in membrane lipids [3]. The intensities of the absorption bands

A.A. Paiziev (✉) • V.A. Krakhmalev
Institute of Electronics, Uzbek Academy of Science, Durmon Yuli 33, Academgorodok, Tashkent, 100125 Uzbekistan
e-mail: adkhampaiziev@gmail.com
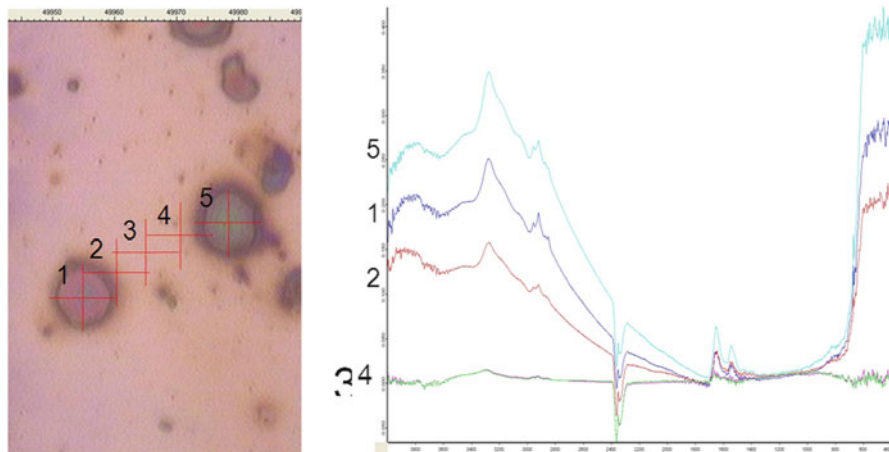
Fig. 49.1

at 2,920 and 2,850 cm^{-1} in green erythrocyte (point 5) were also significantly increased compared to red one (point 1). The protein conformational change of the red and green cells could be expressed as the ratio of the absorbance intensity at wavenumber 1650/1550, which represented the intensity of the amide II band of cells. Lipids have long hydrocarbon chains, so the dominant features in the IR spectrum of lipids are attributed to the asymmetric and symmetric stretching vibrations of CH$_2$ (2,920 and 2,850 cm^{-1}) groups in the molecule. Other biological components, such as proteins, nucleic acids, and carbohydrates, also have unique IR spectra.

References

1. Paiziev A, Krakhmalev V (2010) Color image of red blood cells on the solid surface. Int J Lab Hem 32(suppl1):1–180
2. Paiziev A, Krakhmalev V (2008) Colour visualization of red blood cells in native smears by the new method reflected light microscope. In Aretz A, Hermanns-Sachweh B, Mayer J (eds) Proceedings of 14th European microscopy congress, Aachen, Germany, 1–5 Sept 2008, Life science, vol 3. Springer, Berlin, pp 179–180
3. Dumas P, Sockalingum GD, Sulé-Suso J (2006) Adding synchrotron radiation to infrared microspectroscopy: what's new in biomedical applications? Trends Biotechnol 25(1):40–44

50

Lanthanide Doped Nanocrystalline Alkaline Earth Fluorides: Synthesis, Structural, Morphological and Spectroscopic Investigation

Marco Pedroni, F. Piccinelli, M. Bettinelli, and A. Speghini

Abstract Fluoride based materials doped with lanthanide ions are interesting hosts for efficient luminescence. In particular, $NaYF_4$ codoped with Er^{3+} and Yb^{3+} ions has been demonstrated to be possibly the material in which upconversion is most efficient.

Fluoride based materials can be prepared in colloidal forms, thus opening the doors to their use in important technological applications, especially in biomedical diagnostic. As an example, interesting investigations have been recently reported on the upconversion imaging of Er^{3+}/Yb^{3+} codoped $NaYF_4$ nanoparticles located inside HeLa cancer cells [1].

Lanthanide ions doped CaF_2 nanoparticles very recently have raised attention, due to their strong upconversion emission [2]. It must be emphasized that an easy synthesis of aqueous dispersable nanoparticles of binary fluorides is still a challenging task. In this contribution, we have investigated a variety of preparation methods to obtain alkaline earth fluoride nanoparticles of controlled size while maintaining their upconversion properties. In particular, a hydrothermal one-step procedure has been used to prepare nanocrystalline MF_2 ($M = Ca$, Sr) doped with Er^{3+}/Yb^{3+}, Ho^{3+}/Yb^{3+} and Tm^{3+}/Yb^{3+}. Different temperatures and reaction times have been employed to control the size and morphology of the nanoparticles.

M. Pedroni (✉) • F. Piccinelli • M. Bettinelli • A. Speghini
Laboratory of Solid State Chemistry, DB, University of Verona, Verona, Italy

M. Pedroni • F. Piccinelli • M. Bettinelli • A. Speghini
INSTM, UdR Verona, Verona, Italy
e-mail: marco.pedroni@univr.it

M. Pedroni
Laboratorio di Chimica dello Stato Solido, Dipartimento di Biotecnologie, Univrersità degi Studi di Verona, 37134 Verona, Italy
e-mail: marco.pedroni@univr.it

Their structural and morphological properties have been investigated by X-Ray diffraction and electron microscopy. The obtained nanocrystalline materials are single phase and can be easily dispersed in water. The colloidal solutions show interesting upconversion properties upon laser excitation at 980 nm.

References

1. Vetrone F, Naccache R, Juarranz de la Fuente A, Sanz-Rodriguez F, Blazquez-Castro A, Martin Rodriguez E, Jaque D, Garcia Sole J, Capobianco JA (2010) Intracellular imaging of HeLa cells by non-functionalized NaYF4: Er3+, Yb3+ upconverting nanoparticles. Nanoscale 2:495–498
2. Pedroni M, Piccinelli F, Passuello T, Giarola M, Mariotto G, Polizzi S, Bettinelli M, Speghini A (2011) Lanthanide doped upconverting colloidal CaF_2 nanoparticles prepared by a single-step hydrothermal method: toward efficient materials with near infrared-to-near infrared upconversion emission. Nanoscale 3:1456–1460

51
Observation of Surface Plasmons in Metal-Coated Tapered Fiber Terminated by a Subwavelength Aperture

V. Palm, Mihkel Rähn, and V. Hizhnyakov

Abstract The effect of a tapered Al-coated optical fiber terminated by a subwavelength aperture (SWA) on the spectrum of the transmitted light is investigated experimentally. Under certain conditions a remarkable spectral modulation of the transmitted light can be observed [1]. This effect is of a mesoscopic origin, occurring only for a certain interval of SWA diameters. A noticeable modulation appears when the number of the transmitted fiber modes is small but exceeds unity, thus indicating the presence of a phase shift between different modes.

The observed modulation manifests the phase difference between the two modes passing the 200 nm SWA. In order to establish the origin of this phase shift we performed a series of spectral measurements, gradually reducing the multimode fiber length from 1,075 to 240 mm. It appears that the observed phase shift consists of two clearly distinguishable contributions: (1) the shift in the non-coated multimode fiber, and (2) the shift in the metal-coated tapered region close to SWA. The first one is the result of the inherent modal dispersion of the multimode fiber. The second one is due to the mode-dependent contribution of surface plasmon polaritons: one of the modes (a TM mode) couples to the plasmons stronger than the other one, resulting in a remarkable relative slowdown. Our estimations show that the phase velocity of this TM mode on the last end of a 600 μm long tapered tip is approximately an order of magnitude smaller than the light velocity in vacuum. This means that in the tip area the corresponding mode is mostly plasmon-like.

We also found that the modal dispersion changes its sign at the border of coated and uncoated regions of the fiber, which indicates that the TM mode, having due to hybridization with plasmons a lower phase velocity in the tip region, has

---

V. Palm (✉) • M. Rähn • V. Hizhnyakov
Institute of Physics, University of Tartu, Riia 142, 51014 Tartu, Estonia

M. Rähn
Laboratory of Laser Spectroscopy, Institute of Physics, University of Tartu, 51014 Tartu, Estonia
e-mail: mihkel.rahn@ut.ee

higher phase velocity in the uncoated fiber region. This is actually an expected phenomenon: the phase velocity of this mode in the uncoated fiber region should be higher due to its stronger presence in the fiber cladding, which has lower refractive index.

Reference

1. Rähn M, Pärs M, Palm V, Jaaniso R, Hizhnyakov V (2010) Mesoscopic effect of spectral modulation for the light transmitted by a SNOM tip. Opt Commun 283:2457–2460

52

Fabrication of Single-Photon Sources by Use of Pyramidal Quantum-Dot Microcavities

Daniel Rülke, C. Reinheimer, D.M. Schaadt, H. Kalt, and M. Hetterich

Abstract In recent years the interest in single-photon emitters for quantum-optical applications is strongly increasing. For this purpose, we have investigated In(Ga)As quantum-dots (QDs) embedded in reversed pyramidal GaAs microcavities (Fig. 52.1a). Even though it has been shown recently, that such cavities can act as high-Q optical resonators [1], our focus has been on the directional radiation of the QD emission due to reflection at the facets of the reversed pyramids. With QDs embedded close to the vertex of the four facets and a base angle adaptable between 35° and 55° the pyramids can be perceived as a kind of retroreflector. Since the QD layer is inserted near the tip of the predicted reversed pyramid during molecular-beam epitaxial (MBE) growth, the average number of QDs inside the cavity can be reduced to one, depending on the size of the pyramid and density of QDs. The pyramidal cavities are shaped after MBE growth by a wet-chemical etching process with a solution of H_3PO_4, H_2O_2 and H_2O [2, 3].

Finite-element simulations have been performed to proof the ability of reversed pyra-mids to radiate the QD emission through the top surface and to prevent the emission from being lost into the substrate (Fig. 52.1b). For an optimized geometry we have calcula-ted, that radiation through the surface is more than two orders of magnitude higher than through the substrate.

D. Rülke (✉) • C. Reinheimer • D.M. Schaadt • H. Kalt • M. Hetterich
Institut für Angewandte Physik, Center for Functional Nanostructures, Karlsruhe Institute
of Technology (KIT), Wolfgang-Gaede-Str. 1, 76131 Karlsruhe, Germany

D. Rülke
Institute of Applied Physics, Karlsruhe Institute of Technology (KIT), Wolfgang-Gaede-Strasse 1,
76131 Karlsruhe, Germany
e-mail: daniel.ruelke@kit.edu
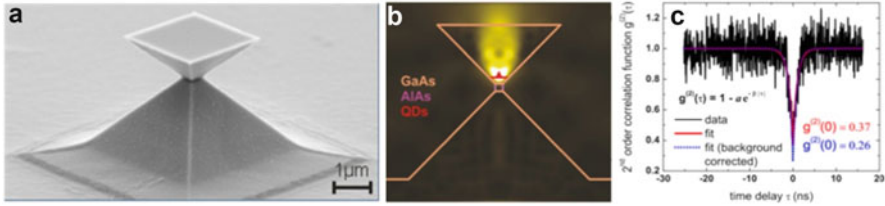
53

Investigation of GaN- and CuInGaSe₂-Based Heterostructures for Optoelectronic Applications

Mikalai V. Rzheutski, E.V. Lutsenko, G.P. Yablonskii, C. Mauder, H. Behmenburg, H. Kalisch, M. Heuken, V. Jmeric, S.V. Ivanov, and V.Y. Shiripov

Abstract GaN-based heterostructures are widely used nowadays in many applications such as high brightness light emitting diodes (LEDs), semiconductor lasers, photodetectors, transistors, solar cells, etc. An advantage of $Al_xIn_yGa_{1-x-y}N$ compound over other wide-gap materials is potential ability to cover spectral region from deep ultraviolet (UV) ($\sim$198 nm corresponding to AlN) to infrared ($\sim$1,770 nm corresponding to InN). Creating of effective optoelectronic devices operating in deep UV region and finding of low-cost and practically feasible substrates for GaN heteroepitaxy are the main objectives in GaN-based technology today. In the present work, several examples of fabrication of GaN-based electronic devices are considered, i. e. blue InGaN/GaN LED ($\sim$475 nm) grown on silicon substrate; blue InGaN/GaN LED emitting polarized light ($\sim$450 nm, polarization degree $\sim$0.42) grown on $LiAlO_2$ substrate; high sensitive metal-semiconductor-metal AlGaN/GaN UV photodetector ($\eta \sim 4 \times 10^7$ A/W); AlGaN-based UV LED (300–340 nm); optically pumped AlGaN-based UV lasers emitting at 303 and 295 nm with laser threshold of $\sim$1 MW/cm².

M.V. Rzheutski (✉) • E.V. Lutsenko • G.P. Yablonskii
Stepanov Institute of Physics, National Academy of Sciences of Belarus, Nezalezhnasci Ave. 68, Minsk 220072, Belarus
e-mail: m.rzheutski@ifanbel.bas-net.by

C. Mauder • H. Behmenburg • H. Kalisch • M. Heuken
GaN Device Technology, RWTH Aachen University, Aachen, Germany

V. Jmeric • S.V. Ivanov
Ioffe Physical-Technical Institute, Russian Academy of Sciences (RAS), St. Petersburg, Russia

V.Y. Shiripov
IZOVAC Company, Minsk, Belarus

CuInGaSe$_2$ compound is promising material for active layers of solar cells because of inexpensive deposition technology (reactive magnetron sputtering) and availability for large-scales. Properties of CuInGaSe$_2$-based solar cell (with efficiency of $\sim$14 %) and monolithically integrated module ($\sim$10 % efficiency) produced by the DC magnetron sputtering of metal alloyed targets in selenium vapor with multistage temperature alteration (from 340 to 550 °C) using Aspira setup of IZOVAC Ltd are demonstrated here.

54

Ebic Investigation of the Recombination at the Edges of GaAs Solar Cells

Andrea Scaccabarozzi and M. Acciarri

Abstract Intermediate band photovoltaics is one of the so-called third generation photovoltaic device designs proposed to increase the efficiency of solar cells. It involves the creation of an intermediate band (IB) inside a semiconductor band gap, that can allow sub-bandgap photon absorption without degrading the output voltage of the device. One possibility to make an IB is through a periodic array of semiconductor quantum dots embedded in a higher bandgap material acting as a barrier. The barrier (matrix) material will be a traditional p-n or p-i-n junction solar cell.

In this work we show the results of the optimization of the matrix solar cell which will host the quantum dots. GaAs single junction solar cells were grown with MBE: the structure (thickness and doping levels) was previously optimized through numerical calculations. Au-based electrical contacts were evaporated and sintered in an inert atmosphere. In the end the single cells were diced out of the wafer with blade cleavage.

The I-V characteristics of the devices were measured and a strong effect of shunt resistance was detected. We mapped the electrical activity and defect density with SEM-EBIC and found that the devices are homogeneous with very few defects and high diffusion length. Since shunt resistance in GaAs devices with high perimeter to area ratio is usually thought to come from perimeter recombination, we imaged the perimeter electrical activity with SEM-EBIC. We saw that different post-growth processing steps can dramatically affect the electrical activity and surface recombination properties of the devices. In particular we found that edge polishing can be effective in reducing the shunt resistance in the I-V curves of the solar cells.

A. Scaccabarozzi (✉) • M. Acciarri
Department of Materials Science, MIB-SOLAR Research Centre,
University of Milano – Bicocca, Via Cozzi, 53, 20125 Milan, Italy
e-mail: a.scaccabarozzi1@campus.unimib.it

55

Dynamical Properties of Cardiomyocytes in Three-Dimensional Polymer Scaffolds

Andrea Scheiwe, B. Richter, M. Bastmeyer, and Martin Wegener

Abstract Cells live in a three-dimensional environment called extracellular matrix (ECM) which offers them multiple possibilities for interactions divided in cell-cell contacts and cell-matrix contacts. These contacts to the cells surrounding play a great role in their proliferation, differentiation and survival. Culturing cells on three-dimensional scaffolds gives the possibility to get closer to the real environment of cells while making experiments in vitro. Offering the freedom to fabricate a wide range of three-dimensional structures Direct Laser Writing [1] became a strong tool for that application [2, 3].

The heart muscle cell (*cardiomyocyte*) spontaneously can apply periodic forces to the matter surrounding it [4]. As far as we know, the synchronization between single cardiomyocytes is based on a chemical process involving Ca^{2+} ions. It is also known that cells can sense their mechanical environment. Therefore we are carrying out single cell experiments in three dimensional structures to test whether a purely mechanical stimulation of *cardiomyocytes* is possible and to which extend.

A. Scheiwe (✉) • M. Wegener
DFG-Center for Functional Nanostructures (CFN), Karlsruhe Institute for Technology (KIT), Karlsruhe, Germany

Institute for Applied Physics, Karlsruhe Institute for Technology (KIT), Karlsruhe, Germany
e-mail: andrea.scheiwe@kit.edu

B. Richter • M. Bastmeyer
DFG-Center for Functional Nanostructures (CFN), Karlsruhe Institute for Technology (KIT), Karlsruhe, Germany

Zoologisches Institut, Karlsruhe Institute for Technology (KIT), Karlsruhe, Germany

M. Wegener
Institut für Nanotechnologie, Karlsruhe Institute for Technology (KIT), Karlsruhe, Germany
e-mail: martin.wegener@physik.uni-karlsruhe.de

References

1. Deubel M, von Freymann G, Wegener M, Pereira S, Busch K, Soukoulis CM (2004) Direct laser writing of three-dimensional photonic-crystal templates for telecommunications. Nat Mater 3:444–447
2. Klein F, Striebel T, Fischer J, Jiang Z, Franz CM, von Freymann G, Wegener M, Bastmeyer M (2010) Elastic fully three-dimensional microstructure scaffolds for cell force measurements. Adv Mater 22:868–871
3. Klein F, Richter B, Striebel T, Franz CM, von Freymann G, Wegener M, Bastmeyer M (2011) Two component polymer scaffolds for controlled three-dimensional cell culture. Adv Mater 23:1341–1345
4. Brady AJ (1991) Mechanical properties of isolated cardiac myocytes. Physiol Rev 71:413–428

56
Femtosecond Laser Doped Silicon for Photovoltaic Applications

Meng-Ju Sher, Yu-Ting Lin, M.T. Winkler, B. Franta, and Eric Mazur

Abstract Doping silicon to concentrations above the metal-insulator transition threshold yields a novel material that has potential for photovoltaic applications. By focusing femtosecond laser pulses on the surface of a silicon wafer in a sulfur hexafluoride (SF_6) environment, silicon is doped with 1 % atomic sulfur. This material exhibits near-unity, broadband absorption from the visible to the near infrared (< 0.5 eV, deep below the silicon bandgap), and metallic-like conduction. These unusual optical and electronic properties suggest the formation of an intermediate band. We report on the femtosecond laser doping techniques and material properties. By changing the laser parameters and ambient environment we can control the dopant profiles, crystallinity, and surface morphology. In addition, we perform mid-infrared absorption measurements as well as temperature-dependent Hall measurements of femtosecond laser doped silicon. These two techniques could shed light on energy levels of dopant states or bands.

M.-J. Sher (✉) • M.T. Winkler
Department of Physics, Harvard University, 9 Oxford Street, McKay 321, Cambridge, MA 02138, USA
e-mail: sher@physics.harvard.edu

Y.-T. Lin • B. Franta
School of Engineering and Applied Sciences, Harvard University, 9 Oxford Street, Cambridge, MA 02138, USA
e-mail: ytlin@fas.harvard.edu

E. Mazur
Department of Physics, Harvard University, 9 Oxford Street, McKay 321, Cambridge, MA 02138, USA

School of Engineering and Applied Sciences, Harvard University, 9 Oxford Street, Cambridge, MA 02138, USA

Division of Applied Sciences, Harvard University, Pierce Hall 225, Cambridge, MA 02138, USA
e-mail: mazur@physics.harvard.edu

57

Laser and Optical Properties of Green-Emitting ZnCdSe Quantum Dot Based Heterostructures

Aliaksei G. Vainilovich, E.V. Lutsenko, G.P. Yablonskii, I.V. Sedova, S.V. Sorokin, S.V. Gronin, S.V. Ivanov, and P.S. Kop'ev

Abstract Green-emitting laser diodes are in great demand for mobile projection media (pico-projector), navigation, underwater communication but they are still absent on the market. InGaN/GaN-based quantum well structures are approaching green spectral region by use of polar, semipolar as well as free-standing GaN substrates. However such heterostructures suffer from high laser thresholds with increase of indium content. A promising alternative way is the use of highly efficient green-emitting undoped ZnCdSe based quantum dot (QD) laser heterostructures optically pumped by blue InGaN laser diodes. Operation of blue-green laser converter based on MBE grown heterostructure with two ZnCdSe QD layers was shown for the first time in [1].

In this work, the results of improvement of the converter performance are presented. Active region of a new heterostructure is comprised of five ZnCdSe QD sheets each placed in ZnSe quantum well and separated from each other by 5 nm ZnSSe layers that is necessary for effective compensation of elastic strain. Adjacent QD sheets are tunnel-coupled due to small thickness of ZnSSe layer that results in homogeneity of optical pumping. The active region is placed non-symmetrically

A.G. Vainilovich (✉)
Institute of Physics, National Academy of Sciences of Belarus, Independence Ave. 68, 220072 Minsk, Belarus

Stepanov Institute of Physics, Laboratory of Physics and Techniques of Semiconductors, National Academy of Sciences of Belarus, Independence Ave., 68, 220072 Minsk, Belarus
e-mail: a.vainilovich@ifanbel.bas-net.by

E.V. Lutsenko • G.P. Yablonskii
Institute of Physics, National Academy of Sciences of Belarus, Independence Ave. 68, 220072 Minsk, Belarus

I.V. Sedova • S.V. Sorokin • S.V. Gronin • S.V. Ivanov • P.S. Kop'ev
Ioffe Physico-Technical Institute, Russian Academy of Sciences (RAS), Politechnicheskaya Street 26, St. Petersburg, Russia

in optical waveguide to reach high optical confinement factor. Optical waveguide contains a set of ZnMgSSe/ZnSe superlattices specially designed for decrease of effective band gap toward QD sheets position in order to stimulate charge carrier transport into the active region. The new heterostructure showed considerable increase of photoluminescence efficiency and effective laser action at 540–550 nm wavelengths. The use of this heterostructure as an active medium of blue-green laser converter results in substantial improvement of its performance. Maximal quantum efficiency of 25 % and relatively high output pulse power ($\tau = 50$ ns, $f = 1$ kHz) of 150 mW were achieved.

Reference

1. Ivanov SV et al (2009) Compact green laser converter with injection pumping, based on MBE grown II–VI nanostructures. J Cryst Growth 311:2120–2122

58

Stokes Parameters Measurements for Whispering Gallery Modes Microcavities Characterization

Francis Vanier, C. La Mela, A. Hayat, and Y.-A. Peter

Abstract When a Whispering Gallery Modes (WGM) optical cavity is coupled to an external waveguide, the total quality factor (Q_T) of a resonance characterizes the combined losses caused by the intrinsic losses, scattering and absorption, via the intrinsic Qfactor (Q_0) and the coupling losses due the waveguide via the coupling Q-factor (Q_c). Using only the transmission spectra, Q_0 and Q_c cannot be determined via a single measurement of Q_T , unless the coupling regime is known [1]. We present a novel method to characterize WGM and ringtype optical resonators [2]. Based on a Stokes parameters analysis, Q_0 and Q_c can be distinctly identified for any coupling regime.

Considering the normalized input amplitudes $a_x \overrightarrow{x} + a_y e^{i\varphi} \overrightarrow{y}$ where φ is the phase difference between $\overrightarrow{a}_x$ and $\overrightarrow{a}_y$, the S_0 and S_3 Stokes parameters can be expressed in terms of the cavity parameters T and θ and the system parameters a_x, a_y and φ as follows [3]:

$$S_0 = a_x^2 + |T|^2 a_y^2 \ \text{ and } \ S_3 = 2a_x a_y |T| \sin(\theta + \varphi) \tag{59.1}$$

where $|T|^2$ and θ are part of the complex response of the cavity $|T|e^{i\theta}$ [4]. Using Q_T definition, $Q_T = Q_0 Q_c / (Q_0 + Q_c)$, it is possible to find that Q_0 and Q_c are approximated by:

$$Q_0^{(e)} = \frac{4a_x a_y Q_T}{4a_x a_y - \Delta S_3} \ \text{ and } \ Q_c^{(e)} = \frac{4a_x a_y Q_T}{\Delta S_3} \tag{59.2}$$

F. Vanier (✉)
Microphotonics Laboratory, École Polytechnique de Montréal, Montreal, Canada

Microphtonics Laboratory, Department of Physical Engineering, Ecole Polytechnique de Montreal, Montreal, QC, Canada
e-mail: francis-2.vanier@polymtl.ca

C. La Mela • A. Hayat • Y.-A. Peter
Microphotonics Laboratory, École Polytechnique de Montréal, Montreal, Canada

where $\Delta S_3 = S_3{}^{max} - S_3{}^{min}$ and when the optical phase accumulation during a cavity round-trip, $\beta_0 L$, can be neglected compared to Q_0 and Q_c. Thus, knowing a_x and a_y, a single measurement of Q_T and S_3 gives $Q_0^{(e)}$ and $Q_c^{(e)}$, assuming Q_0 and Q_c high enough, which is the case generally considering WGM resonator types cavities.

References

1. Spillane SM, Kippenberg TJ, Painter OJ, Vahala KJ (2003) Ideality in a fiber-taper-coupled microresonator system for application to cavity quantum electrodynamics. Phys Rev Lett 91:043902
2. Vanier F, La Mela C, Hayat A, Peter Y-A (2011) Whispering gallery modes intrinsic quality factor and coupling regime extraction using stokes parameters. IEEE/LEOS International Conference on Optical MEMS and Nanophotonics, Istanbul, pp 173–174
3. Bianucci P, Fietz CR, Robertson JW, Shvets G, Shih C-K (2007) Whispering gallery mode microresonators as polarization converters. Opt Lett 32:2224–2226
4. Griffel G, Arnold S, Taskent D, Serpengüzel A, Connolly J, Morris N (1996) Morphology-dependant resonances of a microsphere-optical fiber system. Opt Lett 21:695–697

59

Photonic-Crystal Fiber Synthesizers of Ultrafast Lightwaves

Alexander A. Voronin, I.V. Fedotov, A.B. Fedotov, and Aleksei M. Zheltikov

Abstract Frequency-shifted solitons in a highly nonlinear photonic-crystal fiber (PCF) are shown to give rise to high-visibility interference fringes in PCF output spectra, indicating flat spectral phase profiles of individual solitons in the PCF output (Fig. 59.1). This experimental finding, supported by numerical simulations, suggests a promising method of fiber-format pulse shaping and an attractive technology for few-cycle pulse synthesis through a coherent addition of frequency-shifted solitons generated in a highly nonlinear fiber [1].

Coupling ultrashort optical field waveforms to ultrafast molecular vibrations in an impulsively excited Raman medium is shown to enable the generation of frequency-tunable sub-half-cycle multigigawatt light pulses. In a gas-filled hollow waveguide, this coupled-state dynamics is strongly assisted by soliton effects, which help to suppress temporal stretching of subcycle optical pulses, providing efficient Raman-type impulsive excitation of ultrafast molecular vibrations over large propagation paths [2].

A.A. Voronin • I.V. Fedotov
Physics Department, International Laser Center, M.V. Lomonosov Moscow State University, Moscow 119992, Russia
e-mail: aa.voronin@physics.msu.ru

A.B. Fedotov • A.M. Zheltikov (✉)
Physics Department, International Laser Center, M.V. Lomonosov Moscow State University, Moscow 119992, Russia

Department of Physics and Astronomy, Texas A&M University, College Station, TX 77843-3257, USA
e-mail: zheltikov@phys.msu.ru
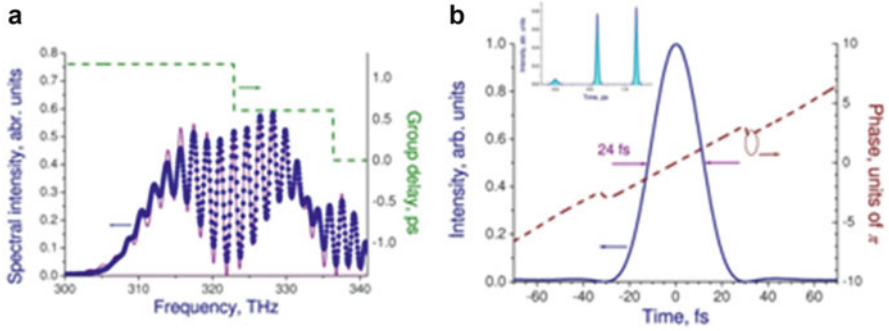
Fig. 59.1 (**a**) Interference fringes in the experimental spectrum of PCF output (*filled circles*) and theoretical fit of the experimental data with three solitons (*solid curve*). The *dashed line* shows the profile of the group delay. (**b**) Temporal envelope (*solid curve*) and the phase (*dashed curve*) of the pulse synthesized after such a group-delay compensation

References

1. Voronin AA, Fedotov IV, Fedotov AB, Zheltikov AM (2009) Spectral interference of frequency-shifted solitons in a photonic-crystal fiber. Opt Lett 34:569
2. Zheltikov AM, Voronin AA, Kienberger R, Krausz F, Korn G (2010) Frequency-tunable multigigawatt sub-half-cycle light pulses from coupled-state dynamics of optical solitons and impulsively driven molecular vibrations. Phys Rev Lett 105:103901

60
Single Nanoparticle Surface Enhanced Fluorescence

Linden R. Webster, K. Suhling, and D. Richards

Abstract It is well established that when in close proximity to gold nanoparticles the optical properties of local fluorescent molecules are dramatically altered. When the localised surface plasmon resonance (LSPR), tuned to the fluorophore absorption band is excited a strong optical enhancement is observed near the nanoparticle due to enhancement in the excitation rate. Both the radiative and non-radiative decay rates undergo significant modification, resulting in either quantum efficiency enhancement, or fluorophore quenching, and a corresponding reduction in the fluorescence lifetime. These effects depend on fluorophore and nanoparticle separation, the fluorophore quantum efficiency, and the alignment of fluorophore excitation and emission wavelength with the LSPR.

Fluorescence lifetime imaging microscopy (FLIM) is used to create high-resolution spatial maps of molecular lifetime and intensity values of single gold nanoparticles deposited on a thin fluorescent-doped polymer film, separated by a SiO spacer layer. A strong enhancement in emission intensity is observed in the region of a single nanoparticle. The fluorescence lifetime images are described well using two contributions to fluorescence decay; an unmodified term, allowing for the fact that the diffraction limited focus is significantly larger than the nanoparticle, and some average modified term, accounting for the reduction in fluorescence lifetime. Large numbers of nanoparticles are interrogated, giving a statistical distribution of intensity enhancement and lifetime reduction, associated with varying nanoparticle

L.R. Webster (✉)
Department of Physics, King's College London, Strand, London WC2R 2LS, UK

School of Natural and Mathematical Sciences, Department of Physics, King's College London, London WC2R 2LS, UK
e-mail: linden.webster@kcl.ac.uk

K. Suhling • D. Richards
Department of Physics, King's College London, Strand, London WC2R 2LS, UK
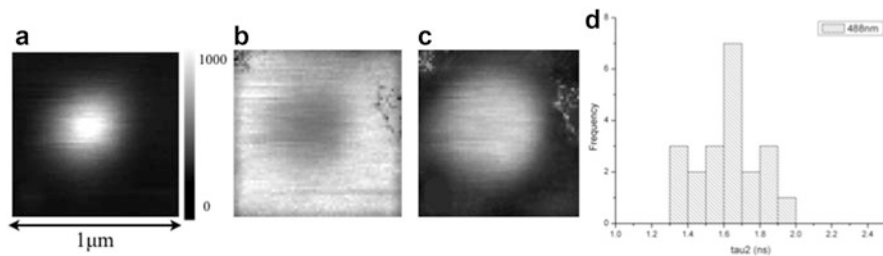
Fig. 60.1 (**a**) Fluorescence intensity of a single gold nanoparticle. (**b**) Amplitude of the unmodified lifetime component of the fluorescence lifetime, normalized with respect to intensity. (**c**) Amplitude of the modified lifetime component, normalized with respect to intensity. (**d**) Statistical distribution of modified lifetime value

size and shape. These nanoparticle populations are measured for a variety of excitation wavelengths, LSPRs, and dyes, allowing analysis of the relationship between LSPR, fluorophore excitation and emission wavelength, and quantum efficiency.

List of Participants

1. Svetlana Afonina
   PhD Student
   GAP-Biophotonics
   University of Geneva
   Ecole de Medecine 20
   1205 Geneva, Switzerland
   Tel.: +41.22.379.61.52
   Svetlana.Afonina@unige.ch

2. Alaa EL-din Eid Abd EL-Aziz Ragab
   Home Address: Mohammed Helal st. Warak EL-Arab Giza, Egypt.
   Mobile: +20143218082
   E-Mail: alaadin85@yahoo.com; alaadin85@niles.edu.eg
   University Address (Correspondence Address):
   Laser Science and Interactions department, National Institute of
      Laser Enhanced Sciences
   (NILES), Cairo University, Egypt.
   Job Tel. No:(+202) 35675223; Fax No.:(+202) 35675341
   alaadin85@niles.edu.eg

3. Trisha Andrew
   Department of Chemistry
   Massachusetts Institute of Technology
   Cambridge, MA
   Tel.: (617) 253–4423 Fax: (617) 253–7929
   Cell: (617) 314–2974
   trishala@mit.edu

4. Steve Arnold
   Polytechnic Institute of NYU - 6 Metroteck Center
   Brooklyn, NY 11201, USA
   Tel. (1) 718 260–3899; 917 568-6549(cell)
   arnold@photon.poly.edu; sarnold935@aol.com

5. Pietro Artoni
   MATIS, IMM-CNR & University of Catania
   c/o Dep. of Physics and Astronomy
   via S. Sofia, 64
   I-95123 Catania, Italy
   pietro.artoni@ct.infn.it

6. Harry Atwater
   California Institute of Technology
   246 Watson Laboratories – MC 128–95
   Pasadena, CA 91125, USA
   Tel.: (1) 626 395–2197
   haa@caltech.edu

7. Gabriele Bellocchi
   MATIS, IMM-CNR & University of Catania
   c/o Dep. of Physics and Astronomy
   via S. Sofia, 64
   I-95123 Catania, Italy
   gabriele.bellocchi@ct.infn.it

8. Francisco Bezares
   ASEE Postdoctoral Researcher
   Naval Research Lab
   Overlook Ave., SW
   Washington, DC 20375
   tel: 202-404-4443
   francisco.bezares.ctr@nrl.navy.mil

9. Palash Bharadwaj
   The Institute of Optics
   University of Rochester
   Wilmot Annex 101
   275 Hutchinson Avenue
   Rochester, NY 14627–4936
   palash@pas.rochester.edu

10. Jorg Bochterle
    Kirchhoff-Institut für Physik
    Universität Heidelberg
    Im Neuenheimer Feld 227

69120 Heidelberg, Germany
Tel. (+49) 6221/54-9892
jboch@kip.uni-heidelberg.de

11. Georges Boulon
Université Claude Bernard- Lyon I
Laboratoire de Physico-Chimie des
Materiaux Luminescents, Bât. 205
43, Boulevard du 11 Novembre 1918
F-69622 Villeurbanne Cedex, France
Tel. (33) 7 244–8271; FAX (33) 7 243–1130
boulon@pcml.univ-lyon1.fr

12. John W. Bowen
The University of Reading – Terahertz Laboratory
Reading RG6 6AH, UK
Tel: (44)(0)118 378 6702; FAX: (44) (0)118 378 8220
cybjb@cyber.reading.ac.uk

13. Angelo Bozzola
Dipartimento di Fisica "A. Volta"
Università degli Studi di Pavia
I-27100 Pavia, Italy
angelo.bozzola@unipv.it

14. Adriano Cacciola
Scuola di Dottorato di Ricerca in Fisica
Università di Messina
98166 Messina, Italy
acacciola@unime.it

15. Joshua D. Caldwell
Physical Scientist
Naval Research Laboratory
4555 Overlook Ave, S.W.
Code 6881
Washington, D.C. 20375
(202) 404–6209 office; (240) 682–5020 cell
jcaldwel@ccs.nrl.navy.mil

16. Dennis M. Callahan Jr.
Department of Materials Science
California Institute of Technology
Thomas J. Watson Laboratories of Applied Physics (MS 128–95)
1200 E. California Blvd.
Pasadena, CA 91106, USA
callahan@caltech.edu

17. Maura Cesaria
    University of Salento-Department of Physics
    Via Arnesano, 73100 Lecce (Italy)
    Ph: +39 0832 297555
    maura.cesaria@le.infn.it

18. Balu Chandra
    Department of Physics and Mathematics
    University of Eastern Finland
    P.O. Box 111
    FI-80101 Joensuu, Finland
    Mobile: +358 41 724 6711
    balu.chandra@uef.fi

19. T. L. Chen
    Optical Sciences (OS)
    University of Twente
    P.O. Box 217, 7500 AE Enschede, The Netherlands
    Phone: +31 53 489 3871
    fax: +31 53 489 3511
    T.L.Chen@utwente.nl

20. Ilaria Cianchetta
    Università degli Studi di Roma "Tor Vergata"
    Dipartimento di Scienze e Tecnologie Chimiche
    Via Della Ricerca Scientifica, 1
    00133 – Roma, ITALY
    Tel: +39 7259 4402; Fax: +39 7259 4328
    E-mail: ilaria.cianchetta@uniroma2.it
    Web: http://minima.stc.uniroma2.it

21. John Collins
    Department of Physics
    Wheaton College
    Norton, MA 02766, USA
    Tel.: (1) 508 286–3977; FAX (1) 508 286–3977
    jcollins@wheatonma.edu

22. Cristiano D'Andrea
    CNR – Istituto per i Processi Chimico-Fisici,
    Viale F. Stagno D'Alcontres, 37
    I-98158, Messina, Italy
    Tel. +39-090-39.76.22.13 direct line
    dandrea@its.me.cnr.it

23. Baldassare Di Bartolo (Co-Director of the Institute)
    Department of Physics, Boston College
    Chestnut Hill, MA 02167, USA

Tel. (1) 617 552–3601; home (1) 781 483–3993
FAX (1) 617 552–8478
dibartob@bc.edu,rinodiba@comcast.net.

24. Dirk Jan Willem Dikken
Optical Science Group
University of Twente
Faculty of Science and Engineering
MESA+Institute of Nanotechnology
7500 AE Enschede, The Netherlands
Tel. (31) 53 489 3172
D.J.W.Dikken@utwente.nl

25. Joren Eilers
Condensed Matter and Interfaces
Debye Institute
University of Utrecht
Princetonplein 5
3584 CC Utrecht, The Netherlands
J.J.Eilers@uu.nl

26. Christopher C. Evans
Mazur Group
Department of Physics, Harvard University
9 Cambridge St. McKay 321,
Cambridge, MA 02138
evans@fas.harvard.edu

27. Joaquin Fernandez
Departamento de Fisica Applicada I- Escuela Tecnica Superior de
Ingenieros Industriales Y de Telecomunicacion-Universidad del Pais Vasco
Alda Urquio, S/N 49013 Bilbao, Spain
Tel.: (34)-94 601 40 52; Fax.: (34) 94 601 41 78
joaquin.fernandez@ehu.es

28. Sergei Gaponenko
National Academy of Sciences
Institute of Physics
Minsk, Belarus
s.gaponenko@dragon.bas-net.by

29. Jacek Gosciniak
University of Southern Denmark
Institute of Technology and Innovation
Niels Bohrs Alle 1
Dk-5230, Odense M, Denmark
Phone +45 6550 7466
jag@iti.sdu.dk

30. Martin M. Greve
University of Bergen
Institute of Physics and Technology
Allegatén 55
5007 Bergen, Norway
mgr066@student.uib.no

31. K*ı*vanç Güngör
Electrical and Electronics Engineering Department
Bilkent University
06800 Bilkent, Ankara, Turkey
kivanc@bilkent.edu.tr

32. Per-Anders Hansen
Centre for Materials Science and Nanotechnology
Department of Chemistry
University of Oslo
P. O. Box 1033, Binden
N-0315 Oslo, NORWAY
p.a.hansen@kjemi.uio.no

33. Alexander Heisterkamp
Biophotonics Group
Department of Biomedical Optics
Hollerithallee 8
D-30419 Hannover, Germany
Tel.: 49 511 2788–484; Fax.: 49 511 2788–100
a.heisterkamp@lzh.de

34. Huttunen Mikko
Tampere University of Technology
Optics Laboratory Korkeakoulunkatu
33720 Tampere, Finland
P. O. Box 692
3FI-33101 Tampere, Finland
mikko.j.huttunen@tut.fi

35. Outi Hyvärinen
Optoelectronics Research Centre
Tampere University of Technology
P.O. Box 692
FIN-33101 Tampere, Finland
outi.hyvarinen@tut.fi

36. Steven G. Johnson
Massachusetts Institute of Technology
MIT Room 2–388
77 Massachusetts Ave

Cambridge, MA 02139, USA
Tel.: (1) 617 253–4073
stevenj@math.mit.edu

37. Seung- Yeon Kang
Mazur Group
Department of Physics, Harvard University
9 Cambridge St. McKay 321,
Cambridge, MA 02138
kang5@fas.harvard.edu

38. Ivan Karbovnyk
National University of Lviv
Department of Electronics
107 Tarnavskogo str, 79017
Lviv, Ukraine,
Ph. 38 032 2394224
ivan_karbovnyck@yahoo.com

39. Johannes Kaschke
Institut für Angewandte Physik- Universität Karlsruhe
D-76128 Karlsruhe, Germany
johannes.kaschke@student.kit.edu

40. Emily Kosten
California Institute of Technology
246 Watson Laboratories – MC 128–95
Pasadena, CA 91125, USA
ekosten@caltech.edu

41. Puskai Kunwar Kubaku
Department of Physics, Optic Laboratory
Tampere University of Technology
P. O. Box 692
FI-33101 Tampere, Finland
puskal.kunwar@tut.fi

42. Nadezda Kuznetsova
Nanophotonic Devices
DTU Fotonik
Technical University of Denmark
Department of Photonics Engineering
Ørsted Plads
Building 345V, room 181
2800 Kgs. Lyngby, Denmark
Direct +45 45256390
www.fotonik.dtu.dk
Nadezda Kuznetsova naku@fotonik.dtu.dk

43. Katri Laaksonen
    Department of Applied Physics
    Aalto University School of Science
    Espoo, Finland
    katri.laaksonen@tkk.fi

44. Antonino La Francesca (Administrative Secretary of the course)
    143 Pine Street
    Medfield, MA 02052, USA
    Tel: (508) 359–5961; Cell. (508) 333–4510
    ninolf@hotmail.com

45. Boris le Feber
    Nano-optics Group at Arnolf
    Institute of the Foundation for Fundamental Research on Matter (FOM)
    P. O. Box 41883
    1009 DB Amsterdam, The Netherlands
    lefeber@amolf.nl

46. Uli Lemmer
    Lichttechnisches Institut
    Universitaet Karlsruhe (TH)
    Kaiserstrasse 12
    76131 Karlsruhe, Germany
    Tel.: +49-721-608-2530; FAX:+49-721-608-2590
    Mobile: +49-175-202-7612
    Secretary: +49-721-608-2531
    uli.lemmer@lti.uni-karlsruhe.de

47. Yu-Ting Lin
    Mazur Group
    Department of Physics, Harvard University
    9 Cambridge St. McKay 321,
    Cambridge, MA 02138
    ytlin@fas.harvard.edu

48. Martin Loncaric
    "Rudjer Boskovic" Institute
    Division of Laser and Atomic Research and
    Development Bijenicka cesta 54
    10000 Zagreb
    tel: +385 1 4680 105; fax: +385 1 4680 104
    mob: +385 95 3092 261
    mail: mloncaric@irb.hr

49. Erik Mannseth
    Department of Physics and Technology
    University of Bergen

Allegatén 55
5007 Bergen, Norway
ema085@webmail.uib.no

50. Michele Manzo
KTH Royal Institute of Technology
Laser Physics, Applied Physics
AlbaNova Universitetscentrum
Roslagstullsbacken
21 SE-106 91 Stockholm, Sweden
Phone: +46 – (0)8 – 55 37 88 60; Fax: +46 – (0)8 - 55 37 82 16
mmanzo@laserphysics.kth.se

51. M. Sc. Eng. Łukasz Marciniak
Polish Academy of Sciences
Institute of Low Temperature and Structure Research
Department of Excited States Spectroscopy
ul. Okolna 2,
50–422 Wroclaw, POLAND
tel. (48–071)-34-35-021 – 029 int. 188; fax. (48–071)-34-41
L.Marciniak@int.pan.wroc.pl

52. Enrico Massa
Centre for Plasmonics and Metamaterials
Department of Physics
Imperial College London
South Kensigton Campus
London SW7 2AZ, UK
enrico.massa08@imperial.ac.uk

53. Eric Mazur
Division of Applied Sciences
Harvard University – Pierce Hall 225
Cambridge, MA 02138, USA
Tel. (1) 617 495–8729; FAX (1) 617 495–1229 or 9837
mazur@physics.harvard.edu

54. Andreas Merz
Karlsruhe Institute of Technology
Institute of Applied Physics
Wolfgang-Gaede-Strasse 1
76131 Karlsruhe, Germany
Phone:+49 721-608-4-3420 Fax:+49 721-608-4-8480
andreas.merz@student.kit.edu

55. Michel Meunier
Department of Engineering Physics
Ecole Polytechnique Montreal
Montreal, Quebec, Canada

Telephone: (514) 340–4711 ext. 4971
Fax: (514) 340–3218
Office: J-4071
michel.meunier@polymtl.ca

56. Niccolò Michieli
    Dipartimento di Fisica
    Univesrsità degli Studi di Padova
    I-35131 Padova, ITALY
    niccolo.michieli@pd.infn.it

57. Julia Mikhailova
    Max-Planck-Institute of Quantum Optics
    Laboratory for Attosecond & High-Field Physics
    Hans-Kopfermann-Str. 1
    85748 Garching, Germany
    Phone: +49 (89) 32905514; Fax: +49 (89) 32905200
    julia.mikhailova@mpq.mpg.de

58. Jonhatan Mueller
    Karlsruhe Institute of Technology
    Institute of Applied Physics
    Wolfgang-Gaede-Strasse 1
    76131 Karlsruhe, Germany
    Tel: +49 721-608-43563
    jonathan.mueller@student.kit.edu

59. Michael J. Naughton
    Department of Physics, Boston College
    Chestnut Hill, MA 02467, USA
    617.552.0635 (office)
    617.552.0968 (admin. asst.)
    617.552.3575 (dept.); 617.552.8478 (fax)
    naughton@bc.edu

60. Oleksandr Navozenko
    Department of Experimental Physics
    Physics Faculty
    National Taras Shevchenko University of Kyiv
    Kyiv, Ukraine
    a.navozenko@gmail.com

61. Michael Grøndahl Nielsen
    Institute of Sensors, Signals and Electrotechnics
    Odense, Denmark University of Southern Denmark
    Niels Bohrs Allé 1
    DK-5230 Odense M, Denmark
    Tel.: +45 6550 7371; Fax: +45 6550 7384
    mgni@sense.sdu.dk

62. Gerd Ulrich Nienhaus
    Institute of Applied Physics and
    Center for Functional Nanostructures (CFN)
    Karlsruhe Institute of Technology (KIT)
    Wolfgang-Gaede-Strasse 1
    D-76131 Karlsruhe, Germany
    TEL: +49-721-608-43401; FAX: +49-721-608-48480
    Email: uli@uiuc.edu

63. Aliaksei Novikau
    B. I. Stepanov Institute of Physics
    National Academy of Sciences
    Minsk, BELARUS
    novalexey@mail.ru

64. Lukas Novotny
    The Institute of Optics
    University of Rochester
    Wilmot Annex 101
    275 Hutchison Avenue
    Rochester, NY 14627–4936
    Tel.: (1) 585 275–2322; FAX; (1) 585 244–4936; → 585 276–2112
    novotny@optics.rochester.edu

65. Lukas Ondic
    Institute of Physics, Academy of Sciences
    Na Slovance 2
    182 21 Prague 8, Czech Repyblic
    Tel.: 420 2–203 18 502; FAX: 420-2-333 43 184
    ondic@fzu.cz

66. Adkhamjon Paiziev
    Institute of Electronics
    UzbekAcademy of Sciences Tashkent
    100125 Academgorodok
    Durmon Yoli 33, Uzbekistan
    Mob.:+(998–97) 7799775
    Tel.: +(998–71) 2470701; Fax: +(998–71) 2628767
    adkhampaiziev@gmail.com

67. Marco Pedroni
    Laboratorio di Chimica dello Stato Solido
    Dipartimento di Biotecnologie
    Univrersità degi Studi di Verona
    37134 Verona, Italy
    marco.pedroni@univr.it

68. Siim Pikker
    Laboratory of Laser Spectroscopy
    Institute of Physics
    University of Tartu
    Tartu, Estonia
    siim.pikker@gmail.com

69. Vitaly Pikulev
    Department of Solid State Physics
    Petrozavodsk State University
    33, Lenin av.
    185910, Petrozavodsk, Russia
    pikulev@petrsu.ru

70. Markus Pollnau
    Chair, Integrated Optical Micro Systems (IOMS) Group
    MESA+ Institute for Nanotechnology
    Department of Electrical Engineering; University of Twente
    P.O. Box 217
    NL-7500 AE Enschede, The Netherlands
    phone: ++31-53-489 1037; fax: ++31-53-489 3996
    e-mail: m.pollnau@ewi.utwente.nl
    URL: http://ioms.ewi.utwente.nl/
    Private phone: ++49-5921-7265688

71. Vitaliy Pustovit
    Centre de Recherche Paul Pascal – CNRS
    115 Av. Dr Albert Schweitzer
    33600 Pessac, FRANCE
    pustovit@crpp-bordeaux.cnrs.fr

72. Mihkel Rahn
    Laboratory of Laser Spectroscopy
    Institute of Physics
    University of Tartu
    Tartu 51014, ESTONIA
    mihkel.rahn@ut.ee

73. Said Rahimzadeh-Kalaleh Rodriguez
    Surface Photonics Group
    FOM-Institute AMOLF c/o Philips Research Laboratories Eindhoven
    HTC 4.1.2.38
    5656 AE Eindhoven, The Netherlands
    Phone. : +31 (0)40 27 43051
    s.rodriguez@amolf.nl and Said.Rahimzadeh@philips.com

74. Daniel Rülke
    Karlsruhe Institute of Technology

Institute of Applied Physics
Wolfgang-Gaede-Strasse 1
76131 Karlsruhe, Germany
Tel.: +49 721 608 4 3402; Fax: +49 721 608 4 8480
daniel.ruelke@kit.edu

75. Mikalai Rzheutski
junior scientist
Stepanov Institute of Physics
National Academy of Sciences of Belarus
Nezalezhnasti Ave, 68
Minsk 220072 BELARUS
Phone: +(375) 29 7480459 – Mobile
m.rzheutski@ifanbel.bas-net.by

76. Andrea Scaccabarozzi
Department of Materials Science
Univrsitty of Milano – Bicocca
Via Cozzi, 53
20125 Milano, Italy
scaccabarozzi.andrea@gmail.com

77. Andrea Scheiwe
Karlsruher Institut für Technologie (KIT)
Institut für Angewandte Physik
Wolfgang-Gaede-Str.1
76131 Karlsruhe, Germany
andrea.scheiwe@kit.edu

78. Meng-Ju Sher
Mazur Group
Department of Physics, Harvard University
9 Cambridge St. McKay 321, Cambridge, MA 02138
sher@physics.harvard.edu

79. Yaroslav Shpotyuk
PhD Student
Faculty of Electronics, Department of Nonlinear Optics
Ivan Franko National University of Lviv
50, Dragomanov str., Lviv, 79005, Ukraine
y_shpotyuk@mail.ru

80. Luciano Silvestri (Scientific Secretary of the course)
Department of Physics
University of Massachusetts Boston
100 Morrissey Blvd.
Boston, MA 02125
Tel.: 617 840–2373
lucianosilvetri88@gmail.com

81. Mark I. Stockman
29 Peachtree Center Avenue
Department of Physics and Astronomy
Georgia State University
Atlanta, GA 30302, USA
Tel.: (1) 678 457–4739
mstockman@gsu.edu

82. Andrea Trabattoni
Department of Physics
University of Milan-Bicocca
Benedek Group
Milano, Italy
sebach.traba@gmail.com

83. Aliaksei Vainilovich
Stepanov Institute of Physics,
National Academy of Sciences of Belarus,
Laboratory of Physics and Techniques of Semiconductors
Independence ave., 68, 220072 Minsk, Belarus
Tel : +375 (17) 294 90 25
Fax : +375 (17) 284 08 79
a.vainilovich@ifanbel.bas-net.by

84. Francis Vanier
Microphtonics Laboratory
Departement of Physical Engineering
Ecole Polytechnique de Montreal
Montreal, Quebec, Canada
francis-2.vanier@polymtl.ca

85. Alessandro S. Villar
Max Planck Institute for the Science of Light
University of Erlangen-Nuremberg
Staudtstr. 7/B2, Room 01.506
91058 Erlangen, Germany
Phone +49 9131 8528377; Fax +49 9131 13508
http://mpl.mpg.de
Alessandro.Villar@mpl.mpg.de

86. Alexander P. Voitovich (Co-Director of the Institute)
President, National Academy of Sciences of Belarus
66 Skaryna Av.
Minsk 220072 Belarus
Tel.: (375) 17 2841801; FAX: 375 17 2393163
voitovich@imaph.bas-net.by

87. Alexander Voronin
    Physics Department
    M.V.Lomonosov Moscow State University
    Moscow, Russia
    aa.voronin@physics.msu.ru

88. Linden Webster
    School of Natural and Mathematical Sciences
    Department of Physics
    King's College London
    London WC2R 2LS, UK
    linden.webster@kcl.ac.uk

89. Martin Wegener
    Institut für Angewandte Physik- Universität Karlsruhe
    D-76128 Karlsruhe, Germany
    Tel. (49) 721 608–3400; FAX (49) 721 607–593
    martin.wegener@physik.uni-karlsruhe.de

90. Jean-Pierre Wolf
    Université de Gèneve
    Biophotonics Group
    Gèneve, Switzerland
    Tel.: (41) 22 37965 94
    jean-pierre.wolf@unige.ch

91. Aleksei Zheltikov
    Moscow State University
    Moscow, Russia
    zheltikov@phys.msu.ru

92. Iurii Zhovtobriukh
    Department of Experimental Physics
    Physics Faculty
    National Taras Shevchenko University of Kyiv
    Kyiv, Ukraine
    zhovtobruh@gmail.com

Index